UNIVERSITY OF ICELAND

UPPSALA UNIVERSITET

Ph.D. Dissertation

The Influence of Pre-existing Fractures and Tectonic Stress on Magmatic Dikes

Sonja H. M. Greiner

2025

FACULTY OF EARTH SCIENCES
UNIVERSITY OF ICELAND

DEPARTMENT OF EARTH SCIENCES
UPPSALA UNIVERSITY

The Influence of Pre-existing Fractures and Tectonic Stress on Magmatic Dikes

Sonja H. M. Greiner

Dissertation submitted in partial fulfillment of a
Philosophiae Doctor degree in Geophysics (University of Iceland) and
Mineralogy, Petrology, Tectonics (Uppsala University)

Ph.D. Committee
Freysteinn Sigmundsson
Steffi Burchardt
Olivier Galland
Halldór Geirsson

Opponents
Meredith R. Townsend
John Browning

Faculty of Earth Sciences
School of Engineering and Natural Sciences
University of Iceland

Department of Earth Sciences
Uppsala University

Reykjavík, 2025

The Influence of Pre-existing Fractures and Tectonic Stress on Magmatic Dikes

Dissertation submitted in partial fulfillment of a *Ph.D.* in Geophysics at the University of Iceland (Iceland) and in Mineralogy, Petrology, Tectonics at Uppsala University (Sweden) as part of a double degree.
Dissertation to be publicly examined in the University Aula, University of Iceland, Main Building, Sæmundargata 2, Reykjavík (Iceland), Friday, 13 June 2025 at 11:30 (CET) for the degree of Doctor of Philosophy. The examination will be conducted in English.

Copyright © 2025 Sonja H. M. Greiner
All rights reserved

Faculty of Earth Sciences
School of Engineering and Natural Sciences
University of Iceland
Askja, Sturlugata 7
102 Reykjavik
Iceland

Department of Earth Sciences
Uppsala University
Villavägen 16
752 36 Uppsala
Sweden

Bibliographic information:
Sonja H. M. Greiner, 2025, *The Influence of Pre-existing Fractures and Tectonic Stress on Magmatic Dikes*, Ph.D.Dissertation, Faculty of Earth Sciences, University of Iceland and Department of Earth Sciences, Uppsala University, 282 pp.

Author ORCID: 0000-0003-1023-6431
ISBN: 978-9935-9772-4-3
ISSN: 1651-6214
URN: urn:nbn:se:uu:diva-554100 (http://urn.kb.se/resolve?urn=urn:nbn:se:uu:diva-554100)

Printing: Kph Print AB
Uppsala, Sweden, 2025

Abstract

Magmatic dikes form an integral part of volcanic systems and transport magma from depth towards the surface. Dike propagation through the Earth's crust is affected by the mechanical properties of the crust, which is important to better understand potential effects on volcanic activity. This thesis investigates the influence of crustal heterogeneity on magmatic dikes, focusing specifically on the interaction between magma and pre-existing weaknesses and on the influence of tectonic stress. Basaltic dikes exposed in moderately fractured hyaloclastite in the extinct Dyrfjöll volcanic system, NE Iceland, showed that dikes can follow existing fractures, change strike when intersecting them without propagating into a fracture or be arrested in front of a fracture. Laboratory models of intrusions into pre-faulted crust demonstrate that the host rock cohesion and the strength contrast between intact and faulted host rock strongly control if and how faults affect intrusions. Faults additionally affect the amplitude and pattern of intrusion-associated surface deformation. Finite Element models simulated dike opening in a tectonic stress field. Comparison of these to surface deformation associated with the 2021 February-March Fagradalsfjall dike, SW Iceland, show that tectonic stress can be a sufficient driving mechanism for dike opening. The relative amount of predicted opening and shearing of the dike plane is consistent with expectations based on geological models and the area's obliquely-spreading tectonic setting. This thesis demonstrates the complexity of dikes interacting with heterogeneous crust and the potential of considering multidisciplinary research as a key to advance understanding of such interactions.



Ágrip

Kvikugangar eru mikilvægir innviðir virkra eldstöðva og flytja kviku djúpt úr rótum eldstöðva til yfirborðs. Breytileiki i aflfræðilegum eiginleikum jarðskorpunnar hefur áhrif á hvernig kvikugangar myndast og þróast, og mikilvægt er að skilja betur hvernig þessi breytileiki getur haft áhrif á mögulega eldvirkni. Þetta doktorsverkefni kannar sérstaklega áhrif breytileika í gerð jarðskorpunnar á kvikuinnskot. Áhersla er lögð á að kanna samspil á milli innskota og misgengja og sprungna sem fyrir eru í berggrunninum og áhrif spennisviðs vegna flekahreyfinga. Basískir kvikugangar sem hafa skotist inn í móberg og sjá má í útkulnuðu eldstöðinni í Dyrfjöllum, Bogafirði eystra, voru kortlaggðir með gerð þrívíddarlíkana af svæðinu. Niðurstöðurnar sýna að kvikugangar geta fylgt sprungunum, þeir geta breytt stefnu sinni þegar þeir koma að sprungu eða þeir geta stoppað fyrir framan sprungu. Líkön voru gerð í tilraunastofu af myndun og þróun kvikuganga í jarðskorpu sem inniheldur sprungur og veikleika. Þau líkön sýna að munur á styrkleika jarðskorpu með og án sprungna, sem og samheldni (e. cohesion) jarðskorpunnar hefur mikil áhrif á hvort og hvernig misgengi hafa áhrif á kvikuganga. Misgengi í jarðskorpunni breyta líka munstri og stærð yfirborðshreyfinga samfara kvikuinnskotum. Þá voru gerð reiknilíkön með bútaaðferð (e. Finite Element Method) af myndun kvikuganga í spennusviði vegna flekahreyfinga. Slík líkön voru borin saman við jarðskorpuhreyfingar sem mældust þegar kvikugangur myndaðist í febrúar-mars 2021 við Fagradalsfjall. Niðurstaðan af þeim samanburði er að togspenna vegna flekahreyfinga getur verið megin drifkraftur kvikuinnskota. Opnun og skúfhreyfing á kvikugangsfletinum skv. reiknilíkönum er sambærileg við það sem má áætla út frá jarðfræðilegum aðstæðum á Reykjanesskaganum og skáreki flekahreyfinga (e. oblique spreading) þar. Þetta doktorsverkefni sýnir að samverkan kvikuganga og breytileika í aflfræðilegum eiginleikum jarðskorpunnar er mjög flókin og það að nota mismunandi rannsóknaraðferðir er lykill að auknum skilningi á slíkri samverkan.



Sammanfattning (Swedish Summary)

Magmatiska gångar är viktiga beståndsdelar i magmatransportsystem. De utgör det huvudsakliga sättet att transportera magma genom jordskorpan. Inte nog med att majoriteten av vulkanutbrott är kopplade till gångar, de bidrar också till bildandet av ny jordskorpa och minskar spänningar vid tektoniska plattgränser. Eftersom gångar är så vanligt förekommande är det viktigt att förstå hur jordskorpans egenskaper påverkar dess bildning. Denna avhandling undersöker hur magmatiska gångar påverkas av jordskorpans heterogenitet, särskilt av befintliga sprickor och tektonisk spänning. Detta görs genom tre artiklar, som är inriktade på en av följande forskningsmetoder: Fältbaserad strukturgeologi, analoga modeller och numeriska modeller av magmagångar i heterogen jordskorpa.

Basaltgångar i det fossila vulkaniska systemet Dyrfjöll på nordöstra Island fotograferades med hjälp av en drönare. Dessa basaltgångar har trängt in lätt uppsprucken hyaloklastit i en vulkanisk kaldera. Utifrån dessa foton skapade vi virtuella 3D-modeller med hjälp av fotogrammetri och kartlade gångarnas och sprickornas orientering. Både gångar och sprickor förekom i stort sett fyra riktningar. Den vanligaste riktningen av dessa kan härröras till den uppskattade tektoniska spänningsfältet vid tidpunkten för uppkomsten av vulkanen (för ca 12,5 miljoner år sedan). Vi observerade tre olika sätt som gångar interagerade med redan existerande sprickor: 1) Gångar kan följa sprickor. 2) Gångar kan ändra riktning när de korsar en spricka utan att följa den. 3) I ett fall stannade en gång framför en befintlig spricka. Här bildades flera små förgreningar nära spetsen på den stannade gången. De flesta av dessa förgreningar korsade samma spricka som stoppade den ursprungliga gången och antingen korsade den eller följde den. Samspel mellan gångar och sprickor observerades oftast när de var nästan parallella med den sannolika tektoniskt kontrollerade riktningen. Observationerna vid Dyrfjöll visar att samverkan mellan gångar och sprickor är en komplex process och magmans flöde måste inte nödvändigtvis följa befintliga sprickor.

Frågan om hur samspelet mellan magma och förkastningar påverkas av de mekaniska materialegenskaperna hos det omgivande berget och magman behandlades med hjälp av laboratorieexperiment med analoga modeller. Analoga modeller återskapar naturliga processer i laboratorieskala med material som i förhållande till varandra beter sig på ett liknande sätt som sina motsvarigheter i naturen. Vi undersökte specifikt betydelsen av det omgivande bergets sammanhållning (också kallad kohesion, dvs. hur starkt eller svagt berget är) och magmans viskositet. Berg med varierande kohesion representerades av blandningar av mikroglaspärlor (låg kohesion) och kiselmjöl (hög kohesion). Smält vegetabilisk olja och glukossirap fungerade som analoga magmor med låg respektive hög viskositet. De injicerades underifrån i en modellbox fylld med antingen kiselmjöl-glaspärleblandningen. Genom att förskjuta en platta i sidled i botten av modellboxen skapade vi en sidoförkastning, som korsade injektionsinloppet. En rad kameror placerade ovanför lådan tog upprepade bilder av modellytan under experimentets gång. Detta gjorde det möjligt för oss att rekonstruera ytdeformationen under magmagångbildning i 3D. Den vegetabiliska oljan stelnar vid rumstemperatur, vilket dessutom gjorde det möjligt att gräva ut magmastrukturerna och dokumentera deras

geometri. Den experimentella intrusionen i stark jordskorpa med hög kohesion påverkades mycket av redan existerande förkastningar. När intrusionen korsade förkastningen ändrade intrusionen riktning och följde förkastningssegmenten. Ytdeformationen påverkades också av förekomsten av förkastningar, eftersom återaktivering av förkastningen i stor utsträckning kompenserade för intrusionsinducerad töjning. Omvänt hade förkastningar i svaga analoga bergarter (med låg kohesion) liten inverkan på intrusioner och deras tillhörande ytdeformation. Tiden från det att injektionen påbörjades till dess att utbrottet bröt igenom ytan förkortades av förekomsten av en förkastning i våra experiment med stark kohesion, eftersom vätska flödade längs förkastningen till ytan. I svagt berg fördröjde dock förekomsten av en förkastning utbrottets början. Bland de båda testade vätskorna var vätskan med låg viskositet (vegetabilisk olja) något känsligare för interaktion med förkastningar än vätskan med högre viskositet. Sammantaget hade dock det omringande bergets kohesion en mycket starkare inverkan på samspelet mellan intrusion och förkastning. Experimenten visar att det är viktigt att ta hänsyn till materialegenskaperna hos jordskorpan och magman när man vill förstå interaktion mellan magma och förkastningar.

Även om det är allmänt känt att tektonisk spänning kan ha en betydande inverkan på magmatiska gångar, beaktas detta sällan kvantitativt i modeller för ytdeformation vid aktiva vulkaner. Den tektoniska spänningens potentiella roll som drivmekanism för gångbildning undersöktes i numeriska modeller baserade på Finite-Element-metoden. En magmatisk gång som bildades under februari-mars 2021 vid Fagradalsfjall på Reykjaneshalvön, sydvästra Island, användes som fallstudie i detta projekt. Vi jämförde förutsägelser från vår modell med geodetiskt observerad ytdeformation när Fagradalsfjallgången bildades. Reykjaneshalvön är särskilt väl lämpad för den här typen av studier, eftersom plattrörelsen i området är skev. Det innebär att den lokala plattrörelsen inte är vinkelrätt mot plattgränsen. Istället är den en blandning av spridning och skjuvning. Den vulkaniska aktiviteten i området är episodisk och sker under en tidsperiod på några hundra år, som växlar med perioder utan vulkanisk aktivitet, som varar i ca. 800–1000 år. Gångintrusionen 2021 och det efterföljande 6 månader långa vulkanutbrottet började efter nästan 800 år utan vulkanisk aktivitet på halvön. Vår numeriska modell är uppdelad i två steg: Först ackumuleras tektonisk stress som en följd av plattornas rörelse under en tidsperiod på 800 år. I det andra modellsteget frigörs spänningen lokalt av gången, som representeras av en spricka i modellskorpan. Den observerade ytdeformationen kunde bäst återskapas när gången frigjorde 60% av den tektoniska spänningen. Att endast en del av den tidigare ackumulerade spänningen frigjordes av 2021 års gång stöds av att tre efterföljande gångar bildades i samma område mellan december 2021 och juli 2023. Den relativa mängden öppning och skjuvning längs med gångarna som förutses av vår modell stämmer väl överens med förväntningarna från geologiska modeller som är baserade på den verkliga gångens riktning i förhållande till det styrande spänningsfältet.

Resultaten i denna avhandling understryker hur komplext samspelet mellan magmatiska gångar, befintliga sprickor och tektonisk spänning är. Ytterligare studier krävs för att bättre förstå samspelet mellan magma och plattektonik och för att bättre integrera båda processerna i geofysiska modeller som kan vara användbara för övervakning av aktiva vulkaniska system.



Table of Contents

List of Figures **xiii**

List of Publications **xv**

Abbreviations **xxi**

Acknowledgements **xxiii**

1 Introduction **1**
1.1 General Introduction 1
1.2 Research Aims 3

2 Background **5**
2.1 Rock Mechanics and Rheology 5
2.1.1 Linear Elasticity 5
2.1.2 Viscoelasticity 7
2.1.3 Brittle Plasticity 7
2.2 Interaction of Dikes with Crustal Heterogeneity 11
2.3 Geological Setting 16
2.3.1 Geological Setting of Iceland 16
2.3.2 The Reykjanes Peninsula 16
2.3.3 The Dyrfjöll Volcanic System 19

3 Methods **25**
3.1 Structure-from-Motion Photogrammetry 25
3.2 Analogue Modeling 28
3.3 The Finite Element Method (FEM) 31
3.4 Geodetic Observations and Analytical Models of Surface Deformation . . . 34
3.4.1 InSAR 34
3.4.2 GNSS 35
3.4.3 Analytical Modelling of Volcano Deformation 37

4 Paper Summaries **39**
4.1 Present Work 39
4.2 Paper I 41
4.2.1 Summary 41
4.2.2 Main findings 43
4.3 Paper II 45
4.3.1 Summary 45
4.3.2 Main findings 49
4.4 Paper III 51

4.4.1 Summary 51
4.4.2 Main findings 55

5 Conclusions and Outlook **57**

References **65**

Plain Language Summary (English) **91**

Zusammenfassung (German Summary) **95**

Information about Photos on Divider Pages **99**

Publications **103**

Paper I **103**

Paper II **137**

Paper III **221**

List of Figures

1.1 Introductory figure illustrating dikes in active and extinct volcanic systems. 2
2.1 Schematic illustration of elastic, Maxwell-viscoelastic and plastic material responses. . . . 6
2.2 Schematic illustration of dikes interacting with various types of crustal heterogeneity. . . . 12
2.3 Map of Iceland marking the locations of study areas. . . . 17
2.4 Map of the Reykjanes Peninsula . . . 18
2.5 Map of the Dyrfjöll volcanic system and caldera . . . 20
3.1 Field- and laboratory-examples of virtual models derived with Structure-from-motion (SfM)-photogrammetry . . . 26
3.2 Examples of analogue models of intrusion processes. . . . 29
3.3 Example of a FEM model . . . 32
3.4 Observation of surface deformation using InSAR and GNSS. . . . 36
4.1 Key findings from **Paper I**. . . . 42
4.2 Key findings from **Paper II**. Surface deformation and intrusion geometries of key experiments. . . . 46
4.3 Key findings from **Paper II**. Quantitative summary of experiments. . . . 48
4.4 Key findings from **Paper III**. Crustal stresses and deformation in the dike plane. . . . 52
4.5 Key findings from **Paper III**. Surface deformation and results from a model driven by overpressure. . . . 53



List of Publications

The following research articles form the basis of this thesis. They are the result of collaborative work of my co-authors and me. Currently unpublished research articles list their status in parentheses. My contribution to each article/manuscript is listed. For a complete list of all authors' contributions please refer to the respective full-texts.

Paper I: **S. H. M. Greiner**, S. Burchardt, F. Sigmundsson, B. V. Óskarsson, O. Galland, H. Geirsson, E. Rhodes, 2023, Interaction between propagating basaltic dikes and pre-existing fractures: A case study in hyaloclastite from Dyrfjöll, Iceland. *Journal of Volcanology and Geothermal Research*, Vol. 442, pp. 107891. Accessed at `https://doi.org/10.1016/j.jvolgeores.2023.107891`.
Contribution: 80% of the total effort. The research question was developed mainly by myself and Steffi Burchardt (SB) and refined together with my other supervisors. I collected the photogrammetry data in the field for outcrops DF1-DF3 under guidance from SB and analyzed the data with guidance from SB and Freysteinn Sigmundsson (FS). I wrote the initial draft of the manuscript, created figures (SB created parts of Figure 1) and implemented reviewer-suggestions during revision of the manuscript.

Paper II: (Accepted) **S. H. M. Greiner**, O. Galland, F. Sigmundsson, S. Burchardt, H. Geirsson, R. Pedersen, X. Wen, (*Accepted April 2025*), The influence of variable host rock cohesion and magma viscosity on intrusion-fault interaction: Insights from laboratory models. *Journal of Geophysical Research: Solid Earth*.
Contribution: 75% of the total effort. The research question was developed by Olivier Galland (OG) and myself. I performed all experiments and analyzed the data, which was interpreted by OG and myself. I contributed to the Dimensional Analysis which was led and described in the manuscript by OG. I wrote the rest of the initial draft of the manuscript and created all figures.

Paper III: (In press) **S. H. M. Greiner**, F. Sigmundsson, H. Geirsson, S. Burchardt, O. Galland, (*2025*), Tectonic stress as the driving mechanism for dike opening in an oblique rift setting: A deformation model of the 2021 Fagradalsfjall dike, Iceland. *Geophysical Research Letters*, 52, e2024GL113970. Will be accessible at `https://doi.org/10.1029/2024GL113970`
Contribution: 85% of the total effort. The research question was developed by FS and myself. I implemented all numerical models and analyzed their output. Interpretation of the modelling results was done by myself, FS and Halldór Geirsson (HG). I wrote the initial draft of the manuscript and created all figures and implemented revisions with input by FS, HG and SB.

Reprints were made with permission from the respective publishers.

Additional Publications

In addition to the above mentioned research articles, I contributed to the following publications during the time of the PhD project. These works do not form a part of the thesis.

1: E. Rhodes, S. Burchardt, **S. H. M. Greiner**, T. Mattsson, F. Sigmundsson, T. Schmiedel, A. K. Barker, T. Witcher, 2024, Volcanic unrest as seen from the magmatic source. *Scientific Reports*, Vol. 14, 962. doi: https://doi.org/10.1038/s41598-023-50880-0 .
Contribution: Implementation of a Finite Element deformation model to simulate surface deformation associated with partial roof subsidence of the Reyðarártindur pluton. Writing of those parts of the initial manuscript that describe the model implementation and results.

2: F. Sigmundsson, M. M. Parks, H: Geirsson, A. Hooper, V. Drouin, K. Vogfjörd, B. G. Ófeigsson, **S. H. M. Greiner**, Y. Yang, C. Lanzi, G. P. De Pascale, K. Jónsdóttir, S. Hreinsdóttir, V. Tolpekin, H: M. Friðriksdóttir, P. Einarsson, S. Barsotti 2024, Fracturing and tectonic stress drive ultrarapid magma flowinto dikes. *Science*, Vol. 383, pp.1228–1235. doi: 10.1126/science.adn2838.
Contribution: Figure preparation, contributions to evaluation of models, discussion of results and comments on initial manuscript.

3: **Sonja. H. M. Greiner**, H. Geirsson (2024), Including a pressure dependent relation between static and dynamic elastic moduli in a Finite Element deformation model of Grímsvötn Volcano, Iceland. *Volcanica*, Vol. 7, Issue 2, pp.907–924. doi: https://doi.org/10.30909/vol.07.02.907924.
Contribution: Based on my MS thesis. I implemented all models, wrote the initial manuscript and created all figures. HG and me both contributed to revisions of the manuscript.

4: (Submitted book chapter) O. Galland, L. Girod, **S. H. M. Greiner**, P. Souloumiac, F. Guldstrand, H: Bertelsen, D. Yagupski, *submitted; Preprint published April 2024* Digitising sandbox experiments using open-source Structure-from-Motion/Photogrammetry/Digital Image Correlation package MicMac. Preprint available at https://doi.org/10.31223/X5QD7Q. Contribution: Partial writing of the initial manuscript, specifically the case study for analogue models of intrusions.

5: (Under Review) O. Quintela, S. Burchardt, T: Mattsson, B. Almqvist, C: Stevensson, W. McMarthy, B. V. Óskarsson, I. Pitcairn, E. L. Rhodes, T. Witcher, **S. H. M. Greiner**, B. Latimer. *Submitted January 2025* The magnetic fingerprint of pulsed granite magma emplacement and alteration: Slaufrudalur, Iceland. Under Review at *Geochemistry, Geophysics, Geosystems.*
Contribution: Data collection and investigation.



Abbreviations

This list contains abbreviations used in this thesis in alphabetical order.

BEL Borgarfjörður eystri-Loðmundarfjörður

DEM Digital Elevation Model

FEM Finite-Element Method

GB Glass Beads

GIA Glacio-isostatic adjustment

GCP Ground Control Point

GNSS Global Navigation Satellite System

GPS Global Satellite System

InSAR Interferometric Synthetic Aperture Radar

LiDAR Light Detection and Ranging

LOS Line-of-sight

MVS Multi-View Stereo

NVZ Northern Volcanic Zone

RMS Root-Mean-Square

SF Silica flour

SfM Structure-from-motion

UAV Unmanned Aerial Vehicle

2D two-dimensional

3D three-dimensional



Acknowledgements

This thesis would not have been completed without the help and support of many people. Trying to list them all makes one realize just how many actually.

First and foremost, my thanks go to my supervisors **Freysteinn Sigmundsson, Steffi Burchardt, Olivier Galland** and **Halldór Geirsson**. Thank you so much for all your support, encouragement and patience, for sharing knowledge, and for feedback on countless paper drafts, abstracts and this thesis. Most of all thank you for always believing in me, even if and especially when I didn't. Thanks for countless discussions, both on how to do research (for this specific project) and on what it is like to be a researcher – and how to hopefully stay one. Thanks for sitting through countless zoom meetings and sticking around independent on whether I was in the office next door or in some other place across the Scandinavian countries. Thanks for encouragement and pushing me to grow outside of my comfort zone – sometimes more and sometimes a bit less gently.

Freysteinn, thanks for encouraging me to find my own questions within the project from the very beginning. Thanks for always finding time to discuss, no matter how busy you were, and for making sure this time was used as efficiently as possible. Takk fyrir að stundum tala íslensku við mig.

Steffi, thanks for opening my eyes to the world of magmatic plumbing systems and for scientific and emotional support throughout the entire four years, but especially the last one. Thanks for creating a space where it is okay to talk about doubts and struggles and for making sure we never forget how amazing and fascinating volcanic systems are. Thanks also for help with the Swedish and German summaries for this thesis.

Olivier, thanks for welcoming me in Oslo and for the introduction to analogue models. Thanks for showing me the geology of the Oslo fjord on foot and on an unforgettable little sailing trip.

Halldór, thanks for letting me rope you into this project and for sitting through yet another thesis written by me. I am afraid it is not really shorter than the last one. But jokes aside, thanks for always being up for spontaneous discussions, especially related to events on Reykjanes.

Thanks to **Rikke Pedersen** for initiating the entire project, for taking care of the logistics of the double degree and of every-day business, and lastly for always having an open door and ear. Thanks to **Sara Lind** at Uppsala university and the people at **PhD SENS** at HÍ for help with figuring out the double degree graduation process and to the **Thesis Production Unit** at the Uppsala University Library for their support with the thesis printing. Thanks to **Nordvulk** and **Uppsala University** for funding the project and for giving me the opportunity to study and work in three different countries and universities.

Thanks to **Birgir Óskarsson** and **Emma Rhodes** for their contribution on the first paper of

this thesis. Thanks to **Rikke Pedersen** and **Xia Wen** for their contribution to the second paper. The Swedish summary in the beginning of this thesis was translated from English with **DeepL** and improved by **Steffi** and by **Tobias Mattsson**. My translation of the abstract into Icelandic was signficiantly improved by **Freysteinn** and **Halldór**.

Thanks to **Michelle Parks** for sharing modelling data for events on Reykjanes, for discussions and for letting me tag along all sorts of events. Thanks to **Erik Sturkell** for advice on how to make the most of large conferences and for good times in the field. Thanks to **Léa Levy** for encouraging words and advice on multidisciplinary and international PhD-projects.

Thanks to the many people in Iceland, Uppsala, Oslo and elsewhere, who contributed to that this whole project stayed interesting and fun rather than feeling like "just work". Thanks for keeping the fascination and the fun alive through seminars (especially the HÍ-Wednesday seminars), workshops, fieldwork, summer schools, courses, random discussions, coffee/tea/hot chocolate breaks, hikes, board game evenings, cookie baking sessions and so much more. Thanks for this go to **Yilin, Jonas, Greta, Siqi, Ylse, Patricia, Daniel**, yet another **Daniel, Noemi, Nico, Didas, Siggi, Páll, Sveinbjörn, Elisa, Nate, Gabriele, Remi, Abi, Chris, Thorben, Janne, Rakel, Marija, Erina, Marte, Janine, Caitlyn, Tegan** and all the others. Special thanks go to **Cat** and **Chiara** for emotional and technical support (don't we all love GMT and Comsol?), and for sharing the good and the more intense times. Special thanks also go to **Emma, Taylor, Orlando** and **Tobias** for welcoming me into the research group long before I actually moved to Uppsala and for introducing a little geophysicist to structural geology!

Thanks to my **parents**. It is difficult to put into few words how much you have supported me in countless different ways. Thanks for all of it and for always believing in me. I wouldn't be where I am now without it.

Thanks to friends spread across the world and everybody back home, especially **Maud, Alexa, Eli, Anne, Birgit, Karl-Michael** and **Markus**. Thanks for sticking around despite me being terrible at staying in touch. Thanks for listening to me rambling on about my work, volcanoes and Iceland, for visiting, letting me visit you and for sending countless care packages with tea, chocolate, candles, words of encouragement and support throughout the past four years (and longer). Thanks to **Mareike** and everybody at Fljótshólar. Who would have thought that a planned stay for eight months in Iceland would eventually lead to this thesis? I certainly didn't. Thanks to **Rakel** for helping me to improve my Icelandic. Thanks to **Niklas, Turid** and little **Astrid** for being great hosts in Uppsala!

Thanks to the many, many sheep whose wool I knitted into countless sweater to stay both sane and warm throughout this PhD project. Thanks on this topic also to **Steffi, Taylor** and **Cat** for combining work and hobby. We need more volcano- and geo-themed woollen sweaters – secret or otherwise. Thanks to **Güntherska** for baking the very best cinnamon buns!

Last but not least, thanks to **Philipp**. How can I adequately summarize your contribution to this thesis? Thanks for following me across countries, for support, encouragement and patience, for clear reminders of when I work too much, for keeping my feet on the ground and for involuntarily learning more about geology and volcanoes than you probably ever planned to do.



1 Introduction

1.1 General Introduction

Volcanoes are highly complex, multi-faceted systems. Although our collective understanding of them grows continuously, many processes happening within them remain poorly understood. This relates largely to that it is currently impossible to directly observe the interior of active volcanic systems. The system within volcanoes, which stores and transports magma from depth towards the Earth's surface is sometimes referred to as the magmatic or volcanic plumbing system (e.g., Burchardt, 2018). It is important to understand processes occurring within this system and how it interacts with its surroundings, since this can affect the location and characteristics of potential eruptions. This in turn is relevant for hazard assessment e.g., if magma reaches the surface by flowing along pre-existing faults (Figure 1.1a).

Eruptions are often fed by magmatic dikes, which are typically subvertical, sheet-like intrusions (Rivalta et al., 2015; Breitkreuz and Rocchi, 2018). Not every dike feeds an eruption. However, they also play an important role for vertical magma transport at depth and contribute to the creation of new crust at divergent plate boundaries (Walker, 1975; van Wyk de Vries and van Wyk de Vries, 2018). Because dikes are such common features in magmatic plumbing systems and often the direct connection to the Earth's surface, understanding how they interact with the surrounding crust is important for assessing risks related to potential volcanic activity.

A series of magmatic dikes have formed since 2021 on the Reykjanes Peninsula in SW Iceland, which is an obliquely spreading, subaerial segment of the Mid-Atlantic Ridge (e.g., Einarsson, 2008; Sigmundsson et al., 2020a). The emplacement of these intrusions, several of which resulted in eruptions, has been well documented with geodetic and seismic monitoring (Sigmundsson et al., 2022; Parks et al., 2023; Sigmundsson et al., 2024; Geirsson et al., 2024). The resulting observations suggest that tectonic processes and volcano-tectonic interactions have a strong influence on this ongoing series of events. Additionally, the presence of numerous fractures and faults in areas prone to dike intrusion emphasizes the importance of better understanding magma-fault interaction (Sigmundsson et al., 2022; Hjartardóttir et al., 2023; Ducrocq et al., 2024; Sigmundsson et al., 2024, and Figure 1.1a). The detailed observations of this series of intrusive events and subsequent eruptive activity provide an excellent opportunity to study dike propagation and how it interacts with its surroundings.

Subsurface processes in active volcanic systems are typically hidden from view and can only be observed indirectly, e.g., through ground deformation and seismicity. In contrast to this, it is possible to directly observe the interior of volcanoes in extinct and partially eroded systems. This can allow to study up close the results of magmatic plumbing systems processes (Burchardt and Galland, 2016, and Figure 1.1b & c). Great care must however be taken when interpreting observations from fossilized volcanic systems, since they present a complete record of the entire systems' lifespan. This record can include several different stages and younger events can overprint or modify structures related to previous processes. It

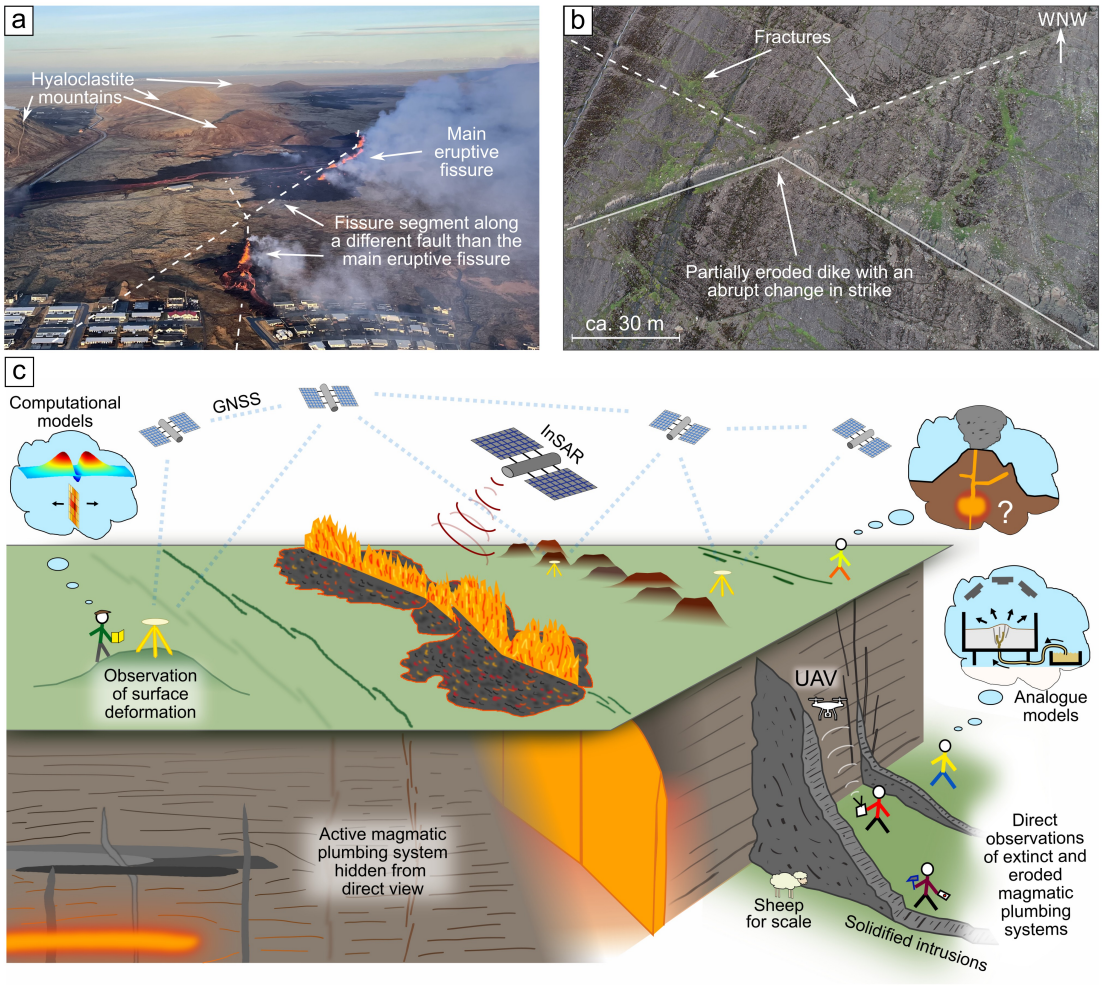

Figure 1.1. a) Example of a fissure eruption on the Reykjanes Peninsula on the 14th of January 2024. Photo: Hólmfríður Dagný Friðjónsdóttir. Pre-existing fault traces (dashed white lines) based on data of the Icelandic Meteorological Office. b) Dike in fractured host rock showing abrupt change in strike. Modified from ***Paper I****. c) Conceptual figure illustrating the different methods used in this thesis: field geology to study extinct systems, numerical and analogue modelling and geodesy. Not to scale. Abbreviations: Global Navigation Satellite System (GNSS), Interferometric Synthetic Aperture Radar (InSAR), Unmanned Aerial Vehicle (UAV).*

may therefore be difficult to separate them (Burchardt and Galland, 2016). However, if the different geological events that contributed to the present picture are carefully separated, they can provide detailed insights into otherwise hidden magmatic processes. Such observations can even be extrapolated to infer, what associated surface signals could look like (e.g., Rhodes et al., 2024). Overall, neither active nor extinct volcanic systems by themselves provide a complete picture of dike propagation because some information is always missing. However, combined evaluation of observations from both can provide further insights.

One tool commonly used to study active or extinct volcanic systems are quantitative models. The host rock response to magmatic intrusions, in the direct proximity to the intrusion and at the Earth's surface, is commonly modelled through either computational (i.e. analytical or numerical) models, or through laboratory experiments, which serve as analogue models.

Analogue models are typically conducted to understand and systematically study aspects of the basic physical processes underlying magma emplacement downscaled to a laboratory setting (Galland et al., 2018; Kavanagh et al., 2018). Computational models are typically implemented to either systematically study basic processes or to reproduce signals observed from individual case studies (Annen et al., 2001; Currenti and Williams, 2014; Browning and Gudmundsson, 2015; Townsend et al., 2015; Vachon and Hieronymus, 2016; Sigmundsson et al., 2022). Computational ground deformation models are often applied together with geodetic observations to infer subsurface processes at active volcanic systems (Amelung et al., 2000; Lundgren et al., 2015; Sigmundsson et al., 2015; Aloisi et al., 2020; Sigmundsson et al., 2022). To gain first-order understanding of a process, especially for near-real time monitoring, models often make simplifying assumptions regarding the intrusion itself and of the mechanical properties of the surrounding host rock, which may, however, not match reality (e.g., Masterlark, 2007; Pascal et al., 2013; Heap et al., 2020; Poppe et al., 2024).

It is well known that the Earth's crust is highly heterogeneous and can behave in an elastic, viscoelastic or brittle-plastic manner (Bertelsen et al., 2018; Galland et al., 2018). The crust can be layered, intersected by fractures and faults, and host older solidified intrusions (Figure 1.1c). Additionally, aspects like the local temperature and the governing stress field vary throughout the crust and can affect not only ground deformation, but also magma propagation dynamics and where magma may stall (e.g., Del Negro et al., 2009; Heimisson and Segall, 2020; Alshembari et al., 2022). While near-real time monitoring requires models with short computation times, models considering more complex crustal properties may help to estimate, if and under which conditions propagating intrusions may deviate from estimates that can be provided by more simplified models.

1.2 Research Aims

In this thesis, I aim to improve our understanding of how magmatic sheet intrusions are influenced by crustal heterogeneity. Guided by recent events on the Reykjanes Peninsula, I will focus on magmatic dikes and how they and the associated surface deformation are affected by tectonic stress and pre-existing fractures and faults. The main research questions addressed here are the following:

1. How are propagating dikes affected by pre-existing fractures and faults in moderately fractured host rock?
2. How do the mechanical properties of the host rock and the magma influence the interaction between sheet intrusions and faults?
3. How does variable tectonic stress affect dike propagation and the associated surface deformation?

These questions are addressed in three projects, each of which corresponds to a research paper or manuscript. Any method used to study volcanic plumbing systems, active or extinct, is inevitably subject to limitations, biases and commonly made assumptions. To work towards a more holistic view and to balance some of the biases of individual methods, this thesis applies a multidisciplinary approach using 1) field-based observations from an extinct and partially eroded volcanic system, 2) laboratory experiments and 3) numerical models, which are compared to geodetic observations of recent activity on the Reykjanes Peninsula.



2 Background

The Earth's crust is a highly complex material. Its behaviour can be approximated through a number of mechanical models depending on the processes and timescales in question (e.g., Turcotte and Schubert, 2014). Each of these models is an idealized description of how a material reacts to stress and can be used to describe a specific aspect of the Earth's crust. However, reality is likely a combination of all of them. I will provide here a brief overview over mechanical models applied throughout this thesis.

2.1 Rock Mechanics and Rheology

Rheology describes how a material, which is subjected to stress, reacts by either deforming internally or by flowing (Jaeger et al., 2007). A solid continuous material in equilibrium (static conditions) can be generally described by (e.g., Jaeger et al., 2007; Segall, 2010)

$$\vec{\nabla}\underline{\sigma} + \rho\vec{F} = 0 \tag{1}$$

Here, $\underline{\sigma}$ is the stress tensor, which describes normal and shear stresses acting on any part of a continuous material, ρ is its density and $\vec{F}$ describes volume forces, such as gravity.

The strain associated with small, relative displacement of individual points within a continuous material is typically expressed through (e.g., Segall, 2010)

$$\varepsilon_{i,j} = \frac{1}{2}\left(\frac{\partial u_i}{\partial x_j} + \frac{\partial u_j}{\partial x_i}\right) \tag{2}$$

where $\varepsilon_{i,j}$ are the components of the strain tensor $\underline{\varepsilon}$ with $i, j \in \{1,2,3\}$ for a three-dimensional (3D) case, u_i and u_j are components of the displacement vector $\vec{u}$, and x_i and x_j are spatial dimensions. How stress and strain are related, depends on the rheology of the individual materials.

2.1.1 Linear Elasticity

The simplest description of the rheology of the Earth's crust is to assume that it behaves as a linearly elastic, isotropic material, which is for example commonly done in analytical models of ground deformation (e.g., Mogi, 1958; Okada, 1985). The stress-strain relation of a linear elastic material is described by Hooke's law and the stress is linearly proportional to the strain (Figure 2.1a). In elastic materials, all strain is recoverable, i.e. once an applied force is removed, the material reverts back to its initial state (Figure 2.1b). Adapted for continuum mechanics, this results in the following generalized form of Hook's law (e.g., Segall, 2010)

$$\sigma_{i,j} = c_{i,j,k,l} : \varepsilon_{k,l} \tag{3}$$

with $c_{i,j,k,l}$ as the entries of the elasticity tensor $\underline{c}$. The symmetry of the stress and strain tensors ($\sigma_{i,j} = \sigma_{j,i}$, $\varepsilon_{k,l} = \varepsilon_{l,k}$) and the assumption of isotropy, i.e. that properties are independent of direction, reduce the number of independent entries of $\underline{c}$ to two, which can for example be the Young's modulus E and Poisson's ratio ν. They are related to the seismic velocities of p- and s-waves, v_p and v_s, respectively through

$$E = \rho v_s^2 \frac{3v_p^2 - 4v_s^2}{v_p^2 - v_s^2} \tag{4}$$

$$\nu = \frac{v_p^2 - 2v_s^2}{2\left(v_p^2 - v_s^2\right)} \tag{5}$$

These relations can be used to implement spatially varying elastic properties of the crust based on seismic tomography studies in more realistic ground deformation models (e.g., Hickey et al., 2015; Gottsmann et al., 2020; Greiner and Geirsson, 2024). In the context of this thesis, a linear elastic rheology is used in **Paper I** for a simple model to estimate tectonic stress and in **Paper III**, where it is used both to convert seismic velocities to depth-dependent elastic moduli and for analytical deformation models of fault motion.

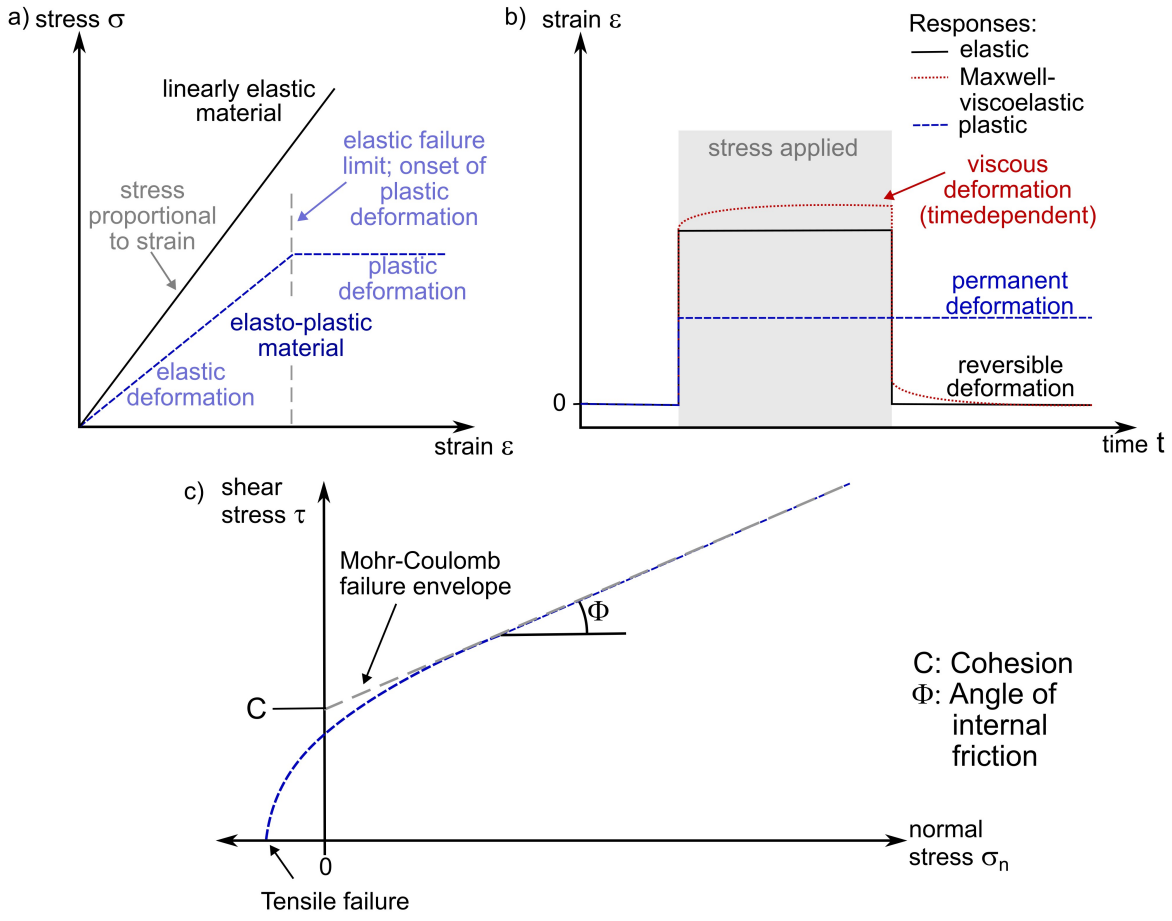

Figure 2.1. Schematic illustration of elastic, Maxwell-viscoelastic and plastic behaviour of materials. a) Stress-strain relation for elastic and elastoplastic materials. b) Strain evolution with time in changing loading conditions. c) Mohr-Coulomb failure envelope of a brittle-plastic material.

2.1.2 Viscoelasticity

Over long timescales, the Earth's crust and mantle can behave in a viscous manner (e.g., Auriac et al., 2013). The Maxwell-viscoelastic model combines linearly elastic behaviour with linearly viscous behaviour, so that the strain is a superposition of the elastic and viscous contributions ε_e and ε_v, respectively (e.g., Turcotte and Schubert, 2014):

$$\varepsilon = \varepsilon_e + \varepsilon_v \tag{6}$$

The strain rate $d\varepsilon/dt$ relates to the stress and its change with time via

$$\frac{d\varepsilon}{dt} = \frac{1}{E}\frac{d\sigma}{dt} + \frac{1}{2\eta}\sigma \tag{7}$$

where d/dt marks time derivatives and η is the viscosity. In this model, the initial response to abrupt changes is elastic. However, the resulting strain and stress do not remain constant, but change with time (Figure 2.1b). The timescale of stress relaxation depends on the viscosity of the system with a lower viscosity resulting in faster relaxation. In models of the Earth's crust, the viscosity is often assumed to be constant in time and for layers of the Earth (e.g., Auriac et al., 2013; Schmidt et al., 2013; Li et al., 2022; Lanzi et al., 2024) and can be constrained for example from Glacio-isostatic adjustment (GIA). The viscosity can also vary gradually as a function of temperature and pressure or be non-linearly related to the strain rate, i.e. it becomes time-dependent. Temperature-dependent viscosities can be used to model viscous relaxation around magma reservoirs (Del Negro et al., 2009; Hickey et al., 2015). For temperature-dependent models, which include the lower part of the crust or the upper mantle, an additional pressure dependency of the viscosity needs to be considered, so that the viscosity increases for high pressure (i.e. at large depths) (e.g., Karato and Wu, 1993). This can for example be achieved by relating the viscosity to the lithostatic pressure and the temperature through an expression describing diffusion creep (Turcotte and Schubert, 2014):

$$\eta = \frac{RTh^2}{24V_aD_0} exp\left(\frac{E_a + pV_a}{RT}\right) \tag{8}$$

where R is the universal gas constant, T is the temperature, h is the size of undeformed individual crystals making up the crust, V_a is the activation volume, D_0 is a frequency factor, E_a is the activation energy and p is the pressure. Alternative approaches can include non-linear viscoelastic models (e.g., Islam et al., 2016; Givens, 2025).

In the context of this thesis, viscoelastic relaxation of the crust is relevant for estimating the distribution of tectonic stress throughout the crust prior to dike intrusions (**Paper III**). Tectonic stress accumulates continuously through plate motion, but based on a lack of seismicity in the lower crust, the stress distribution is not uniform with depth. In the deep parts of the crust, where temperatures are high, stress can relaxe faster than it is supplied by plate motion.

2.1.3 Brittle Plasticity

If the stress exerted on the Earth's crust (or any other material) becomes too large, it fails and experiences non-recoverable deformation (Figure 2.1), which can be brittle or ductile. There are several models and criteria describing the onset of material failure (e.g., Yu, 2002; Labuz et al., 2018), but the focus here lies on the Mohr-Coulomb criterion (Coulomb, 1773; Jaeger et al., 2007), which describes brittle failure and is relevant for **Paper II**. This criterion

assumes that material fails in shear if the shear stress τ exceeds a critical level τ_{crit} described by

$$\tau_{crit} = C + tan(\varphi)\,\sigma_n \tag{9}$$

where C is the cohesion of the material, φ the angle of internal friction and σ_n the normal stress acting on the eventual failure plane. The critical shear stress defined by this criterion as a function of the normal stress is referred to as the Mohr-Coulomb failure envelope (Figure 2.1c). Within this envelope, the material remains intact and may behave for example elastically, but once the shear stress exceeds its limit, failure occurs and the material deforms plastically (Figure 2.1a,b). Plastic deformation is non-linear, since after a material yields and plastic deformation occurs, the stress does not increase anymore even if the strain does (Figure 2.1a). This makes it difficult to describe plastic deformation analytically, but it can be studied through numerical or analogue models (e.g., Trasatti et al., 2005; Abdelmalak et al., 2012; Galland, 2012; Currenti and Williams, 2014; Vachon and Hieronymus, 2016).



2.2 Interaction of Dikes with Crustal Heterogeneity

Magmatic dikes are typically subvertical, sheet-like intrusions with a width much smaller than their length and height (Figure 2.2a), and they tend to cut across existing bedding planes or host rock layers rather than propagating along them like sills do (e.g., Rivalta et al., 2015; Breitkreuz and Rocchi, 2018). It is commonly thought that to a first order, the orientation of dikes – and other sheet intrusions – is controlled by the governing stress field, such that they propagate in the $\sigma_1 - \sigma_2$-plane and open perpendicular to it, parallel to the least compressive principal stress σ_3 (Anderson, 1951, and Figure 2.2b). Dikes are commonly found in volcanic systems across many different geological setting (e.g., Acocella and Neri, 2009, and references therein) and they can cover not only lateral distances of several tens of kilometers and more, but also depth ranges from the lower, ductile parts of the crust all the way up to the Earth's surface (Buck et al., 2006; Wright et al., 2012; Sigmundsson et al., 2015). If a single dike covers such large lateral or vertical distances, the properties of the surrounding host rock can vary dramatically along its path, making it important to better understand the interaction with different types of crustal heterogeneity.

Based on their general alignment with the governing stress field, dikes and other sheet intrusions exposed in partially eroded and extinct volcanic systems are sometimes used as indicators of the paleo-stress field at the time of emplacement (e.g., Nakamura, 1977; Stephens et al., 2018; Maerten et al., 2022). However, not only can the local stress field vary across large study areas, but pre-existing faults, fractures and joints can affect the orientations of dikes on length scales ranging from less than a meter to up to several kilometers (Baer and Beyth, 1990; Khodayar and Einarsson, 2002; Valentine and Krogh, 2006; Gaffney et al., 2007; Browning and Gudmundsson, 2015; Spacapan et al., 2016; Temtime et al., 2020; Poppe et al., 2020; Drymoni et al., 2022; Espinosa-Leal et al., 2025).

One form of dike-fault- or dike-fracture interaction is the deflection of the dike into a fault or fracture (Figure 2.2c). For a pre-existing fault, fracture or joint to be intruded, the magmatic overpressure needs to exceed the normal stress acting on the fault/fracture plane (e.g., Delaney et al., 1986; Baer et al., 1994). If the fluid pressure P_f is sufficiently large for magma to intrude a fracture or fault that is oriented oblique to the principal stress axes, the plane will open as a mixture of tensile opening and shearing. The opening angle μ between the dilation vector and the normal of the intruded fracture/fault plane is described as (Delaney et al., 1986; Jolly and Sanderson, 1997; Stephens et al., 2018):

$$\mu = arctan\left(\frac{\tau}{P_f - \sigma_n}\right) \tag{10}$$

assuming here that the fault/fracture in question is cohesion-less and taking tensile stress as negative. For purely tensile opening, $\mu = 0^\circ$ and it trends towards 90° as the shearing component increases.

Deducing the state of the tectonic stress field based on the opening angle from the field can, however, be challenging. Even if host rock markers are present to indicate fault offset, it may be difficult to separate between offset on a fault that occurred prior to diking and offset related to the dike intrusion (Stephens et al., 2018). When considering magma-fault interaction, it is important to also consider that the propagating intrusion itself modifies the stress field around

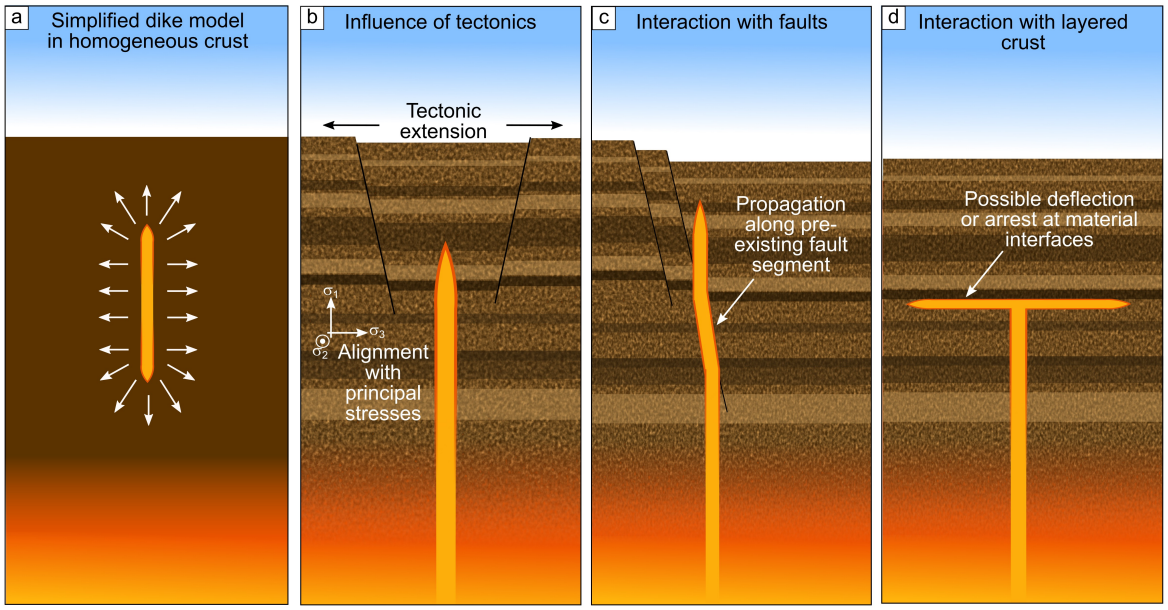

Figure 2.2. Schematic illustration of magmatic dikes in crust with different degrees and types of heterogeneity. a) A simplified dike in uniform crust, as is often assumed in models. b) Dike in an extensional tectonic setting. Alignment with the principal stress axes σ_1-σ_3 indicated (refers to relative stresses). In this view, σ_2 comes out of the paper plain. c) Dike interacting with a pre-existing fault and propagating along it. d) Dike interacting with layers of variable mechanical properties. These can lead to dike arrest or deflection. The example shown here shows deflection into a sill.

it, which may for example lead to the formation of new cracks, that in turn become available for magma to follow (e.g., Ziv et al., 2000). While alignment of volcanic features along fault zones can also be observed on even larger scales up to tens of kilometers and larger (e.g., Tibaldi et al., 2017; Tadesse et al., 2023), different mechanisms may have to be considered on these scales, since they do not deal with a single intrusion or a discrete fault or fracture. In addition to magma flowing along faults, there are indications of dikes being arrested in front of them. However, examples of this are less frequently reported than magma flowing along faults (Maccaferri et al., 2016; Stephens et al., 2018; Smittarello et al., 2022).

In addition to faults and fractures, dikes can also be affected by material contrasts in the host rock. They can be the result of layering, older intrusions or intense fault offsets. Such abrupt changes of the host rock properties can affect both the shape of the dike (e.g. its width) and propagation dynamics (Figure 2.2d). The type of interaction can depend on the strength of the interface as well as the contrast in the elastic properties on either side of it (Bonafede and Rivalta, 1999; Kavanagh et al., 2006; Taisne and Jaupart, 2009; Geshi et al., 2010; Geshi et al., 2012; Browning and Gudmundsson, 2015; Kavanagh et al., 2017; Drymoni et al., 2020). Transition from a softer to a stiffer material may favor arrest (depending also on the magmatic overpressure), while transition to a weaker material may favor onward propagation and either type of contrast may result in deflection of the dike. The intrusion can furthermore be deflected, even to the degree that they propagate along the interface (Kavanagh et al., 2006; Burchardt, 2008; Maccaferri et al., 2010).

Detailed observations of dikes interacting with variable types of crustal heterogeneity are

known from eroded field sites and are compared to laboratory experiments as well as numerical or analytical models. However, they tend to be less frequently recorded in active volcanic systems (e.g., Geshi et al., 2012; Hjartardóttir et al., 2023), because of limited geological exposure of the internal structure of active systems. Many deformation models of relatively recent diking events still approximate the crust with homogeneous elastic half-spaces (e.g., Montgomery-Brown et al., 2010; Neal et al., 2019; Aloisi et al., 2020; Sigmundsson et al., 2022; Parks et al., 2023), whereas fewer studies consider variable crustal properties for modelling dike-induced deformation (e.g., Currenti et al., 2008; Hooper et al., 2011; Currenti et al., 2011). Tectonic stresses are occasionally considered in geophysical models (e.g. Hooper et al., 2011; Spaans and Hooper, 2018; Heimisson and Segall, 2020). Small-scale thickness variations along the dike, segmentation, finger formation and other features observed at depth are generally difficult to observe in active volcanic systems, due to insufficient resolution of currently available geophysical imaging techniques. While some computational models connect directly to geological observations, many are in 2D and there is a lack of connection between them and typical quantitative, geophysical methods and models applicable to active volcanic systems (Rivalta et al., 2015).



2.3 Geological Setting

2.3.1 Geological Setting of Iceland

Iceland is an island located in the North Atlantic where a mantle plume coincides with the divergent plate boundary of the Mid-Atlantic Ridge (e.g. Einarsson, 2008; Sigmundsson et al., 2020a). The plate boundary crosses Iceland approximately from the southwest to northeast (Figure 2.3) and is characterized by volcanically active rift zones as well as transform zones (e.g., Sigmundsson et al., 2020a, and references therein). Within the rift zones, plate motion is accommodated through dike intrusions and faulting that occurs within parallel or en-echelon arranged volcanic systems (blue areas in Figure 2.3). Additionally, volcanic activity sporadically occurs in flank zones, but no plate spreading is observed across them (e.g., Einarsson, 2008; Drouin and Sigmundsson, 2019). Many volcanic systems host a central volcano, often with one or more calderas and silicic eruptive products, as well as a fissure swarm consisting of crater rows, old eruptive fissures and normal faults (Thordarson and Larsen, 2007). These fissure swarms are narrow, stretched out regions thought to be the surface expression of underlying dike swarms (Sæmundsson, 1979; Thordarson and Larsen, 2007). It is commonly assumed that they reflect the orientation of the local principal stresses with their strike being perpendicular to the least compressive stress (e.g., Sigmundsson et al., 2020a).

2.3.2 The Reykjanes Peninsula

The Reykjanes Peninsula is a plate boundary segment in SW Iceland and connects the submarine Reykjanes Ridge to the subaerial plate boundary segments across Iceland. (Figure 2.4a) (e.g., Einarsson, 2008; Sigmundsson et al., 2020a). It is located in close proximity to the towns of Reykjavík, Keflavík and Grindavík as well as to important infrastructure like power plants and the international airport. This, combined with frequent seismicity and ongoing ground deformation, has motivated intense geodetic and seismic monitoring during the past ca. three decades (e.g., Sigmundsson et al., 2020a; Björnsson et al., 2020).

Plate motion in the area is highly oblique and combines spreading with left-lateral shear. The resulting deep motion was estimated at ca. 20^{+4}_{-3} mm/yr towards $\mathrm{N}\left(100^{+8}_{-6}\right)^{\circ}\mathrm{E}$ relative to the fixed North American plate below a locking depth of ca. 5-8 km by Keiding et al. (2008), consistent with farfield plate motion (e.g., Sella et al., 2002; DeMets et al., 2010; Altamimi et al., 2023) and estimates of the depth of the brittle-ductile transition (e.g., Weir et al., 2001). Local deviations in surface deformation occur mainly in the vicinity of high-temperature geothermal areas and power plants in the Reykjanes, Svartsengi and Hengill systems (Vadon and Sigmundsson, 1997; Keiding et al., 2010; Juncu et al., 2017; Parks et al., 2020).

Volcanic features on the Reykjanes Peninsula are arranged en-echelon along the plate boundary (Figure 2.4) and characterized by fissure swarms, which strike ca. N35-45°E (Clifton and Schlische, 2003; Clifton and Kattenhorn, 2006) and consist of normal faults, previous eruptive vents and hyaloclastite ridges (e.g., Sæmundsson et al., 2016; Sæmundsson et al., 2020). Hyaloclastite is commonly found on the Reykjanes Peninsula due to extensive volcanism during past periods of glaciation (Sæmundsson et al., 2016; Jakobsson and Gudmundsson, 2008). The exact number of volcanic systems on the Reykjanes Peninsula varies in the literature (e.g., Thordarson and Larsen, 2007; Sæmundsson et al., 2020) depending on what is counted as an individual system. From west to east they are Reykjanes, Svartsengi,

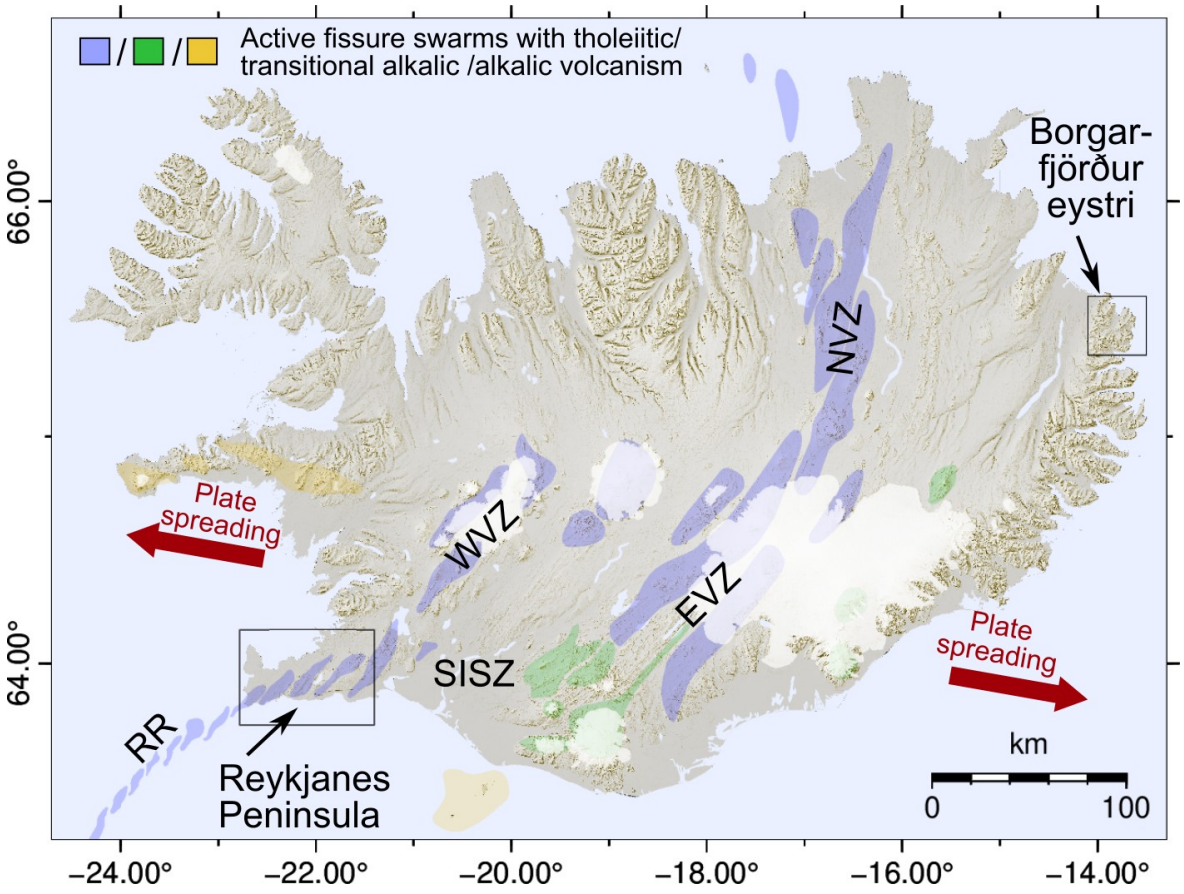

Figure 2.3. Map of Iceland with the location of study areas of this thesis, marked by black rectangles. ***Paper I*** *is based in the extinct Dyrfjöll volcanic system in Borgarfjörður eystri, NE Iceland.* ***Paper III*** *is focused on Fagradalsfjall on the Reykjanes Peninsula, SW Iceland. Fissure swarms (Jakobsson et al., 2008) mark areas of active volcanism. The volcanically active plate boundary segments of the Reykjanes Ridge (RR), Reykjanes Peninsula, Western Volcanic Zone (WVZ), Eastern Volcanic Zone (EVZ) and Northern Volcanic Zone (NVZ) are indicated. SISZ refers to the South Iceland Seismic Zone. Red arrows indicate approximate direction of plate motion.*

Fagradalsfjall, Krýsuvík and Brennisteinfjöll (Figure 2.4a). Sometimes, the Hengill system, located at the triple junction of the plate boundary between the Reykjanes Peninsula, the Western Volcanic Zone and the South Iceland Seismic Zone (Figure 2.3) is counted as being part of the Peninsula's systems as well. The strike of most volcanic features is consistent with and approximately perpendicular to estimates of the strike of the least compressive principal stress and the largest extensional strain rate trending ca. N120°E (Clifton and Schlische, 2003; Clifton and Kattenhorn, 2006; Keiding et al., 2009). None of the systems (except for Hengill) hosts a central volcano (Thordarson and Larsen, 2007) and volcanic products are dominantly basaltic in composition (e.g., Jónsson, 1978; Sæmundsson et al., 2016).

During at least the past 3000 years, volcanism has occurred episodically, lasting for few hundred years and alternating with periods of volcanic quiescence, which last for ca. 800–1000 years (e.g., Einarsson, 2008; Sæmundsson et al., 2020). During periods of volcanic quiescence, activity in the area is characterized by bookshelf faulting on right-lateral N-S-striking strike-slip faults along the plate boundary axis (Clifton and Kattenhorn, 2006;

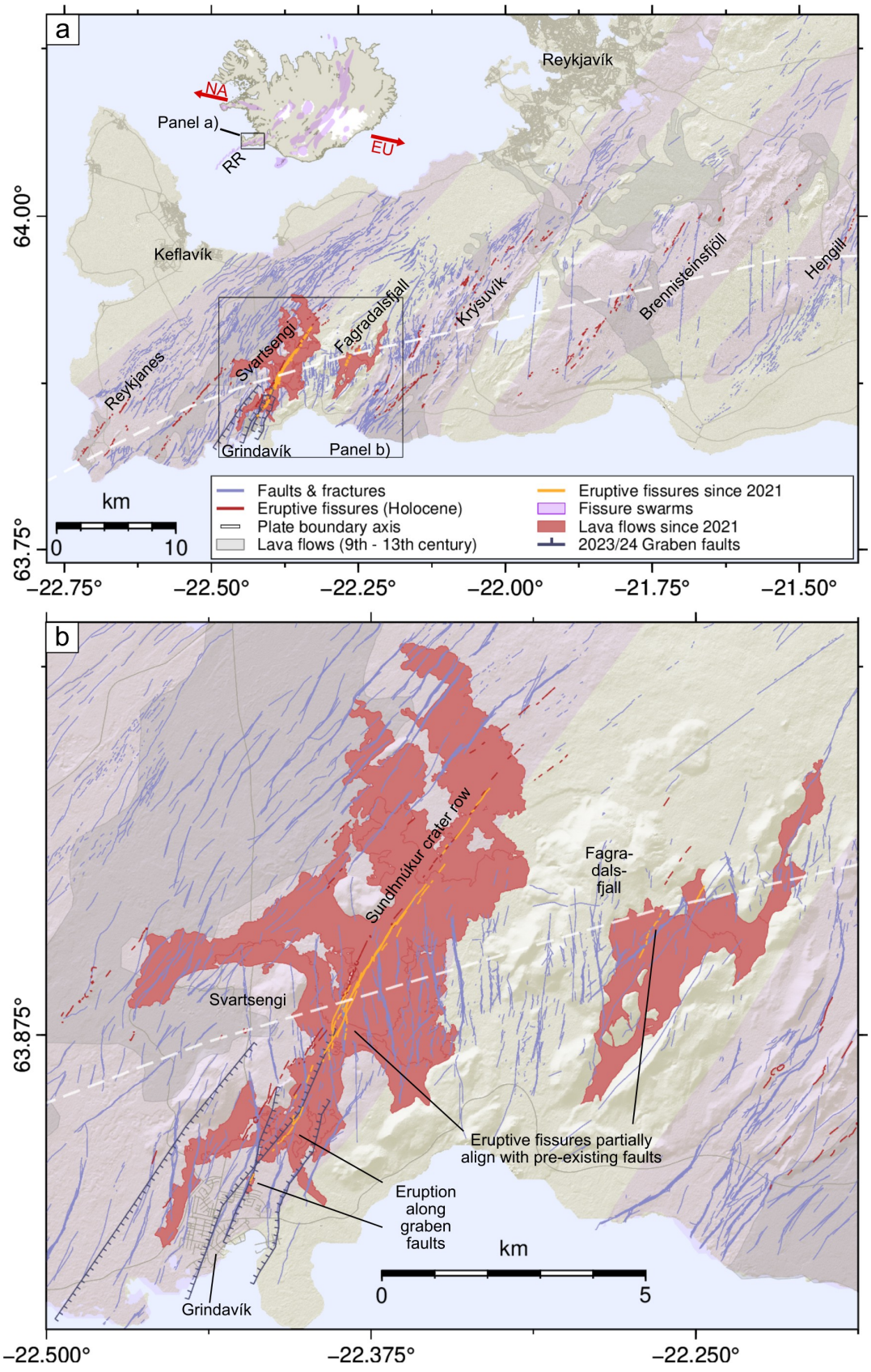

Figure 2.4. See following page for caption.

Figure 2.4. a) Map of the volcanic systems on the Reykjanes Peninsula. Inset: Location of the Reykjanes Peninsula in Iceland. "RR" marks the submarine Reykjanes Ridge. "NA" and "EU" refer to the North American and Eurasian plates, respectively. Red arrows indicate farfield plate motion. b) Parts of the Fagradalsfjall and Svartsengi volcanic systems, which have experienced volcanic activity since 2021. See a) for legend. Fagradalsfjall lava fields: Pedersen et al. (2022), Gunnarson et al. (2023), and Belart et al. (2023), Svartsengi fissures and lava fields: Parks et al. (2025). Fractures and faults: Clifton and Kattenhorn (2006) and Ducrocq et al. (2024). Outlines of the Grindavík graben faults: Veðurstofa Íslands (Accessed 02. 12. 2024). Older eruptive fissures and lava fields: Náttúrufræðistofnun Íslands (Accessed 29. 09. 2024). Fissure swarms: Jakobsson et al. (2008). Plate boundary axis: Michalczewska et al. (2014). Topography: ÍslandsDEM (Landmælingar Íslands, Accessed 26. 07. 2024).

Einarsson et al., 2020).

Since early 2020, unrest expressed by increased seismicity, and surface uplift interpreted as accumulation of magma or gases was observed in at least three volcanic systems (Flóvenz et al., 2022; Geirsson et al., 2024). A magmatic dike propagated in the Fagradalsfjall volcanic system (Figure 2.4) in February–March 2021 (Sigmundsson et al., 2022), leading to a six-month long effusive eruption (Pedersen et al., 2022). This was the first documented dike intrusion and eruption on the Reykjanes Peninsula since the 13th century and the first in the Fagradalsfjall system in >6000 years (Sæmundsson et al., 2016; Sæmundsson et al., 2020).

Between 2021–2024, a total of four dikes and three eruptions have occurred at Fagradalsfjall and at least ten dikes intruded into the neighbouring Svartsengi volcanic system (Figure 2.4), resulting in seven fissure eruptions until December 2024 (Sigmundsson et al., 2022; Parks et al., 2023; Geirsson et al., 2024; Sigmundsson et al., 2024; Parks et al., 2025). The first dikes to propagate at Fagradalsfjall and Svartsengi, respectively, were accompanied by intense seismicity, major tectonic movements, such as graben formation at Svartsengi, and widespread, low-amplitude motion on hundreds of faults and fractures (Sigmundsson et al., 2022; Sigmundsson et al., 2024; Ducrocq et al., 2024; De Pascale et al., 2024). This highlights the importance of understanding and quantifying volcano-tectonic interaction in the area. Furthermore, the alignment of both recent and older eruptive fissures with faults highlight the importance of magma-fault interaction for the Reykjanes Peninsula (Jenness and Clifton, 2009; Sæmundsson et al., 2016; Hjartardóttir et al., 2023). Recent examples of eruptive fissures aligning with faults can be found especially along the Sundhnúkur crater row (just south of the plate boundary axis in Figure 2.4b). Notably, the photo in Figure 1.1a shows a small eruptive fissure that opened along a graben fault on the northern edge of the town of Grindavík in January 2024 (Figure 2.4b).

2.3.3 The Dyrfjöll Volcanic System

The Dyrfjöll volcanic system is located in Northeast Iceland and is a part of the Borgarfjörður eystri-Loðmundarfjörður (BEL) area, a cluster of extinct volcanic centers and smaller volcanic vents from the Miocene, which were active approximately 14–12.2 Ma ago (Berg, 2016; Burchardt et al., 2022b). The volcanoes in the BEL area host several calderas as well as ignimbrite sheets. The upper parts of the magmatic plumbing systems have been exposed by erosion and it is thought that the paleosurface must have been close to the highest present-day

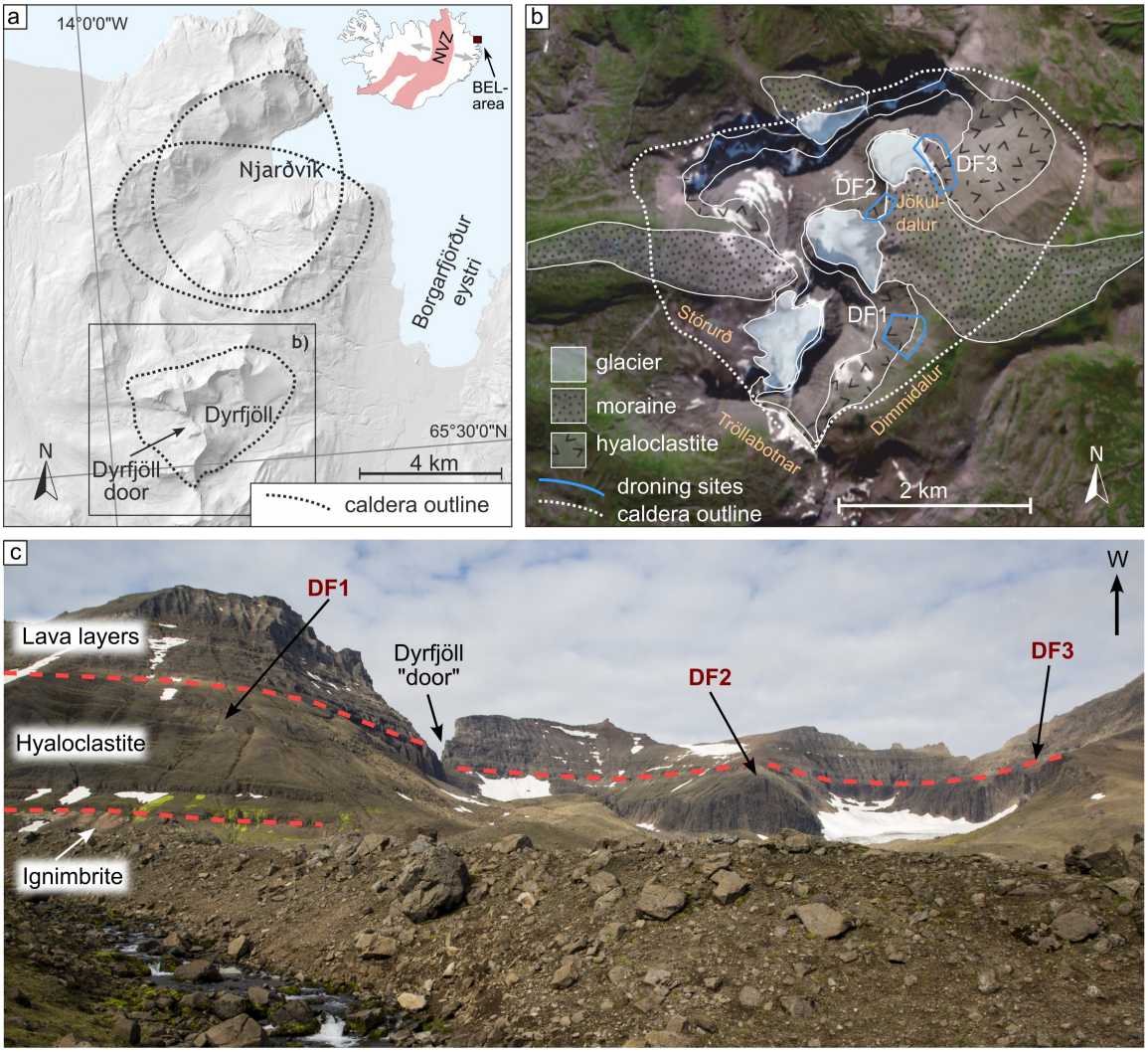

Figure 2.5. a) The Dyrfjöll volcanic system with the Njarðvík and Dyrfjöll calderas on the western side of Borgarfjörður eystri. Inset: Location of the BEL area and the Northern Volcanic Zone (NVZ) in Iceland. b) Geology of the Dyrfjöll caldera and locations where drone images were collected for ***Paper I****. Panels a) and b) are modified from* ***Paper I****. Caldera outlines and geological information from Burchardt et al. (2022b). c) The eastern side of the Dyrfjöll caldera.*

mountain peaks in the area, i.e. around 1100 m a.s.l. (Burchardt et al., 2022b).

The geological context of the BEL area is somewhat poorly understood. Largely contemporaneous activity of the central volcanoes in the BEL area, unusually large volumes of silicic rocks (by Icelandic standards), a lack of well-developed dike swarms, an extensive dip anomaly, and mildly alkaline tendencies of some lavas indicate that the area was not part of a typical rift zone like those making up the present-day plate boundary in Iceland (Burchardt et al., 2022b, and references therein). Instead it could have been a flank zone or indicate a different rift zone structure from the one today.

The Dyrfjöll system is named after a homonymous mountain massive located on the western side of Borgarfjörður eystri and hosts three calderas: the Dyrfjöll caldera and two largely

overlapping calderas near Njarðvík, located north of Dyrfjöll (Figure 2.5a). The Dyrfjöll caldera is a bell-shaped collapse caldera, which measures 4 km across its long, ca. NE-SW aligned axis and is bound by steeply inward dipping ring faults. The caldera floor is covered by at least 30 m of rhyolitic ignimbrite and the remaining caldera is filled by up to 250 m of olivine-basaltic hyaloclastite (Burchardt et al., 2022b, and Figure 2.5b, c). The caldera is overlain by lava layers from the Jónsfjall olivine basalt group, which is a regionally extensive group of lavas not associated with an individual volcanic system and which covered most of the BEL area (Óskarsson and Riishuus, 2013).

After an early, dominantly basaltic phase, the Dyrfjöll volcanic system was characterized by bimodal activity (Gústafsson, 1992; Burchardt et al., 2011; Burchardt et al., 2022b), which likely culminated in the explosive and ignimbrite-producing eruption that resulted in the formation of the Dyrfjöll caldera approximately 12.4 ± 0.19 Ma ago (Berg, 2016; Burchardt et al., 2022b). Gústafsson (1992) concluded that the hyaloclastite filling up the caldera must have formed due to interaction with water in a caldera lake, since there are no indications of the presence of glaciers in the area during the Miocene. Faintly dipping bedding structures within the hyaloclastite, and structures near Tröllabotnar on the southern caldera edge indicate that the hyaloclastite was not erupted from within the caldera. It is instead thought that basaltic lava flowed into the lake from the side. It has furthermore been suggested that the hyaloclastite belongs to the same group of basalts as the overlying lava layers (Gústafsson, 1992; Burchardt et al., 2022b). Dikes mapped in the Dyrfjöll system, some of which intersect the hyaloclastite filling up the Dyrfjöll caldera, strike dominantly N20°E or, to a lesser degree towards NE (Gústafsson, 1992). Some of the dikes in the hyaloclastite can be traced into the overlying lava layers, indicating that they are associated with them rather than with activity from the Dyrfjöll volcanic system itself. The lava layers form the present day top of the Dyrfjöll mountains (Figure 2.5c) and represent the youngest known magmatic event in this area.

Due to glacial erosion, the hyaloclastite and the basaltic dikes intersecting it are exposed in steep hillsides and cliffs around the Dyrfjöll mountains in the valleys of Dimmidalur, Jökuldalur and Stórurð (Figure 2.5 b,c). The curved nature of the exposed cliffs provides a three-dimensional view into the caldera, but the steep terrain makes many of the outcrops inaccessible on foot. This may have contributed to that, apart from work by Gústafsson (1992), little mapping of the Dyrfjöll caldera has been done in the past.



3 Methods

The following sections introduce the main research methods applied in this thesis: 1) Structure-from-Motion photogrammetry, 2) Analogue modelling and 3) the Finite-Element Method. **Paper III** additionally heavily relies on geodetic observations of surface deformation. Therefore, methods of data collection using Global Navigation Satellite System (GNSS) and Interferometric Synthetic Aperture Radar (InSAR) will also be briefly summarized together with a short introduction of analytical modelling of dike-induced surface deformation.

3.1 Structure-from-Motion Photogrammetry

In recent years, documenting field sites, outcrops, and rock samples with the help of virtual 3D models has become a widely used practice in Earth science (Smith et al., 2016; Dering et al., 2019b; Eltner and Sofia, 2020). This has proven useful for mapping and measuring structural features on a wide variety of scales (e.g., James and Robson, 2012; Smith and Vericat, 2015; Townsend et al., 2015; Rhodes et al., 2021), extracting textures and elevation data (e.g., Ben-Yehoshua et al., 2023; Bufféral et al., 2023), correlating excavated subsurface structures from laboratory experiments with surface data (e.g., Schmiedel et al., 2017) and for tracking the temporal evolution of surfaces in the laboratory and in the field (e.g., Galland et al., 2016; Pedersen et al., 2022). Virtual 3D models are typically created from overlapping two-dimensional (2D) images with slightly differing perspectives using a method often referred to as (digital) photogrammetry or Structure-from-motion (SfM)-photogrammetry (e.g., Smith et al., 2016; Dering et al., 2019b). The terms photogrammetry and SfM are sometimes used interchangeably in the literature, although they are technically not the same. While SfM heavily relies on photogrammetry, it also relies on the capability of computers to display images or objects in 3D vision (Dering et al., 2019b; Eltner and Sofia, 2020).

The technique of photogrammetry was developed since the late 19th and throughout the 20th century, to combine several images and remove distortions to create ortho-images. However, its capabilities were for a long time limited by the technical development of photography (Collier, 2020). Independent of photogrammetry, the increasing availability of computers around the 1970s–80s facilitated the development of 3D vision and digital image correlation. These elements were crucial for the development of the first SfM algorithms towards the end of the 20th century (Ullman, 1979; Eltner and Sofia, 2020, and references therein). One of the earliest SfM applications to Earth sciences came from Heimsath and Farid (2002) and by the early 2010s the method had become widely used in Earth sciences (Westoby et al., 2012; Favalli et al., 2012; James and Robson, 2012; Bemis et al., 2014; Townsend et al., 2015; Smith et al., 2016).

The following paragraphs summarize the main steps for creating 3D virtual outcrop models.

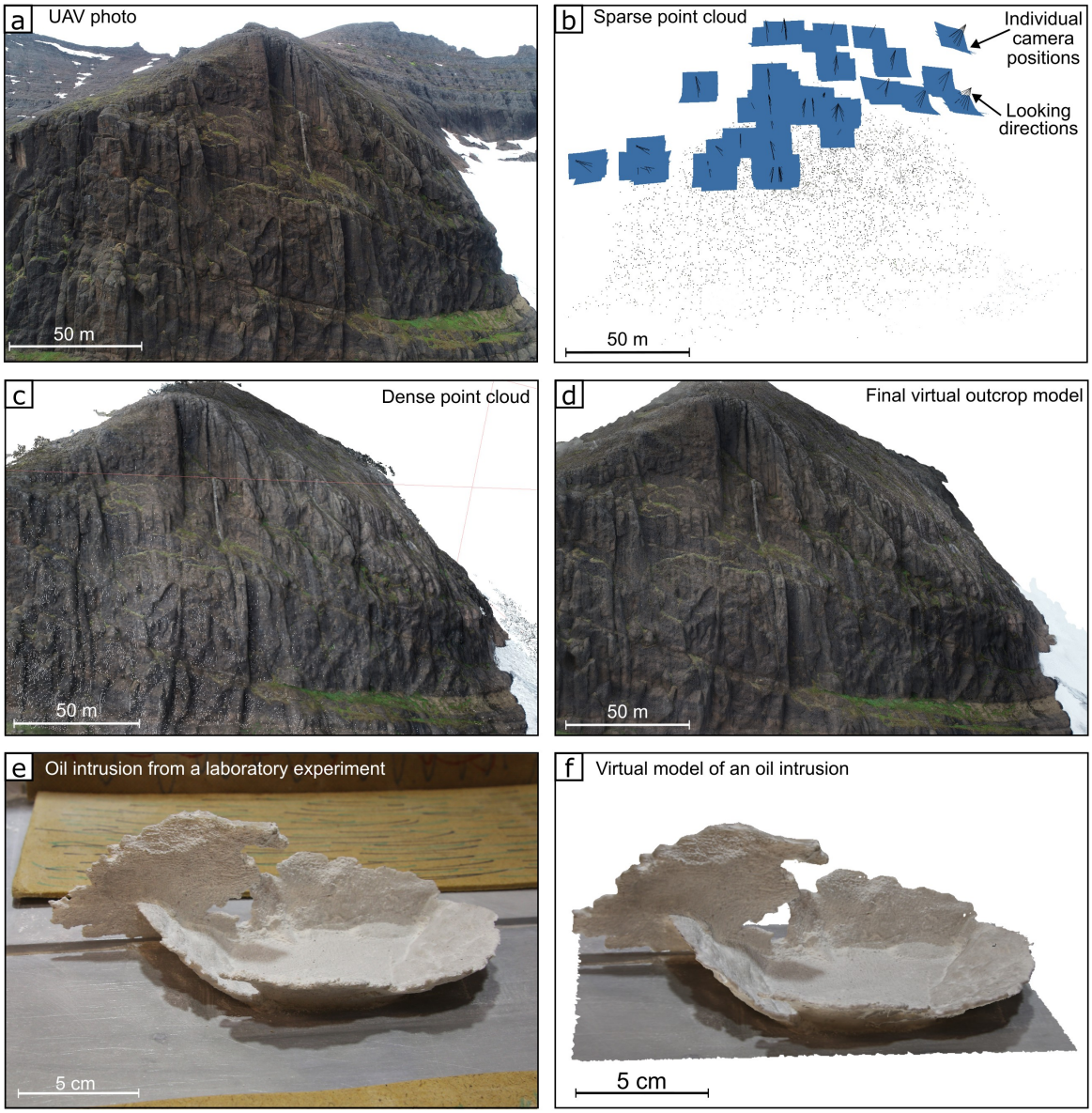

Figure 3.1. Examples outlining the steps to derive 3D virtual models from 2D images using Structure-from-motion (SfM). Point clouds and models shown here are derived in the software Agisoft Metashape. a) Photograph of an outcrop in the field taken with an Unmanned Aerial Vehicle (UAV). b) Sparse point cloud derived from SfM with a similar perspective as in a). Blue planes and black lines indicate positions and line of sight of the camera for each photo. c) Dense point cloud created with Multi-View Stereo (MVS). d) Final virtual 3D model. Note the more detailed texture compared to c). e) Example photograph of a solidified oil intrusion created in a laboratory setting. f) Virtual 3D model of the intrusion shown in e).

While the process is described for field photos collected with a Unmanned Aerial Vehicle (UAV), the underlying principles and steps remain largely unchanged if processing other types of data with SfM, e.g. if they were collected from aerial images rather than with a UAV or in a laboratory setting.

During data collection it is important to ensure large overlap between individual images

(>60 %) to ensure that a sufficiently high number of features, called key points, are common to multiple images (Bemis et al., 2014). Furthermore, angular changes between adjacent images should stay small, i.e. on the order of 10–20° (Bemis et al., 2014). Large and abrupt jumps in scale, i.e. the distance to the object of interest, should be avoided (Smith et al., 2016). It can furthermore be difficult to resolve harsh shadows and strong or varying lighting contrasts during post-processing (James and Robson, 2012; Favalli et al., 2012). Therefore, in the field high clouds with even and soft lighting are preferred conditions for data collection. Many modern processing tools can create a 3D model by reconstructing the relative camera positions based on common key points between images. However, to reduce distortion, increase accuracy of the resulting virtual model and allow for accurate scaling, it is preferable to provide georeferencing information along with the raw images. This can come from several Ground Control Points (GCPs) that are placed around the outcrop at locations determined e.g., via Global Satellite System (GPS) or by using the GPS system internal to most modern UAVs. The precision of the photo locations can be further improved if the UAV in questions can record its position in an real time kinematic mode relative to a base station.

Since SfM algorithms started to be more widely applied, a range of commercial and open-source softwares have become available (e.g., Bemis et al., 2014). While there may be variations in the exact procedure and algorithms used, the basic steps are similar and can be briefly summarized as follows: At first, features, which correspond to patterns of pixels with varying colour- and intensity values are identified by an algorithm in individual images. They can then be identified across several images through cross-correlation and other algorithms. Filters can be applied for quality improvement. Identified keypoint matches are subsequently used in a SfM algorithm to reconstruct the 3D geometry, which is represented in a sparse point cloud (see e.g., Figure 3.1b). The sparse point cloud can then be appropriately scaled and georeferenced based on GCPs or other available information. This forms the basis of a more detailed point cloud, referred to as a dense point cloud, with the help of Multi-View Stereo (MVS) algorithms (e.g., Figure 3.1c). In the example in Figure 3.1c, gaps between individual points are visible especially at the edges of the point cloud and in the lower left corner, where the point density is somewhat lower than in the right and top parts of the model. From the point cloud, a range of different products can be derived such as textured 3D models (e.g., Figure 3.1d), Digital Elevation Models (DEMs) and orthomosaics (Dering et al., 2019b). The resolution and uncertainties of virtual models depend to a large part on the raw data, such as the quality and number of images, the overlap between individual image pairs, the distance from the object of interest, and how stable the lighting conditions were at the time of recording. Furthermore, adjusting parameters and filtering during the processing stage can positively or negatively impact the result.

For capturing scenes in a laboratory setting, the processing steps from individual photos to virtual 3D models (e.g., Figure 3.1e,f) essentially follow those described for processing field-based data. However, instead of recording data with a UAV, photos can be taken on either a fixed array of multiple cameras or with a hand-held camera (e.g., James and Robson, 2012; Galland et al., 2016). The first option is suitable if the evolution of an object through time is to be recorded in 3D, for example surface deformation during analogue experiments (e.g., Galland et al., 2016). Here, it is important that the cameras remain stationary and ideally, record images synchronously. If both the cameras and the object were to move, it may be difficult to isolate motion of the object. Data for stationary/static objects, such as excavated intrusions or rock samples, can be collected using consumer-grade hand-held cameras (James

and Robson, 2012; Schmiedel et al., 2019). Here, the principles outlined above regarding sufficient image overlap, changes in the looking angle and scales, and requirements for even lighting apply in the same way as they do for UAV-assisted surveys in the field.

Once a virtual model e.g., of an outcrop in the field, is created, it can be used for mapping purposes. It is possible to determine the orientation and dimensions of sheet intrusions, rock layers and fractures, or to map contacts, which can later be used to reconstruct larger intrusive bodies (e.g., Dering et al., 2019a; Thiele et al., 2020; Rhodes et al., 2024; Witcher et al., 2024). The orientation of planar features can be determined by fitting them with a plane, the orientation of which is calculated. Depending on the software used for mapping, such a plane can be fitted to three points or to any number of points placed along the feature of interest. The quality of the measurement generally increases, if the points used to fit the plane do not fall on a single line. If they are close to co-linear, the orientation of the fitting plane becomes non-unique (Dering et al., 2019b, and references therein).

Using SfM-MVS workflows can under ideal conditions produce virtual outcrop models with a resolution comparable to other methods such as Light Detection and Ranging (LiDAR). At the same time photogrammetry is significantly cheaper to conduct (Smith et al., 2016; Dering et al., 2019b), since digital cameras or small UAVs are widely available now and easy to bring along in the field. UAV-based virtual outcrop models can cover a variety of scales. Additionally, they allow for data collection in steep terrain, where it is dangerous or impossible to inspect outcrops on foot (Thiele et al., 2020; Rhodes et al., 2024; Witcher et al., 2024). In locations where field-based measurements can be collected, they can be integrated into the virtual outcrop model during post-processing (e.g., Rhodes et al., 2024). Having a virtual version of an outcrop available furthermore allows to revisit the outcrop and repeat or add measurements as needed, which is more difficult if all measurements are to be taken on site. Lastly, virtual outcrop models have in recent years proven useful for improving accessibility and as teaching tools (Dolphin et al., 2019; Guillaume et al., 2023; Watson et al., 2024).

3.2 Analogue Modeling

Geological processes are often highly complex. To better understand them, natural phenomena can be modeled on a smaller scale in a laboratory setting. There, they can be studied in a systematic manner and in a controlled environment. Such models are often referred to as analogue or laboratory models/experiments. Rather than exactly reproducing a geological event, their principal aim is to better understand the underlying physical process or how several processes and material properties interact (Galland et al., 2018; Kavanagh et al., 2018). For this purpose, analogue models rely on the principle of similarity. If all materials and parameters are chosen appropriately, the laboratory model is a scaled-down representation of a natural process (Merle, 2015; Galland et al., 2018; Kavanagh et al., 2018).

One of the first documented applications of analogue models in Earth Sciences was by Hall (1815) to qualitatively explain folding structures in Scotland. One of the first applications of analogue modelling to volcanic processes was by Daubrée (1891). A shift towards more quantitative analyses in analogue modelling began in the 1950s (Hubbert and Willis, 1957; Kavanagh et al., 2018). Dimensional analysis based on the Buckingham-Pi theorem (Buckingham, 1914) was first used as a tool to scale laboratory experiments by Tibaldi (1995) and

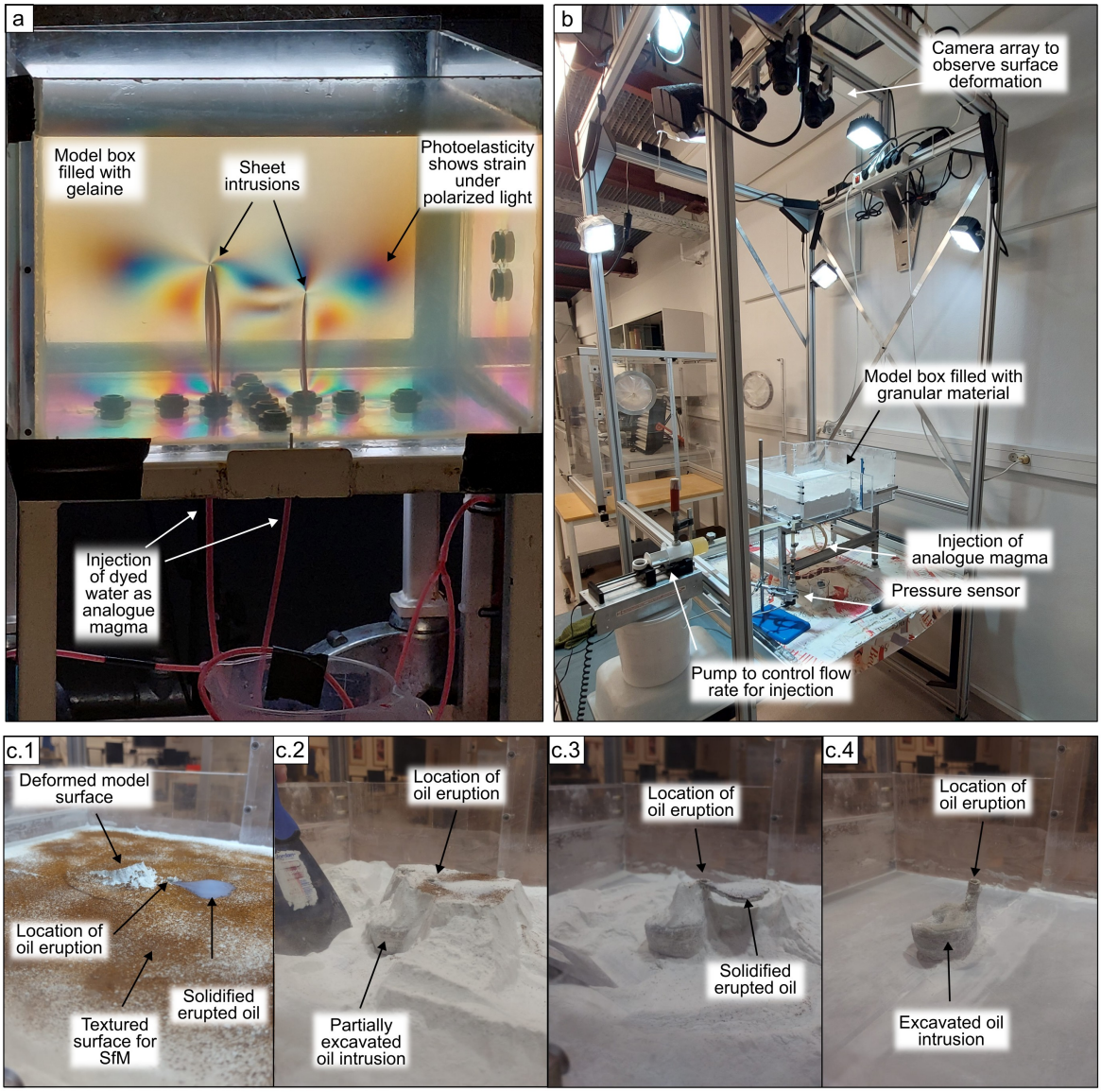

Figure 3.2. Examples of analogue models of magmatic intrusions. a) Experiment with injection of dyed water into gelatine at the Magmalab Liverpool. b) Experimental setup using granular materials as the analogue host rock. Photograph is taken at the analogue laboratory of the NJORD center, University of Oslo. c.1-c.4) Close-up of a solidified oil intrusion into a granular material and gradual excavation of the intrusion. The brown powder sprinkled on the model surface (coffee powder and olivine sand) adds texture. This is required for feature detection to extract surface deformation using SfM photogrammetry.

Merle and Borgia (1996). Today, a wide variety of geologic and volcanic processes is studied with analogue models using different materials and methods (Kavanagh et al., 2018; Galland et al., 2018).

The formation of sheet intrusions in laboratory experiments can be largely split into two groups, which differ in terms of the simulated intrusion mechanisms as well as the materials used: The first uses pig-skin gelatine as the model crust (Figure 3.2a) to represent a dominantly elastic material (e.g., Kavanagh et al., 2013; van Otterloo and Cruden, 2016). The second

one models brittle-plastic behaviour by using granular materials such as mixtures of silica flour and glass beads (e.g., Figure 3.2b; Galland et al., 2006; Merle, 2015; Poppe et al., 2019). One advantage of gelatine models is that the gelatine is transparent and allows to easily observe the propagation of sheet intrusions within the model crust. Materials serving as analogue magmas in combination with gelatine can be for example water or air (Kavanagh et al., 2006; Le Corvec et al., 2013). Furthermore, it is possible to replicate some degree of crustal heterogeneity by creating layers of varying stiffness, interfaces of variable toughness and pre-existing weaknesses, which have been used in the past to study dike-sill transitions, capture of magma into faults and similar processes (Kavanagh et al., 2006; Le Corvec et al., 2013; Kavanagh et al., 2017). However, gelatine typically fails in tension only, not in shear. Therefore, it is typically considered to only represent strong, dominantly elastic crust (Kavanagh et al., 2013).

Brittle-plastic behaviour is more frequently simulated by using granular materials as the analogue host rock (e.g., Galland et al., 2006; Galland, 2012; Abdelmalak et al., 2012; Guldstrand et al., 2017). In such models, oil or syrup often serve as analogue magmas. It should be noted that although the materials serving as model crust are granular, some can have substantial cohesion, especially if they were compacted (Galland et al., 2006). Mixing high- and low-cohesion materials can provide a range of different cohesions (Abdelmalak et al., 2016). With these materials, intrusive processes into host rock with a wide range of cohesions can be studied, but granular materials are generally considered to be more representative of host rock with intermediate to low strength, e.g., in sedimentary basins (e.g., Schmiedel et al., 2017; Schmiedel et al., 2019; Galland et al., 2018). One disadvantage of granular materials is that they are opaque and it is therefore difficult to observe the dynamic propagation of intrusions. While methods like Computed Tomography scanning have been applied (e.g., Poppe et al., 2019), it is often more convenient to use model magmas such as vegetable oil, which solidify after the experiment and can subsequently be excavated (e.g., Figure 3.2c; Schmiedel et al., 2019) or to simulate the intrusion process in quasi-2D by using a Hele-Shaw cell, i.e. a model box that has a very low thickness compared to its width and height (e.g., Abdelmalak et al., 2012).

The key for creating experiments, that are meaningful and representative of geological processes in nature, lies in scaling them correctly. Therefore, great care needs to be taken when selecting materials and experimental parameters for analogue models (Merle, 2015; Galland et al., 2018; Kavanagh et al., 2018). If an experiment is poorly or incorrectly scaled this can severely limit how much can be learned from it about natural processes. The overall aim is to select parameters so that the laboratory model is geometrically, kinematically and dynamically similar to the studied geological process (e.g., Hubbert, 1937; Ramberg, 1981). While some studies use scaling factors, i.e. they directly compare the ratio of characteristic parameters in nature and their models (see e.g., Merle, 2015, and references therein), the focus here will be placed on dimensional analysis, which is the scaling method used in **Paper II** of this thesis.

Dimensional analysis (e.g., Gibbings, 2011) is based on the Buckingham-Pi theorem (Buckingham, 1914). Its aim is to characterize a process through a number of dimensionless ratios. These ratios are determined by first identifying the governing parameters of the experiment. These could for example be the density, cohesion and angle of internal friction of a brittle material as well as the depth, at which the intrusion forms and the width of the feeder. Each of these parameters can be described in terms of its dimensions. The dimension refers in

this context not necessarily to a spatial dimension. For models largely based on mechanics, they are typically combinations of length (L), time (T) and mass (M), but can also include temperature. As an example, the density of a material has the basic unit of kg/m^3, which means that it has the dimension of $[M/L^3]$. According to the Buckingham-Pi theorem, a problem, which is governed by i parameters involving j dimensions, can be fully characterized by $k = i - j$ dimensionless, independent parameters. By combining the individual governing parameters through multiplication and division, their dimension can be canceled out until the final ratios are dimensionless. During this process care must be taken that the resulting ratios remain independent, i.e., that they cannot be recreated through linearly combining other ratios (see e.g., Gibbings, 2011, for a more detailed description of the procedure). One example of a ratio, which is frequently featured in dimensionless analysis but also well known from fluid mechanics is the Reynolds number Re. It characterizes the flow regime, i.e. if a fluid is expected to behave in a turbulent or laminar manner (e.g., Turcotte and Schubert, 2014). Once a set of dimensionless ratios has been derived for a process, one needs to find laboratory materials, which result in similar values for the dimensionless ratios as the natural phenomenon of interest.

Finding appropriate materials for analogue models can be challenging for a number of reasons: 1) It can be difficult to identify the governing parameters for dimensional analysis, especially if the studied process is highly complex or unclear. 2) Natural materials such as the Earth's crust or magma behave in a highly complex manner and a single analogue material may not capture all relevant aspects. For example, magma is a multi-phase non-Newtonian fluid which exhibits a wide range of viscosities (Gonnermann, 2015; Lesher and Spera, 2015; Witcher, 2024). Instead of using a single material to represent this, a number of different fluids are typically used to model magma with different viscosities (Kavanagh et al., 2018). 3) Lastly, even if suitable materials can be found, it may be difficult to constrain the governing parameters in nature.

One advantage of analogue models is that they allow to study processes systematically as opposed to field observations, where it is often challenging to find a sufficiently high number of comparable field sites with good constraints on all parameters and processes of interest. While systematic variation of parameters is easily possible in computational models, they typically only consider physics that are intentionally implemented. Other physical aspects are ignored. A common example of this is gravity or, in case of deformation models, rock failure under high stress. Therefore, such models carry the risk of becoming physically unreasonable even if they are correct from a mathematical standpoint. In contrast to this, analogue experiments are intrinsically physically consistent, since it is not possible to simply "turn off gravity" or to prevent failure of a material if its strength is exceeded. However, their ability to provide insights into natural processes relies entirely on the choice of materials and experimental parameters.

3.3 The Finite Element Method (FEM)

The Finite-Element Method (FEM) is a numerical technique that can solve a wide variety of boundary value problems even if analytical solutions are difficult or impossible to derive. This is achieved by representing the model through a mesh (an unstructured grid), which divides the domain into a finite number of discrete elements with simple geometry (e.g.,

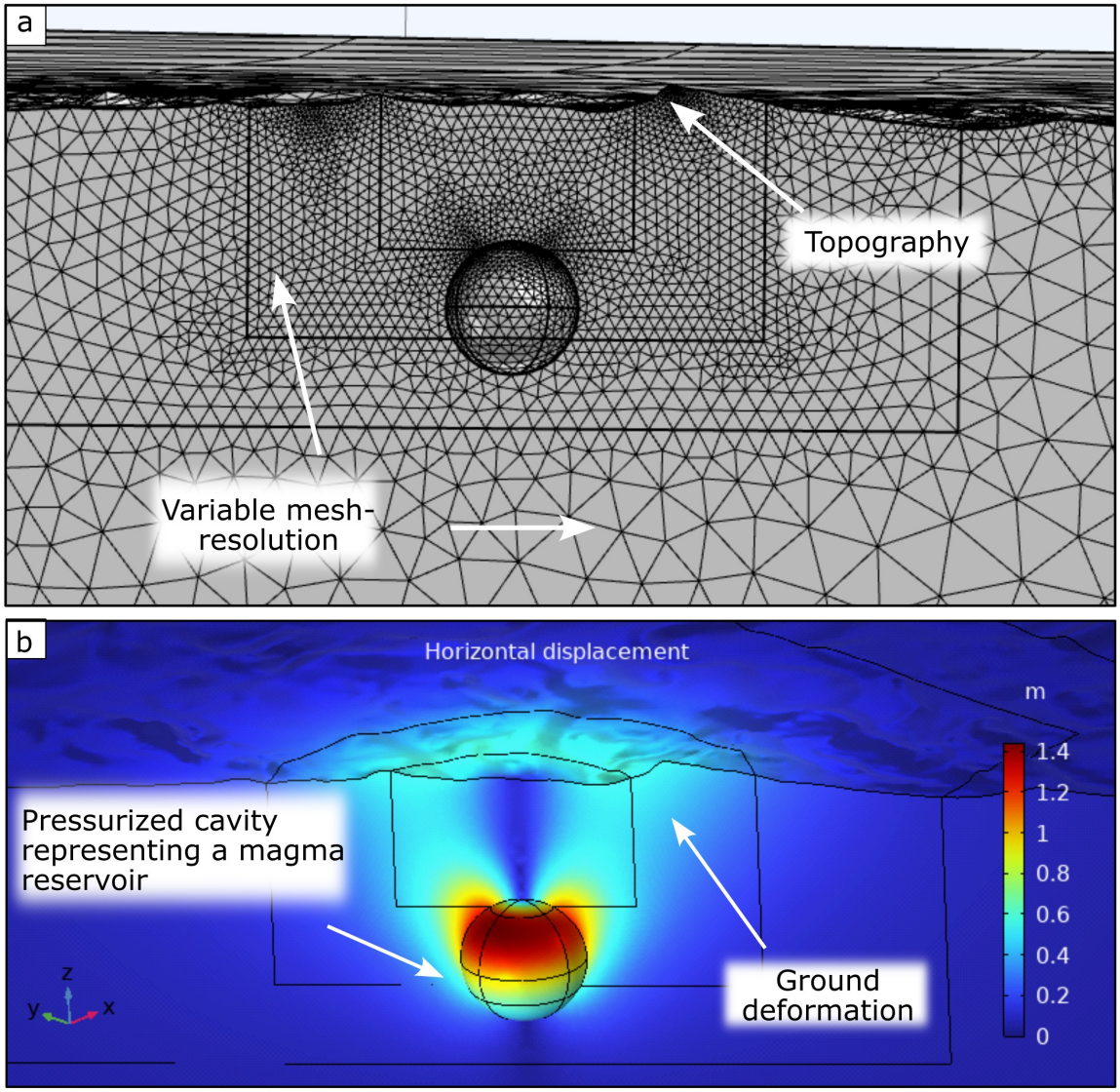

Figure 3.3. Example of a FEM model showing a cross-section through a 3D model domain. a) The model domain is divided into tetrahedral elements of variable size. This allows the representation of irregular geometries like realistic topography derived from DEMs. b) Horizontal deformation as an example for the output of a FEM model (same model as in a). A pressurized cavity representing a magma reservoir causes displacement of the surrounding material, which translates to surface deformation. Model is modified from those presented by Greiner and Geirsson (2024).

Figure 3.3a). The governing physical processes are defined piece-wise with equations for individual elements and then recombined to obtain a solution for the entire model.

The FEM was initially developed in the mid-20th century for structural engineering (Logan, 2017). Early works using similar techniques (e.g., Hrennikoff, 1941; Courant, 1943) had little impact, because solving large systems of equations was not feasible without digital computers (Clough, 1990; Logan, 2017). The work, which is widely considered to be the first application of the FEM and described a 2D problem is that by Turner et al. (1956). The method got termed the "Finite-Element Method" in 1960 (Clough, 1960; Clough, 1990). It developed

rapidly during the 1960s, when it was expanded into three dimensions, implemented more complex rheologies and was applied to non-structural problems involving e.g., heat transfer and fluid flow (Logan, 2017). The potential of the FEM for applications in Earth Sciences was recognized relatively early on, e.g., by Voight and Samuelson (1969) and Stephansson and Berner (1971). Many early applications modeled processes related to tectonics and earthquakes (Stephansson and Berner, 1971; Jungels and Frazier, 1973; Shimazaki, 1974; Miyashita and Matsu'ura, 1978), while applications to volcanic processes came slightly later when the method was already more established (Dieterich and Decker, 1975). This could possibly relate to that robust analytical models of finite dislocations (e.g., Okada, 1985) were developed later than those for e.g., point sources (Mogi, 1958). The FEM is today applied both as forward models and in inversions in many aspects of Earth Sciences, including ground deformation related to tectonics, volcanism and glacio-isostatic adjustment (van Wijk and Blackman, 2005; Currenti et al., 2011; Schmidt et al., 2013; Hickey et al., 2015; Lanzi et al., 2024; Greiner and Geirsson, 2024) as well as cooling of magmatic intrusions (e.g., Rhodes et al., 2021; Burchardt et al., 2022a), hydrology (e.g. Lei et al., 2021) and large-scale tectonics (e.g., Huismans and Beaumont, 2011; Lu and Huismans, 2021).

To solve a model with the FEM, the governing equations of a physical process (e.g., Equations 1-3 for linear elasticity) are expressed as piece-wise continuous functions. They relate e.g., the forces and displacements acting on the mesh nodes of each individual element according to the governing equations. Modern FEM models can contain several hundreds of thousand individual elements. As an example, the mesh in the models in **Paper III** consists of 71 348 nodes that divide the model domain into 394 344 tetrahedral elements. For the entire model, a total of 9 608 604 equations need to be solved. While considering all boundary conditions, they are then re-combined into a single system of equations for the entire model domain, which is solved to obtain the solution for the model (e.g., Logan, 2017). As an example, pressure applied to a surface can be related to displacement in the surrounding material (Figure 3.3). The inherently piece-wise definition of the model makes the FEM well suited to implement variations in material properties, and the discretization into small elements facilitates the simulation of models with complex, irregular geometries.

Since the FEM divides the model domain into a finite number of elements, it cannot simulate truly infinite domains such as a half- or full-space. They are instead approximated by creating a model domain, that is sufficiently large so that there are no edge effects, i.e. further changing the domain size does not influence the model results (Currenti et al., 2008; Hickey and Gottsmann, 2014). The accuracy of a solution furthermore depends to some degree on the number and resolution of the individual elements, which the model is divided into. The element size is typically variable within a single model with a finer mesh, i.e. smaller elements, in areas with high gradients in either material properties or solved-for variables such as displacement or temperature. While the precision of a model increases as the mesh gets finer, the computational requirements, i.e. computation power, cost and time, associated with solving the model increases as well and it is important to balance these requirements.

It is considered good practice to benchmark a model, to ensure that boundary conditions and the underlying physical processes are implemented correctly and that there are no edge- or mesh-effects (Currenti et al., 2008; Hickey and Gottsmann, 2014). For this purpose, the model results are compared quantitatively to a known solution e.g., an analytical model. If the numerical model includes complexities such as variable material properties, a simplified version with homogeneous properties should be benchmarked before complexities are added

(e.g., Masterlark, 2007; Hickey and Gottsmann, 2014).

Individual computers as well as parallel computing on high-performance computers/clusters have become increasingly accessible in recent years and have allowed for the implementation of increasingly large and complex models. However, individual forward models using the FEM typically require significantly more computational resources and time than analytical or semi-analytical methods (Currenti et al., 2010; Hickey et al., 2015). This becomes an issue for inversions, which require a large number of forward models to be run. Consequently, FEM models are not commonly used in near-real-time monitoring. Nonetheless, in the field of modelling ground deformation in general and volcano deformation in particular, advantages of the FEM are that it can produce models based on more realistic assumptions compared to simplified analytical models (e.g., Masterlark, 2007). Such models can include realistic topography (Figure 3.3a) based on DEMs (Trasatti et al., 2003; Johnson et al., 2019), crustal heterogeneity (Hautmann et al., 2010; Greiner and Geirsson, 2024), non-linear rheologies (Trasatti et al., 2005; Islam et al., 2016), actively interacting deformation sources or pre-existing stress fields (Pascal et al., 2013), and thermomechanical or poroelastic coupling (Hickey et al., 2015; Alshembari et al., 2022).

3.4 Geodetic Observations and Analytical Models of Surface Deformation

The measurement of surface deformation is an important geophysical method to obtain information about magma movements in active volcanic systems (e.g., Sigmundsson et al., 2015; Aloisi et al., 2020; Parks et al., 2023). Oftentimes surface deformation is much too small to detect it with the bare eye, especially if magma is relatively deep in the ground or if the amount of magma in motion is small. However, by using geodetic techniques, it is possible to detect motion of the ground down to the centimeter- or even mm scale (Dzurisin, 2007b; Aoki and Kreemer, 2024). While a whole range of geodetic measuring techniques exist (see e.g., Dzurisin, 2007b), the focus here lies on the space geodetic techniques of InSAR and GNSS, which produced the surface deformation data sets used in **Paper III**. Details about how the data are processed are however omitted here, since geodetic data processing was not part of this thesis. The geodetic data sets used in **Paper III** were published by Sigmundsson et al. (2022).

3.4.1 InSAR

The acronym InSAR stands for Interferometric Synthetic Aperture Radar and was established for applications in Earth sciences in the 1990s (Massonnet et al., 1994; Dzurisin and Lu, 2007). The first application to volcano deformation were by Massonnet et al. (1995) for Etna (Italy).

Satellites orbiting the Earth send electromagnetic signals in the microwave spectrum towards the ground and record both the amplitude and phase of reflected signals for each pixel. Later (after typically days, months or years) the satellite flies along the same orbit again and records a second image. If the Earth's surface deformed in the meantime, the recorded phase of the reflected signal will be slightly shifted relative to the initial image, since the distance between the satellite and the ground surface changed (Dzurisin and Lu, 2007). An example

of such an image is shown in Figure 3.4a. The satellite recording this particular image has a wavelength of 56 mm and one full color fringe corresponds to half the wavelength, i.e. 28 mm. This type of image is known as a wrapped interferogram. To extract the cumulative Line-of-sight (LOS) displacement, i.e. the change of distance between the satellite and the ground along the viewing direction of the satellite, the integral over the phase derivative is determined between a chosen reference point and the individual pixel (e.g., Osmanoğlu et al., 2016). A number of corrections need to be applied to account for e.g., surface topography, atmospheric disturbances, noise and slight variations in the position of the satellite. For details see e.g. in Dzurisin and Lu (2007).

InSAR works well if the changes recorded between neighbouring pixels correspond to a fraction of the recording wavelength. If changes get larger due to steep deformation gradients (e.g., large motion along fault scarps), the phases recorded on neighbouring pixel differ too much and coherence between them is lost. Similar issues arise if the reflecting surface is very rough or generally unstable, such as for snow, water, vegetated areas or areas with drifting sand. This makes it difficult to obtain information in e.g., snow-covered areas during the winter.

One of the most important advantages of InSAR is its a high spatial resolution of up to $\approx$1 m, thanks to which it can reveal spatially complex deformation patterns (e.g., Figure 3.4a). Furthermore, InSAR does not require the deployment of instruments in the study area. This is especially useful for areas that are very remote or dangerous to enter. Unfortunately, only the deformation along the LOS vector is recorded rather than the 3D deformation field. By combining images with two different viewing angles, the components of Near-East (i.e. approximate east) and Near-Vertical (i.e. approximate vertical) deformation can be resolved (e.g., Drouin and Sigmundsson, 2019). However, it remains difficult to resolve deformation occurring close to or parallel to the nearly north-south oriented flight direction of the satellite (e.g., Li et al., 2021). The temporal resolution of InSAR is limited by the flight schedule of the orbiting satellites. It is common that days or weeks pass between image acquisitions of a single area by the same satellite, so a number of different InSAR satellites can be beneficial. Due to the temporal resolution and difficulties in acquiring a coherent signal in varying snow conditions, it can be challenging to rely purely on InSAR when monitoring ground deformation of a volcanic system experiencing unrest.

3.4.2 GNSS

GNSS stands for Global Navigation Satellite System and includes a number of positioning systems such as GPS, GLONASS, Galileo and Beidou (e.g., Aoki and Kreemer, 2024). GNSS deformation measurements require ground based stations deployed in the field, as opposed to InSAR, which is purely satellite-based. The first GNSS satellite was launched in 1978 and the first network, GPS, became fully operational in 1993 (Dzurisin, 2007a). Early studies in Iceland were done around a similar time (Foulger et al., 1993; Sturkell et al., 1994).

Each satellite continuously sends electromagnetic signals that contain information on e.g., the satellite itself, its orbit, satellite clocks and clock errors. These signals are received by the ground stations, which consist of an antenna and a receiver (Figure 3.4b). For high-accuracy positioning, i.e. locating the absolute position of the GNSS station in a global reference frame with up to mm-level accuracy, the distance between the station and a minimum of four satellites needs to be accurately determined. To achieve this, the phase of the incoming carrier

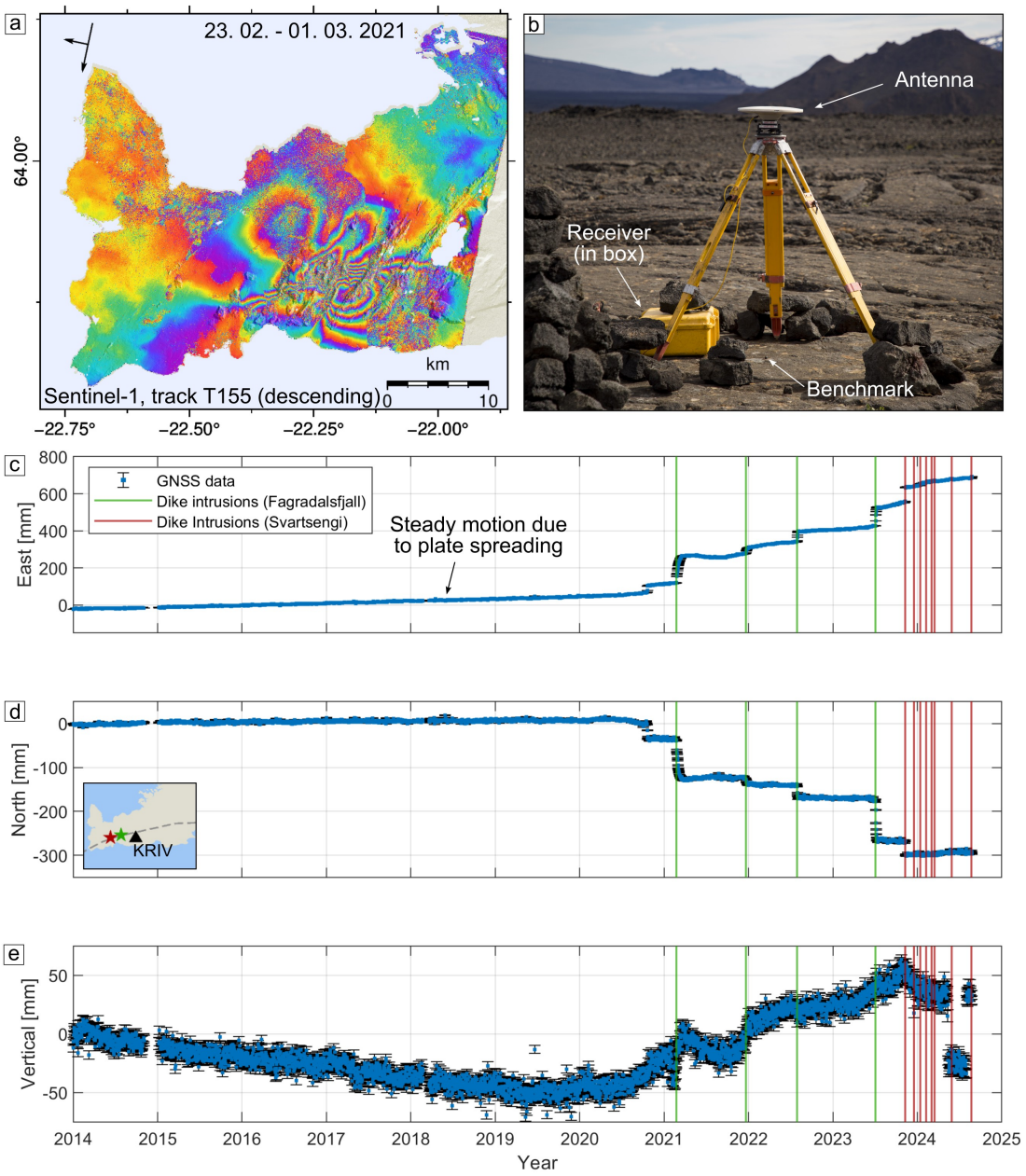

Figure 3.4. Methods of measuring surface deformation relevant for this thesis. a) Wrapped interferogram of the Reykjanes Peninsula obtained with InSAR by Sigmundsson et al. (2022). Image spans the first week of the February–March 2021 dike at Fagradalsfjall. Arrows indicate satellite heading and looking direction. Phase change over one colour fringe corresponds to 28 mm. b) Example of a GNSS station in the field (Photo). This is a battery-powered campaign station (the battery is hidden behind the pile of rocks to the left of the receiver box). c) Eastward, d) northward and e) vertical component of motion for the continuous GNSS station KRIV on the Reykjanes Peninsula relative to the stable North American plate. Green and red lines mark dike intrusions. Locations of KRIV (black triangle), Fagradalsfjall (green star) and Svartsengi (red star) are marked in the inset in d). Plate boundary outline by Michalczewska et al. (2014). GNSS data from KRIV processed using GIPSY Oasis II by H. Geirsson. See Sigmundsson et al. (2022) for details.

waves is recorded in addition to the content of the signal sent by the individual satellites. To account for the dispersive propagation delay through the ionosphere, two or more signal frequencies are used. For further details on this see e.g., Dzurisin (2007a). The accuracy of the ground station's position increases, the longer the time span of data collection is. If data is collected over a 24h interval, the position can be determined with an accuracy of up to 3–5 mm in the horizontal and 10 mm in the vertical direction (Dzurisin, 2007a; Aoki and Kreemer, 2024).

A single position of a single GNSS station by itself does not record any ground deformation. However, repeated measurements of the position can be compiled into a time series (e.g. Figure 3.4c-e), from which both deformation events (e.g., dike intrusions or large earthquakes) and the velocity of observed motion, e.g. due to plate motion, can be extracted. There are two types of GNSS stations used for high-accuracy positioning: 1) spatially fixed, continuously measuring and 2) campaign stations. The latter are set up above fixed benchmarks in the ground, record data for hours to days and are subsequently moved elsewhere. For campaign stations it is therefore important to note that the station records the position of the antenna and it is crucial to determine the position of the antenna relative to the benchmark on the ground. Typically, the station is set up so that the antenna is located directly above the benchmark (Figure 3.4b) and the height of the antenna above the benchmark needs to be measured. GNSS is advantageous compared to InSAR with respect to the three-dimensional nature of the recorded deformation and due to flexible and generally higher temporal resolution. However, the spatial resolution of a GNSS network is highly dependent on the number of stations in the area of interest and inevitably lower than that of a coherent interferogram. Additionally, GNSS stations require regular access to the field.

3.4.3 Analytical Modelling of Volcano Deformation

Analytical deformation models are often used in the context of monitoring volcano deformation since they can produce solutions with very short computation time compared to e.g., FEM models. If a volcanic system experiences unrest e.g., due to a magmatic intrusion, GNSS and InSAR data are often interpreted together. They can serve as input for inversions to constrain the potential location and nature of the unrest source (e.g., Mogi, 1958; Hooper et al., 2011; Bagnardi and Hooper, 2018; Sigmundsson et al., 2022; Sigmundsson et al., 2024). The probably most widely applied analytical solution for inversions of surface deformation associated with a magmatic dike is the Okada model (Okada, 1985; Rivalta et al., 2015). This model predicts the surface deformation caused by uniform tensile opening and/or shearing of a rectangular dislocation of a given length, width, height, strike and dip buried at a certain depth in a homogeneous, isotropic elastic halfspace (e.g., Dzurisin, 2007b; Battaglia et al., 2013). Using this model, a dike (or sill) can be represented by either a single dislocation or by many small patches with varying deformation, in which case the individual solutions are superimposed (e.g., Amelung et al., 2000; Montgomery-Brown et al., 2010; Sigmundsson et al., 2022; Parks et al., 2023).



4 Paper Summaries

This chapter summarizes the three research papers forming the base of this thesis. Each paper focussed one of the main research questions outlined in Section 1.2 and on one of the main research methods of field geology, laboratory experiments and numerical models .

4.1 Present Work

Paper I investigates how dikes that propagated through hyaloclastite are affected by pre-existing fractures in the shallow crust. This question is addressed from a field-based perspective by studying a set of basaltic dikes exposed in a partially eroded caldera-filling hyaloclastite in the extinct Dyrfjöll volcanic system, NE Iceland (Figure 2.3 for location). We collected UAV-assisted photogrammetry data and created virtual 3D outcrops through SfM. We mapped the orientation of dikes and fractures in the virtual outcrop models, characterized and quantified observed changes in the orientation of individual dikes and analyzed them in the context of the local tectonic setting.

Faults and fractures are generally considered to be weaker than their surrounding crust. However, not every weakness is intruded by magma. **Paper II** investigates the role of the host rock cohesion and magma viscosity on magma-fault interaction. We conducted laboratory experiments, during which we injected two liquids with differing viscosities into dry, granular materials with varying cohesion and a pre-existing strike-slip fault. Surface deformation was recorded using SfM. For experiments with the lower viscosity model magma, we could additionally document the intrusion geometry, since the injected fluid solidified after the experiments and could be excavated.

Paper III investigates the role of tectonic stress as a driving mechanism for dike opening and dike-induced deformation. For this purpose, a FEM model of the dike, which formed at Fagradalsfjall on the Reykjanes Peninsula in early 2021 is implemented. The model assumes a temperature- and pressure dependent Maxwell-viscoelastic 3D-variable rheology and depth-dependent elastic properties of the crust, and consists of two model steps. During the first step, tectonic stress accumulates over 800 years due to plate motion (i.e. since the end of the last volcanic eruption on the peninsula). Part of this stress is locally released during the second model step through dike emplacement. The predicted dike-induced surface deformation is compared to geodetic observations from GNSS and InSAR data from Sigmundsson et al. (2022).



4.2 Paper I

4.2.1 Summary

This project studied magma-fault interaction in the shallow crust from a field-based perspective. The main objectives were to 1) characterize the observed interaction and to 2) put it in relation to the estimated tectonic conditions at the time of emplacement. For this purpose, we mapped basaltic dikes and fractures in a moderately fractured, caldera-filling hyaloclastite in the extinct and partially eroded volcanic system of Dyrfjöll in NE Iceland. Above outcrop scale, the hyaloclastite is relatively homogeneous with existing fractures as the dominant type of heterogeneity, making it well suited for this type of study.

We created virtual 3D models of three outcrops within the caldera (Figure 2.5b) through SfM photogrammetry using photos collected with a UAV. Across the three virtual outcrops, we mapped 317 fractures and 45 dikes consisting of 104 segments. Based on their strike, we could identify four groups of orientations, referred to here as sets, which were identified in both the fractures and dike segments (Figure 4.1 a and b, respectively). The most frequently observed strike was NNE-SSW, while the others were ENE-WSW, ESE-WNW and SSE-NNW.

For dike segments, we furthermore determined whether they occupied a pre-existing fracture or likely propagated through intact rock. Out of the 104 identified dike segments, 39 propagated along pre-existing fractures, 61 through intact rock and four were inconclusive. Out of the 61 segments in intact rock, 28 belonged to a single dike, which split into many small segments. Most dike segments, which propagated along fractures, followed the most prominent, NNE-SSW-striking fracture set (Figure 4.1c). Perpendicular to this orientation, no fracture-occupying dikes were observed. The other observed sets were dominated by dike segments in intact rock even though fractures with similar orientations were found across the study sites (Figure 4.1a, c).

We did not quantify the fracture density and lengths due to strongly variable outcrop geometries and fracture spacing within individual outcrops. However, a qualitative assessment did not reveal noticeable changes in the fracture density (or orientation) as a function of distance from individual dikes on UAV photos or in the virtual outcrop models. Such changes could have indicated the presence of damage zones around intrusions and whether fractures pre-dated the intrusions or possibly formed during or after their emplacement (e.g., Townsend et al., 2015).

The influence of tectonic stress was evaluated through a simple stress model. We assumed that the NVZ, a present-day plate boundary segment located west of Borgarfjörður eystri (see Figure 2.3 for location), can serve as an analogue rift zone and estimated the amplitude and orientation of the crustal stresses there at 500 m depth below the surface, which is thought to resembles the paleo-depth of the dikes at Dyrfjöll (Burchardt et al., 2022a). We furthermore assumed a moderate magmatic overpressure of 1.3 MPa during dike emplacement. These parameters were used in the Matlab code *FracTend* (Stephens et al., 2018; Healy, 2018) to estimate the susceptibility of fractures of arbitrary orientation to be intruded by magma. Additionally, the expected opening angle was determined, i.e. the angle between the normal to the fracture plane and the dilation vector (Equation 10). Comparison between this simple stress model and the orientation of the identified dike segments at Dyrfjöll shows that most dike segments fall close to the $\sigma_1 - \sigma_2$ plane (poles to planes close to σ_3). They furthermore have low expected opening angles, i.e. open dominantly tensile (Figure 4.1d). Most segments with a

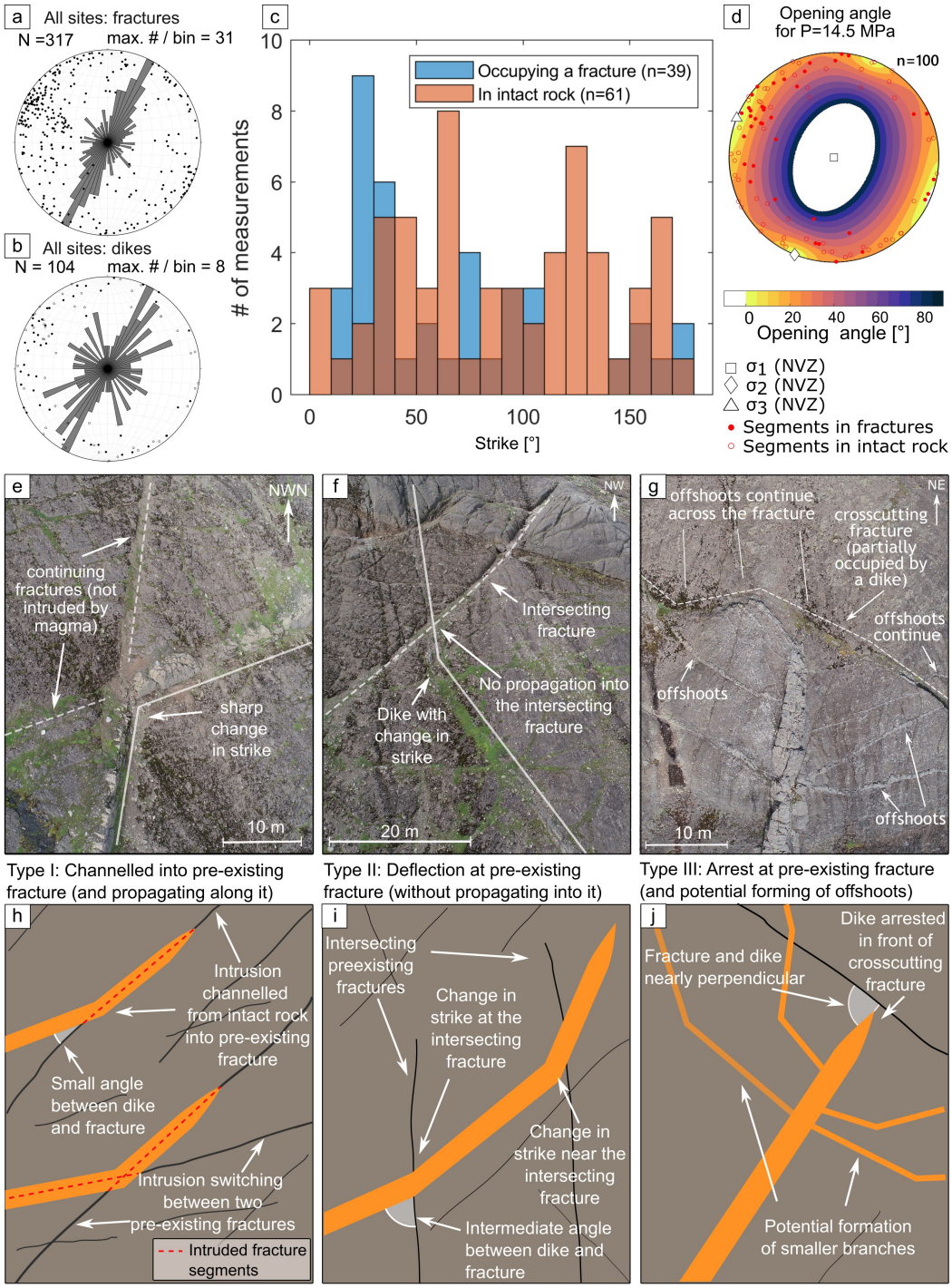

*Figure 4.1. Key results of **Paper I**. Equal area, lower hemisphere stereographic projections of poles to planes overlain by rose diagrams of all a) fractures and b) dike segments mapped at the three locations in the Dyrfjöll caldera. c) Distribution of dike segments in pre-existing fractures or intact rock according to their strike. Four inconclusive segments were excluded. d) Expected opening angle based on the estimated regional stress field. Filled/hollow red dots represent poles to the planes of dike segments in fractured/intact host rock. e)-f) Field photos and g)-j) conceptual illustrations of the three types of dike-fracture interaction observed at Dyrfjöll.*

high predicted shearing component dominantly occupied pre-existing fractures (solid symbols in Figure 4.1d). It was unfortunately not possible to compare the opening angles predicted by *FracTend* to field observations due to a lack of host rock markers in the hyaloclastite.

For each identified change in strike between neighboring dike segments, we measured the angle and tried to constrain from the outcrop models and UAV photos, whether nearby fractures could have influenced dike propagation. We observed three different types of interaction. 1) Most commonly, magma flowed along pre-existing fractures and could switch between fractures with differing orientations (Figure 4.1e,h). 2) Some dikes showed a change in strike at or near an intersection with a fracture (Figure 4.1f, i). At least at the resolution of the UAV images, we did not observe magma propagating into fractures in these instances. Sometimes, the intersecting feature was another dike rather than a fracture. 3) In one instance, a dike was arrested in front of a cross-cutting fracture (Figure 4.1g,j). A number of small branches or offshoots formed near the arrested dike tip. Several of these offshoots intersected the same fracture, although at different angles, and either propagated along or across it. We also observed combinations of the first two types of interaction, i.e. where a dike occupying a fracture switched into a different fracture set where it intersected a third fracture (or a different dike). All observed changes in strike were smaller than 50° and those in intact rock had a generally lower amplitude than changes, where at least one dike segment occupied a pre-existing fracture.

4.2.2 Main findings

- Mapped dikes and fractures at Dyrfjöll dominantly follow four different orientations. The most prominent direction strikes NNE-SSW (Figure 4.1a,b), which is consistent with estimates of the tectonic stress field at the time of emplacement (Figure 4.1d).
- Magma propagation along fractures is more frequently observed if the dike segment strikes close to NNE-SSW, i.e., to the likely tectonically controlled direction (Figure 4.1c). Propagation along fractures becomes less common the farther the strike deviates from this direction. No propagation along fractures is observed perpendicular to the tectonically controlled direction.
- All observed changes in strike are smaller than 50°. We observed three types of interaction between basaltic dikes and pre-existing fractures in the hyaloclastite at Dyrfjöll, which may to some degree be controlled by the angle between the dike and fracture in question:
    1. Dikes can follow pre-existing fractures. This is especially common if the dike/fracture has a strike similar to the estimated paleo-tectonic stress field
    2. Dikes can change strike when intersecting a pre-existing fracture without being channeled into said fracture. We observe that this occurred mainly if the angle between the dike and the fracture was large.
    3. Dikes can be arrested in front of a pre-existing fracture. This was observed when the dike strikes almost perpendicular to the fracture. In at least one instance, small offshoots formed near the tip of the arrested dike, which intersected the same fracture at different angles and could propagate beyond or along it.



4.3 Paper II

4.3.1 Summary

Observations from active and extinct volcanic systems show that magmatic intrusions frequently propagate along pre-existing faults, if they are suitably oriented relative to the local stress field at the time (Delaney et al., 1986; Mathieu et al., 2008; Jenness and Clifton, 2009; Stephens et al., 2018; Hjartardóttir et al., 2023). However, not every fault near an intrusion is exploited by propagating magma, especially in the context of magma reservoirs (Paterson and Schmidt, 1999). Instead, many plutons are to some degree fault-bounded (Rosenberg, 2004; Burchardt et al., 2010; Mattsson et al., 2018; Rhodes et al., 2024). This study investigates the influence of the host rock cohesion and magma viscosity on magma-fault interaction using laboratory experiments as analogue models.

We conducted a series of experiments, during which we injected fluids serving as analogue magmas into the base of a box filled with granular materials, that served as analogue host rock. The experimental setup is shown in Figure 3.2b. We tested five dry, granular, compacted mixtures with varying proportions of Silica flour (SF) and micro-Glass Beads (GB) as the analogue host rock. The relative proportions of GB/SF control the host rock cohesion, which has been quantified in previous studies (Galland et al., 2006; Abdelmalak et al., 2016). The tested proportions ranged from equal amounts of both materials (50/50) to pure glass beads (100/0), which served as end member analogues of high-cohesion (strong) and low-cohesion (weak) host rock, respectively. Two different liquids served as analogue magmas with varying viscosity: molten vegetable oil (O) as a low-viscosity analogue and glucose syrup (S) as a high-viscosity analogue. Percolation into the granular analogue host rock can be considered negligible for both fluids (Galland et al., 2006; Galland et al., 2018). For each of the 10 possible material combinations, one experiment was conducted with intact, unfractured host rock (I) and one where a strike-slip fault was created in the host rock prior to the injection of fluid (F). This created a discontinuity at depth and formed a strike-slip fault in the analogue host rock. Each experiment was given a name based on the fluid used (O/S), the initial host rock status (I/F) and the proportions of the different granular materials (GB/SF).

The analogue magma was injected from below into the center of the model box through a 0.5 cm-wide inlet at constant flow rate. An externally controlled array of four cameras positioned above the box (Figure 3.2b) synchronously recorded images of the model surface from different angles in regular intervals ($\Delta t_s = 2\,min$ and $\Delta t_o = 1\,s$ for syrup and oil, respectively). The experiment ended when the fluid reached the model surface. The images of the model were processed with SfM photogrammetry to extract 3D surface deformation. The vegetable oil solidified after the experiment, which allowed us to additionally excavate the intrusion and create 3D models of them using SfM photogrammetry. This was not possible for experiments with syrup intrusions, since these did not solidify.

We observed three distinct types of intrusions in strong, intermediate and weak analogue host rock. Sheet intrusions formed in high-cohesion analogue host rock. In intact host rock, this resulted in partial cone sheets (Figure 4.2). In the presence of a fault, the intrusions exhibited abrupt changes into planar sheets where they intersected and propagated along a fault segment (Figure 4.2b). Surface deformation was generally characterized by low-amplitude (<1 cm), flat-topped doming (Figure 4.2a,b). The horizontal divergence, which shows deformation gradients, indicated extension along discrete lines above the center of the intrusion (shown

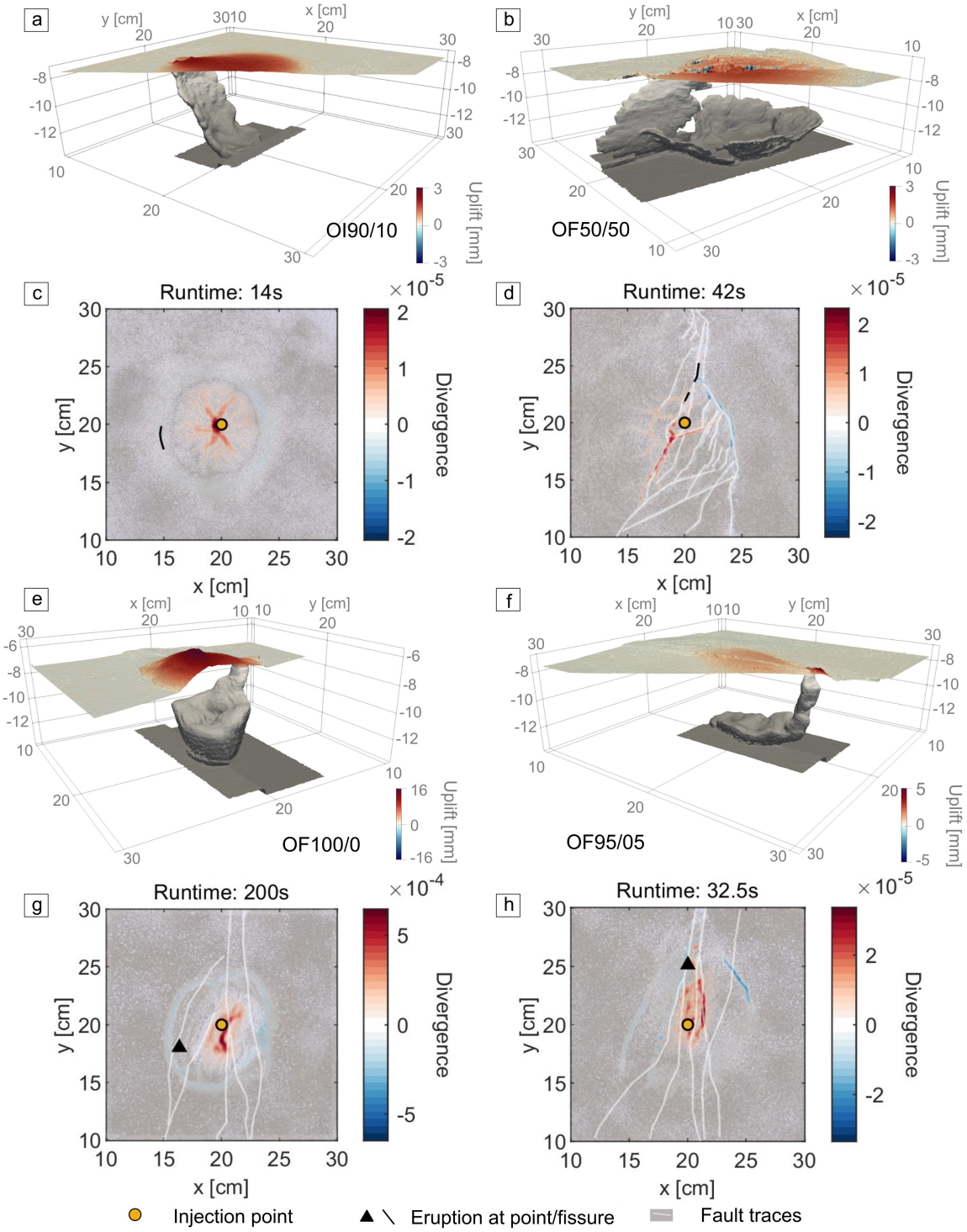

*Figure 4.2. Key experimental results of **Paper II**. Virtual 3D models and surface uplift of a) experiment OI90/10 and b) experiment OF50/50. c) and d) associated divergence of horizontal surface deformation. For the divergence, red corresponds to extension and blue indicates contraction. Virtual 3D models and surface uplift of e) experiment OF100/0 and f) experiment OF95/05. g) and h) associated divergence of horizontal surface deformation.*

in red in Figure 4.2c). This was surrounded by a ring of contraction (shown in blue). In the presence of a fault, deformation gradients in the horizontal and vertical direction were strongly

localized along fault segments rather than forming circular structures (Figure 4.2b, d). This indicates, that the existing faults accommodated a large part of the intrusion-induced strain. In pre-faulted experiments, intrusions consistently breached the surface along fault-segments. All described characteristics were observed for both oil and syrup experiments (excluding the intrusion geometry, which was not observed for syrup).

In low-cohesion (weak) materials, massive intrusions with a low aspect ratio, i.e. a thickness comparable to their width and length, formed and caused high-amplitude ($\geq$ 1.5 cm) uplift. Here, the area of uplift strongly correlated with the shape of the underlying intrusion (Figure 4.2e). Oil intrusions had an elliptic base area, steeply inward-dipping sides and a subcircular conduit connecting to the surface (Figure 4.2e). The horizontal divergence was noticeably more diffuse and lacked discrete extension lines as they were observed in higher-cohesion experiments (Figure 4.2g). The presence of a pre-existing fault did not have visible effects on surface deformation and the divergence was undisturbed across fault segments. As for high-cohesion experiments, the observations were consistent for both tested viscosities.

At intermediate cohesion, oil intrusions in pre-faulted analogue host rock showed a hybrid geometry exhibiting elements of both previously described regimes. Two experiments showed these hybrid geometries. OF95/05 had an elongated, inflated body at depth, the long axis of which aligned with the strike of the fault. It was connected to the model surface through a thick, rounded conduit with an irregular, lobate structure (Figure 4.2f). Experiment OF90/10 did not form an inflated part at depth and the conduit was slightly more planar, but still lobate and twisted resulting in a C-like shape (not shown here). In both cases, the conduits formed in the plane of existing fault segments. For experiment OF95/05, surface deformation showed low amplitude uplift above the elongated, inflated body at depth and extremely localized, moderate uplift above the conduit (Figure 4.2f). The divergence shows extension along the fault above the inflated body and an incomplete contraction ring farther out (Figure 4.2h). Barely any horizontal deformation was observed around the conduit. There are no indications that hybrid intrusions formed in the pre-faulted syrup experiments nor in experiments with intact analogue crust. Instead, surface deformation was consistent with sheet intrusions for GB/SF 90/10 and with massive, low-aspect ratio intrusions for GB/SF 95/05.

Intrusive volumes were mostly lower for pre-faulted, high-cohesion experiments compared to their intact counterparts, while the reverse was observed for low-cohesion experiments (Figure 4.3a). For constant injection rates, this implies that propagation along faults reduced the time until eruption in high-cohesion analogue crust, while they delayed eruption in weak crust.

The ratio of uplifted to injected volume changed systematically between pre-faulted and intact experiments in high- to intermediate cohesion host rock (Figure 4.3b). While intact analogue host rock resulted in ratios $\geq$1, indicating slight decompaction, the ratio was close to, or <1 for pre-faulted analogue host-rock, indicating compaction. This could partially relate to small amounts of dilation occurring during shearing on strike-slip faults. The thereby created space could subsequently be filled by the intrusions without creating much uplift. In contrast to this, fractures only began forming in intact analogue host rock during the intrusion process. This would have resulted in a localized apparent volume increase or decompaction of the crust. Experiments in low-cohesion analogue host rock show this trend to a lesser degree, possibly due to less dilation during deformation processes, independent of if they relate to faulting or intrusions.

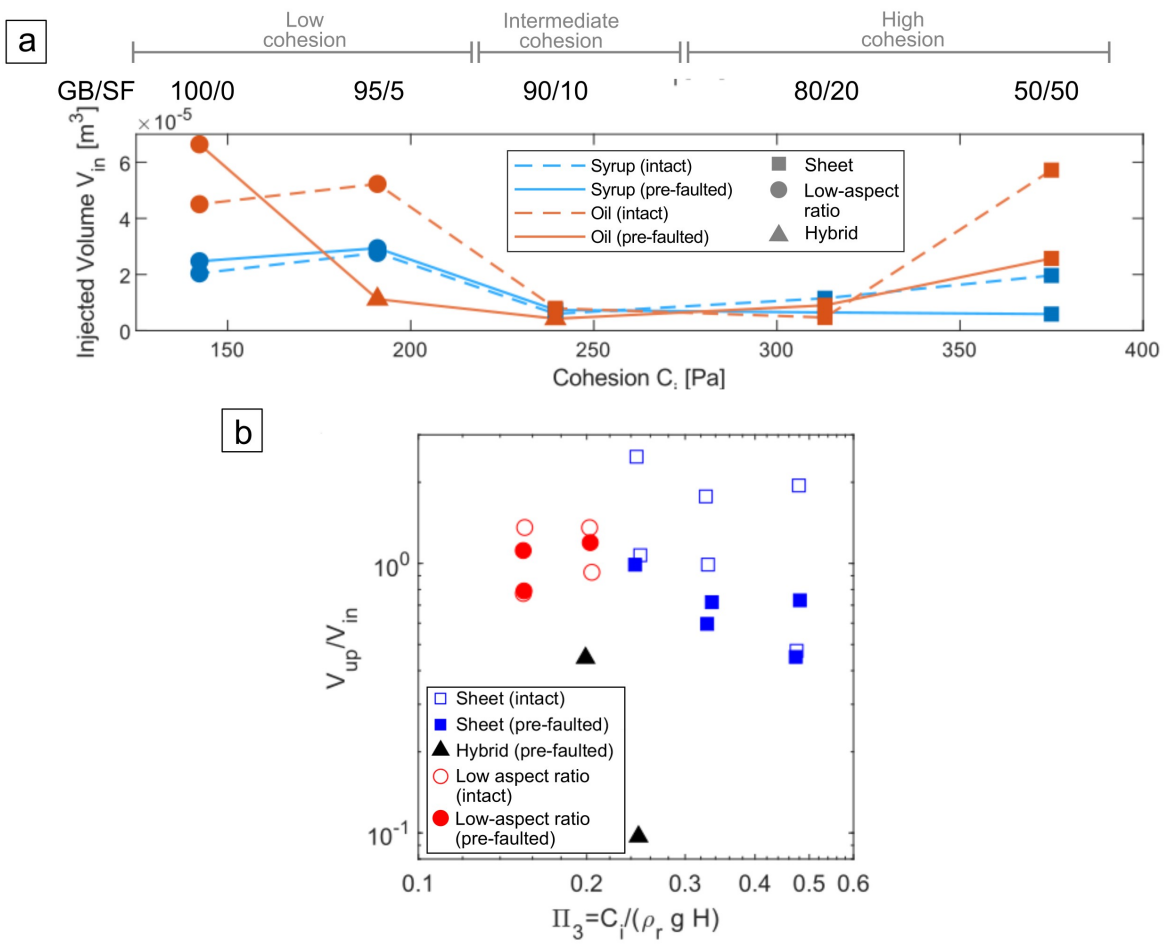

Figure 4.3. Results of ***Paper II****. a) Injected volume as functions of the (intact) host rock cohesion for all experiments in this study. b) Ratio of uplifted to injected volume as a function of the (intact) cohesion relative to the lithostatic stress at the base of the box.*

The presence of faults affects the intrusion and the associated deformation in different ways depending on the intrusion regime, which is in turn controlled by the cohesion of the analogue host rock. In intact host rock, the contrast between intact and faulted analogue crust is very high, which makes it energy efficient for the intrusion to follow the fault segment. Additionally, it is easy to sustain comparatively large dilation of fractures without having their walls collapse (Abdelmalak et al., 2016), which may explain why even higher-viscosity fluids can form sheet intrusions. In low cohesion analogue host-rock, the contrast between the faulted and unfaulted materials is low. Furthermore, the cohesion is not sufficient to sustain and dilate a fracture, independent of whether it already existed or was newly created. Consequently, low-aspect ratio intrusions form irrespective of the presence of the fault. The slightly increased intrusive volume in pre-faulted experiments may indicate that the fault was still slightly more efficient in accommodating strain compared to intact material. This could possibly relate to differing mechanical and frictional properties between intact and faulted low-cohesion analogue crust.

We attribute the formation of hybrid intrusions to the cohesion being very close to the limit of the ability to dilate a fracture. The locally reduced cohesion of the fault may have been unable

to sustain dilation, but the strength contrast was likely high enough to focus deformation to the fault segments. The lobate structure of the conduit may indicate that the intrusion propagated as a viscous indenter, where the intrusion pushes its way through the host rock instead of by dilating a fracture (e.g., Abdelmalak et al., 2012; Guldstrand et al., 2017). This is furthermore supported by the extremely localized surface deformation.

That no hybrid intrusions were observed for syrup experiments is the only observed indication that high-viscosity intrusions may be slightly less sensitive to interaction with faults than those with lower viscosity. Otherwise, the viscosity appeared to have a much weaker control compared to the cohesion and the strength contrast.

The experiments demonstrate the strong control of the cohesion and of the strength contrast between intact and faulted materials on the nature of magma-fault interaction. Different intrusion regimes, mechanisms and types of interactions with faults were observed across a range of host rocks with gradually varying cohesion. Future studies could investigate how the different regimes are affected by the presence of tectonic stress, which was not considered in our experiments. Our findings furthermore emphasize the importance of a more accurate characterization of the mechanical properties of faulted materials both in the context of laboratory experiments and in nature.

4.3.2 Main findings

- Magma-fault interaction is strongly controlled by the strength contrast between intact and faulted host rock, which in turn is a function of the host rock cohesion. In strong host rock, an existing fracture represents a significant weakness, whereas in weak host rock, the strength contrast is much lower between intact and fractured host rock. This affects both the intrusion geometry and the associated surface deformation patterns. We observe three different intrusion regimes with distinct surface deformation:

    1. In strong host rock, magma propagates along fault segments upon intersection, resulting in sheet-like intrusion geometries. Surface deformation is largely accommodated by fault reactivation.

    2. At intermediate host rock cohesion, hybrid intrusions may form through the viscous-indenter mechanism. Surface deformation is strongly localized on the intruded fault.

    3. In weak host rock, low-aspect ratio intrusions form irrespective of the presence of pre-existing faults. No fluid propagation along fault segments is observed. Intrusions push the overburden upwards, causing high-amplitude uplift. Gradients of surface deformation are diffuse and undisturbed by pre-existing faults.

- In high-cohesion host rock, the presence of faults reduces the time until an intrusion breaches the surface. They furthermore reduce the ratio of uplifted volume relative to the volume intruded at depth.

- Compared to the host rock cohesion, the viscosity has a secondary influence on magma-fault interaction. However, low-viscosity intrusions tend to be slightly more susceptible to interaction with faults than the high-viscosity intrusions. We only observed hybrid intrusions in experiments with low-viscosity fluids, which may confirm the slightly higher sensitivity of low-viscosity fluids.



4.4 Paper III

4.4.1 Summary

The presence of tectonic stress affects propagating intrusions and the likelihood of magma reaching the surface (Buck et al., 2006; Wright et al., 2012; Sigmundsson et al., 2024). Although this is well known, the governing stress field is often neglected in deformation models. In February–March 2021, a dike propagated at Fagradalsfjall on the Reykjanes Peninsula, SW Iceland, ending almost 800 years of volcanic quiescene in the area (Sæmundsson et al., 2020; Sigmundsson et al., 2022). Detailed observations of ground motion prior to and during the dike emplacement make this event an excellent case study to explore the role of tectonic stress for dike emplacement.

To investigate the contribution of tectonic stress as a driving mechanism for dike opening, we implemented a multi-step FEM model of the 2021 Fagradalsfjall dike and compare it to surface deformation observed with GNSS and InSAR (Sigmundsson et al., 2022). We first obtained an estimate of the tectonic stress on the Reykjanes Peninsula and subsequently locally released it through dike emplacement. Apart from that the dike was present only in the second step, both model steps used identical mechanical properties and boundary conditions.

The estimate of the tectonic stress was derived from a Maxwell-viscoelastic 3D plate spreading model. To allow for viscoelastic relaxation at depth, we let the viscosity vary with both temperature and pressure (Turcotte and Schubert, 2014). The temperature was derived from a heat-transfer model, which assumed a depth-dependent temperature profile along the plate boundary axis (outline of plate boundary by Michalczewska et al., 2014 in Figure 4.4a) and simulated heat transport away from it through conduction and advection (due to plate motion). We defined the surface corresponding to a viscosity of 10^{21} Pa s as the base of the effectively elastic crust, above which little stress is relaxed on the timescale of our models. It should be noted that this surface was located at variable depths in our model depending on the distance to the plate boundary axis (Figure 4.4b). At this surface, plate spreading was applied for a time span of 800 years, i.e. approximately since the end of the last eruptive period on the Reykjanes Peninsula (e.g., Sæmundsson et al., 2020). The elastic properties of the crust were derived from depth-dependent models of 1) the density (Sigmundsson et al., 2020b) and 2) seismic velocities (Weir et al., 2001). Surface velocities predicted by the tectonic model were compared to GNSS measurements by Keiding et al. (2008).

The predicted tectonic stress field shows a concentration of the least compressive principal stress σ_3 around the plate boundary axis. The highest stress was located at the base of the elastic crust around the plate boundary axis (Figure 4.4a,b). A slight asymmetry in the viscosity structure and, consequently, in the depth of the base of the elastic crust (Figure 4.4b) can be attributed to the curved plate boundary axis, which affected the temperature distribution.

The dike model used the stress field of the tectonic model as initial conditions. The dike consisted of two rectangular, vertical, 4.5 km-long segments, with location, strike and dimensions based on Sigmundsson et al. (2022) and as shown in Figure 4.2c) and d). The dike was represented in the model by a crack reaching from 1 km below the surface down to 6 km depth for the southern segment and 7 km for the northern segment (Figure 4.4e,f). We compared the modelled dike-induced surface deformation driven purely by tectonic stress to observed surface deformation from InSAR and GNSS by Sigmundsson et al. (2022). If the entire tectonic stress acting on the dike plane would be released, predicted surface deformation

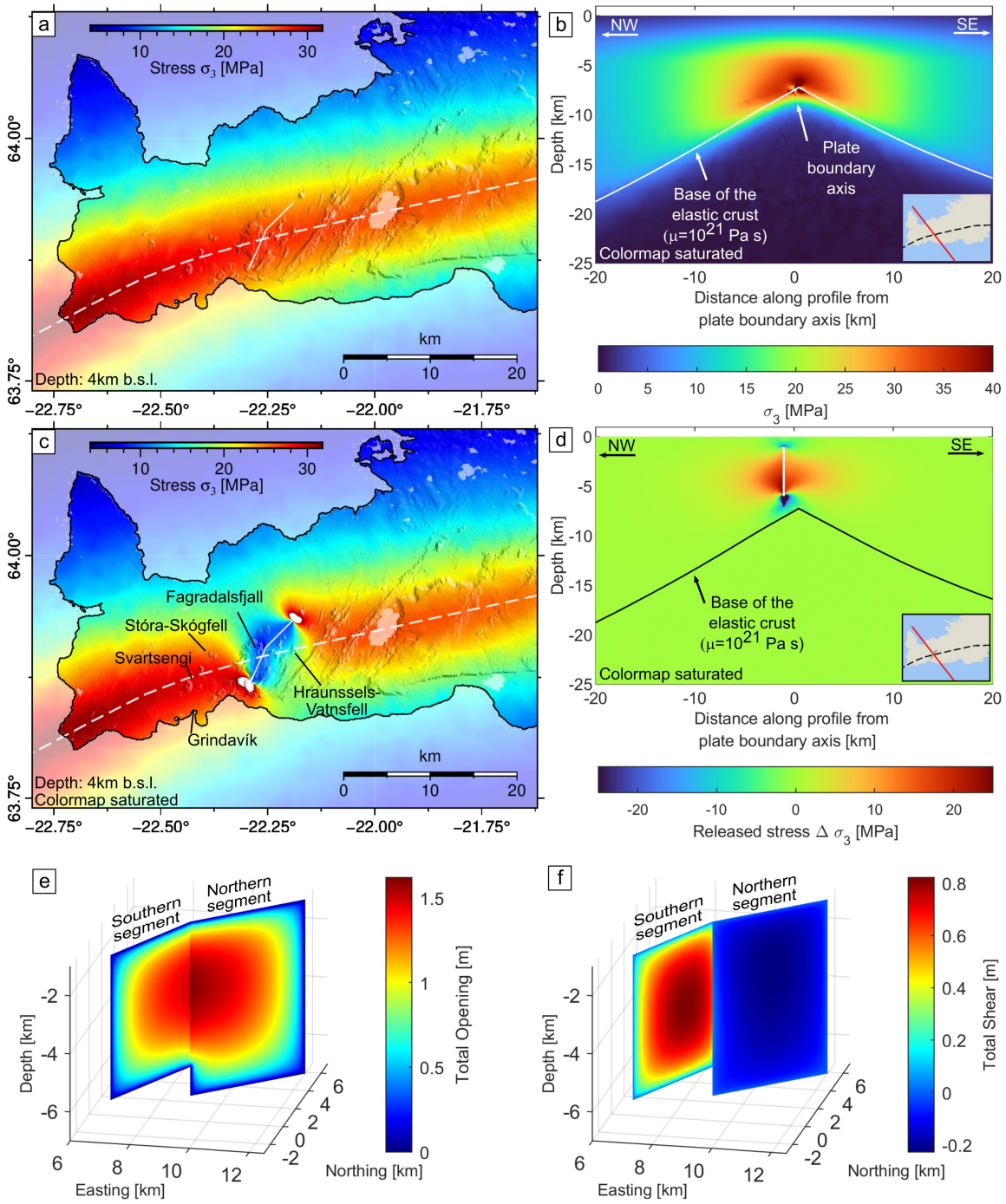

Figure 4.4. Key results of ***Paper III****. Least compressive principal stress* σ_3 *after 800 years of plate spreading a) at 4 km depth and b) along a cross-section parallel to the* σ_3 *axis (see inset for location). Location of the dike in a) is only shown for reference. c) Stress state of* σ_3 *after dike opening at 4 km depth. d) Change of* σ_3 *along the same cross-section shown in b). e) Opening and f) shearing of the dike-plane predicted by the model driven by tectonic stress. Right-lateral shear is shown as positive in f). Location of the dike (solid white line) in a) and c) by Sigmundsson et al. (2022) and plate boundary outline (dashed white line) by Michalczewska et al. (2014).*

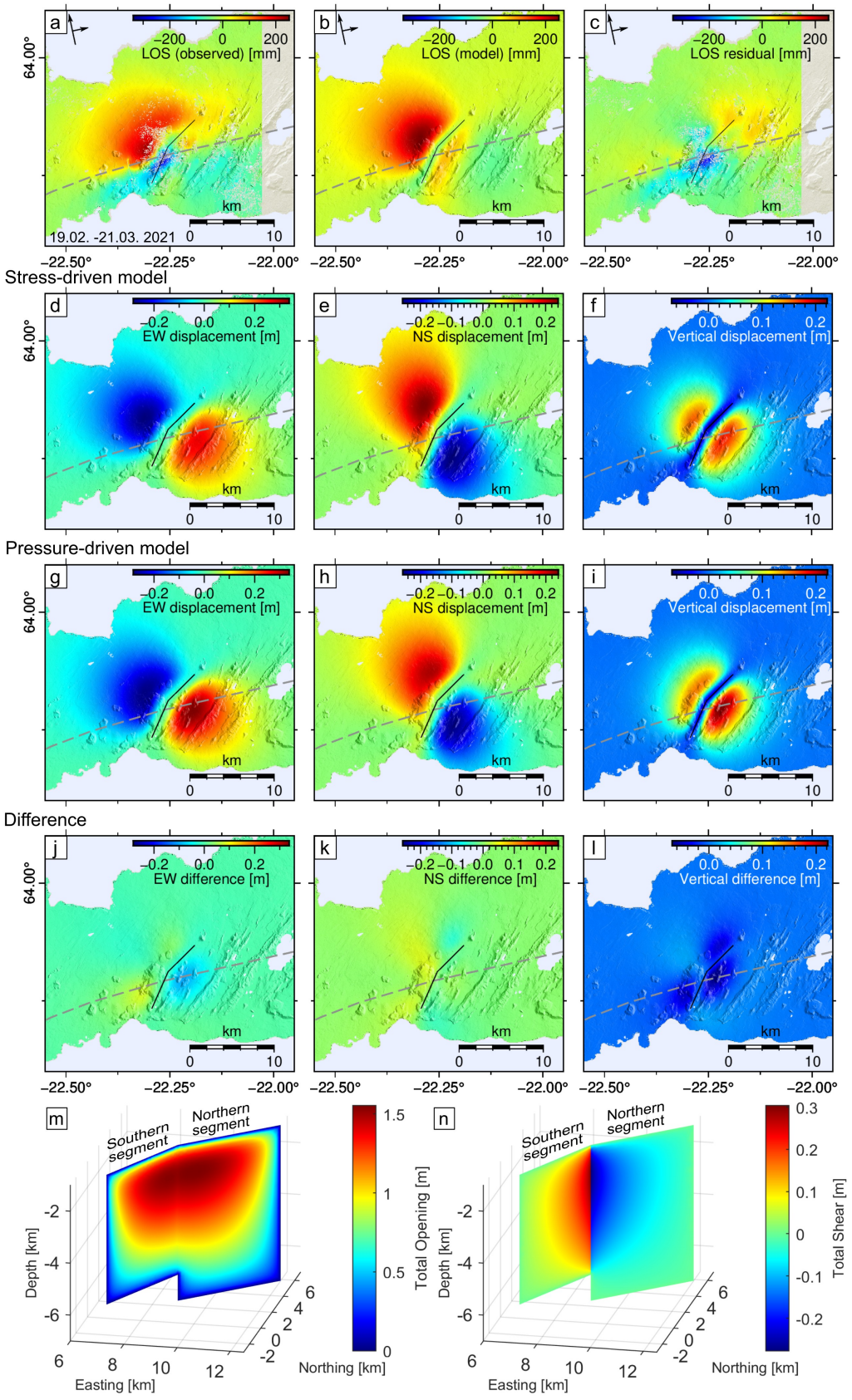

Figure 4.5. See following page for caption.

*Figure 4.5. Comparison of **Paper III** model results with observed surface deformation. a) LOS displacement measured from an ascending Sentinel-1 satellite on track T16 spanning the 2021 February–March Fagradalsfjall dike intrusion (time span indicated in the lower left corner). Large and small black arrows indicate flying and looking direction of the satellite, respectively. Dike position as inferred by Sigmundsson et al. (2022). Plate boundary outline (dashed gray line) for reference by Michalczewska et al. (2014). b) Projection of modelled dike-induced deformation onto the LOS vector. c) LOS residual (difference between a) and b)). d)-f) East, North, and vertical surface deformation by the tectonic-stress driven dike-model. g)-i) East, North, and vertical surface deformation predicted by a uniform-magma-overpressure-driven dike-model. j)-l) difference of the stress- and pressure-driven models. m) Opening and n) shearing of the dike plane for the pressure-driven model. Right-lateral shear shown as positive.*

would greatly exceeded observed deformation. To avoid this, we applied a negative pressure condition to the dike plane, which was scaled to the component of the tectonic stress normal to the planes of each dike segment. We varied the fraction of released stress in increments of 10% to minimize the residual to observed surface deformation using the Root-Mean-Square (RMS) as a criterion.

Observed deformation was best reproduced when ca. 60% of the accumulated tectonic stress were released by the dike (Figure 4.5a-c). One aspect, that can for example affect the fraction of stress released is the availability of magma. We anticipate however, that this does not affect the component of the stress field, which is oriented parallel to the dike. Once magma began to spread in the dike plane, it is unlikely that the dike plane could have held significant shear stress. In agreement with this, the application of underpressure only affected the dike-normal component of the stress field. Partial release of tectonic stress during the 2021 dike is consistent with the emplacement of subsequent dikes between late 2021–2023 (Parks et al., 2023). Furthermore, the need in our model to apply underpressure to the dike rather than magmatic overpressure is consistent with very low eruptive flow rates during the early stage of the subsequent eruption (Pedersen et al., 2022).

The dike model reproduces first-order features of the observed surface deformation. However, it underestimates subsidence above the dike close to the eventual location of the eruptive fissures and lacks a shearing signal symmetric around the plate boundary axis, which is especially pronounced west of Fagradalsfjall (Figure 4.5c). Parts of this deviation may relate to distributed motion across numerous shallow faults and opening of the initial eruptive fissure (Hjartardóttir et al., 2023; Ducrocq et al., 2024).

Opening of the dike effectively releases stress in its immediate surroundings, between Mt. Stóra-Skógfell to the west and Mt. Hraunssels-Vatnsfell to the east (Figure 4.4c). Due to the curved geometry of the dike, slightly more stress is released towards the west. Furthermore, the stress change due to dike opening is larger at depth compared to the shallow parts of the crust. This reflects the larger initial stress deeper in the crust (Figure 4.4d). Despite this, the largest opening of the dike is observed at intermediate depth of ca. 2–4 km with the maximum located close to the center of the dike, but on the northern dike segment (Figure 4.4e). Shearing is predicted on both dike segments, but with opposing shearing sense. The southern segment is predicted to have experienced significantly more shear (Figure 4.4e). The relative amounts of shear and opening on each segment are consistent with the orientation of the tectonic stress.

The σ_1 stress axis has a strike that is larger than that of the southern segment and slightly less than that of the northern dike segment (e.g., Delaney et al., 1986; Jolly and Sanderson, 1997). Since the northern segment is oriented less oblique to σ_1, it experiences less shear.

If the surface deformation of the stress-driven model is compared to a model driven purely by uniform magmatic overpressure, it becomes apparent that they are overall similar (Figure 4.5d-l). However, the pressure-driven model predicts more elongated areas of uplift on both sides of the dike (Figure 4.5f, i) and less shear directly above it. This is best visible in the difference of the north-component between both models (Figure 4.5k). The slightly more elongated uplift bulges compared to the stress-driven model reflect the more elongated and shallower area of maximum opening of the dike plane (Figure 4.5m). The lack of shearing at the surface is matched by less shear in the dike plane and although the sense of motion is the same as in the stress-driven model, pressure-driven shearing has a lower maximum amplitude, is symmetric and occurs mainly close to the connection of the dike segments.

The model presented in this study provides an opportunity to study the interaction of the tectonic stress field and magmatic intrusions. Modelling subsequent intrusions both at Fagradalsfjall and the neighboring Svartsengi system furthermore has the potential to investigate the temporal evolution of the crustal stress throughout this ongoing rifting episode.

4.4.2 Main findings

- Deformation associated with the February–March 2021 Fagradalsfjall dike, which formed on the Reykjanes Peninsula, SW Iceland, can be reasonably well reproduced with a Finite-Element deformation model by releasing ca. 60 % of the previously accumulated tectonic stress. No additional magmatic overpressure is required by the model to produce this deformation.
- In an obliquely spreading tectonic setting, nearfield shearing above the dike may help to distinguish between tectonic stress and magmatic overpressure as the driving mechanism. However, this shearing signal may be small and difficult to distinguish from near-surface fault motion occurring simultaneous to the dike emplacement.
- Despite similar surface deformation, the opening patterns of the dike plane may differ significantly between dikes opening due to magmatic overpressure and tectonic stress in heterogeneous host rock. For the model driven by tectonic stress, the amount of opening and shearing in the dike plane varies between the northern and southern dike segments. The relative amounts are consistent with the segments' respective orientations relative to those of the principal stress axes.



5 Conclusions and Outlook

This thesis investigated the interaction of magmatic dikes with different types of crustal heterogeneity. The main focus is the interaction with pre-existing fractures/faults (**Paper I**, **Paper II**) as well as a variable governing stress field (**Paper III**). Regarding the initially posed research questions, the work conducted here has lead to the following conclusions:

How are propagating dikes affected by pre-existing fractures in moderately fractured host rock?

Dike-fracture interaction is a complex process and pre-existing fractures or faults can affect propagating dikes with regards to their path and dynamics. The interaction in each case depends on several factors, which include the orientations of the dike and the fault/fracture in question relative to the governing stress field, the angle of both to each other as well as the magmatic overpressure and amplitude of the governing stress field.

At the extinct Dyrfjöll volcanic system we observed three different ways in which fractures affected dike propagation (**Paper I**):

1. Dikes propagating along a pre-existing fracture. This can mean that a dike, which previously propagated through intact host rock, was diverted into a fracture upon intersection. Alternatively, a dike, which already propagated along a fracture, switched to a fracture with a different orientation even though the initial fracture continues.
2. Dikes being deflected, i.e. changing strike, upon intersecting a pre-existing fracture. However, at least from what is visible in the available data, magma did not propagate along the fracture in question.
3. Dikes being arrested close to an intersecting fracture.

While dikes propagating along existing fractures or faults are observed in the field relatively frequently (Delaney et al., 1986; Valentine and Krogh, 2006; Browning and Gudmundsson, 2015; Stephens et al., 2018), the second type of interaction observed at Dyrfjöll tends to find less mentioning in the scientific literature. It is unclear if this is the case because it simply occurs less frequently or if there may be an observational or reporting bias. Recent examples of this type of interaction are the later fissures opening during the 2021 Fagradalsfjall eruption (Hjartardóttir et al., 2023). Deflection of a dike across a fracture or fault without propagation along it is to some degree reminiscent of dikes being deflected when propagating across mechanical interfaces (e.g., Maccaferri et al., 2010; Geshi et al., 2012). However, it differs from these in two ways: 1) the fractures at Dyrfjöll were subvertically dipping, while most material interfaces considered for dike deflection are subhorizontal and 2) there was no apparent contrast in material properties, as there was the presumably same hyaloclastite on either side. However, material properties could have varied within the fractures on a scale that

is below the resolution of our data (Mitchell and Faulkner, 2009; Browning and Gudmundsson, 2015; Hofer-Apostolidis et al., 2024).

The question, under which exact circumstances which type of interaction occurs could and should be addressed in future studies. Our findings from Dyrfjöll indicate that the angle between the dike and the fracture could have some influence on this. However, the potential role of additional controlling factors needs to be investigated further, involving for example more detailed mechanical analysis of the stresses involved. Furthermore, the spacing and density of fractures could be analyzed quantitatively, which would allow to better characterize how dike-fracture interaction changes in variably fractured host rocks.

Paper II provided insights into how fractures can affect the dynamics of magmatic sheet propagation. In strong host rock, magma being channeled through pre-existing faults can accelerate the ascent towards the surface. This effect became more pronounced, the stronger the host rock was. As a consequence, the ratio of intruded vs. erupted material would tip towards a higher fraction being erupted.

The February–March 2021 Fagradalsfjall dike was oriented slightly oblique to the tectonic stress field of the Reykjanes Peninsula. However, it is not entirely clear what caused this obliqueness. **Paper I** demonstrated that interaction with pre-existing fractures could be a potential cause. While there are indications of magma-fault interaction in the shallowest few hundred meters of the crust (Hjartardóttir et al., 2023; Einarsson et al., 2023), evidence is less clear for larger depths. Sigmundsson et al. (2022) and Ducrocq et al. (2024) reported localized creep along faults and increased strain accumulation in the years prior to 2021, which suggests the presence of a weakness. However, based on the findings from **Paper II**, the relatively long propagation period of the dike (ca. three weeks until the eruption onset) is not an indication for propagation along a well defined weak plane, although other factors may have also contributed to the slow propagation. These could have for example been a small cross-sectional area of the dike-feeding magma channel and an overall low amount of total driving pressure available for dike formation if compared to e.g., the dike that formed in November 2023 at Svartsengi (Sigmundsson et al., 2024).

If the obliqueness of the dike was not related to propagation along a weak plane, one or both of the following processes could have contributed to it: 1) The creep observed in this area could have locally altered and rotated the stress field. The strain anomalies described by Sigmundsson et al. (2022) and Ducrocq et al. (2024) mainly coincide with the southern dike segment of the 2021 Fagradalsfjall dike, which was modelled as the more oblique of the two segments. Local rotation of the stress field caused by the mentioned creep prior to magma emplacement could therefore explain the obliqueness of the southern dike segment and the difference in strike compared to the northern segment. In this case, the dike would not necessarily have to propagate along the plane of weakness to be affected by it. Local rotation of the stress field could also relate to potential segmentation of the plate boundary axis and a step-over structure identified from seismicity close to the eventual eruption sites by Fischer et al. (2022). 2) Alternatively, it is possible that the dike propagated along pre-existing fractures and fault segments of slightly varying strike, length and strength. The area around Fagradalsfjall has experienced frequent seismicity well before 2021 (e.g., Björnsson et al., 2020; Fischer et al., 2022) and there are almost certainly several faults and fractures at depth. Dikes propagating along fractures of variable strike were observed at Dyrfjöll (**Paper I**), but it is not clear, how the propagation dynamics are affected by flow along several connected

fractures of different strength contrasts and varying orientations relative to the governing stress field. It is challenging to resolve small-scale (less than hundreds of meters) features of intrusions at depth with geophysical methods, which makes it difficult to further constrain the detailed structure of the 2021 Fagradalsfjall dike at depth. It is possible that the two major segments of the 2021 dike modelled by Sigmundsson et al. (2022) and **Paper III** represent the average strike of several shorter segments.

Overall, the work presented here shows that dike-fracture interaction is a complex process controlled by many different parameters. The field observations show that magma-fault interaction involves more than magma diversion into a fault. Future work including both additional quantitative field-based studies and modelling of dynamic dike propagation may help to advance our understanding of the other types of interaction. Furthermore, the implications of the different resolutions achieved by field-based studies of exposed intrusions and geophysical monitoring techniques of active volcanic systems could be explored further.

How do the mechanical properties of the host rock and the magma influence the interaction between sheet intrusions and faults?

The laboratory experiments from **Paper II** indicate that the host rock cohesion exerts a primary control on magma-fault interaction. It influences the ability of the host rock to sustain the dilation of fractures and the formation of sheet intrusions (compared to the formation of other intrusion shapes). Additionally, it affects the strength contrast between faulted and intact crust as well as the degree, to which intrusion-induced strain is accommodated by existing faults.

In high-cohesion host rock, the strength contrast between intact and faulted material tends to be high. Consequently, pre-existing fractures represent a considerable weakness, which can be exploited by propagating intrusions upon intersection. The weaker the host rock, the lower is the strength contrast to the surrounding intact host rock and the less influencial are pre-existing fault segments.

How much of a weakness a fault represents is, however, not only controlled by the host rock cohesion. In nature, the complexity of a fault, its maturity and the question of how active it is can also affect the strength contrast. A fracture or fault may be located in very strong host rock, but still have a low strength contrast to intact rock. This could for example be the case if it is only a single, relatively short fault plane or if it has been locked for a long time and some degree of healing has occurred. Characterizing the mechanical properties of faulted materials is generally challenging for both natural faults and laboratory materials. While the characterization of fault zones and their associated mechanical properties is an active field of research and important information can be retrieved e.g., from partially exhumed faults and laboratory measurements (e.g., Mitchell and Faulkner, 2009; Faulkner et al., 2010), it can often be challenging to characterize the structure and properties of active faults at depth without drilling through the fault in question (e.g., Carpenter et al., 2012; Ikari et al., 2015). More detailed analysis of the role of the strength contrast would require a better understanding of the mechanical properties, especially the cohesion of faulted (analogue and natural) materials and how they evolve with depth and with time.

On the Reykjanes Peninsula, intrusions such as the 2021 Fagradalsfjall dike have caused

extensive seismicity and movement on fractures and faults (Sigmundsson et al., 2022; Ducrocq et al., 2024). This widespread reactivation could imply that a high number of faults currently represent relative weaknesses that could be exploited by future intrusions. Identifying, which of the many reactivated fractures and faults connect to deeper-reaching faults rather than just near-surface fractures, could help to constrain and identify faults especially susceptible to magma intrusion. In other settings, active fault zones related to tectonic stresses, gravitational loading or landslides could form potential pathways for propagating intrusions.

The presence of faults in the experiments of **Paper II** affected the ratio of the uplift volume to the intruded volume. This effect was most pronounced in high-cohesion experiments. If one only observed the surface deformation, as is the case in active systems, this effect could lead to an underestimation of the actual intrusive volume at depth. The reduced ratio of uplifted to intruded volumes is likely related to that strongly faulted materials are slightly more dilated than their intact counterparts. They can accommodate some degree of strain through compaction. Laboratory experiments provide an excellent opportunity to study this effect, since it is possible to collect quantitative information about the intrusive volumes as well as the associated surface deformation.

The range of intermediate cohesion, where a pre-existing fault can be the deciding factor between (analogue) magma pooling at depth or quick ascent towards the surface, was comparatively narrow in the laboratory experiments. It is very likely, that this requires somewhat specific conditions to occur in nature.

The analogue magma viscosities tested in **Paper II** appeared to be a secondary control on intrusion-fault interaction compared to the properties of the host rock. However, magma in nature can span an immense range of viscosities (Gonnermann, 2015; Lesher and Spera, 2015) and our experiments did not capture the full spectrum of natural viscosities.

The dikes mapped at Dyrfjöll for **Paper I** propagated through hyaloclastite that is homogeneous on outcrop scale apart from the presence of fractures. Although hyaloclastite is a relatively soft material (e.g., Eggertsson et al., 2020), it clearly has sufficiently high cohesion to support the formation of sheet intrusions. Some of the dikes at Dyrfjöll furthermore propagated into the lava layers overlying the hyaloclastite. Spatial variations in the host rock material affect not only the cohesion of the crust, but also the fracture density and elastic properties. Variations in the fracture density become evident e.g., by visually comparing the hyaloclastite and overlying lava layers at Dyrfjöll (e.g., photo on Page xxvi at the beginning of Section 1). Hyalcolastite and subaerially erupted lavas are also common on the Reykjanes Peninsula. While **Paper III** did not consider dynamic dike propagation and only considered very simple depth-dependent variations of the elastic properties of the crust, it could be interesting to investigate if propagating dikes are more likely to interact with fractures in one or the other material. This could be done through models of dynamic dike propagation as well as by additional mapping and quantification of fracture populations at locations such as Dyrfjöll to compare interaction of dikes with fractures in both hyaloclastite and in lava layers. Material-dependent variations of the elastic properties may also affect the accumulation of stress in response to e.g., plate motion. Localized stress anomalies could possibly affect the susceptibility of fractures and faults towards reactivation as well as the opening/thickness of intruding dikes, as observed in previous studies (e.g., Geshi et al., 2012).

The experiments of **Paper II** did not consider effects of tectonic stress. This was primarily done to reduce the number of variable parameters in the experiments and to systematically

study the influence of the mechanical material properties. However, considering observations from e.g., the Reykjanes Peninsula and Dyrfjöll, investigating how different tectonic stress fields affect intrusions and intrusion-fault interaction in host rocks of variable cohesion would be a logical topic for future studies. Another parameter worth exploring in the context of magma-fault interaction is the effect of the strain rate and fluid pressure, which both relate to the flow rate of the intruding fluid. The experiments in **Paper II** used a single fluid flow rate for each of the two analogue magmas, but investigating how intrusion geometry and dynamics change with varying flow rates could provide further interesting insights.

How does variable tectonic stress affect dike propagation and the associated surface deformation?

The effect of tectonic stress on surface deformation models was evaluated in **Paper III**. Using the 2021 Fagradalsfjall dike on the Reykjanes Peninsula as a case study demonstrated that tectonic stress can be a sufficient driving mechanism for dike opening. This implies that, given enough magma is available at depth to fill the created space, diking could occur largely passively without requiring significant magmatic overpressure in excess of lithostatic conditions. That tectonic stress played a major role in the emplacement of the 2021 Fagradalsfjall dike is supported by the intense, distributed seismicity and widespread fracture movements that accompanied its emplacement (Sigmundsson et al., 2022; Ducrocq et al., 2024). Additionally, the initial flow rates into the dike as well as initial eruption rates were relatively low (Sigmundsson et al., 2022; Pedersen et al., 2022), indicating that tectonic stresses dominated over magma pressure.

Observed surface deformation could to a large extent be reproduced by a model driven by tectonic stress. Many of the residual signals can likely be related to shallow fault movement. This links well with the observations from **Paper II** that existing fault networks can accommodate intrusion-induced strain and modify surface deformation patterns. Since the dike segments were modelled as striking slightly oblique to the principal stress axes, some amount of shearing was predicted directly above the dike. However, if a hypothetical dike would be perfectly aligned with the governing stress field, it would likely be difficult to differentiate between tectonic stress and magmatic overpressure as the driving mechanism based on surface deformation alone. That tectonic stress can serve as the principal driving mechanism for dike emplacement, as demonstrated by **Paper III**, emphasizes how closely volcanism and tectonics are linked during a magmatic rifting episode. It furthermore emphasizes the importance of considering both together rather than as separate processes.

Although the tectonic stress in our models increased with depth, the opening pattern of the dike plane did not follow this trend. Instead, the area of maximum opening remained close to the center of the modelled dike. When considering depth-dependent variations of the tectonic stress, in general, it may additionally be important to also consider vertical and ideally lateral variations in the elastic properties of the crust for an appropriate estimate of stress associated with the strain caused by plate motion at depth.

The area of maximum dike opening in the stress-driven model was not only located at a different depth than the initial maximum tectonic stress. It additionally was laterally offset from the plate boundary axis, where the driving stress was highest. Instead, the model predicted maximum dike opening to occur on the northern dike segment. This demonstrates

that dike opening in such models is highly sensitive to the orientation of the dike in addition to the amplitude of the stress field. The relative amount of shearing to opening predicted for the two modelled dike segments was furthermore consistent with expectations based on field studies of eroded intrusions (Delaney et al., 1986; Stephens et al., 2018), demonstrating how modelling and field studies can help to inform and validate each other.

In the same manner as the tectonic stress field was used to simulate the emplacement of the 2021 Fagradalsfjall dike, subsequent dike intrusions (at Fagradalsfjall in December 2021, July/August 2022 and July 2023) could be simulated in additional model steps. This could help to track the evolution of the local stress field through time, which may be useful for estimating future rifting and magma emplacement in the area.

Variations of the orientation of dikes mapped at Dyrfjöll in **Paper I** that correlate with their position in the caldera emphasize the importance of considering locally prominent structures when modelling the local stress field. At Dyrfjöll, it is unclear if these local variations in the governing stress field relate to the caldera-bounding faults, material contrasts due to the caldera-filling hyaloclastite or potential topographic effects. If models similar to the one presented in **Paper III** would be implemented for other volcanic systems on the Reykjanes Peninsula, it could be important to consider how the local stress field is affected by e.g., high-temperature geothermal areas and power plants.

An additional aspect to consider in future models are distributed fracture networks. Using the Finite-Element Method, it should be possible to implement them as passive deformation sources in the sense that they are free to move and affect the deformation of the model domain, but without the need to prescribe motion on them. A separate path to advance numerical models is to couple dynamic dike propagation to surface deformation models. This would reduce the number of assumptions enforced on simulated intrusions in term s of their shape and orientation.

About the Multidisciplinary Aspect of This Thesis

The work presented in his thesis demonstrates that the interaction of sheet intrusions with the surrounding host rock is a complex process and that no single method can capture it in all its complexity. I attempted to combine insights from field-based studies of eroded volcanic systems, laboratory experiments and numerical models (Figure 1.1c). Although the individual research projects/papers each focused on a single main method, working with all of them allowed me to view and interpret findings from different standpoints and to reflect on assumptions commonly made (and sometimes forgotten) in the context of individual methods. While this can be challenging, I believe it is generally beneficial and could help to improve communication between researchers of different backgrounds.

Scope for Future Work

While the work in this thesis has provided some new insights about how sheet intrusions interact with crustal heterogeneities, there are many ways in which this work could be continued.

Building on the field-based observations related to research questions 1) and 2), more detailed field studies of different types of dike-fracture interaction would be beneficial. This could

include mapping of new field areas as well as re-examining of already mapped areas. For this purpose, the increasing number of published virtual outcrop models could be very useful. Differentiation between different types of dike-fracture interaction could furthermore be supported by models.

To better understand how weak a fault/fracture needs to be relative to the surrounding crust to be exploited by intruding magma, a more detailed characterization of the mechanical properties of faulted materials and how they change with depth is needed. This applies to faults in nature as well as to materials used in laboratory experiments.

Being able to simulate dike propagation in three dimensions, ideally even with considering variable material properties and pre-existing faults, would be a major advancement, especially related to research question 3). The Finite-Element Method has great potential for being able to advance the current state of research on this topic due the ability to consider complex geometries and variable material properties. If a potential mechanism is found that can simulate dynamic dike propagation in a heterogeneous, pre-fractured 3D model, it would need extensive testing to validate it against commonly used approaches and models. Additionally, any simulation of 3D-propagating dikes would require high mesh resolution and consequently, high computation times and cost. Much work is therefore needed before any such model could be of use in near-real time monitoring. They could, however, proof useful both for simulating different scenarios in long-term hazard assessment as well as to better understand fundamental processes in magmatic plumbing systems. They could thereby help bridge the gap between field-based geological studies of magmatic plumbing systems and largely surface-based geophysical models of active volcanic systems.

The continued rapid development of new technology keeps opening up possibilities to address both new and older research questions. Given that there seems to be no shortage of open questions to explore, now promises to be an exciting time for studying magmatic systems and processes.



References

Abdelmalak, M.M., C. Bulois, R. Mourgues, O. Galland, J.-B. Legland, and C. Gruber. "Description of new dry granular materials of variable cohesion and friction coefficient: Implications for laboratory modeling of the brittle crust." In: *Tectonophysics* 684 (2016). Special Issue on GeoMod 2014 – Modelling in Geoscience, pp. 39–51. ISSN: 0040-1951. DOI: https://doi.org/10.1016/j.tecto.2016.03.003. URL: https://www.sciencedirect.com/science/article/pii/S0040195116001591.

Abdelmalak, M.M., R. Mourgues, O. Galland, and D. Bureau. "Fracture mode analysis and related surface deformation during dyke intrusion: Results from 2D experimental modelling." In: *Earth and Planetary Science Letters* 359-360 (2012), pp. 93–105. ISSN: 0012-821X. DOI: https://doi.org/10.1016/j.epsl.2012.10.008. URL: https://www.sciencedirect.com/science/article/pii/S0012821X12005675.

Acocella, V. and M. Neri. "Dike propagation in volcanic edifices: Overview and possible developments." In: *Tectonophysics* 471.1 (2009). Understanding stress and deformation in active volcanoes, pp. 67–77. ISSN: 0040-1951. DOI: https://doi.org/10.1016/j.tecto.2008.10.002. URL: https://www.sciencedirect.com/science/article/pii/S0040195108004745.

Aloisi, M., A. Bonaccorso, F. Cannavò, G. Currenti, and S. Gambino. "The 24 December 2018 Eruptive Intrusion at Etna Volcano as Revealed by Multidisciplinary Continuous Deformation Networks (CGPS, Borehole Strainmeters and Tiltmeters)." In: *Journal of Geophysical Research: Solid Earth* 125.8 (2020), e2019JB019117. DOI: https://doi.org/10.1029/2019JB019117. eprint: https://agupubs.onlinelibrary.wiley.com/doi/pdf/10.1029/2019JB019117. URL: https://agupubs.onlinelibrary.wiley.com/doi/abs/10.1029/2019JB019117.

Alshembari, R., J. Hickey, B. J. Williamson, and K. Cashman. "Poroelastic Mechanical Behavior of Crystal Mush Reservoirs: Insights Into the Spatio-Temporal Evolution of Volcano Surface Deformation." In: *Journal of Geophysical Research: Solid Earth* 127.10 (2022), e2022JB024332. DOI: https://doi.org/10.1029/2022JB024332. eprint: https://agupubs.onlinelibrary.wiley.com/doi/pdf/10.1029/2022JB024332. URL: https://agupubs.onlinelibrary.wiley.com/doi/abs/10.1029/2022JB024332.

Altamimi, Z., L. Métivier, P. Rebischung, X. Collilieux, K. Chanard, and J. Barnéoud. "ITRF2020 Plate Motion Model." In: *Geophysical Research Letters* 50.24 (2023). e2023GL106373 2023GL106373, e2023GL106373. DOI: https://doi.org/10.1029/2023GL106373. eprint: https://agupubs.onlinelibrary.wiley.com/doi/pdf/10.1029/2023GL106373. URL: https://agupubs.onlinelibrary.wiley.com/doi/abs/10.1029/2023GL106373.

Amelung, Falk, Sigurjón Jónsson, Howard Zebker, and Paul Segall. "Widespread uplift and 'trapdoor' faulting on Galapagos volcanoes observed with radar interferometry." In: *Nature* 407.6807 (2000), pp. 993–996. DOI: https://doi.org/10.1038/35039604.

Anderson, E. M. *The dynamics of faulting and dyke formation with applications to Britain*. 2nd ed. Edinburgh, UK: Oliver and Boyd, 1951.

Annen, C., J.-F. Lénat, and A. Provost. "The long-term growth of volcanic edifices: numerical modelling of the role of dyke intrusion and lava-flow emplacement." In: *Journal of Volcanology and Geothermal Research* 105.4 (2001), pp. 263–289. ISSN: 0377-0273. DOI: https://doi.org/10.1016/S0377-0273(00)00257-2. URL: https://www.sciencedirect.com/science/article/pii/S0377027300002572.

Aoki, Yosuke and Corné Kreemer. "Chapter 1 - Introduction." In: *GNSS Monitoring of the Terrestrial Environment*. Ed. by Y. Aoki and C. Kreemer. Elsevier, 2024, pp. 1–10. ISBN: 978-0-323-95507-2. DOI: https://doi.org/10.1016/B978-0-323-95507-2.00001-3. URL: https://www.sciencedirect.com/science/article/pii/B9780323955072000013.

Auriac, A., K. H. Spaans, F. Sigmundsson, A. Hooper, P. Schmidt, and B. Lund. "Iceland rising: Solid Earth response to ice retreat inferred from satellite radar interferometry and visocelastic modeling." In: *Journal of Geophysical Research: Solid Earth* 118.4 (2013), pp. 1331–1344. DOI: https://doi.org/10.1002/jgrb.50082. eprint: https://agupubs.onlinelibrary.wiley.com/doi/pdf/10.1002/jgrb.50082. URL: https://agupubs.onlinelibrary.wiley.com/doi/abs/10.1002/jgrb.50082.

Baer, G. and M. Beyth. "A mechanism of dyke segmentation in fractured host rock." In: *Mafic dykes and emplacement mechanisms. Balkema, Rotterdam* 3.11 (1990).

Baer, G., M. Beyth, and Z. Reches. "Dikes emplaced into fractured basement, Timna igneous complex, Israel." In: *Journal of Geophysical Research: Solid Earth* 99.B12 (1994), pp. 24039–24050.

Bagnardi, M. and A. Hooper. "Inversion of Surface Deformation Data for Rapid Estimates of Source Parameters and Uncertainties: A Bayesian Approach." In: *Geochemistry, Geophysics, Geosystems* 19.7 (2018), pp. 2194–2211. DOI: https://doi.org/10.1029/2018GC007585. eprint: https://agupubs.onlinelibrary.wiley.com/doi/pdf/10.1029/2018GC007585. URL: https://agupubs.onlinelibrary.wiley.com/doi/abs/10.1029/2018GC007585.

Battaglia, M., P. F. Cervelli, and J. R. Murray. "dMODELS: A MATLAB software package for modeling crustal deformation near active faults and volcanic centers." In: *Journal of Volcanology and Geothermal Research* 254 (2013), pp. 1–4. ISSN: 0377-0273. DOI: https://doi.org/10.1016/j.jvolgeores.2012.12.018. URL: https://www.sciencedirect.com/science/article/pii/S0377027312003836.

Belart, J. M.C., V. Pinel, H. I. Reynolds, E. Berthier, and S. R. Gunnarson. *Digital Elevation Models (DEMs) and lava outlines from the 2023 Litla-Hrútur eruption, Iceland, from Pléiades satellite stereoimages*. Version 1. Oct. 2023. DOI: 10.5281/zenodo.8414866. URL: https://doi.org/10.5281/zenodo.8414866.

Bemis, S. P., S. Micklethwaite, D. Turner, M. R. James, S. Akciz, S. T. Thiele, and H. A. Bangash. "Ground-based and UAV-Based photogrammetry: A multi-scale, high-resolution mapping tool for structural geology and paleoseismology." In: *Journal of Structural Geology* 69 (2014), pp. 163–178. ISSN: 0191-8141. DOI: https://doi.org/10.1016/j.jsg.2014.10.007. URL: https://www.sciencedirect.com/science/article/pii/S0191814114002429.

Ben-Yehoshua, D., Þ. Sæmundsson, S. Erlingsson, J. K. Helgason, R. L. Hermanns, E. Magnússon, B. G. Ófeigsson, J. M.C. Belart, Á. R. Hjartardóttir, H. Geirsson, S. Guðmundsson,

H. Hannesdóttir, F. Pálsson, V. Drouin, and B. H. Bergsson. “The destabilization of a large mountain slope controlled by thinning of Svínafellsjökull glacier, SE Iceland.” In: *Jökull* 73 (2023). DOI: https://doi.org/10.33799/jokull2023.73.001.

Berg, S. E. “Silicic magma genesis in basalt-dominated oceanic settings: examples from Iceland and the Canary Islands.” PhD thesis. Acta Universitatis Upsaliensis, 2016.

Bertelsen, H. S., B.D. Rogers, O. Galland, G. Dumazer, and Al Abbana Bennani. “Laboratory modelling of coeval brittle and ductile deformation during magma emplacement into viscoelastic rocks.” In: *Frontiers in Earth Science* 6 (2018). DOI: https://doi.org/10.3389/feart.2018.00199.

Björnsson, S., P. Einarsson, H. Tulinius, and Á. R. Hjartardóttir. “Seismicity of the Reykjanes Peninsula 1971–1976.” In: *Journal of Volcanology and Geothermal Research* 391 (2020), p. 106369. ISSN: 0377-0273. DOI: https://doi.org/10.1016/j.jvolgeores.2018.04.026. URL: https://www.sciencedirect.com/science/article/pii/S0377027317306315.

Bonafede, M. and E. Rivalta. “On tensile cracks close to and across the interface between two welded elastic half-spaces.” In: *Geophysical Journal International* 138.2 (Aug. 1999), pp. 410–434. ISSN: 0956-540X. DOI: 10.1046/j.1365-246X.1999.00880.x. eprint: https://academic.oup.com/gji/article-pdf/138/2/410/6089640/138-2-410.pdf. URL: https://doi.org/10.1046/j.1365-246X.1999.00880.x.

Breitkreuz, C. and S. Rocchi. *Physical geology of shallow magmatic systems — Dykes, sills and laccoliths*. Advances in Volcanology. Springer Berlin Heidelberg, 2018. ISBN: 978-3-319-14084-1. DOI: https://doi.org/10.1007/978-3-319-14084-1.

Browning, J. and A. Gudmundsson. “Caldera faults capture and deflect inclined sheets: an alternative mechanism of ring dike formation.” In: *Bulletin of Volcanology* 77 (2015), pp. 1–13. DOI: https://doi.org/10.1007/s00445-014-0889-4.

Buck, W. R., P. Einarsson, and B. Brandsdóttir. “Tectonic stress and magma chamber size as controls on dike propagation: Constraints from the 1975–1984 Krafla rifting episode.” In: *Journal of Geophysical Research: Solid Earth* 111.B12 (2006). DOI: https://doi.org/10.1029/2005JB003879. eprint: https://agupubs.onlinelibrary.wiley.com/doi/pdf/10.1029/2005JB003879. URL: https://agupubs.onlinelibrary.wiley.com/doi/abs/10.1029/2005JB003879.

Buckingham, E. “On Physically Similar Systems; Illustrations of the Use of Dimensional Equations.” In: *Phys. Rev.* 4 (4 1914), pp. 345–376. DOI: 10.1103/PhysRev.4.345. URL: https://link.aps.org/doi/10.1103/PhysRev.4.345.

Bufféral, S., E. Panza, S. Mannini, Á. R. Hjartardóttir, A. Nobile, N. Gies, B. V. Óskarsson, and J. Ruch. “Surface fractures generated during the 2021 Reykjanes oblique rifting event (SW Iceland).” In: *Bulletin of Volcanology* 85.11 (2023), p. 64. DOI: https://doi.org/10.1007/s00445-023-01666-9.

Burchardt, S. “New insights into the mechanics of sill emplacement provided by field observations of the Njardvik Sill, Northeast Iceland.” In: *Journal of Volcanology and Geothermal Research* 173.3 (2008), pp. 280–288. ISSN: 0377-0273. DOI: https://doi.org/10.1016/j.jvolgeores.2008.02.009. URL: https://www.sciencedirect.com/science/article/pii/S0377027308000838.

– *Volcanic and Igneous Plumbing Systems: Understanding Magma Transport, Storage, and Evolution in the Earth’s Crust*. Elsevier, 2018. DOI: https://doi.org/10.1016/C2015-0-06837-X.

Burchardt, S., M. Bazargan, E. Bessi Gestsson, C. Hieronymus, E. Ronchin, H. Tuffen, M. J. Heap, J. Davidson, B. Kennedy, A. Hobé, and E. Saubin. "Geothermal potential of small sub-volcanic intrusions in a typical Icelandic caldera setting." In: *Volcanica* 5.2 (2022), 477–507. DOI: 10.30909/vol.05.02.477507. URL: https://www.jvolcanica.org/ojs/index.php/volcanica/article/view/118.

Burchardt, S. and O. Galland. "Studying Volcanic Plumbing Systems – Multidisciplinary Approaches to a Multifaceted Problem." In: *Updates in Volcanology*. Ed. by K. Nemeth. Rijeka: IntechOpen, 2016. Chap. 2. DOI: 10.5772/63959. URL: https://doi.org/10.5772/63959.

Burchardt, S., B. Oskarsson, L. Gustafsson, S. E. Berg, and M. S. Riishuus. "Geology of a Neogene caldera cluster in the Borgarfjörður eystri - Loðmundarfjörður area, Eastern Iceland." In: *Volcanica* 5.1 (2022), 133–161. DOI: 10.30909/vol.05.01.133161. URL: http://jvolcanica.org/ojs/index.php/volcanica/article/view/120.

Burchardt, S., D. C. Tanner, and M. Krumbholz. "Mode of emplacement of the Slaufrudalur Pluton, Southeast Iceland inferred from three-dimensional GPS mapping and model building." In: *Tectonophysics* 480.1 (2010), pp. 232–240. ISSN: 0040-1951. DOI: https://doi.org/10.1016/j.tecto.2009.10.010. URL: https://www.sciencedirect.com/science/article/pii/S0040195109005800.

Burchardt, S., D. C. Tanner, V. R. Troll, M. Krumbholz, and L. E. Gustafsson. "Three-dimensional geometry of concentric intrusive sheet swarms in the Geitafell and the Dyrfjöll volcanoes, eastern Iceland." In: *Geochemistry, Geophysics, Geosystems* 12.7 (2011). DOI: https://doi.org/10.1029/2011GC003527. URL: https://agupubs.onlinelibrary.wiley.com/doi/abs/10.1029/2011GC003527.

Carpenter, B.M., D.M. Saffer, and C. Marone. "Frictional properties and sliding stability of the San Andreas fault from deep drill core." In: *Geology* 40.8 (Aug. 2012), pp. 759–762. ISSN: 0091-7613. DOI: 10.1130/G33007.1. eprint: https://pubs.geoscienceworld.org/gsa/geology/article-pdf/40/8/759/3543748/759.pdf. URL: https://doi.org/10.1130/G33007.1.

Clifton, A. E. and S. A. Kattenhorn. "Structural architecture of a highly oblique divergent plate boundary segment." In: *Tectonophysics* 419.1 (2006), pp. 27–40. ISSN: 0040-1951. DOI: https://doi.org/10.1016/j.tecto.2006.03.016. URL: https://www.sciencedirect.com/science/article/pii/S0040195106001673.

Clifton, A. E. and R. W. Schlische. "Fracture populations on the Reykjanes Peninsula, Iceland: Comparison with experimental clay models of oblique rifting." In: *Journal of Geophysical Research: Solid Earth* 108.B2 (2003). DOI: https://doi.org/10.1029/2001JB000635. eprint: https://agupubs.onlinelibrary.wiley.com/doi/pdf/10.1029/2001JB000635. URL: https://agupubs.onlinelibrary.wiley.com/doi/abs/10.1029/2001JB000635.

Clough, R. W. "Original formulation of the finite element method." In: *Finite Elements in Analysis and Design* 7.2 (1990), pp. 89–101. ISSN: 0168-874X. DOI: https://doi.org/10.1016/0168-874X(90)90001-U. URL: https://www.sciencedirect.com/science/article/pii/0168874X9090001U.

– "The Finite Element Method in Plane Stress Analysis." In: *Proceedings*. American Society of Civil Engineers, 2nd Conference on Electronic Computation, Pittsburgh, PA, 1960, pp. 345–378.

Collier, P. “Photogrammetry and Aerial Photography.” In: *International Encyclopedia of Human Geography (Second Edition)*. Ed. by A. Kobayashi. Second Edition. Oxford: Elsevier, 2020, pp. 91–98. ISBN: 978-0-08-102296-2. DOI: https://doi.org/10.1016/B978-0-08-102295-5.10583-9. URL: https://www.sciencedirect.com/science/article/pii/B9780081022955105839.

Coulomb, C. A. “Application des règles de maxima et minima à quelques problèmes de statique relatifs à l’Architecture [Application of the rules of maxima and minima to some problems of statics related to architecture].” In: *Acad. Roy. Sci. Mem. Math. Phys.* 7 (1773), pp. 343–82.

Courant, R. “Variational Methods for the Solution of Problems of Equilibrium and Vibrations.” In: *Bullettin of the American Mathematical Society* 49 (1943), pp. 1–23.

Currenti, G., A. Bonaccorso, C. Del Negro, F. Guglielmino, D. Scandura, and E. Boschi. “FEM-based inversion for heterogeneous fault mechanisms: application at Etna volcano by DInSAR data.” In: *Geophysical Journal International* 183.2 (2010), pp. 765–773. ISSN: 0956-540X. DOI: 10.1111/j.1365-246X.2010.04769.x. eprint: https://academic.oup.com/gji/article-pdf/183/2/765/1854509/183-2-765.pdf. URL: https://doi.org/10.1111/j.1365-246X.2010.04769.x.

Currenti, G., C. Del Negro, G. Ganci, and D. Scandura. “3D numerical deformation model of the intrusive event forerunning the 2001 Etna eruption.” In: *Physics of the Earth and Planetary Interiors* 168.1 (2008), pp. 88–96. ISSN: 0031-9201. DOI: https://doi.org/10.1016/j.pepi.2008.05.004. URL: https://www.sciencedirect.com/science/article/pii/S0031920108000897.

Currenti, G., R. Napoli, A. Di Stefano, F. Greco, and C. Del Negro. “3D integrated geophysical modeling for the 2008 magma intrusion at Etna: Constraints on rheology and dike overpressure.” In: *Physics of the Earth and Planetary Interiors* 185.1 (2011), pp. 44–52. ISSN: 0031-9201. DOI: https://doi.org/10.1016/j.pepi.2011.01.002. URL: https://www.sciencedirect.com/science/article/pii/S0031920111000124.

Currenti, G. and C. A. Williams. “Numerical modeling of deformation and stress fields around a magma chamber: Constraints on failure conditions and rheology.” In: *Physics of the Earth and Planetary Interiors* 226 (2014), pp. 14–27. ISSN: 0031-9201. DOI: https://doi.org/10.1016/j.pepi.2013.11.003. URL: https://www.sciencedirect.com/science/article/pii/S0031920113001623.

Daubrée, A. *Recherches expérimentales sur le rôle possible des gaz à hautes températures doués de très fortes pressions et animés d’un mouvement fort rapide dans divers phénomènes géologiques*. Société géologique de France, 1891.

De Pascale, G. P., T. J. Fischer, W. M. Moreland, H. Geirsson, P. Hrubcová, V. Drouin, D. Forester, M. Payet-Clerc, D. B. da Silveira, J. Vlček, B. G. Ófeigsson, Á. Höskuldsson, H. K. Torfadóttir, I. K. Valdimarsdóttir, B. D. Jónsdóttir Blöndal, I. Jónsdóttir, S. Jónsson, and Th. Thordarson. “On the Move: 2023 Observations on Real Time Graben Formation, Grindavík, Iceland.” In: *Geophysical Research Letters* 51.14 (2024). e2024GL110150 2024GL110150, e2024GL110150. DOI: https://doi.org/10.1029/2024GL110150. eprint: https://agupubs.onlinelibrary.wiley.com/doi/pdf/10.1029/2024GL110150. URL: https://agupubs.onlinelibrary.wiley.com/doi/abs/10.1029/2024GL110150.

Del Negro, C., G. Currenti, and D. Scandura. "Temperature-dependent viscoelastic modeling of ground deformation: Application to Etna volcano during the 1993–1997 inflation period." In: *Physics of the Earth and Planetary Interiors* 172.3 (2009), pp. 299–309. ISSN: 0031-9201. DOI: https://doi.org/10.1016/j.pepi.2008.10.019. URL: https://www.sciencedirect.com/science/article/pii/S0031920108003087.

Delaney, P. T., D. D. Pollard, J. I. Ziony, and E. H. McKee. "Field relations between dikes and joints: Emplacement processes and paleostress analysis." In: *Journal of Geophysical Research: Solid Earth* 91.B5 (1986), pp. 4920–4938. DOI: https://doi.org/10.1029/JB091iB05p04920. URL: https://agupubs.onlinelibrary.wiley.com/doi/abs/10.1029/JB091iB05p04920.

DeMets, C., R. G. Gordon, and D. F. Argus. "Geologically current plate motions." In: *Geophysical Journal International* 181.1 (Apr. 2010), pp. 1–80. ISSN: 0956-540X. DOI: 10.1111/j.1365-246X.2009.04491.x. eprint: https://academic.oup.com/gji/article-pdf/181/1/1/17360517/181-1-1.pdf. URL: https://doi.org/10.1111/j.1365-246X.2009.04491.x.

Dering, G. M., S. Micklethwaite, A. R. Cruden, S. J. Barnes, and M. L. Fiorentini. "Evidence for dyke-parallel shear during syn-intrusion fracturing." In: *Earth and Planetary Science Letters* 507 (2019), pp. 119–130. ISSN: 0012-821X. DOI: https://doi.org/10.1016/j.epsl.2018.10.024. URL: https://www.sciencedirect.com/science/article/pii/S0012821X18306204.

Dering, G. M., S. Micklethwaite, S. T. Thiele, S. A. Vollgger, and A. R. Cruden. "Review of drones, photogrammetry and emerging sensor technology for the study of dykes: Best practises and future potential." In: *Journal of Volcanology and Geothermal Research* 373 (2019), pp. 148–166. ISSN: 0377-0273. DOI: https://doi.org/10.1016/j.jvolgeores.2019.01.018. URL: https://www.sciencedirect.com/science/article/pii/S0377027318302294.

Dieterich, James H. and Robert W. Decker. "Finite element modeling of surface deformation associated with volcanism." In: *Journal of Geophysical Research (1896-1977)* 80.29 (1975), pp. 4094–4102. DOI: https://doi.org/10.1029/JB080i029p04094. eprint: https://agupubs.onlinelibrary.wiley.com/doi/pdf/10.1029/JB080i029p04094. URL: https://agupubs.onlinelibrary.wiley.com/doi/abs/10.1029/JB080i029p04094.

Dolphin, G., A. Dutchak, B. Karchewski, and J. Cooper. "Virtual field experiences in introductory geology: Addressing a capacity problem, but finding a pedagogical one." In: *Journal of Geoscience Education* 67.2 (2019), pp. 114–130. DOI: 10.1080/10899995.2018.1547034. eprint: https://doi.org/10.1080/10899995.2018.1547034. URL: https://doi.org/10.1080/10899995.2018.1547034.

Drouin, V. and F. Sigmundsson. "Countrywide Observations of Plate Spreading and Glacial Isostatic Adjustment in Iceland Inferred by Sentinel-1 Radar Interferometry, 2015–2018." In: *Geophysical Research Letters* 46.14 (2019), pp. 8046–8055. DOI: https://doi.org/10.1029/2019GL082629. eprint: https://agupubs.onlinelibrary.wiley.com/doi/pdf/10.1029/2019GL082629. URL: https://agupubs.onlinelibrary.wiley.com/doi/abs/10.1029/2019GL082629.

Drymoni, K., J. Browning, and A. Gudmundsson. "Dyke-arrest scenarios in extensional regimes: Insights from field observations and numerical models, Santorini, Greece." In: *Journal of Volcanology and Geothermal Research* 396 (2020), p. 106854. ISSN: 0377-

0273. DOI: https://doi.org/10.1016/j.jvolgeores.2020.106854. URL: https://www.sciencedirect.com/science/article/pii/S0377027319305293.
– "Spatial and temporal volcanotectonic evolution of Santorini volcano, Greece." In: *Bulletin of Volcanology* 84.6 (2022), p. 60. DOI: https://doi.org/10.1007/s00445-022-01566-4.
Ducrocq, C., Th. Árnadóttir, P. Einarsson, S. Jónsson, V. Drouin, H. Geirsson, and Á. R. Hjartardóttir. "Widespread fracture movements during a volcano-tectonic unrest: the Reykjanes Peninsula, Iceland, from 2019–2021 TerraSAR-X interferometry." In: *Bulletin of Volcanology* 86.2 (2024), p. 14. DOI: https://doi.org/10.1007/s00445-023-01699-0.
Dzurisin, D. "The global positioning system: A multipurpose tool." In: *Volcano Deformation: Geodetic Monitoring Techniques*. Ed. by D. Dzurisin. Springer, 2007, pp. 111–152. DOI: https://doi.org/10.1007/978-3-540-49302-0_4.
– *Volcano deformation: new geodetic monitoring techniques*. Springer, 2007. DOI: https://doi.org/10.1007/978-3-540-49302-0.
Dzurisin, D. and Z. Lu. "Interferometric synthetic-aperture radar (InSAR)." In: *Volcano deformation: Geodetic monitoring techniques*. Springer, 2007, pp. 153–194. DOI: https://doi.org/10.1007/978-3-540-49302-0_5.
Eggertsson, G. H., J. E. Kendrick, J. Weaver, P. A Wallace, J. E.P. Utley, J. D. Bedford, M. J. Allen, S. H. Markússon, R. H. Worden, D. R. Faulkner, and Y. Lavallée. "Compaction of hyaloclastite from the active geothermal system at Krafla volcano, Iceland." In: *Geofluids* (2020), pp. 1–17. DOI: 10.1155/2020/3878503. URL: https://doi.org/10.1155/2020/3878503.
Einarsson, P. "Plate boundaries, rifts and transforms in Iceland." In: *Jökull* 58 (2008), pp. 35–58.
Einarsson, P., V. Eyjólfsson, and Á. R. Hjartardóttir. "Tectonic framework and fault structures in the Fagradalsfjall segment of the Reykjanes Peninsula Oblique Rift, Iceland." In: *Bulletin of Volcanology* 85.2 (2023), p. 9. DOI: https://doi.org/10.1007/s00445-022-01624-x.
Einarsson, P., Á. R. Hjartardóttir, S. Hreinsdóttir, and P. Imsland. "The structure of seismogenic strike-slip faults in the eastern part of the Reykjanes Peninsula Oblique Rift, SW Iceland." In: *Journal of Volcanology and Geothermal Research* 391 (2020), p. 106372. ISSN: 0377-0273. DOI: https://doi.org/10.1016/j.jvolgeores.2018.04.029. URL: https://www.sciencedirect.com/science/article/pii/S0377027317303955.
Eltner, Anette and Giulia Sofia. "Chapter 1 - Structure from motion photogrammetric technique." In: *Remote Sensing of Geomorphology*. Ed. by Paolo Tarolli and Simon M. Mudd. Vol. 23. Developments in Earth Surface Processes. Elsevier, 2020, pp. 1–24. DOI: https://doi.org/10.1016/B978-0-444-64177-9.00001-1. URL: https://www.sciencedirect.com/science/article/pii/B9780444641779000011.
Espinosa-Leal, J., J. Browning, J. Cembrano, T. Mitchell, F. Rojas, M. Moorkamp, W. A. Griffith, and P. Meredith. "Fault intersection-related stress rotation controls magma emplacement at the Nevados de Chillán Volcanic Complex." In: *Journal of Volcanology and Geothermal Research* 458 (2025), p. 108255. ISSN: 0377-0273. DOI: https://

doi.org/10.1016/j.jvolgeores.2024.108255. URL: https://www.sciencedirect.com/science/article/pii/S0377027324002488.

Faulkner, D.R., C.A.L. Jackson, R.J. Lunn, R.W. Schlische, Z.K. Shipton, C.A.J. Wibberley, and M.O. Withjack. "A review of recent developments concerning the structure, mechanics and fluid flow properties of fault zones." In: *Journal of Structural Geology* 32.11 (2010). Fault Zones, pp. 1557–1575. ISSN: 0191-8141. DOI: https://doi.org/10.1016/j.jsg.2010.06.009. URL: https://www.sciencedirect.com/science/article/pii/S019181411000101X.

Favalli, M., A. Fornaciai, I. Isola, S. Tarquini, and L. Nannipieri. "Multiview 3D reconstruction in geosciences." In: *Computers & Geosciences* 44 (2012), pp. 168–176. ISSN: 0098-3004. DOI: https://doi.org/10.1016/j.cageo.2011.09.012. URL: https://www.sciencedirect.com/science/article/pii/S0098300411003128.

Fischer, T., P. Hrubcová, A. Salama, J. Doubravová, T. Ágústsdóttir, E.Á. Gudnason, J. Horálek, and G.P. Hersir. "Swarm seismicity illuminates stress transfer prior to the 2021 Fagradalsfjall eruption in Iceland." In: *Earth and Planetary Science Letters* 594 (2022), p. 117685. ISSN: 0012-821X. DOI: https://doi.org/10.1016/j.epsl.2022.117685. URL: https://www.sciencedirect.com/science/article/pii/S0012821X22003211.

Flóvenz, Ó. G., R. Wang, G. P. Hersir, T. Dahm, S. Hainzl, M. Vassileva, V. Drouin, S. Heimann, M. P. Isken, E. Á. Gudnason, K. Ágústsson, Th. Ágústsdóttir, J. Horálek, M. Motagh, T. R. Walter, E. Rivalta, R. Jousset, C. M. Krawczyk, and C. Milkereit. "Cyclical geothermal unrest as a precursor to Iceland's 2021 Fagradalsfjall eruption." In: *Nature Geoscience* 15.5 (2022), pp. 397–404. DOI: https://doi.org/10.1038/s41561-022-00930-5.

Foulger, G.R., G. Beutler, R. Bilham, P. Einarsson, S. Fankhauser, W. Gurtner, U. Hugentobler, W. J. Morgan, M. Rothacher, G. Thorbergsson, and U. Wild. "The Iceland 1986 GPS geodetic survey: Tectonic goals and data processing results." In: *Bulletin géodésique* 67 (1993), pp. 148–172. DOI: https://doi.org/10.1007/BF00806254.

Gaffney, E. S., B. Damjanac, and G. A. Valentine. "Localization of volcanic activity: 2. Effects of pre-existing structure." In: *Earth and Planetary Science Letters* 263.3 (2007), pp. 323–338. ISSN: 0012-821X. DOI: https://doi.org/10.1016/j.epsl.2007.09.002. URL: https://www.sciencedirect.com/science/article/pii/S0012821X07005614.

Galland, O. "Experimental modelling of ground deformation associated with shallow magma intrusions." In: *Earth and Planetary Science Letters* 317-318 (2012), pp. 145–156. ISSN: 0012-821X. DOI: https://doi.org/10.1016/j.epsl.2011.10.017. URL: https://www.sciencedirect.com/science/article/pii/S0012821X11006121.

Galland, O., H. S. Bertelsen, F. Guldstrand, L. Girod, R. F. Johannessen, F. Bjugger, S. Burchardt, and K. Mair. "Application of open-source photogrammetric software MicMac for monitoring surface deformation in laboratory models." In: *Journal of Geophysical Research: Solid Earth* 121.4 (2016), pp. 2852–2872. DOI: https://doi.org/10.1002/2015JB012564. URL: https://agupubs.onlinelibrary.wiley.com/doi/abs/10.1002/2015JB012564.

Galland, O., P. R. Cobbold, E. Hallot, J. de Bremond d'Ars, and G. Delavaud. "Use of vegetable oil and silica powder for scale modelling of magmatic intrusion in a deforming brittle crust." In: *Earth and Planetary Science Letters* 243.3 (2006), pp. 786–804. ISSN:

0012-821X. DOI: https://doi.org/10.1016/j.epsl.2006.01.014. URL: https://www.sciencedirect.com/science/article/pii/S0012821X06000276.

Galland, O., E. Holohan, B. Van Wyk de Vries, and S. Burchardt. "Laboratory modelling of volcano plumbing systems: a review." In: *Physical Geology of Shallow Magmatic Systems: Dykes, Sills and Laccoliths* (2018), pp. 147–214.

Geirsson, H., M. M. Parks, F. Sigmundsson, V. Drouin, B. G. Ófeigsson, C. Lanzi, Á. G. Birgisdóttir, C. Ducrocq, A. Hooper, P. Einarsson, K. Jónsdóttir, S. Hreinsdóttir, and S. H. M. Greiner. "Deformation patterns of the Reykjanes Peninsula unrest 2020-2024, Iceland: evidence for interconnected neighboring volcanic systems." In: 2024. DOI: https://doi.org/10.5194/egusphere-egu24-18235.

Geshi, N., S. Kusumoto, and A. Gudmundsson. "Effects of mechanical layering of host rocks on dike growth and arrest." In: *Journal of Volcanology and Geothermal Research* 223-224 (2012), pp. 74–82. ISSN: 0377-0273. DOI: https://doi.org/10.1016/j.jvolgeores.2012.02.004. URL: https://www.sciencedirect.com/science/article/pii/S0377027312000340.

– "Geometric difference between non-feeder and feeder dikes." In: *Geology* 38.3 (Mar. 2010), pp. 195–198. ISSN: 0091-7613. DOI: 10.1130/G30350.1. eprint: https://pubs.geoscienceworld.org/gsa/geology/article-pdf/38/3/195/3538185/195.pdf. URL: https://doi.org/10.1130/G30350.1.

Gibbings, J. C. *Dimensional analysis*. Springer Science & Business Media, 2011. DOI: https://doi.org/10.1007/978-1-84996-317-6.

Givens, T. "Modeling Holocene Glacial Isostatic Adjustment in Iceland Using Composite Asthenosphere Viscosity, Comparisons to Linear Rheology and Implications for Glacially Induced Asthenosphere Melting." PhD thesis. Pennsylvania State University, 2025.

Gonnermann, H. M. "Magma Fragmentation." In: *Annual Review of Earth and Planetary Sciences* 43.1 (2015), pp. 431–458. DOI: 10.1146/annurev-earth-060614-105206. eprint: https://doi.org/10.1146/annurev-earth-060614-105206. URL: https://doi.org/10.1146/annurev-earth-060614-105206.

Gottsmann, J., M. Flynn, and J. Hickey. "The Transcrustal Magma Reservoir Beneath Soufrière Hills Volcano, Montserrat: Insights From 3-D Geodetic Inversions." In: *Geophysical Research Letters* 47.20 (2020). e2020GL089239 2020GL089239, e2020GL089239. DOI: https://doi.org/10.1029/2020GL089239. eprint: https://agupubs.onlinelibrary.wiley.com/doi/pdf/10.1029/2020GL089239. URL: https://agupubs.onlinelibrary.wiley.com/doi/abs/10.1029/2020GL089239.

Greiner, S. H. M. and H. Geirsson. "Including a pressure dependent relation between static and dynamic elastic moduli in a Finite Element deformation model of Grímsvötn Volcano, Iceland." In: *Volcanica* 7.2 (2024), 907–924. DOI: 10.30909/vol.07.02.907924. URL: https://www.jvolcanica.org/ojs/index.php/volcanica/article/view/300.

Guillaume, L., V. Laurent, and M. J. Genge. "Immersive and interactive three-dimensional virtual fieldwork: Assessing the student learning experience and value to improve inclusivity of geosciences degrees." In: *Journal of Geoscience Education* 71.4 (2023), pp. 462–475. DOI: 10.1080/10899995.2023.2200361. eprint: https://doi.org/10.

1080/10899995.2023.2200361. URL: https://doi.org/10.1080/10899995.2023.2200361.

Guldstrand, F., S. Burchardt, E. Hallot, and O. Galland. "Dynamics of Surface Deformation Induced by Dikes and Cone Sheets in a Cohesive Coulomb Brittle Crust." In: *Journal of Geophysical Research: Solid Earth* 122.10 (2017), pp. 8511–8524. DOI: https://doi.org/10.1002/2017JB014346. eprint: https://agupubs.onlinelibrary.wiley.com/doi/pdf/10.1002/2017JB014346. URL: https://agupubs.onlinelibrary.wiley.com/doi/abs/10.1002/2017JB014346.

Gunnarson, S. R., J. M. C. Belart, B. V. Óskarsson, M. T. Gudmundsson, Th. Högnadóttir, G. B. M. Pedersen, T. Dürig, and V. Pinel. *Automated processing of aerial imagery for geohazards monitoring: Results from Fagradalsfjall eruption, SW Iceland, August 2022*. Version 1.1. Apr. 2023. DOI: 10.5281/zenodo.7871187. URL: https://doi.org/10.5281/zenodo.7871187.

Gústafsson, L. E. "Geology and petrography of the Dyrfjöll Central Volcano, eastern Iceland." PhD thesis. Fachbereich Geowiss., FU, 1992.

Hall, James. "II. On the Vertical Position and Convolutions of certain Strata, and their relation with Granite." In: *Transactions of the Royal Society of Edinburgh* 7.1 (1815), 79–108. DOI: 10.1017/S0080456800019268.

Hautmann, Stefanie, Joachim Gottsmann, R. Stephen J. Sparks, Glen S. Mattioli, I. Selwyn Sacks, and Michael H. Strutt. "Effect of mechanical heterogeneity in arc crust on volcano deformation with application to Soufrière Hills Volcano, Montserrat, West Indies." In: *Journal of Geophysical Research: Solid Earth* 115.B9 (2010). DOI: https://doi.org/10.1029/2009JB006909. eprint: https://agupubs.onlinelibrary.wiley.com/doi/pdf/10.1029/2009JB006909. URL: https://agupubs.onlinelibrary.wiley.com/doi/abs/10.1029/2009JB006909.

Healy, D. *FracTend*. Accessed 12. April 2022. 2018. URL: https://github.com/DaveHealy-github/FracTend.

Heap, M. J., M. Villeneuve, F. Albino, J. I. Farquharson, E. Brothelande, F. Amelung, J.-L. Got, and P. Baud. "Towards more realistic values of elastic moduli for volcano modelling." In: *Journal of Volcanology and Geothermal Research* 390 (2020), p. 106684. ISSN: 0377-0273. DOI: https://doi.org/10.1016/j.jvolgeores.2019.106684. URL: https://www.sciencedirect.com/science/article/pii/S0377027319304044.

Heimisson, E. R. and P. Segall. "Physically Consistent Modeling of Dike-Induced Deformation and Seismicity: Application to the 2014 Bárdarbunga Dike, Iceland." In: *Journal of Geophysical Research: Solid Earth* 125.2 (2020). e2019JB018141 10.1029/2019JB018141, e2019JB018141. DOI: https://doi.org/10.1029/2019JB018141. eprint: https://agupubs.onlinelibrary.wiley.com/doi/pdf/10.1029/2019JB018141. URL: https://agupubs.onlinelibrary.wiley.com/doi/abs/10.1029/2019JB018141.

Heimsath, A. M and H. Farid. "Hillslope topography from unconstrained photographs." In: *Mathematical Geology* 34 (2002), pp. 929–952. DOI: https://doi.org/10.1023/A:1021364623017.

Hickey, J. and J. Gottsmann. "Benchmarking and developing numerical Finite Element models of volcanic deformation." In: *Journal of Volcanology and Geothermal Research* 280 (2014), pp. 126–130. ISSN: 0377-0273. DOI: https://doi.org/10.1016/

j.jvolgeores.2014.05.011. URL: https://www.sciencedirect.com/science/article/pii/S037702731400153X.

Hickey, J., J. Gottsmann, and P. Mothes. "Estimating volcanic deformation source parameters with a finite element inversion: The 2001–2002 unrest at Cotopaxi volcano, Ecuador." In: *Journal of Geophysical Research: Solid Earth* 120.3 (2015), pp. 1473–1486. DOI: https://doi.org/10.1002/2014JB011731. eprint: https://agupubs.onlinelibrary.wiley.com/doi/pdf/10.1002/2014JB011731. URL: https://agupubs.onlinelibrary.wiley.com/doi/abs/10.1002/2014JB011731.

Hjartardóttir, Á. R., T. Dürig, M. Parks, V. Drouin, V. Eyjólfsson, H. Reynolds, P. Einarsson, E. H. Jensen, B. V. Óskarsson, J. M.C. Belart, J. Ruch, N. B. Gies, and G. B. M. Pedersen. "Pre-existing fractures and eruptive vent openings during the 2021 Fagradalsfjall eruption, Iceland." In: *Bulletin of Volcanology* 85.10 (2023), p. 56. DOI: https://doi.org/10.1007/s00445-023-01670-z.

Hofer-Apostolidis, K., J. Cembrano, J. Browning, P. Pérez-Flores, T. M. Mitchell, P. G. Meredith, F. Rojas, and T. Xu. "Fracture growth and damage zone evolution in fault-vein systems determined through scaling relations in alteration halo-bearing hydrothermal veins." In: *Journal of Structural Geology* 187 (2024), p. 105219. ISSN: 0191-8141. DOI: https://doi.org/10.1016/j.jsg.2024.105219. URL: https://www.sciencedirect.com/science/article/pii/S0191814124001718.

Hooper, A., B. Ófeigsson, F. Sigmundsson, B. Lund, P. Einarsson, H. Geirsson, and E. Sturkell. "Increased capture of magma in the crust promoted by ice-cap retreat in Iceland." In: *Nature Geoscience* 4.11 (2011), pp. 783–786. DOI: https://doi.org/10.1038/ngeo1269.

Hrennikoff, A. "Solution of problems of elasticity by the framework method." In: (1941).

Hubbert, M. King. "Theory of scale models as applied to the study of geologic structures." In: *GSA Bulletin* 48.10 (Oct. 1937), pp. 1459–1520. ISSN: 0016-7606. DOI: 10.1130/GSAB-48-1459. eprint: https://pubs.geoscienceworld.org/gsa/gsabulletin/article-pdf/48/10/1459/3415436/BUL48_10-1459.pdf. URL: https://doi.org/10.1130/GSAB-48-1459.

Hubbert, M. King and David G. Willis. "Mechanics Of Hydraulic Fracturing." In: *Transactions of the AIME* 210.01 (1957), pp. 153–168. ISSN: 0081-1696. DOI: 10.2118/686-G. eprint: https://onepetro.org/TRANS/article-pdf/210/01/153/2176767/spe-686-g.pdf. URL: https://doi.org/10.2118/686-G.

Huismans, R. and C. Beaumont. "Depth-dependent extension, two-stage breakup and cratonic underplating at rifted margins." In: *Nature* 473.7345 (2011), pp. 74–78. DOI: https://doi.org/10.1038/nature09988.

Ikari, M. J., J. Kameda, D. M. Saffer, and A. J. Kopf. "Strength characteristics of Japan Trench borehole samples in the high-slip region of the 2011 Tohoku-Oki earthquake." In: *Earth and Planetary Science Letters* 412 (2015), pp. 35–41. ISSN: 0012-821X. DOI: https://doi.org/10.1016/j.epsl.2014.12.014. URL: https://www.sciencedirect.com/science/article/pii/S0012821X14007675.

Islam, Md. Tariqul, Erik Sturkell, Peter LaFemina, Halldór Geirsson, Freysteinn Sigmundsson, and Halldór Ólafsson. "Continuous subsidence in the Thingvellir rift graben, Iceland: Geodetic observations since 1967 compared to rheological models of plate spreading." In: *Journal of Geophysical Research: Solid Earth* 121.1 (2016), pp. 321–338. DOI: https://doi.org/10.1002/2015JB012306. eprint: https://agupubs.

onlinelibrary.wiley.com/doi/pdf/10.1002/2015JB012306. URL: https://agupubs.onlinelibrary.wiley.com/doi/abs/10.1002/2015JB012306.

Jaeger, J. C., N.G.W. Cook, and R.W. Zimmerman. *Rock Mechanics and Engineering*. 4th ed. Blackwell Publishing Ltd, 2007. ISBN: 978-0-632-05759-7. URL: https://www.wiley.com/en-fr/Fundamentals+of+Rock+Mechanics%2C+4th+Edition-p-9780632057597.

Jakobsson, S. P. and M. T. Gudmundsson. "Subglacial and intraglacial volcanic formations in Iceland." In: *Jökull* 58 (2008), pp. 179–196. URL: https://jokull.jorfi.is/articles/jokull2008.58/jokull2008.58.179.pdf.

Jakobsson, S. P., K. Jónasson, and I. A. Sigurdsson. "The three igneous rock series of Iceland." In: *Jökull* 58.1 (2008), pp. 117–138.

James, M. R. and S. Robson. "Straightforward reconstruction of 3D surfaces and topography with a camera: Accuracy and geoscience application." In: *Journal of Geophysical Research: Earth Surface* 117.F3 (2012). DOI: https://doi.org/10.1029/2011JF002289. URL: https://agupubs.onlinelibrary.wiley.com/doi/abs/10.1029/2011JF002289.

Jenness, M. H and A. E. Clifton. "Controls on the geometry of a Holocene crater row: a field study from southwest Iceland." In: *Bulletin of volcanology* 71 (2009), pp. 715–728. DOI: https://doi.org/10.1007/s00445-009-0267-9.

Johnson, J. H., M. P. Poland, K. R. Anderson, and J. Biggs. "A Cautionary Tale of Topography and Tilt from Kīlauea Caldera." In: *Geophysical Research Letters* 46.8 (2019), pp. 4221–4229. DOI: https://doi.org/10.1029/2018GL081757. eprint: https://agupubs.onlinelibrary.wiley.com/doi/pdf/10.1029/2018GL081757. URL: https://agupubs.onlinelibrary.wiley.com/doi/abs/10.1029/2018GL081757.

Jolly, R.J.H. and D.J. Sanderson. "A Mohr circle construction for the opening of a pre-existing fracture." In: *Journal of Structural Geology* 19.6 (1997), pp. 887–892. ISSN: 0191-8141. DOI: https://doi.org/10.1016/S0191-8141(97)00014-X. URL: https://www.sciencedirect.com/science/article/pii/S019181419700014X.

Juncu, D., Th. Árnadóttir, A. Hooper, and G. Gunnarsson. "Anthropogenic and natural ground deformation in the Hengill geothermal area, Iceland." In: *Journal of Geophysical Research: Solid Earth* 122.1 (2017), pp. 692–709. DOI: https://doi.org/10.1002/2016JB013626. eprint: https://agupubs.onlinelibrary.wiley.com/doi/pdf/10.1002/2016JB013626. URL: https://agupubs.onlinelibrary.wiley.com/doi/abs/10.1002/2016JB013626.

Jungels, P. H. and G. A. Frazier. "Finite element analysis of the residual displacements for an earthquake rupture: Source parameters for the San Fernando earthquake." In: *Journal of Geophysical Research (1896-1977)* 78.23 (1973), pp. 5062–5083. DOI: https://doi.org/10.1029/JB078i023p05062. eprint: https://agupubs.onlinelibrary.wiley.com/doi/pdf/10.1029/JB078i023p05062. URL: https://agupubs.onlinelibrary.wiley.com/doi/abs/10.1029/JB078i023p05062.

Jónsson, J. *Jarðfræðikort af Reykjanesskaga (Geological map of the Reykjanes Peninsula*. Orkustofnun JHD (Iceland Energy Authority), 7831, 303 p., 30 plates, 20 map sheets 1:25,000. 1978.

Karato, S.i. and P. Wu. “Rheology of the Upper Mantle: A Synthesis.” In: *Science* 260.5109 (1993), pp. 771–778. DOI: 10.1126/science.260.5109.771. eprint: https://www.science.org/doi/pdf/10.1126/science.260.5109.771. URL: https://www.science.org/doi/abs/10.1126/science.260.5109.771.

Kavanagh, J. L., S. L. Engwell, and S. A. Martin. “A review of laboratory and numerical modelling in volcanology.” In: *Solid Earth* 9.2 (2018), pp. 531–571. DOI: 10.5194/se-9-531-2018. URL: https://se.copernicus.org/articles/9/531/2018/.

Kavanagh, J. L., T. Menand, and R. S. J. Sparks. “An experimental investigation of sill formation and propagation in layered elastic media.” In: *Earth and Planetary Science Letters* 245.3 (2006), pp. 799–813. ISSN: 0012-821X. DOI: https://doi.org/10.1016/j.epsl.2006.03.025. URL: https://www.sciencedirect.com/science/article/pii/S0012821X06002421.

Kavanagh, J. L., B. D. Rogers, D. Boutelier, and A. R. Cruden. “Controls on sill and dyke-sill hybrid geometry and propagation in the crust: The role of fracture toughness.” In: *Tectonophysics* 698 (2017), pp. 109–120. ISSN: 0040-1951. DOI: https://doi.org/10.1016/j.tecto.2016.12.027. URL: https://www.sciencedirect.com/science/article/pii/S0040195116306412.

Kavanagh, J.L., T. Menand, and K.A. Daniels. “Gelatine as a crustal analogue: Determining elastic properties for modelling magmatic intrusions.” In: *Tectonophysics* 582 (2013), pp. 101–111. ISSN: 0040-1951. DOI: https://doi.org/10.1016/j.tecto.2012.09.032. URL: https://www.sciencedirect.com/science/article/pii/S0040195112006336.

Keiding, M., B. Lund, and T. Árnadóttir. “Earthquakes, stress, and strain along an obliquely divergent plate boundary: Reykjanes Peninsula, southwest Iceland.” In: *Journal of Geophysical Research: Solid Earth* 114.B9 (2009). DOI: https://doi.org/10.1029/2008JB006253. eprint: https://agupubs.onlinelibrary.wiley.com/doi/pdf/10.1029/2008JB006253. URL: https://agupubs.onlinelibrary.wiley.com/doi/abs/10.1029/2008JB006253.

Keiding, M., T. Árnadóttir, S. Jónsson, J. Decriem, and A. Hooper. “Plate boundary deformation and man-made subsidence around geothermal fields on the Reykjanes Peninsula, Iceland.” In: *Journal of Volcanology and Geothermal Research* 194.4 (2010), pp. 139–149. ISSN: 0377-0273. DOI: https://doi.org/10.1016/j.jvolgeores.2010.04.011. URL: https://www.sciencedirect.com/science/article/pii/S0377027310001290.

Keiding, M., T. Árnadóttir, E. Sturkell, H. Geirsson, and B. Lund. “Strain accumulation along an oblique plate boundary: The Reykjanes Peninsula, southwest Iceland.” In: *Geophysical Journal International* 172.2 (Feb. 2008), pp. 861–872. ISSN: 0956-540X. DOI: 10.1111/j.1365-246X.2007.03655.x. eprint: https://academic.oup.com/gji/article-pdf/172/2/861/5985592/172-2-861.pdf. URL: https://doi.org/10.1111/j.1365-246X.2007.03655.x.

Khodayar, M. and P. Einarsson. “Strike-slip faulting, normal faulting, and lateral dike injections along a single fault: Field example of the Gljúfurá fault near a Tertiary oblique rift-transform zone, Borgarfjörður, west Iceland.” In: *Journal of Geophysical Research: Solid Earth* 107.B5 (2002), ETG 5–1–ETG 5–16. DOI: https://doi.org/10.1029/

2001JB000150. URL: https://agupubs.onlinelibrary.wiley.com/doi/abs/10.1029/2001JB000150.

Labuz, J. F., F.eitao Zeng, R. Makhnenko, and Y. Li. "Brittle failure of rock: A review and general linear criterion." In: *Journal of Structural Geology* 112 (2018), pp. 7–28. ISSN: 0191-8141. DOI: https://doi.org/10.1016/j.jsg.2018.04.007. URL: https://www.sciencedirect.com/science/article/pii/S0191814118301986.

Landmælingar Íslands. *ÍslandsDEM*. Dec. Accessed 26. 07. 2024. URL: https://atlas.lmi.is/mapview/?application=DEM.

Lanzi, C., F. Sigmundsson, M. M. Parks, H. Geirsson, and V. Drouin. "Strain Localization at Volcanoes Undergoing Extension: Investigation of Long-Term Deformation at Krafla and Askja Volcanic Systems in North Iceland." In: *Geophysical Research Letters* 51.21 (2024). e2024GL110299 2024GL110299, e2024GL110299. DOI: https://doi.org/10.1029/2024GL110299. eprint: https://agupubs.onlinelibrary.wiley.com/doi/pdf/10.1029/2024GL110299. URL: https://agupubs.onlinelibrary.wiley.com/doi/abs/10.1029/2024GL110299.

Le Corvec, N., T. Menand, and J. Lindsay. "Interaction of ascending magma with pre-existing crustal fractures in monogenetic basaltic volcanism: an experimental approach." In: *Journal of Geophysical Research: Solid Earth* 118.3 (2013), pp. 968–984. DOI: https://doi.org/10.1002/jgrb.50142. eprint: https://agupubs.onlinelibrary.wiley.com/doi/pdf/10.1002/jgrb.50142. URL: https://agupubs.onlinelibrary.wiley.com/doi/abs/10.1002/jgrb.50142.

Lei, Q., N. Gholizadeh Doonechaly, and C.-F. Tsang. "Modelling fluid injection-induced fracture activation, damage growth, seismicity occurrence and connectivity change in naturally fractured rocks." In: *International Journal of Rock Mechanics and Mining Sciences* 138 (2021), p. 104598. ISSN: 1365-1609. DOI: https://doi.org/10.1016/j.ijrmms.2020.104598. URL: https://www.sciencedirect.com/science/article/pii/S1365160920309643.

Lesher, C. E. and F. J. Spera. "Chapter 5 - Thermodynamic and Transport Properties of Silicate Melts and Magma." In: *The Encyclopedia of Volcanoes (Second Edition)*. Ed. by H. Sigurdsson. Second Edition. Amsterdam: Academic Press, 2015, pp. 113–141. ISBN: 978-0-12-385938-9. DOI: https://doi.org/10.1016/B978-0-12-385938-9.00005-5. URL: https://www.sciencedirect.com/science/article/pii/B9780123859389000055.

Li, S., R. Grapenthin, F. Sigmundsson, V. Drouin, S. Hreinsdóttir, and B. G. Ófeigsson. "Post-Rifting Relaxation During 2015–2020 Following the Bárðarbunga-Holuhraun Dike Intrusion and Eruption in Iceland." In: *Geophysical Research Letters* 49.13 (2022), e2022GL098977. DOI: https://doi.org/10.1029/2022GL098977. eprint: https://agupubs.onlinelibrary.wiley.com/doi/pdf/10.1029/2022GL098977. URL: https://agupubs.onlinelibrary.wiley.com/doi/abs/10.1029/2022GL098977.

Li, X., S. Jónsson, and Y. Cao. "Interseismic Deformation From Sentinel-1 Burst-Overlap Interferometry: Application to the Southern Dead Sea Fault." In: *Geophysical Research Letters* 48.16 (2021). e2021GL093481 2021GL093481, e2021GL093481. DOI: https://doi.org/10.1029/2021GL093481. eprint: https://agupubs.onlinelibrary.wiley.com/doi/pdf/10.1029/2021GL093481. URL: https://agupubs.onlinelibrary.wiley.com/doi/abs/10.1029/2021GL093481.

Logan, D. L. *A first course in the Finite Element Method*. 6th ed. Cengage Learning, 2017.
Lu, G. and R. S. Huismans. "Melt volume at Atlantic volcanic rifted margins controlled by depth-dependent extension and mantle temperature." In: *Nature Communications* 12.1 (2021), p. 3894. DOI: https://doi.org/10.1038/s41467-021-23981-5.
Lundgren, P., A. Kiryukhin, P. Milillo, and S. Samsonov. "Dike model for the 2012–2013 Tolbachik eruption constrained by satellite radar interferometry observations." In: *Journal of Volcanology and Geothermal Research* 307 (2015). SI: 2012-13 Tolbachik eruption, pp. 79–88. ISSN: 0377-0273. DOI: https://doi.org/10.1016/j.jvolgeores.2015.05.011. URL: https://www.sciencedirect.com/science/article/pii/S0377027315001432.
Maccaferri, F., M. Bonafede, and E. Rivalta. "A numerical model of dyke propagation in layered elastic media." In: *Geophysical Journal International* 180.3 (Mar. 2010), pp. 1107–1123. ISSN: 0956-540X. DOI: 10.1111/j.1365-246X.2009.04495.x. eprint: https://academic.oup.com/gji/article-pdf/180/3/1107/5887291/180-3-1107.pdf. URL: https://doi.org/10.1111/j.1365-246X.2009.04495.x.
Maccaferri, F., E. Rivalta, L. Passarelli, and Y. Aoki. "On the mechanisms governing dike arrest: Insight from the 2000 Miyakejima dike injection." In: *Earth and Planetary Science Letters* 434 (2016), pp. 64–74. ISSN: 0012-821X. DOI: https://doi.org/10.1016/j.epsl.2015.11.024. URL: https://www.sciencedirect.com/science/article/pii/S0012821X15007281.
Maerten, F., L. Maerten, R. Plateaux, and P. H. Cornard. "Joint inversion of tectonic stress and magma pressures using dyke trajectories." In: *Geological Magazine* 159.11–12 (2022), 2379–2394. DOI: 10.1017/S001675682200067X.
Massonnet, D., K. Feigl, M. Rossi, and F. Adragna. "Radar interferometric mapping of deformation in the year after the Landers earthquake." In: *Nature* 369.6477 (1994), pp. 227–230. DOI: https://doi.org/10.1038/369227a0.
Massonnet, Didier, Pierre Briole, and Alain Arnaud. "Deflation of Mount Etna monitored by spaceborne radar interferometry." In: *Nature* 375.6532 (1995), pp. 567–570. DOI: https://doi.org/10.1038/375567a0.
Masterlark, T. "Magma intrusion and deformation predictions: Sensitivities to the Mogi assumptions." In: *Journal of Geophysical Research: Solid Earth* 112.B6 (2007). DOI: https://doi.org/10.1029/2006JB004860. eprint: https://agupubs.onlinelibrary.wiley.com/doi/pdf/10.1029/2006JB004860. URL: https://agupubs.onlinelibrary.wiley.com/doi/abs/10.1029/2006JB004860.
Mathieu, L., B. van Wyk de Vries, E. P. Holohan, and V. R. Troll. "Dykes, cups, saucers and sills: Analogue experiments on magma intrusion into brittle rocks." In: *Earth and Planetary Science Letters* 271.1 (2008), pp. 1–13. ISSN: 0012-821X. DOI: https://doi.org/10.1016/j.epsl.2008.02.020. URL: https://www.sciencedirect.com/science/article/pii/S0012821X08001155.
Mattsson, T., S. Burchardt, B. S.G. Almqvist, and E. Ronchin. "Syn-emplacement fracturing in the Sandfell laccolith, eastern Iceland—Implications for rhyolite intrusion growth and volcanic hazards." In: *Frontiers in Earth Science* 6 (2018), p. 5. DOI: https://doi.org/10.3389/feart.2018.00005.
Merle, O. "The scaling of experiments on volcanic systems." In: *Frontiers in Earth Science* 3 (2015). ISSN: 2296-6463. DOI: 10.3389/feart.2015.00026. URL: https:

//www.frontiersin.org/journals/earth-science/articles/10.3389/feart.2015.00026.

Merle, O. and A. Borgia. "Scaled experiments of volcanic spreading." In: *Journal of Geophysical Research: Solid Earth* 101.B6 (1996), pp. 13805–13817. DOI: https://doi.org/10.1029/95JB03736. URL: https://agupubs.onlinelibrary.wiley.com/doi/abs/10.1029/95JB03736.

Michalczewska, K., S. Hreinsdóttir, S. Dumont, and F. Sigmundsson. *Crustal deformation on the Western Reykjanes Peninsula 2009 to 2014 mapped by InSAR and GPS measurements*. Tech. rep. Sturlugata 7, 101 Reykjavík, Iceland: Institute of Earth Sciences, 2014.

Mitchell, T.M. and D.R. Faulkner. "The nature and origin of off-fault damage surrounding strike-slip fault zones with a wide range of displacements: A field study from the Atacama fault system, northern Chile." In: *Journal of Structural Geology* 31.8 (2009), pp. 802–816. ISSN: 0191-8141. DOI: https://doi.org/10.1016/j.jsg.2009.05.002. URL: https://www.sciencedirect.com/science/article/pii/S0191814109001060.

Miyashita, K. and M. Matsu'ura. "Inversion Analysis of Static Displacement Data associated with the Alaska Earthquake of 1964." In: *Journal of Physics of the Earth* 26.4 (1978), pp. 333–349. DOI: 10.4294/jpe1952.26.333.

Mogi, K. "Relations between the eruptions of various volcanoes and the deformations of the ground surfaces around them." In: *Bulletin of the Earthquake Research Institute* 36 (1958), pp. 99–134.

Montgomery-Brown, E. K., D. K. Sinnett, M. Poland, P. Segall, T. Orr, H. Zebker, and A. Miklius. "Geodetic evidence for en echelon dike emplacement and concurrent slow slip during the June 2007 intrusion and eruption at Kīlauea volcano, Hawaii." In: *Journal of Geophysical Research: Solid Earth* 115.B7 (2010). DOI: https://doi.org/10.1029/2009JB006658. eprint: https://agupubs.onlinelibrary.wiley.com/doi/pdf/10.1029/2009JB006658. URL: https://agupubs.onlinelibrary.wiley.com/doi/abs/10.1029/2009JB006658.

Nakamura, K. "Volcanoes as possible indicators of tectonic stress orientation — principle and proposal." In: *Journal of Volcanology and Geothermal Research* 2.1 (1977), pp. 1–16. ISSN: 0377-0273. DOI: https://doi.org/10.1016/0377-0273(77)90012-9. URL: https://www.sciencedirect.com/science/article/pii/0377027377900129.

Neal, C. A., S. R. Brantley, L. Antolik, J. L. Babb, M. Burgess, K. Calles, M. Cappos, J. C. Chang, S. Conway, L. Desmither, P. Dotray, T. Elias, P. Fukunaga, S. Fuke, I. A. Johanson, K. Kamibayashi, J. Kauahikaua, R. L. Lee, S. Pekalib, A. Miklius, W. Million, C. J. Moniz, P. A. Nadeau, P. Okubo, C. Parcheta, M. R. Patrick, B. Shiro, D. A. Swanson, W. Tollett, F. Trusdell, E. F. Younger, M. H. Zoeller, E. K. Montgomery-Brown, K. R. Anderson, M. P. Poland, J. L. Ball, J. Bard, M. Coombs, H. R. Dietterich, C. Kern, W. A. Thelen, P. F. Cervelli, T. Orr, B. F. Houghton, C. Gansecki, R. Hazlett, P. Lundgren, A. K. Diefenbach, A. H. Lerner, G. Waite, P. Kelly, L. Clor, C. Werner, K. Mulliken, G. Fisher, and D. Damby. "The 2018 rift eruption and summit collapse of Kīlauea Volcano." In: *Science* 363.6425 (2019), pp. 367–374. DOI: 10.1126/science.aav7046. eprint: https://www.science.org/doi/pdf/10.1126/science.aav7046. URL: https://www.science.org/doi/abs/10.1126/science.aav7046.

Náttúrufræðistofnun Íslands. *Eldvörp, gervigígar og eldhraun á nútíma*. Compiled from published geological maps, aerial images and data from the Icelandic Meteorological

occice. Scale is 1:25.000; identifier: 8817e173-8e2b-4dc4-a57c-348f75bfb85b. Accessed 29. 09. 2024. URL: https://gatt.lmi.is/geonetwork/srv/eng/catalog.search#/metadata/8817e173-8e2b-4dc4-a57c-348f75bfb85b.

Okada, Y. "Surface deformation due to shear and tensile faults in a half-space." In: *Bulletin of the Seismological Society of America* 75.4 (Aug. 1985), pp. 1135–1154. ISSN: 0037-1106. DOI: 10.1785/BSSA0750041135. eprint: https://pubs.geoscienceworld.org/ssa/bssa/article-pdf/75/4/1135/5332841/bssa0750041135.pdf. URL: https://doi.org/10.1785/BSSA0750041135.

Osmanoğlu, B., F. Sunar, S. Wdowinski, and E. Cabral-Cano. "Time series analysis of InSAR data: Methods and trends." In: *ISPRS Journal of Photogrammetry and Remote Sensing* 115 (2016). Theme issue 'State-of-the-art in photogrammetry, remote sensing and spatial information science', pp. 90–102. ISSN: 0924-2716. DOI: https://doi.org/10.1016/j.isprsjprs.2015.10.003. URL: https://www.sciencedirect.com/science/article/pii/S0924271615002269.

Parks, M., V. Drouin, F. Sigmundsson, Á. R. Hjartardóttir, H. Geirsson, G. B.M. Pedersen, J. M.C. Belart, S. Barsotti, C. Lanzi, K. Vogfjörd, A. Hooper, B. Ófeigsson, S. Hreinsdóttir, E. B. Gestsson, R. H. Þrastarson, P. Einarsson, V. Tolpekin, D. Rotheram-Clarke, S. R. Gunnarsson, B. V. Óskarsson, and V. Pinel. "2023–2024 inflation-deflation cycles at Svartsengi and repeated dike injections and eruptions at the Sundhnúkur crater row, Reykjanes Peninsula, Iceland." In: *Earth and Planetary Science Letters* 658 (2025), p. 119324. ISSN: 0012-821X. DOI: https://doi.org/10.1016/j.epsl.2025.119324. URL: https://www.sciencedirect.com/science/article/pii/S0012821X25001232.

Parks, M., F. Sigmundsson, V. Drouin, Á. R. Hjartardóttir, H. Geirsson, A. Hooper, K. S. Vogfjörd, B. G. Ófeigsson, S. Hreinsdóttir, E. H. Jensen, P. Einarsson, S. Barsotti, and H. M. Fridriksdottir. "Deformation, seismicity, and monitoring response preceding and during the 2022 Fagradalsfjall eruption, Iceland." In: *Bulletin of Volcanology* 85.10 (2023), p. 60. DOI: https://doi.org/10.1007/s00445-023-01671-y.

Parks, M., F. Sigmundsson, Ó. Sigurdsson, A. Hooper, S. Hreinsdóttir, B. Ófeigsson, and K. Michalczewska. "Deformation due to geothermal exploitation at Reykjanes, Iceland." In: *Journal of Volcanology and Geothermal Research* 391 (2020), p. 106438. ISSN: 0377-0273. DOI: https://doi.org/10.1016/j.jvolgeores.2018.08.016. URL: https://www.sciencedirect.com/science/article/pii/S0377027317305887.

Pascal, K., J. Neuberg, and E. Rivalta. "On precisely modelling surface deformation due to interacting magma chambers and dykes." In: *Geophysical Journal International* 196.1 (2013), pp. 253–278. ISSN: 0956-540X. DOI: 10.1093/gji/ggt343. eprint: https://academic.oup.com/gji/article-pdf/196/1/253/27640822/ggt343.pdf. URL: https://doi.org/10.1093/gji/ggt343.

Paterson, S.R. and K.L. Schmidt. "Is there a close spatial relationship between faults and plutons?" In: *Journal of Structural Geology* 21.8 (1999), pp. 1131–1142. ISSN: 0191-8141. DOI: https://doi.org/10.1016/S0191-8141(99)00024-3. URL: https://www.sciencedirect.com/science/article/pii/S0191814199000243.

Pedersen, G. B. M., J. M. C. Belart, B. V. Óskarsson, M. T. Gudmundsson, N. Gies, Th. Högnadóttir, Á. R. Hjartardóttir, V. Pinel, E. Berthier, T. Dürig, H. I. Reynolds, C. W. Hamilton, G. Valsson, P. Einarsson, D. Ben-Yehosua, A. Gunnarsson, and B. Oddsson. "Volume, Effusion Rate, and Lava Transport During the 2021 Fagradalsfjall Eruption:

Results From Near Real-Time Photogrammetric Monitoring." In: *Geophysical Research Letters* 49.13 (2022). e2021GL097125 2021GL097125, e2021GL097125. DOI: https://doi.org/10.1029/2021GL097125. eprint: https://agupubs.onlinelibrary.wiley.com/doi/pdf/10.1029/2021GL097125. URL: https://agupubs.onlinelibrary.wiley.com/doi/abs/10.1029/2021GL097125.

Poppe, S., O. Galland, N. J. de Winter, S. Goderis, P. Claeys, V. Debaille, P. Boulvais, and M. Kervyn. "Structural and Geochemical Interactions Between Magma and Sedimentary Host Rock: The Hovedøya Case, Oslo Rift, Norway." In: *Geochemistry, Geophysics, Geosystems* 21.3 (2020), e2019GC008685. DOI: https://doi.org/10.1029/2019GC008685. URL: https://agupubs.onlinelibrary.wiley.com/doi/abs/10.1029/2019GC008685.

Poppe, S., E. P. Holohan, O. Galland, N. Buls, G. Van Gompel, B. Keelson, P.-Y. Tournigand, J. Brancart, D. Hollis, A. Nila, and M. Kervyn. "An Inside Perspective on Magma Intrusion: Quantifying 3D Displacement and Strain in Laboratory Experiments by Dynamic X-Ray Computed Tomography." In: *Frontiers in Earth Science* 7 (2019). ISSN: 2296-6463. DOI: 10.3389/feart.2019.00062. URL: https://www.frontiersin.org/journals/earth-science/articles/10.3389/feart.2019.00062.

Poppe, S., C. Wauthier, and K. Fontijn. "Inversions of Surface Displacements in Scaled Experiments of Analog Magma Intrusion." In: *Geophysical Research Letters* 51.8 (2024). e2023GL106805 2023GL106805, e2023GL106805. DOI: https://doi.org/10.1029/2023GL106805. eprint: https://agupubs.onlinelibrary.wiley.com/doi/pdf/10.1029/2023GL106805. URL: https://agupubs.onlinelibrary.wiley.com/doi/abs/10.1029/2023GL106805.

Ramberg, H. *Gravity, Deformation and the Earth'crust*. Academic Press, London, 1981.

Rhodes, E., S. Burchardt, S. H. M. Greiner, T. Mattsson, F. Sigmundsson, T. Schmiedel, A. K. Barker, and T. Witcher. "Volcanic unrest as seen from the magmatic source: Reyðarártindur pluton, Iceland." In: *Scientific Reports* 14.1 (2024), p. 962. DOI: https://doi.org/10.1038/s41598-023-50880-0.

Rhodes, E. L., A. K. Barker, S. Burchardt, C. F. Hieronymus, S. N. Rousku, D. W. McGarvie, T. Mattsson, T. Schmiedel, E. Ronchin, and T. Witcher. "Rapid Assembly and Eruption of a Shallow Silicic Magma Reservoir, Reyðarártindur Pluton, Southeast Iceland." In: *Geochemistry, Geophysics, Geosystems* 22.11 (2021). e2021GC009999 2021GC009999, e2021GC009999. DOI: https://doi.org/10.1029/2021GC009999. eprint: https://agupubs.onlinelibrary.wiley.com/doi/pdf/10.1029/2021GC009999. URL: https://agupubs.onlinelibrary.wiley.com/doi/abs/10.1029/2021GC009999.

Rivalta, E., B. Taisne, A.P. Bunger, and R.F. Katz. "A review of mechanical models of dike propagation: Schools of thought, results and future directions." In: *Tectonophysics* 638 (2015), pp. 1–42. ISSN: 0040-1951. DOI: https://doi.org/10.1016/j.tecto.2014.10.003. URL: https://www.sciencedirect.com/science/article/pii/S0040195114005174.

Rosenberg, C. L. "Shear zones and magma ascent: A model based on a review of the Tertiary magmatism in the Alps." In: *Tectonics* 23.3 (2004). DOI: https://doi.org/10.1029/2003TC001526. URL: https://agupubs.onlinelibrary.wiley.com/doi/abs/10.1029/2003TC001526.

Sæmundsson, K. "Outline of the geology of Iceland." In: *Jökull* 29 (1979), pp. 7–28.

Sæmundsson, K., M.Á. Sigurgeirsson, Á. Hjartarson, I. Kaldal, S.G. Kristinsson, and S. Víkingsson. *Geological map of SW Iceland, 1: 100 000*. 2016.

Schmidt, P., B. Lund, C. Hieronymus, J. Maclennan, T. Árnadóttir, and C. Pagli. "Effects of present-day deglaciation in Iceland on mantle melt production rates." In: *Journal of Geophysical Research: Solid Earth* 118.7 (2013), pp. 3366–3379. DOI: https://doi.org/10.1002/jgrb.50273. eprint: https://agupubs.onlinelibrary.wiley.com/doi/pdf/10.1002/jgrb.50273. URL: https://agupubs.onlinelibrary.wiley.com/doi/abs/10.1002/jgrb.50273.

Schmiedel, T., O. Galland, and C. Breitkreuz. "Dynamics of Sill and Laccolith Emplacement in the Brittle Crust: Role of Host Rock Strength and Deformation Mode." In: *Journal of Geophysical Research: Solid Earth* 122.11 (2017), pp. 8860–8871. DOI: https://doi.org/10.1002/2017JB014468. URL: https://agupubs.onlinelibrary.wiley.com/doi/abs/10.1002/2017JB014468.

Schmiedel, T., O. Galland, O. T. Haug, G. Dumazer, and C. Breitkreuz. "Coulomb failure of Earth's brittle crust controls growth, emplacement and shapes of igneous sills, saucer-shaped sills and laccoliths." In: *Earth and Planetary Science Letters* 510 (2019), pp. 161–172. ISSN: 0012-821X. DOI: https://doi.org/10.1016/j.epsl.2019.01.011. URL: https://www.sciencedirect.com/science/article/pii/S0012821X19300214.

Segall, Paul. *Earthquake and Volcano Deformation*. Princeton: Princeton University Press, 2010. ISBN: 9781400833856. DOI: doi:10.1515/9781400833856. URL: https://doi.org/10.1515/9781400833856.

Sella, G. F., T. H. Dixon, and A. Mao. "REVEL: A model for Recent plate velocities from space geodesy." In: *Journal of Geophysical Research: Solid Earth* 107.B4 (2002), ETG 11–1–ETG 11–30. DOI: https://doi.org/10.1029/2000JB000033. eprint: https://agupubs.onlinelibrary.wiley.com/doi/pdf/10.1029/2000JB000033. URL: https://agupubs.onlinelibrary.wiley.com/doi/abs/10.1029/2000JB000033.

Shimazaki, K. "Pre-seismic crustal deformation caused by an underthrusting oceanic plate, in eastern Hokkaido, Japan." In: *Physics of the Earth and Planetary Interiors* 8.2 (1974), pp. 148–157. ISSN: 0031-9201. DOI: https://doi.org/10.1016/0031-9201(74)90127-7. URL: https://www.sciencedirect.com/science/article/pii/0031920174901277.

Sigmundsson, F., P. Einarsson, Á. R. Hjartardóttir, V. Drouin, K. Jónsdóttir, T. Árnadóttir, H. Geirsson, S. Hreinsdóttir, S. Li, and B. G. Ófeigsson. "Geodynamics of Iceland and the signatures of plate spreading." In: *Journal of Volcanology and Geothermal Research* 391 (2020a), p. 106436. ISSN: 0377-0273. DOI: https://doi.org/10.1016/j.jvolgeores.2018.08.014. URL: https://www.sciencedirect.com/science/article/pii/S0377027317306376.

Sigmundsson, F., A. Hooper, S. Hreinsdóttir, K.S. Vogfjörd, B.G. Ófeigsson, E.R. Heimisson, S. Dumont, M. Parks, K. Spaans, G.B. Gudmundsson, V. Drouin, T. Árnadóttir, K. Jónsdóttir, M.T. Gudmundsson, T. Högnadóttir, H.M. Fridriksdóttir, M. Hensch, P. Einarsson, E. Magnússon, S. Samsonov, B. Brandsdóttir, R.S. White, T. Ágústsdóttir, T. Greenfield, R.G. Green, Á.R. Hjartardóttir, R. Pedersen, R.A. Bennett, H. Geirsson, P.C. La Femina, H. Björnsson, F. Pálsson, E. Sturkell, C.J. Bean, M. Möllhoff, A.K. Braiden, and E.P.S. Eibl. "Segmented lateral dyke growth in a rifting event at Bárdarbunga volcanic system, Iceland." In: *Nature* 517 (2015), p. 191. DOI: 10.1038/nature14111https://www.

nature.com/articles/nature14111#supplementary-information. URL: http://dx.doi.org/10.1038/nature14111https://www.nature.com/articles/nature14111.pdf.

Sigmundsson, F., M. Parks, H. Geirsson, A. Hooper, V. Drouin, K. S. Vogfjörd, B. G. Ófeigsson, S. H. M. Greiner, Y. Yang, C. Lanzi, G. P. De Pascale, K. Jónsdóttir, S. Hreinsdóttir, V. Tolpekin, H. M. Fridriksdóttir, P. Einarsson, and S. Barsotti. "Fracturing and tectonic stress drive ultrarapid magma flow into dikes." In: *Science* 383.6688 (2024), pp. 1228–1235. DOI: 10.1126/science.adn2838. eprint: https://www.science.org/doi/pdf/10.1126/science.adn2838. URL: https://www.science.org/doi/abs/10.1126/science.adn2838.

Sigmundsson, F., M. Parks, A. Hooper, H. Geirsson, K. S. Vogfjörd, V. Drouin, B. G. Ófeigsson, S. Hreinsdóttir, S. Hjaltadóttir, K. Jónsdóttir, P. Einarsson, S. Barsotti, J. Horálek, and Th. Ágústsdóttir. "Deformation and seismicity decline before the 2021 Fagradalsfjall eruption." In: *Nature* 609.7927 (2022), pp. 523–528. DOI: https://doi.org/10.1038/s41586-022-05083-4. URL: https://doi.org/10.1038/s41586-022-05083-4.

Sigmundsson, F., V. Pinel, R. Grapenthin, A. Hooper, S. A Halldórsson, P. Einarsson, B. G. Ófeigsson, E. R. Heimisson, K. Jónsdóttir, M. T. Gudmundsson, K. Vogfjörd, S. Li, V. Drouin, H. Geirsson, S. Dumont, H. M. Fridriksdottir, G. B. Gudmundsson, T. J. Wright, and T. Yamasaki. "Unexpected large eruptions from buoyant magma bodies within viscoelastic crust." In: *Nature Communications* 11.1 (2020b), p. 2403. DOI: https://doi.org/10.1038/s41467-020-16054-6.

Smith, Mark William and Damià Vericat. "From experimental plots to experimental landscapes: topography, erosion and deposition in sub-humid badlands from Structure-from-Motion photogrammetry." In: *Earth Surface Processes and Landforms* 40.12 (2015), pp. 1656–1671. DOI: https://doi.org/10.1002/esp.3747. eprint: https://onlinelibrary.wiley.com/doi/pdf/10.1002/esp.3747. URL: https://onlinelibrary.wiley.com/doi/abs/10.1002/esp.3747.

Smith, M.W., J.L. Carrivick, and D.J. Quincey. "Structure from motion photogrammetry in physical geography." In: *Progress in Physical Geography: Earth and Environment* 40.2 (2016), pp. 247–275. DOI: 10.1177/0309133315615805. URL: https://doi.org/10.1177/0309133315615805.

Smittarello, D., B. Smets, J. Barrière, C. Michellier, A. Oth, T. Shreve, R. Grandin, N. Theys, H. Brenot, V. Cayol, P. Allard, C. Caudron, O. Chevrel, F. Darchambeau, P. de Buyl, L. Delhaye, D. Derauw, G. Ganci, H. Geirsson, E. Kamate Kaleghetso, J. Kambale Makundi, I. Kambale Nguomoja, C. Kasereka Mahinda, M. Kervyn, C. Kimanuka Ruriho, H. Le Mével, S. Molendijk, O. Namur, S. Poppe, M. Schmid, J. Subira, C. Wauthier, M. Yalire, N. d'Oreye, F. Kervyn, and A. Syavulisembo Muhindo. "Precursor-free eruption triggered by edifice rupture at Nyiragongo volcano." In: *Nature* 609.7925 (2022), pp. 83–88. DOI: https://doi.org/10.1038/s41586-022-05047-8.

Spaans, K. and A. Hooper. "Insights Into the Stress Field Around Bárdarbunga Volcano From the 2014/2015 Holuhraun Rifting Event." In: *Journal of Geophysical Research: Solid Earth* 123.4 (2018), pp. 3238–3249. DOI: https://doi.org/10.1002/2017JB015274. eprint: https://agupubs.onlinelibrary.wiley.com/doi/pdf/10.1002/2017JB015274. URL: https://agupubs.onlinelibrary.wiley.com/doi/abs/10.1002/2017JB015274.

Spacapan, J. B., O. Galland, H. A. Leanza, and S. Planke. "Control of strike-slip fault on dyke emplacement and morphology." In: *Journal of the Geological Society* 173.4 (Apr. 2016), pp. 573–576. ISSN: 0016-7649. DOI: 10.1144/jgs2015-166. eprint: https://pubs.geoscienceworld.org/jgs/article-pdf/173/4/573/3683310/jgs2015-166.pdf. URL: https://doi.org/10.1144/jgs2015-166.

Stephansson, O. and H. Berner. "The Finite Element Method in tectonic processes." In: *Physics of the Earth and Planetary Interiors* 4.4 (1971), pp. 301–321. ISSN: 0031-9201. DOI: https://doi.org/10.1016/0031-9201(71)90014-8. URL: https://www.sciencedirect.com/science/article/pii/0031920171900148.

Stephens, T. L., R. J. Walker, D. Healy, A. Bubeck, and R. W. England. "Mechanical models to estimate the paleostress state from igneous intrusions." In: *Solid Earth* 9.4 (2018), pp. 847–858. DOI: 10.5194/se-9-847-2018. URL: https://se.copernicus.org/articles/9/847/2018/.

Sturkell, E., F. Sigmundsson, P. Einarsson, and R. Bilham. "Strain accumulation 1986–1992 across the Reykjanes Peninsula Plate Boundary, Iceland, determined from GPS measurements." In: *Geophysical Research Letters* 21.2 (1994), pp. 125–128. DOI: https://doi.org/10.1029/93GL03421. eprint: https://agupubs.onlinelibrary.wiley.com/doi/pdf/10.1029/93GL03421. URL: https://agupubs.onlinelibrary.wiley.com/doi/abs/10.1029/93GL03421.

Sæmundsson, K., M. Á. Sigurgeirsson, and G. Ó. Fridleifsson. "Geology and structure of the Reykjanes volcanic system, Iceland." In: *Journal of Volcanology and Geothermal Research* 391 (2020), p. 106501. ISSN: 0377-0273. DOI: https://doi.org/10.1016/j.jvolgeores.2018.11.022. URL: https://www.sciencedirect.com/science/article/pii/S0377027317305474.

Tadesse, A. Z., G. Bedassa, M. Kervyn, A. A. Muluneh, S. Gudbrandsson, G. Yirgu, D. Ayalew, and K. Fontijn. "Structural controls on magma pathways in Bora-Baricha-Tullu Moye (BBTM) volcanic system, Main Ethiopian Rift." In: *Volcanica* 6.2 (2023), 367–390. DOI: 10.30909/vol.06.02.367390. URL: http://jvolcanica.org/ojs/index.php/volcanica/article/view/206.

Taisne, B. and C. Jaupart. "Dike propagation through layered rocks." In: *Journal of Geophysical Research: Solid Earth* 114.B9 (2009). DOI: https://doi.org/10.1029/2008JB006228. eprint: https://agupubs.onlinelibrary.wiley.com/doi/pdf/10.1029/2008JB006228. URL: https://agupubs.onlinelibrary.wiley.com/doi/abs/10.1029/2008JB006228.

Temtime, T., J. Biggs, E. Lewi, and A. Ayele. "Evidence for Active Rhyolitic dike Intrusion in the Northern Main Ethiopian Rift from the 2015 Fentale Seismic Swarm." In: *Geochemistry, Geophysics, Geosystems* 21.6 (2020), e2019GC008550. DOI: https://doi.org/10.1029/2019GC008550. eprint: https://agupubs.onlinelibrary.wiley.com/doi/pdf/10.1029/2019GC008550. URL: https://agupubs.onlinelibrary.wiley.com/doi/abs/10.1029/2019GC008550.

Thiele, S. T., A. R. Cruden, S. Micklethwaite, A. P. Bunger, and J. Köpping. "Dyke apertures record stress accumulation during sustained volcanism." In: *Scientific reports* 10.1 (2020), p. 17335. DOI: https://doi.org/10.1038/s41598-020-74361-w.

Thordarson, T. and G. Larsen. "Volcanism in Iceland in historical time: Volcano types, eruption styles and eruptive history." In: *Journal of Geodynamics* 43.1 (2007). Hotspot Iceland, pp. 118–152. ISSN: 0264-3707. DOI: https://doi.org/10.1016/j.

jog.2006.09.005. URL: https://www.sciencedirect.com/science/article/pii/S0264370706000652.

Tibaldi, A. "Morphology of pyroclastic cones and tectonics." In: *Journal of Geophysical Research: Solid Earth* 100.B12 (1995), pp. 24521–24535. DOI: https://doi.org/10.1029/95JB02250. eprint: https://agupubs.onlinelibrary.wiley.com/doi/pdf/10.1029/95JB02250. URL: https://agupubs.onlinelibrary.wiley.com/doi/abs/10.1029/95JB02250.

Tibaldi, A., F.L. Bonali, and C. Corazzato. "Structural control on volcanoes and magma paths from local- to orogen-scale: The central Andes case." In: *Tectonophysics* 699 (2017), pp. 16–41. ISSN: 0040-1951. DOI: https://doi.org/10.1016/j.tecto.2017.01.005. URL: https://www.sciencedirect.com/science/article/pii/S0040195117300045.

Townsend, M., D. D. Pollard, K. Johnson, and C. Culha. "Jointing around magmatic dikes as a precursor to the development of volcanic plugs." In: *Bulletin of Volcanology* 77 (2015), pp. 1–13. DOI: https://doi.org/10.1007/s00445-015-0978-z.

Trasatti, E., C. Giunchi, and M. Bonafede. "Effects of topography and rheological layering on ground deformation in volcanic regions." In: *Journal of Volcanology and Geothermal Research* 122.1 (2003), pp. 89–110. ISSN: 0377-0273. DOI: https://doi.org/10.1016/S0377-0273(02)00473-0. URL: https://www.sciencedirect.com/science/article/pii/S0377027302004730.

– "Structural and rheological constraints on source depth and overpressure estimates at the Campi Flegrei caldera, Italy." In: *Journal of Volcanology and Geothermal Research* 144.1 (2005). The Tectonics and Physics of Volcanoes, pp. 105–118. ISSN: 0377-0273. DOI: https://doi.org/10.1016/j.jvolgeores.2004.11.019. URL: https://www.sciencedirect.com/science/article/pii/S0377027304004202.

Turcotte, D. L. and G. Schubert. *Geodynamics*. 3rd. Cambridge university press, 2014.

Turner, M. J., R. W. Clough, H. C. Martin, and L. J. Topp. "Stiffness and Deflection Analysis of Complex Structures." In: *Journal of the Aeronautical Sciences* 23.9 (1956), pp. 805–823. DOI: 10.2514/8.3664. eprint: https://doi.org/10.2514/8.3664. URL: https://doi.org/10.2514/8.3664.

Ullman, S. "The interpretation of structure from motion." In: *Proceedings of the Royal Society of London. Series B. Biological Sciences* 203.1153 (1979), pp. 405–426. DOI: https://doi.org/10.1098/rspb.1979.0006.

Vachon, R. and C. F. Hieronymus. "Effect of host-rock rheology on dyke shape, thickness and magma overpressure." In: *Geophysical Journal International* 208.3 (2016), pp. 1414–1429. ISSN: 0956-540X. DOI: 10.1093/gji/ggw448. eprint: https://academic.oup.com/gji/article-pdf/208/3/1414/9589657/ggw448.pdf. URL: https://doi.org/10.1093/gji/ggw448.

Vadon, H. and F. Sigmundsson. "Crustal Deformation from 1992 to 1995 at the Mid-Atlantic Ridge, Southwest Iceland, Mapped by Satellite Radar Interferometry." In: *Science* 275.5297 (1997), pp. 194–197. DOI: 10.1126/science.275.5297.194. eprint: https://www.science.org/doi/pdf/10.1126/science.275.5297.194. URL: https://www.science.org/doi/abs/10.1126/science.275.5297.194.

Valentine, G. A. and K. E.C. Krogh. "Emplacement of shallow dikes and sills beneath a small basaltic volcanic center – The role of pre-existing structure (Paiute Ridge, southern Nevada, USA)." In: *Earth and Planetary Science Letters* 246.3 (2006), pp. 217–230.

ISSN: 0012-821X. DOI: https://doi.org/10.1016/j.epsl.2006.04.031. URL: https://www.sciencedirect.com/science/article/pii/S0012821X06003347.

van Otterloo, J. and A. R. Cruden. "Rheology of pig skin gelatine: Defining the elastic domain and its thermal and mechanical properties for geological analogue experiment applications." In: *Tectonophysics* 683 (2016), pp. 86–97. ISSN: 0040-1951. DOI: https://doi.org/10.1016/j.tecto.2016.06.019. URL: https://www.sciencedirect.com/science/article/pii/S0040195116302256.

van Wijk, J.W. and D.K. Blackman. "Deformation of oceanic lithosphere near slow-spreading ridge discontinuities." In: *Tectonophysics* 407.3 (2005), pp. 211–225. ISSN: 0040-1951. DOI: https://doi.org/10.1016/j.tecto.2005.08.009. URL: https://www.sciencedirect.com/science/article/pii/S0040195105003653.

van Wyk de Vries, B. and M. van Wyk de Vries. "Chapter 7 - Tectonics and Volcanic and Igneous Plumbing Systems." In: *Volcanic and Igneous Plumbing Systems*. Ed. by Steffi Burchardt. Elsevier, 2018, pp. 167–189. ISBN: 978-0-12-809749-6. DOI: https://doi.org/10.1016/B978-0-12-809749-6.00007-8. URL: https://www.sciencedirect.com/science/article/pii/B9780128097496000078.

Veðurstofa Íslands. *Mörk sigdals við Svartsengi og Grindavík*. Accessed 02. 12. 2024. URL: https://gatt.natt.is/geonetwork/srv/ice/catalog.search#/metadata/03173bf2-87b9-4905-b033-f21268adaef5.

Voight, B. and A. C. Samuelson. "On the application of finite-element techniques to problems concerning potential distribution and stress analysis in the earth sciences." In: *Pure and Applied Geophysics* 76 (1969), pp. 40–55. DOI: https://doi.org/10.1007/BF00877835.

Walker, G. P.L. "Intrusive sheet swarms and the identity of Crustal Layer 3 in Iceland." In: *Journal of the Geological Society* 131.2 (1975), pp. 143–159. DOI: 10.1144/gsjgs.131.2.0143. eprint: https://www.lyellcollection.org/doi/pdf/10.1144/gsjgs.131.2.0143. URL: https://www.lyellcollection.org/doi/abs/10.1144/gsjgs.131.2.0143.

Watson, A., B. M. Kennedy, J. Davidson, E. Brogt, and A. Jolley. "The implementation of a virtual field trip to aid geological interpretation within an undergraduate volcanology course." In: *Journal of Geoscience Education* 72.3 (2024), pp. 220–232. DOI: 10.1080/10899995.2023.2279016. eprint: https://doi.org/10.1080/10899995.2023.2279016. URL: https://doi.org/10.1080/10899995.2023.2279016.

Weir, N. R. W., R. S. White, B. Brandsdóttir, P. Einarsson, H. Shimamura, and H. Shiobara. "Crustal structure of the northern Reykjanes Ridge and Reykjanes Peninsula, southwest Iceland." In: *Journal of Geophysical Research: Solid Earth* 106.B4 (2001), pp. 6347–6368. DOI: https://doi.org/10.1029/2000JB900358. eprint: https://agupubs.onlinelibrary.wiley.com/doi/pdf/10.1029/2000JB900358. URL: https://agupubs.onlinelibrary.wiley.com/doi/abs/10.1029/2000JB900358.

Westoby, M.J., J. Brasington, N.F. Glasser, M.J. Hambrey, and J.M. Reynolds. "'Structure-from-Motion' photogrammetry: A low-cost, effective tool for geoscience applications." In: *Geomorphology* 179 (2012), pp. 300–314. ISSN: 0169-555X. DOI: https://doi.org/10.1016/j.geomorph.2012.08.021. URL: https://www.sciencedirect.com/science/article/pii/S0169555X12004217.

Witcher, T. “Viscous-brittle deformation of shallowly emplaced silicic magma: Implications for outgassing and volcanic hazards.” PhD thesis. Acta Universitatis Upsaliensis, 2024. URL: https://urn.kb.se/resolve?urn=urn:nbn:se:uu:diva-524861.

Witcher, T., S. Burchardt, T. Mattsson, M. J. Heap, and W. McCarthy. “Development of permeable networks by viscous-brittle deformation in a shallow rhyolite intrusion. Part 1: Field evidence.” In: *Journal of Volcanology and Geothermal Research* 454 (2024), p. 108166. ISSN: 0377-0273. DOI: https://doi.org/10.1016/j.jvolgeores.2024.108166. URL: https://www.sciencedirect.com/science/article/pii/S0377027324001586.

Wright, T. J., F. Sigmundsson, C. Pagli, M. Belachew, I. J. Hamling, B. Brandsdóttir, D. Keir, R. Pedersen, A. Ayele, C. Ebinger, P. Einarsson, E. Lewi, and E. Calais. “Geophysical constraints on the dynamics of spreading centres from rifting episodes on land.” In: *Nature Geoscience* 5.4 (2012), pp. 242–250. DOI: https://doi.org/10.1038/ngeo1428.

Yu, M. “Advances in strength theories for materials under complex stress state in the 20th Century.” In: *Applied Mechanics Reviews* 55.3 (June 2002), pp. 169–218. ISSN: 0003-6900. DOI: 10.1115/1.1472455. eprint: https://asmedigitalcollection.asme.org/appliedmechanicsreviews/article-pdf/55/3/169/5438834/169_1.pdf. URL: https://doi.org/10.1115/1.1472455.

Ziv, A., A. M. Rubin, and A. Agnon. “Stability of dike intrusion along preexisting fractures.” In: *Journal of Geophysical Research: Solid Earth* 105.B3 (2000), pp. 5947–5961. DOI: https://doi.org/10.1029/1999JB900410. URL: https://agupubs.onlinelibrary.wiley.com/doi/abs/10.1029/1999JB900410.

Óskarsson, B. V. and M. S. Riishuus. “The mode of emplacement of Neogene flood basalts in Eastern Iceland: Facies architecture and structure of the Hólmar and Grjótá olivine basalt groups.” In: *Journal of Volcanology and Geothermal Research* 267 (2013), pp. 92–118. ISSN: 0377-0273. DOI: https://doi.org/10.1016/j.jvolgeores.2013.09.010. URL: https://www.sciencedirect.com/science/article/pii/S0377027313002989.

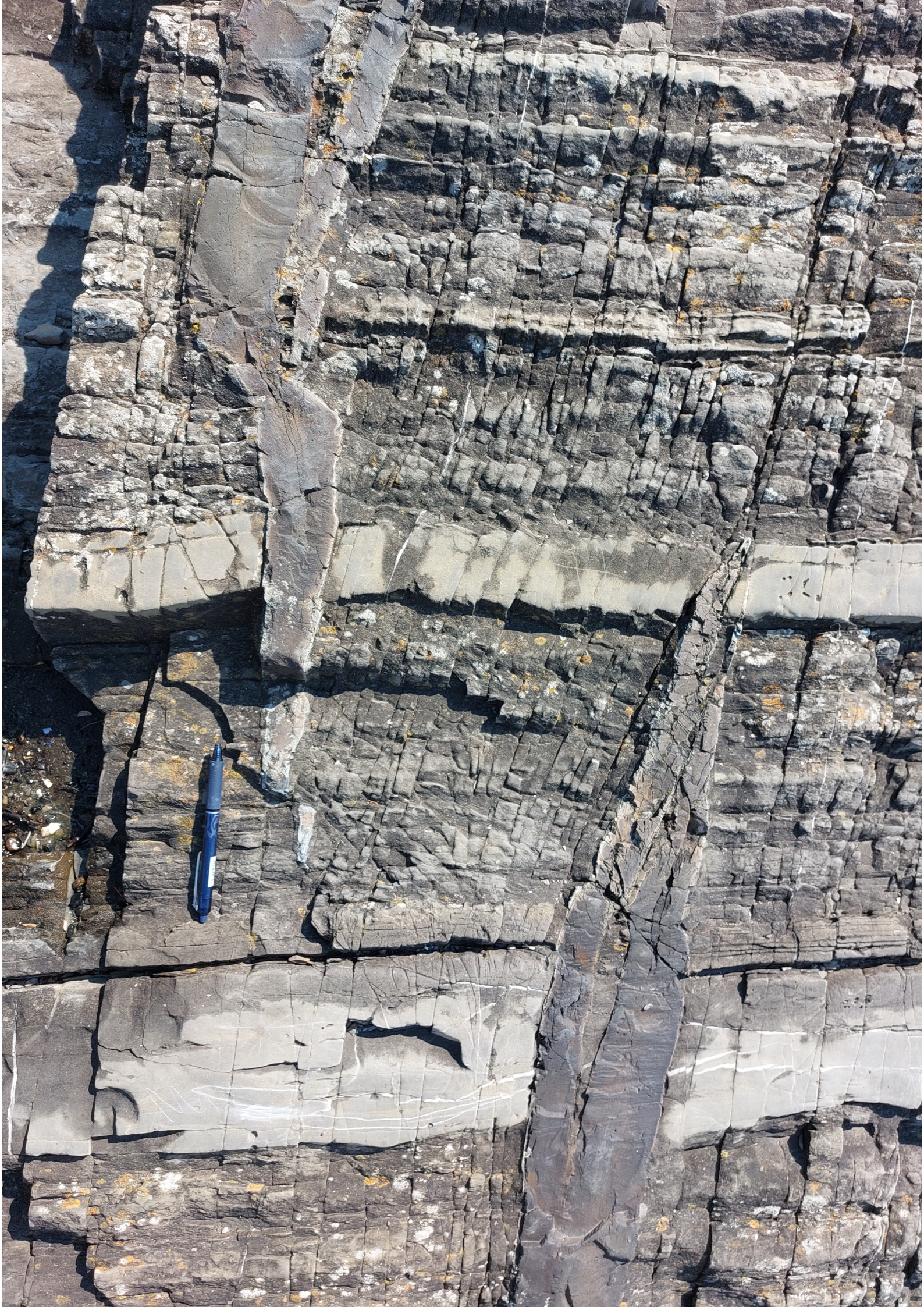

Plain Language Summary

Magmatic dikes are crucial parts of magmatic plumbing systems and represent the primary pathway of magma through the Earth´s crust. Not only is the majority of volcanic eruptions fed by dikes, but they also contribute to the formation of new crust and release tensional stress at tectonic plate boundaries. Because they are such common features, it is important to better understand how dikes are affected by the crust they intrude. This thesis investigates how magmatic dikes are influenced by crustal heterogeneity, specifically by pre-existing fractures and tectonic stress. This is done through three research projects, which are focused on one of the following research methods: Field-based structural geology, analogue models and numerical models.

Basaltic dikes that intruded a caldera-filling, mildly fractured hyaloclastite in the extinct volcanic system of Dyrfjöll in NE Iceland were photographed with the help of a drone. From these photos, we created virtual 3D models using Structure-from-motion photogrammetry and mapped the orientation of dikes and fractures in the hyaloclastite. Both features followed largely four directions. The most prominent of these likely aligned with the estimated tectonic stress field at the time of emplacement (ca. 12.5 Mio years ago). We observed three different ways, in which dikes interacted with pre-existing fractures: 1) Dikes can change direction to follow fractures and propagate along them. 2) Dikes can change strike upon intersection without following the fracture. 3) In one instance a dike got arrested in front of a pre-existing fracture. Here, several small branches formed near the arrested dike tip. Most of these intersected the same fracture that arrested the initial dike tip and either crosscut it or followed it. Dike-fracture interaction was observed most frequently if the strike was close to the likely tectonically controlled direction. The observations at Dyrfjöll show that dike-fracture interaction is a complex process that goes beyond magma simply flowing along existing fractures.

The question of how magma-fault interaction is affected by the mechanical material properties of the host rock and of the magma is addressed with the help of laboratory experiments that served as analogue models. Analogue models reproduce natural processes on a laboratory scale with materials that relative to each other behave in a similar manner as their counterparts in nature. We specifically investigated the role of the host rock cohesion (i.e. how strong or weak the host rock is) and of the magma viscosity. Host rock of variable cohesion was represented by mixtures of micro-glass beads (low cohesion) and silica flour (high cohesion). Molten vegetable oil and glucose syrup served as analogue magmas with low and high viscosity, respectively. They were injected from below into a model box filled with the granular host rock. By laterally displacing a plate at the base of the model box we created a strike-slip fault, which ran past the injection inlet. An array of cameras positioned above the box repeatedly recorded images of the model surface. This allowed us to reconstruct surface deformation in 3D. The vegetable oil solidifies at room temperature, which additionally made it possible to excavate the intrusion and record its geometry. Intrusions into strong, high-cohesion crust were strongly affected by pre-existing faults. Upon intersection they

were deflected and followed fault segments. Surface deformation was also affected by the presence of faults, since fault reactivation largely accommodated intrusion-induced strain. Conversely, faults in low-cohesion, weak analogue host rock had little influence on intrusions and their associated surface deformation. The duration between the start of injection until the eruption breached the surface was reduced by the presence of a fault in strong-cohesion analogue host rock, because fluid flowed along the fault to the surface. However, in weak host rock, the presence of a fault delayed the onset of eruption. Among both tested fluids, the low-viscosity fluid (vegetable oil) was slightly more sensitive to interaction with faults than the higher viscosity fluid. However, overall, the host rock cohesion was a much stronger control on intrusion-fault interaction. The experiments show that it is important to take material properties of the Earth's crust and magma into account when considering magma-fault interaction.

Although it is commonly known that tectonic stress can significantly affect magmatic dikes, this is rarely considered quantitatively in surface deformation models of active volcanoes. The potential role of tectonic stress as a driving mechanism for dike emplacement is investigated with numerical models based on the Finite-Element Method. A magmatic dike, which formed during February–March 2021 at Fagradalsfjall on the Reykjanes Peninsula, SW Iceland, is taken as a case study here; and we compare predictions from our model to geodetically observed surface deformation. The Reykjanes Peninsula is especially well suited for this type of study, because plate motion in the area is oblique. This means that the local plate motion is not oriented perpendicular to the plate boundary and instead is a mixture of spreading and shearing. Volcanic activity in the area is episodic and occurs over a time period of a few hundred years, which alternate with episodes of volcanic quiescence, that last for ca. 800-1000 years. The dike intrusion in 2021 and the subsequent 6-month-long eruption ended almost 800 years of volcanic quiescence on the peninsula. Our numerical model is divided into two steps: First, tectonic stress accumulates as a consequence of plate motion over a time span of 800 years. In the second model step, the stress is locally released by the dike, which is represented by a crack in the model crust. Observed surface deformation could be best reproduced when the dike released ca. 60% of the tectonic stress. That only a part of the previously accumulated stress was released by the 2021 dike is supported by the emplacement of three subsequent dikes in the same area between December 2021 and July 2023. The relative amount of opening and shearing in the dike plane predicted by our model fits well with expectations from geological models that are based on the strike of the dike relative to the governing stress field.

The findings of this thesis emphasize how complex the interaction of dikes with pre-existing fractures and tectonic stress is. Further studies are required to better understand them and to better integrate both processes into geophysical models that could be useful for monitoring of active volcanic systems.



Zusammenfassung

Magmatische Gänge sind platten- oder klingenförmige magmagefüllte Brüche, durch die flüssiges Magma durch die Erdkruste transportiert wird. Sie speisen nicht nur den Großteil aller Vulkanausbrüche, sondern tragen auch zur Lösung von Spannung an tektonischen Plattengrenzen und zur Bildung neuer Erdkruste bei. All das macht es wichtig zu verstehen, wie die Bildung magmatischer Gänge, ihre Form und ihr Wachstum von dem sie umgebenden Gestein und seinem Spannungszustand beeinflusst werden.

Diese Dissertation untersucht, wie magmatische Gänge von Diskontinuitäten in der Erdkruste beeinflusst werden, insbesondere mit Hinsicht auf die Wechselwirkung zwischen Gängen und schon vorher bestehenden Brüchen, sowie auf den Einfluss tektonischer Spannung. Die hier vorgestellte Arbeit unterteilt sich in drei Unterprojekte, die jeweils auf eine der folgenden Forschungsmethoden fokussiert sind: Strukturgeologie, laborbasierte Analogmodelle und numerische Simulationen, die mit geodetischen Daten verglichen werden.

Eine Gruppe basaltischer Gänge, die in leicht geklüfteten Hyaloklastit in den Dyrfjöll-Bergen in Borgarfjörður Eystri, Nordost-Island, intrudiert sind, wurden mit Hilfe einer Drohne photographiert. Durch Photogrammetrie wurden virtuelle 3D-Modelle von drei Aufschlüssen auf der Ostseite der Dyrfjöll-Berge erstellt und die Orientierung von Gängen und Brüchen im Hyaloklastit kartiert. Die untersuchten Gänge folgen überwiegend vier Streichrichtungen. Die am häufigsten vertretene Richtung folgt der mutmaßlichen Richtung der Plattengrenze zur Zeit der Gangintrusionen (vor ca. 12,5 Millionen Jahren). Wir beobachten drei unterschiedliche Arten, auf die Gänge mit schon vorher existierenden Brüchen interagieren: 1) Gänge können Brüchen folgen, sodass Magma entlang der Brüche fließt. 2) Gänge können ihre Richtung ändern, wenn sie einen Bruch kreuzen, ohne ihm zu folgen. 3) In einem Fall wurde ein Gang vor einem Bruch gestoppt. Nahe der Gangspitze spaltete sich der Gang in mehrere kleine Gänge auf, die denselben Bruch in einem anderen Winkel trafen. Viele von diesen kleinen Gängen kreuzten entweder den Bruch oder folgtem ihm zumindest für eine gewisse Strecke. Interaktion mit Brüchen wurde besonders häufig beobachtet, wenn die Gänge der mutmaßlich tektonisch kontrollierten Richtung folgten und wurde seltener, je weiter sich die Gang- bzw. Bruchrichtungen von der hauptsächlichen tektonischen Richtung unterschieden. Die Beobachtungen von Dyrfjöll zeigen, dass die Wechselwirkung zwischen Magma und Brüchen ein komplexer Vorgang ist, der darüber hinausgehen kann, dass Magma notwendigerweise entlang von Brüchen fließt.

Wie magmatische Gänge von bestehenden Störungen, den Materialeigenschaften des Umgebungsgesteins und der Magmaviskosität beeinflusst werden, wurde mit Hilfe von laborbasierten Analogmodellen untersucht. Analogmodelle stellen natürliche Prozesse nach, wobei der gesamte Prozess auf Laborgröße „herunterskaliert“ wird. In unseren Modellen wurde die Erdkruste durch Mischungen aus winzigen Glasskugeln (sehr feinem Sand) und Silikatpulver dargestellt. Das Modellmagma wurde entweder von geschmolzenem Kokosfett (niedrigviskos) oder Zuckersirup (höhere Viskosität) repräsentiert und von unten in die Modellbox injiziert.

Das jeweilige Verhältnis, in dem Sand und Silikatpulver gemischt wurden, beeinflusst die Kohäsion des Materials, wobei ein hoher Sandanteil niedrigere Kohäsion impliziert, also insgesamt schwächeres Material. Die Mitte der Modellkuste wurde durch eine Blattverschiebung gestört, die durch 4 cm horizontalen Versatz entlang des Bodens der Box erzeugt wurde. Vier Kameras, die oberhalb des Modellaufbaus positioniert wurden, nahmen in regelmäßigen Abständen Bilder der Modelloberfläche auf. Basierend auf diesen Bildern konnte die dreidimensionale Oberflächendeformation durch Photogrammetrie rekonstruiert werden. Kokosfett wird bei Raumtemperatur fest und konnte nach dem Experiment ausgegraben werden, sodass die Form der gebildeten Intrusionen offenbart wurde. Intrusionen in starke, kohäsive Modellkruste werden stark von schon bestehenden Störungen beeinflusst. Wenn Gangintrusionen auf Störungen treffen, werden sie umgelenkt und folgen der Störung. Zusätzlich beeinflussen die Störungen, wie Deformation des umgebenden Materials ausgeglichen werden. Dies geschieht, indem die Störungen reaktiviert werden und ein Großteil der von der Intrusion erzeugten Spannung entlang dieser existierenden Schwachstellen gelöst wird. Im Gegenteil dazu haben Störungen kaum Einfluss auf Intrusionen in schwachem Gestein, wo weder die Form der Intrusion noch Oberflächendeformation sichtbare Effekte aufweisen. Störungen in starkem umgebendem Gestein reduzieren die Zeit, die benötigt wird, bis das Modellmagma die Oberfläche erreicht, während der Effekt umgekehrt ist, wenn das umgebende Gestein schwach ist. Unter den beiden getesteten Modellmagmen war das niedrigviskosere Kokosfett etwas empfindlicher in Bezug auf Störungen als der Sirup. Allerdings war der Einfluss der Viskosität deutlich weniger stark ausgeprägt als der der Kohäsion des umgebenden Gesteins. Diese Experimente zeigen, dass es wichtig ist, die Materialeigenschaften der Erdkruste und des Magmas zu berücksichtigen, wenn die Wechselwirkung zwischen Gängen und Störungen untersucht wird.

Obwohl allgemein bekannt und ist, dass magmatische Gänge maßgeblich von tektonischer Spannung beeinflusst werden können, wird dies selten quantitativ in Modellen, die Oberflächendeformation simulieren, berücksichtigt. Das Potential tektonischer Spannung als primärer Antrieb für Gangintrusion wurde mit numerischen Modellen, die auf der Finite-Element Methode beruhen, getestet. Als Fallstudie dient der Gang, der sich im Februar–März 2021 bei Fagradalsfjall auf der Reykjanes Halbinsel in Südwestisland gebildet hat. Die Reykjaneshalbinsel ist besonders gut für diese Studie geeignet, da die lokale Plattenbewegung eine Mischung aus divergierender und scherender Bewegung ist. Das bedeutend, dass die Bewegungsrichtung der tektonischen Platten nicht senkrecht auf die Plattengrenze steht, sondern in einem Winkel dazu verläuft, was eine Rotation der Hauptspannungsrichtungen erzeugt. Episoden vulkanischer Aktivität konzentrieren sich auf Reykjanes üblicherweise auf Zeiträume in der Größenordnung von 200–300 Jahren, wonach Ruhephasen folgen, die etwa 800–1000 Jahre andauern. Die Gangintrusion 2021 und die darauffolgende sechs Monate andauernde Eruption haben eine beinahe 800 Jahre dauernde Pause vulkanischer Aktivität auf der Halbinsel beendet. Das numerische Modell der Gangintrusion ist in zwei Schritte unterteilt: Im ersten Schritt baut sich tektonische Spannung über einen Zeitraum von 800 Jahren auf. Im zweiten Schritt wird die angesammelte Spannung lokal gelöst, indem der Gang als Riss in der Modellkruste gebildet wird. Die Öffnung des Gangs wurde ausschließlich von tektonischer Spannung getrieben. Das Modell zeigt, dass geodetisch beobachtete Oberflächendeformation am besten reproduziert werden kann, wenn etwa 60% der lokal angesammelten Spannung durch den Gang gelöst werden. Dass nur ein Bruchteil der Spannung gelöst wurde, ist konsistent mit drei nachfolgenden Gängen, die sich zwischen Dezember 2021 und Juli 2023 in derselben Gegend gebildet haben. Die relative Scherung und Öffnung entlang des Ganges,

die von dem numerischen Modell vorhergesagt werden, zeigen gute Übereinstimmung mit Werten, die geologische Modelle basierend auf der Streichrichtung des Ganges im Vergleich zum Spannungsfeld erwarten.

Die Ergebnisse der hier vorgestellten Arbeit zeigen, dass die Interaktion zwischen magmatischen Gängen und Brüchen/Störungen sowie mit dem tektonischen Spannungsfeld hochkomplexe Vorgänge sind. Weitere Forschung ist notwendig, um sie besser zu verstehen und um ihre Wechselwirkung in geophysikalische Modelle zu integrieren, die für die Überwachung aktiver Vulkane hilfreich sein können.



Information about Photos on Divider Pages

This list provides information on all photos on divider pages. All photos were taken by myself and most during or shortly before the beginning of this PhD project.

Page iv:

> Eruptive fissure of the 2022 Fagradalsfjall eruption. Photo was taken within the first hours of the eruption on 03.08.2022.

Page vi:

> Field site DF1 at Dyrfjöll as seen from Dimmidalur looking westward. Toward the left, the pink ignimbrite underlying the caldera-filling hyaloclastite is visible (just below the lower snow patches). Photo taken August 2021.

Page x:

> The second day of the 2022 Fagradalsfjall eruption (04.08.2022).

Page xiv:

> Crater of the 2022 Fagradalsfjall eruption on 14.08.2022. Behind the crater are several hyaloclastite mountains, emphasizing how common this type of rock is in the area.

Page xx:

> The Krýsuvík fissure swarm and Búrfellsgjá with Reykjavík and Esja in the background. Photo taken with a UAV from flying above the top of Helgafell in August 2024.

Page xxii:

> A partially eroded dike in hyaloclastite north of Kleifarvatn (Reykjanes Peninsula). Photo from July 2023.

Page xxvi:

> Some local inhabitants of the Dyrfjöll mountains. In the upper third the transition between the hyaloclastite and the overlying lava layers is visible. Photo from August 2021.

Page 4:

> Sheet intrusions at Hovedøya (Oslo fjord, Norway). For more information on this outcrop see Poppe et al. (2020). Photo from May 2023.

Page 10:

Magma-fracture interaction of a sheet intrusions at Hovedøya (Oslo fjord, Norway). For more information on this outcrop see Poppe et al. (2020). Photo from May 2023.

Page 15:

The 2021 Fagradalsfjall eruption during the phase, where multiple fissures were active simultaneously. Photo taken (23.04.2021).

Page 23:

The Reykjanes Peninsula as seen from Helgafell looking westwards. Photo taken with a UAV in August 2024.

Page 38:

Channel of lava flowing downhill from the crater of the 2021 Fagradalsfjall eruption (21.03.2021).

Page 40:

View from the Dyrfjöll caldera towards east across Borgarfjörður eystri. In the foreground is the tree-dike at DF3, described in **Paper I**. Additionally, the transition between the hyaloclastite and the lava layers above is visible. Photo taken in August 2021.

Page 44:

Solidified and excavated oil intrusion of analogue experiment OF50/50. See **Paper II** for more information. The segment parallel to the fault is hollow because the oil drained downwards into the fault after the volumetric pump was shut down.

Page 50:

The 2021 Fagradalfjall eruption on the third day of the eruption (21.3.2021).

Page 56:

View over the Reykjanes Peninsula with the gas plume of the 2021 Fagradalsfjall eruption as seen from Ægisíða, Reykjavík. Taken 02.05.2021. Fun fact: I went to the coast to think about if I should take the PhD position, which resulted in this exact thesis.

Page 64:

Multiple dike cutting through the lava pile near the Sandfell laccolith in Fáskrúðsfjörður (East Iceland). Photo taken in August 2021.

Page 90:

Fractured crust between disconnected sheet intrusion tips at Hovedøya (Oslo fjord, Norway). Pen for scale. For more information on this outcrop see Poppe et al. (2020). Photo from May 2024.

Page 94:

Northward view over the January-2024 fissure/craters at Svartsengi. Note the bend in the fissure. Photo taken in February from near the point where the fissure cut through the protective barriers.

Page 98:

View of the Dyrfjöll mountains in Borgarfjörður eystri from Jökuldalur (looking westward). The fieldsite DF2 of **Paper I** can be seen in the middle on the right edge of the photo. A small part of site DF1 is at the same level on the left edge, but most of it is outside of the frame.

Page 102:

Westward view into the Dyrfjöll caldera and onto field site DF2.

Page 136:

Solidified and excavated oil intrusion of analogue experiment OF50/50. See **Paper II** for more information.

Page 220:

The 2021 Fagradalsfjall eruption seen from Fagradalsfjall (21.04.2021).

Page 282:

View over the December 2023/February 20024 lava fields at Svartsengi. Stóra-Skógfell in the background. Photo taken in February 2024.



Paper I

Interaction between propagating basaltic dikes and pre-existing fractures: A case study in hyaloclastite from Dyrfjöll, Iceland

Sonja H. M. Greiner, Steffi Burchardt, Freysteinn Sigmundsson, Birgir V. Óskarsson, Olivier Galland, Halldór Geirsson, Emma Rhodes

Journal of Volcanology and Geothermal Research, Vol. 442, 107891

doi: https://doi.org/10.1016/j.jvolgeores.2023.107891

Status: Published (2023)

Journal of Volcanology and Geothermal Research 442 (2023) 107891

Contents lists available at ScienceDirect

Journal of Volcanology and Geothermal Research

journal homepage: www.journals.elsevier.com/journal-of-volcanology-and-geothermal-research

Interaction between propagating basaltic dikes and pre-existing fractures: A case study in hyaloclastite from Dyrfjöll, Iceland

Sonja H.M. Greiner [a,b,c,*], Steffi Burchardt [b,c], Freysteinn Sigmundsson [a], Birgir V. Óskarsson [d], Olivier Galland [e], Halldór Geirsson [a], Emma Rhodes [b,c,f]

[a] Nordic Volcanological Center, Institute of Earth Sciences, University of Iceland, Reykjavík, Iceland
[b] Department of Earth Sciences, Uppsala University, Uppsala, Sweden
[c] Center for Natural Hazard and Disaster Science (CNDS), Sweden
[d] Icelandic Institute of Natural History, Garðabær, Iceland
[e] NJORD Center, Department of Geosciences, University of Oslo, Oslo, Norway
[f] Pattle Delamore Partners, Christchurch, New Zealand

ARTICLE INFO

Keywords:
Dike propagation
Dike-fracture interaction
Volcano-tectonic interaction
Hyaloclastite
Photogrammetry
Iceland

ABSTRACT

Magma in the Earth's crust is commonly transported through dikes. Fractures and faults, which are common in the shallow crust, form structural weaknesses that can act as energy-efficient propagation pathways. Although examples of this are known from active and extinct volcanoes in varying host rocks, the conditions and mechanisms of how and when dikes are influenced by these structures are not yet fully understood. This study investigates how basaltic dikes propagating through hyaloclastite in the shallow crust interact with pre-existing fractures. Using virtual 3D-models from drone-based photogrammetry, we mapped basaltic dikes exposed in a caldera-filling hyaloclastite in the extinct Dyrfjöll volcano, NE-Iceland, to measure the orientations of fractures and dikes, and quantify their interactions. We observe 39 changes in strike among 45 dikes and found a strong control of the governing stress field on orientations and interactions. Three types of dike-fracture interaction were identified: (1) Dikes propagating along pre-existing fractures. This is most frequently observed for dikes following the tectonic stress field. (2) Dikes with an abrupt change in strike occurring near or at a crosscutting fracture, but without magma flow into the fracture. (3) Dikes arrested at a crosscutting fracture. Such dikes may develop offshoots near the dike tip, which may approach the fracture at different angles and be able to cut across. Understanding how dikes interact with pre-existing fractures in moderately fractured host rock such as hyaloclastite is relevant for hazard assessment and monitoring of volcanically active areas.

1. Introduction

Dikes represent an important mode of magma transport through the Earth's crust. In the upper parts of the crust, they can form due to failure of a pressurized magma reservoir and to relax tensile stresses which accumulate due to plate spreading (e.g., Rivalta et al., 2015, and references therein). Dikes are vertical to subvertical sheet intrusions and can transport magma vertically and laterally across tens of kilometers away from the main volcanic center (Sigmundsson et al., 2015; Wauthier et al., 2012). The characteristics of propagating dikes (e.g., geometry, mode of failure, associated surface deformation) vary in different types of host rocks (Bertelsen et al., 2021).

The shape and propagation path of dikes is often assumed to be determined by the prevailing stress conditions with the dike opening as a tensile, planar fracture parallel to the direction of the least compressive stress (Anderson, 1951). Deformation models, which are frequently used to constrain magmatic processes at depth, tend to represent dikes as dislocations opening in a homogeneous, often fully elastic volume (Okada, 1985, 1992; Wright et al., 2006; Wauthier et al., 2012; Sigmundsson et al., 2015). However, numerous studies based on field observations of exposed dikes and analogue models, suggest that propagation can be more complex, e.g., because of a shearing component during the opening of the dike (Stephens et al., 2018; Dering et al., 2019), interaction with pre-existing fractures (Spacapan et al., 2016;

* Corresponding author at: Nordic Volcanological Center, Institute of Earth Sciences, University of Iceland, Reykjavík, Iceland.
E-mail addresses: shmgreiner@hi.is (S.H.M. Greiner), steffi.burchardt@geo.uu.se (S. Burchardt), fs@hi.is (F. Sigmundsson), birgir.v.oskarsson@ni.is (B.V. Óskarsson), olivier.galland@geo.uio.no (O. Galland), hgeirs@hi.is (H. Geirsson), nzemmarhodes@gmail.com (E. Rhodes).

https://doi.org/10.1016/j.jvolgeores.2023.107891
Received 31 May 2023; Received in revised form 8 August 2023; Accepted 14 August 2023
Available online 19 August 2023
0377-0273/© 2023 Elsevier B.V. All rights reserved.

Poppe et al., 2020), varying material properties of the host rock such as layers of different rock types (Kjøll et al., 2019; Bertelsen et al., 2021; Drymoni et al., 2021), and the composition of the intruding magma (Schmiedel et al., 2021). Another important aspect is that the stress field is affected by various geological processes, such as plate tectonics, the inflation/deflation of magma reservoirs, glacio-isostatic adjustment and the diking process itself causing spatio-temporal complexities in the field (Heimisson et al., 2015; Drymoni et al., 2020). Furthermore, on smaller scales effects can be caused by host rock heterogeneities like material interfaces and layering (Kavanagh et al., 2006; Burchardt, 2008; Mathieu et al., 2015). All of these aspects influence and can change the propagation direction of dikes. Different types of host rock may also show varying intensity and types of fracturing, e.g., cooling joints in magmatic rocks and tectonic fractures. Some studies of dikes exposed in eroded volcanic systems indicate that propagation paths in the uppermost crust can be influenced by pre-existing weaknesses, such as fractures and fault zones (e.g., Delaney et al., 1986; Baer and Beyth, 1990; Baer et al., 1994; Jolly and Sanderson, 1997; Martínez-Poza et al., 2014; Browning and Gudmundsson, 2015; Spacapan et al., 2016; Stephens et al., 2018; Poppe et al., 2020; Drymoni et al., 2021), while other studies propose dike propagation is unaffected by such weaknesses, e.g., Lister and Kerr (1991), Rubin (1993), Rubin (1995). Despite decades of research into the details of when and how dikes use pre-existing weaknesses (e.g., Delaney et al., 1986; Ziv et al., 2000; Valentine and Krogh, 2006; Le Corvec et al., 2013), the mechanisms are still not fully understood. An improved understanding of dike-fracture interaction may help to better constrain possible propagation paths, and thus potential eruption locations, during volcanic unrest periods and therefore be of value for hazard assessment.

Here, we apply structural analysis of well-exposed basaltic dikes in hyaloclastite at the extinct Dyrfjöll caldera in NE-Iceland. Glacial erosion of a caldera-infill hyaloclastite has exposed numerous regional dikes emplaced after volcanic activity associated with the Dyrfjöll caldera ceased. We study the arrangement of dikes and fractures to understand to what degree dike propagation was influenced by pre-existing fractures. Our results help to understand scenarios of eruptive

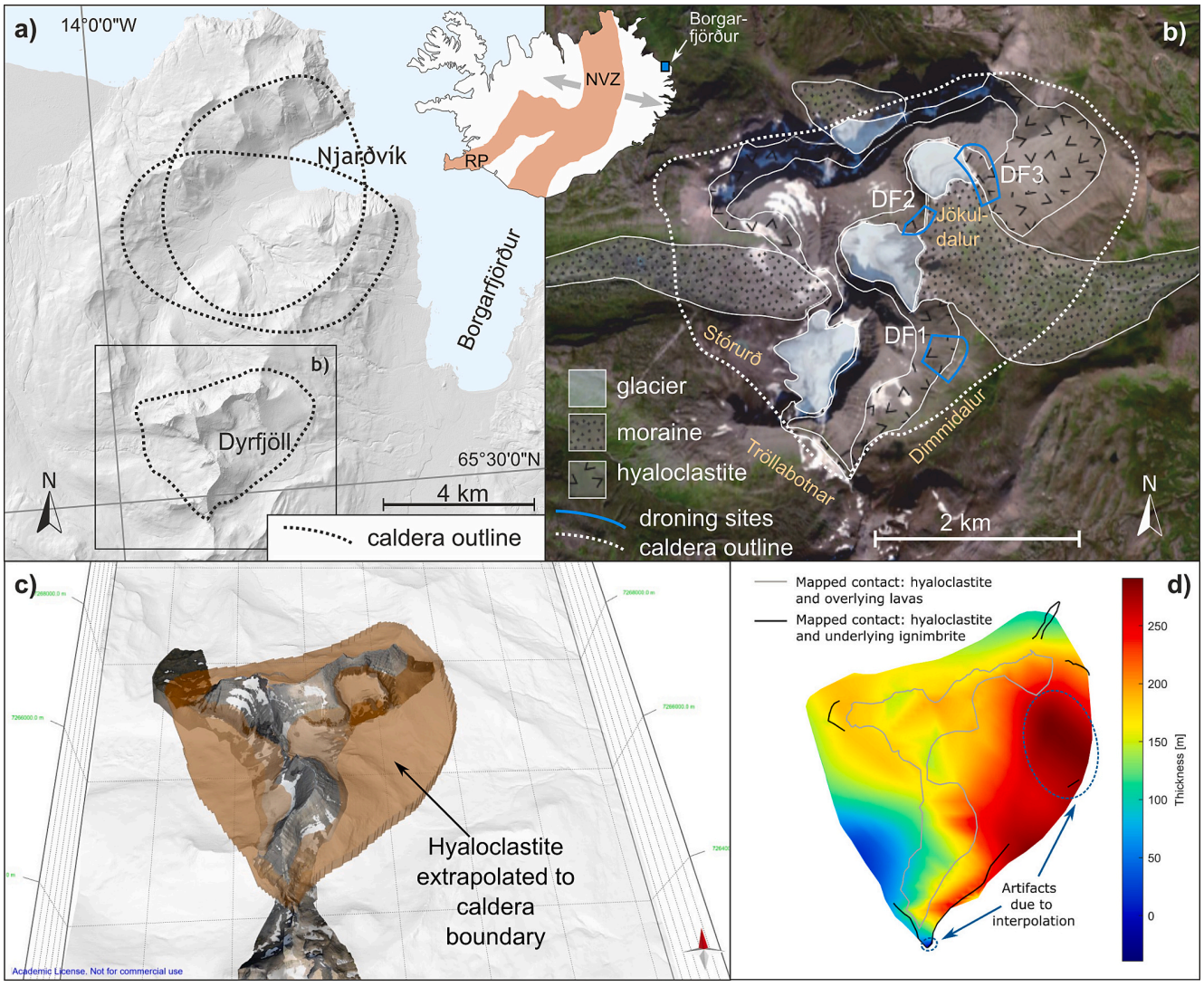

Fig. 1. Overview maps of (a) the north-western part of the Borgarfjörður-eystri-Loðmundarfjörður (BEL) area and (b) the Dyrfjöll caldera. Caldera outlines and surface geology in panels (a) and (b) from Burchardt et al. (2022). Droning sites DF1–DF3 in (b) are marked in blue. Small inset: Iceland with the plate boundary outlined by the shaded area. The blue box in the North-East of Iceland marks the location of the Borgarfjörður area. Grey arrows indicate far-field plate motion. The Northern Volcanic Zone (NVZ) and Reykjanes Peninsula (RP) are two of the volcanically active segments of the plate boundary (e.g., Sigmundsson et al., 2020). (c) Volumetric extent for the caldera-filling hyaloclastite based on extrapolating the exposed top and bottom contacts to the caldera boundary. (d) Thickness of the extrapolated hyaloclastite layer.

fissures following existing fractures in areas with significant amounts of moderately fractured hyaloclastite, but may further be applied to other, structurally similar host rocks (e.g., tuff or sandstone) with a comparable degree of fracturing.

2. Geological setting

Iceland is located at the intersection between the Mid-Atlantic Ridge, which crosses the island approximately from Southwest to Northeast (Fig. 1), and a mantle plume. Active volcanism occurs along rift zones, which accommodate plate spreading and are connected by transform zones, as well as in flank zones, where no plate spreading is observed (e.g., Einarsson, 2008; Árnadóttir et al., 2009; Sigmundsson et al., 2020). Far-field plate motion occurs at 18–19 mm/yr towards N(100–105 °) E relative to the stable North-American plate (see e.g., Sigmundsson et al., 2020, and references therein), and is locally accommodated by faulting and dike emplacement.

Due to periods of extensive glaciations in the past, volcanic products characteristic for magma-ice interaction are commonly found in Iceland. One such product is hyaloclastite (Schopka et al., 2006; Jakobsson and Gudmundsson, 2008; Jarosch et al., 2008). The term hyaloclastite is somewhat loosely defined (e.g., Watton et al., 2013, and references therein), but refers here to basaltic magma which was fragmented and solidified to varying degrees due to contact with water or ice during eruption and consolidated due to subsequent hydrothermal alteration (e.g., Jarosch et al., 2008), producing a heterogeneous material with brecciated pillows in a matrix of fine, glassy fragments. The amount and size of pillow fragments can vary significantly within individual rock units (Fig. 2a, b), but this does not affect the large-scale structure of the formations (Fig. 2c). This large scale homogeneity is what makes hyaloclastite well suited to study dike-fracture interaction.

Many presently active volcanic systems in Iceland consist of a central volcano, often with a caldera and silicic eruptive products, and an elongated fissure swarm, which is the surface-expression of an underlying dike swarm (Sæmundsson, 1979; Thordarson and Larsen, 2007). Fissure swarms are generally thought to reflect the orientation of the principal stresses with the least compressive stress perpendicular to their strike (e.g., Sigmundsson et al., 2020). Due to motion of the mantle plume relative to the plate boundary and potential variations in the size of the plume with time (Óskarsson and Riishuus, 2014), episodic rift-jumps have occurred in Iceland, when the active plate boundary shifts by several tens to a hundred kilometers to stay above the mantle plume (Helgason, 1984). These jumps, together with plate motion, limit the lifetime of volcanic systems and produce extinct volcanic zones, where varying degrees of burial and subsequent erosion have resulted in the exposure of the shallow volcanic plumbing system (Walker, 1974; Helgason, 1984).

The Borgarfjörður eystri-Loðmundarfjörður area (BEL; Fig. 1) in NE-Iceland hosts a cluster of several volcanic centers (Burchardt et al., 2022). The area was active during the Miocene, dated to 14–12.2 Ma ago, and the different centers appear to have been active roughly simultaneously (Burchardt et al., 2011; Berg, 2016; Burchardt et al., 2022). The area contains three collapse calderas and ignimbrite sheets, among them the Dyrfjöll caldera which is located west of Borgarfjörður eystri (Fig. 1a). It is bound by steeply dipping ring-faults and has a maximum diameter of ca. 4 km. The caldera floor is covered by rhyolitic ignimbrite (Fig. 1b), which is at least 30 m thick. Above the ignimbrite, an up to 250 m thick layer of hyaloclastite is exposed, which fills up the entire caldera and compositionally corresponds to an olivine-basalt (Burchardt et al., 2022). There is no evidence of glaciers in the area during the Miocene, when Dyrfjöll was active (Gústafsson, 1992), suggesting that in contrast to many other hyaloclastite formations in Iceland, magma likely interacted with water rather than ice. Gústafsson (1992) suggested the presence of a caldera lake and compared the setting in the caldera with the Öskjuvatn caldera, the youngest caldera of the Askja volcanic system in North Iceland. Structures observed at the caldera edge near Tröllabotnar and the dipping of faint bedding layers within the hyaloclastite towards the center of the caldera (Fig. 2b) may indicate that the lava, which formed the hyaloclastite, flowed into the lake from the sides rather than originating from within the caldera (Gústafsson, 1992; Burchardt et al., 2022). The lava flows which overlie the hyaloclastite (e.g., Fig. 2c) belong to the Jónsfjall olivine basalt group (Óskarsson and Riishuus, 2013), and the hyaloclastite likely belongs to the same group (Burchardt et al., 2022). These regionally extensive basalts were erupted from fissures not associated with any central volcano and buried the caldera cluster in the BEL area (Óskarsson and Riishuus, 2013). Secondary minerals as well as unaltered olivine crystals within the lava flows indicate that they have not been significantly buried (Burchardt et al., 2022). They represent the youngest magmatic event in the area (Walker, 1960).

The hyaloclastite and the underlying ignimbrite are exposed around the Dyrfjöll massive in steep glacial valleys, e.g., at Stórurð and Tröllabotnar, as well as in Dimmidalur and Jökuldalur. The exposures often have the form of steep cliffs (see e.g., Fig. 2c), which makes them difficult to access and study in close detail. Basaltic dikes cut through the hyaloclastite all over the caldera, and some dikes can be traced into the overlying lava layers. Hence, the dikes in the hyaloclastite may represent the feeders to the lavas. Gústafsson (1992) described 76 dikes for

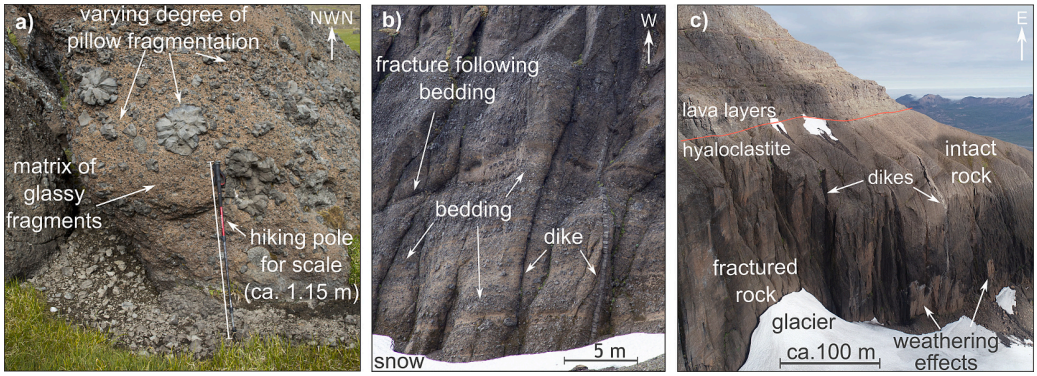

Fig. 2. Hyaloclastite on three different scales. (a) Hyaloclastite boulder in Dimmidalur (see Fig. 1b, coordinates: N65.500180 °, W13.917145 °) shows varying degrees of fragmentation from pillow breccia to a matrix of glassy fragments. The hiking pole for scale has a height of approximately 1.15 m. (b) Part of the base of site DF2 showing two small dikes and faint bedding in the hyaloclastite. Photo taken from ca. N65.51495 °, W13.92707 °. (c) Outcrop scale UAV-photo of the DF3 site (taken from just northeast of the site at ca. N65.52148 °, W13.92560 °) showing large-scale homogeneity of hyaloclastite and the contrast with the overlying lava layers (above the red line). In the left half of the image the host rock is cut by vertical fractures, while the right side consists of largely intact rock. Color variations in the host rock are attributed to varying degrees of weathering. Scale varies with perspective.

the Dyrfjöll and Njarðvík areas (Fig. 1a), with an average strike of N20 °E and a minor set striking NE. Dike thicknesses were found ranging from 0.3 to 5 m with an average of just below 2 m. The dominant NNE-strike agrees well with the strike of dikes found all over the BEL area (Burchardt et al., 2011; Burchardt et al., 2022) and the regional plate motion.

The tectonic setting of the BEL area is somewhat poorly understood. The lack of clearly visible dike swarms, the closely spaced cluster of calderas and the slightly transitional alkaline composition of some lavas were taken as indications that the area may not have been a typical rift zone but rather resembled a flank zone (Gústafsson, 1992; Óskarsson and Riishuus, 2013; Burchardt et al., 2022). Additionally, the overall rift zone configuration in Iceland may have been different from the present one. It has for example been suggested that the plume head was somewhat larger and located further north than at present (Walker, 1974, 1975; Óskarsson and Riishuus, 2014), which would have likely influenced the stress field in the BEL to some degree.

3. Methods

3.1. Photogrammetry

Most dikes in the Dyrfjöll caldera are exposed in steep hillsides and cliffs, which are difficult or impossible to access on foot. In the past decade, numerous studies have successfully mapped such inaccessible or large areas by collecting images with Unmanned Aerial Vehicles (UAVs) and creating virtual outcrops through Structure from motion (SfM) algorithms (Niethammer et al., 2012; James and Robson, 2012; Bemis et al., 2014; Eltner et al., 2016; Dering et al., 2019; Thiele et al., 2021; Rhodes et al., 2021).

We collected photogrammetry data using a DJI Phantom 4 Pro UAV with an FC6310 camera and an 8.8 mm lens at three sites on the eastern side of the Dyrfjöll mountains, which are referred to from here on as DF1–DF3 (Fig. 1b). They have base elevations of ca. 520 m a.s.l. (DF1), 560 m a.s.l. (DF2) and 580 m a.s.l. (DF3) and were selected based on the size of the outcrops and accessibility. Both the flight path of the drone and the recording of images were controlled manually. While both the yaw and the pitch of the camera were varied manually, the roll remained unchanged at 0 °. Photographs were taken with a minimum of 50% overlap and with varying viewing angles to ensure the alignment of the individual images and adequate representation of three-dimensional (3D) features during processing. Individual photographs have a resolution of 5472 × 3648 pixels. The geographical location, at which each image was taken was recorded using the UAV-internal GPS. The horizontal and vertical uncertainty of camera locations is listed in the Supplementary Materials, Table S1. A total of 130, 146 and 120 images were taken at DF1–DF3, respectively.

Additionally, 236 aerial images of the entire Dyrfjöll mountains were taken with a handheld NIKON D850 camera (35 mm focal length, 8256 × 5504 pixels resolution) from a small airplane, which flew around the mountains at an elevation slightly above the mountain tops (ca. 1300 m a.s.l.).

Virtual 3D outcrop models were created from the UAV and aerial images in Agisoft Metashape Professional version 1.6.3 (https://www.agisoft.com/). Pictures with insufficient overlap or quality were excluded from the process by using software-internal tools to estimate the alignment and image quality. The software uses the camera locations connected to each image to georeference the outcrop model automatically using the WSG84 reference system. Although the use of ground control points would have improved the accuracy of the model, this was not feasible due to the inaccessibility of the outcrops. The final models of DF1–DF3 had resolutions of 28 cm/pixel, 24.9 cm/pixel and 31.2 cm/pixel, respectively and additional details as well as images of the cameras relative to the final models can be found in Section S2 in the Supplementary Materials.

Five 3D models based on the aerial images were combined into a single model of the entire Dyrfjöll mountains. They were georeferenced and fitted on the IslandsDEM, a digital elevation model available on the webpage of the National Land Survey of Iceland, in the software MOVE by Petroleum Experts. The model was used to trace the top and bottom of the hyaloclastite as lines and subsequently create the top and bottom surfaces from these lines. Extending these surfaces to the caldera fault, the position of which is given by Burchardt et al. (2022), provides an estimate of the volume of the hyaloclastite.

3.2. Dike and fracture mapping

Individual dikes and fractures were identified using the virtual outcrops and the UAV photographs. Orientations of dikes and fractures (strike and dip) were then measured in the virtual outcrop models in LIME v 2.2.2 (Buckley et al., 2019) using the "Measure from 3 points" tool, which fits a plane to three selected points on the dike or fracture. LIME does not provide a quality or uncertainty estimate for the orientations, thus we self-derived a method for measuring the orientation quality (Supplementary Materials, Section S1). In the following, we present orientation data according to the 'American right-hand rule', i.e. that the dip direction is read clockwise from the strike. While only the orientation was measured for fractures, dikes were analyzed with regards to their orientation, evidence for the potential use of pre-existing fractures and possible changes in strike along individual dikes (Supplementary Materials, Table S3 along with Figs. S8–S10, where all dike segments are marked). In many instances, dikes consist of more than one segment. Here, we define a new segment either after a change in strike (Fig. 3a) or if the dike is broken up into disconnected segments, which may or may not have the same strike (Fig. 3b). A dike was defined as occupying a fracture if the fracture visibly continued beyond the

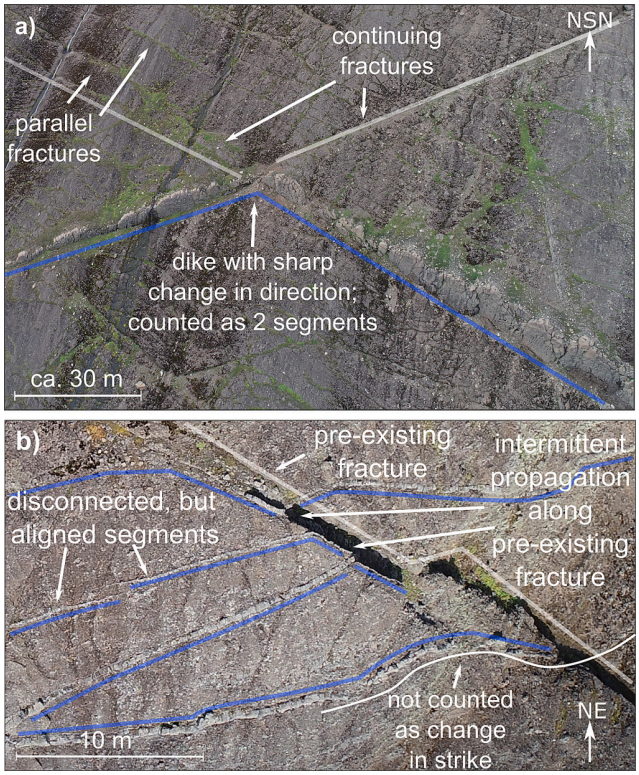

Fig. 3. Examples of dikes in hyaloclastite, how they interact with pre-existing fractures, and in which cases a new segment is or is not defined. All dike segments are marked in blue, and fractures, with which dike segments interact, are marked in gray. (a) Example of a sharp change in strike observed at DF1. Scale varies with perspective. (b) Examples from branches of a dike at DF3 (see Fig. 7 for entire dike).

exposed part of the dike or if there were somewhat regularly spaced fractures found parallel to and on either or both sides of an exposed dike (Fig. 3a). The orientations of dikes and fractures were plotted in Stereonet 10 (Allmendinger et al., 2011; Cardozo and Allmendinger, 2013). Further analysis of the properties of dikes and fractures was performed using Matlab.

3.3. Stress field analysis

The Matlab-code FracTend (Stephens et al., 2018; Healy, 2022) models the expected tendency of pre-existing fractures of any orientation to slip or dilate when they are intruded by a sheet intrusion. It additionally estimates the minimum magmatic pressure required for this and the expected opening angle (angle between dilatation vector and the vector expected for purely tensile opening) in a uniform stress field and for a specified uniform magmatic pressure. This is done under the assumption that a fracture dilates when the magmatic overpressure exceeds the stress component normal to the fracture plane. The code allows to compare measured orientations to the values expected in the specified stress field by providing estimates for the fracture susceptibility, that shows at which magma pressure individual fractures are expected to be susceptible to intrusion. Here, we use FracTend to compare orientations of different groups of dikes to a uniform tectonic stress field. It is important to note that the opening angle of the dikes at Dyrfjöll cannot be constrained from the data collected in this study. However, dikes are often assumed to mostly open in a tensile manner and deviations from this in the data set may provide insights into the stress field at the time of emplacement.

We use the present-day stress field of the Northern Volcanic Zone (NVZ, inset in Fig. 1) of Iceland as an analogue for the tectonic stress field at Dyrfjöll at the time of dike emplacement. While the specific configuration of rift zones is unclear for the times of volcanic activity in the BEL area, the orientation of dikes and faults is consistent with the NVZ configuration (cf. Burchardt et al., 2022). We estimate values for the principal stresses σ_1, σ_2 and σ_3 in a strongly simplified model of the tectonic stresses. It is important to note that only the ratio of the principal stresses to each other and their directions influence the results in FracTend, not their amplitudes (Stephens et al., 2018). The amplitudes mainly influence the corresponding magmatic pressure required to reactivate fractures and scale with the assumed spreading rate and the elastic moduli chosen for the modeled crust. The values chosen here may serve as examples and provide an order of magnitude. Plate spreading in the NVZ occurs currently at a rate of $s = 17.4$ mm/yr in direction 292 ° relative to the stable Eurasian plate (Drouin et al., 2017). It is assumed here that stresses accumulate over a period of t = 200 years, after which rifting episodes occur and release the accumulated stress. It is furthermore assumed that the plate spreading is purely tensile. Deformation is assumed to be limited to a $w = 50$ km wide strip of crust and the locking depth, below which the plates can move freely, is set to $h = 7$ km depth, which is representative for the NVZ (Heimisson et al., 2015). The Young's modulus and Poisson ratio are assumed as $E = 45$ GPa and $\nu = 0.27$, respectively (e.g., Grapenthin et al., 2006; Heap et al., 2020). A coordinate system is placed in the crust with the x- and y-axes parallel to the plate boundary and spreading direction, respectively, and the z-axis vertical. Extension and tensile stresses are taken as < 0. No deformation parallel to the plate boundary is assumed, and then the condition of plane strain applies with $e_x = 0$. Assuming the conservation of area in the cross-section through the deformation zone, the other two strain components can be calculated (Turcotte and Schubert, 2014):

$$e_y = \frac{w - (w + dw)}{w} = \frac{-dw}{w} \tag{1}$$

$$e_z = \frac{-dh}{h} \tag{2}$$

where $dw = s\,t = 3.48$ m equals the plate spreading throughout 200 years and dh can be calculated using the conservation of the cross-sectional area $dA = A - A' = w\,h - (w + dw)(d + dh) = 0$ as

$$dh = \frac{w\,h}{w + dw} - h = -\frac{h\,s\,t}{w + s\,t} \tag{3}$$

The resulting principal strains are $e_1 = e_z = 7.0{\cdot}10^{-5}, e_2 = e_x = 0$ and $e_3 = e_y = -7{\cdot}10^{-5}$.

With the assumed values for the elastic moduli, these strains correspond to stresses $\sigma_x = \sigma_2 = 0$ MPa, $\sigma_y = \sigma_3 = -2.5$ MPa and $\sigma_z = \sigma_1 = 2.5$ MPa (Turcotte and Schubert, 2014).

The stretching-parallel stress agrees well with stress-accumulation rate estimated by Sigmundsson (2006). It is important to note here that plane stress does not always follow from plane strain. It does here due to the combined assumptions of plane strain and conservation of cross-sectional area. Assuming that the peaks of the Dyrfjöll mountains represent the paleo-surface, the dikes were located at approximately $d = 0.5$ km depth and assuming an average density of $\rho = 2700$ kg/m^3, this results in a lithostatic pressure of $\sigma_{lith} = \rho\,g\,d = 13.2$ MPa. The estimates for the principal stresses used for FracTend are the sum of the lithostatic pressure and the principal components of the deviatoric stress, which leads to the least compressive stress of $\sigma_{3,abs} = 10.7$ MPa towards 292 ° (horizontal; perpendicular to rift direction), the maximum compressive stress of $\sigma_{1,abs} = 15.7$ MPa (vertical) and $\sigma_{2,abs} = 13.2$ MPa perpendicular to these two striking 22 ° (horizontal; along the rift direction). Lastly, the magmatic pressure was assumed to be 14.5 MPa, which equals an overpressure of 1.3 MPa. This value was chosen somewhat arbitrarily so that all dikes in fractures were predicted to indeed be intruded by magma in the modeled stress field. It falls well into the range commonly inferred for large-scale tensile rock-strengths at shallow depth (Jónsson, 2012; Haimson and Rummel, 1982).

4. Results

4.1. The Dyrfjöll caldera-filling hyaloclastite

3D reconstruction of the hyaloclastite filling the Dyrfjöll caldera (Fig. 1c and d) shows that the bottom of the hyaloclastite forms a wide bowl and that the layer is thickest near the center of the caldera and thins towards the edges. The thickness in the eastern part of the caldera is poorly constrained and likely an artifact of the extrapolation, due to poor or no exposure of the contacts in this area (see Fig. 1b). Similarly, the negative thickness at the southern tip of the caldera, where the top surface was extrapolated to be below the base, is an artifact. At the sites DF1–DF3, the thickness of the hyaloclastite is better constrained and estimated to be approximately 200–250 m (Fig. 1d).

Based on the extrapolation towards the caldera edge, the pre-erosional volume is estimated to have been around 1.8 km^3.

4.2. Fractures

The majority of fractures at all three sites are steeply dipping (> 60 °). Shallow-dipping fractures (< 30 °) were mainly observed at DF2. Most of the shallowly dipping fractures at DF2 strike 350 ± 10 and follow faintly visible bedding in the hyaloclastite (see e.g., Fig. 2b). There was no visible interaction between magmatic intrusions and these fractures and they were therefore excluded from further analysis since they do not directly relate to the tectonic stress field (Supplementary Materials, Fig. S11). For steeply dipping fractures, observations can be divided into sets, which are understood as a strike direction which occurs with a higher frequency compared to other directions. We distinguish between two main and two minor fracture sets. The major sets, named FI and FII respectively, strike centered around 025 and 065, and the minor ones around 135 and 170 (Fig. 4, Table 1). There is some variation between sites with respect to the representation of individual sets and the exact strike of the identified sets (Fig. 4c, e & g; for

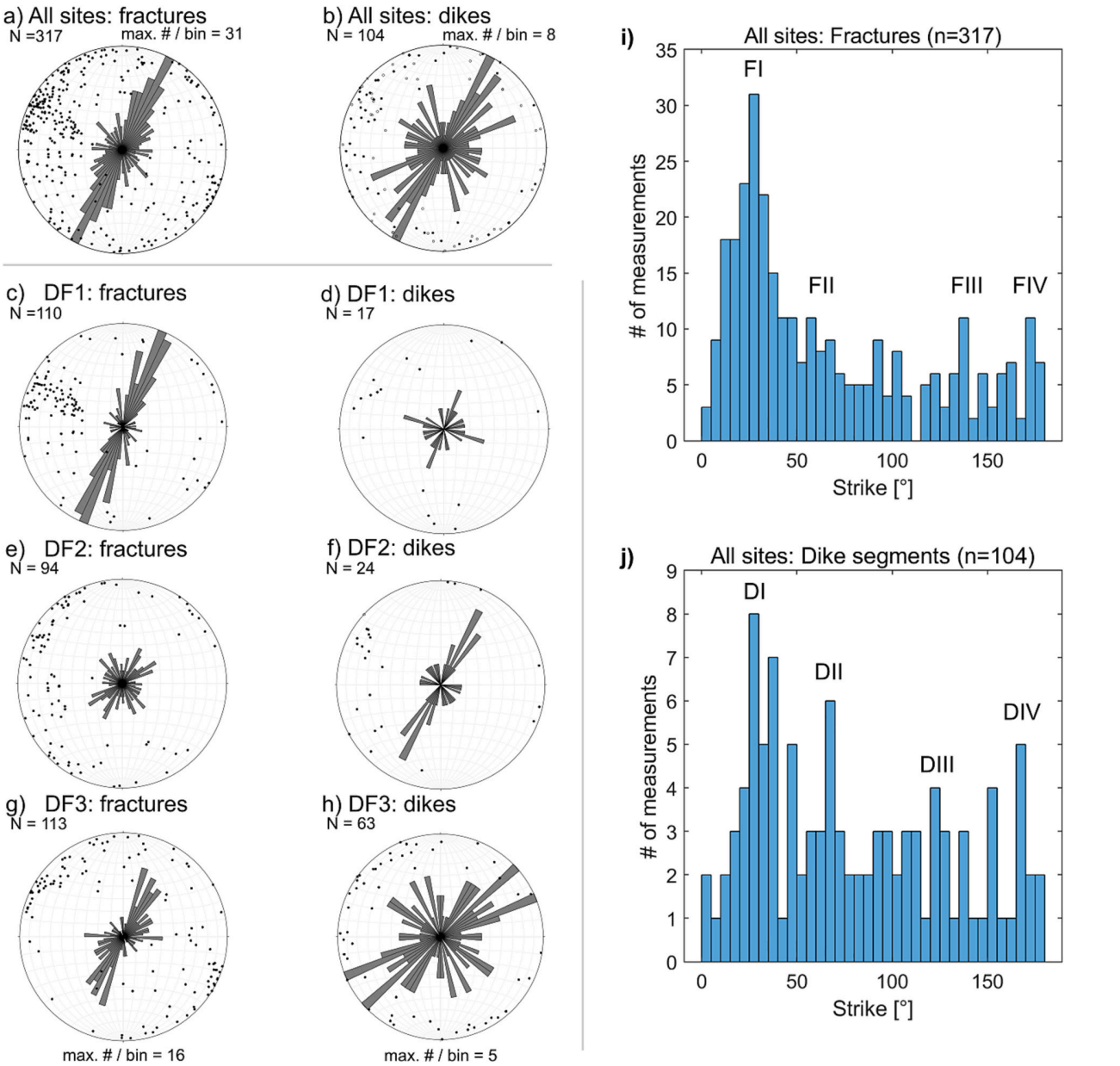

Fig. 4. Rose diagrams and poles for orientations of (a) fractures and (b) dikes at all sites and (c–h) fractures and dike segments at each site individually. For each individual site, rose plots were normalized for the maximum number of measurements per bin for all three sites (max. #/bin; 16 for fractures at DF1, 5 for dikes at DF3. N denotes the total number of measurements per plots. Fractures following bedding planes were excluded from e). Bin size for rose plots equals 5 °. (i) Histogram of the strike of all fractures in 5 ° bins. (j) Histogram of the strike of all dike segments in 5 ° bins. See Table 2 for details on fracture and dike sets marked in (i) and (j).

Table 1
Characteristics of individual sets of fractures and dike segments in the caldera shown in Fig. 4. Sets are numbered clockwise from north and given Roman numerals to avoid confusion with the names of droning sites. The color refers to dike segments marked according to their strike in Fig. 5–Fig. 6.

Set	FI	FII	FIII	FIV	DI	DII	DIII	DIV
Centre strike [°]	025	060	135	170	030	065	125	170
Lower limit strike [°]	010	050	120	155	020	055	110	160
Upper limit strike [°]	040	070	145	180	040	075	140	005
Color	–	–	–	-	Red	Green	Blue	Yellow

histograms of individual sites see Fig. S12 a–c in the Supplementary Materials).

Most fractures observed at DF1 belong to FI and are semi-regularly spaced. Although they are oriented almost parallel to the strike of the outcrop, they are well visible due to the lower cutting angle of the outcrop compared to the cliff-like exposure of the other two sites. At DF2, fractures strike along almost all directions with a more balanced distribution (Fig. 4e) compared to DF1. The major sets, FI and FII, are notably perpendicular to the two minor sets, FIII and FIV and all four sets are similarly pronounced. The outcrop appears blockier than DF1 and is more affected by weathering. The last site, DF3, can be divided into two distinct parts. The south-eastern part consists of largely intact rock with few fractures. Towards the north-western part of the outcrop the number of large, dominantly NNE-striking fractures increases

significantly (Fig. 2c). Fracture orientations are similar to DF1, but the distribution is more balanced, and the dominant direction shows a wider scatter. Changes in the fracture density with distance from individual dikes or in the vertical direction along outcrops were not observed anywhere.

4.3. Dikes

Across the three studied sites, a total of 45 dikes consisting of 104 segments were identified. At all three sites, but especially at DF1 and DF2, the majority of dikes strike NNE and belong to set DI (parallel to the main fracture set FI, see Table 1). Some strike sets identified for the fractures are missing, e.g., DIII at DF1 is barely represented and DII is missing entirely at DF2 (Fig. 4d and f). At DF3, DII is more pronounced than DI and almost any strike is found (Fig. 4h).

In the following we will describe three dikes in more detail to illustrate intermittent use of pre-existing fractures, frequent changes in strike and propagation through intact rock, respectively.

The clearest example of a dike using pre-existing fractures is located at DF1 (Fig. 5). The dike stretches diagonally across the entire outcrop and is exposed along a distance of approximately 360 m. The exposed section of the dike is composed of five segments and shows two significant changes in strike at either end of a centrally located, SSE–NNW-striking segment (yellow line in Fig. 5a; colors identify sets as listed in Table 1). Both changes have similar magnitudes, but in opposite directions. The corner connecting the solid red and the yellow segments coincides with a clearly visible fracture, which is occupied by another dike. Clearly visible fractures also continue beyond both corners marking either end of the yellow segment (Fig. 5a and b). It is unclear if the dashed red segment, which connects to the main dike at the lower corner, does indeed connect to the rest of the dike since the exposure is significantly worse than the previously described segments. The same applies to the dashed-dotted segment connecting to the southwestern end of the solid red segment.

At DF2, five changes in strike were observed along a single dike, which consists of seven segments and is exposed over a length of

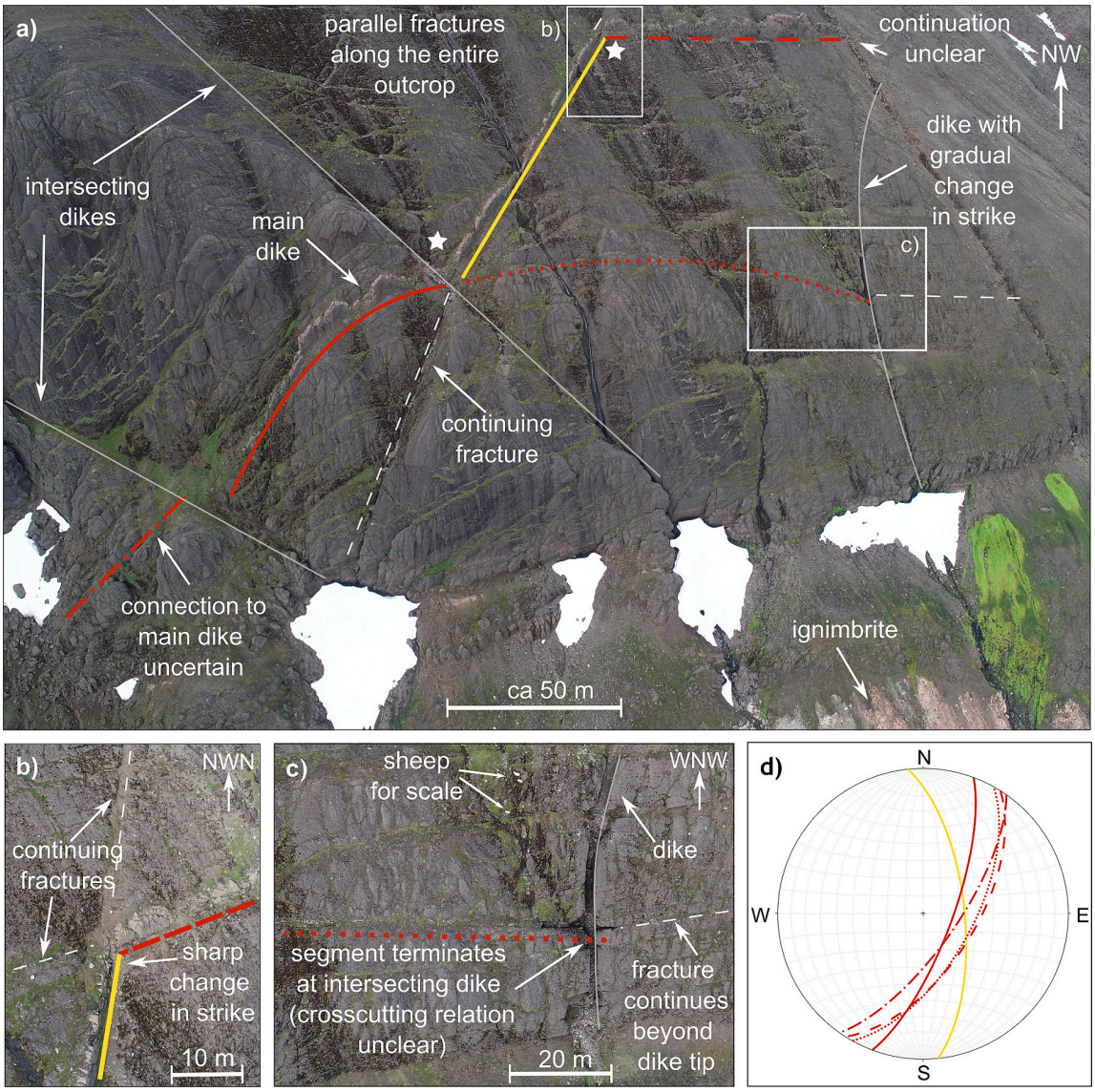

Fig. 5. (a) Example of a dike being channeled into a pre-existing fracture (yellow segment). White stars mark changes in strike. Grey lines mark intersecting dikes, but no clear cross-cutting relations can be established. Scale varies with perspective. (b) Close-up of the upper change in strike to illustrate the continuing fractures (white dashed lines). (c) Close-up of an eroded dike-tip, with a fracture continuing beyond the tip. (d) Orientations of the segments of the main dike in (a)–(c). Colors correspond to dike sets as listed in Table 1.

approximately 100 m (Fig. 6). The northern end (red dotted line in Fig. 6) may have extended further towards the northeast, but the southernmost segment (solid yellow in Fig. 6) narrows significantly towards the end (Fig. 6b). Four out of the five observed changes in strike occur where the dike intersects one of the more prominent fractures in the outcrop (Fig. 6e). The only exception is the connection between the dashed red and the solid white segments (Fig. 6a, b & e). In this instance, the change occurs distinctly next to a fracture (Fig. 6b and e).

A dike which is unique compared to all other studied dikes is located at DF3 (Fig. 7) and will hereafter be referred to as the 'Tree-dike'. Both tips are exposed and the main part of the dike is ca. 150 m long. Both tips are surrounded by vein- or branch-like magmatic structures, which connect to the main dike (Fig. 7b–e). At the lower tip, the veins are very thin (maximum thickness around a few tens of centimeters) and form an asymmetric, triangular pattern with low angles to the main dike (area with veins surrounded by white dotted lines in Fig. 7b). At the upper tip, thicker veins (up to several tens of centimeters) branch off at larger angles (up to almost 90 °) on either side of the main dike. The upper tip is located in front of a fracture, which, at least partially, is occupied by another dike and strikes almost perpendicular to the main part of the dike. Branches to the right of the main dike show clear evidence of intermittent use of the crosscutting discontinuity. Most of these segments appear to merge after crossing the discontinuity. Despite being rather thin, the merged branch can be traced along the outcrop for close to 160 m. A number of very thin veins accompany the dike, but they were considered too narrow to confidently determine their orientation or thickness and it is unclear how they relate to the dike.

The large number of interactions of dike branches with the crosscutting discontinuity suggest that it pre-dates the dike. The change in strike between the segments marked in solid red and dotted green in

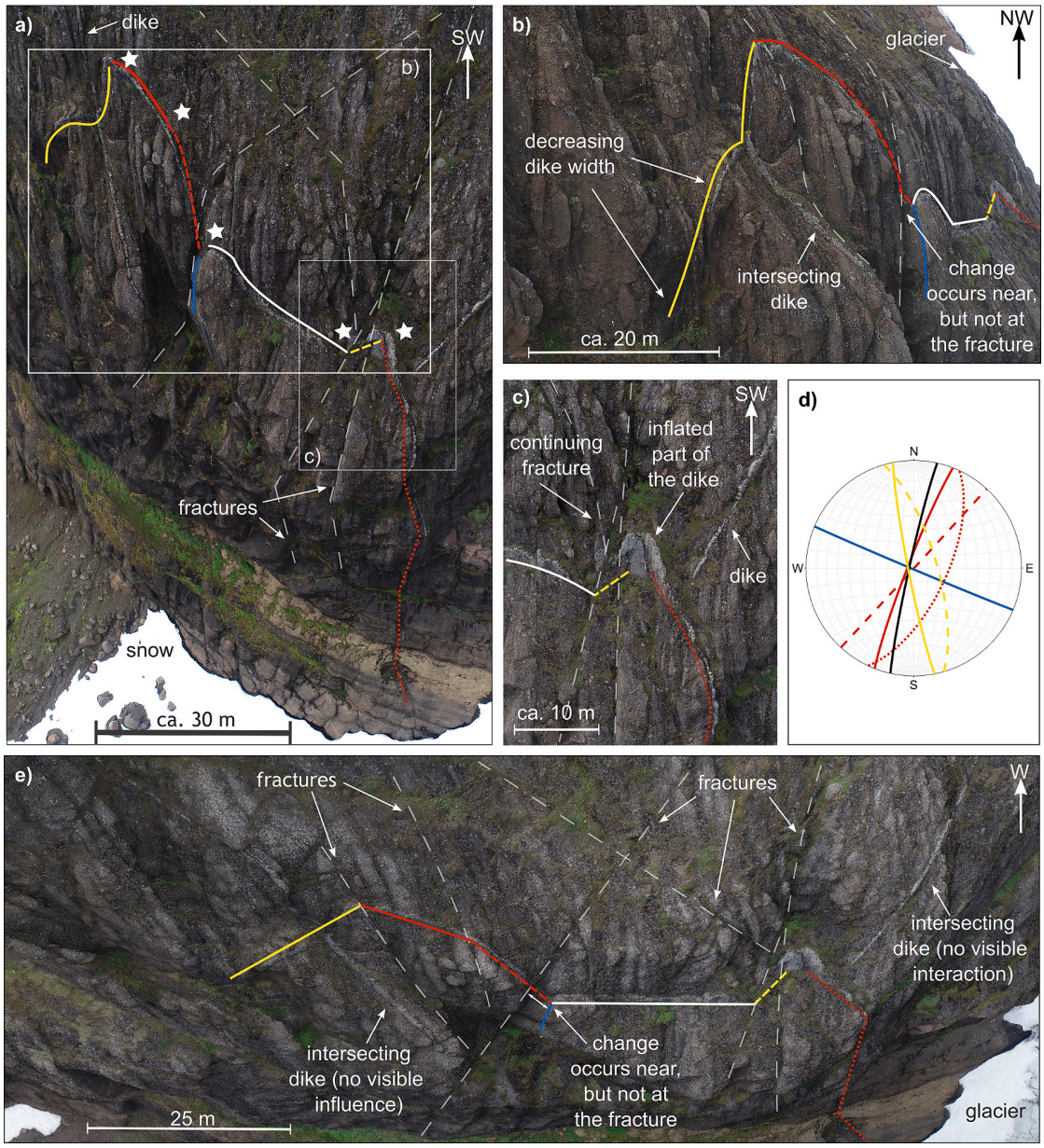

Fig. 6. Example of a dike at DF2 with numerous changes in strike (white stars in (a)). Fractures are marked by dashed gray lines. (b) and (c) show the dike from different perspectives. (d) Orientations of all dike segments coded by color and pattern as shown in the photographs, except black line in (d) corresponds to the white line in the photographs. Colors correspond to dike set as listed in Table 1. Dike segments outside of any sets are marked in black. (e) Map-view of the dike from the virtual outcrop model. Scale in (a)–(c) varies with perspective.

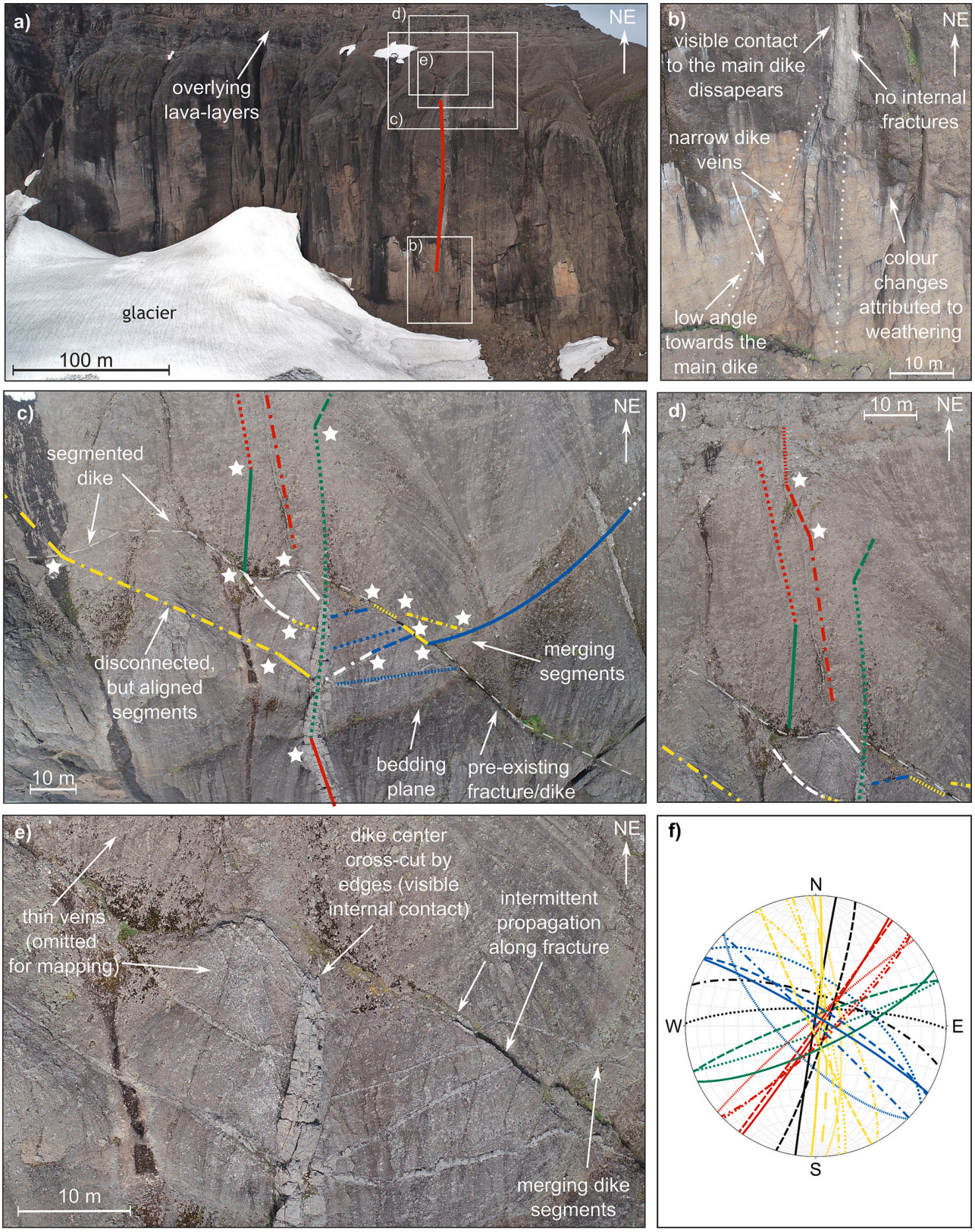

Fig. 7. Tree-dike. (a) Overview over the entire Tree-dike indicating the locations of panels b–d. (b) Lower dike tip surrounded by numerous veins. Thin veins were omitted from mapping due to insufficient resolution. (c) Individual dike segments around the upper tip. White stars mark changes in strike. Color and line style of dike segments allow to identify each segment in the stereonet in (f). (d) Dike segments extending beyond the upper edge of the photograph in (c). (e) Close up of the upper tip. (f) Orientations of the individual segments with colors and patterns of each line corresponding to (a)–(d), except white lines in the photographs are represented in black. Colors correspond to major set in Table 1.

Fig. 7c may be related to a bedding plane. Apart from short distances where the crosscutting discontinuity was occupied, all branching segments appear to have propagated through previously intact rock. This is not only supported by the lack of nearby fractures, but also from the narrow width of many segments, frequent changes in direction and strong segmentation of individual branches.

4.4. Use of fractures

Of the 104 identified dike segments, 39 segments occupy fractures, while 61 segments were identified in intact rock and 4 were inconclusive (Fig. 8a, Table 2). It should be noted however, that of the 61 segments in intact rock, 28 belong to the Tree-dike. Most dike segments which occupy fractures belong to sets DI and DII, while dikes which propagated through intact rock show the entire range of strikes (Fig. 8a). There is a notable gap in the use of fractures between ca. 110–140 °, which mostly overlaps with DIII/FIII and is perpendicular to the strike of the most commonly occupied fractures (FI/DI). Slightly more than half of all dikes identified in the three study areas used fractures either partially or entirely.

4.5. Changes in strike

A total of 39 changes in strike were identified across 14 dikes (Table 2) and most of them were sharp. Gradual changes were observed only in two instances (one example is marked in Fig. 5a). In most cases, the segments on either side of a change in strike were connected at the corner (e.g., Fig. 5b or Fig. 6e) rather than separated by a clearly visible part of the host rock (e.g., some segments in Fig. 7e). Most changes in strike had a magnitude of 10–40 ° and no changes were larger than 50 ° (Fig. 8b). It should be noted here that angles between the main part of the Tree-dike and the branches near the upper tip were not counted as changes in strike, since they represent splitting up rather than simple changes in the strike. These angles are for the most part much larger than most other changes in strike (Fig. 8b), and no other dikes were observed to split up more than once (and not into more than two segments). This may suggest different conditions or mechanisms involved in the formation of these branches compared to most other dikes.

Intermittent use of pre-existing fractures and changes in strike at or close to fractures were observed for several dikes in the study areas. Out of the 39 identified changes in strike, eleven occurred at intersections with fractures and seven occurred close to an intersection with a fracture (Table 3). This was mostly observed for dikes which already occupied fractures and where multiple fractures intersected at the point of strike change. Five dikes were channeled into a fracture (or left it) without a nearby third intersecting fracture. In nine cases, the change in strike was not directly related to a fracture in its immediate surroundings. Of those nine changes, seven belong to the Tree-dike at DF3. These numbers indicate that in at least 23 out of 39 cases, fractures may have influenced or caused a change in the strike of propagating dikes.

The distribution of change in strike and dike use of fractures are shown in Fig. 8c. The change is counted as in intact rock only if both segments adjacent to the change in strike are in intact rock. If at least one of the two segments occupied a fracture, they were counted as involving a fracture (2 instances). It is important to note that here, fracture use explicitly implies the occupation of a pre-existing fracture, not the intersection of one, as was the case in Table 3. Most of the larger changes in strike involve fractures, while the number of changes in intact rock decreases the larger the change in strike. No sharp changes in dip were observed, unless related to a change in strike.

4.6. Tectonic constraints on dike orientation

To test if the observed orientations of dike segments at Dyrfjöll can provide constraints on the stress field at the time of emplacement, they are compared to a stress field modeled after the Northern Volcanic Zone,

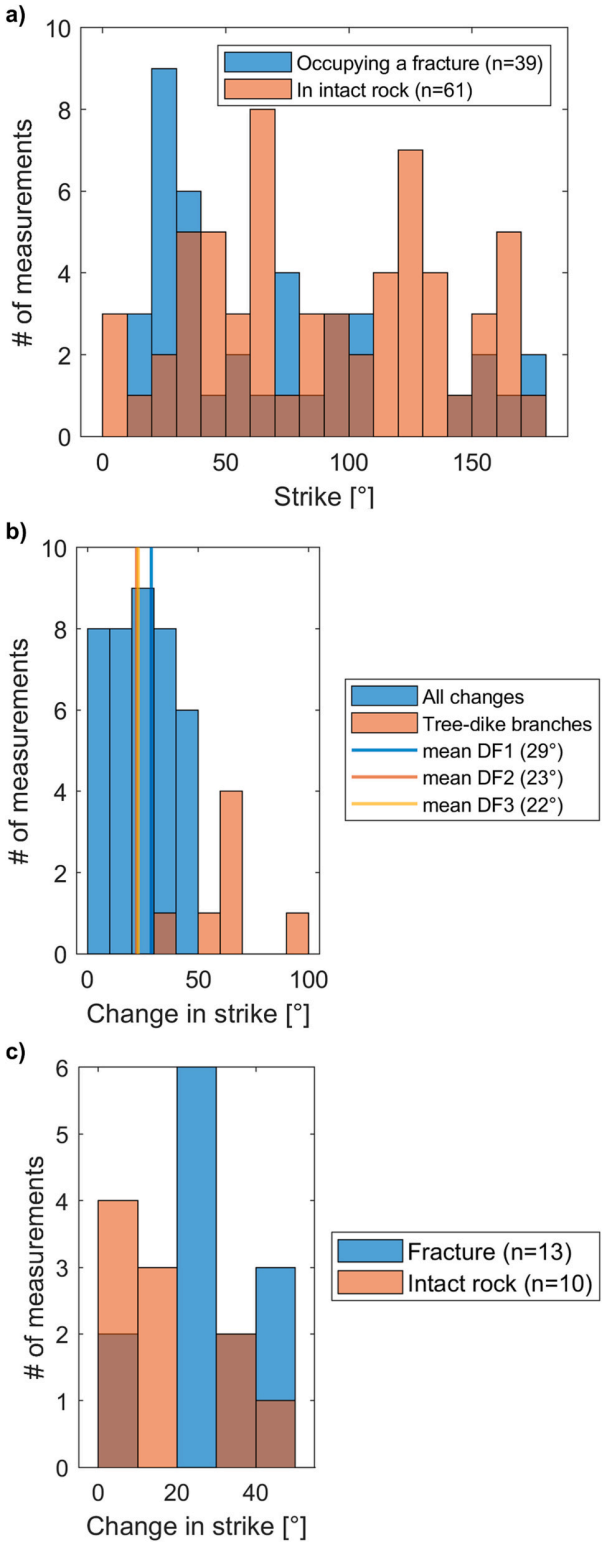

Fig. 8. (a) Strike of dike segments in intact rock and fractures at all three sites. Four segments, where the use of fractures could not be determined, are omitted. Brown color represents overlap of both data sets (blue and orange). (b) Distribution of strike changes and the angle of branches near the upper tip of the Tree-dike to its main part. (c) Changes in strike divided between those in intact rock and those involving a fracture. Changes observed at the Tree-dike were omitted here due to their high number and the possibly unique formation conditions compared to other dikes in the study area (for the complete set of changes, see Supplementary Materials, Fig. S13).

Table 2
Summary of dike segmentation at DF1–DF3. Since individual dikes can consist of several segments, the use of fractures vs propagation in intact rock and recorded changes in direction are listed both per dike and per segment (numbers of segments listed in parentheses). Conditions at the Tree-dike at DF3 were possibly different than for the other dikes at this site and therefore, it is listed separately.

Site	Identified dike segments	Dikes with changes in direction			Use of fractures (segments)		
		Yes (number of identified changes)	No	Inconclusive	Yes/partially	In intact rock	Inconclusive segments
DF1	8 (17)	4 (7)	2	2	6 (10)	2 (6)	1
DF2	9 (24)	4 (10)	4	1	7 (15)	2 (7)	2
DF3 (all)	28 (63)	6 (22)	22	-	12 (14)	15 (48)	1
DF3 (other than Tree-dike)	27 (33)	5 (6)	22	-	11 (12)	15 (20)	1
DF3 (Tree-dike)	1 (30)	1 (16)	-	-	1 (2)	(23)	-
Total	45 (104)	14 (39)	28	3	25 (39)	19 (61)	4

Table 3
List of potential ways of dike-fracture interaction. The term "channeled" refers to changes in strike where one or both of the segments adjacent to the change in strike propagated along a pre-existing fracture. The second and third row refer to corners, where the dike was intersected by a fracture close to or at the change in strike, but where the dike was deflected without propagating along the intersecting fracture.

Changes in strike	DF1	DF2	DF3	All sites
Channeled	1	-	4	5
At a fracture	1	5	5	11
Near a fracture	2	2	3	7
Unrelated	1	1	7	9
Unclear	2	2	3	7
All changes	7	10	22	39

which serves as a present day analogue to the rift zones in Iceland at the time of dike emplacement. The poles of most dike segments fall close to the direction of σ_3, and thus are expected to have opened dominantly tensile and would have required comparatively low magmatic overpressures to intrude (Fig. 9 a, b). Dike segments which occupied pre-existing fractures (filled circles in Fig. 9a & b) are clustered more closely around σ_3 than those in intact rock (hollow circles). According to this model, most segments in intact rock would have opened dominantly tensile, whereas the segments which required a larger shearing component occupied fractures (Fig. 9b). The poles of dikes corresponding mostly to the set DIII fall close to σ_2. Although FracTend predicts almost purely tensile opening for these dikes (Fig. 9b), high fluid pressure is required for fractures of this strike to be susceptible to reactivation (Fig. 9a), which is consistent with that most of these segments propagated through intact rock.

There is some variation in the orientations of fracture-occupying dike segments between the three study sites (Fig. 9c & d). Most segments from DF2 strike close to the plane spanned by σ_1 and σ_2 and show little variation in strike. Segments from DF1 mostly have a more northerly strike than those at DF2 and show a wider scatter of both strike and dip. Segments from DF3 have little variation in dip, but show a broad variation of strikes, which are nearly all rotated further towards East compared to the other two sites (i.e., their poles are rotated more towards North). The rotations of dikes from DF1 and DF3 relative to DF2 appear to mirror the positions of the sites relative to the caldera center with DF1 located south of the caldera center, DF2 close to it and DF3 furthest away from the caldera center towards Northeast (Fig. 1b).

5. Discussion

This section discusses insights into potential local and regional components of the stress field at the time of dike emplacements provided by the mapped and described structures. Furthermore, the different types of dike-fracture interaction are compared to observations in other volcanic systems and settings. Finally, implications for future work and active volcanic systems are discussed. Before interpreting our results and comparing them to previous work, the limitations of the presented data set are discussed briefly.

5.1. Limitations

The selected droning sites (DF1–3) in the Dyrfjöll caldera are considered to give a representative view of the caldera, although deviations in the dike orientations in less well-preserved parts of the caldera cannot be excluded. The outcrop geometry and the degree of weathering is variable at the droning sites. At DF2, the hyaloclastite appears to be more affected by weathering than at the other two sites. At DF1, the rock was cut at an oblique, shallower angle than the cliff-like outcrops at DF2 and DF3, resulting in less bare rock and more loose rocks. Because of this, the lateral exposure of dikes varied greatly, ranging from a few tens of meters or even less (particularly at DF2 and DF3) to several hundreds of meters. This may have affected the probability of observing changes in strike along individual dikes.

DF1 is located at a slightly lower elevation than the other two sites and the lowest part of the outcrop is close to the contact to the underlying ignimbrite (lower left corner in Fig. 5a). Similarly, the upper part of DF3 is located close to the top contact of the hyaloclastite (see e.g. Fig. 2c & Fig. 7a) and it cannot be excluded that the proximity to the interface with the overlying lava layers influenced the propagation and shape of some of the dikes. However, no significant changes or trends in the behaviour of dikes or fractures were observed close to the bottom or top contact of the hyaloclastite and since additionally, the sites are closer to the center of the caldera than to its boundary, we conclude that the three sites were largely unaffected by material interfaces.

The use of a UAV made previously unstudied parts of the caldera accessible, but the resolution of the data is limited and provides less detailed information compared to outcrops which can be reached on foot. Therefore, details that could indicate propagation or flow directions of magma (e.g., Galland et al., 2019), small fractures potentially caused by a propagating dike, or markers in the host rock indicating offset due to a shear component during emplacement (e.g., Stephens et al., 2018) are not resolved in our data. The difficulty of identifying markers for shearing is further increased due to the hyaloclastite providing few markers in itself. Moreover, the exposed intrusions are likely the result of numerous rifting events resulting in frequent crosscutting of dikes. Nevertheless, the degree of weathering combined with the resolution of our data rarely allowed to establish crosscutting relationships between individual dikes. The number of dikes identified in the study areas are likely underestimated. A few individual very short dike segments were identified, but omitted from measurements because it was not possible to confidently measure their orientation. Other dikes may have gone entirely unnoticed due to the data resolution.

Uncertainty estimates for the measured dike orientations (Supplementary Materials, Section S1) indicate that it is difficult to differentiate between dike sets if their orientations differ by less than 15-25 °. The identified dike sets are each scattered across 20–30 ° (Table 1) and may be difficult to clearly separate at individual sites (e.g., DI and DII at DF3, see Fig. 4g). In these cases, the uncertainty makes it difficult to confidently attribute individual dikes to one or another set. However, since

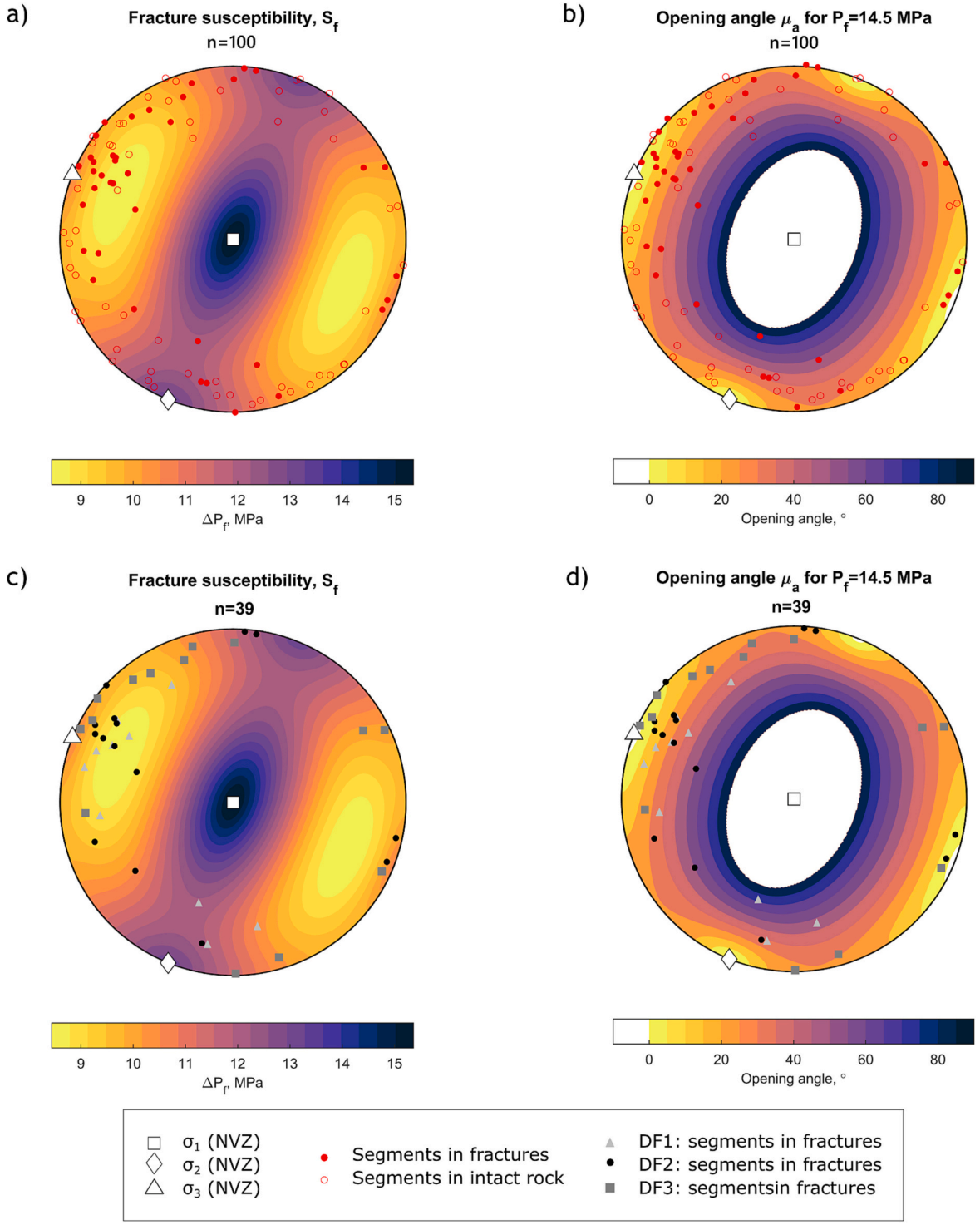

Fig. 9. Comparison of dike orientations from Dyrfjöll, represented as poles, and the NVZ-stress field, modelled in FracTend and represented by the color map. (a) & (b) Fluid pressure ΔP_f, at which fractures become susceptible to intrusion and expected opening angle for all dike segments in fractures/intact rock. Four inconclusive segments were omitted. The fracture susceptibility indicates the minimum magmatic pressure ΔP_f required to make fractures of a given orientation susceptible to dike intrusion. The opening angle refers to the angle between the normal to the dike plane and direction of motion during opening. An opening angle of 0 corresponds to purely tensile opening and higher angles represent an increasing shear component. (c) & (d) Fluid pressure ΔP_f, at which fractures become susceptible to intrusion and expected opening angle for all dikes in fractures grouped by droning sites.

the calculated uncertainties are an upper estimate for the uncertainty and the presumed centers of the sets are separated by at least 30 ° in all cases, we conclude that the four identified sets of orientations for dikes and fractures respectively are indeed individual sets.

The tectonic stress field modeled after the NVZ and assumed to be homogeneous is strongly simplified. Additionally, it is important to be aware that FracTend models the tendency of pre-existing fractures to be intruded by propagating intrusions and may therefore not be entirely representative for dikes propagating through intact rock.

5.2. Regional and local stress field

The most prominent sets for both fractures and dikes found within the caldera (DI, FI) have similar directions (Fig. 4, Table 1). DI strikes also similar to the average strike of 76 dikes (*N*20 °*E*) found by Gústafsson (1992) across the entire Dyrfjöll system including the intrusive complex at Njarðvík. Gústafsson (1992) mentioned basaltic dikes along the caldera rim, but dikes within the caldera are not specifically mentioned and most of the dikes measured for this study are inaccessible on foot, so there is probably little overlap between both studies. NNE or similarly trending dikes (equivalent to DI in this study) are found all across the BEL-area (Dearnley, 1954; Burchardt et al., 2022), as well as in active and extinct fissure swarms in other parts of Iceland (Hjartardóttir et al., 2012; Hjartardóttir et al., 2016; Rhodes, 2022). If DI aligns with the regional principal stresses, the orientation of σ_3 may have been similar to the current spreading direction of 292 ° obtained for the NVZ by Drouin et al. (2017). If the spreading direction remained overall similar since the Miocene as indicated e.g., by Merkouriev and DeMets (2008) and if the BEL area was indeed located in or near a rift zone, this would indicate that spreading had a rather small, if any, oblique component, comparable to the NVZ at present.

In addition to the tectonically controlled dike and fracture sets, we observed at least three other sets of orientations. All of them are less prominent, and there are clear variations between the sites, especially for the dikes, where some sets are specific to individual sites (Fig. 4, Fig. 9). There are several factors which may have resulted in varying degrees of representation of individual sets at the three study sites: (1) There could be a bias due to the shape of the outcrop, where certain fractures or dikes are sub-parallel to the outcrop and thus, more difficult to identify. This is unlikely to be the case due to either a low angle of the mountain side to the horizontal (at DF1) or due to vertical, but laterally curved cliffs (at DF2 and DF3). (2) Temporal variations in the stress field during different rifting episodes could have resulted in different orientations of the dikes. However, since Iceland has always been located at a divergent plate boundary, it can be assumed that the far field principal stress axes did not change significantly until today. Therefore, temporal variations in the stress field would have to have been local. (3) Although the stress field was likely to a large extent controlled by plate spreading, it may have been superimposed with a more local component. It is unclear, how long after the caldera-forming eruption the hyaloclastite and lavas formed and the dikes were emplaced, but a lack of sediments from the proposed caldera lake may indicate that little time passed between them (Gústafsson, 1992). In this case, a remnant of the central-volcano stress field could have still been present. An approximately radial component centered near the middle of the caldera could explain why some orientations are more or less frequently found at different sites in the caldera and why the propagation of dikes in pre-existing fractures appears to correlate with the position in the caldera (Fig. 9c & d). Alternatively, even if little or no influence of the central volcano-stress field remained, hyaloclastite has very different elastic properties than regular basalt (e.g., Eggertsson et al., 2020). This in combination with the irregularly shaped caldera may have resulted in inhomogeneous stress distributions within the caldera. Dikes striking different from NNE are also found elsewhere in the BEL area (e.g., Burchardt et al., 2022; Kennedy et al., 2022) but further and more systematic studies are needed to better constrain potential local influences.

5.3. Interaction with fractures

We observe that basaltic dikes in hyaloclastite may propagate through intact rock or use pre-existing fractures either entirely or intermittently. The observation that dikes more frequently occupied fractures if they strike closer to DI/FI may to some degree be explained by the larger amount of fractures present. However, fractures perpendicular to this direction were also present (Fig. 4a, i) but were apparently not suitable for dikes to propagate into (Fig. 8a, Fig. 9a), which may be related to the stress field (e.g., Stephens et al., 2018).

We also observed that changes in strike of dikes tend to be larger if fractures are involved (Fig. 8c) and more frequent in stronger fractured host rock, especially if more than one fracture direction is represented in a similar strength (compare e.g., fracture distributions at DF1 and DF2). Large and frequent changes in strike following fracture networks are also known from other locations (Delaney et al., 1986; Baer and Beyth, 1990; Martínez-Poza et al., 2014; Poppe et al., 2020), but the results of this study show that even in moderately fractured host rock, fractures notably influence propagating dikes. We can classify interactions of dikes and fractures observed in this study into three groups: (1) Dikes that are channeled into a pre-existing fracture. (2) Dikes that change direction near or at a crosscutting fracture. (3) Dikes that are arrested in front of a crosscutting discontinuity. All three types are schematically depicted in Fig. 10.

The first type of interaction (Fig. 10a) has been observed in the field and analogue models before. This may occur when a dike which previously propagated through intact host rock (Le Corvec et al., 2013; Drymoni et al., 2021), changes direction to move into a fracture of a different orientation. Alternatively, a dike may have followed an entire fracture network, in which cases changes can occur frequently between individual fracture sets (Baer and Beyth, 1990; Martínez-Poza et al., 2014; Stephens et al., 2018). A clear example of this type of behavior is the upper change in strike of the dike described at DF1 (Fig. 5b), where two different fracture sets are involved and independent of the direction of propagation, one set was changed for another one despite both continuing beyond the dike segments. The individual segments, however, are much longer than those described by Baer and Beyth (1990), Martínez-Poza et al. (2014), Stephens et al. (2018) and the angle between the dike and fractures, along which it propagated, tend to be relatively small. Similar behavior was described by Bureau et al. (2013) for sandstone-intrusions, which were channeled into faults.

The second type of dike-fracture interaction (Fig. 10b) describes changes in strike occurring where the propagating dike intersects a fracture or another dike. The propagating dike does not propagate into the fracture but rather changes direction. Such crosscutting fractures or dikes were found either directly at the change or close to it. Due to limited resolution it is not possible to confidently state that the crosscutting element always pre-dates the dike in question. However, the repeated observations at least suggest a systematic reason. An alternative explanation could be that the crosscutting fracture formed after the dike and that it was guided by the stress field to pass the dike exactly at or near its change in strike, where the local stress field may be irregular. However, we did not observe any systematic curving of the crosscutting fractures and it is deemed therefore unlikely that, by coincidence, often prominent crosscutting fractures would pass through the corner of dikes (which in some cases were rather small). The best-exposed example of a dike being redirected can be observed at the lower change in strike of the dike at DF1 (Fig. 5a, marked by the lower white star). It is important to note that the two types of interactions described so far can occur simultaneously if more than two fractures intersect, as is the case in the just mentioned example. Furthermore, it may be possible that this type of interaction occurs if the angle between the propagating dike and the intersecting element is large enough that propagation into the fracture is not energy efficient.

Examples of dikes propagating along older intrusions are known from both field studies and recent volcanic eruptions (Browning and

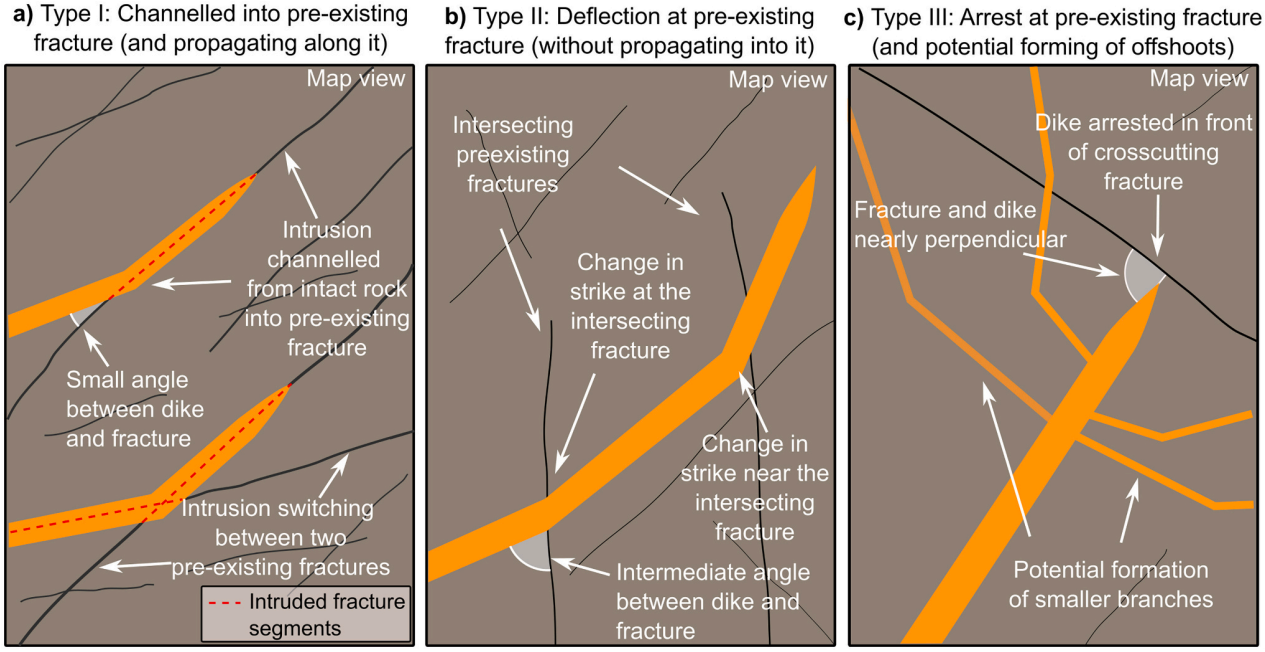

Fig. 10. Schematic representation of the three types of dike-fracture interaction observed in the Dyrfjöll caldera. (a) Type I interaction: Dikes are channeled into pre-existing fractures. The parts of the fractures which were intruded by a dike are indicated by red dashed lines. (b) Type II interaction: Dikes are deflected at or near an intersecting, preexisting fracture without magma propagating into the fracture. (c) Type III interaction: Dikes arrest in front of a pre-existing fracture and may form smaller branches. All panels are in map view.

Gudmundsson, 2015; Ruch et al., 2016; Drymoni et al., 2021; Thiele et al., 2021). In the present cases, the crosscutting dike/fracture may have rotated the stresses very locally. For the dike shown in Fig. 5a, the propagation into the direction of the yellow segment was more energy efficient. This dike is one of the few that could potentially be reached on foot and therefore be studied in more detail. An analysis to constrain the flow direction of the dike may provide additional information and help to understand the processes related to the formation of this specific dike. The question, if dikes are more likely to interact with fractures if the angle between them is smaller or larger is still a matter of discussion. Some studies indicate that the chances of interaction are higher if they are closer to perpendicular (Ziv et al., 2000; Le Corvec et al., 2013; Drymoni et al., 2021), while others indicate that it gets more difficult to open fractures or follow other intrusions under higher angles to the initial propagation direction (Stephens et al., 2018; Thiele et al., 2021). Our observations are more compatible with the second option. Most changes in strike were between 10–40° and no larger than 50 ° (not counting the offshoots from the Tree-dike), while angles to crosscutting fractures were often slightly higher. The changes in strike associated with type-II interaction may have occurred if the angle to the intersecting element was too large and the magmatic overpressure was not sufficient to overcome the normal stress acting on the fracture and propagate into it. If the change in strike resulted in capture into yet another pre-existing fracture (as proposed for the yellow segment in Fig. 5), the dike may continue along this orientation for some distance before eventually reverting back to a strike closer to its initial propagation direction. This type of dike-fracture interaction is not commonly observed or mentioned, which could be due to several reasons: (1) The fractures may be entirely unrelated and even postdate the dikes. (2) The crosscutting fractures may be more common but could have been overlooked in other locations. (3) There could be a lack of suitable outcrops, where fracture networks do not dominate the dike propagation entirely, but where enough dikes and fractures are present to show some degree of interaction. This would mean that this type of interaction would require somewhat specific conditions. Further work is needed here to clarify this.

The third and last type of interaction (Fig. 10c) is the arrest of a dike in front of a crosscutting feature, and this refers in our study mainly to the Tree-dike at DF3 (Fig. 7). In this case, the main body of the dike stopped propagating in front of a fracture which is at least partially occupied by another dike. The magmatic overpressure of the Tree-dike may have been insufficient to directly propagate through the crosscutting discontinuity, resulting instead in small self-propagating cracks, that possibly exploited minor weaknesses in the host rock in the absence of a well-developed pre-existing fracture-network. Several of these branches eventually found a way across the dike, but all meet it at a shallower angle than the initial dike. The Tree-dike eventually demonstrates two things: Firstly, this dike may be an example of what happens if, in the absence of fractures, the magmatic overpressure was not sufficient to cross-cut the pre-existing dike in the first attempt. The main part of the dike shows internal contacts near the upper tip as well as crosscutting and suggests that only branches which formed sometime after the initial emplacement found a way (Fig. 7e) e), and they are much smaller than the main body of the dike. Secondly, the deflection of dikes at crosscutting elements without channeling (in this case the branches of the Tree-dike) can occur even in the absence of additional fractures. The segments soon return to orientations which are seen elsewhere in the caldera, but this is not necessarily the orientation of the main part of the dike. The formation of small cracks which start out almost perpendicular to the main dike and later align with the remote stress field are reminiscent of the wing-cracks predicted by Ziv et al. (2000), although in that case the main dike occupied a pre-existing fracture, while we did not find evidence for such a pre-existing fracture at the Tree-dike. Further studies would be needed to resolve the role of the dike, which partially occupied the crosscutting fracture here. Another example of a dike being arrested may be the example shown in Fig. 5, where both the dashed and the dotted segments terminate at a dike/fracture which is oriented nearly perpendicular to the segments. However, the exposure at both segments is insufficient to confirm this with certainty and neither segment showed branching similar to what is observed at the Tree-dike. Models by Drymoni et al. (2021) suggest that the mechanical properties (the stiffness) of faults influence how a

propagating dike interacts with it. At Dyrfjöll, we did not find well-developed fault zones with a fault-core surrounded by a damage zone. Instead, there are individual fractures, but a dike occupying a fracture may have somewhat similar effects to the inactive faults with a stiff core described and modeled by Drymoni et al. (2021).

5.4. Implications

The different types of dike-fracture interaction observed at Dyrfjöll show that these are complex processes. Even in a case with little variation in material properties, discontinuities have an influence on propagation paths and can offset dikes laterally by potentially tens to hundreds of meters.

Hyaloclastite is not commonly found in volcanic products from the Miocene in Iceland due to the absence of glaciers, but the volume at Dyrfjöll is large enough to suggest that our findings may be applicable to the present day rift zones in Iceland, where hyaloclastite is more abundant. Furthermore, even though this study focused on hyaloclastite, similar effects may apply to other, mechanically similar host rocks like tuffs or sandstones, if they show a similar degree of fracturing.

Considering the shallow depth in the crust, our findings could have implications for volcanic hazards and risks in areas prone to dike intrusions, especially if these areas are accessible and attract public interest. One such area is the Reykjanes Peninsula in southwest Iceland, where two basaltic eruptions occurred at Fagradalsfjall in 2021 and 2022 (Barsotti et al., 2023). Hyaloclastite is commonly exposed at the surface in the area. An improved understanding of which areas have an increased risk of additional eruptive fissures opening, especially in the early phases of such eruptions, would be helpful for limiting the risk for visitors and infrastructure around the eruption site. The suggested influence of strike-slip faults on the location of the eruptive fissures of the 2021 Fagradalsfjall eruption (Einarsson et al., 2023) together with this study show the relevance of this topic for the Reykjanes Peninsula. Eruptions may be expected in other volcanic systems in the area in the coming years and decades (Sæmundsson et al., 2020), and this study emphasizes the importance of mapping fractures and faults for hazard assessment. It remains to be tested if the three types of dike-fracture interaction observed in the present study can also be applied to dikes on larger scales, e.g., changes in strike that occur on the scale of several kilometers and may be influenced by large fault zones or if it is mainly valid on scales of at most a few hundred meters for small dikes and dike segments intruding into moderately fractured rocks.

Our findings indicate that the Dyrfjöll caldera provides an excellent view into the upper crust. A more systematic and complete study of the caldera is expected to show additional dikes and could shed further light onto the stress field in the area at the time of emplacement and possibly the tectonic setting of the BEL area.

6. Conclusion

Digital outcrop models from UAV-based photogrammetry were used to map the orientations of basaltic dikes and fractures in hyaloclastite at the extinct Dyrfjöll volcano, and to quantify their interactions. Our main findings are: Dikes and fractures in the Dyrfjöll caldera mostly followed one of four orientations, the most prominent of which strikes NNE-SSW and is controlled by the regional divergent tectonic stress field. The orientations of dikes and fractures are similar, suggesting that they formed in similar stress conditions. Dikes tend to use fractures along their entire length or intermittently. Interaction is more common in more fractured host rock but all observed changes in strike were smaller than 50 °. Three different types of dike-fracture interaction were identified:

i) Dikes being channeled into pre-existing fractures. This may have happened for dikes which already occupied a fracture of a different orientation or dikes, which previously propagated through intact rock.

ii) Dikes were found to change strike at or near a crosscutting fracture, without magma flow into the fracture. Further work is needed to fully understand the exact mechanics resulting in this type of interaction.

iii) Upon hitting a barrier such as an intersecting fracture or dike, which could not be overcome and in the absence of suitable fracture networks to follow, a dike can be arrested and may split up into several thinner branches, potentially with different propagation directions.

CRediT authorship contribution statement

Sonja H.M. Greiner: Conceptualization, Investigation, Formal-analysis, Writing – original draft. **Steffi Burchardt:** Conceptualization, Funding-acquisition, Formal-analysis, Investigation, Resources, Supervision, Writing – review & editing. **Freysteinn Sigmundsson:** Conceptualization, Investigation, Formal-analysis, Funding-acquisition, Writing – review & editing. **Birgir V. Óskarsson:** Investigation, Writing – review & editing. **Olivier Galland:** Conceptualization, Funding-acquisition, Writing – review & editing. **Halldór Geirsson:** Conceptualization, Writing – review & editing. **Emma Rhodes:** Investigation, Formal-analysis, Writing – review & editing.

Declaration of Competing Interest

The authors declared that there is no conflict of interest.

Data availability

Virtual outcrop models of DF1–DF3 are accessible here: DF1 https://skfb.ly/oKDCy, DF2 https://skfb.ly/oKDCD, DF3 https://skfb.ly/oKDCG

Acknowledgments

We thank the Nordic Volcanological Center for funding S. Greiner's PhD position. Furthermore we thank Orlando Quintela for helpful discussions and everyone who participated in the Volcanic Plumbing System fieldwork during 2021 in East-Iceland. We additionally thank the editor Ed Llewellin and two anonymous reviewers for helpful suggestions to improve the initial manuscript.

Appendix A. Supplementary material

Supplementary data associated with this article can be found, in the online version, at https://doi.org/10.1016/j.jvolgeores.2023.107891.

References

Allmendinger, R.W., Cardozo, N., Fisher, D.M., 2011. Structural Geology Algorithms: Vectors and Tensors. Cambridge University Press.

Anderson, E.M., 1951. The Dynamics of Faulting and Dyke Formation with Applications to Britain, second ed. Oliver and Boyd, Edinburgh, UK.

Árnadóttir, T., Lund, B., Jiang, W., Geirsson, H., Björnsson, H., Einarsson, P., Sigurdsson, T., 2009. Glacial rebound and plate spreading: Results from the first countrywide GPS observations in Iceland. Geophys. J. Int. 177, 691–716. https://doi.org/10.1111/j.1365-246X.2008.04059.x.

Baer, G., Beyth, M., 1990. A Mechanism of Dyke Segmentation in Fractured Host Rock. Mafic Dykes and Emplacement Mechanisms. Balkema, Rotterdam, p. 3.

Baer, G., Beyth, M., Reches, Z., 1994. Dikes emplaced into fractured basement, timna igneous complex, israel. J. Geophys. Res.: Solid Earth 99, 24039–24050.

Barsotti, S., Parks, M.M., Pfeffer, M.A., Óladóttir, B.A., Barnie, T., Titos, M.M., Jónsdóttir, K., Pedersen, G.B.M., Hjartardóttir, Á.R., Stefansdóttir, G., Johannsson, T., Arason, T., Gudmundsson, M.T., Oddsson, B., þrastarson, R.H., Ófeigsson, B.G., Vogfjörd, K., Geirsson, H., Hjörvar, T., von Löwis, S., Petersen, G.N., Sigurðsson, E.M., 2023. The eruption in Fagradalsfjall (2021, Iceland): How the operational monitoring and the volcanic hazard assessment contributed to its safe access. Nat. Hazards 1–30. https://doi.org/10.1007/s11069-022-05798-7.

Bemis, S.P., Micklethwaite, S., Turner, D., James, M.R., Akciz, S., Thiele, S.T., Bangash, H.A., 2014. Ground-based and UAV-based photogrammetry: A multi-scale, high-resolution mapping tool for structural geology and paleoseismology. J. Struct. Geol. 69, 163–178. https://doi.org/10.1016/j.jsg.2014.10.007.

Berg, S.E., 2016. Silicic Magma Genesis in Basalt-dominated Oceanic Settings: Examples from Iceland and the Canary Islands (Ph.D. thesis). Acta Universitatis Upsaliensis.

Bertelsen, H.S., Guldstrand, F., Sigmundsson, F., Pedersen, R., Mair, K., Galland, O., 2021. Beyond elasticity: Are Coulomb properties of the Earth's crust important for volcano geodesy? J. Volcanol. Geoth. Res. 410, 107153 https://doi.org/10.1016/j.jvolgeores.2020.107153.

Browning, J., Gudmundsson, A., 2015. Caldera faults capture and deflect inclined sheets: an alternative mechanism of ring dike formation. Bull. Volcanol. 77, 1–13. https://doi.org/10.1007/s00445-014-0889-4.

Buckley, S.J., Ringdal, K., Naumann, N., Dolva, B., Kurz, T.H., Howell, J.A., Dewez, T.J. B., 2019. LIME: Software for 3-D visualization, interpretation, and communication of virtual geoscience models. Geosphere 15, 222–235. https://doi.org/10.1130/GES02002.1.

Burchardt, S., 2008. New insights into the mechanics of sill emplacement provided by field observations of the Njardvik Sill, Northeast Iceland. J. Volcanol. Geoth. Res. 173, 280–288. https://doi.org/10.1016/j.jvolgeores.2008.02.009.

Burchardt, S., Oskarsson, B., Gustafsson, L., Berg, S.E., Riishuus, M.S., 2022. Geology of a neogene caldera cluster in the Borgarfjörður eystri - Loðmundarfjörður area, eastern Iceland. Volcanica 5, 133–161. https://doi.org/10.30909/vol.05.01.133161. URL:

Burchardt, S., Tanner, D.C., Troll, V.R., Krumbholz, M., Gustafsson, L.E., 2011. Three-dimensional geometry of concentric intrusive sheet swarms in the Geitafell and the Dyrfjöll volcanoes, eastern Iceland. Geochem. Geophys. Geosyst. 12 https://doi.org/10.1029/2011GC003527.

Bureau, D., Mourgues, R., Cartwright, J., Foschi, M., Abdelmalak, M., 2013. Characterisation of interactions between a pre-existing polygonal fault system and sandstone intrusions and the determination of paleo-stresses in the faroe-shetland basin. J. Struct. Geol. 46, 186–199. https://doi.org/10.1016/j.jsg.2012.09.003.

Cardozo, N., Allmendinger, R.W., 2013. Spherical projections with osxstereonet. Comput. Geosci. 51, 193–205. https://doi.org/10.1016/j.cageo.2012.07.021.

Dearnley, R., 1954. A Contribution to the Geology of Loðmundarfjörður. Náttúrugripasafnið i Reykjavík/Museum rerum naturalium Reyknavikensis.

Delaney, P.T., Pollard, D.D., Ziony, J.I., McKee, E.H., 1986. Field relations between dikes and joints: Emplacement processes and paleostress analysis. J. Geophys. Res.: Solid Earth 91, 4920–4938. https://doi.org/10.1029/JB091iB05p04920.

Dering, G.M., Micklethwaite, S., Cruden, A.R., Barnes, S.J., Fiorentini, M.L., 2019. Evidence for dyke-parallel shear during syn-intrusion fracturing. Earth Planet. Sci. Lett. 507, 119–130. https://doi.org/10.1016/j.epsl.2018.10.024.

Dering, G.M., Micklethwaite, S., Thiele, S.T., Vollgger, S.A., Cruden, A.R., 2019. Review of drones, photogrammetry and emerging sensor technology for the study of dykes: Best practises and future potential. J. Volcanol. Geoth. Res. 373, 148–166. https://doi.org/10.1016/j.jvolgeores.2019.01.018.

Drouin, V., Sigmundsson, F., Ófeigsson, B.G., Hreinsdóttir, S., Sturkell, E., Einarsson, P., 2017. Deformation in the Northern Volcanic Zone of Iceland 2008–2014: An interplay of tectonic, magmatic, and glacial isostatic deformation. J. Geophys. Res.: Solid Earth 122, 3158–3178. https://doi.org/10.1002/2016JB013206. URL:

Drymoni, K., Browning, J., Gudmundsson, A., 2020. Dyke-arrest scenarios in extensional regimes: Insights from field observations and numerical models, Santorini, Greece. J. Volcanol. Geoth. Res. 396, 106854 https://doi.org/10.1016/j.jvolgeores.2020.106854.

Drymoni, K., Browning, J., Gudmundsson, A., 2021. Volcanotectonic interactions between inclined sheets, dykes, and faults at the Santorini volcano, Greece. J. Volcanol. Geoth. Res. 416, 107294 https://doi.org/10.1016/j.jvolgeores.2021.107294.

Eggertsson, G.H., Kendrick, J.E., Weaver, J., Wallace, P.A., Utley, J.E., Bedford, J.D., Allen, M.J., Markússon, S.H., Worden, R.H., Faulkner, D.R., Lavallée, Y., 2020. Compaction of hyaloclastite from the active geothermal system at Krafla volcano, Iceland. Geofluids 1–17. https://doi.org/10.1155/2020/3878503.

Einarsson, P., 2008. Plate boundaries, rifts and transforms in Iceland. Jökull 58, 35–58.

Einarsson, P., Eyjólfsson, V., Hjartardóttir, A.R., 2023. Tectonic framework and fault structures in the Fagradalsfjall segment of the Reykjanes Peninsula Oblique Rift, Iceland. Bull. Volcanol. 85, 9. https://doi.org/10.1007/s00445-022-01624-x.

Eltner, A., Kaiser, A., Castillo, C., Rock, G., Neugirg, F., Abellán, A., 2016. Image-based surface reconstruction in geomorphometry – merits, limits and developments. Earth Surf. Dyn. 4, 359–389. https://doi.org/10.5194/esurf-4-359-2016.

Galland, O., Spacapan, J.B., R., O., Mair, K., Soto, F.G., Eiken, T., Schiuma, M., Leanza, H.A., 2019. Structure, emplacement mechanism and magma-flow significance of igneous fingers – implications for sill emplacement in sedimentary basins. J. Struct. Geol. 124, 120–135. https://doi.org/10.1016/j.jsg.2019.04.013.

Grapenthin, R., Sigmundsson, F., Geirsson, H., Árnadóttir, T., Pinel, V., 2006. Icelandic rhythmics: Annual modulation of land elevation and plate spreading by snow load. Geophys. Res. Lett. 33 https://doi.org/10.1029/2006GL028081.

Gústafsson, L.E., 1992. Geology and Petrography of the Dyrfjöll Central Volcano, Eastern Iceland. Ph.D. thesis. Fachbereich Geowiss, FU.

Haimson, B.C., Rummel, F., 1982. Hydrofracturing stress measurements in the iceland research drilling project drill hole at reydarfjordur, Iceland. J. Geophys. Res.: Solid Earth 87, 6631–6649. https://doi.org/10.1029/JB087iB08p06631.

Healy, D., 2022. Fractend. URL: <https://github.com/DaveHealy-github/FracTend. downloaded 12. April 2022.

Heap, M.J., Villeneuve, M., Albino, F., Farquharson, J.I., Brothelande, E., Amelung, F., Got, J.L., Baud, P., 2020. Towards more realistic values of elastic moduli for volcano modelling. J. Volcanol. Geoth. Res. 390, 106684 https://doi.org/10.1016/j.jvolgeores.2019.106684.

Heimisson, E.R., Hooper, A., Sigmundsson, F., 2015. Forecasting the path of a laterally propagating dike. J. Geophys. Res.: Solid Earth 120, 8774–8792. https://doi.org/10.1002/2015JB012402.

Helgason, J., 1984. Frequent shifts of the volcanic zone in Iceland. Geology 12, 212–216. https://doi.org/10.1130/0091-7613(1984)12<212:FSOTVZ>2.0.CO;2.

Hjartardóttir, Á.R., Einarsson, P., Björgvinsdóttir, S.G., 2016. Fissure swarms and fracture systems within the Western Volcanic Zone, Iceland – effects of spreading rates. J. Struct. Geol. 91, 39–53. https://doi.org/10.1016/j.jsg.2016.08.007.

Hjartardóttir, Á.R., Einarsson, P., Bramham, E., Wright, T.J., 2012. The Krafla fissure swarm, Iceland, and its formation by rifting events. Bull. Volcanol. 74, 2139–2153. https://doi.org/10.1007/s00445-012-0659-0.

Jakobsson, S.P., Gudmundsson, M.T., 2008. Subglacial and intraglacial volcanic formations in Iceland. Jökull 58, 179–196.

James, M.R., Robson, S., 2012. Straightforward reconstruction of 3d surfaces and topography with a camera: Accuracy and geoscience application. J. Geophys. Res.: Earth Surf. 117 https://doi.org/10.1029/2011JF002289.

Jarosch, A., Gudmundsson, M.T., Högnadóttir, T., Axelsson, G., 2008. Progressive cooling of the hyaloclastite ridge at Gjálp, Iceland, 1996–2005. J. Volcanol. Geoth. Res. 170, 218–229. https://doi.org/10.1016/j.jvolgeores.2007.10.012.

Jolly, R., Sanderson, D., 1997. A Mohr circle construction for the opening of a pre-existing fracture. J. Struct. Geol. 19, 887–892. https://doi.org/10.1016/S0191-8141(97)00014-X.

Jónsson, S., 2012. Tensile rock mass strength estimated using InSAR. Geophys. Res. Lett. 39 https://doi.org/10.1029/2012GL053309.

Kavanagh, J.L., Menand, T., Sparks, R.S.J., 2006. An experimental investigation of sill formation and propagation in layered elastic media. Earth Planet. Sci. Lett. 245, 799–813. https://doi.org/10.1016/j.epsl.2006.03.025.

Kennedy, B., Heap, M., Burchardt, S., Villeneuve, M., Tuffen, H., Gilg, H.A., Davidson, J., Duncan, N., Saubin, E., Gestsson, E.B., Anjomrouz, M., Butler, P., 2022. Thermal impact of dykes on ignimbrite and implications for fluid flow compartmentalisation in calderas. Volcanica 5, 75–93. https://doi.org/10.30909/vol.05.01.7593.

Kjøll, H.J., Galland, O., Labrousse, L., Andersen, T.B., 2019. Emplacement mechanisms of a dyke swarm across the brittle-ductile transition and the geodynamic implications for magma-rich margins. Earth Planet. Sci. Lett. 518, 223–235. https://doi.org/10.1016/j.epsl.2019.04.016.

Le Corvec, N., Menand, T., Lindsay, J., 2013. Interaction of ascending magma with pre-existing crustal fractures in monogenetic basaltic volcanism: an experimental approach. J. Geophys. Res.: Solid Earth 118, 968–984. https://doi.org/10.1002/jgrb.50142.

Lister, J.R., Kerr, R.C., 1991. Fluid-mechanical models of crack propagation and their application to magma transport in dykes. J. Geophys. Res.: Solid Earth 96, 10049–10077, doi: 10.1029/91JB00600. URL: https://agupubs.onlinelibrary.wiley.com/doi/abs/10.1029/91JB00600, arXiv:https://agupubs.onlinelibrary.wiley.com/doi/pdf/10.1029/91JB00600.

Martínez-Poza, A., Druguet, E., Castano, L., Carreras, J., 2014. Dyke intrusion into a pre-existing joint network: The Aiguablava lamprophyre dyke swarm (Catalan Coastal Ranges). Tectonophysics 630, 75–90. https://doi.org/10.1016/j.tecto.2014.05.015.

Mathieu, L., Burchardt, S., Troll, V.R., Krumbholz, M., Delcamp, A., 2015. Geological constraints on the dynamic emplacement of cone-sheets – the Ardnamurchan cone-sheet swarm, NW Scotland. J. Struct. Geol. 80, 133–141. https://doi.org/10.1016/j.jsg.2015.08.012.

Merkouriev, S., DeMets, C., 2008. A high-resolution model for Eurasia-North America plate kinematics since 20 Ma. Geophys. J. Int. 173, 1064–1083. https://doi.org/10.1111/j.1365-246X.2008.03761.x.

Niethammer, U., James, M., Rothmund, S., Travelletti, J., Joswig, M., 2012. UAV-based remote sensing of the Super-Sauze Landslide: Evaluation and results. Eng. Geol. 128, 2–11. https://doi.org/10.1016/j.enggeo.2011.03.012.

Okada, Y., 1985. Surface deformation due to shear and tensile faults in a half-space. Bull. Seismol. Soc. Am. 75, 1135–1154. https://doi.org/10.1785/BSSA0750041135.

Okada, Y., 1992. Internal deformation due to shear and tensile faults in a half-space. Bull. Seismol. Soc. Am. 82, 1018–1040. https://doi.org/10.1785/BSSA0820021018.

Óskarsson, B.V., Riishuus, M.S., 2013. The mode of emplacement of neogene flood basalts in eastern Iceland: Facies architecture and structure of the Hólmar and Grjótá olivine basalt groups. J. Volcanol. Geoth. Res. 267, 92–118. https://doi.org/10.1016/j.jvolgeores.2013.09.010.

Óskarsson, B.V., Riishuus, M.S., 2014. The mode of emplacement of neogene flood basalts in eastern Iceland: Facies architecture and structure of simple aphyric basalt groups. J. Volcanol. Geoth. Res. 289, 170–192. https://doi.org/10.1016/j.jvolgeores.2014.11.009.

Poppe, S., Galland, O., de Winter, N., Goderis, S., Claeys, P., Debaille, V., Boulvais, P., Kervyn, M., 2020. Structural and geochemical interactions between magma and sedimentary host rock: The Hovedøya case, Oslo Rift, Norway. Geochem. Geophys. Geosyst. 21, e2019GC008685 https://doi.org/10.1029/2019GC008685.

Rhodes, E., 2022. Evolution of a silicic magma reservoir in the upper crust: Reyðarártindur pluton, Southeast Iceland. Ph.D. thesis. Acta Universitatis Upsaliensis.

Rhodes, E.L., Barker, A.K., Burchardt, S., Hieronymus, C.F., Rousku, S.N., McGarvie, D. W., Mattsson, T., Schmiedel, T., Ronchin, E., Witcher, T., 2021. Rapid assembly and eruption of a shallow silicic magma reservoir, Reyðarártindur pluton, Southeast Iceland. Geochem. Geophys. Geosyst. 22, e2021GC009999 https://doi.org/10.1029/2021GC009999.

Rivalta, E., Taisne, B., Bunger, A., Katz, R., 2015. A review of mechanical models of dike propagation: Schools of thought, results and future directions. Tectonophysics 638, 1–42. https://doi.org/10.1016/j.tecto.2014.10.003.

Rubin, A.M., 1993. Tensile fracture of rock at high confining pressure: Implications for dike propagation. J. Geophys. Res.: Solid Earth 98, 15919–15935, doi: 10.1029/

93JB01391. URL: <https://agupubs.onlinelibrary.wiley.com/doi/abs/10.1029/93JB01391>, arXiv:https://agupubs.onlinelibrary.wiley.com/doi/pdf/10.1029/93JB01391.

Rubin, A.M., 1995. Propagation of magma-filled cracks. Annu. Rev. Earth Planet. Sci. 23, 287–336.

Ruch, J., Wang, T., Xu, W., Hensch, M., Jónsson, S., 2016. Oblique rift opening revealed by reoccurring magma injection in central iceland. Nature Commun. 7, 12352. https://doi.org/10.1038/ncomms12352.

Sæmundsson, K., 1979. Outline of the geology of Iceland. Jökull 29, 7–28.

Schmiedel, T., Burchardt, S., Mattsson, T., Guldstrand, F., Galland, O., Palma, J.O., Skogby, H., 2021. Emplacement and segment geometry of large, high-viscosity magmatic sheets. Minerals 11. https://doi.org/10.3390/min11101113.

Schopka, H.H., Gudmundsson, M.T., Tuffen, H., 2006. The formation of Helgafell, Southwest Iceland, a monogenetic subglacial hyaloclastite ridge: Sedimentology, hydrology and volcano–ice interaction. J. Volcanol. Geoth. Res. 152, 359–377. https://doi.org/10.1016/j.jvolgeores.2005.11.010.

Sigmundsson, F., 2006. Iceland Geodynamics: Crustal Deformation and Divergent Plate Tectonics. Springer Science & Business Media.

Sigmundsson, F., Einarsson, P., Hjartardóttir, A.R., Drouin, V., Jónsdóttir, K., Árnadóttir, T., Geirsson, H., Hreinsdóttir, S., Li, S., Ófeigsson, B.G., 2020. Geodynamics of Iceland and the signatures of plate spreading. J. Volcanol. Geoth. Res. 391, 106436 https://doi.org/10.1016/j.jvolgeores.2018.08.014.

Sigmundsson, F., Hooper, A., Hreinsdóttir, S., Vogfjörd, K.S., Ófeigsson, B.G., Heimisson, E.R., Dumont, S., Parks, M., Spaans, K., Gudmundsson, G.B., Drouin, V., Árnadóttir, T., Jónsdóttir, K., Gudmundsson, M.T., Högnadóttir, T., Fridriksdóttir, H. M., Hensch, M., Einarsson, P., Magnússon, E., Samsonov, S., Brandsdóttir, B., White, R.S., Ágústsdóttir, T., Greenfield, T., Green, R.G., Hjartardóttir, A.R., Pedersen, R., Bennett, R.A., Geirsson, H., La Femina, P.C., Björnsson, H., Pálsson, F., Sturkell, E., Bean, C.J., Möllhoff, M., Braiden, A.K., Eibl, E.P.S., 2015. Segmented lateral dyke growth in a rifting event at Bárðarbunga volcanic system, Iceland. Nature 517, 191–195. https://doi.org/10.1038/nature14111.

Spacapan, J.B., Galland, O., Leanza, H.A., Planke, S., 2016. Control of strike-slip fault on dyke emplacement and morphology. J. Geol. Soc. 173, 573–576. https://doi.org/10.1144/jgs2015-166.

Stephens, T.L., Walker, R.J., Healy, D., Bubeck, A., England, R.W., 2018. Mechanical models to estimate the paleostress state from igneous intrusions. Solid Earth 9, 847–858. https://doi.org/10.5194/se-9-847-2018.

Sæmundsson, K., Sigurgeirsson, M.A., Friðleifsson, G.O., 2020. Geology and structure of the Reykjanes volcanic system, Iceland. J. Volcanol. Geotherm. Res. 391, 106501. https://doi.org/10.1016/j.jvolgeores.2018.11.022.

Thiele, S.T., Cruden, A.R., Zhang, X., Micklethwaite, S., Matchan, E.L., 2021. Reactivation of magma pathways: insights from field observations, geochronology, geomechanical tests, and numerical models. J. Geophys. Res.: Solid Earth 126, e2020JB021477. https://doi.org/10.1029/2020JB021477.

Thordarson, T., Larsen, G., 2007. Volcanism in iceland in historical time: Volcano types, eruption styles and eruptive history. J. Geodyn. 43, 118–152. https://doi.org/10.1016/j.jog.2006.09.005.

Turcotte, D.L., Schubert, G., 2014. Geodynamics, thir ed.,. Cambridge University Press.

Valentine, G.A., Krogh, K.E., 2006. Emplacement of shallow dikes and sills beneath a small basaltic volcanic center – the role of pre-existing structure (Paiute Ridge, southern Nevada, USA). Earth Planet. Sci. Lett. 246, 217–230. https://doi.org/10.1016/j.epsl.2006.04.031.

Walker, G.P.L., 1960. Zeolite zones and dike distribution in relation to the structure of the basalts of eastern Iceland. J. Geol. 68, 515–528. https://doi.org/10.1086/626685.

Walker, G.P.L., 1974. The structure of eastern iceland. Geodynamics of Iceland and the North Atlantic Area, 177–188.

Walker, G.P.L., 1975. Excess spreading axes and spreading rate in Iceland. Nature 255, 468–471. https://doi.org/10.1038/255468a0.

Watton, T., Jerram, D., Thordarson, T., Davies, R., 2013. Three-dimensional lithofacies variations in hyaloclastite deposits. J. Volcanol. Geoth. Res. 250, 19–33. https://doi.org/10.1016/j.jvolgeores.2012.10.011.

Wauthier, C., Cayol, V., Kervyn, F., d'Oreye, N., 2012. Magma sources involved in the 2002 nyiragongo eruption, as inferred from an insar analysis. J. Geophys. Res.: Solid Earth 117. https://doi.org/10.1029/2011JB008257.

Wright, T.J., Ebinger, C., Biggs, J., Ayele, A., Yirgu, G., Keir, D., Stork, A., 2006. Magma-maintained rift segmentation at continental rupture in the 2005 Afar dyking episode. Nature 442, 291–294. https://doi.org/10.1038/nature04978.

Ziv, A., Rubin, A.M., Agnon, A., 2000. Stability of dike intrusion along preexisting fractures. J. Geophys. Res.: Solid Earth 105, 5947–5961. https://doi.org/10.1029/1999JB900410. URL: <https://agupubs.onlinelibrary.wiley.com/doi/abs/10.1029/1999JB900410>.

Supplementary Materials

Interaction between propagating basaltic dikes and pre-existing fractures: A case study in hyaloclastite from Dyrfjöll, Iceland (Greiner et al.)

S1 Uncertainty estimates for fracture/dike mapping

When using the software LIME (Buckley et al., 2019), the strike and dip of planar features is determined by picking three points, which fall onto the plane in question. The software itself does not provide an uncertainty estimate or any other measurement of quality for such measurements. However, some measure of quality would be useful to estimate, which results can be treated as significant and which not. It is important to note that the method, which is used here, only considers the error connected to picking the planes, but they do not provide any information regarding e.g., differences between the virtual outcrop model and the real outcrops, which undoubtedly have some influence on the measured strikes and dips as well. If the orientation of a single plane would be measured many times, the three points picked for each plane would be slightly different every time, resulting in small variations of the strike and dip. Gaussian error propagation can be used to derive an estimate of this type of uncertainty (Willink, 2013). The method allows the calculation of the standard deviation of a parameter, which is connected to measured parameters through analytical functions. It is well known in physics, where it is commonly taught in undergraduate studies, as well as other sciences, where quantitative data is commonly used in connection with analytical equations (e.g., Ku, 1966; Lo, 2005), and can be applied if the measured parameters have at least approximately Gaussian distributed uncertainties. It is important to note that the uncertainty estimate calculated with this method does not include potential inaccuracies in the applied model (here: the analytical equation) but only those related to the measurement itself.

The uncertainty Δf of a variable $f(\vec{x})$, which is a function of uncorrelated parameters x_i is calculated based on the standard deviations of the individual parameters, Δx_i as

$$\Delta f = \sqrt{\sum_i \left(\left(\frac{\partial f}{\partial x_i} \right)^2 \Delta x_i^2 \right)} \tag{1}$$

Here the parameters x_i correspond to coordinates and a coordinate system is placed in such a way that the positive x, y and z axes correspond to East, North and Up, respectively. Since all three coordinates correspond to different directions, they are clearly independent of each other. It is assumed, that the coordinates of all measured points are realizations of random variables and that they all have the same standard deviation called *sd*. In the following, all calculated uncertainties (i.e. standard deviations according to error propagation) are denoted by a Δ in front of the variable in question.

In LIME, three points are picked, which lie on the planar feature of interest. These three points define a plane, which should be parallel to the feature of interest and thus allow the determination of the planar feature's orientation. These three points will in the following be referred to by their position vectors $\vec{a}$, $\vec{b}$ and $\vec{c}$. The normal vector of the plane spanned by $\vec{a}$, $\vec{b}$ and $\vec{c}$ is defined as the cross-product of the two vectors $\left(\vec{a} - \vec{b}\right)$

and $(\vec{a}-\vec{c})$:

$$\vec{n} = \begin{pmatrix} n_1 \\ n_2 \\ n_3 \end{pmatrix} = \left(\vec{a}-\vec{b}\right) \times (\vec{a}-\vec{c}) \tag{2}$$

From the normal vector of the plane, the dip direction can be calculated as the angle between the projection of $\vec{n}$ onto the xy plane $n_{xy} = \begin{pmatrix} n_1 \\ n_2 \end{pmatrix}$ and North, which corresponds to the vector $\vec{e}_N = \begin{pmatrix} 0 \\ 1 \end{pmatrix}$. Rearranging

$$cos\,(\alpha) = \frac{\vec{n}_{xy} \cdot \vec{e}_N}{|n_{xy}| \cdot |\vec{e}_N|} \tag{3}$$

to isolate α gives

$$\alpha = arccos\left(\frac{n_2}{\sqrt{{n_1}^2 + {n_2}^2}}\right) \tag{4}$$

The dip can be calculated as the angle between $\vec{n}$ and the normal vector of the xy-plane, which corresponds to a vertical vector $\begin{pmatrix} 0 \\ 0 \\ 1 \end{pmatrix}$. This is calculated as

$$\delta = arccos\left(\frac{n_3}{\sqrt{{n_1}^2 + {n_2}^2 + {n_3}^2}}\right) \tag{5}$$

Now, the uncertainties of n, α and δ need to be calculated using error propagation. With $x_j = a_1, a_2, a_3, b_1, b_2, b_3, c_1, c_2, c_3$, the uncertainty of each component of $\vec{n}$ can be calculated as

$$\Delta n_i = \sqrt{\sum_j \left(\frac{\partial n_i}{\partial x_j}\right)^2 sd^2} \tag{6}$$

This results in

$$\Delta n_1 = \sqrt{(-c_3+b_3)^2 + (-b_2+c_2)^2 + (-a_3+c_3)^2 + (a_2-c_2)^2 + (a_3-b_3)^2 + (-a_2+b_2)^2}\,sd \tag{7}$$

$$\Delta n_2 = \sqrt{(-b_3+c_3)^2 + (-c_1+b_1)^2 + (a_3-c_3)^2 + (-a_1+c_1)^2 + (-a_3+b_3)^2 + (a_1-b_1)^2}\,sd \tag{8}$$

$$\Delta n_3 = \sqrt{(-c_2+b_2)^2 + (-b_1+c_1)^2 + (-a_2+c_2)^2 + (a_1-c_1)^2 + (a_2-b_2)^2 + (-a_1+b_1)^2}\,sd \tag{9}$$

The uncertainty for α and δ is calculated based on Δn_1, Δn_2 and Δn_3:

$$\Delta\alpha = \sqrt{\sum_{i=1}^{2} \left(\frac{\partial \alpha}{\partial n_i}\right)^2 {\Delta n_i}^2} \tag{10}$$

$$= \sqrt{{\Delta n_1}^2 \left(\frac{n_1 n_2}{\sqrt{\frac{{n_1}^2}{{n_1}^2+{n_2}^2}}\,({n_1}^2+{n_2}^2)^{3/2}}\right)^2 + {\Delta n_2}^2 \left(\frac{n_1}{{n_1}^2+{n_2}^2}\right)^2} \tag{11}$$

as well as

$$\Delta\delta = \sqrt{\sum_{i=1}^{3} \left(\frac{\partial\delta}{\partial n_i}\right)^2 \Delta {n_i}^2} \tag{12}$$

$$\frac{\partial\delta}{\partial n_1} = \frac{n_1 n_3}{\sqrt{\frac{{n_1}^2+{n_2}^2}{{n_1}^2+{n_2}^2+{n_3}^2}}\left({n_1}^2+{n_2}^2+{n_3}^2\right)^{3/2}} \tag{13}$$

$$\frac{\partial\delta}{\partial n_2} = \frac{n_2 n_3}{\sqrt{\frac{{n_1}^2+{n_2}^2}{{n_1}^2+{n_2}^2+{n_3}^2}}\left({n_1}^2+{n_2}^2+{n_3}^2\right)^{3/2}} \tag{14}$$

$$\frac{\partial\delta}{\partial n_3} = -\frac{\sqrt{{n_1}^2+{n_2}^2}}{{n_1}^2+{n_2}^2+{n_3}^2} \tag{15}$$

We applied these equations to points for the 104 dike segments from Dyrfjöll, assuming as a start a standard deviation of $0.3\,m$ for the x-y and z coordinates for each point Figure S1, Figure S2. Since currently each point as to be manually read out of LIME, we omitted measuring fracture orientation uncertainty, assuming that the results will be similar to those of the dikes.

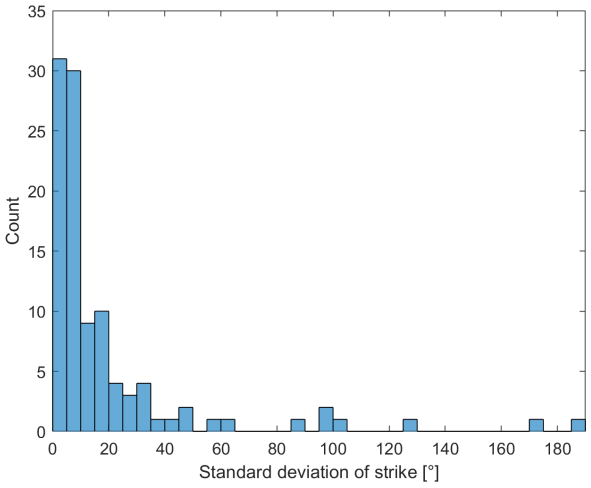

Figure S1: Standard deviation of the strike of dike segments from Dyrfjöll. Bin size is 5°.

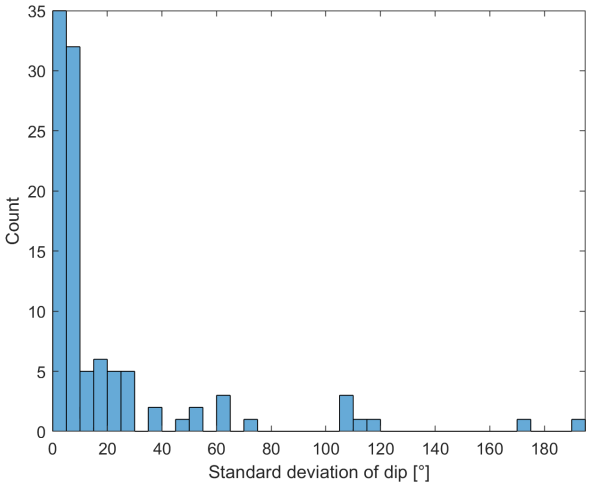

Figure S2: Standard deviation of the dip of dike segments from Dyrfjöll. Bin size is 5°.

There are outliers with very large uncertainties, but the bulk of the measurements has uncertainties of less than 25° (81% and 80% for strike and dip, respectively). For strike and dip respectively, 67% and 69% of the measurements show uncertainties of less than 15°. The segments with very large uncertainties correspond to elements where the points fall close to being on a single line. In these cases even very small deviations from this line result in drastically different orientations. For comparison the length of each segment and the surface area of each triangle abc are also plotted in histograms Figure S3, Figure S4.

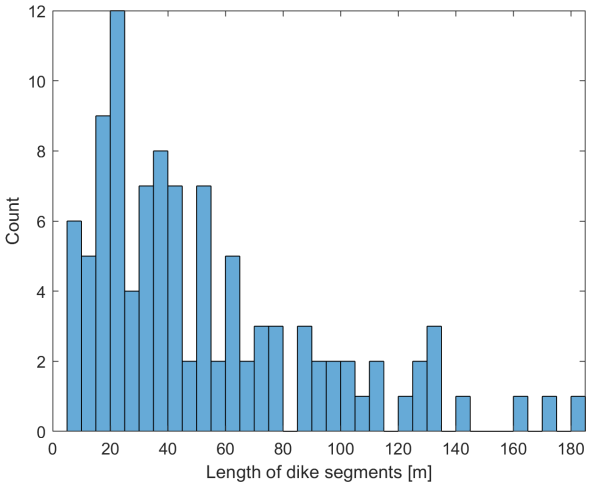

Figure S3: Distribution of the exposed length of the dike segments.

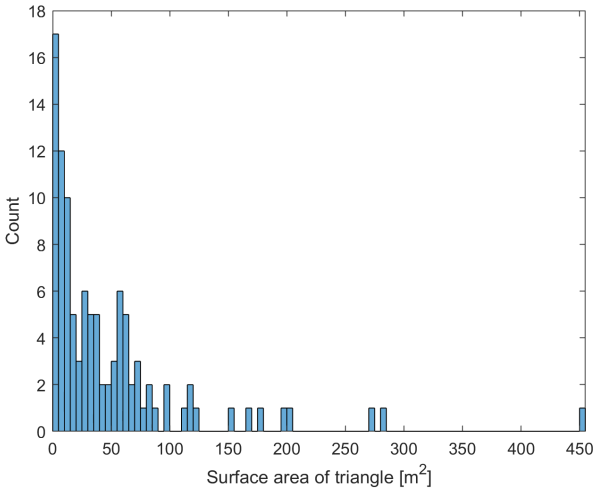

Figure S4: Distribution of the surface area of the triangles spanned by the three points which defined each dike segment's orientation.

LIME offers the possibility to manually adjust the orientation of the fit plane, which is especially useful for dike segments, where the exposure was close to being along a straight line. This was done by adjusting the point of view in LIME to look along the plane (which sticks out of the virtual outcrop model) after it was placed into the model based on the three specified points. The fit could then be improved by rotating the plane until it was aligned with the segment of interest, which should lie directly behind the plane when looking along it. The influence of this procedure onto the fit cannot be quantified easily, but it likely improved the fits to some dike segments significantly. Therefore, the numbers plotted in Figure S1, Figure S2 can be taken as an upper estimate of the uncertainty related to measuring orientations.
These uncertainty estimates show that inaccuracies during picking of the points may, to some degree, contribute to scatter observed at all sets of orientations measured at Dyrfjöll.

References

Buckley, S. J., K. Ringdal, N. Naumann, B. Dolva, T. H. Kurz, J. A. Howell, and T. J. B. Dewez. "LIME: Software for 3-D visualization, interpretation, and communication of virtual geoscience models". In: *Geosphere* 15.1 (Jan. 2019), pp. 222–235. ISSN: 1553-040X. DOI: 10.1130/GES02002.1. eprint: https://pubs.geoscienceworld.org/gsa/geosphere/article-pdf/15/1/222/4619098/222.pdf. URL: https://doi.org/10.1130/GES02002.1.

Ku, H. .H. "Notes on the use of propagation of error formulas". In: *Journal of Research of the National Bureau of Standards* 70.4 (1966).

Lo, E. "Gaussian error propagation applied to ecological data:Post-ice-storm-downed woody biomass". In: *Ecological Monographs* 75.4 (2005), pp. 451–466. DOI: https://doi.org/10.1890/05-0030. eprint: https://esajournals.onlinelibrary.wiley.com/doi/pdf/10.1890/05-0030. URL: https://esajournals.onlinelibrary.wiley.com/doi/abs/10.1890/05-0030.

Willink, Robin. *Measurement uncertainty and probability*. Cambridge University Press, 2013, p. 101.

S2 Photogrammetry

Quantitative information related to the UAV-based survey and outcrop models:

Table S1: Quantitative information related to the collected photogrammetry data for the three studied sites. The effective ground resolution corresponds to the average resolution across all images and the horizontal and vertical errors correspond to the average uncertainty of the camera locations at the time at which individual images were recorded.

Site	# images	Effective ground resolution $[cm/pix]$	Horizontal error [m]	Vertical error [m]
DF1	130	3.50	0.68	1.04
DF2	146	3.12	0.70	1.07
DF3	120	3.90	1.48	2.45

Table S2: Quantitative information related to the virtual outcrop models for the three studied sites. Surface area, numbers of tie points (points in the sparse cloud), dense cloud points, vertices and triangular faces, which approximate the surface of the virtual outcrop models. Resolution and point density correspond to the final virtual models.

Site	Surface area $[m^2]$	# Tie points	# Dense cloud points	# vertices	# faces	Resolution $[cm/pix]$	Point density $[pts./m^2]$
DF1	241 616	3566	3 085 600	104 220	205 694	28.0	12.7
DF2	116 449	6350	1 918 865	64 956	127 924	24.9	16.1
DF3	306 023	4544	3 268 862	110 121	217 921	31.2	10.3

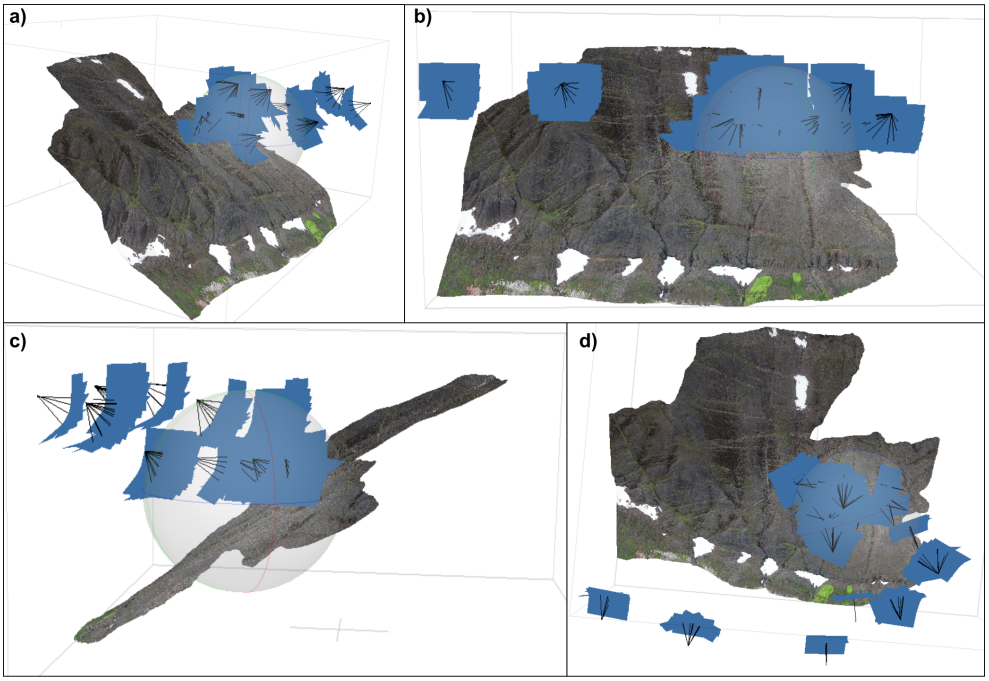

Figure S5: Location and viewing direction of the camera (indicated by black lines) relative to the outcrop at DF1. View towards a) the left of the outcrop (looking ca. NNW), b) the front of the outcrop (looking ca. WSW), c) the right side of the outcrop (looking ca. SSW) and d) looking downwards (direction WSW up).

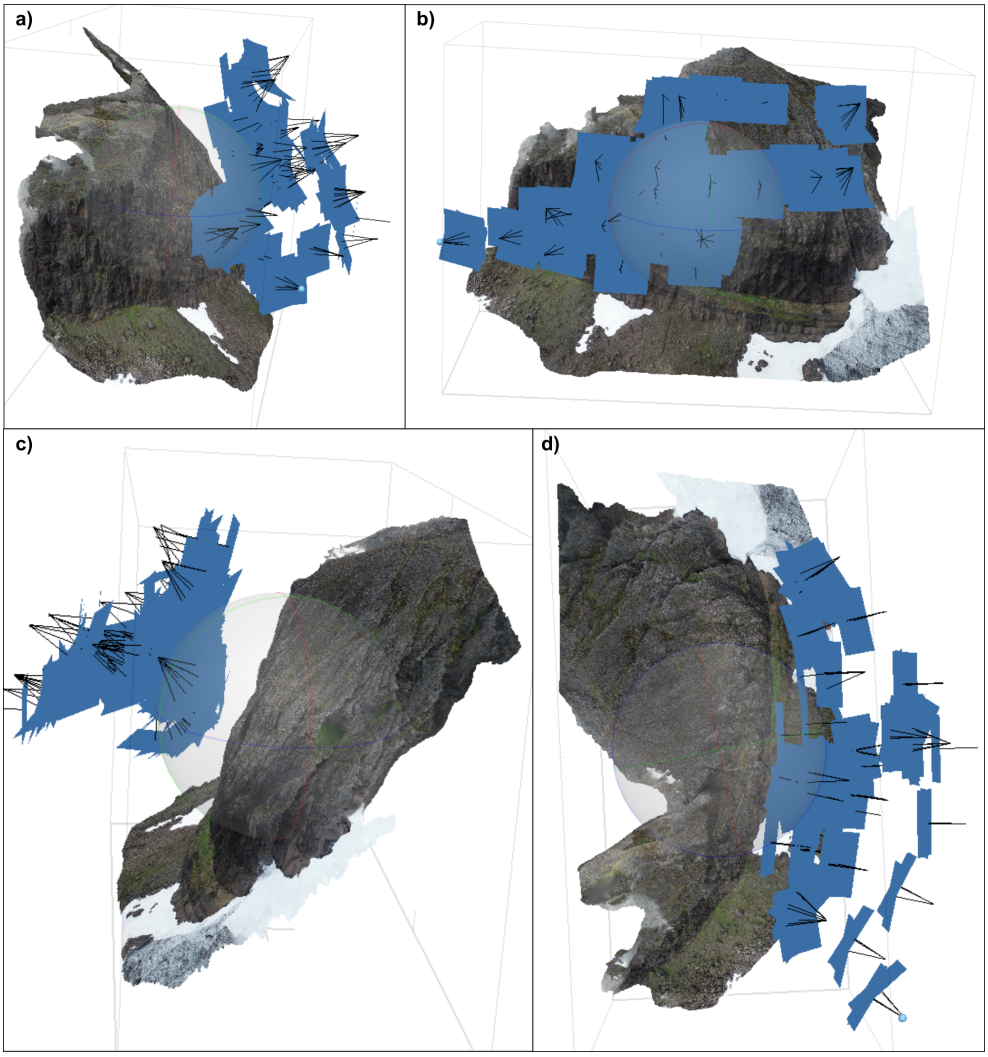

Figure S6: Location and viewing direction of the camera (indicated by black lines) relative to the outcrop at DF2. View towards a) the left of the outcrop (looking ca. N), b) the front of the outcrop (looking ca. W), c) the right side of the outcrop (looking ca. SW) and d) looking downwards (direction N up).

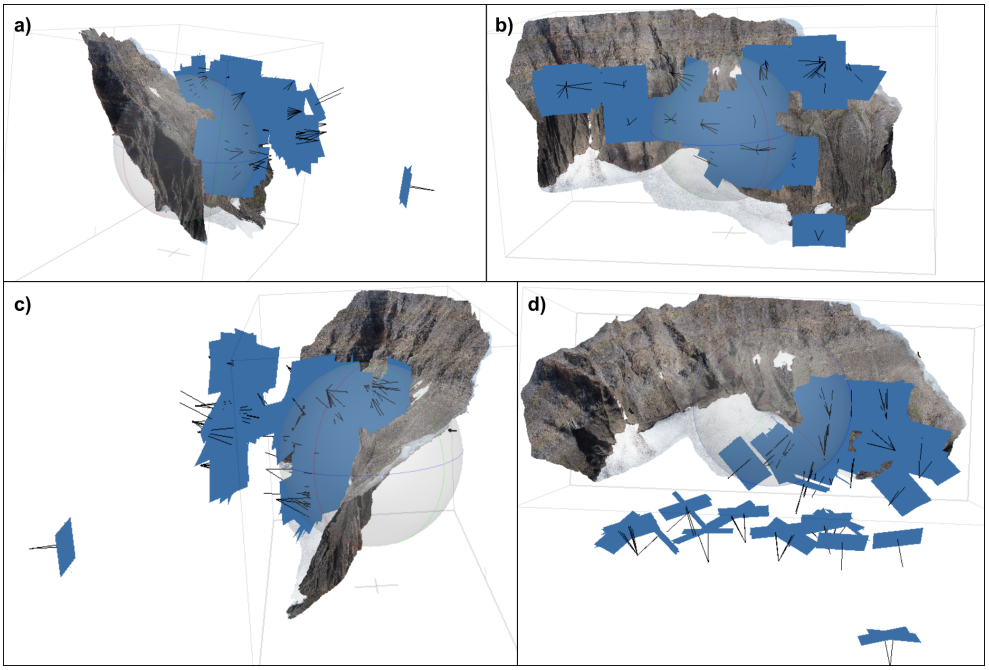

Figure S7: Location and viewing direction of the camera (indicated by black lines) relative to the outcrop at DF3. View towards a) the left of the outcrop (looking ca. SE), b) the front of the outcrop (looking ca. NE), c) the right side of the outcrop (looking ca. NW) and d) looking downwards (direction NE up).

S3 Mapping of dikes

Table S3: List of all mapped dike segments, if they have a change in strike at the end and if they occupied a pre-existing fracture. For changes in strike and use of pre-existing fractures: 0 = no, 1 = yes, 2 = inconclusive. All segments are marked on Figure S8 (DF1), Figure S9 (DF2) or Figure S10 (DF3).

Strike [°]	Dip [°]	Change in strike	Propagating along fracture	Site	Dike	Segment number
20.4	73.7	1	1	DF1	I	1
354.1	66.7	1	1	DF1	I	2
35.1	71.1	2	1	DF1	I	3
32.2	60.6	2	1	DF1	I	4
209.5	117.8	0	2	DF1	I	5
96.0	100.0	1	0	DF1	II	1
83.5	94.6	1	0	DF1	II	2
68.0	52.0	1	0	DF1	II	3
287.3	102.4	0	0	DF1	II	4
123.6	89.9	1	0	DF1	III	1
349.2	99.2	2	0	DF1	III	2
258.9	62.8	1	1	DF1	IV	1

Strike [°]	Dip [°]	Change in strike	Propagating along fracture	Site	Dike	Segment number
100.1	107.1	0	1	DF1	IV	2
108.7	128.0	0	1	DF1	V	1
242.3	114.5	2	1	DF1	VI	1
205.0	113.6	0	1	DF1	VII	1
13.0	77.6	0	1	DF1	VIII	1
144.7	121.1	1	1	DF2	I	1
277.9	92.1	1	1	DF2	I	2
94.0	88.8	0	1	DF2	I	3
209.1	99.1	0	1	DF2	II	1
282.4	72.9	0	1	DF2	III	1
26.0	72.9	0	1	DF2	IV	1
217.4	103.7	0	0	DF2	V	1
215.0	106.9	1	1	DF2	VI	1
26.1	78.2	0	1	DF2	VI	2
37.1	78.0	0	0	DF2	VI	3
171.9	122.0	2	2	DF2	VII	1
19.6	65.9	2	2	DF2	VII	2
213.9	109.6	0	1	DF2	VII	3
197.1	131.1	0	1	DF2	VII	4
136.4	98.2	1	0	DF2	VIII	1
325.0	65.9	1	0	DF2	VIII	2
331.7	89.7	0	0	DF2	VIII	3
348.9	94.2	1	0	DF2	IX	1
201.3	85.4	1	1	DF2	IX	2
222.6	90.2	1	1	DF2	IX	3
12.5	93.4	1	1	DF2	IX	4
343.8	72.5	1	1	DF2	IX	5
205.1	115.0	0	1	DF2	IX	6
112.8	89.1	0	0	DF2	IX	7
34.1	87.5	1	0	DF3	I	1
69.9	85.6	0	0	DF3	I	2
182.0	92.8	1	0	DF3	I	3
349.7	84.7	0	0	DF3	I	4
358.3	83.6	2	0	DF3	I	5
166.9	97.7	1	0	DF3	I	6
17.7	83.3	1	0	DF3	I	7
64.8	76.2	1	0	DF3	I	8
45.2	82.1	2	0	DF3	I	9
9.0	91.1	1	0	DF3	I	10
46.3	80.5	0	0	DF3	I	11
35.9	89.7	1	0	DF3	I	12
228.8	85.9	2	0	DF3	I	13
69.5	96.5	2	0	DF3	I	14
134.5	91.0	1	0	DF3	I	15
355.6	74.9	1	1	DF3	I	16
331.9	72.1	1	0	DF3	I	17
120.8	95.4	1	0	DF3	I	18
271.2	79.0	2	0	DF3	I	19
126.3	118.1	0	0	DF3	I	20

Strike [°]	Dip [°]	Change in strike	Propagating along fracture	Site	Dike	Segment number
154.7	87.1	2	1	DF3	I	21
120.8	95.4	2	0	DF3	I	22
288.4	70.8	1	0	DF3	I	23
301.7	79.0	2	0	DF3	I	24
315.3	110.0	0	0	DF3	I	25
349.7	84.7	1	0	DF3	I	26
126.3	118.1	1	0	DF3	I	27
46.3	80.5	1	0	DF3	I	28
69.9	85.6	2	0	DF3	I	29
315.3	110.0	2	0	DF3	I	30
250.9	104.2	2	1	DF3	II	1
228.5	86.1	0	0	DF3	III	2
249.5	119.4	0	0	DF3	IV	3
291.7	92.4	0	0	DF3	V	4
57.8	97.8	0	0	DF3	VI	5
276.9	71.7	0	0	DF3	VII	1
89.1	90.4	0	1	DF3	VIII	1
90.5	81.6	0	1	DF3	IX	2
22.5	61.3	1	0	DF3	X	1
38.8	65.9	0	0	DF3	X	2
335.2	90.0	0	0	DF3	XI	1
54.6	94.0	0	0	DF3	XII	2
208.7	75.7	0	0	DF3	XIII	3
85.0	74.1	0	0	DF3	XIV	1
247.1	90.1	0	0	DF3	XV	3
253.5	83.5	0	1	DF3	XVI	4
238.9	95.8	1	0	DF3	XVII	1
242.3	84.3	0	0	DF3	XVII	2
30.1	83.7	0	1	DF3	XVIII	1
71.9	101.0	0	0	DF3	XIX	1
205.5	92.1	0	1	DF3	XX	1
57.3	77.6	0	1	DF3	XXI	1
34.9	79.8	0	2	DF3	XXII	1
217.3	91.3	0	1	DF3	XXIII	1
331.3	104.9	1	1	DF3	XXIV	1
125.8	78.7	1	0	DF3	XXIV	2
118.0	93.6	2	0	DF3	XXIV	3
230.7	99.2	1	1	DF3	XXV	1
75.4	82.3	0	1	DF3	XXV	2
2.8	79.7	0	0	DF3	XXVI	1
25.0	95.1	0	1	DF3	XXVII	2
260.4	83.6	1	0	DF3	XXVIII	1
291.0	119.0	2	0	DF3	XXVIII	2

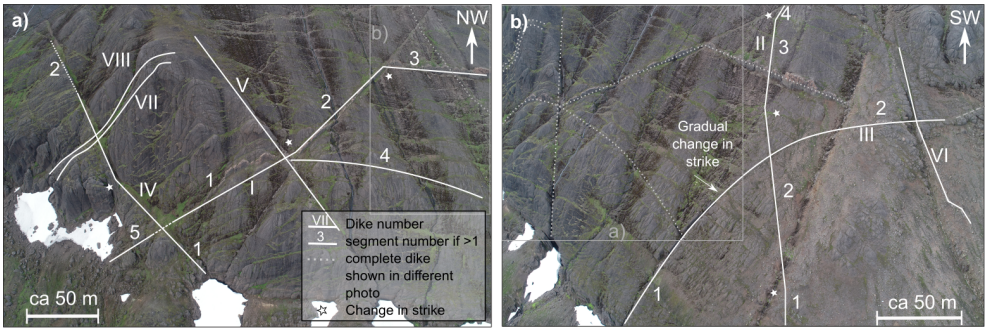

Figure S8: Dike segments at DF1 with labels according to tab. S3. Roman numerals correspond to dikes, Arabic to dike segments. Legend shown in a) also applies to b). Scale varies with perspective.

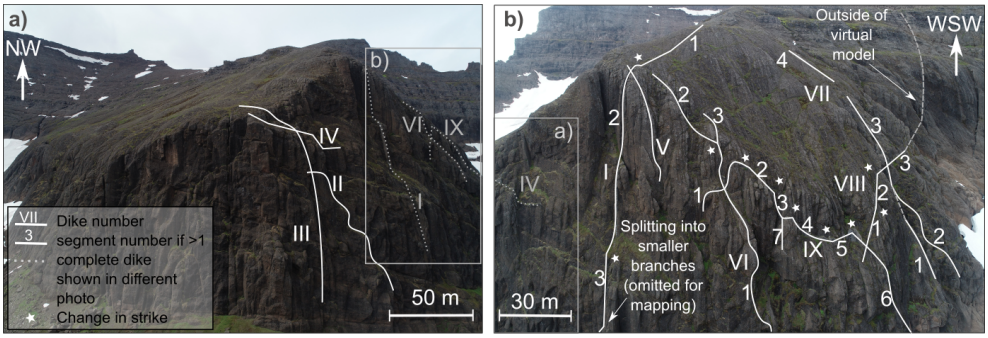

Figure S9: Dike segments at D2 with labels according to tab. S3. Roman numerals correspond to dikes, Arabic to dike segments. Legend shown in a) also applies to b).

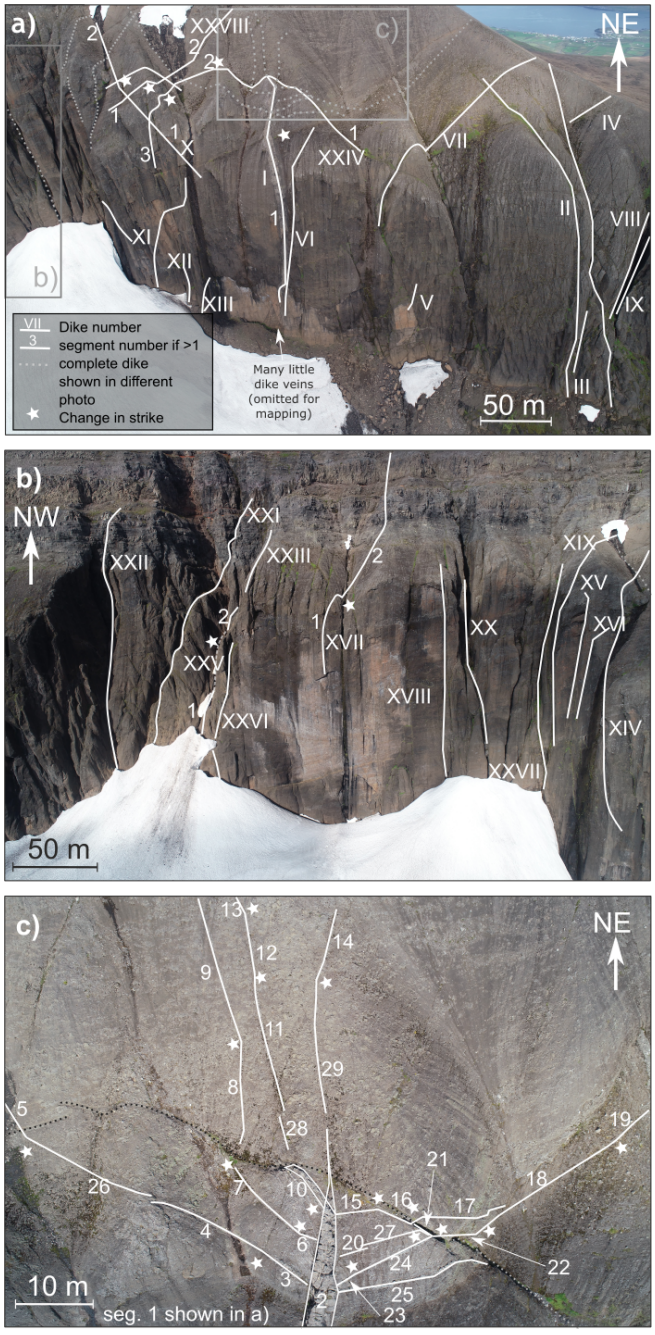

Figure S10: Dike segments at DF3 with labels according to tab. S3. Roman numerals correspond to dikes, Arabic to dike segments. Legend shown in a) also applies to b) and c).

S4 Additional plots for the results

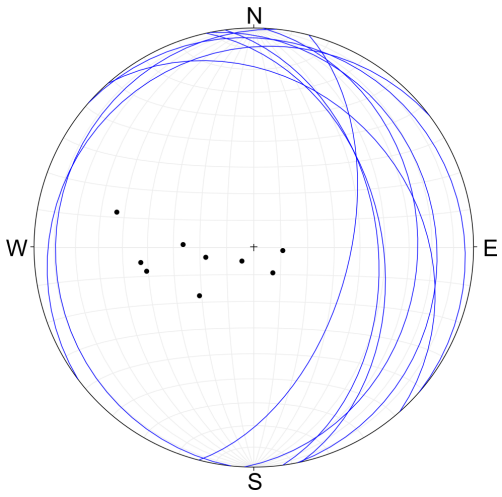

Figure S11: Orientation of fractures following the bedding in the hyaloclastite at DF2. N=9

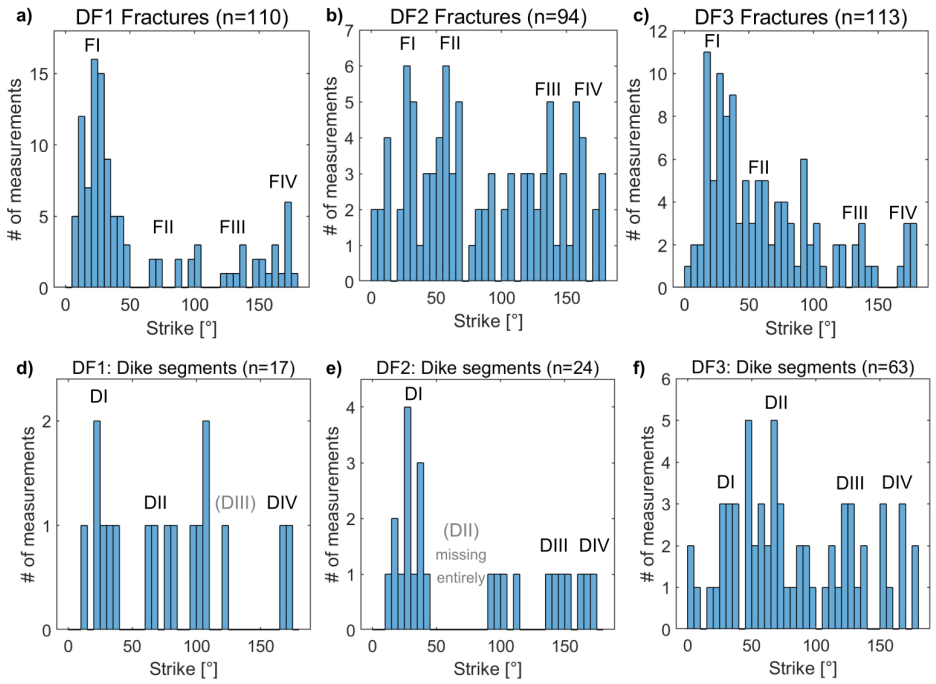

Figure S12: Strike distributions of fractures and dike segments by site. a)-c) Strike of fractures at DF1, DF2 and DF3, respectively. d)-f) Strike of dike segments at DF1, DF2 and DF3, respectively. Orientation sets FI-FIV and DI-DIV as defined in Table 1 are marked. Grey indicates that the set is only weakly visible or missing entirely.

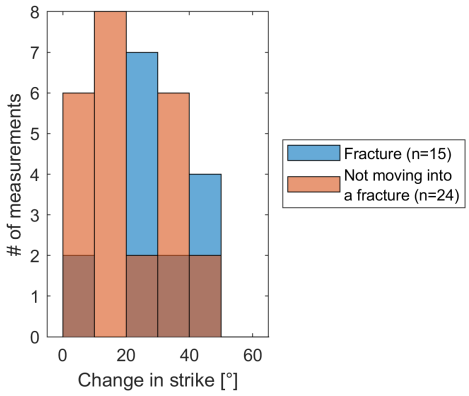

Figure S13: Changes in strike by amplitude divided into those in fractures/intact rock. In contrast to fig. 6c, the changes associated with the Tree-dike were included here.



Paper II

The influence of variable host rock cohesion and magma viscosity on intrusion-fault interaction: Insights from laboratory models

Sonja H. M. Greiner, Olivier Galland, Freysteinn Sigmundsson, Steffi Burchardt, Halldór Geirsson, Rikke Pedersen, Xia Wen

Journal of Geophysical Research: Solid Earth

Status: Accepted (2025)

The influence of variable host rock cohesion and magma viscosity on intrusion-fault interaction: Insights from laboratory models

Sonja H. M. Greiner [1,2,3], Olivier Galland [4], Freysteinn Sigmundsson [1], Steffi Burchardt[2,3], Halldór Geirsson [1], Rikke Pedersen [1], Xia Wen[5]

[1]Nordic Volcanological Center, Institute of Earth Sciences, University of Iceland, Reykjavík, Iceland
[2]Department of Earth Sciences, Uppsala University, Uppsala, Sweden
[3]Center for Natural Hazard and Disaster Science (CNDS), Sweden
[4]Physics of Geological Processes, the NJORD Center, Department of Geosciences, University of Oslo, Oslo, Norway
[5]School of Resource Environment and Saftey Engineering, University of South China, Hengyang, Hunan, China

Key Points:

- Laboratory experiments indicate that the host rock cohesion strongly affects the nature of intrusion-fault interaction
- Pre-existing faults in strong host rock are exploited by intruding fluid, while this is not observed in weak host rock
- The tested viscosity range has a secondary effect on intrusion-fault interaction, but low-viscosity fluids are more sensitive to faults

Corresponding author: Sonja H. M. Greiner, shmgreiner@hi.is

Abstract

Magma transport through the Earth's shallow crust can be affected by pre-existing weaknesses like faults. Consequently, fault-channeled magma may reach the surface in unexpected locations. Hence, better understanding of magma-fault interaction is needed to improve hazard assesment. We investigate the effect of host rock cohesion and magma viscosity on intrusion-fault interaction using laboratory experiments. Vegetable oil and glucose syrup, serving as low- and high-viscosity analogue magmas, were injected into intact and faulted granular materials with variable cohesion (mixtures of silica flour and micro-glass beads), serving as a brittle plastic model crust. High-cohesion models produced sheet intrusions, that propagated along fault segments upon intersection. Low-cohesion models produced low-aspect ratio intrusions low width/thickness ratio. Without tectonic stresses, the cohesion strongly controls intrusion-fault interaction, while tested model magma viscosities exerted a weaker control. Our findings show that intrusion-fault interaction is a highly complex process and important to consider at active volcanoes.

Plain Language Summary

Magma moving through the Earth's crust sometimes flows through pre-existing cracks. Thereby, cracks can influence where eruptions occur. Although this is well known, much about this process is unclear. We studied how different magmas behave when they meet cracks in different types of rocks. For this, we used laboratory experiments with materials that behave in a similar way to magma moving through the Earth's crust. Our model magmas were molten vegetable oil, representing runny magma, and sugar syrup, which represented magma of a thicker consistency. The Earth's crust was modelled with mixtures of silica powder and very small glass beads. In strong crust, the fluid can save energy by moving into existing cracks rather than by creating a new crack. The magma body's shape showed a sudden change where the fluid had met the crack and flowed into it, resulting in a plate-like shape. If the surrounding rock was weak, the fluid did not flow into cracks, which resulted in a "tea pot-shaped" intrusion. We found that the strength of the surrounding rock has more influence on magma interacting with cracks than the fluid properties of the magma. This is important to know for people who monitor active volcanoes.

1 Introduction

Magma transport through the Earth's crust can feed volcanic eruptions or lead to magma storage at depth (e.g., Breitkreuz & Rocchi, 2018; Burchardt, 2018). This often

occurs in areas, where the Earth's crust is heavily faulted. It is commonly assumed that pre-existing faults can affect magma pathways and emplacement as documented by field and seismic studies (Delaney et al., 1986; Valentine & Krogh, 2006; Jenness & Clifton, 2009; Magee et al., 2013; Spacapan et al., 2016; Maccaferri et al., 2016; Tibaldi et al., 2017; Stephens et al., 2018; Drymoni et al., 2021). Magma-fault interaction generally depends on the orientation of the intrusion and fault to the governing stress field (Jolly & Sanderson, 1997; Mathieu et al., 2015; Stephens et al., 2018; Greiner et al., 2023). However, magma-fault interaction can be so prominent that arrays of pre-existing faults influence the orientation of entire dike swarms (Spacapan et al., 2016). Few examples are reported of silicic magma propagating along faults compared to their mafic counterparts (de Silva et al., 1994; Corti et al., 2013; Burchardt et al., 2019; Temtime et al., 2020; Schmiedel et al., 2021; Rhodes et al., 2024). Furthermore, the importance of faults for the emplacement of magma reservoirs remains debated. Several studies suggest some influence (Kalakay et al., 2001; Rosenberg, 2004; Grocott et al., 2009; Burchardt et al., 2010, 2012; Cruden & Weinberg, 2018), while others argue that faults only weakly affect pluton emplacement (Paterson & Schmidt, 1999).

Observations at active volcanoes further document the relevance of understanding magma-fault interaction beyond the potential to influence magma-pathways. The reactivation of pre-existing faults as a response to magma emplacement can affect surface deformation (Temtime et al., 2020; Hjartardóttir et al., 2023; Ducrocq et al., 2024; Sigmundsson et al., 2024). However, this is rarely considered in inversions of geodetic data (Wright et al., 2006; Calais et al., 2008; Ruch et al., 2016; Sigmundsson et al., 2022). Better understanding the potential impact of faults on shallow subsurface magma movement is thus important for hazard assessment (e.g., Barsotti et al., 2023).

In field studies, magma-fault interaction is often solely ascribed to the influence of deviatoric stress, which may relate to e.g., tectonic movements or gravitational loading (Delaney et al., 1986; Acocella & Neri, 2009; Stephens et al., 2018). However, not every dike shows evidence of propagation along faults and not every fault in a volcanically active area is intruded by magma (e.g., Gudmundsson, 1983; Pedicini et al., 2023). The influence of and interplay between the underlying mechanical properties of the magma and faulted host rock are often neglected in this context. While active faults are typically considered to be weaker than the surrounding host rock, faults can be complex structures, and processes such as fault healing can influence how weak a fault is relative to largely unfractured material (e.g., Caine et al., 1996; Carpenter et al., 2012; Ikari et al., 2015). Because of the difficulty to separate the material property-based control on magma-

fault interaction from effects of tectonic processes in the field, other approaches are required that allow for systematic separation of the two.

Laboratory modelling is frequently employed to study magma emplacement under controlled conditions (Galland et al., 2018; Kavanagh et al., 2018). Magma-fault interaction has previously been investigated through two main types of models. Firstly, models with cohesion-less sand and high-viscosity silicone putty studied pluton emplacement in actively deforming faults (Román-Berdiel et al., 1997; Corti et al., 2005; Montanari et al., 2010; Mathieu & van Wyk de Vries, 2011). These studies found that although the resulting intrusions were elongated parallel to the main fault structures, the model magma never intruded into the faults. Notably, magma emplacement was simulated at the same time scale as tectonic processes (>100,000 years) although the time scale of dike emplacement (Sigmundsson et al., 2015, 2024), laccoliths and cryptodomes (Minakami et al., 1951; Donnadieu & Merle, 2001; Castro et al., 2016), and small plutons (de Saint Blanquat et al., 2011; Caricchi et al., 2014; Rhodes et al., 2021), is typically orders of magnitude shorter (days to thousands of years). It is therefore unclear, if the elongated intrusion shapes in these sand/silicone models were controlled by the active fault motion or by the mechanical weakness represented by the fault.

Secondly, elastic gelatin-models with low-viscosity intrusions (air, water) simulated dike and sill emplacement in the presence of pre-existing weak planes (Le Corvec et al., 2013; Kavanagh et al., 2017). In contrast to the sand-silicone models, intrusions in gelatin models were more systematically channeled into weaknesses upon intersection. The cohesion of gelatin is unknown and it exhibits a high tensile strength with respect to granular materials (Kavanagh et al., 2015). Although the strength contrast between intact gelatin and pre-existing cuts in the models of Le Corvec et al. (2013) has not been quantified, it is likely to be large if compared to the strength contrasts in the sand/silicone models. In summary, the analgoue host rock in sand/silicone models may have too low cohesion to simulate fault-controlled magma emplacement, while gelatin is so strong that pre-existing faults systematically control propagating intrusions.

The gradual transition between different intrusion regimes has been successfully investigated in laboratory models by injecting oil or syrup into granular materials of variable cohesion (e.g., Schmiedel et al., 2019; Poppe et al., 2019). In these experiments, the crust was represented by homogenized mixtures of glass beads and either silica flour or gypsum powder. The cohesion varied depending on the ratio of mixed materials. Intrusions into high-cohesion granular materials, i.e. strong analogue host rock produced sheet intrusions like dikes and cone sheets. They have a high-aspect ratio, i.e. their height and length are large compared to their thickness. Conversely, intrusions into low-cohesion,

weak granular materials resulted in massive intrusions with a low aspect ratio, i.e. their thickness is comparable to their length and height. They resembled to some degree laccoliths or crypto-domes and erupted through subcircular or elongated conduits. Such massive intrusions will hereafter be referred to as *low-aspect ratio* intrusions. These studies indicate the potential to investigate the gradual transition from strong to weak host rock using granular materials with physically consistent properties.

Here, we use analogue modelling to systematically study the role of mechanical material properties on magma-fault interaction, focusing on the host rock cohesion and magma viscosity. This is done by injecting two different liquids – with high and low viscosity, respectively – into granular host rocks of varying cohesion with a pre-existing fault. These experiments help to better understand the potential role of faults during intrusions into the shallow crust, and their effect on associated surface deformation. Testing different viscosities may provide insights into magma-fault interaction even for more viscous types of magma. In nature, magma-fault interaction is strongly affected by tectonic stress. However, deviatoric stress fields are not considered in the present study to isolate and investigate specifically the influence of the mechanical host rock and fluid properties on magma-fault interaction.

2 Materials and Methods

All experiments were conducted using molten vegetable oil or glucose syrup as model magma. They were injected into five mixtures of dry granular materials, simulating host rocks of varying strength. For each material combination, one experiment was conducted, for which the host rock was subjected to strike-slip faulting prior to the intrusion emplacement, and one with non-faulted, intact host rock, resulting in 20 experiments (Table 1).

2.1 Materials

The model crust in this study consisted of mixtures of microglass beads (GB; diameter of $\approx 30\,\mu$m) and silica flour (SF; average grain size $10-20\,\mu$m) (Galland et al., 2006). Both behave as brittle plastic Coulomb materials, but while silica flour is cohesive, glass beads have almost negligible cohesion (Galland et al., 2006; Abdelmalak et al., 2016). This allows to use them as end-member analogues of strong, competent and weak, incompetent natural rocks. Mixtures of both materials have cohesions between those of the end-member materials (Galland et al., 2006; Abdelmalak et al., 2016) and have been used in analogue experiments for several years (Galland et al., 2006; Galland, 2012; Abdelmalak et al., 2012; Galland et al., 2018; Schmiedel et al., 2017, 2019; Bertelsen et

Table 1. Material properties of granular materials and liquids used in this study. Composition correspond to the weight fraction of glass beads (GB) and Silica flour (SF), respectively. Cohesion and angle of internal friction refer to non-faulted material. The density was measured after compaction.

Model name	Liquid	Analogue host rock composition	Initial host rock status	Cohesion[a] C_i [Pa]	Angle of internal friction[a] Φ [°]	Density (compacted) ρ_c [kg/m^3]
OI50/50	Oil	50% GB, 50% SF	intact	375	44	1342
OI80/20	Oil	80% GB, 20% SF	intact	313	28	1614
OI90/10	Oil	90% GB, 10% SF	intact	240	27	1632
OI95/5	Oil	95% GB, 5% SF	intact	191	27	1587
OI100/0	Oil	100% GB, 0% SF	intact	142	26	1569
OF50/50	Oil	50% GB, 50% SF	faulted	375	44	1347
OF80/20	Oil	80% GB, 20% SF	faulted	313	28	1620
OF90/10	Oil	90% GB, 10% SF	faulted	240	27	1643
OF95/5	Oil	95% GB, 5% SF	faulted	191	27	1629
OF100/0	Oil	100% GB, 0% SF	faulted	142	26	1565
SI50/50	Syrup	50% GB, 50% SF	intact	375	44	1329
SI80/20	Syrup	80% GB, 20% SF	intact	313	28	1628
SI90/10	Syrup	90% GB, 10% SF	intact	240	27	1657
SI95/5	Syrup	95% GB, 5% SF	intact	191	27	1602
SI100/0	Syrup	100% GB, 0% SF	intact	142	26	1560
SF50/50	Syrup	50% GB, 50% SF	faulted	375	44	1324
SF80/20	Syrup	80% GB, 20% SF	faulted	313	28	1589
SF90/10	Syrup	90% GB, 10% SF	faulted	240	27	1667
SF95/5	Syrup	95% GB, 5% SF	faulted	191	27	1598
SF100/0	Syrup	100% GB, 0% SF	faulted	142	26	1570

[a] From Abdelmalak et al. (2016). Values for 95%GB, 5% SF mix calculated as average of 90%GB, 10% SF mix and 100 % GB.

al., 2021). In the series of experiments presented here, we used five mixtures ranging from 50% SF and 50% GB to pure glass beads (Table 1).

The two liquids used here as model magmas represent low- and high-viscosity magma, respectively. The low-viscosity model magma was molten vegetable oil, called Vegetaline by Unilever (France) and it has been used in several previous studies (Galland et al., 2006;

Galland, 2012; Galland et al., 2014; Schmiedel et al., 2017, 2019; Bertelsen et al., 2021). The oil is solid at room temperature, but melts above ca. 31°C. At the injection temperature (50 °C), it has a viscosity of $\eta_o = 0.02\,\mathrm{Pa\,s}$ and a density of $\rho_o = 890\,\mathrm{kg/m^3}$ (Galland et al., 2006).

We used Eldorado Syrup Lys, a glucose syrup produced in Sweden, as an example of a high-viscosity liquid. It was injected at room temperature (ca. 22°C), where it has a viscosity of η_s =70 Pa s and a density of $\rho_s = 1400\,\mathrm{kg/m^3}$ (Supporting Information S2). It resembles Golden Syrup, which has been used in analogue models before (Mathieu et al., 2008; Abdelmalak et al., 2012; Poppe et al., 2019)

Hereafter, experiments will be referred to by the liquid used ("O" for oil or "S" for syrup), the initial host rock status ("I" for intact and "F" for faulted) and relative GB/SF proportions (Table 1).

2.2 Experimental Setup and Procedure

The model box has a base area of $38\,cm \times 39\,cm$ with a circular inlet (5 mm diameter) at its center, through which liquid is injected. A half-open, second box, W_S = 18.5 cm wide, was placed into the initial box (right side in Figure 1a). Moving this second box creates a discontinuity at depth (Figure 1b), which nucleates a strike-slip fault in the model crust (Le Guerroué & Cobbold, 2006; Visage et al., 2023). The sliding plate introduces a 5 mm-high step along the length of the box and directly past the injection inlet (Figure 1a).

The analogue host rock was poured into the box and compacted by pressing a metal plate onto the surface while using a compressed air shaker (Houston Vibrator, model GT-25). The amount of material was chosen so that the thickness after compaction was 6 cm (max. deviation < 3 mm). During compaction, the inlet was closed with a plug to prevent clogging and loss of material. The cohesion of the 95/5 and 100/0 mixtures was so low that material would fall through the inlet after the plug was removed. Therefore, all experiments using either of these materials had a 1 cm-thick layer of the 80/20 mix at their base (thickness refers to the non-sliding side of the box). For all pre-faulted experiments, the sliding box was pulled, creating 4 cm of right-lateral slip (Figure 1b). For consistency, the sliding-box was also part of the setup in intact experiments, although remaining undisplaced. All external fault motion occurred before liquid was injected. The structure of the fault zone created by movement of the sliding plate varied to some degree as a function of the cohesion fo the analogue host rock. However, comparison of fault patterns suggest that the position of the largest fault segments is comparable between

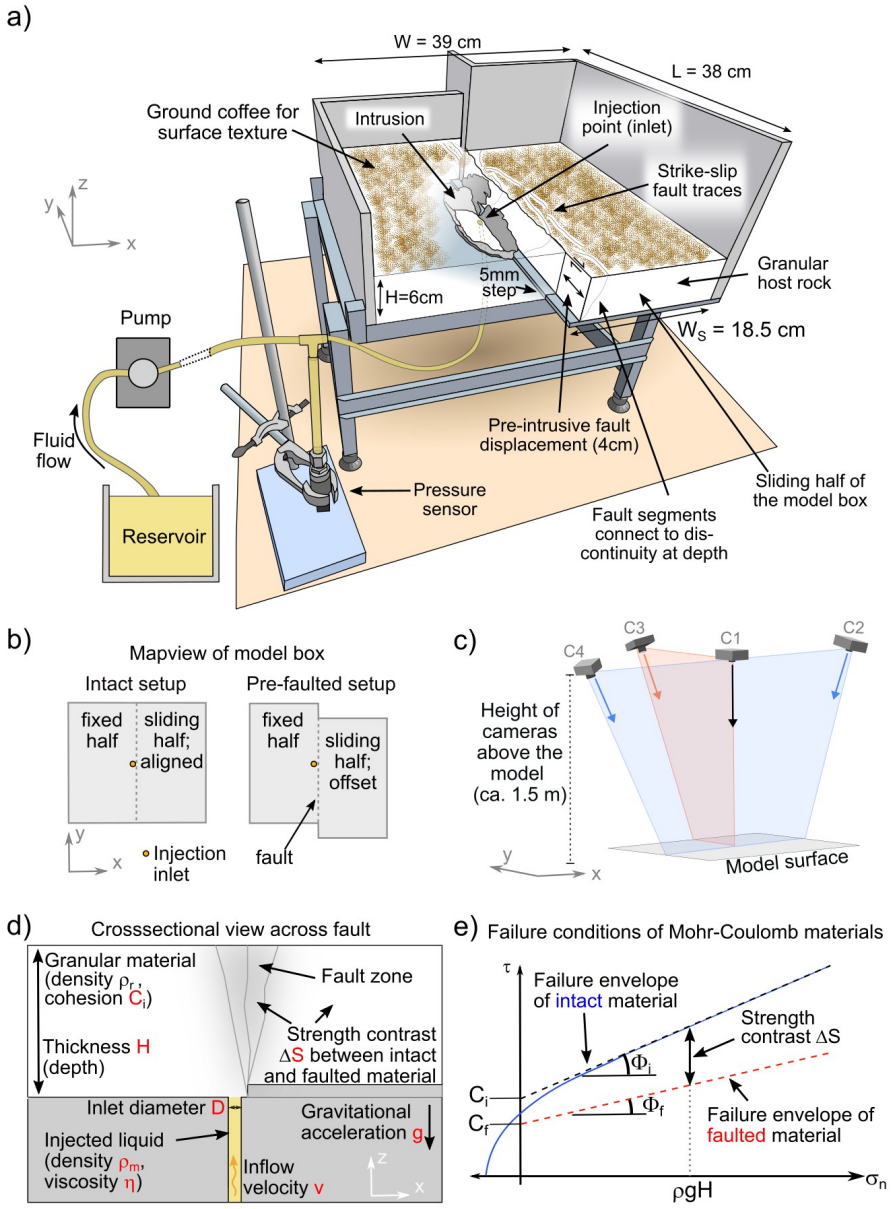

Figure 1. a) Illustration of the experimental set up. b) Schematic mapview of the starting geometry of the model box. c) Schematic camera positions. Coloured polygons mark planes spanned by the camera positions and looking directions. For photos of the experimental setup see Supporting Figure S1. d) Schematic cross-section through the model box showing the physical parameters controlling the intrusion process. e) Schematic comparison of failure conditions for intact and faulted materials based on the Mohr-Coulomb failure criterion.

experiments (Supporting Figure S10), and we argue here that the fault pattern is broadly reproducible between experiments.

To facilitate observation of surface motion, the model needed to have a sufficient amount of surface texture. For this purpose, we sprinkled grains of ground coffee and olivine sand onto the surface of the otherwise white analogue host rock, which however did not affect the mechanical properties of the underlying material. This was done prior to any faulting. An array of four cameras (Nikon 3200 with 35 mm fixed-focal length lenses) was set up approximately 1.5 m above the model to record surface deformation (Figure 1c). One camera faced straight downwards; the others had oblique looking angles to allow reconstruction of surface deformation in three dimensions (3D). All cameras were remote-controlled to record images synchronously at rates of $\Delta t_o = 1\,\mathrm{s}$ (2 s-intervals for OI100/0 and OF100/0) for oil, and $\Delta t_s = 2\,\mathrm{min}$ for syrup experiments. The camera resolution was set to 6016×4000 pixels for oil and 4512×3000 pixels for syrup experiments, respectively.

A syringe pump was used to inject syrup at a rate of $Q_s = 0.2\,\mathrm{ml/min}$. The oil was heated to $50^\circ\,C$ in a pot to ensure that it did not cool before injection and fluid flow was regulated through a volumetric pump to a flow rate of $Q_o = 20\,\mathrm{ml/min}$. Both types of pumps controlled the flow rate of injected fluid. The different pumps were required due to the different viscosities and the requirement to keep the oil heated prior to injection. A pressure sensor between the pump and the injection inlet recorded the fluid pressure at frequencies of $f_o = 10\,\mathrm{Hz}$ and $f_s = 2\,\mathrm{Hz}$ for oil and syrup, respectively. Based on this measurement we derived the fluid pressure at the injection inlet at the base of the model box (Supporting Information S7).

The oil solidifies at room temperature, so the final intrusion shape could be observed after removing the surrounding material. To create virtual models of the solidified intrusion geometry through photogrammetry, we took images of the intrusion from many different perspectives using a handheld camera (Canon EOS 6D with a 24 mm fixed-focal length lens). Since the syrup does not solidify at room temperature, we did not retrieve the final intrusion geometry for syrup experiments.

During some experiments, one of the recorded data sets was compromised. Such experiments were excluded from further analysis and repeated. However, if only the pressure sensor was affected, the experiments contained information about the surface deformation and, where applicable, the intrusion geometry and can be compared to successful experiments (Supporting Information S6). We note that very similar results were

produced in repeated experiments, strongly suggesting that our experimental results are overall reproducible.

2.3 Data Processing

2.3.1 Surface Deformation

Surface data was processed using a structure-from-motion approach through the photogrammetry software MicMac v.1.1.1 (Pierrot-Deseilligny et al., 2016; Galland et al., 2016; Rupnik et al., 2017; Galland et al., 2024). The georeferencing of the model was imposed through six ground control points on the edges of the model box. The output from MicMac included time-resolved Digital Elevation Models (DEM) and horizontal surface displacement maps. A geo-referenced point cloud of the initial surface was used to map the surface traces of the strike-slip fault (if present) using the software CloudCompare.

The experimental deformation data and DEMs were further analyzed using Matlab following the same workflows as used by Galland et al. (2024). One parameter of interest is the topography change. For each pixel, the cumulative topography change $\Delta_{DEM,i}$ at any time step i is the difference between the DEM in question and the initial surface:

$$\Delta_{DEM,i} = DEM_i - DEM_0. \tag{1}$$

Note that in faulted experiments, DEM_0 refers to the surface after faulting.

The divergence of the horizontal displacement field $\vec{u}_{hor}$ highlights its gradients. It is calculated as

$$div\,(\vec{u}_{hor}) = \nabla \vec{u}_{hor} = \frac{\partial u_x}{\partial x} + \frac{\partial u_y}{\partial y} \tag{2}$$

where the suffix x and y refer to directions as indicated in Figure 1. Positive values correspond to lengthening/extension while negative values indicate shortening/compression.

2.3.2 Intrusion Geometry and Volume

3D virtual models of oil intrusions were created with the software Agisoft Metashape 1.6.4, using photogrammetry and structure-from-motion. To place the model in the same reference system as the overlying surface, we used Ground Control Points at the base and the edge of the model box. Models of the final intrusion geometry were combined with the overlying surface in the software ParaView.

The intrusion volume can be determined by multiplying the duration of an experiment with the constant injection rate. In the earliest phase of each experiment, the fluid

flowed along the pipe before reaching the contact to the granular material, which was taken as the beginning of the actual intrusion process and marked by an abrupt increase in the recorded pressure. The eruption onset, which defined the end of the experiment, was identified from images of the model surface.

2.4 Model Parameters and Dimensional Analysis

Scaling and similarity of the experiments to natural systems are important because they ensure that the processes observed in the laboratory are at least at first order similar to nature (Hubbert, 1937; Ramberg, 1970, 1981). The relevant material properties and experimental parameters are shown in Figure 1d and listed in Table 2. All except for the strength parameter ΔS are straightforward to constrain for laboratory materials and have been used in previous studies (Galland et al., 2006; Galland, 2012; Abdelmalak et al., 2012; Guldstrand et al., 2017; Schmiedel et al., 2017; Bertelsen et al., 2021). The host rock cohesion of the granular materials has been quantified through shear tests, tensile and extensional tests by Abdelmalak et al. (2016) and for a more detailed discussion of this topic the reader is referred to that study. It should be noted that we calculated the fluid flow velocity at the injection inlet (Table 2). While the tip-velocity of a propagating intrusion may be more meaningful for intrusions, it was not possible to observe this due to the opaque analogue host rock. However, at least in unfractured materials, the tip velocity can be assumed to be to a first order proportional to the inflow velocity (Chalk & Kavanagh, 2024).

We apply here dimensional analysis based on the Buckingham-Π theorem to scale our experiments (Buckingham, 1914; Gibbings, 2011) and derived six dimensionless ratios $\Pi_1 - \Pi_6$ from the governing parameters (Table 2). All except for Π_2 have been used in previous studies (e.g., Abdelmalak et al., 2012; Galland et al., 2014; Schmiedel et al., 2017). For details on the derivation of the parameters, see these studies and Supporting Information S3. In the context of magmatic intrusions, the fluid viscosity is a parameter of special interest (e.g., Stinton et al., 2024). Based on the range of Π_5 for our laboratory models and the estimated range for the inlet diameter, flow velocity and host rock cohesion in nature, we estimate that our experiments are representative of magma viscosities ranging from ca. $\eta = 20 - 600\,Pa\,s$ and $\eta = 9 \times 10^5 - 3 \times 10^7\,Pa\,s$ for the low- and high-viscosity experiments, respectively (Tables 2 and S2). It should however be noted that these values depend on the estimated range of the other parameters affecting Π_5 and that additionally, our experiments may not be representative of the magmas on the very high end of the sprectrum of natural viscosities (Gonnermann, 2015; Lesher & Spera, 2015).

297 Faulted host rock is generally weaker than intact rock, which affects its cohesion
298 and angle of internal friction (Thompson et al., 2008; Ikari et al., 2015; Carpenter et al.,

Table 2. Governing parameters and dimensionless ratios with values for our experiments and nature. See Supporting Information S3 for details and derivation of dimensionless ratios.

Parameter/Ratio	Laboratory range	Natural range
Rock density ρ_r	1324 – 1667 kg/m^3 $^{(a)}$	1600 – 3000 kg/m$^{3(f)}$
Intact cohesion C_i	142 – 375 Pa $^{(b)}$	$10^6 - 10^8$ Pa$^{(g)}$
Depth H	6 cm $^{(a)}$	1000-5000 m $^{(h)}$
Strength contrast ΔS	22 – 630 Pa $^{(a),(c)}$	Uncertain
Liquid density ρ_m	890 kg/m^3 $^{(d)}$ / 1400 kg/m^3 $^{(e)}$	2260 – 2750 kg/m^3 $^{(i)}$
Viscosity η	0.02 Pa^d/ 70 Pa$^{(e)}$	100 – 10^{10} Pa s$^{(i),(j)}$
Inflow velocity v	$7 \times 10^{-3}\, m/s$ / $9 \times 10^{-5}\, m/s$ $^{(a)}$	0.1–12 $m/s^{(k)}$
Inlet diameter D	0.5 cm $^{(a)}$	1-10 m $^{(l)}$
Gravit. accelerat. g	9.81 m/s^2	9.81 m/s^2
$\Pi_1 < \Pi_{1,max} = \frac{\rho_r - \rho_m}{\rho_r}$	-0.06 – 0.47	-0.71–0.24
$\Pi_2 = \frac{\Delta S}{C_i}$	0.16 – 1.68	Uncertain
$\Pi_3 = \frac{C_i}{\rho_r g H}$	0.15 – 0.5	0.01-6.37
$\Pi_4 = Re = \frac{\rho_m v D}{\eta}$ $^{(m)}$	1.5 / 9×10^{-6}	$2 \times 10^{-8} - 3300$
$\Pi_5 = \frac{\tau_v}{C_i} = \frac{\eta v}{D C_i}$	$7 \times 10^{-5} - 9 \times 10^{-3}$	$10^{-8} - 1.2 \times 10^6$
$\Pi_6 = \frac{D}{H}$	0.09	$1.7 \times 10^{-4} - 0.01$

$^{(a)}$ From experimental set up

$^{(b)}$ Abdelmalak et al. (2016)

$^{(c)}$ Poppe et al. (2021b)

$^{(d)}$ Galland et al. (2006)

$^{(e)}$ Supplementarty Section S2

$^{(f)}$ Turcotte and Schubert (2014)

$^{(g)}$ Schultz (1995); Schellart (2000) and references therein; Heap and Violay (2021)

$^{(h)}$ Galland et al. (2014); Schmiedel et al. (2017)

$^{(i)}$ Lesher and Spera (2015)

$^{(j)}$ Gonnermann (2015)

$^{(k)}$ Spera (1980); Peltier et al. (2005); Sigmundsson et al. (2022)

$^{(l)}$ Spence and Turcotte (1985); Clemens and Mawer (1992)

$^{(m)}$ Refers to the flow at the injection inlet. Velocity derived from volumetric flow rate.

2012; Poppe et al., 2021b). Assuming a Mohr-Coulomb failure criterion (e.g., Abdelmalak et al., 2016), the failure envelopes differ between intact and faulted rock (Figure 1e). The strength contrast is defined here as the difference in critical shear stresses of intact and faulted rock at a given normal stress, which we chose to be the lithostatic stress at the base of the box (Figure 1e):

$$\Delta S = C_i + \rho_r g H tan\left(\varphi_i\right) - \left[C_f + \rho_r g H tan\left(\varphi_f\right)\right] \tag{3}$$

The indices i and f correspond to faulted and intact material, respectively, and C and φ are the cohesion and the angle of internal friction. In our study, the strength contrast affects the dimensionless parameter Π_2, which relates it to the cohesion of intact host rock C_i (Table 2). This parameter is a measure for how much of a weakness a fault represents. If the strength contrast is significant compared to the cohesion of the intact material, the fault represents a strong weakness, while it represents a less pronounced weakness if the contrast is small compared to the cohesion of the intact material.

The strength contrast is difficult to constrain since the properties of fractured rocks are difficult to constrain in nature (e.g., Schultz, 1995; Thompson et al., 2008; Heap & Violay, 2021). No information is available for the properties of the faulted material mixtures used in this study. However, ring shear tests with gypsum powder/quartz sand mixtures indicate that C_f remains approximately constant across varying proportions although C_i changes (Poppe et al., 2021a, 2021b). We assume similar behaviour here and set $C_f = 120\,\mathrm{Pa}$, which is slightly lower than the cohesion of pure glass beads. The angle of internal friction of faulted materials is assumed as equal to that of pure glass beads for all materials.

Throughout the current study we refer to fluids interacting with faults or fault segments. Our findings may be partially transferrable to other structural weaknesses such as fractures and joints, although the applicability of our findings may be limited due to the scaling if they are very small.

2.5 Model Limitations

The Earth's crust can behave as a visco-elasto-plastic material. This is difficult to accurately reproduce in analogue models (Bertelsen et al., 2018; Galland et al., 2018; Arachchige et al., 2021). Our model crust behaves in a dominantly brittle-plastic manner and therefore mainly represents brittle deformation in the upper crust, although the elastic properties of dry granular materials are poorly understood (Bodet et al., 2010; Abdelmalak et al., 2016).

Faults are complex structures, and it is challenging to accurately characterize their bulk material properties (Heap & Violay, 2021). The mechanical properties of the faulted material in our models are unknown. The strength contrast between faulted and intact materials is particularly challenging to assess, limiting direct quantitative relationships, which we can extract from our models at this time. More quantitative information about the mechanical properties of faulted materials (in nature and for laboratory materials) are required before any quantitative relationships can be derived.

For low-cohesion experiments, a 1 cm-thick layer of more cohesive material (80/20-mix) covered the base of the box to prevent material from falling through the injection inlet. We tested whether this affected the final geometry, by repeating experiment OI90/10 with a 1 cm thick layer of the 80/20-mix at the model base and found that it did not significantly affect the intrusive process (Supporting Information S5).

The final oil intrusion geometries might differ slightly from their shape at the eruption onset. This can relate to minor percolation of the oil into the host rock (Galland et al., 2006), continued propagation along faults after the eruption onset and, in case of low-aspect ratio intrusions, because the roof partially subsided once the eruption started. We hypothesize however, that these processes do not affect the main findings of this study.

Our models neglect many processes and aspects relevant to magma emplacement. This not only includes tectonics, but also heterogeneous crustal material properties, topography, thermal effects, repeated intrusions, non-Newtonian magma rheology and changes in magmatic properties with time e.g., due to degassing (Jolly & Sanderson, 1997; Fialko & Rubin, 1999; Pinel & Jaupart, 2000; Glazner et al., 2004; Kervyn et al., 2009; Burchardt et al., 2010; Leuthold et al., 2012; Burchardt et al., 2019; Galland et al., 2019; Kjøll et al., 2019; Witcher et al., 2024). Furthermore, the fault zone in our model had one dominant orientation and sense of motion, and we did not investigate effects of fault maturity. Further studies could incorporate some of these processes and evaluate their influence on intrusion-fault interaction.

3 Results

3.1 High-viscosity Experiments (Syrup)

Syrup intrusions into intact model crust of high and intermediate cohesion (SI50/50-SI90/10; Figure 2a, c and e) produced gentle subcircular doming approximately centered around the injection inlet. Eruptions occurred at the edge of the uplifting area. Low-cohesion model crust (SI95/5-SI100/0; Figure 2g and i) produced low-amplitude subcircular uplift superimposed by asymmetric uplift with higher amplitudes compared to more

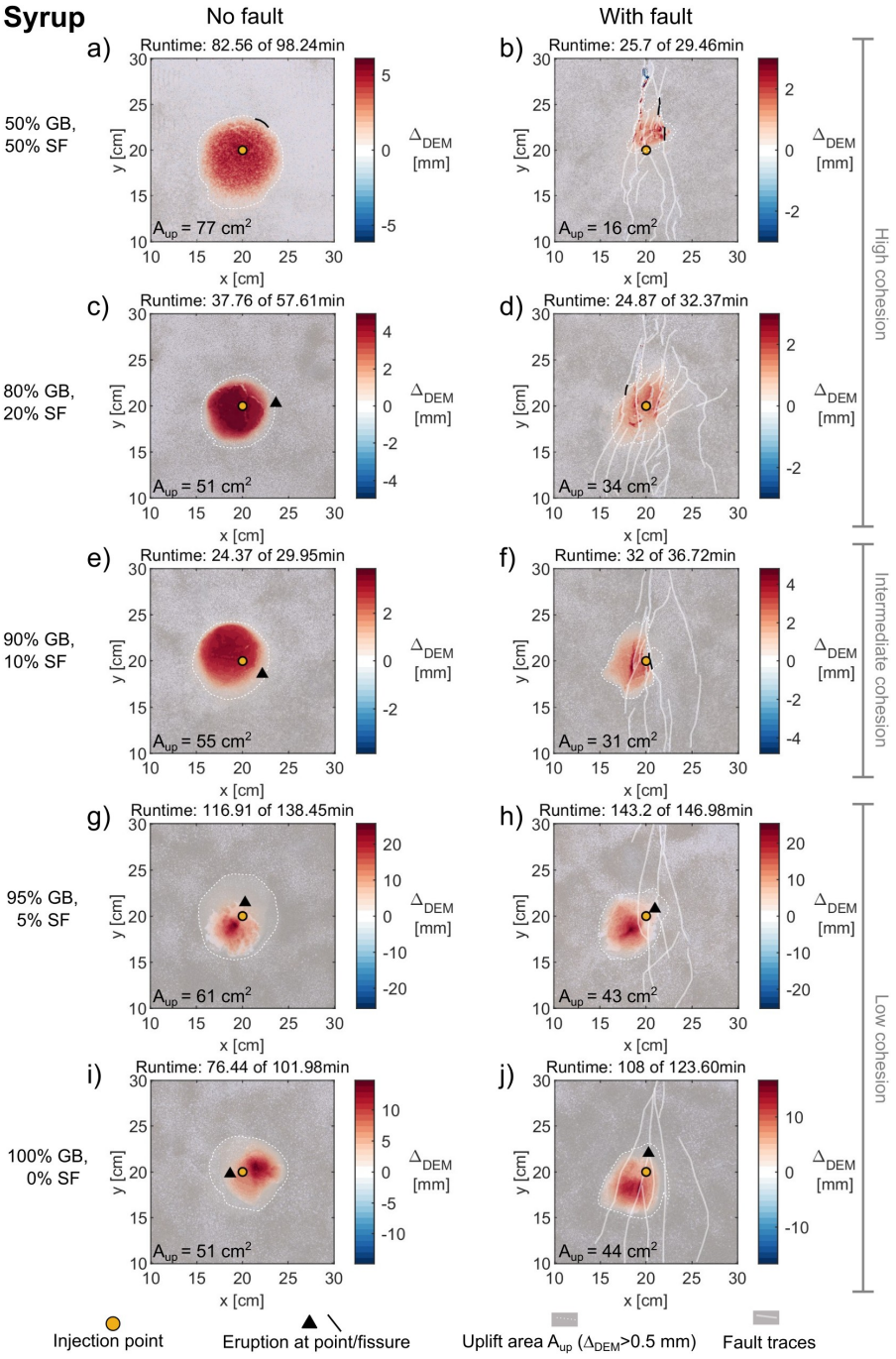

Figure 2. Vertical surface displacement of high-viscosity models (syrup) with varying cohesion and intact or pre-faulted model crust. Yellow circle marks injection point for each experiment. In the right column, white lines outline pre-intrusion fault traces.

366 cohesive model crust. In experiment SI50/50, syrup breached the surface along a fissure,

whereas in all other intact models the eruptions were subcircular in map view, i.e. point-sources.

Uplift was strictly confined between pre-existing fault segments in experiment SF50/50 (Figure 2b). In models SF80/20 and SF90/10, the confinement of deformation to fault-bounded areas was less pronounced but still visible (Figure 2d and f). Instead, the uplifted area became increasingly elliptical with the long axis sub-parallel to the direction of the fault. Although less pronounced than in Figure 2b, deformation gradients were still localized along fault traces. Deformation in low-cohesion materials (Figure 2h and j) resembled patterns observed in intact host rock, *i.e.* the uplift pattern was undisturbed by the presence of existing fault segments. In all faulted models, eruptions occurred along a fault segment. In high to intermediate cohesion experiments (SF50/50, SF80/20 and SF90/10), fissures formed, whereas in low-cohesion experiments the eruptions were point-sources.

The divergence maps for intrusions into intact high- and intermediate-cohesion host rock showed a network of lines with positive divergence (extension) across the uplifted area, surrounded by a narrow sub-circular band of negative divergence, indicating shortening (Figure 3a, c and e). The convergence largely coincided with the edge of the uplifted area, outlined by white dotted lines in Figure 3. Some extension lines appeared visually as tensile cracks in the uplift pattern (e.g., Figure 2c). The eventual eruption sites were located along the convergence bands. However, immediately before the fluid breached the surface, the shortening turned into extension. The divergence patterns in low-cohesion experiments showed fewer discrete lines, which could be identified as fractures (Figure 3g and i). Instead, internal deformation occurred more broadly distributed across the uplifted area. The faint band of convergence, however, was still visible, although the eruptions did not coincide with them.

Strong localization of deformation gradients along pre-existing faults was observed in experiment SF50/50 (Figure 3b), indicating that the block between the fault segments moved with little internal deformation and no new surface structures formed. In SF80/20 and SF90/10, the divergence was partially localized along fractures. Additionally, subtle shortening bands that do not align with pre-existing faults occurred (left of the faults, Figure 3d and f), which may indicate newly formed structures. In low-cohesion experiments, convergence bands formed subcircular structures that intersect fault segments without visible disturbance (Figure 3h and j), strongly resembling their intact host rock counterparts. However, extensional zones seemed to concentrate at the ridge of the uplifted zones aligned with fault segments.

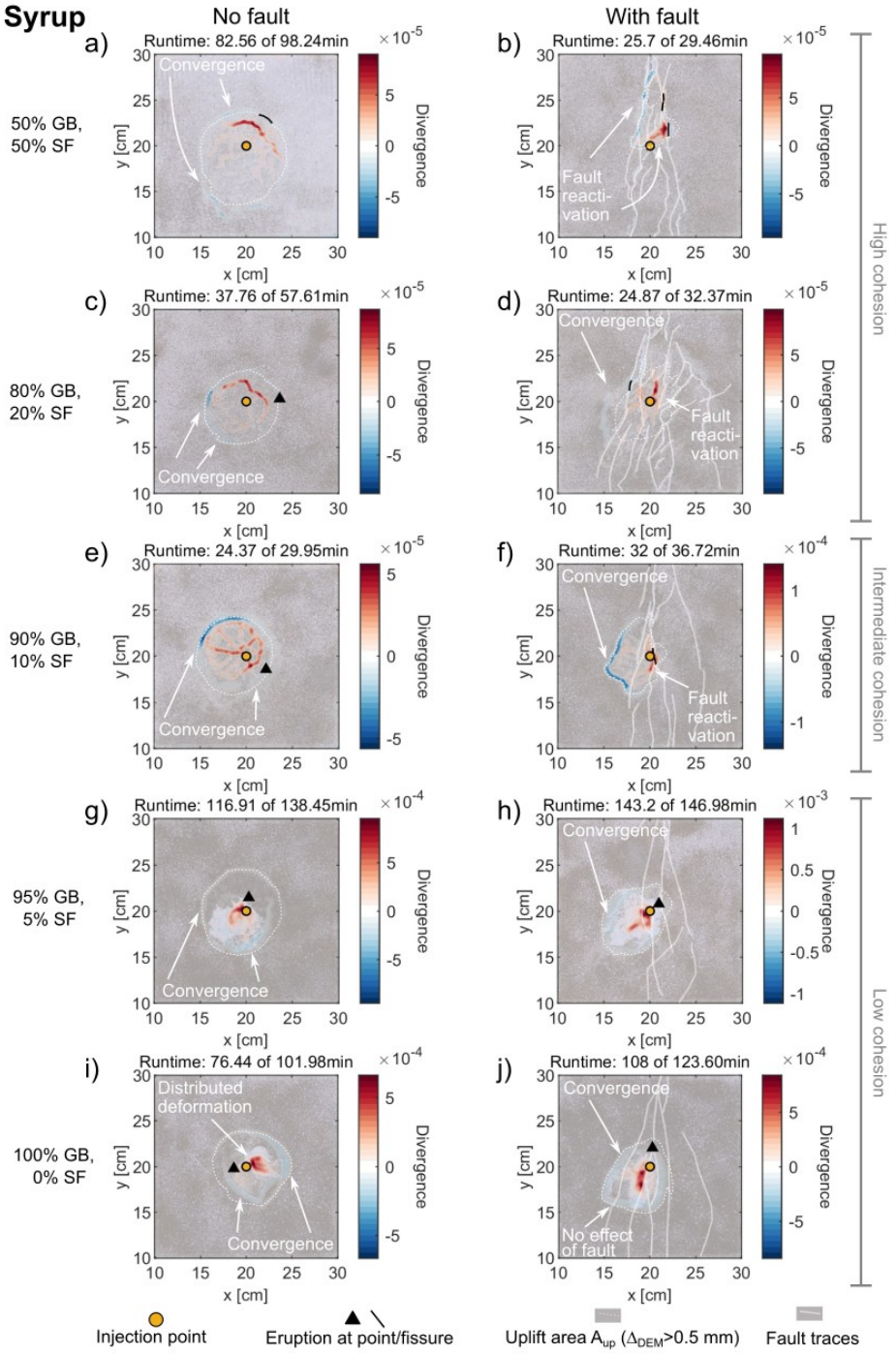

Figure 3. Horizontal divergence of high-viscosity models (syrup) with varying cohesion and intact or pre-faulted model crust. Yellow circle marks injection point for each experiment. In the right column, white lines outline pre-intrusion fault traces.

3.2 Low-viscosity Experiments (Oil)

3.2.1 Surface Deformation

Oil intrusions in intact high- to intermediate-cohesion models (OI50/50, OI80/20, OI90/10) caused smooth, sub-circular doming (Figure 4a, c, e). Uplift was symmetric around the injection point in the early stages of the experiments. The domes gradually became more asymmetrical with time (e.g., Figure 4c). Deformation in low-cohesion models became asymmetric early on (OI95/5 and OI100/0; Figure 4g and i). A low-amplitude outer zone and a higher-amplitude, inner zone developed on one side of the injection inlet. This high-uplift zone grew along clear faults in a trapdoor-like manner (Figure 4g,i). In high- and intermediate-cohesion models oil breached the model surface along one or two short fissures, whereas a localized point source formed in low-cohesion models (Figure 4).

The high-cohesion pre-faulted model OF50/50 showed gentle uplift to the left of the injection inlet (Figure 4b). Away from the faults, it resembled intact high-cohesion models. The dome was sharply bounded where it intersected a fault segment and little uplift was observed in faulted model crust. Similar, but less pronounced features occurred in experiment OF80/20 (Figure 4d). In model OF90/10, uplift was strongly localized around the eventual eruption site. A similar pattern was observed in OF95/5 (Figure 4h), although in this case, the eruption and associated localized uplift occurred farther away from the inlet. Additionally, a low-amplitude elongated uplifted zone was observed, the long axis of which was sub-parallel to the fault and did not seem to be bounded by the fault segments (Figure 4h). Experiment OF100/0 exhibited an elongated uplifted zone, the edges of which were not affected by pre-existing faults (Figure 4j). Additionally, the uplift amplitude in this experiment was much larger compared to the other pre-faulted oil experiments. Eruptions occurred along fissures in experiments OF50/50 and OF80/20 and at point sources for the other experiments (Figure 4). In all faulted experiments, the eruption occurred along or in prolongation of mapped pre-existing fault segments.

Divergence maps of high- and intermediate-cohesion experiments (OI50/50, OI80/20, OI90/10), highlighted a network of localized opening fractures across the uplifted areas, surrounded by subcircular shortening zones, along which eruptions occurred as fissures and that coincided with the edge of the uplifted areas (Figure 5a, c, e). In low-cohesion models (OI95/5, OI100/0), the divergence fields appeared less localized and the eruptions occurred between the growing extensional features and the surrounding convergence bands (Figure 5g, i).

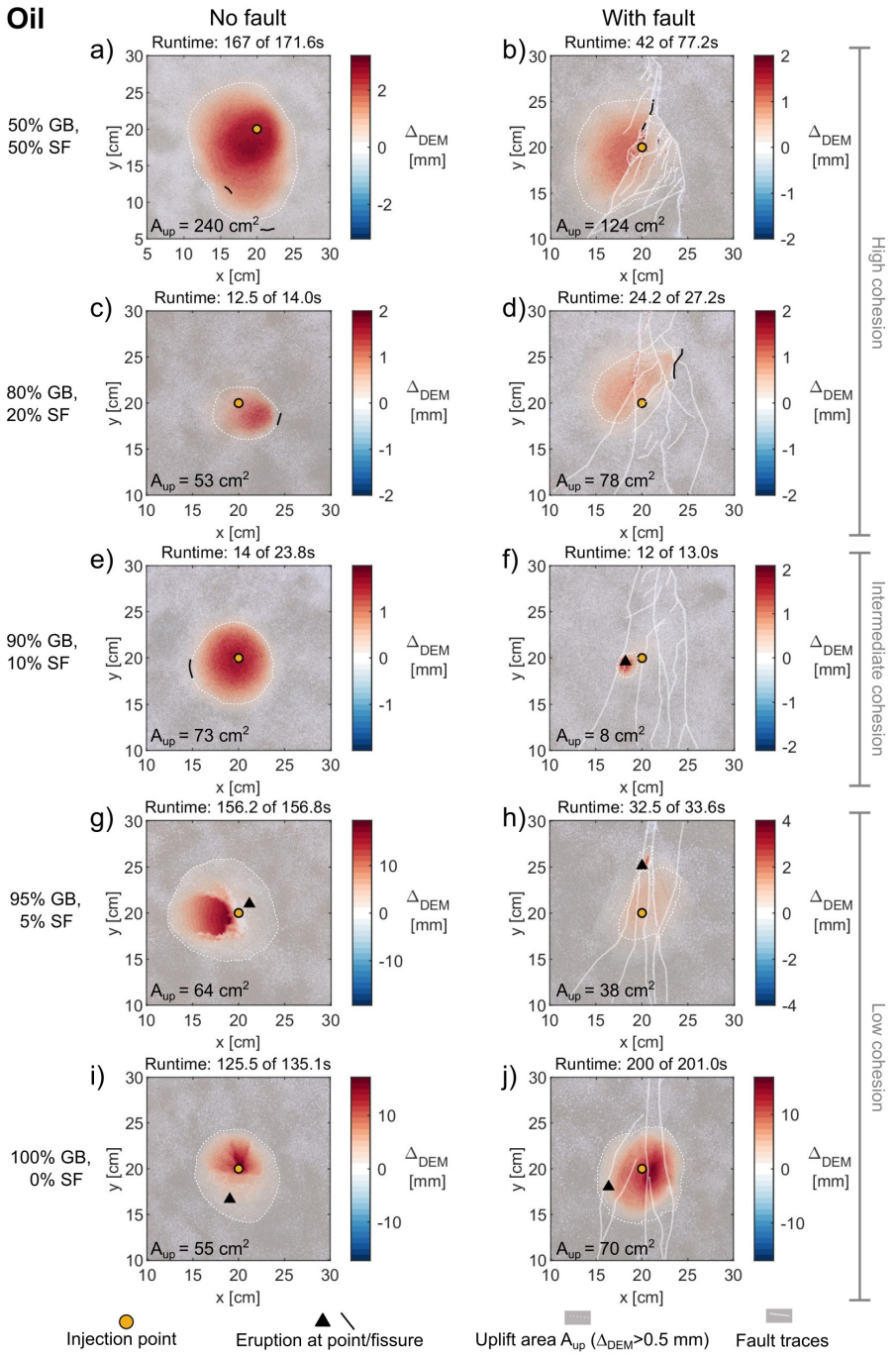

Figure 4. Vertical surface displacement of low-viscosity models (oil) with varying cohesion and intact or pre-faulted model crust. Yellow circle marks injection point for each experiment. In the right column, white lines outline pre-intrusion fault traces.

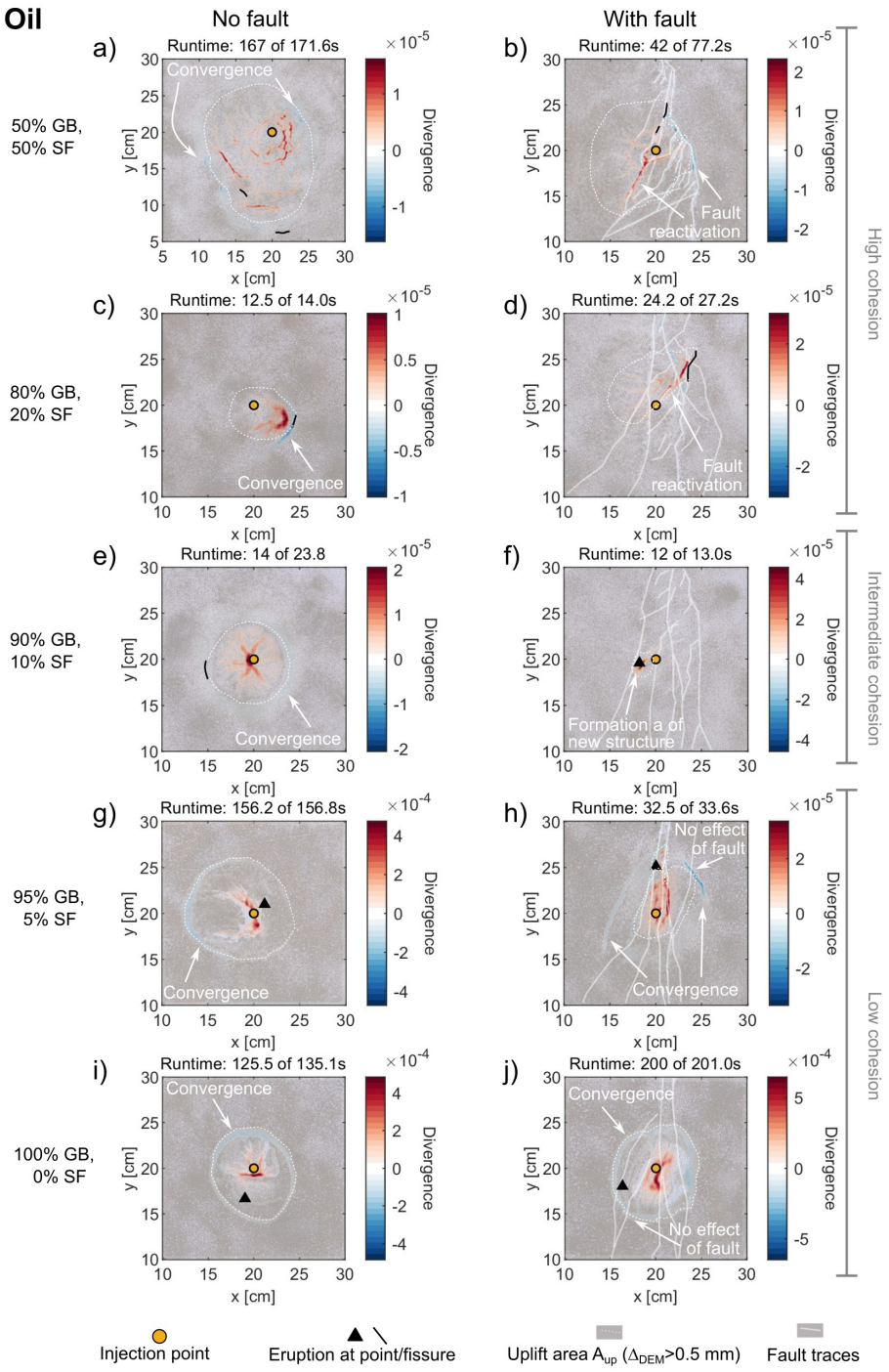

Figure 5. Horizontal divergence of low-viscosity models (oil) with varying cohesion and intact or pre-faulted model crust. Yellow circle marks injection point for each experiment. In the right column, white lines outline pre-intrusion fault traces.

In pre-faulted high-cohesion models (OF50/50 and OF80/20; Figure 5b and d), the divergence fields highlighted both extensional and compressional features that coincided with pre-existing fault segments. Although some newly formed features were observed outside of the fault zone in Figure 5b, the highest gradients followed pre-existing fault segments. In experiment OF90/10, a single short fracture accommodated the intrusion (Figure 5f). It is unclear whether this fracture is controlled by pre-existing faults. In the low-cohesion experiments (OF95/5, OF100/0) divergence patterns were diffuse (Figure 5h, j). Nevertheless, extensional features at the apex of the uplifted zones appeared parallel to the pre-existing faults, whereas the concentric compressional structures appeared along the edges of the uplift area, independent of pre-existing faults. Localized areas of compression closer to the uplift center in OF100/0 related to small "landslides", which occurred along the slopes of the uplifted dome.

3.2.2 Intrusion Geometries

Oil intrusions excavated from intact high and intermediate-cohesion experiments produced a saucer-shaped sill (OI50/50; Figure 6a) and partial cone sheets (OI80/20 and OI90/10; Figure 6c, e). Approximately ellipsoidal, low-aspect ratio intrusions i.e., with a thickness comparable to their length and height, formed in intact low-cohesion experiments. They connected to the surface through a thin conduit at their edge (OI95/5 and OI100/0; Figure 6g, i). The rounded structure only formed in the low-cohesion-part of the granular material, i.e. above the thin layer of more cohesive material at the base of the box.

Intrusion into pre-faulted, high-cohesion host rock (OF50/50) formed a saucer-shaped sill (Figure 6) underneath the left side of the uplift pattern in Figure 6b. Connected through a sharp, perpendicular transition to this, an additional, vertical sheet formed aligned with a fault segment, through which the oil reached the surface. The intrusion of OF80/20 (Figure 6d) propagated dominantly subvertically, although a small part propagated along the bottom of the box. Circa 2 cm above the inlet, the intrusion sharply transitioned into variably dipping, planar segments. Several of those segments reached the surface, resulting in a bent eruptive fissure (Figure 4d). The intrusion of OF90/10 (Figure 6f) formed a slightly thickened sheet with small lobes. Although it propagated approximately in a sub-vertical plane, it changed direction within this plane, resulting in a C-shaped geometry, which differed from other observed geometries. The intrusion of OF100/0 (Figure 6j) was a low-aspect ratio intrusion. It strongly resembled intrusions into intact low-cohesion experiments (Figure 6g, i), but was slightly elongated along the fault. Although the OF95/5 intrusion consisted of an inflated body at depth and a conduit connecting to the surface

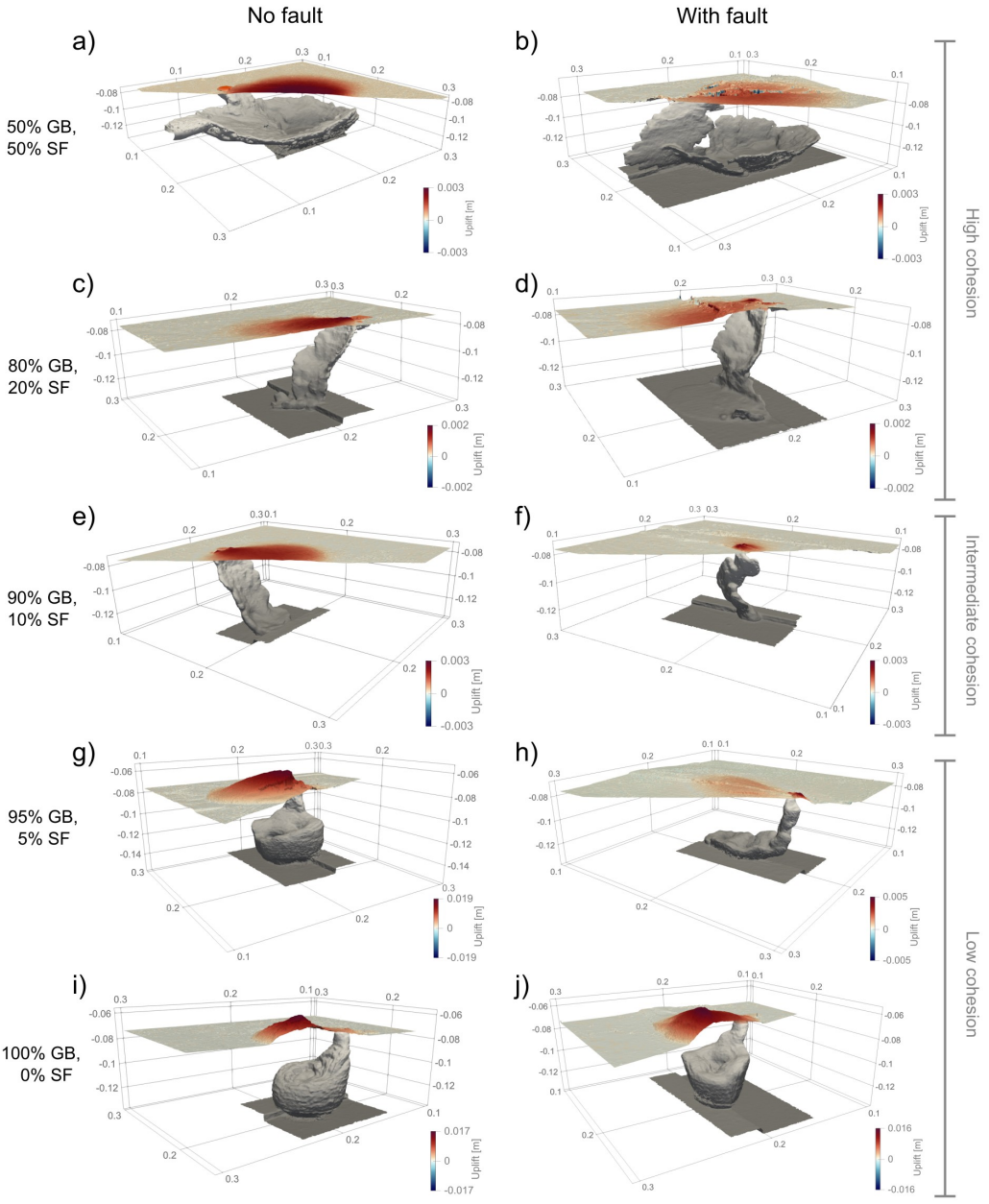

Figure 6. 3D models of solidified oil intrusions and uplift of the overlying surface. The step in the bottom plate marks the edge of the sliding plate and the strike of the fault zone.

(Figure 6h), the proportions differed from other low-cohesion experiments. The more massive part was small in volume, elongated along the fault and confined to the deepest parts of the model crust. The conduit was more pronounced with lobe-like structures similar to the OF90/10 intrusion.

The intrusion geometry of syrup experiments was not retrieved systematically. However, the observed surface deformation and locations of eruptive fissures/point sources closely resembled those observed in oil experiments. X-ray Computed Tomography (CT) scans of experiments with similar materials and experimental parameters to our syrup experiments were done by Poppe et al. (2019). They showed intrusion shapes and associated surface deformation similar to the sheet intrusions and low-aspect ratio intrusions observed in the oil–intrusions and to the surface deformation of syrup experiments in unfractured high- and low-cohesion analogue host rock, respectively. We furthermore found remains consistent with a low-aspect ratio intrusion from experiment SF100/0 (Supporting Figure S14). Based on these indications, we infer that the syrup intrusions in high- to intermediate-cohesion host rock (50/50-90/10) resulted in sheets, and the syrup injection into low-cohesion materials produced low-aspect ratio intrusions.

3.3 Data Correlation and Scaling

The maximum uplift and total uplifted volumes are greater in low-aspect ratio intrusion-producing, low-cohesion experiments than in high-cohesion experiments for both model magmas (Figure 7a, b). Among sheet intrusions, the uplifted volume decreases with decreasing cohesion and is greater in intact than in pre-faulted models (Figure 7b). The deformation in experiments OF90/10 and OF95/5, which produced intrusions fitting neither the sheet- nor low-aspect ratio geometry, fell closer to models that produced sheet intrusions.

Low-aspect ratio intrusions have a larger intrusive volume than sheet intrusions except for the intrusions in OI50/50 and SI50/50 (Figure 7c). While sheet intrusions in intact analogue host rock have a larger volume compared to faulted rock, the trend is notably reversed for low-aspect ratio intrusions. Differences between faulted and intact experiments are most pronounced for very high cohesion and to a lower degree for low cohesion. In between, the differences in terms of volume become very small with the exception of OI95/5 and OF95/5. OF90/10 and OF95/5 are closer to the volumes of sheet intrusions than to those of low-aspect ratio intrusions.

Systematically lower ratios of the uplifted to injected volume V_{up}/V_{in} as a function of the cohesion scaled to gravitational stresses ($\Pi_3 = C_i/(\rho_r g H)$) are observed in pre-faulted experiments compared to intact experiments, except for OI50/50 and OI100/0 (Figure 7d). The difference is more pronounced for sheet intrusions than for low-aspect ratio intrusions. OF90/10 has an exceptionally low ratio, which may be attributed to unusually low and localized surface deformation (Figure 7b). For both intact and pre-faulted experiments, the V_{up}/V_{in} ratio gets closer to one with decreasing cohesion.

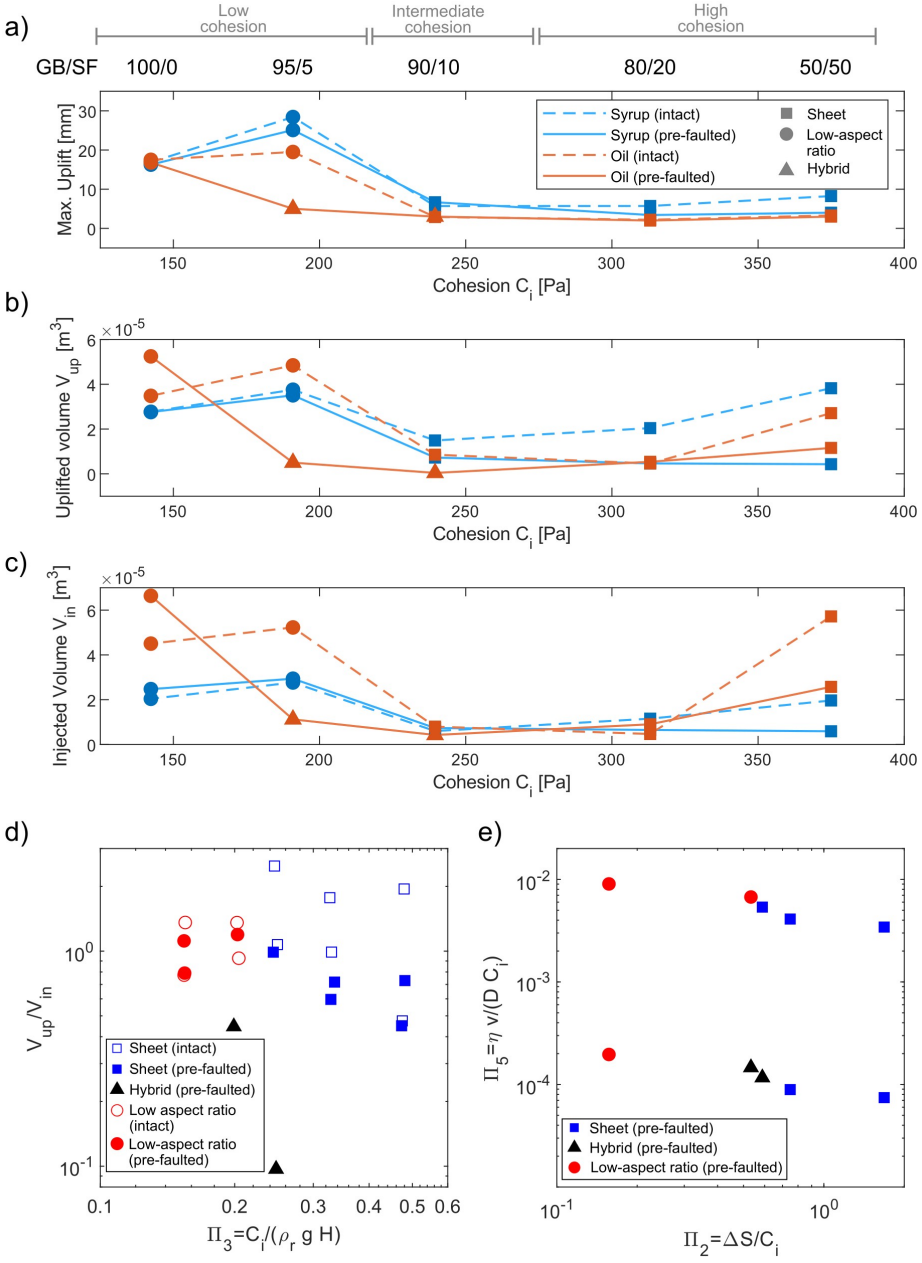

Figure 7. a) Maximum uplift, b) uplifted volume and c) injected volume at the last timestep before the onset of eruption for all experiments. d) Ratio of uplifted to injected volume as a function of Π_3. Dimensionless parameters Π_2 and Π_5 (Table 2). e) Dimensionless parameters Π_2 and Π_5 plotted against each other relating the viscous stresses in the fluid and the strength contrast of the analogue host rock, both scaled by the intact cohesion.

A physical phase diagram helps to constrain the conditions of formation of sheet versus low-aspect ratio intrusions depending on the viscous stress to cohesion ratio ($\Pi_5 = \eta v/(DC_i)$) and the strength contrast to cohesion ratio ($\Pi_2 = \Delta S/C_i$) (Figure 7e). Only pre-faulted experiments are shown here, since the strength contrast is not applicable for intact models. Low-aspect ratio intrusions formed in models with low Π_2 values, while sheet-intrusions formed in models with higher values of Π_2. Hybrid intrusions plot between the two other regimes, defining a transition between them. The transition between the low-aspect ratio intrusion and the sheet intrusion regimes appears to occur at similar values of Π_2 for varying values of Π_5 (Figure 7e), suggesting a weak effect of Π_5 on the transition between the two emplacement regimes.

4 Interpretation

4.1 Intrusions in Intact Host Rock

Intrusions into intact model crust resulted in two intrusion regimes. They differ from each other in terms of intrusion geometry, injected volume and amplitude and pattern of the corresponding surface deformation (Figures 2-6).

In high- to intermediate-cohesion host rock (50-90% GB), sheet intrusions formed, transitioning from saucer-shaped sills to partial cone sheets as the cohesion decreases (Figure 6). Narrow bands of convergence along the edges of the uplifted area may indicate shear damage zones. Eruptions occurring along them are consistent with emplacement dominated by tensile opening and propagation into these shear zones (Figure 8a, Schmiedel et al., 2019; Poppe et al., 2019).

Intrusions in low-cohesion models (95-100% GB) exhibit low-aspect ratio shapes (Figure 6). Localized surface deformation and diffuse divergence patterns suggest that the host rock fails across a wider area compared to higher cohesion experiments. The analogue host rock cannot sustain dilation and instead, fluid pushes the entire overburden upwards (Figure 8d, Schmiedel et al. (2019); Poppe et al. (2019)).

4.2 Effects of Faulting

The experimental data highlight complex, variable interactions between the model magma and faults, depending on the cohesion of the model crust. In the presence of a pre-existing fault, we observed two major emplacement regimes with distinct intrusion morphologies and surface deformation. Localized deformation gradients and abrupt changes in intrusion geometry indicate that intrusion emplacement is accommodated by fault reactivation in high-cohesion models (Figures 3b,d,f, 5b,d, 6b,d, 8b). Conversely, intrusion

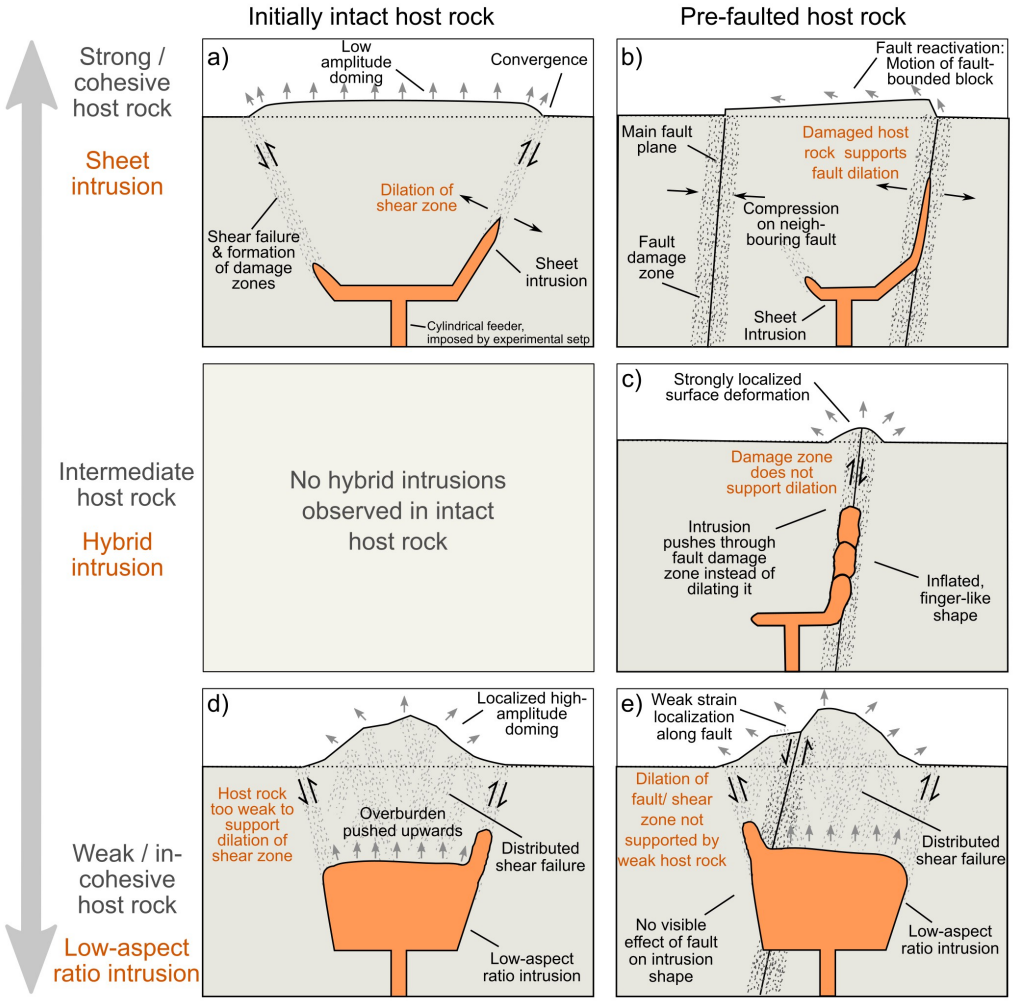

Figure 8. Conceptual model of intrusion regimes in strong, intermediate and weak host rock with and without fault. The lowest, vertical part of the depicted intrusions represents a circular feeder and is an imposed structure related to our experiments. Feeders to shallowly emplaced intrusions in nature may deviate from the geometry depicted here. The depicted intrusion regimes are assumed to be valid for both low- and high-viscosity intrusions. However, no hybrid intrusions were observed for high-viscosity fluids.

543 geometries appear largely unaffected by faults in low-cohesion models (Figures 3i,j, 5j,
544 8e). Here, newly formed structures accommodate the emplacement of low-aspect ratio
545 intrusions and the associated uplift of the overburden without indications of fluid prop-
546 agation along existing faults (Figures 3 and 5). The effects of the faults are slightly less

pronounced for high-viscosity intrusions compared to those of low analogue magma viscosity.

Lowered intrusive volumes of pre-faulted experiments in high-cohesion material compared to intact experiments indicate that faults facilitate faster fluid ascent towards the surface (Figure 7c). Conversely, greater intrusion volumes in low-cohesion experiments indicate that faults delay eruption onset in this case. This may relate to more efficient strain accommodation along faults compared to intact host rock, possibly due to differing frictional properties.

The presence of a fault led to hybrid intrusions at intermediate cohesion for low-viscosity fluids (OF90/10 and OF95/05). They formed dominantly in the plane of the fault, but exhibited elements of both sheet and low-aspect ratio intrusions. We interpret their lobate structure as indications that they propagated by pushing through the damaged host rock rather than dilating the fault plane, similar to the viscous-indenter mechanism (Abdelmalak et al., 2012; Guldstrand et al., 2017; Bertelsen et al., 2021, and Figure 8c). In the phase diagram in Figure 7e, OF90/10 and OF95/5 plot between the sheet- and low-aspect ratio intrusion fields. We infer that this mechanism mainly occurs when the host rock is close to the limit of being able to sustain sheet intrusions. This implies that somewhat specific conditions are required for such intrusions to form.

The values of the cohesion to gravitational stress ratio $\Pi_3 = C_i/(\rho g H)$ in the low-cohesion models are lower than 0.2 (Figure 7d), suggesting that cohesive forces are almost negligible at the scale of the models. This implies that cohesive forces are too low to sustain dilational structures such as tensile cracks, which is supported by the absence of tensile fractures at the surface. This suggests that the model crust needs to hold sufficient cohesion for the analogue magma to form sheets. Therefore, faults can control the formation of sheet intrusions only if cohesive forces allow dilational opening of the fault planes. When cohesive forces are too low, magma is emplaced as a low-aspect ratio intrusion instead.

Figure 7e shows that intrusion emplacement channeled through faults occurs only when $\Pi_2 > 0.5$, We therefore infer that fault-controlled emplacement occurs when the strength contrast between the fault and the surrounding model crust is significant, *i.e.* the strength of the fault is significantly lower than the strength of the surrounding model crust. In our models, Π_2 increases with increasing cohesion (Figure 7e), and thus fault-controlled intrusion emplacement is observed in high-cohesion models. In low cohesion models, even the intact material does not support dilation and we infer that the strength

contrast between faulted and intact materials is too low to localize the emplacement-related stresses.

Deforming granular materials experience dilation and decompaction prior to failure (e.g., Lohrmann et al., 2003; Panien et al., 2006). The ratio of $V_{up}/V_{in} \geq 1$ for intact experiments (Figure 7d) indicates that this decompaction occurs during the intrusion process. In pre-faulted experiments, decompaction may instead be associated with the formation of the strike-slip fault prior to the actual experiment and is likely localized to the fault zone (e.g., Holland et al., 2011; Ellingsen, 2020). We hypothesize that the subsequently intruding fluid can exploit and fill these areas, while possibly re-compacting neighbouring fault segments, resulting in the observed lowered V_{up}/V_{in}-ratio. The weakening of this effect at lower cohesion possibly relates to the materials' decreasing ability to sustain dilation, especially along planes (Panien et al., 2006; Abdelmalak et al., 2016; Ellingsen, 2020).

5 Discussion

5.1 Fluid Viscosity

There are no indications of hybrid intrusions having formed in any syrup experiments. High-viscosity intrusions often have a greater thickness than low-viscosity intrusions to accommodate the dissipation of mechanical work due to viscous flow (Wada, 1994; Schmiedel et al., 2019). High-viscosity magmas would therefore require relatively larger dilation. The smaller dilation required by low-viscosity intrusions may still be sustainable at a cohesion that cannot sustain higher-viscosity sheets anymore, which could explain why the transition to proper low-aspect ratio intrusions occurs at lower cohesion for the oil. Apart from this, surface deformation showed similar characteristics, indicating that the fluid viscosity and viscous stresses only weakly influences intrusion-fault interaction. The viscosity-estimate of ca. $2.2{\times}10^5 Pa\,s$ for the presumably fault-guided 2015 Fentale dike, Ethiopia (Temtime et al., 2020) is of a similar order of magnitude as the lower limit of viscosities represented by the syrup experiments of the present study ($\eta = 9 \times 10^5\ Pa\,s$). While our experiments suggested that higher viscosity liquids can be captured by fault segments in high-cohesion host rock in a similar manner to low-viscosity fluids, it should be noted that our findings do not apply to viscosities significantly higher than $10^7\ Pa\,s$.

5.2 Comparison to Experimental and Computational Studies

The surface deformation data and where applicable, geometry, of intrusions into intact, unfaulted experiments are consistent with results by Schmiedel et al. (2019) and Poppe et al. (2019). The systematic intrusion along fault segments in pre-faulted, high-cohesion models agrees well with the observations of previous models of intrusions into high-cohesion analogue host rock (Le Corvec et al., 2013; Galland et al., 2006, 2014). Conversely, the lack of observed propagation along fault segments in low-cohesion experiments is consistent with sand/silicone models by e.g., Corti et al. (2005). Overall, our findings agree well with previous laboratory experiments and can fill the gap between faulted high- and low-cohesion host rocks in a series of materials with physically consistent properties.

It is generally challenging to model the dynamic, three-dimensional propagation of sheet intrusions (e.g., Rivalta et al., 2015). However, analytical and numerical models of pre-faulted crust suggest that vertically propagating magma is more likely to be captured by steeper dipping faults (Ziv et al., 2000; Gaffney et al., 2007). Intrusion geometries in the present study that indicate capture by faults generally agree with this. The clearest example is likely experiment OF80/20 (Figure 6d), where the uppermost right segment of the intrusion dips steeper than the underlying segment. Comparison to mapped fault traces suggests that the intrusion may have followed one of the bounding fault segments at depth (segment to the right of the lower part of the eruptive fissure in Figure 4d) and was subsequently captured by a smaller segment within the fault zone with a presumably steeper dip. Gaffney et al. (2007) furthermore suggest that faults in weaker host rocks are expected to only capture intrusions in the very shallowest parts of the crust, if at all, which agrees with the observed lack of intrusion-fault interaction in low-cohesion experiments.

Rubin and Gillard (1998) investigated fault reactivation around propagating dikes. Their findings suggest that significant motion (corresponding in their case to seismicity between M1-M2) is unlikely to occur at large distances from the dike. While we did not record signals corresponding to seismicity, we observe spatially distributed fault reactivation, which is not limited to the direct vicinity of the propagating intrusions. It is unclear if this discrepancy relates to differences e.g., due to granular vs. dominantly elastic materials, to the more complex fault zone architecture in the experiments or to some sort of cascading effect of fault reactivation. This question may be relevant for extensively faulted areas prone to intrusions and could be a subject for future studies.

5.3 Geological and Geophysical Implications

Based on the presented experiments, intrusions into strong host rock are expected to propagate into existing fault segments upon intersection. However, based on field observations, only a fraction of dikes propagate along existing fractures (e.g., Gudmundsson, 1983; Pedicini et al., 2023; Greiner et al., 2023). In nature this may relate to the orientation of faults relative to the governing stress field (Stephens et al., 2018) or to a reduced strength contrast due to faults being inactive, healing or similar processes. Our findings may therefore be most meaningful in the context of active faults. They furthermore highlight the need to consider mechanical material properties in the context of magma-fault interaction in addition to tectonics.

In active volcanic settings, deviatoric stresses often fluctuate with time. At divergent plate boundaries, tectonic stress is relieved during rifting episodes (e.g., Buck et al., 2006; Wright et al., 2012). Our results can provide insights for intrusions occurring especially in the later phase of such events, when the majority of tectonic stress has been released as well as in areas with weak deviatoric stress fields. Our findings furthermore suggest that magma could generally reach the surface in significantly shorter time by following weaknesses compared to propagation through intact rock.

Surface deformation in our models was strongly affected by pre-existing faults resembling small-scale movements across an extensive fracture network during the 2019–2021 volcano-tectonic episode on the Reykjanes Peninsula, Iceland (Ducrocq et al., 2024). Such movements are rarely considered during geodetic inversions, where - if at all - only the main rift faults are considered or those which caused significant earthquakes (Wright et al., 2006; Calais et al., 2008; Ruch et al., 2016; Sigmundsson et al., 2022). Our models suggest that widespread fault reactivation may systematically reduce surface deformation, which could result in underestimation of deformation-derived estimates of intrusive volumes.

6 Conclusions

The effect of host rock cohesion and magma viscosity on intrusion-fault interaction in brittle plastic materials was studied with analogue models. We find that the host rock cohesion and, if present, the strength contrast between intact and faulted rock strongly control the emplacement mechanism, intrusion shape and surface deformation. In the presence of a pre-existing fault and absence of tectonic stresses, we observed three distinct types of intrusions:

1. Sheet intrusions form in strong host rock through dilation of existing weaknesses. Deformation is primarily accommodated by fault reactivation. Intruded volumes are low and fluid is efficiently transported through the crust.
2. Low-aspect ratio intrusions form in weak host rock through doming of the overburden, resulting in high amplitude surface deformation. This is accommodated by distributed shear failure of the roof, since the weak host rock cannot sustain dilation of existing weaknesses. The intrusion geometry is barely influenced by pre-existing faults, which, however, still affect strain accommodation.
3. Hybrid intrusions may form in intermediately-cohesive host rock, where emplacement takes place through the viscous indenter mechanism and is focused to the fault zone due to the strength contrast to intact host rock. Surface deformation is strongly localized.

In the range explored in this study, the analogue magma viscosity exerts a weak influence on intrusion-fault interaction compared to the cohesion. We find that low-viscosity fluids interact slightly more with pre-existing faults and can form sheet or hybrid intrusions in weaker host rock than high-viscosity fluids.

Our findings highlight the importance of constraining the crustal properties in volcanic areas, since they affect the emplacement mechanism of magmatic intrusions and help to assess the relevance of existing structures for volcanic activity. It is furthermore important to further investigate how our findings change in the context of tectonic stresses.

Open Research Section

Additional information on experimental procedures and the dimensional analysis can be found in the Supporting Information. The data presented in this article will be available at the following repositories: Raw data: Greiner et al. (2025a); Processed data: Greiner et al. (2025b); Data related to repeat experiments: Greiner et al. (2025c).

Acknowledgments
We thank the Nordic Volcanological Center and Uppsala University for funding S. Greiner's PhD position. X. Wen was supported by a grant from the China Scholarship Council (No. 201902505002). All experiments were carried out in the analogue laboratory of the NJORD center at the University of Oslo. We thank editor Alexandre Schubnel, the associate editor and reviewers Janine Kavanagh and Alessandro Tibaldi for helpful comments that improved the initial manuscript.

References

Abdelmalak, M., Bulois, C., Mourgues, R., Galland, O., Legland, J.-B., & Gruber, C. (2016). Description of new dry granular materials of variable cohesion and friction coefficient: Implications for laboratory modeling of the brittle crust. *Tectonophysics*, *684*, 39-51. Retrieved from `https://www.sciencedirect.com/science/article/pii/S0040195116001591` (Special Issue on GeoMod 2014 – Modelling in Geoscience) doi: https://doi.org/10.1016/j.tecto.2016.03.003

Abdelmalak, M., Mourgues, R., Galland, O., & Bureau, D. (2012). Fracture mode analysis and related surface deformation during dyke intrusion: Results from 2d experimental modelling. *Earth and Planetary Science Letters*, *359-360*, 93-105. Retrieved from `https://www.sciencedirect.com/science/article/pii/S0012821X12005675` doi: https://doi.org/10.1016/j.epsl.2012.10.008

Acocella, V., & Neri, M. (2009). Dike propagation in volcanic edifices: Overview and possible developments. *Tectonophysics*, *471*(1), 67-77. Retrieved from `https://www.sciencedirect.com/science/article/pii/S0040195108004745` (Understanding stress and deformation in active volcanoes) doi: https://doi.org/10.1016/j.tecto.2008.10.002

Arachchige, U., Cruden, A., & Weinberg, R. (2021). Laponite gels - visco-elasto-plastic analogues for geological laboratory modelling [Journal Article]. *Tectonophysics*, *805*, 228773. Retrieved from `https://www.sciencedirect.com/science/article/pii/S0040195121000573` doi: https://doi.org/10.1016/j.tecto.2021.228773

Barsotti, S., Parks, M. M., Pfeffer, M. A., Óladóttir, B. A., Barnie, T., Titos, M. M., ... Sigurdsson, E. M. (2023). The eruption in fagradalsfjall (2021, iceland): how the operational monitoring and the volcanic hazard assessment contributed to its safe access. *Natural Hazards*, *116*(3), 3063–3092. doi: https://doi.org/10.1007/s11069-022-05798-7

Bertelsen, H. S., Guldstrand, F., Sigmundsson, F., Pedersen, R., Mair, K., & Galland, O. (2021). Beyond elasticity: Are coulomb properties of the earth's crust important for volcano geodesy? *Journal of Volcanology and Geothermal Research*, *410*, 107153. Retrieved from `https://www.sciencedirect.com/science/article/pii/S0377027320305898` doi: https://doi.org/10.1016/j.jvolgeores.2020.107153

Bertelsen, H. S., Rogers, B., Galland, O., Dumazer, G., & Abbana Bennani, A. (2018). Laboratory modelling of coeval brittle and ductile deformation during magma emplacement into viscoelastic rocks [Journal Article]. *Frontiers in*

Earth Science, *6*. doi: https://doi.org/10.3389/feart.2018.00199

Bodet, L., Jacob, X., Tournat, V., Mourgues, R., & Gusev, V. (2010). Elasticity profile of an unconsolidated granular medium inferred from guided waves: Toward acoustic monitoring of analogue models. *Tectonophysics*, *496*(1), 99-104. Retrieved from `https://www.sciencedirect.com/science/article/pii/S0040195110004269` doi: https://doi.org/10.1016/j.tecto.2010.10.004

Breitkreuz, C., & Rocchi, S. (2018). *Physical geology of shallow magmatic systems — dykes, sills and laccoliths* [Edited Book]. Springer Berlin Heidelberg. doi: https://doi.org/10.1007/978-3-319-14084-1

Buck, W. R., Einarsson, P., & Brandsdóttir, B. (2006). Tectonic stress and magma chamber size as controls on dike propagation: Constraints from the 1975–1984 krafla rifting episode. *Journal of Geophysical Research: Solid Earth*, *111*(B12). Retrieved from `https://agupubs.onlinelibrary.wiley.com/doi/abs/10.1029/2005JB003879` doi: https://doi.org/10.1029/2005JB003879

Buckingham, E. (1914). On physically similar systems; illustrations of the use of dimensional equations. *Phys. Rev.*, *4*, 345–376. Retrieved from `https://link.aps.org/doi/10.1103/PhysRev.4.345` doi: 10.1103/PhysRev.4.345

Burchardt, S. (2018). *Volcanic and igneous plumbing systems: Understanding magma transport, storage, and evolution in the earth's crust*. Elsevier.

Burchardt, S., Mattsson, T., Palma, J. O., Galland, O., Almqvist, B., Mair, K., ... Sun, Y. (2019). Progressive growth of the cerro bayo cryptodome, chachahuén volcano, argentina—implications for viscous magma emplacement. *Journal of Geophysical Research: Solid Earth*, *124*(8), 7934-7961. Retrieved from `https://agupubs.onlinelibrary.wiley.com/doi/abs/10.1029/2019JB017543` doi: https://doi.org/10.1029/2019JB017543

Burchardt, S., Tanner, D., & Krumbholz, M. (2012, 01). The slaufrudalur pluton, southeast iceland — an example of shallow magma emplacement by coupled cauldron subsidence and magmatic stoping. *GSA Bulletin*, *124*(1-2), 213-227. Retrieved from `https://doi.org/10.1130/B30430.1` doi: 10.1130/B30430.1

Burchardt, S., Tanner, D. C., & Krumbholz, M. (2010). Mode of emplacement of the slaufrudalur pluton, southeast iceland inferred from three-dimensional gps mapping and model building. *Tectonophysics*, *480*(1), 232-240. Retrieved from `https://www.sciencedirect.com/science/article/pii/S0040195109005800` doi: https://doi.org/10.1016/j.tecto.2009.10.010

Caine, J. S., Evans, J. P., & Forster, C. B. (1996, 11). Fault zone architecture and permeability structure. *Geology*, *24*(11), 1025-1028. Retrieved from

https://doi.org/10.1130/0091-7613(1996)024<1025:FZAAPS>2.3.CO;2
doi: 10.1130/0091-7613(1996)024⟨1025:FZAAPS⟩2.3.CO;2

Calais, E., d'Oreye, N., Albaric, J., Deschamps, A., Delvaux, D., Déverchère, J., ... Wauthier, C. (2008). Strain accommodation by slow slip and dyking in a youthful continental rift, east africa [Journal Article]. *Nature*, *456*(7223), 783-787. Retrieved from https://doi.org/10.1038/nature07478 doi: 10.1038/nature07478

Caricchi, L., Simpson, G., & Schaltegger, U. (2014). Zircons reveal magma fluxes in the earth/'s crust [Journal Article]. *Nature*, *511*(7510), 457-461. Retrieved from http://dx.doi.org/10.1038/nature13532 doi: 10.1038/nature13532http://www.nature.com/nature/journal/v511/n7510/abs/nature13532.html#supplementary-information

Carpenter, B., Saffer, D., & Marone, C. (2012, 08). Frictional properties and sliding stability of the San Andreas fault from deep drill core. *Geology*, *40*(8), 759-762. Retrieved from https://doi.org/10.1130/G33007.1 doi: 10.1130/G33007.1

Castro, J. M., Cordonnier, B., Schipper, C. I., Tuffen, H., Baumann, T. S., & Feisel, Y. (2016). Rapid laccolith intrusion driven by explosive volcanic eruption [Journal Article]. *Nature Communications*, *7*(1), 13585. Retrieved from https://doi.org/10.1038/ncomms13585 doi: 10.1038/ncomms13585

Chalk, C. M., & Kavanagh, J. L. (2024, 03). Up, down, and round again: The circulating flow dynamics of flux-driven fractures. *Physics of Fluids*, *36*(3), 036622. Retrieved from https://doi.org/10.1063/5.0187217 doi: 10.1063/5.0187217

Clemens, J., & Mawer, C. (1992). Granitic magma transport by fracture propagation. *Tectonophysics*, *204*(3), 339-360. Retrieved from https://www.sciencedirect.com/science/article/pii/004019519290316X doi: https://doi.org/10.1016/0040-1951(92)90316-X

Corti, G., Moratti, G., & Sani, F. (2005). Relations between surface faulting and granite intrusions in analogue models of strike-slip deformation. *Journal of Structural Geology*, *27*(9), 1547-1562. Retrieved from https://www.sciencedirect.com/science/article/pii/S0191814105000921 doi: https://doi.org/10.1016/j.jsg.2005.05.011

Corti, G., Sani, F., Philippon, M., Sokoutis, D., Willingshofer, E., & Molin, P. (2013). Quaternary volcano-tectonic activity in the soddo region, western margin of the southern main ethiopian rift. *Tectonics*, *32*(4), 861-879. Retrieved from https://agupubs.onlinelibrary.wiley.com/doi/abs/

10.1002/tect.20052 doi: https://doi.org/10.1002/tect.20052

Cruden, A., & Weinberg, R. (2018). Chapter 2 - mechanisms of magma transport and storage in the lower and middle crust—magma segregation, ascent and emplacement. In S. Burchardt (Ed.), *Volcanic and igneous plumbing systems* (p. 13-53). Elsevier. Retrieved from https://www.sciencedirect.com/science/article/pii/B9780128097496000029 doi: https://doi.org/10.1016/B978-0-12-809749-6.00002-9

de Saint Blanquat, M., Horsman, E., Habert, G., Morgan, S. S., Vanderhaeghe, O., Law, R., & Tikoff, B. (2011). Multiscale magmatic cyclicity, duration of pluton construction, and the paradoxical relationship between tectonism and plutonism in continental arcs [Journal Article]. *Tectonophysics*, *500*(1), 20-33. Retrieved from https://www.sciencedirect.com/science/article/pii/S0040195109006970 doi: https://doi.org/10.1016/j.tecto.2009.12.009

de Silva, S. L., Self, S., Francis, P. W., Drake, R. E., & Carlos, R. R. (1994). Effusive silicic volcanism in the central andes: The chao dacite and other young lavas of the altiplano-puna volcanic complex. *Journal of Geophysical Research: Solid Earth*, *99*(B9), 17805-17825. Retrieved from https://agupubs.onlinelibrary.wiley.com/doi/abs/10.1029/94JB00652 doi: https://doi.org/10.1029/94JB00652

Delaney, P. T., Pollard, D. D., Ziony, J. I., & McKee, E. H. (1986). Field relations between dikes and joints: Emplacement processes and paleostress analysis. *Journal of Geophysical Research: Solid Earth*, *91*(B5), 4920-4938. Retrieved from https://agupubs.onlinelibrary.wiley.com/doi/abs/10.1029/JB091iB05p04920 doi: https://doi.org/10.1029/JB091iB05p04920

Donnadieu, F., & Merle, O. (2001). Geometrical constraints of the 1980 mount st. helens intrusion from analogue models [Journal Article]. *Geophysical Research Letters*, *28*(4), 639-642. Retrieved from http://dx.doi.org/10.1029/2000GL011869 doi: 10.1029/2000gl011869

Drymoni, K., Browning, J., & Gudmundsson, A. (2021). Volcanotectonic interactions between inclined sheets, dykes, and faults at the santorini volcano, greece. *Journal of Volcanology and Geothermal Research*, *416*, 107294. Retrieved from https://www.sciencedirect.com/science/article/pii/S0377027321001232 doi: https://doi.org/10.1016/j.jvolgeores.2021.107294

Ducrocq, C., Árnadóttir, T., Einarsson, P., Jónsson, S., Drouin, V., Geirsson, H., & Hjartardóttir, Á. R. (2024). Widespread fracture movements during a volcano-tectonic unrest: the reykjanes peninsula, iceland, from 2019–2021 terrasar-x interferometry. *Bulletin of Volcanology*, *86*(2), 14. doi:

https://doi.org/10.1007/s00445-023-01699-0

Ellingsen, T. L. (2020). *Laboratory modeling of the initiation of strike-slip faulting* (Master's thesis, Department of Geosciences, University of Oslo). Retrieved from `http://urn.nb.no/URN:NBN:no-83139`

Fialko, Y. A., & Rubin, A. M. (1999). What controls the along-strike slopes of volcanic rift zones? [Journal Article]. *Journal of Geophysical Research*, *104*(B9), 20007-20020. Retrieved from `http://www.sciencedirect.com/science/article/B6WS6-407H5KY-458/2/013ddb0f115596b70c0093b523656a9f`

Gaffney, E. S., Damjanac, B., & Valentine, G. A. (2007). Localization of volcanic activity: 2. effects of pre-existing structure. *Earth and Planetary Science Letters*, *263*(3), 323-338. Retrieved from `https://www.sciencedirect.com/science/article/pii/S0012821X07005614` doi: https://doi.org/10.1016/j.epsl.2007.09.002

Galland, O. (2012). Experimental modelling of ground deformation associated with shallow magma intrusions. *Earth and Planetary Science Letters*, *317-318*, 145-156. Retrieved from `https://www.sciencedirect.com/science/article/pii/S0012821X11006121` doi: https://doi.org/10.1016/j.epsl.2011.10.017

Galland, O., Bertelsen, H. S., Guldstrand, F., Girod, L., Johannessen, R. F., Bjugger, F., ... Mair, K. (2016). Application of open-source photogrammetric software micmac for monitoring surface deformation in laboratory models. *Journal of Geophysical Research: Solid Earth*, *121*(4), 2852-2872. Retrieved from `https://agupubs.onlinelibrary.wiley.com/doi/abs/10.1002/2015JB012564` doi: https://doi.org/10.1002/2015JB012564

Galland, O., Burchardt, S., Hallot, E., Mourgues, R., & Bulois, C. (2014). Dynamics of dikes versus cone sheets in volcanic systems. *Journal of Geophysical Research: Solid Earth*, *119*(8), 6178-6192. Retrieved from `https://agupubs.onlinelibrary.wiley.com/doi/abs/10.1002/2014JB011059` doi: https://doi.org/10.1002/2014JB011059

Galland, O., Cobbold, P. R., Hallot, E., de Bremond d'Ars, J., & Delavaud, G. (2006). Use of vegetable oil and silica powder for scale modelling of magmatic intrusion in a deforming brittle crust. *Earth and Planetary Science Letters*, *243*(3), 786-804. Retrieved from `https://www.sciencedirect.com/science/article/pii/S0012821X06000276` doi: https://doi.org/10.1016/j.epsl.2006.01.014

Galland, O., Girod, L., Greiner, S., Souloumiac, P., Guldstrand, F., Bertelsen, H., & Yagupski, D. (2024). Digitising sandbox experiments using open-source structure-from-motion/photogrammetry/digital image correlation package

micmac.
doi: https://doi.org/10.31223/X5QD7Q

Galland, O., Holohan, E., Van Wyk de Vries, B., & Burchardt, S. (2018). Laboratory modelling of volcano plumbing systems: a review. *Physical Geology of Shallow Magmatic Systems: Dykes, Sills and Laccoliths*, 147–214.

Galland, O., Spacapan, J. B., Rabbel, O., Mair, K., Soto, F. G., Eiken, T., ... Leanza, H. A. (2019). Structure, emplacement mechanism and magma-flow significance of igneous fingers – implications for sill emplacement in sedimentary basins. *Journal of Structural Geology*, *124*, 120-135. Retrieved from `https://www.sciencedirect.com/science/article/pii/S0191814118305121` doi: https://doi.org/10.1016/j.jsg.2019.04.013

Gibbings, J. C. (2011). *Dimensional analysis*. Springer Science & Business Media. doi: https://doi.org/10.1007/978-1-84996-317-6

Glazner, A. F., Bartley, J. M., Coleman, D. S., Gray, W., & Taylor, R. Z. (2004). Are plutons assembled over millions of years by amalgamation from small magma chambers? *GSA today*, *14*(5-Apr), 4–11. doi: https://doi.org/10.17615/nspy-zk53

Gonnermann, H. M. (2015). Magma fragmentation. *Annual Review of Earth and Planetary Sciences*, *43*(1), 431-458. Retrieved from `https://doi.org/10.1146/annurev-earth-060614-105206` doi: 10.1146/annurev-earth-060614-105206

Greiner, S. H. M., Burchardt, S., Sigmundsson, F., Óskarsson, B. V., Galland, O., Geirsson, H., & Rhodes, E. (2023). Interaction between propagating basaltic dikes and pre-existing fractures: A case study in hyaloclastite from dyrfjöll, iceland. *Journal of Volcanology and Geothermal Research*, *442*, 107891. Retrieved from `https://www.sciencedirect.com/science/article/pii/S0377027323001488` doi: https://doi.org/10.1016/j.jvolgeores.2023.107891

Greiner, S. H. M., Galland, O., Sigmundsson, F., Burchardt, S., Geirsson, H., Pedersen, R., & Wen, X. (2025a). *Source data (unprocessed) for "The influence of variable host rock cohesion and magma viscosity on intrusion-fault interaction: Insights from laboratory models"*. Zenodo. Retrieved from `https://doi.org/10.5281/zenodo.14930127` (Data set) doi: 10.5281/zenodo.14930127

Greiner, S. H. M., Galland, O., Sigmundsson, F., Burchardt, S., Geirsson, H., Pedersen, R., & Wen, X. (2025b). *Processed data for "The influence of variable host rock cohesion and magma viscosity on intrusion-fault interaction: Insights from laboratory models"*. Zenodo. Retrieved from `https://doi.org/10.5281/`

zenodo.14935450 (Data set) doi: 10.5281/zenodo.14935450

Greiner, S. H. M., Galland, O., Sigmundsson, F., Burchardt, S., Geirsson, H., Pedersen, R., & Wen, X. (2025c). *Data of repeat experiments for "The influence of variable host rock cohesion and magma viscosity on intrusion-fault interaction: Insights from laboratory models".* Zenodo. Retrieved from https://doi.org/10.5281/zenodo.14937427 (Data set) doi: 10.5281/zenodo.14937427

Grocott, J., Arévalo, C., Welkner, D., & Cruden, A. (2009). Fault-assisted vertical pluton growth: Coastal cordillera, north chilean andes. *Journal of the Geological Society*, *166*(2), 295-301. Retrieved from https://www.lyellcollection.org/doi/abs/10.1144/0016-76492007-165 doi: 10.1144/0016-76492007-165

Gudmundsson, A. (1983). Form and dimensions of dykes in eastern iceland. *Tectonophysics*, *95*(3), 295-307. Retrieved from https://www.sciencedirect.com/science/article/pii/0040195183900744 doi: https://doi.org/10.1016/0040-1951(83)90074-4

Guldstrand, F., Burchardt, S., Hallot, E., & Galland, O. (2017). Dynamics of surface deformation induced by dikes and cone sheets in a cohesive coulomb brittle crust. *Journal of Geophysical Research: Solid Earth*, *122*(10), 8511-8524. Retrieved from https://agupubs.onlinelibrary.wiley.com/doi/abs/10.1002/2017JB014346 doi: https://doi.org/10.1002/2017JB014346

Heap, M. J., & Violay, M. E. (2021). The mechanical behaviour and failure modes of volcanic rocks: a review. *Bulletin of Volcanology*, *83*(5), 33. doi: https://doi.org/10.1007/s00445-021-01447-2

Hjartardóttir, Á. R., Dürig, T., Parks, M., Drouin, V., Eyjólfsson, V., Reynolds, H., ... Pedersen, G. B. M. (2023). Pre-existing fractures and eruptive vent openings during the 2021 fagradalsfjall eruption, iceland. *Bulletin of Volcanology*, *85*(10), 56. doi: https://doi.org/10.1007/s00445-023-01670-z

Holland, M., van Gent, H., Bazalgette, L., Yassir, N., Hoogerduijn Strating, E. H., & Urai, J. L. (2011). Evolution of dilatant fracture networks in a normal fault — evidence from 4d model experiments. *Earth and Planetary Science Letters*, *304*(3), 399-406. Retrieved from https://www.sciencedirect.com/science/article/pii/S0012821X11000884 doi: https://doi.org/10.1016/j.epsl.2011.02.017

Hubbert, M. K. (1937, 10). Theory of scale models as applied to the study of geologic structures. *GSA Bulletin*, *48*(10), 1459-1520. Retrieved from https://doi.org/10.1130/GSAB-48-1459 doi: 10.1130/GSAB-48-1459

Ikari, M. J., Kameda, J., Saffer, D. M., & Kopf, A. J. (2015). Strength characteristics of japan trench borehole samples in the high-slip region of the 2011 tohoku-oki earthquake. *Earth and Planetary Science Letters*, *412*, 35-41. Retrieved from https://www.sciencedirect.com/science/article/pii/S0012821X14007675 doi: https://doi.org/10.1016/j.epsl.2014.12.014

Jenness, M. H., & Clifton, A. E. (2009). Controls on the geometry of a holocene crater row: a field study from southwest iceland. *Bulletin of volcanology*, *71*, 715–728. doi: https://doi.org/10.1007/s00445-009-0267-9

Jolly, R. J. H., & Sanderson, D. J. (1997). A mohr circle construction for the opening of a pre-existing fracture. *Journal of Structural Geology*, *19*(6), 887-892. Retrieved from https://www.sciencedirect.com/science/article/pii/S019181419700014X doi: https://doi.org/10.1016/S0191-8141(97)00014-X

Kalakay, T. J., John, B. E., & Lageson, D. R. (2001). Fault-controlled pluton emplacement in the sevier fold-and-thrust belt of southwest montana, usa. *Journal of Structural Geology*, *23*(6), 1151-1165. Retrieved from https://www.sciencedirect.com/science/article/pii/S0191814100001826 doi: https://doi.org/10.1016/S0191-8141(00)00182-6

Kavanagh, J. L., Boutelier, D., & Cruden, A. R. (2015). The mechanics of sill inception, propagation and growth: Experimental evidence for rapid reduction in magmatic overpressure. *Earth and Planetary Science Letters*, *421*, 117-128. Retrieved from https://www.sciencedirect.com/science/article/pii/S0012821X15001879 doi: https://doi.org/10.1016/j.epsl.2015.03.038

Kavanagh, J. L., Engwell, S. L., & Martin, S. A. (2018). A review of laboratory and numerical modelling in volcanology. *Solid Earth*, *9*(2), 531–571. Retrieved from https://se.copernicus.org/articles/9/531/2018/ doi: 10.5194/se-9-531-2018

Kavanagh, J. L., Rogers, B. D., Boutelier, D., & Cruden, A. R. (2017). Controls on sill and dyke-sill hybrid geometry and propagation in the crust: The role of fracture toughness. *Tectonophysics*, *698*, 109-120. Retrieved from https://www.sciencedirect.com/science/article/pii/S0040195116306412 doi: https://doi.org/10.1016/j.tecto.2016.12.027

Kervyn, M., Ernst, G. G. J., van Wyk de Vries, B., Mathieu, L., & Jacobs, P. (2009). Volcano load control on dyke propagation and vent distribution: Insights from analogue modeling [Journal Article]. *Journal of Geophysical Research*, *114*(B3), B03401. Retrieved from http://dx.doi.org/10.1029/2008JB005653 doi: 10.1029/2008jb005653

Kjøll, H. J., Galland, O., Labrousse, L., & Andersen, T. B. (2019). Emplacement mechanisms of a dyke swarm across the brittle-ductile transition and the geodynamic implications for magma-rich margins. *Earth and Planetary Science Letters*, *518*, 223-235. Retrieved from https://www.sciencedirect.com/science/article/pii/S0012821X19302195 doi: https://doi.org/10.1016/j.epsl.2019.04.016

Le Corvec, N., Menand, T., & Lindsay, J. (2013). Interaction of ascending magma with pre-existing crustal fractures in monogenetic basaltic volcanism: an experimental approach. *Journal of Geophysical Research: Solid Earth*, *118*(3), 968-984. Retrieved from https://agupubs.onlinelibrary.wiley.com/doi/abs/10.1002/jgrb.50142 doi: https://doi.org/10.1002/jgrb.50142

Le Guerroué, E., & Cobbold, P. (2006). Influence of erosion and sedimentation on strike-slip fault systems: insights from analogue models [Journal Article]. *Journal of Structural Geology*, *28*(3), 421-430. Retrieved from http://www.sciencedirect.com/science/article/B6V9D-4J90VSP-1/2/1a4b13bf1e067c8c4a720c374a5851b4

Lesher, C. E., & Spera, F. J. (2015). Chapter 5 - thermodynamic and transport properties of silicate melts and magma. In H. Sigurdsson (Ed.), *The encyclopedia of volcanoes (second edition)* (Second Edition ed., p. 113-141). Amsterdam: Academic Press. Retrieved from https://www.sciencedirect.com/science/article/pii/B9780123859389000055 doi: https://doi.org/10.1016/B978-0-12-385938-9.00005-5

Leuthold, J., Müntener, O., Baumgartner, L. P., Putlitz, B., Ovtcharova, M., & Schaltegger, U. (2012). Time resolved construction of a bimodal laccolith (torres del paine, patagonia). *Earth and Planetary Science Letters*, *325-326*, 85-92. Retrieved from https://www.sciencedirect.com/science/article/pii/S0012821X12000593 doi: https://doi.org/10.1016/j.epsl.2012.01.032

Lohrmann, J., Kukowski, N., Adam, J., & Oncken, O. (2003). The impact of analogue material properties on the geometry, kinematics, and dynamics of convergent sand wedges. *Journal of Structural Geology*, *25*(10), 1691-1711. Retrieved from https://www.sciencedirect.com/science/article/pii/S0191814103000051 doi: https://doi.org/10.1016/S0191-8141(03)00005-1

Maccaferri, F., Rivalta, E., Passarelli, L., & Aoki, Y. (2016). On the mechanisms governing dike arrest: Insight from the 2000 miyakejima dike injection. *Earth and Planetary Science Letters*, *434*, 64-74. Retrieved from https://www.sciencedirect.com/science/article/pii/S0012821X15007281 doi: https://doi.org/10.1016/j.epsl.2015.11.024

Magee, C., Jackson, C. A.-L., & Schofield, N. (2013). The influence of normal fault geometry on igneous sill emplacement and morphology [Journal Article]. *Geology*, *41*(4), 407-410. Retrieved from http://geology.gsapubs.org/content/41/4/407.abstract doi: 10.1130/g33824.1

Mathieu, L., Burchardt, S., Troll, V. R., Krumbholz, M., & Delcamp, A. (2015). Geological constraints on the dynamic emplacement of cone-sheets – the ardnamurchan cone-sheet swarm, nw scotland. *Journal of Structural Geology*, *80*, 133-141. Retrieved from https://www.sciencedirect.com/science/article/pii/S0191814115300304 doi: https://doi.org/10.1016/j.jsg.2015.08.012

Mathieu, L., & van Wyk de Vries, B. (2011). The impact of strike-slip, transtensional and transpressional fault zones on volcanoes. part1: scaled experiments [Journal Article]. *Journal of Structural Geology*, *33*(5), 907-917. Retrieved from http://www.sciencedirect.com/science/article/B6V9D-52C8FPG-1/2/291ddecd3620c1c1ee835d73018de3cc doi: 10.1016/j.jsg.2011.03.002

Mathieu, L., van Wyk de Vries, B., Holohan, E. P., & Troll, V. R. (2008). Dykes, cups, saucers and sills: Analogue experiments on magma intrusion into brittle rocks. *Earth and Planetary Science Letters*, *271*(1), 1-13. Retrieved from https://www.sciencedirect.com/science/article/pii/S0012821X08001155 doi: https://doi.org/10.1016/j.epsl.2008.02.020

Minakami, T., Ishikawa, T., & Yagi, K. (1951). The 1944 eruption of volcano usu in hokkaido, japan [Journal Article]. *Volcanological Bulletin, series 2*, *11*, 5-157.

Montanari, D., Corti, G., Sani, F., Ventisette, C. D., Bonini, M., & Moratti, G. (2010). Experimental investigation on granite emplacement during shortening [Journal Article]. *Tectonophysics*, *484*(1-4), 147-155. Retrieved from http://www.sciencedirect.com/science/article/B6V72-4X9FGNN-1/2/85fb7113bc1c9239088d1c59fa0b60df

Panien, M., Schreurs, G., & Pfiffner, A. (2006). Mechanical behaviour of granular materials used in analogue modelling: insights from grain characterisation, ring-shear tests and analogue experiments. *Journal of Structural Geology*, *28*(9), 1710-1724. Retrieved from https://www.sciencedirect.com/science/article/pii/S0191814106001295 doi: https://doi.org/10.1016/j.jsg.2006.05.004

Paterson, S., & Schmidt, K. (1999). Is there a close spatial relationship between faults and plutons? *Journal of Structural Geology*, *21*(8), 1131-1142. Retrieved from https://www.sciencedirect.com/science/article/pii/S0191814199000243 doi: https://doi.org/10.1016/S0191-8141(99)00024-3

Pedicini, M., Bonali, F. L., Corti, N., Pasquaré M., F. A., Drymoni, K., & Tibaldi, A. (2023). A step forward to understanding the development of volcanotectonic rifts: the structure of the fremrinamar fissure swarm (iceland). *Frontiers in Earth Science*, *11*. Retrieved from https://www.frontiersin.org/journals/earth-science/articles/10.3389/feart.2023.1271721 doi: 10.3389/feart.2023.1271721

Peltier, A., Ferrazzini, V., Staudacher, T., & Bachèlery, P. (2005). Imaging the dynamics of dyke propagation prior to the 2000–2003 flank eruptions at piton de la fournaise, reunion island. *Geophysical Research Letters*, *32*(22). Retrieved from https://agupubs.onlinelibrary.wiley.com/doi/abs/10.1029/2005GL023720 doi: https://doi.org/10.1029/2005GL023720

Pierrot-Deseilligny, M., Rupnik, E., Girod, L., Belvaux, J., Maillet, G., Deveau, M., & Choqueux, G. (2016). Micmac, apero, pastis and other beverages in a nutshell.

Pinel, V., & Jaupart, C. (2000). The effect of edifice load on magma ascent beneath a volcano [Journal Article]. *Philosophical Transactions: Mathematical, Physical and Engineering Sciences*, *358*(1770), 1515-1532. Retrieved from http://www.jstor.org/stable/2666926

Poppe, S., Holohan, E. P., Galland, O., Buls, N., Van Gompel, G., Keelson, B., ... Kervyn, M. (2019). An inside perspective on magma intrusion: Quantifying 3d displacement and strain in laboratory experiments by dynamic x-ray computed tomography. *Frontiers in Earth Science*, *7*. Retrieved from https://www.frontiersin.org/journals/earth-science/articles/10.3389/feart.2019.00062 doi: 10.3389/feart.2019.00062

Poppe, S., Holohan, E. P., Rudolf, M., Rosenau, M., Galland, O., Delcamp, A., & K., M. (2021a). Mechanical properties of quartz sand and gypsum powder (plaster) mixtures: Implications for laboratory model analogues for the earth's upper crust. *Tectonophysics*, *814*, 228976. Retrieved from https://www.sciencedirect.com/science/article/pii/S0040195121002584 doi: https://doi.org/10.1016/j.tecto.2021.228976

Poppe, S., Holohan, E. P., Rudolf, M., Rosenau, M., Galland, O., Delcamp, A., ... Kervyn, M. (2021b). Mechanical test data of quartz sand, garnet sand, gypsum powder (plaster), kaolin and sand-plaster mixtures used as granular analogue materials in geoscience laboratory experiments.

Ramberg, H. (1970). Model studies in relation to plutonic bodies. *Mechanism of igneous intrusion*.

Ramberg, H. (1981). *Gravity, deformation and the earth'crust*. Academic Press, London.

Rhodes, E., Barker, A. K., Burchardt, S., Hieronymus, C. F., Rousku, S. N., McGarvie, D. W., ... Witcher, T. (2021). Rapid assembly and eruption of a shallow silicic magma reservoir, reydarártindur pluton, southeast iceland. *Geochemistry, Geophysics, Geosystems*, *22*(11), e2021GC009999. Retrieved from `https://agupubs.onlinelibrary.wiley.com/doi/abs/10.1029/2021GC009999` (e2021GC009999 2021GC009999) doi: https://doi.org/10.1029/2021GC009999

Rhodes, E., Burchardt, S., Greiner, S. H. M., Mattsson, T., Sigmundsson, F., Schmiedel, T., ... Witcher, T. (2024). Volcanic unrest as seen from the magmatic source: Reydarártindur pluton, iceland. *Scientific Reports*, *14*(1), 962. doi: https://doi.org/10.1038/s41598-023-50880-0

Rivalta, E., Taisne, B., Bunger, A., & Katz, R. (2015). A review of mechanical models of dike propagation: Schools of thought, results and future directions. *Tectonophysics*, *638*, 1-42. Retrieved from `https://www.sciencedirect.com/science/article/pii/S0040195114005174` doi: https://doi.org/10.1016/j.tecto.2014.10.003

Román-Berdiel, T., Gapais, D., & Brun, J. (1997). Granite intrusion along strike-slip zones in experiment and nature [Journal Article]. *American Journal of Science*, *297*(6), 651-678. Retrieved from `http://www.ajsonline.org/content/297/6/651.abstract` doi: 10.2475/ajs.297.6.651

Rosenberg, C. L. (2004). Shear zones and magma ascent: A model based on a review of the tertiary magmatism in the alps. *Tectonics*, *23*(3). Retrieved from `https://agupubs.onlinelibrary.wiley.com/doi/abs/10.1029/2003TC001526` doi: https://doi.org/10.1029/2003TC001526

Rubin, A. M., & Gillard, D. (1998). Dike-induced earthquakes: Theoretical considerations. *Journal of Geophysical Research: Solid Earth*, *103*(B5), 10017-10030. Retrieved from `https://agupubs.onlinelibrary.wiley.com/doi/abs/10.1029/97JB03514` doi: https://doi.org/10.1029/97JB03514

Ruch, J., Wang, T., Xu, W., Hensch, M., & Jónsson, S. (2016). Oblique rift opening revealed by reoccurring magma injection in central iceland. *Nature communications*, *7*(1), 12352. doi: https://doi.org/10.1038/ncomms12352

Rupnik, E., Daakir, M., & Pierrot-Deseilligny, M. (2017). Micmac–a free, open-source solution for photogrammetry. *Open geospatial data, software and standards*, *2*(1), 1–9. Retrieved from `https://doi.org/10.1186/s40965-017-0027-2` doi: 10.1186/s40965-017-0027-2

Schellart, W. (2000). Shear test results for cohesion and friction coefficients for different granular materials: scaling implications for their usage in analogue modelling. *Tectonophysics*, *324*(1), 1-16. Retrieved from https://www.sciencedirect.com/science/article/pii/S0040195100001116 doi: https://doi.org/10.1016/S0040-1951(00)00111-6

Schmiedel, T., Burchardt, S., Mattsson, T., Guldstrand, F., Galland, O., Palma, J. O., & Skogby, H. (2021). Emplacement and segment geometry of large, high-viscosity magmatic sheets. *Minerals*, *11*(10). Retrieved from https://www.mdpi.com/2075-163X/11/10/1113 doi: 10.3390/min11101113

Schmiedel, T., Galland, O., & Breitkreuz, C. (2017). Dynamics of sill and laccolith emplacement in the brittle crust: Role of host rock strength and deformation mode. *Journal of Geophysical Research: Solid Earth*, *122*(11), 8860-8871. Retrieved from https://agupubs.onlinelibrary.wiley.com/doi/abs/10.1002/2017JB014468 doi: https://doi.org/10.1002/2017JB014468

Schmiedel, T., Galland, O., Haug, O. T., Dumazer, G., & Breitkreuz, C. (2019). Coulomb failure of earth's brittle crust controls growth, emplacement and shapes of igneous sills, saucer-shaped sills and laccoliths. *Earth and Planetary Science Letters*, *510*, 161-172. Retrieved from https://www.sciencedirect.com/science/article/pii/S0012821X19300214 doi: https://doi.org/10.1016/j.epsl.2019.01.011

Schultz, R. (1995). Limits on strength and deformation properties of jointed basaltic rock masses. *Rock Mechanics and Rock Engineering*, *28*, 1–15. doi: https://doi.org/10.1007/BF01024770

Sigmundsson, F., Hooper, A., Hreinsdóttir, S., Vogfjörd, K., Ófeigsson, B., Heimisson, E., ... Eibl, E. (2015). Segmented lateral dyke growth in a rifting event at bárdarbunga volcanic system, iceland [Journal Article]. *Nature*, *517*, 191. Retrieved from http://dx.doi.org/10.1038/nature14111https://www.nature.com/articles/nature14111.pdf doi: 10.1038/nature14111https://www.nature.com/articles/nature14111#supplementary-information

Sigmundsson, F., Parks, M., Geirsson, H., Hooper, A., Drouin, V., Vogfjörd, K. S., ... Barsotti, S. (2024). Fracturing and tectonic stress drives ultrarapid magma flow into dikes. *Science*, eadn2838. Retrieved from https://www.science.org/doi/abs/10.1126/science.adn2838 doi: 10.1126/science.adn2838

Sigmundsson, F., Parks, M., Hooper, A., Geirsson, H., Vogfjörd, K. S., Drouin, V., ... Ágústsdóttir, T. (2022). Deformation and seismicity decline before the 2021 fagradalsfjall eruption. *Nature*, *609*(7927), 523–528. Re-

trieved from https://doi.org/10.1038/s41586-022-05083-4 doi: https://doi.org/10.1038/s41586-022-05083-4

Spacapan, J. B., Galland, O., Leanza, H. A., & Planke, S. (2016, 04). Control of strike-slip fault on dyke emplacement and morphology. *Journal of the Geological Society*, *173*(4), 573-576. Retrieved from https://doi.org/10.1144/jgs2015-166 doi: 10.1144/jgs2015-166

Spence, D. A., & Turcotte, D. L. (1985). Magma-driven propagation of cracks. *Journal of Geophysical Research: Solid Earth*, *90*(B1), 575-580. Retrieved from https://agupubs.onlinelibrary.wiley.com/doi/abs/10.1029/JB090iB01p00575 doi: https://doi.org/10.1029/JB090iB01p00575

Spera, F. J. (1980). Chapter 7. aspects of magma transport. In *Physics of magmatic processes* (pp. 265–324). Princeton: Princeton University Press. Retrieved 2024-07-02, from https://doi.org/10.1515/9781400854493.265 doi: doi:10.1515/9781400854493.265

Stephens, T. L., Walker, R. J., Healy, D., Bubeck, A., & England, R. W. (2018). Mechanical models to estimate the paleostress state from igneous intrusions. *Solid Earth*, *9*(4), 847–858. Retrieved from https://se.copernicus.org/articles/9/847/2018/ doi: 10.5194/se-9-847-2018

Stinton, A., Sparks, R. S. J., & Huppert, H. E. (2024). Analysis of magma rheology from lava spreading and explosive activity during the 2020–21 eruption of la soufrière, st vincent, with implications for eruption dynamics. *Geological Society, London, Special Publications*, *539*(1), 153-169. Retrieved from https://www.lyellcollection.org/doi/abs/10.1144/SP539-2022-284 doi: 10.1144/SP539-2022-284

Temtime, T., Biggs, J., Lewi, E., & Ayele, A. (2020). Evidence for active rhyolitic dike intrusion in the northern main ethiopian rift from the 2015 fentale seismic swarm. *Geochemistry, Geophysics, Geosystems*, *21*(6), e2019GC008550. Retrieved from https://agupubs.onlinelibrary.wiley.com/doi/abs/10.1029/2019GC008550 doi: https://doi.org/10.1029/2019GC008550

Thompson, N., Watters, R. J., & Schiffman, P. (2008). Stability analysis of hawaiian island flanks using insight gained from strength testing of the hsdp core. *Journal of Volcanology and Geothermal Research*, *171*(3), 163-177. Retrieved from https://www.sciencedirect.com/science/article/pii/S0377027307003678 doi: https://doi.org/10.1016/j.jvolgeores.2007.11.008

Tibaldi, A., Bonali, F., & Corazzato, C. (2017). Structural control on volcanoes and magma paths from local- to orogen-scale: The central andes case. *Tectonophysics*, *699*, 16-41. Retrieved from https://www.sciencedirect.com/

science/article/pii/S0040195117300045 doi: https://doi.org/10.1016/j.tecto.2017.01.005

Turcotte, D. L., & Schubert, G. (2014). *Geodynamics* (3rd ed.). Cambridge University Press.

Valentine, G. A., & Krogh, K. E. (2006). Emplacement of shallow dikes and sills beneath a small basaltic volcanic center – the role of pre-existing structure (paiute ridge, southern nevada, usa). *Earth and Planetary Science Letters*, *246*(3), 217-230. Retrieved from https://www.sciencedirect.com/science/article/pii/S0012821X06003347 doi: https://doi.org/10.1016/j.epsl.2006.04.031

Visage, S., Souloumiac, P., Cubas, N., Maillot, B., Antoine, S., Delorme, A., & Klinger, Y. (2023). Evolution of the off-fault deformation of strike-slip faults in a sand-box experiment [Journal Article]. *Tectonophysics*, *847*, 229704. Retrieved from https://www.sciencedirect.com/science/article/pii/S0040195123000021 doi: https://doi.org/10.1016/j.tecto.2023.229704

Wada, Y. (1994). On the relationship between dike width and magma viscosity. *Journal of Geophysical Research: Solid Earth*, *99*(B9), 17743-17755. Retrieved from https://agupubs.onlinelibrary.wiley.com/doi/abs/10.1029/94JB00929 doi: https://doi.org/10.1029/94JB00929

Witcher, T., Burchardt, S., Mattsson, T., Heap, M. J., & McCarthy, W. (2024). Development of permeable networks by viscous-brittle deformation in a shallow rhyolite intrusion. part 1: Field evidence. *Journal of Volcanology and Geothermal Research*, *454*, 108166. Retrieved from https://www.sciencedirect.com/science/article/pii/S0377027324001586 doi: https://doi.org/10.1016/j.jvolgeores.2024.108166

Wright, T. J., Ebinger, C., Biggs, J., Ayele, G., A.and Yirgu, Keir, D., & Stork, A. (2006). Magma-maintained rift segmentation at continental rupture in the 2005 afar dyking episode [Journal Article]. *Nature*, *442*(7100), 291-294. Retrieved from http://dx.doi.org/10.1038/nature04978 doi: http://www.nature.com/nature/journal/v442/n7100/suppinfo/nature04978_S1.html

Wright, T. J., Sigmundsson, F., Pagli, C., Belachew, M., Hamling, I. J., Brandsdóttir, B., ... Calais, E. (2012). Geophysical constraints on the dynamics of spreading centres from rifting episodes on land. *Nature Geoscience*, *5*(4), 242–250. doi: https://doi.org/10.1038/ngeo1428

Ziv, A., Rubin, A. M., & Agnon, A. (2000). Stability of dike intrusion along preexisting fractures. *Journal of Geophysical Research: Solid Earth*, *105*(B3), 5947-5961. Retrieved from https://agupubs.onlinelibrary.wiley.com/doi/abs/

1264 10.1029/1999JB900410 doi: https://doi.org/10.1029/1999JB900410

JGR: *Solid Earth*

Supporting information for

The influence of variable host rock cohesion and magma viscosity on intrusion-fault interaction: Insights from laboratory models

Sonja H. M. Greiner [1,2,3], Olivier Galland [4], Freysteinn Sigmundsson [1], Steffi Burchardt[2,3], Halldór Geirsson [1], Rikke Pedersen [1], Xia Wen[5]

[1]Nordic Volcanological Center, Institute of Earth Sciences, University of Iceland, Reykjavík, Iceland
[2]Department of Earth Sciences, Uppsala University, Uppsala, Sweden
[3]Center for Natural Hazard and Disaster Science (CNDS), Sweden
[4]Physics of Geological Processes, the NJORD Center, Department of Geosciences, University of Oslo, Oslo, Norway
[5] School of Resource Environment and Saftey Engineering, University of South China, Hengyang, Hunan, China

Contents

S1 Experimental Data Set **3**

S2 Material Properties of Glucose Syrup **3**

S3 Dimensional Analysis **4**

S4 Additional Information on the Experimental Setup **9**

S5 Addition of a cohesive layer at the base of low-cohesion experiments **10**

S6 Repeated Experiments **12**
S6.1 SF90/10 12
S6.2 SF100/0 13
S6.3 OF50/50 14
S6.4 OF95/05 16
S6.5 OF100/0 17
S6.6 Fault Structure 19

S7 Pressure **21**
S7.1 Methods 21
S7.2 Results 22
S7.2.1 Syrup 22
S7.2.2 Oil 23

S8 Syrup Intrusion Geometries **25**

S9 Oil Intrusion Geometries **25**

S1 Experimental Data Set

The full data set produced for the experiments will be made publically available once the article has been accepted for publication.

S2 Material Properties of Glucose Syrup

In this study, high-viscosity intrusions are represented by a glucose syrup, produced in Sweden under the name *Eldorado syrup Lys*. The density of the syrup has been determined as 1416 kg/m^3 (Figure S1a). The syrup is a Newtonian fluid and its viscosity has been measured at various temperatures ranging between around 15 °C and 65 °C (Figure S1b) using a VEB MLW falling ball viscosimeter. The inferred viscosities vary between 59.39 Pa s and 86.21 Pa s at room temperature (20.3–23.1 °C) and for this study, we take the viscosity as 70 Pa s. Since the laboratory, in which the experiments were conducted is located in a basement,

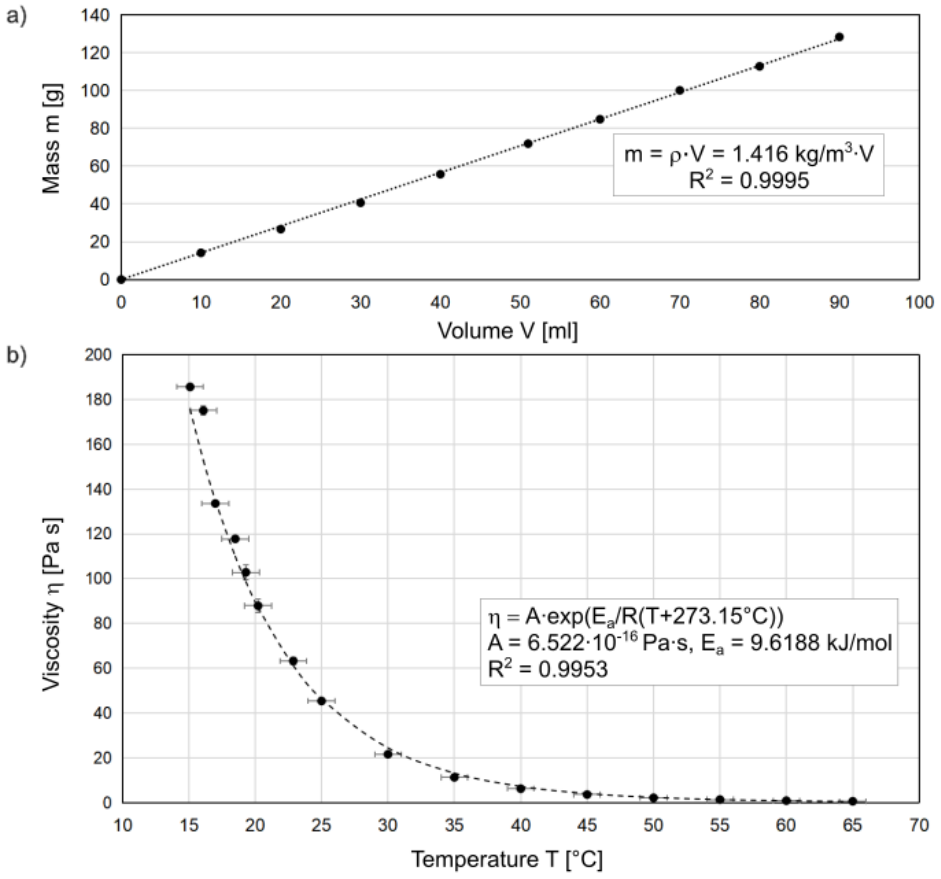

Figure S1: Material properties of Eldorado syrup Lys (glucose syrup). a) Density derived from measurements of the mass and volume. b) Temperature-dependent evolution of the viscosity.

temperature variations are largely unaffected by daily weather variations and the room temperature is assumed to be near-constant across all experiments in this study.

S3 Dimensional Analysis

In this section we discuss how our laboratory results are relevant for geological processes with the help of dimensional analysis of the modelled system and its similarity to their natural counterparts (Gibbings, 2011; Merle, 2015; Galland et al., 2018). This is not straightforward since we need to consider (1) the host rock response to the intrusion, (2) effect of faults in the host rock, (3) the flow of a viscous fluid, and (4) the coupling between the fluid and the deforming and partially faulted host. This system is highly complex in terms of the physics involved and no analytical model exists at this time, from which we could extract scaling parameters (see e.g., Bunger and Cruden, 2011; Michaut, 2011). Instead, we apply the procedure described by e.g., Gibbings (2011) to derive parameters for dimensional analysis. Furthermore, the similarity of our models to their geological equivalent is challenging to assess due to (1) a broad range of possible magma viscosities, (2) variable deformation mechanisms in the host (Galland et al., 2018), and (3) the poorly constrained properties of fault rocks. The derivation of parameters described below is based on the procedures outlined by Merle and Borgia (1996), Galland et al. (2009), Galland (2012), and Galland et al. (2014).

We chose a model-to-nature scale ratio between 10^{-4} and 10^{-5}, i.e. 1 cm represents 100 m to 1 km in nature (Galland et al., 2006; Galland et al., 2014). The physical parameters governing the intrusion process in our experiments are (see Table 2 in the main text): (1) (analogue) magma velocity at the injection inlet v, (2) viscosity η, and (3) density ρ_m as well as (4) the inlet diameter D. The physical parameters controlling the intact brittle analogue host rock are (see Table 2 in the main text): (1) the thickness of the overburden H, (2) rock density ρ_r, (3) intact cohesion C_i, and (4) the angle of friction φ_i. In our experiments, the overburden thickness H corresponds to the injection depth, i.e., 6 cm.

A novelty of our models is to account for the mechanical effects of a fault, which may represent a pre-existing weakness. Faulted rock is generally weaker than intact rock, with lower cohesion and angle of internal friction (Thompson et al., 2008; Ikari et al., 2015; Carpenter et al., 2012). Assuming a Mohr-Coulomb failure criterion for dry granular materials (e.g., Abdelmalak et al., 2016), we expect the failure envelopes to differ between intact and faulted granular media (Figure 1e in the main text). We quantify the weakness due to a fault by defining the strength ratio at the base of the model:

$$\Delta S = C_i + \rho_r g H tan\left(\varphi_i\right) - \left[C_f + \rho_r g H tan\left(\varphi_f\right)\right] \tag{S1}$$

where C_f and φ_f are the cohesion and angle of friction, respectively, of the faults.

The experiment is furthermore subjected to gravity, i.e. the gravitational acceleration g. For simplicity, we will not consider φ_i as a separate parameter in the dimensional analysis, as it is already dimensionless, and the geological relevance of the values of φ_i has previously been discussed by Abdelmalak et al. (2016).

According the Buckingham Π-theorem (Buckingham, 1914; Gibbings, 2011), nine variables with three independent dimensions require six independent dimensionless ratios (Table 2 in the main text). We applied the open-source software BuckinghamPy (Karam and Saad, 2021), with the following list of input parameters (ρ_r, C_i, ΔS, H, g, ρ_m, η, v, D, in this order), to compute the different combinations of the physical parameters into six dimensionless ratios. BuckinghamPy returned 55 sets of dimensionless Π' ratios; we selected Set 4 (Table S1).

In order to make the dimensionless parameters physically relevant for our model system, we recombined some of the Π' numbers to derive six new Π numbers (Table S1), listed in Table 2 of the main text; such a procedure is possible as long as we ensure that none of the original Π' numbers cancel out in the recombination (Gibbings, 2011).

The six dimensionless numbers characterize the physical processes relevant to our models; the experiments can be considered similar to their geological counterparts if the dimensionless ratios in both experiments and nature are comparable. Here, we discuss the individual dimensionless parameters that account for (1) fluid flow, (2) the host rock behavior, (3) the weakness due to the faults, and (4) the physical coupling between the host and the magma. The range of each governing parameter and of each dimensionless Π-number for both our experiments and (approximately) in nature is listed in Table 2 of the main text.

The first dimensionless parameter $\Pi_1 = (\rho_r - \rho_m)/\rho_r$ concerns the (analogue) magma buoyancy and is formed by the ratio of hydrostatic to lithostatic stresses. In our models, Π_1 ranges from 0.34 to 0.47 in the oil experiments and -0.06 and 0.17 in the syrup experiments. In nature, rock densities vary between $1600\,kg/m^3$ and $3000\,kg/m^3$ have an average density of about $2500\,kg/m^3$ (Turcotte and Schubert, 2014). Magma densities range from $2260\,kg/m^3$ for felsic magma to $2750\,kg/m^3$ for mafic magma (Lesher and Spera, 2015). If $\Pi_1 < 0$, the

Table S1: List of Π' numbers derived from BuckinghamPy software (Set 4) (Karam and Saad, 2021). Bottom two rows: recombination of Π' numbers to Π numbers with physical meaning.

Set 4					
$\Pi'_1 = \frac{v^2\rho_r}{C_i}$	$\Pi'_2 = \frac{\Delta S}{C_i}$	$\Pi'_3 = \frac{Hg}{v^2}$	$\Pi'_4 = \frac{v^2\rho_m}{C_i}$	$\Pi'_5 = \frac{v\eta}{C_i H}$	$\Pi'_6 = \frac{D}{H}$
Recombining Π'-numbers:					
$1 - \frac{\Pi'_4}{\Pi'_1}$	Π'_2	$\frac{1}{\Pi'_1\Pi'_3}$	$\frac{\Pi'_4\Pi'_6}{\Pi'_5}$	$\frac{\Pi'_5}{\Pi'_6}$	Π'_6
Resulting Π-numbers					
$\Pi_1 = \frac{\rho_r - \rho_m}{\rho_r}$	$\Pi_2 = \frac{\Delta S}{C_i}$	$\Pi_3 = \frac{C_i}{\rho_r g H}$	$\Pi_4 = Re = \frac{\rho_m D v}{\eta}$	$\Pi_5 = \frac{v\eta}{DC_i}$	$\Pi_6 = \frac{D}{H}$

magma is denser than the surrounding host rock, and locally negatively buoyant. However, if $\Pi_1 > 0$, the magma is less dense than the host rock, resulting in locally buoyant magma. In nature, Π_1 ranges between -0.71 and 0.24, so that magma can be gently positively buoyant to negatively buoyant (Table 2). Therefore, the oil experiments only account for positively buoyant magmas, whereas the syrup experiments account for both negatively and positively buoyant magmas, which is however considered negligible at this scale (Galland et al., 2009). Note here that neither our experiments nor the dimensional analysis consider effects of gas on buoyancy, even though they might affect ascending magma in nature. In geological systems, Hogan et al. (1998) describes didactically that the driving pressure of a magma at a given depth is the result of the integrated buoyancy along the entire magmatic system, i.e. from deep in the source. They assume that magma will propagate as long as the driving pressure, i.e. the integrated buoyancy, is positive. In our experiments, the volumetric pump imposes injection, assuming that the driving pressure of the magma, i.e. the integrated buoyancy, is sufficient for magma injection. Galland et al. (2009) discussed that the local buoyancy contribution at the scale of the modelled processes (i.e. the shallowest few kilometres of the crust) is negligible. This assumption is confirmed a-posteriori by our experimental results by comparing models OI50/50 and SI50/50. Even though Π_1 is positive in OI50/50 and negative in SI50/50, the oil in OI50/50 spread laterally at the bottom of the model more than the syrup in SI50/50, suggesting that positive buoyancy of the oil in OI50/50 was not sufficient to favor upward propagation of the oil.

The second dimensionless ratio characterizes the pre-faulted host rock through the ratio between the strength contrast at the base of the model box and the cohesion of the intact rock $\Pi_2 = \Delta S/C_i$. There are limited constraints on the properties of faulted granular materials used for analogue models. Ring shear tests with gypsum powder/quartz sand mixtures indicate that C_f remains approximately constant across varying proportions although C_i varies (Poppe et al., 2021a; Poppe et al., 2021b). We assume similar behavior for our granular materials and set $C_f = 120\,Pa$ for all mixtures, which is slightly lower than the cohesion of pure glass beads. This implies that the strength ratio between between intact and faulted granular material increases with increasing content of SF. In natural systems, estimating ΔS is challenging as there are large uncertainties on the values of both C_f and φ_f.

The third dimensionless parameter also describes the brittle host rock and scales the cohesion with the lithostatic stress at the injection depth, i.e. the base of the model box: $\Pi_3 = C_i/\rho_r g H$. In our experiments, injection occurs at 6 cm depth, and the model rock cohesion varies from ca. 100 to ca. 300 Pa (Abdelmalak et al., 2016). The experimental values of Π_3 thus range between 0.15 and 0.5 in our models, meaning that cohesive forces are negligible in models made of 100% GB ($\Pi_3 \approx 0.1$), whereas cohesive forces are not negligible in other models. In nature, the cohesion of rocks ranges approximately between $10^6 - 10^8\,Pa$ (Schultz, 1995; Schellart, 2000 and references therein). In sedimentary basins,

intrusion depths are typically between 1 and 5 km (Schmiedel et al., 2017). The values of Π_3 in nature thus range between 1.3×10^{-2} and 6.37 (Table 2). The model values of Π_3 are in the middle of the natural Π_3 values, therefore the brittle deformation regime in our models is representative of those of the corresponding geological systems.

The fourth dimensionless parameter characterizes the (analogue) magma flow regime and is the Reynolds number $\Pi_4 = Re = \rho_m D v/\eta$, i.e. the ratio between inertial and viscous forces within the (analogue) magma. In our models, the values of Re are 1.5 for oil experiments and 9×10^{-6} for syrup experiments. This suggests that the fluid flow in our experiments is laminar at the injection inlet. In nature, the magma velocity v in feeder dikes can vary between 0.01 and ca. $12\,m/s$ (Spera, 1980; Peltier et al., 2005; Sigmundsson et al., 2022). The thickness of feeder dykes D typically varies between 1 and 10 m (Spence and Turcotte, 1985; Clemens and Mawer, 1992). The magma viscosity η can range between 100 up to $> 10^{10}\,Pa\,s$ for mafic and felsic magmas, respectively (Gonnermann, 2015; Lesher and Spera, 2015). Therefore, in nature the values calculated for Re may range between 2×10^{-9} and ≈3300, based on purely mathematical combinations. However, although exceptions may exist, when magma flow is exceptionally high and may become turbulent, fast-flowing magma of low viscosity often flows through feeders on the orders of maximum a few rather than tens of meters (e.g., Sigmundsson et al., 2022). It is furthermore difficult to constrain the dimensions of feeders and subsurface flow velcoities due to a lack of direct observations and high uncertainties associated with indirect methods of observation such as seismicity and ground deformation. Nonetheless, the derived values for Π_4 indicate that the magma flow within intrusions is mostly laminar, indicating that the flow regimes in our model intrusions is representative for magma flow in most intrusions in nature.

The fifth dimensionless parameter, $\Pi_5 = v\eta/C_i D$, accounts for the coupling between the flowing magma and the deforming host rock and scales the viscous stresses within the flowing magma to the cohesion of the host rock. In our experiments, the values of Π_5 range between $9 \times 10^{-5}$and 2.8×10^{-4} in the oil models, and between 3.4×10^{-3} and 9×10^{-3} in the syrup experiments. The broad range of magma viscosities in nature due to e.g., magma composition results in a wide theoretical range of values of Π_5 between 1×10^{-9} and 6×10^{4} (Table 2). Consequently, our experimental values of Π_5 fall within the range of natural systems. It should however be noted, that our models do not account for cases where the viscous stresses dominate over to the cohesive stresses ($\Pi_5 > 1$). Note furthermore that we do not consider changes of the magma viscosity and other parameters associated with cooling, which can occur over intrusive time scales in nature (Thorey and Michaut, 2016).

Paragraph added in partial response to major comment 4.The viscosity of magma is a parameter of special interest, since it can have important effects on e.g., eruption dynamics (e.g., Stinton et al., 2024). While our experimental values

Table S2: Derivation of estimates of natural viscosities represented by the experiments in this study. Values are derived from Eq. S2 and values listed in Table 2 of the main text.

Viscosity end member	Cohesion C_i [Pa]	$\Pi_{5,exp}$	Inlet diameter [m]	Inflow velocity [m/s]	Resulting viscosity [Pa s]
low	10^6	2×10^{-4}	1	12	17
	10^8	7×10^{-5}	1	12	583
high	10^6	9×10^{-3}	10	0.1	9×10^5
	10^8	3×10^{-3}	10	0.1	3×10^7

for Π_5 lie within the range of natural values, we attempt here to constrain further which types of magma are represented by our experiments. For this purpose, the dimensionless parameter Π_5 (Table S1) is rearranged to isolate the viscosity η:

$$\eta = \frac{\Pi_{5,exp} D C_i}{v} \tag{S2}$$

While low- and high-viscosity intrusions can form in both high- or low-cohesion host rock, we will assume here that high-viscosity intrusions are associated with lower flow velocities (assuming $v = 0.1\,m/s$) and larger feeder diameters (assuming $D = 10\,m$) and vice versa for low-viscosity intrusions (assuming $v = 12\,m/s$ and $D = 1\,m$). Table S2 shows that depending on the host rock cohesion, the low-viscosity experiments can represent viscosities of ca. $20-600\,Pa\,s$, while the high-viscosity experiments would represent viscosities between $9 \times 10^5 - 3 \times 10^7\,Pa\,s$. These values roughly correspond to basaltic-andesitic and dacitic- to mildly rhyolitic magmatic compositions, respectively (e.g., Gonnermann, 2015; Lesher and Spera, 2015). It is however crucial to note that these values strongly depend on and scale with the assumed inlet diameter and inflow velocities. The experiments should not be directly translated to natural viscosity ranges without this context.

The sixth and last dimensionless ratio defined here is the geometric ration $\Pi_6 = D/H$, which expresses the relative size of the feeder of the intrusion with respect to its depth. In our experiments, $\Pi_6 = 0.08$, whereas in nature Π_6 ranges between 1.7×10^{-4} and 1.7×10^{-2}. Even though the value Π_6 in our model is larger than its upper bound in nature, it is significantly lower than 1, meaning that in both our models and nature the size of the magma source is very small with respect to its depth.

S4 Additional Information on the Experimental Setup

Photos of the experimental setup (Figure S2) show the general setup, the injection set up for both syrup and oil as well as the box with intact and faulted analogue host rock.

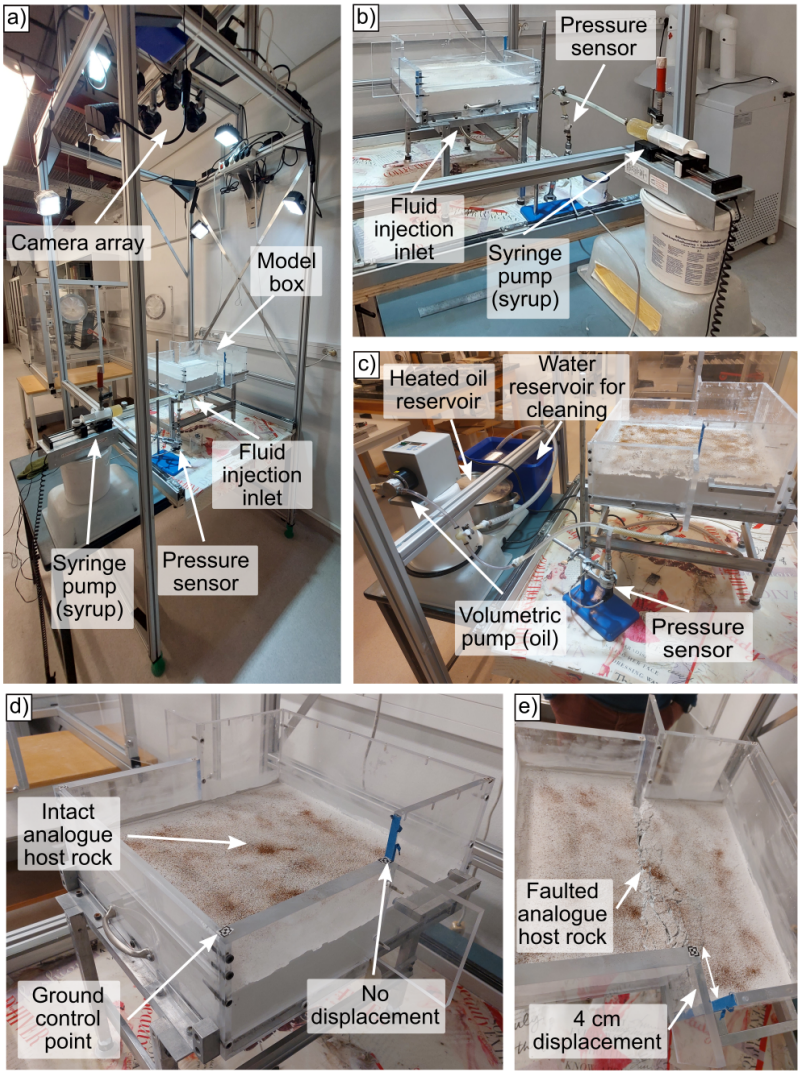

Figure S2: Photos of the experimental set up. a) The entire experimental setup with the injection set up for syrup experiments. b) Close-up of the syrup injection setup with the syringe pump. c). Close-up of the oil injection set up. The water reservoir is used to clean the pump of oil after the experiment, but it is not used during the experiment. d) Intact model without pre-existing displacement. e) Pre-faulted model with pre-existing displacement enforced by moving the left half of the box.

S5 Addition of a cohesive layer at the base of low-cohesion experiments

The two analogue host rock materials with the lowest cohesion (95%GB/5% SF and 100%GB) were sufficiently weak, that material fell through the injection inlet once the plug was removed after compaction. To prevent this from occurring, we added a 1 cm-thick layer of the 80% GB/20% SF mixture at the base of the model (thickness refers to the non-sliding side of the model box). To evaluate whether this cohesive base layer affected the resulting intrusion, we repeated experiment NF9010 with the cohesive layer. The 90/10 mixture was the material with the lowest cohesion, which did not require a base layer. The two experiments can be compared in Figure S3.

Both experiments are sheet intrusions and produced partial cone sheets. Compared to the experiment without the base layer (Figure S3a), the experiment with the cohesive base (Figure S3b) has a more pronounced base, which however still has a low thickness. This becomes clear by the step of the base plate, which is visible through the center of the intrusion (Figure S3d). At depth, the angular fraction of a full circle that is covered by the cone-sheet is larger than for the intrusion without a base layer. This can potentially be related to the absence of the step of the sliding plate, which does not perturb the interface between the two layers.

Vertical surface deformation immediately before the oil breaches the surface is of similar amplitude for both experiments (max. 2.5–3 mm; Figure S3e and f). In both cases, the uplifted area is subcircular with slight concentrations in the lower left corner, which is where the oil approached the surface. The asymmetry is more pronounced in the case without the base layer (Figure S3e), which is consistent with the less well developed base.

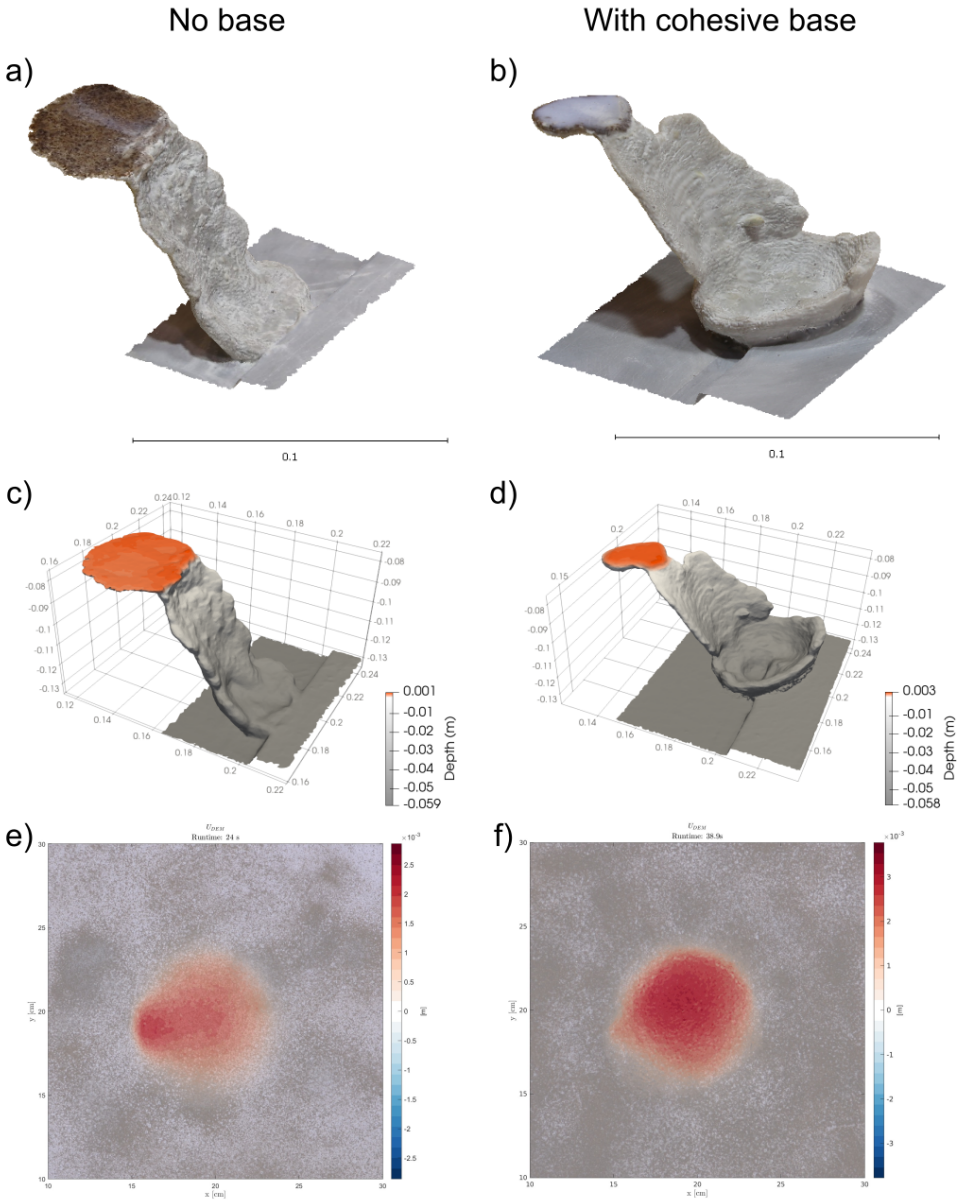

Figure S3: Comparison of the OI90/10 without and with a 1 cm-thick cohesive layer of the 80%GB/20%SF mixture at the base. a) and b) Virtual model of the intrusions from the experiments without and with the cohesive base layer, respectively. Scale bar is in m. c) and d) Virtual models of the intrusion colored by depth without and with the cohesive base layer, respectively. Orange colored parts are at or above the model surface. e) and f) Vertical surface deformation immediately before oil breached the surface.



Figure S4: Side view of the intrusion from experiment WF1000. The massive, low-aspect ratio part of the intrusion noticably forms above the cohesive layer, i.e. above the dashed black line, which marks the top of the cohesive base layer.

S6 Repeated Experiments

Experiments were repeated if one of the recorded data sets (surface deformation and recorded pressure) were compromised or if the model box was not functioning properly, e.g. if a small amount of material fell through the injection inlet creating a cavity at the base of the model box. Even though such experiments were excluded from further analysis, they provide insights into the reproducibility of our experiments. Below we will compare a few "failed" experiments with their successful counterparts. In total we conducted 28 experiments (out of which 20 were considered for analysis) and one reference experiment for the cohesive base layer (see section S5).

S6.1 SF90/10

Experiment SF9010 was conducted a total of four times. The first two failed due to drift in the camera array, which resulted in unusable surface deformation data. During the third iteration, a failure of the pressure sensor occurred, which made it difficult to accurately determine the beginning of the intrusion process and therefore, the intruded volume. However the experiment produced usable surface deformation data. The fourth iteration of this experiment is the one presented in the main text.

Comparison of the uplift of the third and fourth iteration (Figure S5a, b)

shows several common key features, which include an elliptical deformation pattern which is elongated along the fault, the amplitude of displacement and divergence as well as noticeably higher deformation along the fault. The horizontal divergence shows in both iterations compression along a semicircular band away from the fault segments but extension within the faulted host rock, which aligns in parts with existing fault segments.

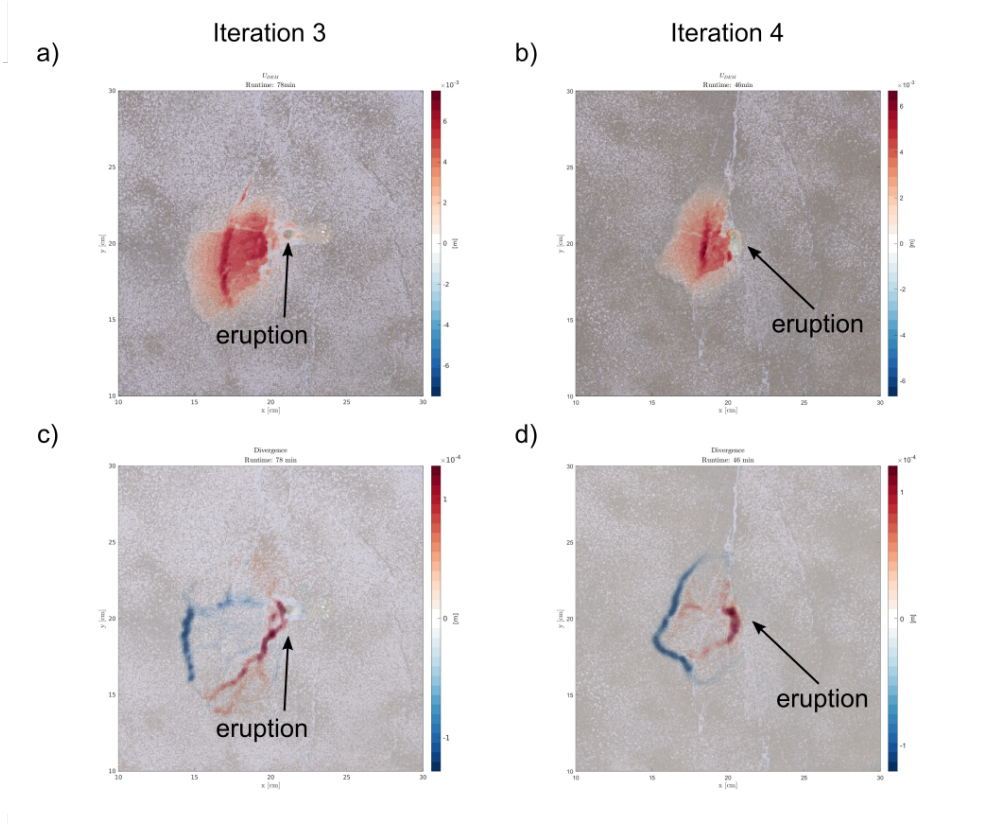

Figure S5: Vertical deformation of a) the third and b) the fourth iteration of experiment SF90/10. c) and d) show the corresponding horizontal divergence.

S6.2 SF100/0

Two iterations of experiment SF100/0 were conducted. The first one was excluded due to a failure of the pressure sensor, but surface deformation data was not compromised. The second iteration is presented in the main text. Comparison of the two iterations shows, that the amplitude and pattern of surface deformation are remarkably similar (Figure S6). In both iterations material was pushed upwards, resulting in a dome, which is asymmetric and elongated in the direction of the fault. The horizontal divergence shows distributed tensile failure in an area roughly aligned with the fault, but it is much wider than for more cohesive experiments (e.g., Figure S5c, d). The surrounding band of convergence is not perturbed significantly where it crosses pre-existing fault segments. In

both cases, the syrup breached the surface on a fault segment.

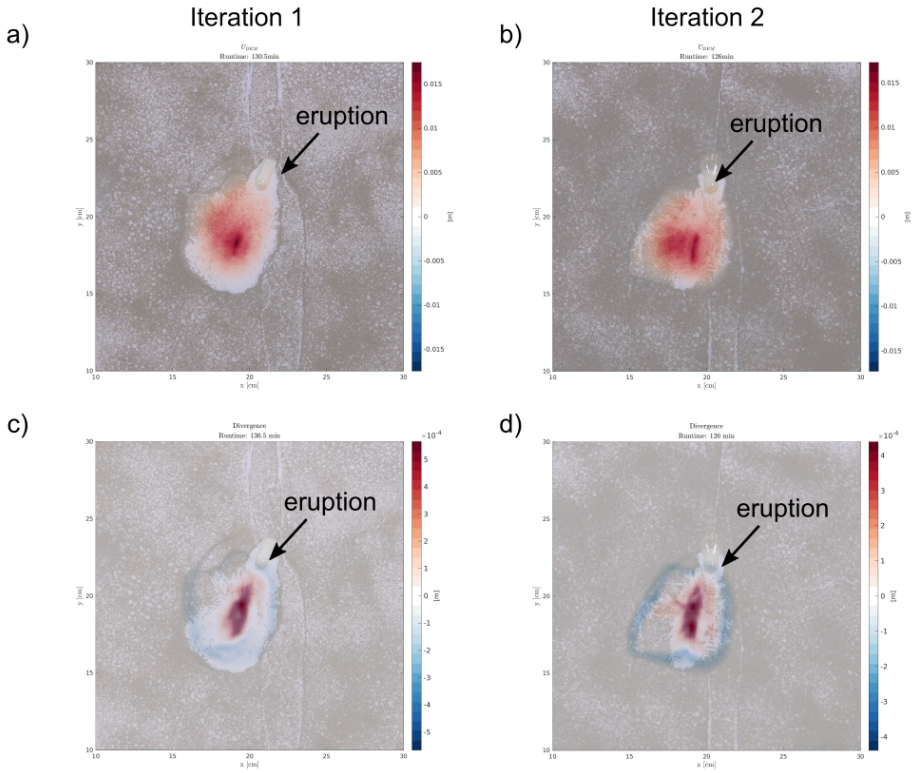

Figure S6: Vertical deformation of a) the first and b) the second iteration of experiment SF100/0. c) and d) show the corresponding horizontal divergence.

S6.3 OF50/50

Two iterations of experiment OF50/50 were conducted. The first one was excluded from analysis, because of a failure of the pressure sensor. Additionally, slight changes were made to the setup of the camera array, which was used to record surface deformation. To have all experiments with the same camera setup, we conducted a second iteration.

The vertical deformation is similar in pattern and amplitude between both iterations (Figure S7), with uplift being concentrated to the left of the faulted model crust. However, in iteration 2 small amounts of deformation are also observed within the faulted part of the model.

The horizontal divergence of the first iteration is strongly dominated by the tensile opening of the fault segment, through which the oil reached the surface. However, on the fault segments on the other side of the injection inlet (lower half of Figure S7c), very faint lines along the fault segments indicate weak fault reactivation. A much more pronounced pattern is observed for the second iteration (Figure S7d), where the fault segment to the right gets compressed, the one to

the experiences tension and there is a fine network of tensional lines to the left of the faulted crust.

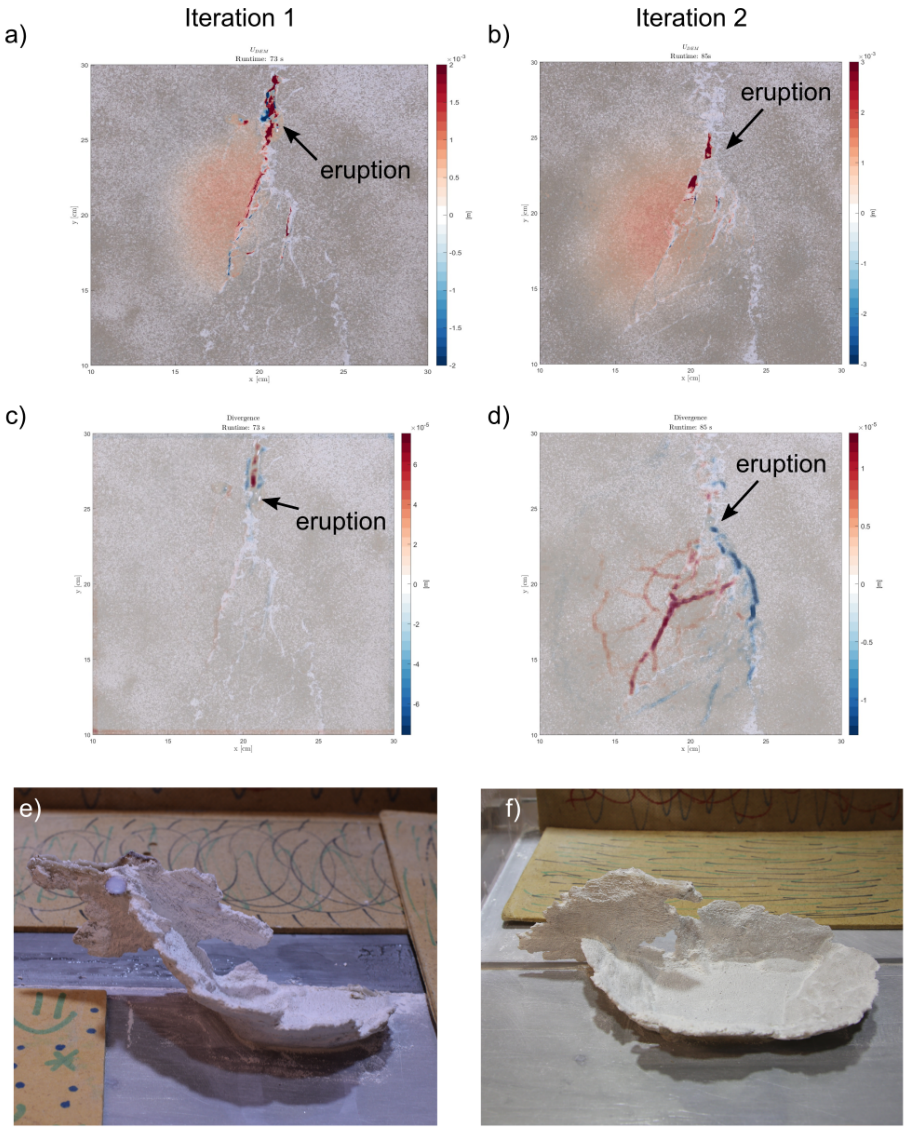

Figure S7: Vertical deformation of a) the first and b) the second iteration of experiment OF50/50. c) and d) show the corresponding horizontal divergence and e) and f) show the final intrusion geometries. The left side of the photos in e) and f) corresponds to the upper edge of the other panels.

The intrusion geometries of both iterations (Figure S7e, f) share that oil initially propagated along the base of the model box before transitioning into a partial saucer-shaped sill. Eventually, the oil intersected a fault segment and propagated along it in both directions and to the surface. However, in iter-

ation 2, the saucer shaped sill is more developed and although segmented, is almost complete (Figure S7e), while only about a third is developed in iteration 1 (Figure S7e). The better developed saucer-shaped sill of iteration 2 underlies the observed more pronounced horizontal divergence. The sharp transition to fault-occupying segments and bi-directional propagation are observed in both iterations, although this only occurs in the shallower half of the crust in iteration 1, but across most of the depth range in iteration 2.

S6.4 OF95/05

Experiment OF95/5 was conducted twice. During the first iteration, a small amount of material fell through the injection inlet when the plug was removed, which is placed there to prevent material falling through the inlet during compaction. It is unclear if the material was loose because the plug was sitting too high or too low, if material was insufficiently compacted or if the cohesive base layer was not continuous. The second iteration is presented in the main text.

For this experiment, surface deformation patterns vary significantly in terms of shape. While iteration 1 resulted in a subcircular to elliptical low-amplitude uplift pattern, which is superimposed by a somewhat higher-amplitude, crescent-shaped pattern around the lower left edge (Figure S8a). Iteration 2 (Figure S8b) resulted in the pattern described in the main text, where a strongly elongated (along the fault) pattern of low amplitude uplift is superimposed by a very localized uplifted area, close to where the oil eventually breached the surface.

Both divergence patterns (Figure S8c, d) show convergence surrounding tensional lines. However, in iteration 1 they form a ring-like structure, while they are elongated along and disconnected on either site of the fault zone in iteration 2.

The intrusive geometries mirror this difference. While both intrusions have a poorly developed inlfated part at depth and a feeder to the surface, their shapes mirror the respective rounded or elongated pattern observed at the surface. Iteration 1 formed a conduit underneath the low-aspect ratio part, which possibly formed when oil filled the cavity, that formed when material fell through the injection inlet. Such a feature was not observed in any other experiment. The connection to the model surface had the form of a rounded sheet, which followed the edge of the inflatedpart in a similar manner to other low-aspect ratio intrusions. However, the feeder is larger relative to the inflated part if compared to other low-cohesion experiments. It furthermore has a more pronounced sheet-like shape and it is hard to tell if it has a lobate structure or not. It is also noticeable that it terminates against the fault zone (left side of the feeder in Figure S8d) instead of propagating in plane with the fault zone. The inflated part formed on both sides of the fault zone and does not show any perturbations in its geometry or surface deformation where it crosses the fault. This differs from iteration 2, where the inflated part is deeper and initiated directly above the cohesive base layer, is elongated along the fault and the lobate structure of the conduit, which connects to the surface is in the fault plane as well.

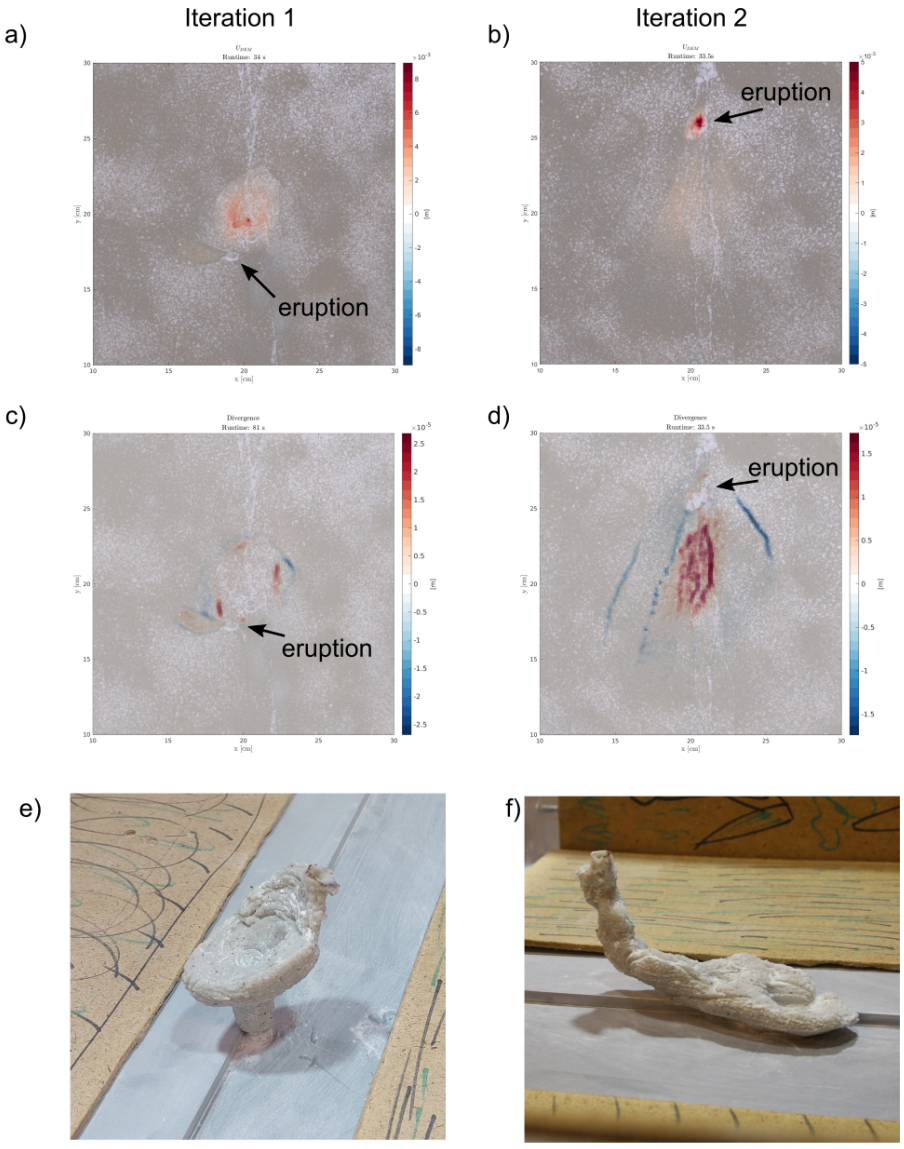

Figure S8: Vertical deformation of a) the first and b) the second iteration of experiment OF95/5. c) and d) show the corresponding horizontal divergence and e) and f) show the final intrusion geometries. The left side of the photos in e) corresponds to the right edge of the map view in a) and c). The left side of the photo in f) corresponds to the top edge of the map view in b) and d).

S6.5 OF100/0

Experiment OF100/0 was conducted twice due to a failure of the pressure sensor in the first iteration and because Iteration 1 was the first experiment, which had the cohesive base layer. We therefore repeated the experiment to ensure that

the results were reproducible. Both iterations produced asymmetric domes of pushed-up material, which were slightly elongated along the fault (Figure S9a, b). The amplitude of uplift is very comparable between both experiments. During the first iteration, oil breached the surface along one of the main fault segments, while it did so along one of the outer, less clearly visible segments in iteration 2.

For both iterations, the horizontal divergence shows a band of convergence surrounding an area of distributed extension, which is elongated along the fault, but does not localized well along individual segments. (Figure S9c,d) There is little disturbance where the convergence band crosses the fault.

Intrusion geometries of both iterations look alike with a pronounced low-aspect ratio body at depth connecting to the surface through a slightly inclined, round conduit (Figure S9e, f). Both intrusions only formed above the cohesive base layer, which can be seen by a small gap between the base of the model box and the base of the intrusion. This is especially well visible for iteration 2 (Figure S9f).

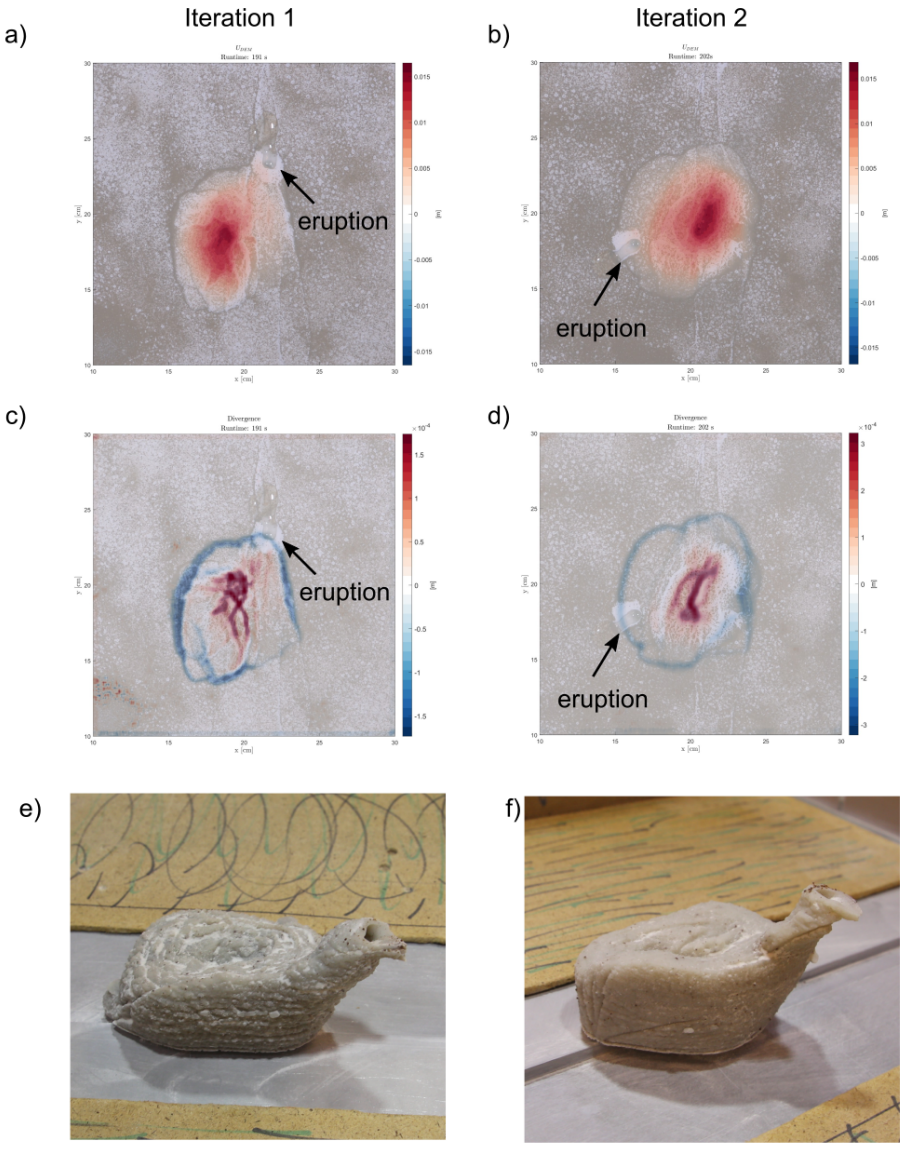

Figure S9: Vertical deformation of a) the first and b) the second iteration of experiment OF100/0. c) and d) show the corresponding horizontal divergence and e) and f) show the final intrusion geometries. The left side of the photos in e) corresponds to the bottom edge of the map view in a) and c). The left side of the photo in f) corresponds to the top edge of the map view in b) and d).

S6.6 Fault Structure

To assess variations of the structure of the strike-slip fault in pre-faulted experiments we compare here mapped fault patterns of individual experiments with GB/SF corresponding to 50/50, 90/10 and 100/0 (Figure S10). To increase the

number of models considered for comparison, we consider not only experiments included in the main text, but also repeat experiments. Fault segments were mapped on the (pre-intrusion) ortho-images shown in Figure S10.

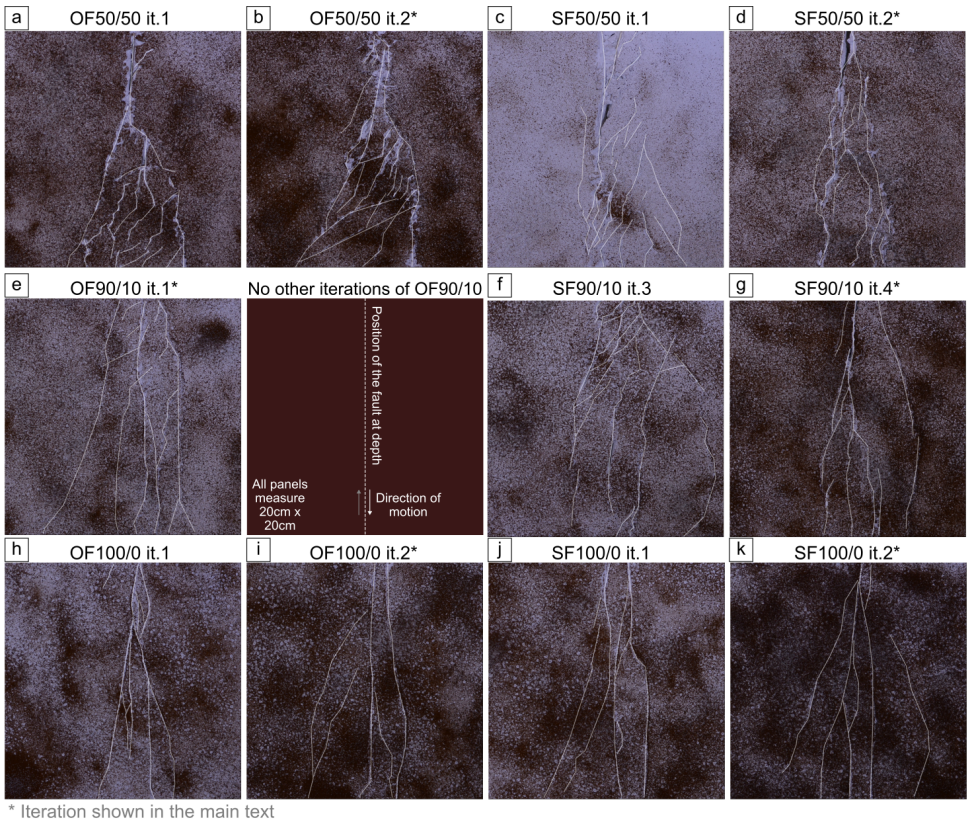

Figure S10: Comparison of fault structures with variable cohesion indicated by white lines in ortho-images (cropped mapview of the model box). Outlines correspond to 20 cm x 20 cm and is equal to the plots in Figures 2-5 in the main text. a)-d) show experiments with GB/SF equal to 50/50, e)-g) show 90/10-mixtures and h)-k) show pure glass beads (100/0). Iterations marked with an asterisk (*) are included in the analysis in the main text.

In experiments using GB/SF 50/50 the fault zone is bound by long fault segments sub-parallel to the direction of the fault (Figure S10a-d). Additionally, several shorter fault segments form between them with a more oblique orientation to the general trend of the fault zone. The fault structure is wider at the base of the images than at the top. Several of the longest and some of the shorter fault segments are visually dilated. The edges of individual segments are frequently jagged rather than forming smooth lines.

Experiments using a 90/10-mixture show long fault segments bounding the fault zone similar to those in the 50/50 mixture (Figure S10e-g). However, the number of shorter segments is noticeably reduced. Furthermore, dilation is much less pronounced. As before, the fault zone is somewhat wider at the base of the

images compared to the top.

Experiments with pure glass beads (Figure S10h-k) are mainly characterized by long fault segments. The number of shorter segments in between is again reduced compared to more cohesive experiments. Furthermore, the segments are more straight, appear less jagged and show no sign of dilation.

While there are variations between individual experiments with the same materials as model host rock show, they appear similar enough that we assume the fracture patterns to be generally reproducible. Furthermore, while the smoothness of individual fault segments, the degree of dilation and the number of small segments vary between the different materials, the presence of longer fault segments bounding the fault zone remains consistent. The width of the fault zone towards the base of the photos is slightly narrower for low-cohesion experiments. However, we assume here that variations of the structure of the fault zone are small enough to allow for comparison of the individual experiments within the framework of this study.

S7 Pressure

S7.1 Methods

For the experiments, the pressure value of interest is the pressure at the injection inlet at the base of the model box. However, the pressure recorded at the sensor, p_{rec}, includes not only the fluid overpressure which builds up at the inlet, but also a hydrostatic contribution p_{ob} due to the height difference between the injection inlet and the pressure sensor. We therefore applied corrections to the measured pressure to account for these effects and derive the pressure at the inlet. In case of the syrup, the fluid column above the sensor was filled by syrup only, whereas in case of the oil part of it was covered by water as well. The water was required for oil experiments to prevent the pressure sensor from being clogged and potentially damaged by oil solidifying within it. However, the density difference between water and oil prevented water from rising up and being injected into the model box. The water was considered assuming a density of $\rho_w = 1000\,kg/m^3$ and measuring the height of the water column h_w above the pressure sensor. Therefore, the pressure contribution due to the height difference can be calculate for syrup and oil, respectively as:

$$p_{h,s} = \rho_s g \Delta h \tag{S3}$$

$$p_{h,o} = \rho_o g \left(\Delta h - h_w\right) + \rho_w g h_w \tag{S4}$$

Additionally, a pressure drop p_{visc} occured due to viscous flow through the pipe walls. Assuming that the fluid flow at the injection inlet is laminar, the contribution of the viscous drop depends on the inner diameter D_i of the pipe connecting the sensor and the injection inlet, its length L as well as the flow velocity and its viscosity through

$$p_{visc} = \frac{32 \eta v L}{D_i^2} \tag{S5}$$

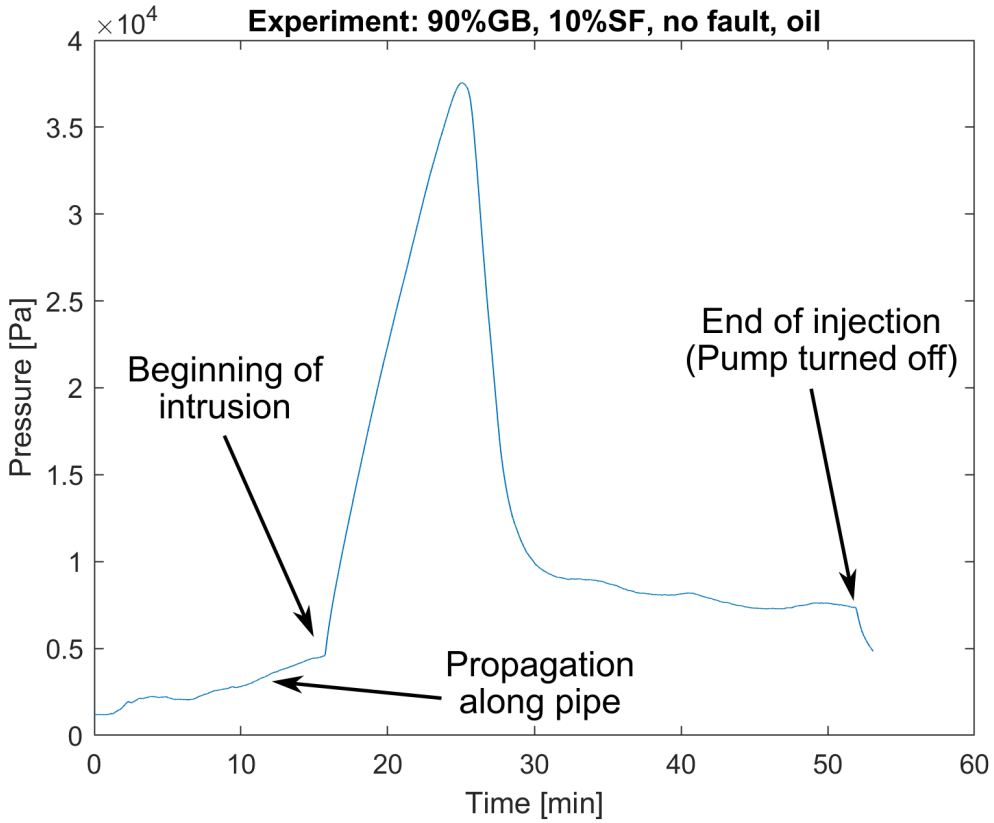

Figure S11: Example of a pressure curve without any corrections applied.

The fluid overpressure p can therefore be calculated as

$$p = p_{rec} - p_{ob} - p_{visc} \tag{S6}$$

In the initial phase of the experiment, before the analogue magma comes into contact with the host rock, it travels along the pipe. This phase is characterized by a steady increase of the recorded pressure. Once the fluid comes into contact with the analogue host rock, which is defined as the beginning of the intrusion process itself, the pressure rapidly increases until the host rock fails and the intrusion begins to propagate. An example of a pressure curve without any corrections applied is shown in Figure S11.

S7.2 Results

S7.2.1 Syrup

For syrup experiments, the evolution of the fluid overpressure with time shows a steep increase in pressure which is followed by a rapid decrease (Figure S12). This decrease gradually tapers out before the pressure stabilizes, although for pre-faulted high-cohesion materials the experiment ended (i.e. eruption occurred) before the pressure level could stabilize properly (solid black and blue lines). The

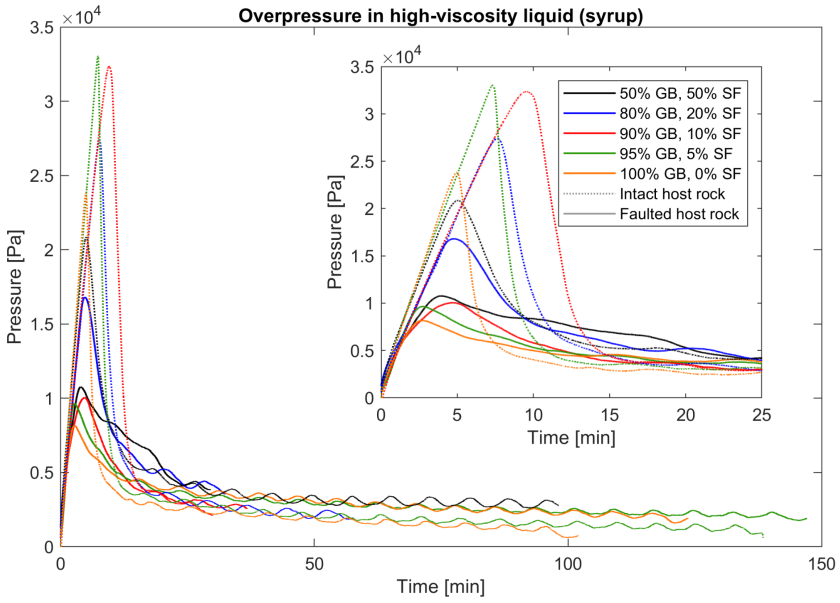

Figure S12: Fluid overpressure at the injection point at the base of the modelling box for high-viscosity (syrup) experiments. Dotted lines correspond to experiments with initially intact host rock, solid lines to experiments with a pre-existing strike-slip fault.

oscillations visible for all experiments once the pressure has stabilized likely relate to slight variations in the flow rate due to the syringe pump. Experiments in intact host rock recorded systematically higher peak-pressures than experiments in pre-faulted host rock. Additionally, intermediate and low-cohesion experiments tend to require higher over-pressures. For both intact and pre-faulted host rock, high-cohesion materials tend to require lower peak-pressures than those with lower cohesion. The peak pressure in low cohesion materials (orange and green lines) is potentially affected by the presence of the more cohesive layer at the base of these models.

S7.2.2 Oil

The evolution of the fluid overpressure as a function of time shows that for all oil experiments pressure builds up at the beginning of the experiment and then rapidly decreases before stabilizing (Figure S13). When comparing the experiments with and without pre-existing faults for each material, the higher overpressure is always observed for the intact host rock. Additionally, the maximum overpressure increases as the cohesion decreases for high and intermediate cohesion materials. This is not the case for the low cohesion materials (95-100% GB), however, these sets of experiments had the 1 cm thick layer of more cohesive material at the base, which may have influenced the initiation of the propagating intrusion. The duration of experiments was generally longest for low-cohesion

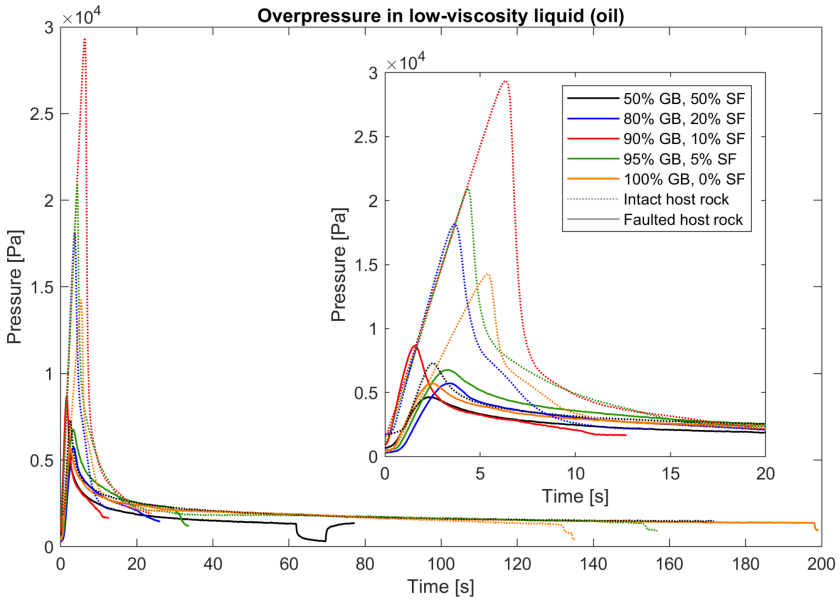

Figure S13: Fluid overpressure at the injection point at the base of the modelling box for low viscosity (vegetable oil) experiments. Dotted lines correspond to experiments with initially intact host rock, solid lines to experiments with a pre-existing strike-slip fault. Inlet shows a more detailed view of the first 20 s of the experiment.

experiments, with the exception of experiment OF95/5. The low-cohesion experiments, both with intact and previously faulted host rock, show a clear pressure drop a few seconds prior to the onset of eruption, which is not observed for high-cohesion materials. At intermediate cohesion, a slightly accelerated decrease may be visible for OF90/10, but not for the intact host rock experiment (OI90/10). The decrease in pressure for experiment OF50/50 (solid black line) between ca. 60-70 s relates to a temporary decrease in flow rate due to the pump and is not a signal caused by the propagating intrusion.

S8 Syrup Intrusion Geometries

Syrup does not solidify at room temperature. Due to this, the intrusions in syrup experiments were not retrieved or recorded in a systematic manner. However, after the experiment finished, the pipe connecting the syringe to the injection inlet was disconnected so that syrup, which did not stick to the analogue host rock could drain back through the injection inlet.

The intrusion of experiment SF1000 was partially retrieved (i.e. the part which came into contact with the host rock and did not drain back through the injection inlet) and is shown in Figure S14. The outline of the intrusion notably resembles those of the low-aspect ratio oil intrusions with steep, inclined walls at the base and a narrow feeder at the edge connecting to the surface.



Figure S14: Parts of the SF1000 syrup intrusion after syrup drained back through the injection inlet.

S9 Oil Intrusion Geometries

Below is a collection of the figures of all oil intrusions at a larger resolution than shown in the main text.

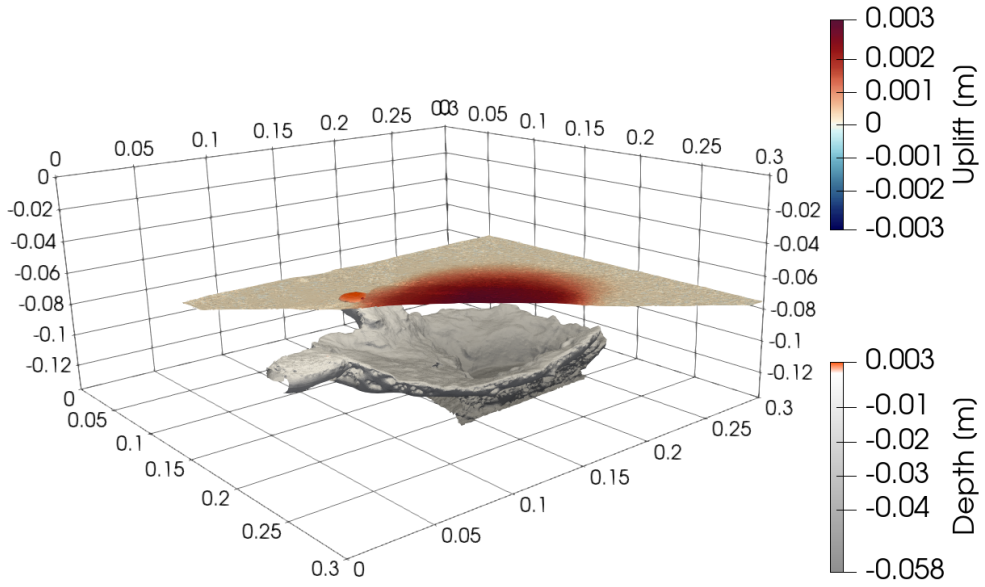

Figure S15: Intrusion of OI50/50.

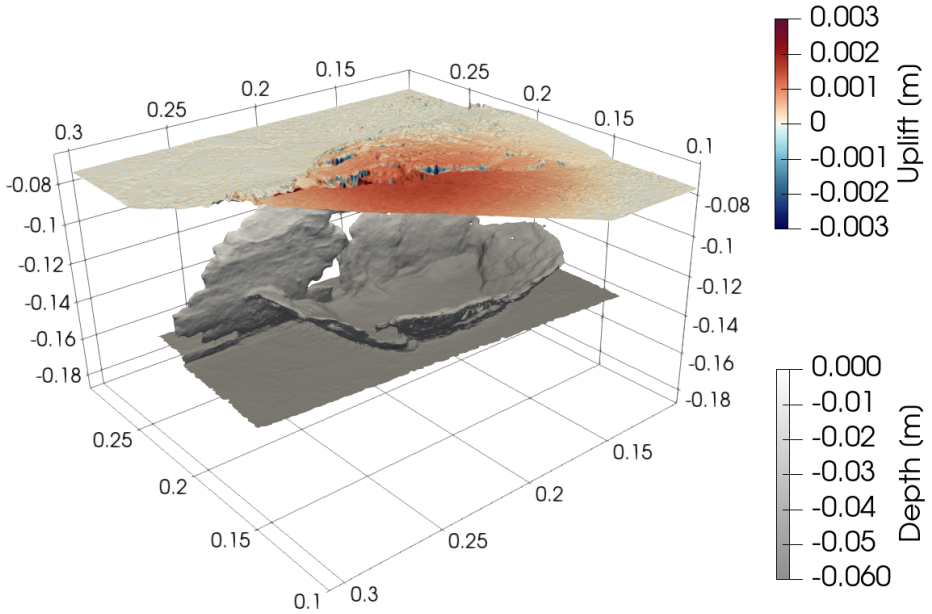

Figure S16: Intrusion of OF50/50.

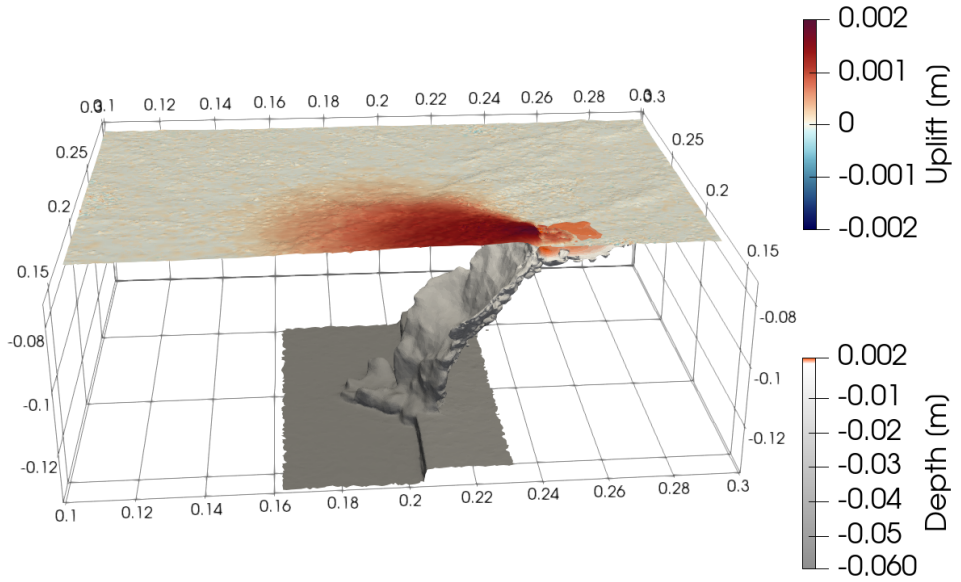

Figure S17: Intrusion of OI80/20.

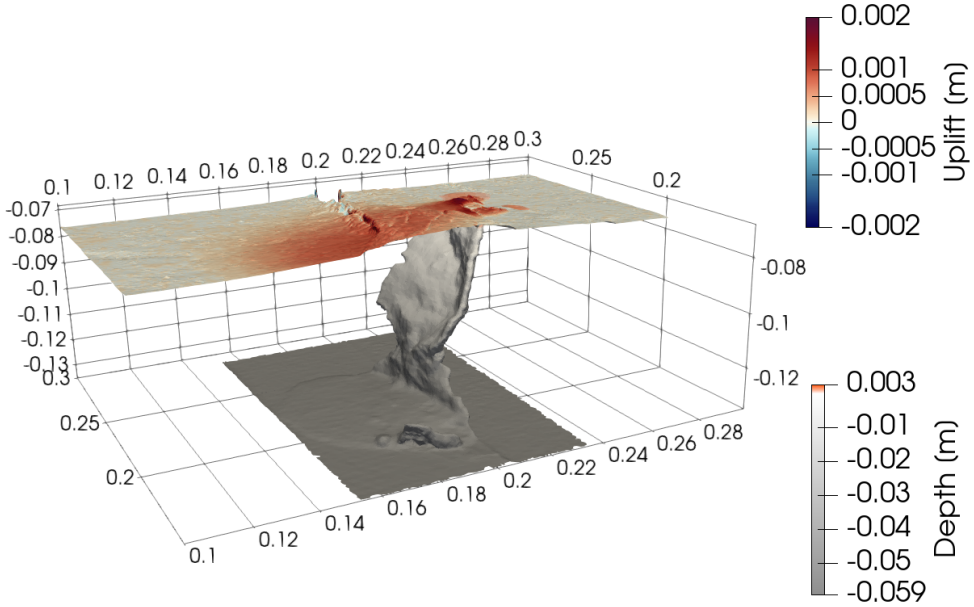

Figure S18: Intrusion of OF80/20.

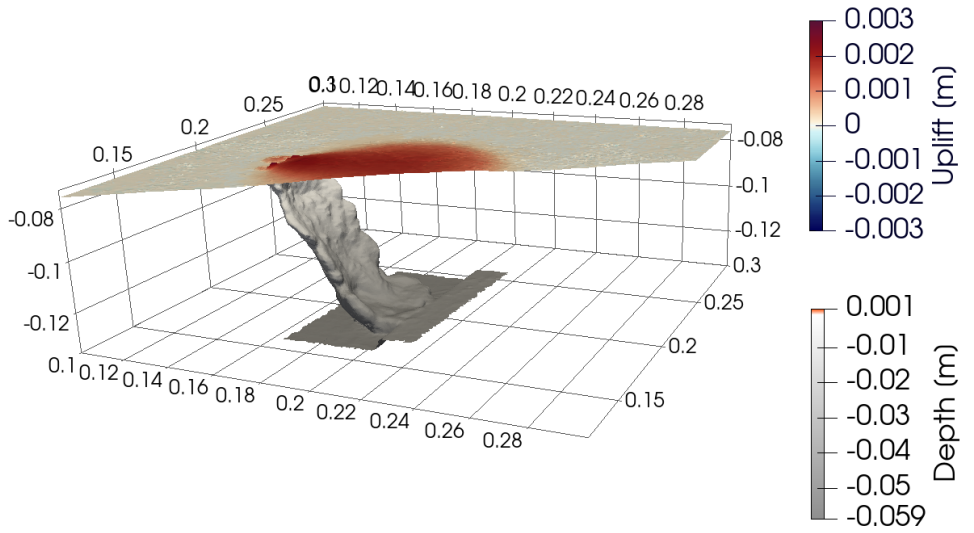

Figure S19: Intrusion of OI90/10.

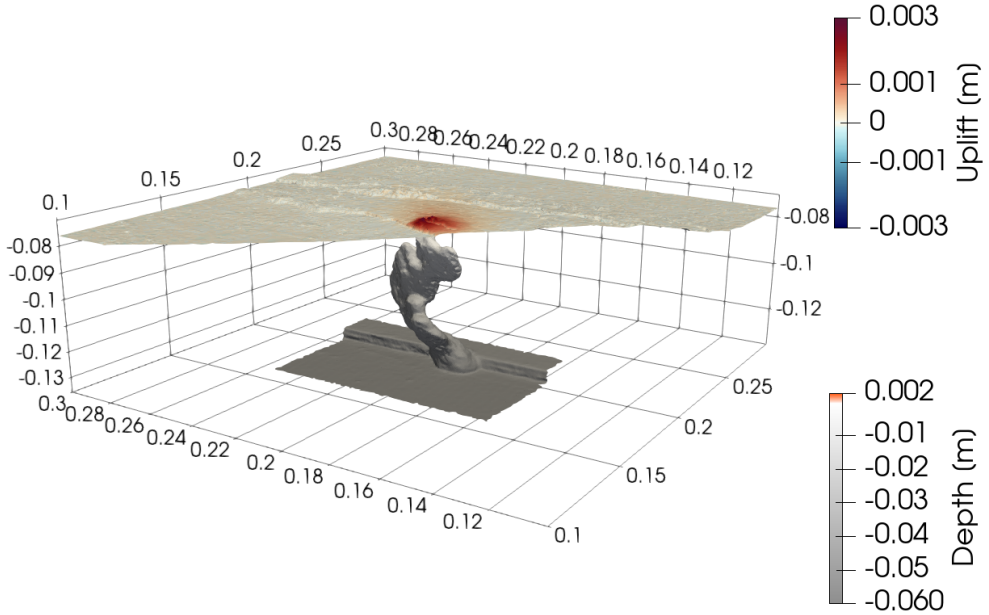

Figure S20: Intrusion of OF90/10.

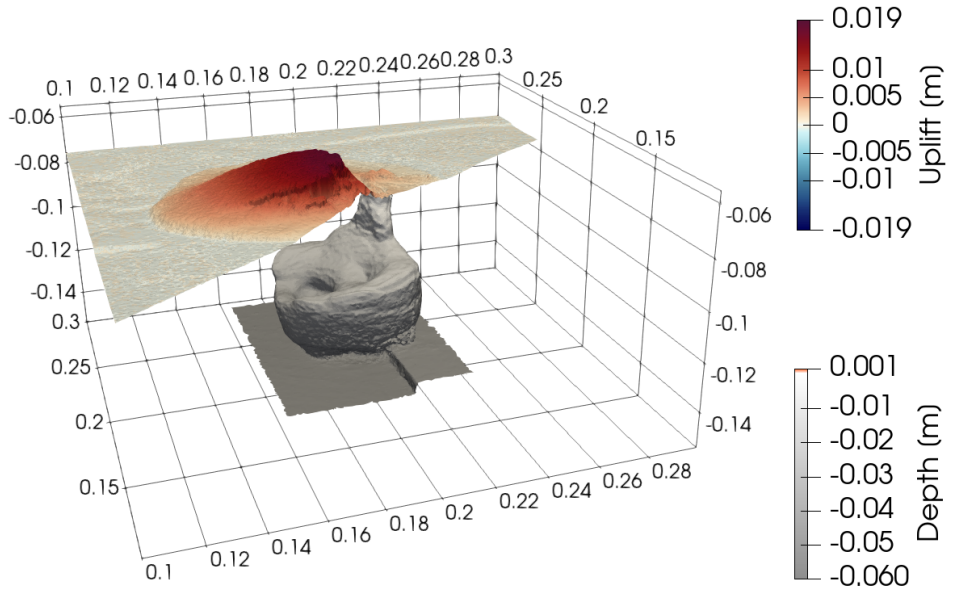

Figure S21: Intrusion of OI95/05.

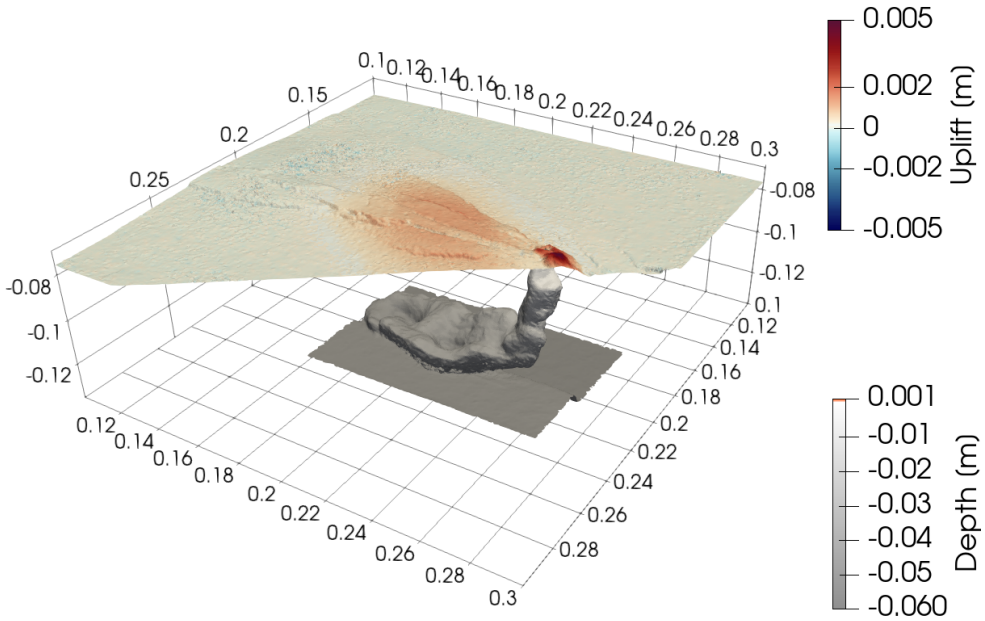

Figure S22: Intrusion of OF95/05.

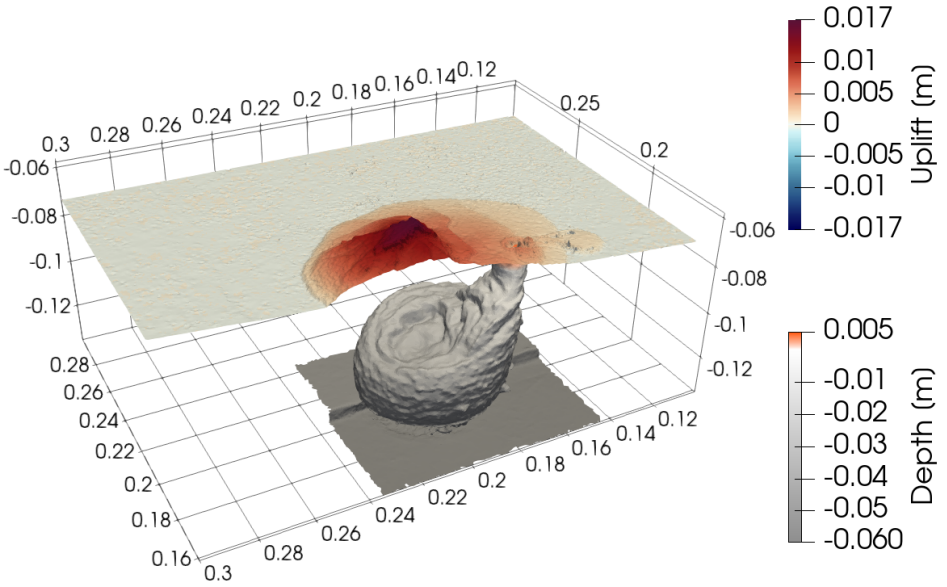

Figure S23: Intrusion of OI100/00.

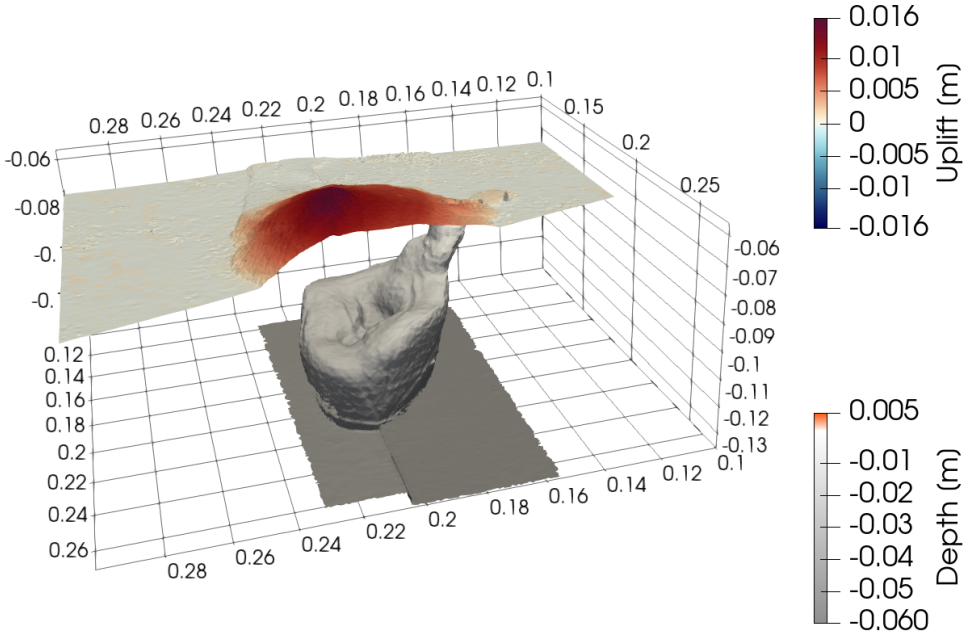

Figure S24: Intrusion of OF100/0.

References

Abdelmalak, M.M., C. Bulois, R. Mourgues, O. Galland, J.-B. Legland, and C. Gruber. "Description of new dry granular materials of variable cohesion and friction coefficient: Implications for laboratory modeling of the brittle crust". In: *Tectonophysics* 684 (2016). Special Issue on GeoMod 2014 – Modelling in Geoscience, pp. 39–51. ISSN: 0040-1951. DOI: https://doi.org/10.1016/j.tecto.2016.03.003. URL: https://www.sciencedirect.com/science/article/pii/S0040195116001591.

Buckingham, E. "On Physically Similar Systems; Illustrations of the Use of Dimensional Equations". In: *Phys. Rev.* 4 (4 1914), pp. 345–376. DOI: 10.1103/PhysRev.4.345. URL: https://link.aps.org/doi/10.1103/PhysRev.4.345.

Bunger, A. P. and A. R. Cruden. "Modeling the growth of laccoliths and large mafic sills: Role of magma body forces". In: *Journal of Geophysical Research: Solid Earth* 116.B2 (2011). DOI: https://doi.org/10.1029/2010JB007648. URL: https://agupubs.onlinelibrary.wiley.com/doi/abs/10.1029/2010JB007648.

Carpenter, B.M., D.M. Saffer, and C. Marone. "Frictional properties and sliding stability of the San Andreas fault from deep drill core". In: *Geology* 40.8 (Aug. 2012), pp. 759–762. ISSN: 0091-7613. DOI: 10.1130/G33007.1. eprint: https://pubs.geoscienceworld.org/gsa/geology/article-pdf/40/8/759/3543748/759.pdf. URL: https://doi.org/10.1130/G33007.1.

Clemens, J.D. and C.K. Mawer. "Granitic magma transport by fracture propagation". In: *Tectonophysics* 204.3 (1992), pp. 339–360. ISSN: 0040-1951. DOI: https://doi.org/10.1016/0040-1951(92)90316-X. URL: https://www.sciencedirect.com/science/article/pii/004019519290316X.

Galland, O. "Experimental modelling of ground deformation associated with shallow magma intrusions". In: *Earth and Planetary Science Letters* 317-318 (2012), pp. 145–156. ISSN: 0012-821X. DOI: https://doi.org/10.1016/j.epsl.2011.10.017. URL: https://www.sciencedirect.com/science/article/pii/S0012821X11006121.

Galland, O., S. Burchardt, E. Hallot, R. Mourgues, and C. Bulois. "Dynamics of dikes versus cone sheets in volcanic systems". In: *Journal of Geophysical Research: Solid Earth* 119.8 (2014), pp. 6178–6192. DOI: https://doi.org/10.1002/2014JB011059. eprint: https://agupubs.onlinelibrary.wiley.com/doi/pdf/10.1002/2014JB011059. URL: https://agupubs.onlinelibrary.wiley.com/doi/abs/10.1002/2014JB011059.

Galland, O., P. R. Cobbold, E. Hallot, J. de Bremond d'Ars, and G. Delavaud. "Use of vegetable oil and silica powder for scale modelling of magmatic intrusion in a deforming brittle crust". In: *Earth and Planetary Science Letters* 243.3 (2006), pp. 786–804. ISSN: 0012-821X. DOI: https://doi.org/10.1016/j.epsl.2006.01.014. URL: https://www.sciencedirect.com/science/article/pii/S0012821X06000276.

551 Galland, O., E. Holohan, B. Van Wyk de Vries, and S. Burchardt. "Laboratory
552 modelling of volcano plumbing systems: a review". In: *Physical Geology of*
553 *Shallow Magmatic Systems: Dykes, Sills and Laccoliths* (2018), pp. 147–214.
554 Galland, O., S. Planke, E.-R. Neumann, and A. Malthe-Sørenssen. "Experimen-
555 tal modelling of shallow magma emplacement: Application to saucer-shaped
556 intrusions". In: *Earth and Planetary Science Letters* 277.3 (2009), pp. 373–
557 383. DOI: https://doi.org/10.1016/j.epsl.2008.11.003. URL: https:
558 //www.sciencedirect.com/science/article/pii/S0012821X08007073.
559 Gibbings, J. C. *Dimensional analysis*. Springer Science & Business Media, 2011.
560 DOI: https://doi.org/10.1007/978-1-84996-317-6.
561 Gonnermann, H. M. "Magma Fragmentation". In: *Annual Review of Earth and*
562 *Planetary Sciences* 43.1 (2015), pp. 431–458. DOI: 10.1146/annurev-earth-
563 060614-105206. eprint: https://doi.org/10.1146/annurev-earth-
564 060614-105206. URL: https://doi.org/10.1146/annurev-earth-060614-
565 105206.
566 Hogan, J. P., J. D. Price, and M. C. Gilbert. "Magma traps and driving pressure:
567 consequences for pluton shape and emplacement in an extensional regime".
568 In: *Journal of Structural Geology* 20.9 (1998), pp. 1155–1168. DOI: https:
569 //doi.org/10.1016/S0191-8141(98)00063-7. URL: https://www.
570 sciencedirect.com/science/article/pii/S0191814198000637.
571 Ikari, M. J., J. Kameda, D. M. Saffer, and A. J. Kopf. "Strength characteristics
572 of Japan Trench borehole samples in the high-slip region of the 2011 Tohoku-
573 Oki earthquake". In: *Earth and Planetary Science Letters* 412 (2015), pp. 35–
574 41. ISSN: 0012-821X. DOI: https://doi.org/10.1016/j.epsl.2014.
575 12.014. URL: https://www.sciencedirect.com/science/article/pii/
576 S0012821X14007675.
577 Karam, M. and T. Saad. "BuckinghamPy: A Python software for dimensional
578 analysis". In: *SoftwareX* 16 (2021), p. 100851. ISSN: 2352-7110. DOI: https:
579 //doi.org/10.1016/j.softx.2021.100851. URL: https://www.sciencedi
580 rect.com/science/article/pii/S2352711021001291.
581 Lesher, C. E. and F. J. Spera. "Chapter 5 - Thermodynamic and Transport
582 Properties of Silicate Melts and Magma". In: *The Encyclopedia of Volca-*
583 *noes (Second Edition)*. Ed. by H. Sigurdsson. Second Edition. Amsterdam:
584 Academic Press, 2015, pp. 113–141. ISBN: 978-0-12-385938-9. DOI: https:
585 //doi.org/10.1016/B978-0-12-385938-9.00005-5. URL: https://www.
586 sciencedirect.com/science/article/pii/B9780123859389000055.
587 Merle, O. "The scaling of experiments on volcanic systems". In: *Frontiers in Earth*
588 *Science* 3 (2015), p. 26. DOI: https://doi.org/10.3389/feart.2015.00026.
589 Merle, O. and A. Borgia. "Scaled experiments of volcanic spreading". In: *Journal*
590 *of Geophysical Research: Solid Earth* 101.B6 (1996), pp. 13805–13817. DOI:
591 https://doi.org/10.1029/95JB03736. URL: https://agupubs.onlinelib
592 rary.wiley.com/doi/abs/10.1029/95JB03736.
593 Michaut, C. "Dynamics of magmatic intrusions in the upper crust: Theory and
594 applications to laccoliths on Earth and the Moon". In: *Journal of Geophysical*
595 *Research: Solid Earth* 116.B5 (2011). DOI: https://doi.org/10.1029/

2010JB008108. URL: https://agupubs.onlinelibrary.wiley.com/doi/abs/10.1029/2010JB008108.

Peltier, A., V. Ferrazzini, T. Staudacher, and P. Bachèlery. "Imaging the dynamics of dyke propagation prior to the 2000–2003 flank eruptions at Piton de La Fournaise, Reunion Island". In: *Geophysical Research Letters* 32.22 (2005). DOI: https://doi.org/10.1029/2005GL023720. eprint: https://agupubs.onlinelibrary.wiley.com/doi/pdf/10.1029/2005GL023720. URL: https://agupubs.onlinelibrary.wiley.com/doi/abs/10.1029/2005GL023720.

Poppe, S., E. P. Holohan, M. Rudolf, M. Rosenau, O. Galland, A. Delcamp, and Matthieu K. "Mechanical properties of quartz sand and gypsum powder (plaster) mixtures: Implications for laboratory model analogues for the Earth's upper crust". In: *Tectonophysics* 814 (2021), p. 228976. ISSN: 0040-1951. DOI: https://doi.org/10.1016/j.tecto.2021.228976. URL: https://www.sciencedirect.com/science/article/pii/S0040195121002584.

Poppe, S., E. P. Holohan, M. Rudolf, M. Rosenau, O. Galland, A. Delcamp, G. Van Gompel, N. Buls, B. Soens, A. Pohlenz, R. Mourgues, and M. Kervyn. "Mechanical test data of quartz sand, garnet sand, gypsum powder (plaster), kaolin and sand-plaster mixtures used as granular analogue materials in geoscience laboratory experiments". In: (2021).

Schellart, W.P. "Shear test results for cohesion and friction coefficients for different granular materials: scaling implications for their usage in analogue modelling". In: *Tectonophysics* 324.1 (2000), pp. 1–16. ISSN: 0040-1951. DOI: https://doi.org/10.1016/S0040-1951(00)00111-6. URL: https://www.sciencedirect.com/science/article/pii/S0040195100001116.

Schmiedel, T., O. Galland, and C. Breitkreuz. "Dynamics of Sill and Laccolith Emplacement in the Brittle Crust: Role of Host Rock Strength and Deformation Mode". In: *Journal of Geophysical Research: Solid Earth* 122.11 (2017), pp. 8860–8871. DOI: https://doi.org/10.1002/2017JB014468. URL: https://agupubs.onlinelibrary.wiley.com/doi/abs/10.1002/2017JB014468.

Schultz, RA2233126. "Limits on strength and deformation properties of jointed basaltic rock masses". In: *Rock Mechanics and Rock Engineering* 28 (1995), pp. 1–15. DOI: https://doi.org/10.1007/BF01024770.

Sigmundsson, F., M. Parks, A. Hooper, H. Geirsson, K. S. Vogfjörd, V. Drouin, B. G. Ófeigsson, S. Hreinsdóttir, S. Hjaltadóttir, K. Jónsdóttir, P. Einarsson, S. Barsotti, J. Horálek, and Th. Ágústsdóttir. "Deformation and seismicity decline before the 2021 Fagradalsfjall eruption". In: *Nature* 609.7927 (2022), pp. 523–528. DOI: https://doi.org/10.1038/s41586-022-05083-4. URL: https://doi.org/10.1038/s41586-022-05083-4.

Spence, D. A. and D. L. Turcotte. "Magma-driven propagation of cracks". In: *Journal of Geophysical Research: Solid Earth* 90.B1 (1985), pp. 575–580. DOI: https://doi.org/10.1029/JB090iB01p00575. eprint: https://agupubs.onlinelibrary.wiley.com/doi/pdf/10.1029/JB090iB01p00575. URL: https://agupubs.onlinelibrary.wiley.com/doi/abs/10.1029/JB090iB01p00575.

Spera, Frank J. "Chapter 7. Aspects of Magma Transport". In: *Physics of Magmatic Processes*. Princeton: Princeton University Press, 1980, pp. 265–324.

642 ISBN: 9781400854493. DOI: doi:10.1515/9781400854493.265. URL: https:
643 //doi.org/10.1515/9781400854493.265.
644 Stinton, A., R. S. J. Sparks, and H. E. Huppert. "Analysis of magma rheology
645 from lava spreading and explosive activity during the 2020–21 eruption of La
646 Soufrière, St Vincent, with implications for eruption dynamics". In: *Geological*
647 *Society, London, Special Publications* 539.1 (2024), pp. 153–169. DOI: 10.
648 1144/SP539-2022-284. eprint: https://www.lyellcollection.org/doi/
649 pdf/10.1144/SP539-2022-284. URL: https://www.lyellcollection.org/
650 doi/abs/10.1144/SP539-2022-284.
651 Thompson, N., R. J. Watters, and P. Schiffman. "Stability analysis of Hawaiian
652 Island flanks using insight gained from strength testing of the HSDP core".
653 In: *Journal of Volcanology and Geothermal Research* 171.3 (2008), pp. 163–
654 177. ISSN: 0377-0273. DOI: https://doi.org/10.1016/j.jvolgeores.2007.
655 11.008. URL: https://www.sciencedirect.com/science/article/pii/
656 S0377027307003678.
657 Thorey, C. and C. Michaut. "Elastic-plated gravity currents with a temperature-
658 dependent viscosity". In: *Journal of Fluid Mechanics* 805 (2016), 88–117. DOI:
659 10.1017/jfm.2016.538.
660 Turcotte, D. L. and G. Schubert. *Geodynamics*. 3rd. Cambridge University Press,
661 2014, p. 575.



Paper III

Tectonic stress as the driving mechanism for dike opening in an oblique rift setting: A deformation model of the 2021 Fagradalsfjall dike, Iceland

Sonja H. M. Greiner, Freysteinn Sigmundsson, Halldór Geirsson, Steffi Burchardt, Olivier Galland,

Geophysical Research Letters, 52, e2024GL113970

doi: https://doi.org/10.1029/2024GL113970

Status: In press. (2025)

Tectonic stress as the driving mechanism for dike opening in an oblique rift setting: A deformation model of the 2021 Fagradalsfjall dike, Iceland

Sonja H. M. Greiner [1,2,3], Freysteinn Sigmundsson [1], Halldór Geirsson [1], Steffi Burchardt[2,3], Olivier Galland [4]

[1]Nordic Volcanological Center, Institute of Earth Sciences, University of Iceland, Reykjavík, Iceland
[2]Department of Earth Sciences, Uppsala University, Uppsala, Sweden
[3]Center for Natural Hazard and Disaster Science (CNDS), Sweden
[4]Physics of Geological Processes, the NJORD Center, Department of Geosciences, University of Oslo, Oslo, Norway

Key Points:

- We model the interaction between diking and tectonic stress in the oblique rift setting of the Reykjanes Peninsula, Iceland
- Tectonic stress release can explain the 2021 Fagradalsfjall-dike emplacement and associated surface deformation
- Our model of tectonic-driven diking predicts shearing along the dike, and similar surface deformation as magma overpressure-driven models

Corresponding author: Sonja H. M. Greiner, shmgreiner@hi.is

Abstract

Repeated dike-intrusions often occur in zones where extensional stress has accumulated. Still, geodetic modelling of observed dike-induced ground deformation often ignores the contribution of tectonic stress. On the obliquely-spreading Reykjanes Peninsula, Iceland, tectonic strain build-up had been geodetically documented for three decades when a magmatic dike formed at Fagradalsfjall in 2021. We explore the contribution of tectonic stress on dike emplacement in a viscoelastic three-dimensional Finite-Element deformation model. Tectonic stress accumulation is initially simulated through plate motion, and later partially released by opening of a segmented rectangular dike. We find that surface deformation can be largely reproduced by releasing ∼60% of the accumulated tectonic stress. Partial stress release and low magma overpressure are consistent with successive dike intrusions and low-intensity eruptions in the area. Our model provides an approach to consistently model stress-release constrained by surface deformation.

Plain Language Summary

In areas where two tectonic plates move apart, tension builds up in the Earth's crust, which can be relaxed by the repeated formation of magma-filled cracks. Although it is well known that stress influences the way in which magma moves through the Earth's crust, this is rarely taken into account in models. In 2021 a magma-filled crack formed at Fagradalsfjall on the Reykjanes Peninsula, SW-Iceland. We simulate the tension that built up in the past 800 years and investigate the opening of this crack and how it affected movement of the ground. Our model has two steps: first, tension builds up because of the plates drifting apart, then a part of this tension is released by the opening of a crack resembling the one in Fagradalsfjall. We find that our model predicts ground motion similar to what was measured in 2021 if the crack releases ca. 60% of the built-up tension. Models like this help to understand the complex interplay between plate movements and magma moving through the crust.

1 Introduction

Magmatic dikes are a key mode of magma transport through the Earth's crust (Rivalta et al., 2015; Breitkreuz & Rocchi, 2018; Burchardt, 2018). They are strongly influenced by the governing stress field, mechanical properties of the crust, and pre-existing host rock structures (Anderson, 1951; P. T. Delaney et al., 1986; Krumbholz et al., 2014; Bertelsen et al., 2021; Greiner et al., 2023). Tectonic stress and pre-existing structures such

as faults can affect the orientation and shape of magmatic dikes as well as propagation dynamics, all of which are important when it comes to hazard assessment (Buck et al., 2006; Sigmundsson et al., 2024). Gradual stress/strain accumulation at plate boundaries, punctuated by rapid release, has long been acknowledged (e.g., Reid, 1910). Diking during rifting episodes plays a similar role in the deformation cycle as large earthquakes, i.e. as modes of stress release (e.g., J. R. Delaney et al., 1998).

The Reykjanes Peninsula, SW Iceland (Figure 1a) connects the divergent plate boundary across Iceland to the submarine Reykjanes Ridge (e.g., Einarsson, 2008; Sigmundsson et al., 2020a). Oblique plate spreading locally rotates the principal stresses and strain accumulation has been geodetically documented during past decades (Hreinsdóttir et al., 2001; Clifton & Schlische, 2003; Keiding et al., 2008). Eruptions in en-echelon arranged systems on the peninsula (Figure 1a) occur in phases lasting a few hundred years, followed by non-eruptive periods of 800-1000 years (Sæmundsson et al., 2020). After 800 years since the last eruption on the peninsula, a dike formed at Fagradalsfjall (Figure 1b) in February–March 2021, preceeding an eruption (Sigmundsson et al., 2022). Since then, repeated eruptions occurred and more than ten dikes have formed in two volcanic systems (Parks et al., 2023; Sigmundsson et al., 2024; Geirsson et al., 2024). As intruding dikes successively release tectonic stress, the importance of magmatic overpressure may increases, which affects the likelihood of magma reaching the surface (Buck et al., 2006).

Ground deformation provides insights into subsurface magmatic processes. Most dike-induced surface deformation models fall into two categories: 1) kinematically driven models with uniform or distributed opening/shearing (Okada, 1985; Amelung et al., 2000; Montgomery-Brown et al., 2010; Sigmundsson et al., 2022) and 2) traction-based models, where the intrusion opens due to pre-stress on the dike plane (Fukushima et al., 2005; Yun et al., 2006; Hooper et al., 2011; Currenti et al., 2011; Heimisson & Segall, 2020). While low computation times make the first group especially valuable during volcanic unrest, they require simplifications regarding the intrusion and surrounding crust (Masterlark, 2007; Pascal et al., 2013). In contrast, traction-driven models using the Boundary Element Method or the Finite-Element Method (FEM) can consider uniform or variable material properties and stress along the dike due to e.g., magmatic overpressure, magma buoyancy or tectonics (Heimisson & Segall, 2020; Hooper et al., 2011; Currenti et al., 2011).

We simulate dike opening driven by tectonic stress in a FEM model, which is applied to the magmatic dike that propagated in early 2021 at Fagradalsfjall on the Reykjanes Peninsula. We explore the effect of tectonic stress on dike opening and surface de-

formation, and quantify the stress-release. Centuries of stress buildup since the last eruption and the geodetically well documented pre- and co-diking surface deformation provide an excellent case study and help to evaluate the contribution of tectonic stress relative to magmatic pressure as driving mechanisms in the onset of a rifting episode.

2 Methods

2.1 Tectonic Model

Plate spreading has been well documented on the Reykjanes Peninsula through ground deformation and seismicity for three decades prior to 2021 (Vadon & Sigmundsson, 1997; Hreinsdóttir et al., 2001; Keiding et al., 2008, 2009). This allows to compare modelled pre-diking surface velocities to Global Navigation Satellite System (GNSS) observations.

Our Finite-Element models were implemented using COMSOL Multiphysics version 6.1 (see Supporting Information S2 for modelling approach). Further analysis was done in Matlab. To create a realistic tectonic stress distribution, which considers partial stress relaxation at depth, we implemented a three-dimensional variable Maxwell-viscoelastic rheology. Elastic moduli were calculated from a 1D density model by Sigmundsson et al. (2020b) (Figure 1c) and p-wave velocities by Weir et al. (2001). Weir et al. (2001) estimated a seismic velocity ratio of $v_p/v_s = 1.78$, corresponding to a Poisson's ratio of $\nu = 0.27$. The resulting Young's modulus (Figure 1d) is depth-dependent. The viscosity depends on the temperature and confining pressure, which we set equal to the lithostatic stress. We derived a 3D temperature model from a steady-state heat-transfer model, where we applied a depth-dependent temperature profile (Figure 1e) along the plate boundary axis (constrained by geodetic observations by Michalczewska et al., 2014). Heat was transported through advection and conduction (Supporting Information S3). The derived temperatures were related to the viscosity η based on diffusion creep (Turcotte & Schubert, 2014):

$$\eta = \frac{RTh^2}{24V_a D_0} exp\left(\frac{E_a + pV_a}{RT}\right) \tag{1}$$

We assumed dry conditions for the crust and mantle with the following parameters: activation energy $E_a = 300\,kJ/mol$, activation volume $V_a = 6\,cm^3/mol$, grain size $h = 3\,mm$, frequency factor $D_0 = 10^{-4}\,m^2/s$ (Turcotte & Schubert, 2014; Karato & Wu, 1993; Turner et al., 2017). The lowest values of the viscosity ($\sim 10^{18} Pa\,s$) match estimates derived from glacioisostatic adjustment around Iceland (e.g., Auriac et al., 2013). We define the 10^{21} Pa s isosurface as the base of the elastically deforming crust (Figure 1f). There and at the lateral model edges, horizontal spreading rates based on Savage

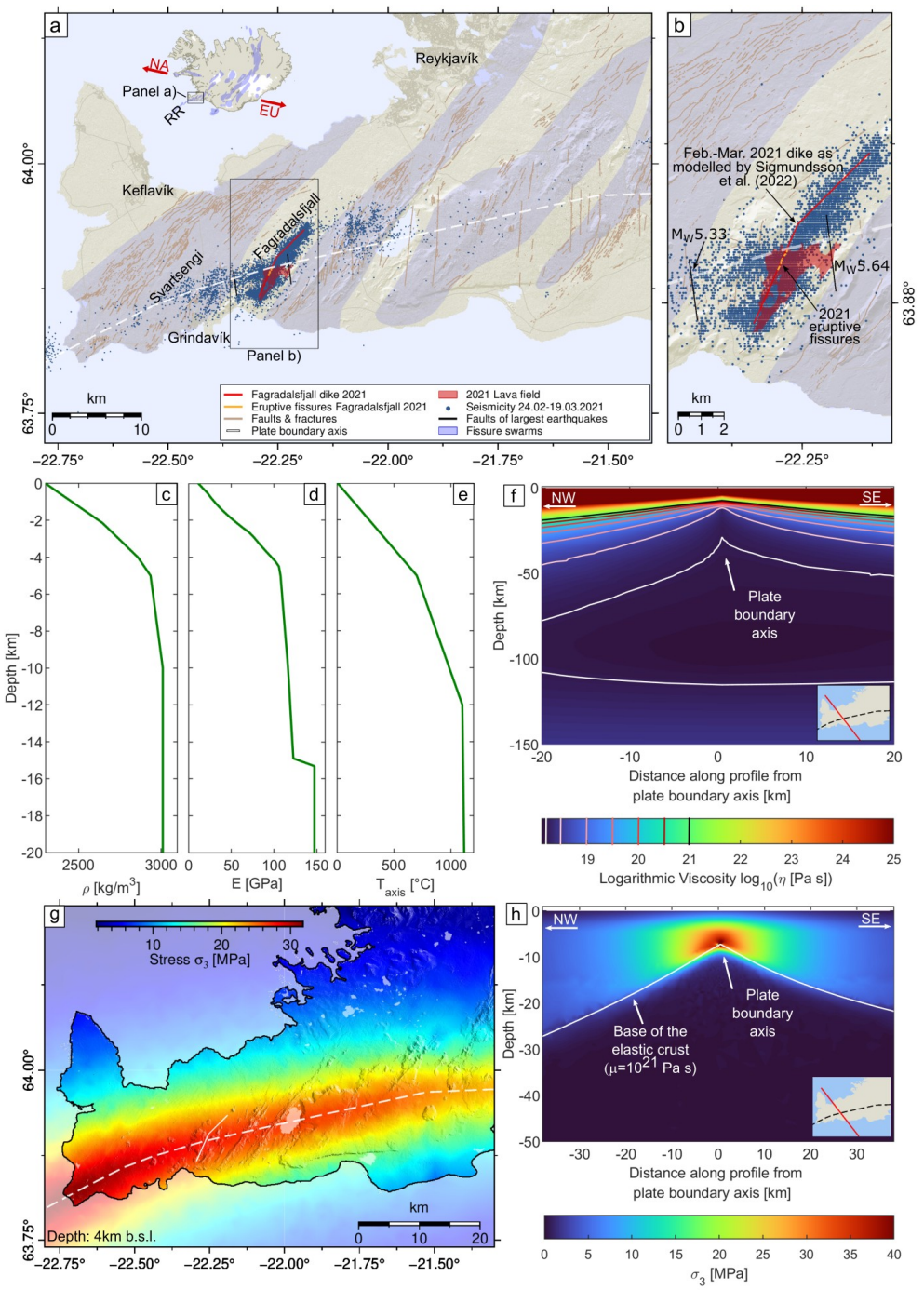

Figure 1. a) The Reykjanes Peninsula in SW-Iceland. Inlet: Volcanic systems across Iceland and the Reykjanes Ridge (RR). b) The surroundings of the Fagradalsfjall volcanic system. Fissure swarms by Jóhannesson and Sæmundsson (2009). Location of the dike and faults of the largest earthquakes by Sigmundsson et al. (2022). Caption continued on the following page.

Figure 1. 2021-lava field and fissure locations by G. B. M. Pedersen et al. (2022) and Hjartardóttir et al. (2023). Seismicity: Icelandic Meteorological Office Earthquake Catalogue (2024); faults/fractures: Clifton and Kattenhorn (2006). Plate boundary axis: Michalczewska et al. (2014). Depth dependent models of c) the density (Sigmundsson et al., 2020b), d) Young's modulus and e) temperature applied to the plate boundary axis (Islam et al., 2016). f) Temperature- and pressure dependent viscosity model along an NW-SE-crosssection (see inlet for location). Color-scale saturated. g) Modelled least compressive stress σ_3 at 4 km depthafter t=800 yrs. Plate boundary axis and eventual dike location in dashed/solid lines. h) Least compressive stress (same cross section as for f) predicted prior to dike emplacement.

and Burford (1973) were applied:

$$u = \frac{u_{full}}{\pi} atan \frac{d}{s} \tag{2}$$

where $u_{full} = 2\,cm/yr$ is the full farfield spreading rate, d the distance from the plate boundary and $s = 7$ km the plate boundary locking depth (Savage & Burford, 1973; Keiding et al., 2008). No vertical motion was allowed along the 10^{21} $Pa\,s$-isoviscous surface. This approach was found to be the only one of several approaches tested that created sufficient focusing of plate boundary deformation to match geodetic observations of plate movements (Supporting Information S6), while allowing for the later implementation of a dike-opening model (see also first paragraph in the Discussion). Plate motion was simulated for 800 years. Although the lithostatic stress affects the viscosity, we did not consider gravity and all stresses are deviatoric. We furthermore neglected other processes, which may affect the local stress field e.g., seismicity, glacio-isostatic adjustment or geothermal processes.

2.2 Dike Model

Dike opening in the stress/strain field created by the tectonic model after 800 years of spreading was simulated by introducing a crack boundary condition on a vertical dike, with two 4.5 km long segments: A northern segment from 1-7 km depth, striking N45°E, and a southern segment from 1-6 km depth, striking N23.5°E. This is a slightly modified version of the dike plane inferred by Sigmundsson et al. (2022) from geodetic observations (Figure 1b). Their model found mostly minor opening in the top kilometer of the crust. We fixed the upper edge of the dike at 1 km depth to ensure our model predicted observed subsidence above it. When compared to their model, the lower edge of our northern segment is 0.5 km shallower so it is not too close to the 10^{21} Pa s isosurface

to prevent unrealistic results. At $t = 800$ years, the crack boundary condition on the dike plane was activated, releasing stress and decoupling displacements on either side of the dike. The dike displacement field was extracted after a time step of 0.1 years, so it is essentially elastic as only insignificant viscous relaxation occurs in the model over that time interval.

Dike opening was driven by tectonic loading, i.e. we did not consider effects of magmatic overpressure (in excess of lithostatic pressure) or buoyancy. The emplacement of additional dikes after 2021 indicates that only a part of the accumulated tectonic stress was released by the first intrusion. We therefore applied a negative pressure condition onto the dike segments to control the released fraction f of the tectonic stress, so that only a part of the tectonic stress was released by the dike. We varied f in 10%-increments to find which value fits the observed data best (Supporting Information S10.1). The negative pressure only affected the component of the stress field oriented normal to the dike planes. We did not consider dynamic propagation of the dike and instead simulated instantaneous opening.

Surface deformation predicted by the dike model was compared to two geodetic data sets by Sigmundsson et al. (2022): GNSS data and a Sentinel-1 interferogram (track T16), after removing the deformation of the two largest earthquakes (Figure 1b and Supporting Information S4). We also compared the dike model to a model driven by uniform magmatic overpressure, which we chose based on minimizing the difference to the stress-driven model.

3 Results

3.1 Tectonic Model

The viscosity model is asymmetric around the plate boundary with higher viscosity deeper to the north compared to south (Figure 1f), caused by the temperature model and curved plate boundary. Thermal energy collects on the southern, concave side of the plate boundary axis due to conductive heat transport, but is dispersed in the northern, convex side (Supporting Figure S2).

Along the peninsula, the least compressive principal stress is largest at the plate boundary axis (Figure 1g, h). It is higher in the western portion of the peninsula and offshore along the Reykjanes Ridge where plate spreading is less oblique (Figure 1g). The modelled least compressive principal stress σ_3 is directed towards ∼N130°E. The part of the model below the 10^{21} $Pa\,s$-isosurface relaxes stress faster than it is accumulated by plate motion (Figure 1h).

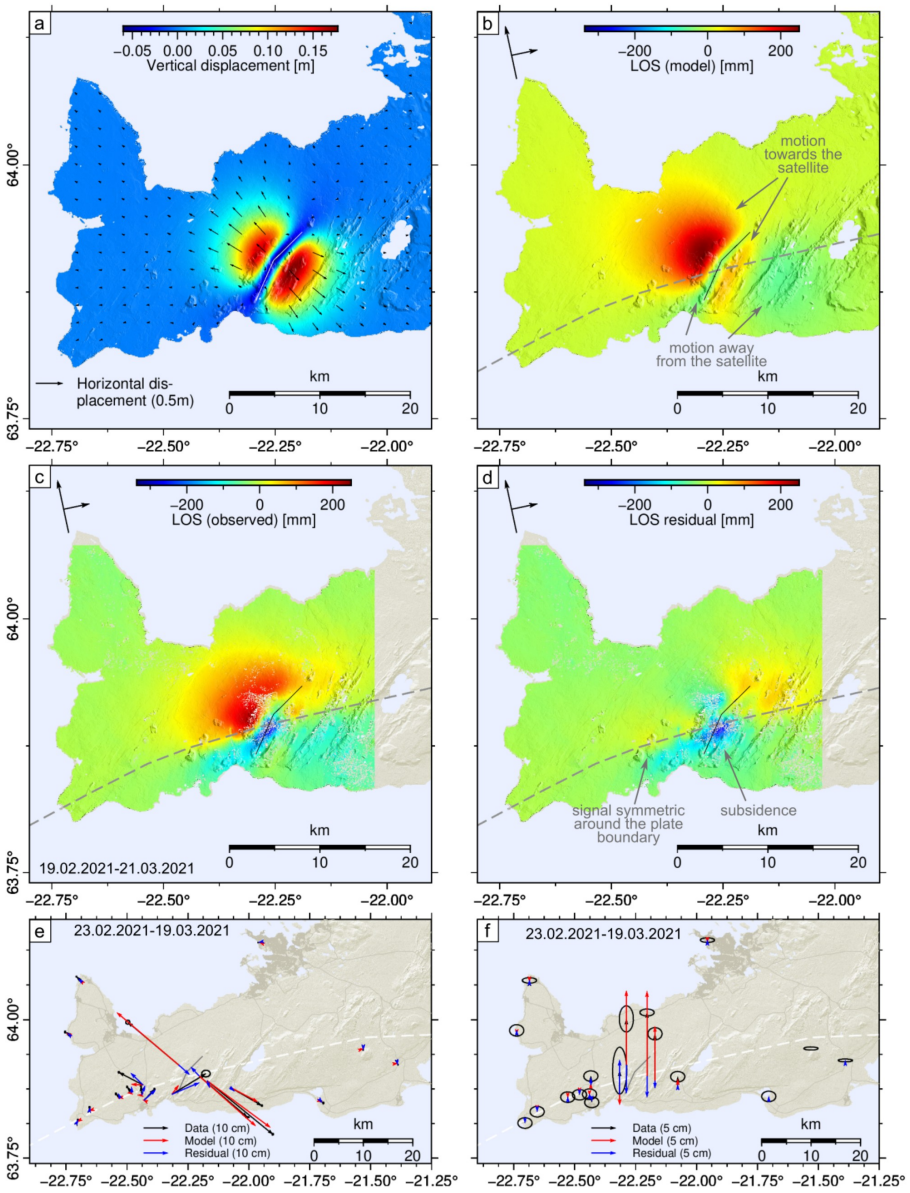

Figure 2. a) Modelled dike-induced surface deformation. Colormap shows vertical motion, arrows indicate horizontal motion. b) Modelled deformation projected onto the Line-of-sight (LOS) of an ascending Sentinel-1 satellite on T16. Black arrows indicate heading and looking direction. c) Observed LOS displacement. d) Residual between observed and modelled LOS displacement. e) and f) Comparison of observed and modelled e) horizontal and f) vertical surface deformation at GNSS benchmarks. Observational data from Sigmundsson et al. (2022).

178 ### 3.2 Dike Model

The observed surface deformation was best reproduced (Figure 2) when $f \sim 60\%$ of the dike-normal component of the tectonic stress were released. The best-fitting value ranges between 40−60% depending on which observational data our model is compared to (Supporting Information S10.1). Modelled deformation shows outward horizontal motion away from the dike, combined with subsidence above the intrusion flanked by uplift (Figure 2a). This pattern is frequently associated with dikes (e.g., Okada, 1985; Sigmundsson et al., 2015). Projection onto the Line-of-sight (LOS) vector of the Sentinel-1 interferogram shows motion towards the satellite northwest of the dike, while the crust above the dike moves away from it (Figure 2b). Southeast of the dike, motion is partially towards and partially away from the satellite. This matches InSAR observations spanning the unrest period and two days into the eruption (Figure 2c). The LOS residual (Figure 2d) shows a subsidence signal above the southern segment. There is also a residual signal symmetric around the plate boundary axis, especially southwest of the dike. This signal locally coincides with observed fault movements during dike emplacement (Supporting Figure S13). Observed horizontal GNSS displacements close to the dike are well reproduced (Figure 2e), but differ in direction and amplitude further west. Vertical deformation is overestimated for nearfield GNSS stations (Figure 2f).

The largest dike opening is predicted at intermediate depths on the northern segment (Figure 3a). This is notably not the location of highest normal stress on the dike (Supporting Figure S10). Shearing occurs along both segments, but has opposing directions and higher amplitude on the southern segment (Figure 3b). The sharp transition between both segments relates to their differing strikes, but motion is continuous across the connection (Figure 3c). Relative displacement is asymmetric across the dike with more shearing occurring on its western side (Figure 3c). At the segment connection, deformation points towards ∼N130°E, which agrees well with the direction of the least compressive principal stress σ_3 predicted by the tectonic model.

Dike opening reduced stress in the vicinity of the intrusion (Figure 3d-e). More stress is released at depth compared to the shallow parts of the dike, which reflects the variable stress of the tectonic model (Figure 1h). In the nearfield, the stress-release is limited to the depth range covered by dike opening. Above and below the dike, stress remains unchanged or increased (shown here as negative release). Due to the angled dike geometry, the stress release around the dike is also asymmetric (Figure 3d-e). Stress is released across a larger area towards the west and around the northern segment, while it is narrower around the southern one (Figure 3d,e). Towards the west, stress is reduced by several MPa until Mt. Stóra-Skógfell, but remains largely unaffected further west. To-

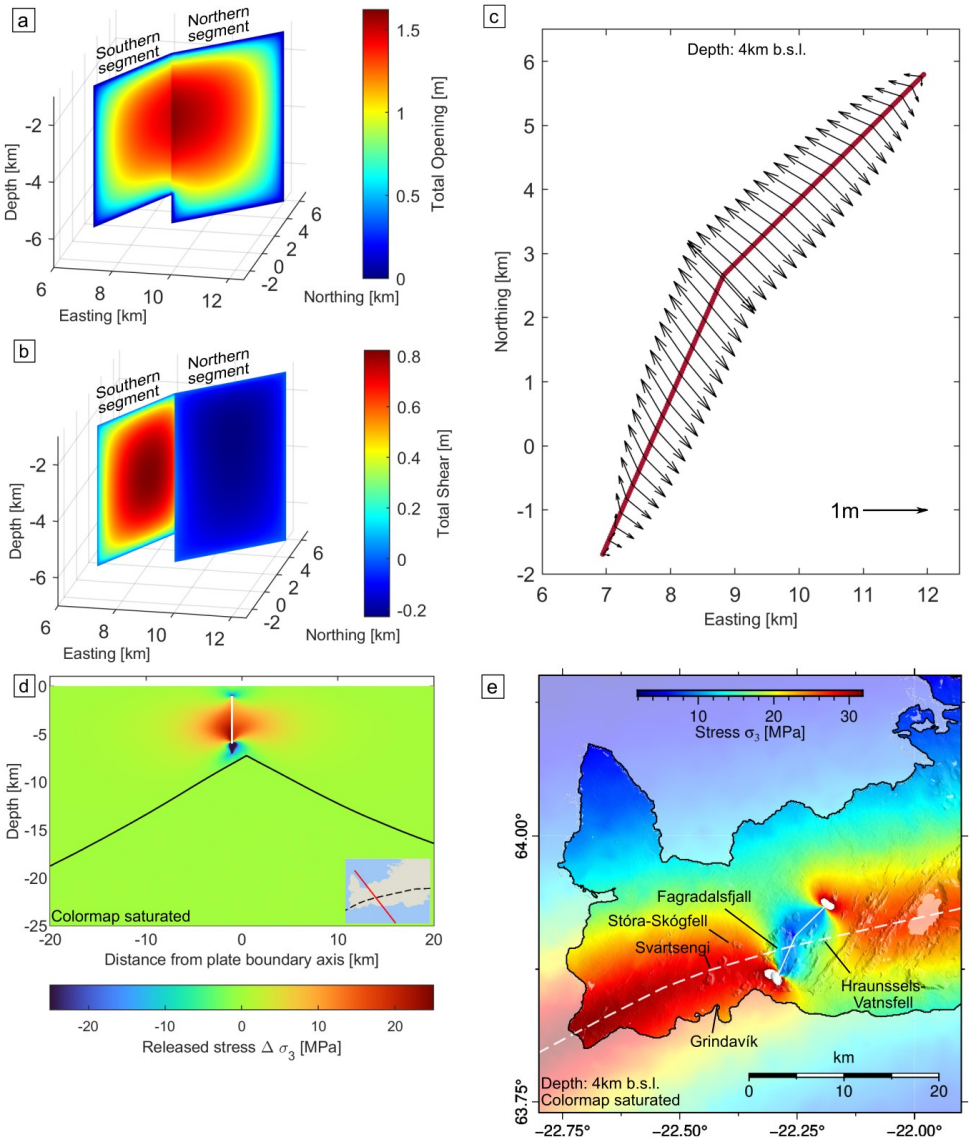

Figure 3. a) Opening and b) shearing along the dike segments. Right-lateral shear shown as positive. c) Directions of motion along the dike at 4 km depth. d) Tensional stress released by dike opening along a ca. N130°E striking cross-section through the center of the dike. e) State of the least compressive stress at 4 km depth after dike opening.

wards the east, stress along the plate boundary axis is reduced significantly until approximately Mt. Hraunssels-Vatnsfell.

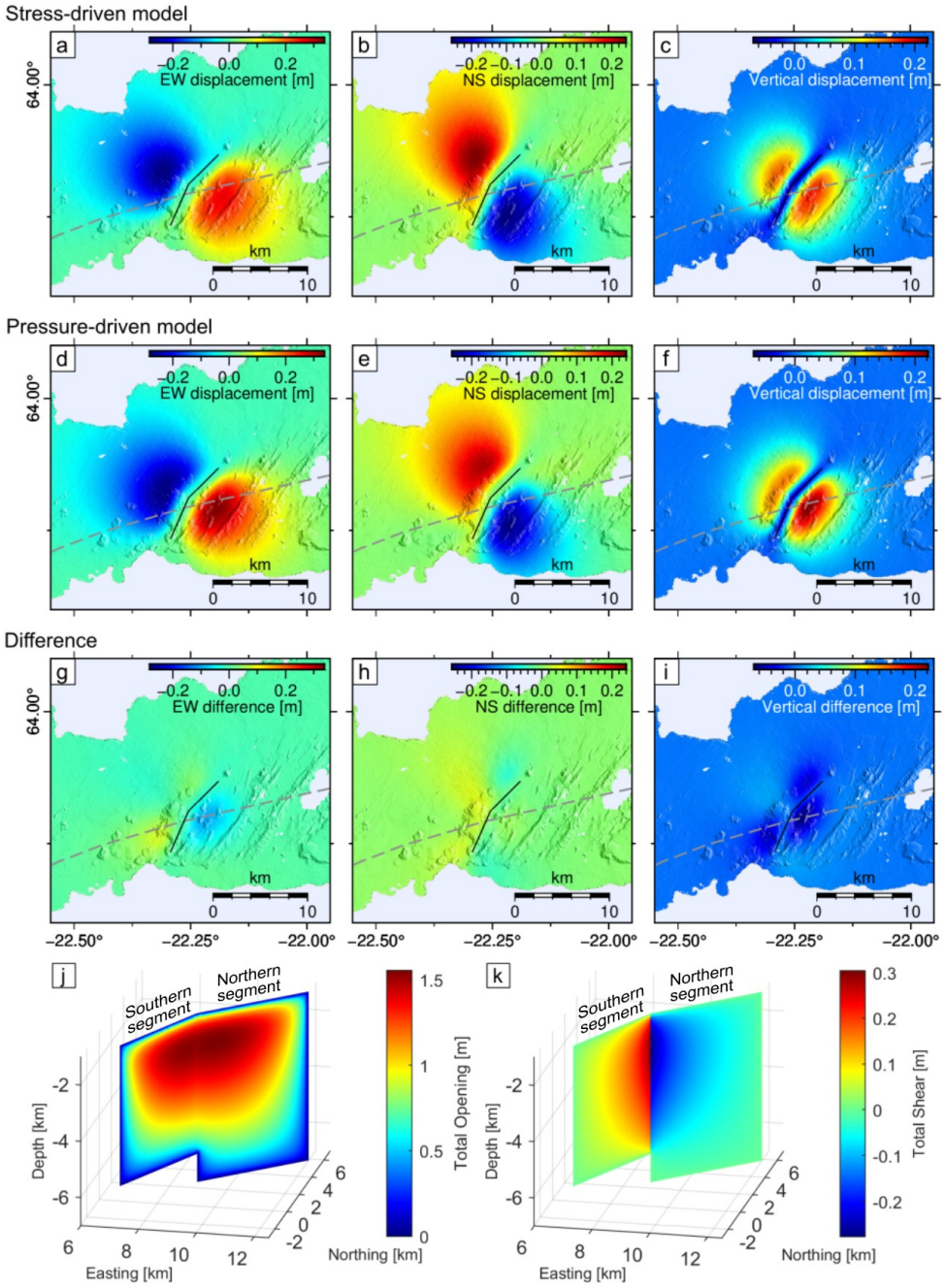

Figure 4. a) East-West, b) North-South and c) vertical surface displacement of the dike model, in which opening is driven by tectonic stresses. d)- f) Same as a)-c), but for a dike driven by uniform overpressure of 12 MPa without tectonic stresses. g)-i) Associated differences. j) Opening and k) shear on the dike plane for the pressure-driven dike.

3.3 Pressure-driven Dike Opening

The pattern and amplitude of surface deformation are similar between models driven by tectonic stress and uniform overpressure of 12 MPa (Figure 4a-f). The main difference is shear in the N-S component (Figure 4h, Supporting Figure S14). Uplift west of the dike is more elongated in the pressure-driven model compared to the stress-driven model (Figure 4c, f).

The largest opening in the pressure-driven model occurs near the top of the dike and is centered around the segment connection (Figure 4j). This differs from the stress-driven model (Figure 3a). The pressure-driven model shows shear close to the segment connectopn (Figure 4k). However, although it has the same sense of motion as the stress-driven model (Figure 3b), the affected area is much smaller for the pressure-driven model, and motion is less than for the stress-driven model and equal for both segments.

4 Discussion

Modelling strain localization in a physically consistent manner rather than forcing it through boundary conditions is generally challenging (e.g., Mulyukova & Bercovici, 2019) and studies on similar spatial dimensions as the present study have used various approaches (van Wijk & Blackman, 2005; R. Pedersen et al., 2009; Turner et al., 2017; Lanzi et al., 2024). We applied a prescribed velocity profile at the base of the elastic crust to localize the plate boundary strain into a narrow region centered on the plate boundary axis. We find that this artificial boundary condition locally affected dike-induced surface deformation by up to 15 mm (Supporting Information S5), which is small compared to observed deformation. Plate spreading and dike emplacement produce very different strain rates and therefore the transition between brittle and ductile deformation likely occurs at larger depths for dikes compared to plate spreading (White et al., 2011; Molnar, 2020, and references therein). Our tectonic model does not account for long-term coseismic stress release (e.g., Árnadóttir et al., 2004; Björnsson et al., 2020), which leads to overestimation of crustal stress by our model. However, this may be partially balanced by our assumption that all tectonic stress had been released during the last rifting episode. Although the 2021 Fagradalsfjall dike formed over three weeks and possibly partially solidified early on while other parts continued to widen, we did not consider thermal effects. Furthermore, we did not consider the density difference between magma and the surrounding crust that may be depth-dependent and can influence dike-pressure conditions.

In our model, the dike released a fraction of the normal component of the tectonic stress, but the entire tangential component. This is consistent with emplacement of three additional dikes at Fagradalsfjall and that geodetic models of these events do not include shear on their planes (Parks et al., 2023; Geirsson et al., 2024). Releasing the entire tangential component also agrees with the idea that once magma spreads in the dike plane, that plane cannot hold shear stress. In contrast, the fraction of released tectonic stress and amount of dike opening are influenced by magma availability. The repeated emplacement of dikes during rifting episodes supports the idea that some dikes release only a fraction of the accumulated tectonic stress (Buck et al., 2006; Hamling et al., 2009; Wright et al., 2012; Parks et al., 2023), while, if enough magma is available, it may be released in a single event (Ruch et al., 2016). It should be noted that the best-fitting fraction of released tectonic stress (∼60% for the present study) depends to some degree on the dike dimensions and the absolute stress before diking (Supporting Information S10).

The stress-driven dike model reproduces first-order features of the observed deformation field. Two remaining signals include left-lateral shear along the plate boundary axis and subsidence around the eventual eruptive fissures (Figure 2d). The residual shear is especially pronounced west of the dike in the area between Svartsengi and Fagradalsfjall. It largely coincides with individual faults that moved during the dike intrusion (Ducrocq et al., 2024)(Supporting Figure S13) and was modelled as slip along the plate boundary segment by Sigmundsson et al. (2022). The subsidence was modelled as a contracting Mogi-source by Sigmundsson et al. (2022), while Hjartardóttir et al. (2023) suggested a combination of opening of the first eruptive fissure and shallow fault motion. Surface deformation near Svartsengi was likely also affected by shallow fault motion.

While our model predicts the largest opening on the northern segment, the geodetic inversion by Sigmundsson et al. (2022) finds maximum opening on the southern segment. However, both models predict similar surface deformation. Their model could have locally overestimated opening due to the contracting point-source, which is located directly above their predicted area of maximum opening. That the eruptive fissures opened above the southern segment could relate to the presence of pre-existing fractures and faults above the southern segment (Einarsson et al., 2023; Hjartardóttir et al., 2023). Sigmundsson et al. (2022) modelled the 2021 dike as a combination of opening and right-lateral shear, while left-lateral shear was only attributed to the plate boundary, resulting in possible tradeoff in shear between the plate boundary and the dike segments. In contrast, in the present study, the dike segments have opposing shear, the direction and amplitudes of which are consistent with expected motion based on the resepective segment strike relative to the principal stress axes (P. T. Delaney et al., 1986; Jolly & Sanderson, 1997).

The maximum compressive principal stress σ_1∼N40°E strikes close to the average of the strike of both segments (N34°E), but closer to the northern one, which strikes N45°E compared to N23.5°E for the southern segment (Supporting Figure S10b).

Overall, observations of the 2021 Fagradalsfjall dike were largely reproduced by our model driven by tectonic stress without requiring magmatic overpressure. A strong contribution of tectonic stress relative to magmatic overpressure is supported for the 2021 eruption by low initial eruptive flow rates (G. B. M. Pedersen et al., 2022). A purely pressure-driven dike can produce a similar deformation field apart from a shearing signal directly above the dike. Such signals may however be difficult to resolve if the dike is accompanied by intense seismicity and near-surface fault motion. Despite similar surface deformation patterns, the modelled opening of the dike plane varies significantly; a reminder of the non-uniqueness of deformation models.

Stress change in a diking event may influence the location of future events. Magmatic activity jumped westwards to Svartsengi in fall 2023 (Sigmundsson et al., 2024), where a major dike injection occurred in a region of slightly increased tensile stress due to the 2021 Fagradalsfjall dike (Figure 3e Supporting Figure S12), as also noted by Birgisdóttir (2023). The stress shadow of the Fagradalsfjall dike east of Stóra-Skógfell may have limited the NE-ward propagation of this dike. In models like the one presented here, stress changes can be directly considered in successive deformation models. As the role of tectonic stress relative to magmatic overpressure changes, the risk of magma reaching the surface in high-discharge eruptions increases (e.g., Buck et al., 2006; Wright et al., 2012).

5 Conclusions

We explored the importance of tectonic stress as a driver for the 2021 Fagradalsfjall dike, using FEM deformation models. Reasonable fits to observations were produced without applying magmatic overpressure, highlighting the importance of tectonic stress for dike propagation. The model suggests that about 60% of the accumulated tectonic stress was released by the dike. Partial release of tectonic stress is supported by the emplacement of three additional dikes between 2021 and 2023. Pressure-driven models can produce similar surface deformation as stress-driven models, differing mainly in shearing signals above the dike, even though deformation in the dike plane can vary significantly. For the stress-driven model, the amount and sense of shear relative to opening in the dike plane are consistent with the local tectonic setting. Our study emphasizes the potential of process-driven deformation models, that allow to directly consider knowledge of the local geology during dike emplacement.

Open Research Section

The surface deformation data (InSAR and GNSS) and source parameters of the 2021 Fagradalsfjall dike and of the two largest earthquakes are from Sigmundsson et al. (2022) and can be accessed in the supporting information of their study. The p-wave velocity model used in the present study was puplished by Weir et al. (2001), the 1D-density-model was published by Sigmundsson et al. (2020b) and the values of the temperature at the plate-boundary axis are found in Islam et al. (2016). Plate spreading velocities from GNSS-measurements are listed in Keiding et al. (2008). The model files created for this study are accessible from Greiner et al. (2025).

Acknowledgments

We thank editor Germán Prieto as well as Roger Buck and an anonymous reviewer for helpful comments that improved the initial manuscript. We thank Nordvulk and Uppsala University for funding SG's PhD. This project was partly supported by the MADRE project (RANNÍS grant no. 228933-051). We also thank Chiara Lanzi for helpful discussions. We are grateful for the computing resources provided by the University of Iceland through the Icelandic Research e-Infrastructure project (IREI). All maps in this manuscript were created in GMT (Wessel et al., 2013).

References

Amelung, F., Jónsson, S., Zebker, H., & Segall, P. (2000). Widespread uplift and 'trapdoor' faulting on Galapagos volcanoes observed with radar interferometry. *Nature*, *407*(6807), 993–996. doi: https://doi.org/10.1038/35039604

Anderson, E. M. (1951). *The dynamics of faulting and dyke formation with applications to Britain* (2nd ed.). Edinburgh, UK: Oliver and Boyd.

Auriac, A., Spaans, K. H., Sigmundsson, F., Hooper, A., Schmidt, P., & Lund, B. (2013). Iceland rising: Solid Earth response to ice retreat inferred from satellite radar interferometry and visocelastic modeling. *Journal of Geophysical Research: Solid Earth*, *118*(4), 1331-1344. Retrieved from `https://agupubs.onlinelibrary.wiley.com/doi/abs/10.1002/jgrb.50082` doi: https://doi.org/10.1002/jgrb.50082

Battaglia, M., Cervelli, P. F., & Murray, J. R. (2013). dMODELS: A MATLAB software package for modeling crustal deformation near active faults and volcanic centers. *Journal of Volcanology and Geothermal Research*, *254*, 1-4. Retrieved from `https://www.sciencedirect.com/science/article/pii/S0377027312003836` doi: https://doi.org/10.1016/j.jvolgeores.2012.12.018

Bertelsen, H. S., Guldstrand, F., Sigmundsson, F., Pedersen, R., Mair, K., & Galland, O. (2021). Beyond elasticity: Are Coulomb properties of the Earth's crust important for volcano geodesy? *Journal of Volcanology and Geothermal Research*, *410*, 107153. Retrieved from https://www.sciencedirect.com/science/article/pii/S0377027320305898 doi: https://doi.org/10.1016/j.jvolgeores.2020.107153

Birgisdóttir, Á. G. (2023). Coulomb stress changes on the Reykjanes Peninsula from 1998-2022 and earthquake triggering. Retrieved from http://hdl.handle.net/1946/44537 (BS thesis; University of Iceland)

Björnsson, S., Einarsson, P., Tulinius, H., & Hjartardóttir, Á. R. (2020). Seismicity of the Reykjanes Peninsula 1971–1976. *Journal of Volcanology and Geothermal Research*, *391*, 106369. Retrieved from https://www.sciencedirect.com/science/article/pii/S0377027317306315 doi: https://doi.org/10.1016/j.jvolgeores.2018.04.026

Breitkreuz, C., & Rocchi, S. (2018). *Physical geology of shallow magmatic systems — Dykes, sills and laccoliths* [Edited Book]. Springer Berlin Heidelberg. doi: https://doi.org/10.1007/978-3-319-14084-1

Buck, W. R., Einarsson, P., & Brandsdóttir, B. (2006). Tectonic stress and magma chamber size as controls on dike propagation: Constraints from the 1975–1984 Krafla rifting episode. *Journal of Geophysical Research: Solid Earth*, *111*(B12). Retrieved from https://agupubs.onlinelibrary.wiley.com/doi/abs/10.1029/2005JB003879 doi: https://doi.org/10.1029/2005JB003879

Burchardt, S. (2018). *Volcanic and Igneous Plumbing Systems: Understanding Magma Transport, Storage, and Evolution in the Earth's Crust*. Elsevier.

Caracciolo, A., Bali, E., Halldórsson, S., Gudfinnsson, G., Kahl, M., Thórdardóttir, I., ... Silvestri, V. (2023). Magma plumbing architectures and timescales of magmatic processes during historical magmatism on the Reykjanes Peninsula, Iceland. *Earth and Planetary Science Letters*, *621*, 118378. Retrieved from https://www.sciencedirect.com/science/article/pii/S0012821X23003916 doi: https://doi.org/10.1016/j.epsl.2023.118378

Clifton, A. E., & Kattenhorn, S. A. (2006). Structural architecture of a highly oblique divergent plate boundary segment. *Tectonophysics*, *419*(1), 27-40. Retrieved from https://www.sciencedirect.com/science/article/pii/S0040195106001673 doi: https://doi.org/10.1016/j.tecto.2006.03.016

Clifton, A. E., & Schlische, R. W. (2003). Fracture populations on the Reykjanes Peninsula, Iceland: Comparison with experimental clay models of oblique rifting. *Journal of Geophysical Research: Solid Earth*, *108*(B2). Retrieved

391 from https://agupubs.onlinelibrary.wiley.com/doi/abs/10.1029/
392 2001JB000635 doi: https://doi.org/10.1029/2001JB000635
393 Currenti, G., Napoli, R., Di Stefano, A., Greco, F., & Del Negro, C. (2011). 3D
394 integrated geophysical modeling for the 2008 magma intrusion at Etna: Con-
395 straints on rheology and dike overpressure. *Physics of the Earth and Planetary*
396 *Interiors*, *185*(1), 44-52. Retrieved from https://www.sciencedirect.com/
397 science/article/pii/S0031920111000124 doi: https://doi.org/10.1016/
398 j.pepi.2011.01.002
399 Delaney, J. R., Kelley, D. S., Lilley, M. D., Butterfield, D. A., Baross, J. A.,
400 Wilcock, W. S. D., ... Summit, M. (1998). The quantum event of oceanic
401 crustal accretion: Impacts of diking at mid-ocean ridges. *Science*, *281*(5374),
402 222-230. Retrieved from https://www.science.org/doi/abs/10.1126/
403 science.281.5374.222 doi: 10.1126/science.281.5374.222
404 Delaney, P. T., Pollard, D. D., Ziony, J. I., & McKee, E. H. (1986). Field re-
405 lations between dikes and joints: Emplacement processes and paleostress
406 analysis. *Journal of Geophysical Research: Solid Earth*, *91*(B5), 4920-4938.
407 Retrieved from https://agupubs.onlinelibrary.wiley.com/doi/abs/
408 10.1029/JB091iB05p04920 doi: https://doi.org/10.1029/JB091iB05p04920
409 Drouin, V., & Sigmundsson, F. (2019). Countrywide Observations of Plate Spread-
410 ing and Glacial Isostatic Adjustment in Iceland Inferred by Sentinel-1 Radar
411 Interferometry, 2015–2018. *Geophysical Research Letters*, *46*(14), 8046-8055.
412 Retrieved from https://agupubs.onlinelibrary.wiley.com/doi/abs/
413 10.1029/2019GL082629 doi: https://doi.org/10.1029/2019GL082629
414 Ducrocq, C., Árnadóttir, T., Einarsson, P., Jónsson, S., Drouin, V., Geirsson, H.,
415 & Hjartardóttir, Á. R. (2024). Widespread fracture movements during
416 a volcano-tectonic unrest: the Reykjanes Peninsula, Iceland, from 2019–
417 2021 TerraSAR-X interferometry. *Bulletin of Volcanology*, *86*(2), 14. doi:
418 https://doi.org/10.1007/s00445-023-01699-0
419 Ducrocq, C., Árnadóttir, T., Einarsson, P., Jónsson, S., Drouin, V., Geirsson,
420 H., & Hjartardóttir, Á. R. (2023). *Additional material for the article*
421 *"Widespread fracture movements during a volcano-tectonic unrest: the Reyk-*
422 *janes Peninsula, Iceland, from 2019–2021 TerraSAR-X interferometry".* Zen-
423 odo. Retrieved from https://doi.org/10.5281/zenodo.10433761 doi:
424 10.5281/zenodo.10433761
425 Einarsson, P. (2008). Plate boundaries, rifts and transforms in Iceland. *Jökull*, *58*,
426 35-58.
427 Einarsson, P., Eyjólfsson, V., & Hjartardóttir, Á. R. (2023). Tectonic frame-

work and fault structures in the Fagradalsfjall segment of the Reykjanes Peninsula Oblique Rift, Iceland. *Bulletin of Volcanology*, *85*(2), 9. doi: https://doi.org/10.1007/s00445-022-01624-x

Fukushima, Y., Cayol, V., & Durand, P. (2005). Finding realistic dike models from interferometric synthetic aperture radar data: The february 2000 eruption at piton de la fournaise. *Journal of Geophysical Research: Solid Earth*, *110*(B3). Retrieved from `https://agupubs.onlinelibrary.wiley.com/doi/abs/10.1029/2004JB003268` doi: https://doi.org/10.1029/2004JB003268

Geirsson, H., Parks, M. M., Sigmundsson, F., Drouin, V., Ófeigsson, B. G., Lanzi, C., ... Greiner, S. H. M. (2024). Deformation patterns of the Reykjanes Peninsula unrest 2020-2024, Iceland: evidence for interconnected neighboring volcanic systems.. doi: https://doi.org/10.5194/egusphere-egu24-18235

Greiner, S. H. M., Burchardt, S., Sigmundsson, F., Óskarsson, B. V., Galland, O., Geirsson, H., & Rhodes, E. (2023). Interaction between propagating basaltic dikes and pre-existing fractures: A case study in hyaloclastite from Dyrfjöll, Iceland. *Journal of Volcanology and Geothermal Research*, *442*, 107891. Retrieved from `https://www.sciencedirect.com/science/article/pii/S0377027323001488` doi: https://doi.org/10.1016/j.jvolgeores.2023.107891

Greiner, S. H. M., Sigmundsson, F., Geirsson, H., Burchardt, S., & Galland, O. (2025). *Model files to "Tectonic stress as the driving mechanism for dike opening in an oblique rift setting: A deformation model of the 2021 Fagradalsfjall dike, Iceland".* Zenodo. Retrieved from `https://doi.org/10.5281/zenodo.14882630` (Data set) doi: 10.5281/zenodo.14882630

Hamling, I. J., Ayele, A., Bennati, L., Calais, E., Ebinger, C. J., Keir, D., ... Yirgu, G. (2009, 08). Geodetic observations of the ongoing Dabbahu rifting episode: New dyke intrusions in 2006 and 2007. *Geophysical Journal International*, *178*(2), 989-1003. Retrieved from `https://doi.org/10.1111/j.1365-246X.2009.04163.x` doi: 10.1111/j.1365-246X.2009.04163.x

Heimisson, E. R., Hooper, A., & Sigmundsson, F. (2015). Forecasting the path of a laterally propagating dike. *Journal of Geophysical Research: Solid Earth*, *120*(12), 8774-8792. Retrieved from `https://agupubs.onlinelibrary.wiley.com/doi/abs/10.1002/2015JB012402` doi: https://doi.org/10.1002/2015JB012402

Heimisson, E. R., & Segall, P. (2020). Physically Consistent Modeling of Dike-Induced Deformation and Seismicity: Application to the 2014 Bárdarbunga Dike, Iceland. *Journal of Geophysical Research: Solid Earth*, *125*(2), e2019JB018141. Retrieved from `https://agupubs.onlinelibrary`

.wiley.com/doi/abs/10.1029/2019JB018141 (e2019JB018141 10.1029/2019JB018141) doi: https://doi.org/10.1029/2019JB018141

Hjartardóttir, Á. R., Dürig, T., Parks, M., Drouin, V., Eyjólfsson, V., Reynolds, H., ... Pedersen, G. B. M. (2023). Pre-existing fractures and eruptive vent openings during the 2021 Fagradalsfjall eruption, Iceland. *Bulletin of Volcanology*, *85*(10), 56. doi: https://doi.org/10.1007/s00445-023-01670-z

Hooper, A., Ófeigsson, B., Sigmundsson, F., Lund, B., Einarsson, P., Geirsson, H., & Sturkell, E. (2011). Increased capture of magma in the crust promoted by ice-cap retreat in Iceland. *Nature Geoscience*, *4*(11), 783–786. doi: https://doi.org/10.1038/ngeo1269

Hreinsdóttir, S., Einarsson, P., & Sigmundsson, F. (2001). Crustal deformation at the oblique spreading Reykjanes Peninsula, SW Iceland: GPS measurements from 1993 to 1998. *Journal of Geophysical Research: Solid Earth*, *106*(B7), 13803-13816. Retrieved from https://agupubs.onlinelibrary.wiley.com/doi/abs/10.1029/2001JB000428 doi: https://doi.org/10.1029/2001JB000428

Icelandic Meteorological Office Earthquake Catalogue. (2024). Skjálftalísa. Retrieved from https://skjalftalisa.vedur.is/#/page/map (Accessed 12. 09. 2024)

Islam, M. T., Sturkell, E., LaFemina, P., Geirsson, H., Sigmundsson, F., & Ólafsson, H. (2016). Continuous subsidence in the Thingvellir rift graben, Iceland: Geodetic observations since 1967 compared to rheological models of plate spreading. *Journal of Geophysical Research: Solid Earth*, *121*(1), 321-338. Retrieved from https://agupubs.onlinelibrary.wiley.com/doi/abs/10.1002/2015JB012306 doi: https://doi.org/10.1002/2015JB012306

Jolly, R., & Sanderson, D. (1997). A Mohr circle construction for the opening of a pre-existing fracture. *Journal of Structural Geology*, *19*(6), 887-892. Retrieved from https://www.sciencedirect.com/science/article/pii/S019181419700014X doi: https://doi.org/10.1016/S0191-8141(97)00014-X

Jóhannesson, H., & Sæmundsson, K. (2009). *Geological map of Iceland 1:600,000–Tectonics.*

Karato, S., & Wu, P. (1993). Rheology of the Upper Mantle: A Synthesis. *Science*, *260*(5109), 771-778. Retrieved from https://www.science.org/doi/abs/10.1126/science.260.5109.771 doi: 10.1126/science.260.5109.771

Keiding, M., Lund, B., & Árnadóttir, T. (2009). Earthquakes, stress, and strain along an obliquely divergent plate boundary: Reykjanes Peninsula, southwest Iceland. *Journal of Geophysical Research: Solid Earth*, *114*(B9). Retrieved from https://agupubs.onlinelibrary.wiley.com/doi/abs/10.1029/

2008JB006253 doi: https://doi.org/10.1029/2008JB006253

Keiding, M., Árnadóttir, T., Jónsson, S., Decriem, J., & Hooper, A. (2010). Plate boundary deformation and man-made subsidence around geothermal fields on the Reykjanes Peninsula, Iceland. *Journal of Volcanology and Geothermal Research*, *194*(4), 139-149. Retrieved from https://www.sciencedirect.com/science/article/pii/S0377027310001290 doi: https://doi.org/10.1016/j.jvolgeores.2010.04.011

Keiding, M., Árnadóttir, T., Sturkell, E., Geirsson, H., & Lund, B. (2008). Strain accumulation along an oblique plate boundary: The Reykjanes Peninsula, southwest Iceland. *Geophysical Journal International*, *172*(2), 861-872. Retrieved from https://doi.org/10.1111/j.1365-246X.2007.03655.x doi: 10.1111/j.1365-246X.2007.03655.x

Krumbholz, M., Hieronymus, C. F., Burchardt, S., Troll, V. R., Tanner, D. C., & Friese, N. (2014). Weibull-distributed dyke thickness reflects probabilistic character of host-rock strength. *Nature communications*, *5*(1), 3272. doi: https://doi.org/10.1038/ncomms4272

Lanzi, C., Sigmundsson, F., Parks, M. M., Geirsson, H., & Drouin, V. (2024). Strain localization at volcanoes undergoing extension: Investigation of long-term deformation at krafla and askja volcanic systems in north iceland. *Geophysical Research Letters*, *51*(21), e2024GL110299. Retrieved from https://agupubs.onlinelibrary.wiley.com/doi/abs/10.1029/2024GL110299 (e2024GL110299 2024GL110299) doi: https://doi.org/10.1029/2024GL110299

Masterlark, T. (2007). Magma intrusion and deformation predictions: Sensitivities to the Mogi assumptions. *Journal of Geophysical Research: Solid Earth*, *112*(B6). Retrieved from https://agupubs.onlinelibrary.wiley.com/doi/abs/10.1029/2006JB004860 doi: https://doi.org/10.1029/2006JB004860

Michalczewska, K., Hreinsdóttir, S., Dumont, S., & Sigmundsson, F. (2014). *Crustal deformation on the Western Reykjanes Peninsula 2009 to 2014 mapped by InSAR and GPS measurements* (Tech. Rep.). Sturlugata 7, 101 Reykjavík, Iceland: Institute of Earth Sciences.

Molnar, P. (2020). The brittle-plastic transition, earthquakes, temperatures, and strain rates. *Journal of Geophysical Research: Solid Earth*, *125*(7), e2019JB019335. Retrieved from https://agupubs.onlinelibrary.wiley.com/doi/abs/10.1029/2019JB019335 (e2019JB019335 2019JB019335) doi: https://doi.org/10.1029/2019JB019335

Montgomery-Brown, E. K., Sinnett, D. K., Poland, M., Segall, P., Orr, T., Zebker, H., & Miklius, A. (2010). Geodetic evidence for en echelon dike emplace-

ment and concurrent slow slip during the June 2007 intrusion and eruption at Kīlauea volcano, Hawaii. *Journal of Geophysical Research: Solid Earth*, *115*(B7). Retrieved from https://agupubs.onlinelibrary.wiley.com/doi/abs/10.1029/2009JB006658 doi: https://doi.org/10.1029/2009JB006658

Mulyukova, E., & Bercovici, D. (2019). The Generation of Plate Tectonics From Grains to Global Scales: A Brief Review. *Tectonics*, *38*(12), 4058-4076. Retrieved from https://agupubs.onlinelibrary.wiley.com/doi/abs/10.1029/2018TC005447 doi: https://doi.org/10.1029/2018TC005447

Okada, Y. (1985). Surface deformation due to shear and tensile faults in a half-space. *Bulletin of the Seismological Society of America*, *75*(4), 1135-1154. Retrieved from https://doi.org/10.1785/BSSA0750041135 doi: 10.1785/BSSA0750041135

Parks, M., Sigmundsson, F., Drouin, V., Hjartardóttir, Á. R., Geirsson, H., Hooper, A., ... Fridriksdottir, H. M. (2023). Deformation, seismicity, and monitoring response preceding and during the 2022 Fagradalsfjall eruption, Iceland. *Bulletin of Volcanology*, *85*(10), 60. doi: https://doi.org/10.1007/s00445-023-01671-y

Parks, M., Sigmundsson, F., Sigurdsson, Ó., Hooper, A., Hreinsdóttir, S., Ófeigsson, B., & Michalczewska, K. (2020). Deformation due to geothermal exploitation at Reykjanes, Iceland. *Journal of Volcanology and Geothermal Research*, *391*, 106438. Retrieved from https://www.sciencedirect.com/science/article/pii/S0377027317305887 doi: https://doi.org/10.1016/j.jvolgeores.2018.08.016

Pascal, K., Neuberg, J., & Rivalta, E. (2013). On precisely modelling surface deformation due to interacting magma chambers and dykes. *Geophysical Journal International*, *196*(1), 253-278. Retrieved from https://doi.org/10.1093/gji/ggt343 doi: 10.1093/gji/ggt343

Pedersen, G. B. M., Belart, J. M. C., Óskarsson, B. V., Gudmundsson, M. T., Gies, N., Högnadóttir, T., ... Oddsson, B. (2022). Volume, Effusion Rate, and Lava Transport During the 2021 Fagradalsfjall Eruption: Results From Near Real-Time Photogrammetric Monitoring. *Geophysical Research Letters*, *49*(13), e2021GL097125. Retrieved from https://agupubs.onlinelibrary.wiley.com/doi/abs/10.1029/2021GL097125 (e2021GL097125 2021GL097125) doi: https://doi.org/10.1029/2021GL097125

Pedersen, R., Sigmundsson, F., & Masterlark, T. (2009). Rheologic controls on inter-rifting deformation of the Northern Volcanic Zone, Iceland. *Earth and Planetary Science Letters*, *281*(1), 14-26. Retrieved from https://

www.sciencedirect.com/science/article/pii/S0012821X09000806 doi: https://doi.org/10.1016/j.epsl.2009.02.003

Reid, H. (1910). The mechanics of the earthquake, the california earthquake of april 18, 1906. *Report of the State Investigation Commission, Carnegie Institution of Washington, Washington DC*.

Rivalta, E., Taisne, B., Bunger, A., & Katz, R. (2015). A review of mechanical models of dike propagation: Schools of thought, results and future directions. *Tectonophysics*, *638*, 1-42. Retrieved from https://www.sciencedirect.com/science/article/pii/S0040195114005174 doi: https://doi.org/10.1016/j.tecto.2014.10.003

Ruch, J., Wang, W., T.and Xu, Hensch, M., & Jónsson, S. (2016). Oblique rift opening revealed by reoccurring magma injection in central Iceland. *Nature communications*, *7*(1), 12352. doi: https://doi.org/10.1038/ncomms12352

Savage, J. C., & Burford, R. O. (1973). Geodetic determination of relative plate motion in central California. *Journal of Geophysical Research (1896-1977)*, *78*(5), 832-845. Retrieved from https://agupubs.onlinelibrary.wiley.com/doi/abs/10.1029/JB078i005p00832 doi: https://doi.org/10.1029/JB078i005p00832

Sigmundsson, F., Einarsson, P., Hjartardóttir, Á. R., Drouin, V., Jónsdóttir, K., Árnadóttir, T., ... Ófeigsson, B. G. (2020a). Geodynamics of Iceland and the signatures of plate spreading. *Journal of Volcanology and Geothermal Research*, *391*, 106436. Retrieved from https://www.sciencedirect.com/science/article/pii/S0377027317306376 doi: https://doi.org/10.1016/j.jvolgeores.2018.08.014

Sigmundsson, F., Hooper, A., Hreinsdóttir, S., Vogfjörd, K., Ófeigsson, B., Heimisson, E., ... Eibl, E. (2015). Segmented lateral dyke growth in a rifting event at Bárdarbunga volcanic system, Iceland [Journal Article]. *Nature*, *517*, 191. Retrieved from http://dx.doi.org/10.1038/nature14111https://www.nature.com/articles/nature14111.pdf doi: 10.1038/nature14111https://www.nature.com/articles/nature14111#supplementary-information

Sigmundsson, F., Parks, M., Geirsson, H., Hooper, A., Drouin, V., Vogfjörd, K. S., ... Barsotti, S. (2024). Fracturing and tectonic stress drive ultrarapid magma flow into dikes. *Science*, *383*(6688), 1228-1235. Retrieved from https://www.science.org/doi/abs/10.1126/science.adn2838 doi: 10.1126/science.adn2838

Sigmundsson, F., Parks, M., Hooper, A., Geirsson, H., Vogfjörd, K. S., Drouin, V., ... Ágústsdóttir, T. (2022). Deformation and seismicity decline be-

fore the 2021 Fagradalsfjall eruption. *Nature*, *609*(7927), 523–528. Retrieved from https://doi.org/10.1038/s41586-022-05083-4 doi: https://doi.org/10.1038/s41586-022-05083-4

Sigmundsson, F., Pinel, V., Grapenthin, R., Hooper, A., Halldórsson, S. A., Einarsson, P., ... Yamasaki, T. (2020b). Unexpected large eruptions from buoyant magma bodies within viscoelastic crust. *Nature Communications*, *11*(1), 2403. doi: https://doi.org/10.1038/s41467-020-16054-6

Spaans, K., & Hooper, A. (2018). Insights Into the Stress Field Around Bárdarbunga Volcano From the 2014/2015 Holuhraun Rifting Event. *Journal of Geophysical Research: Solid Earth*, *123*(4), 3238-3249. Retrieved from https://agupubs.onlinelibrary.wiley.com/doi/abs/10.1002/2017JB015274 doi: https://doi.org/10.1002/2017JB015274

Sæmundsson, K., Sigurgeirsson, M. Á., & Fridleifsson, G. Ó. (2020). Geology and structure of the Reykjanes volcanic system, Iceland. *Journal of Volcanology and Geothermal Research*, *391*, 106501. Retrieved from https://www.sciencedirect.com/science/article/pii/S0377027317305474 doi: https://doi.org/10.1016/j.jvolgeores.2018.11.022

Turcotte, D. L., & Schubert, G. (2014). *Geodynamics* (3rd ed.). Cambridge university press.

Turner, A. J., Katz, R. F., Behn, M. D., & Keller, T. (2017). Magmatic focusing to mid-ocean ridges: The role of grain-size variability and non-newtonian viscosity. *Geochemistry, Geophysics, Geosystems*, *18*(12), 4342-4355. Retrieved from https://agupubs.onlinelibrary.wiley.com/doi/abs/10.1002/2017GC007048 doi: https://doi.org/10.1002/2017GC007048

Vadon, H., & Sigmundsson, F. (1997). Crustal Deformation from 1992 to 1995 at the Mid-Atlantic Ridge, Southwest Iceland, Mapped by Satellite Radar Interferometry. *Science*, *275*(5297), 194-197. Retrieved from https://www.science.org/doi/abs/10.1126/science.275.5297.194 doi: 10.1126/science.275.5297.194

van Wijk, J., & Blackman, D. (2005). Deformation of oceanic lithosphere near slow-spreading ridge discontinuities. *Tectonophysics*, *407*(3), 211-225. Retrieved from https://www.sciencedirect.com/science/article/pii/S0040195105003653 doi: https://doi.org/10.1016/j.tecto.2005.08.009

Weir, N. R. W., White, R. S., Brandsdóttir, B., Einarsson, P., Shimamura, H., & Shiobara, H. (2001). Crustal structure of the northern Reykjanes Ridge and Reykjanes Peninsula, southwest Iceland. *Journal of Geophysical Research: Solid Earth*, *106*(B4), 6347-6368. Retrieved from https://

agupubs.onlinelibrary.wiley.com/doi/abs/10.1029/2000JB900358 doi: https://doi.org/10.1029/2000JB900358

Wessel, P., Smith, W. H. F., Scharroo, R., Luis, J., & Wobbe, F. (2013). Generic mapping tools: Improved version released. *Eos, Transactions American Geophysical Union*, *94*(45), 409-410. Retrieved from https://agupubs.onlinelibrary.wiley.com/doi/abs/10.1002/2013EO450001 doi: https://doi.org/10.1002/2013EO450001

White, R. S., Drew, J., Martens, H. R., Key, J., Soosalu, H., & Jakobsdóttir, S. S. (2011). Dynamics of dyke intrusion in the mid-crust of iceland. *Earth and Planetary Science Letters*, *304*(3), 300-312. Retrieved from https://www.sciencedirect.com/science/article/pii/S0012821X11001178 doi: https://doi.org/10.1016/j.epsl.2011.02.038

Wright, T. J., Sigmundsson, F., Pagli, C., Belachew, M., Hamling, I. J., Brandsdóttir, B., ... Calais, E. (2012). Geophysical constraints on the dynamics of spreading centres from rifting episodes on land. *Nature Geoscience*, *5*(4), 242–250. doi: https://doi.org/10.1038/ngeo1428

Yun, S., Segall, P., & Zebker, H. (2006). Constraints on magma chamber geometry at Sierra Negra Volcano, Galápagos Islands, based on InSAR observations. *Journal of Volcanology and Geothermal Research*, *150*(1), 232-243. Retrieved from https://www.sciencedirect.com/science/article/pii/S0377027305002611 (The Changing Shapes of Active Volcanoes) doi: https://doi.org/10.1016/j.jvolgeores.2005.07.009

Árnadóttir, T., Geirsson, H., & Einarsson, P. (2004). Coseismic stress changes and crustal deformation on the reykjanes peninsula due to triggered earthquakes on 17 june 2000. *Journal of Geophysical Research: Solid Earth*, *109*(B9). Retrieved from https://agupubs.onlinelibrary.wiley.com/doi/abs/10.1029/2004JB003130 doi: https://doi.org/10.1029/2004JB003130

Árnadóttir, T., Jiang, W., Feigl, K. L., Geirsson, H., & Sturkell, E. (2006). Kinematic models of plate boundary deformation in southwest Iceland derived from GPS observations. *Journal of Geophysical Research: Solid Earth*, *111*(B7). Retrieved from https://agupubs.onlinelibrary.wiley.com/doi/abs/10.1029/2005JB003907 doi: https://doi.org/10.1029/2005JB003907

Árnadóttir, T., Lund, B., Jiang, W., Geirsson, H., Björnsson, H., Einarsson, P., & Sigurdsson, T. (2009). Glacial rebound and plate spreading: Results from the first countrywide GPS observations in Iceland. *Geophysical Journal International*, *177*(2), 691-716. Retrieved from https://doi.org/10.1111/j.1365-246X.2008.04059.x doi: 10.1111/j.1365-246X.2008.04059.x

Geophysical Research Letters

Supporting information for

Tectonic stress as the driving mechanism for dike opening in an oblique rift setting: A deformation model of the 2021 Fagradalsfjall dike, Iceland

Sonja H. M. Greiner [1,2,3], Freysteinn Sigmundsson [1], Halldór Geirsson [1], Steffi Burchardt[2,3], Olivier Galland [4]

[1]Nordic Volcanological Center, Institute of Earth Sciences, University of Iceland, Reykjavík, Iceland
[2]Department of Earth Sciences, Uppsala University, Uppsala, Sweden
[3]Center for Natural Hazard and Disaster Science (CNDS), Sweden
[4]Physics of Geological Processes, the NJORD Center, Department of Geosciences, University of Oslo, Oslo, Norway

Contents

S1 Model Coordinate System **3**

S2 Model Setup, Parameters and Mesh **4**
S2.1 Model Setup and Parameters 4
S2.2 Mesh 5

S3 Heat-Transfer Model **6**

S4 Preparation of Surface Deformation Data **9**
S4.1 GNSS-velocities for the Tectonic Model 9
S4.2 Dike-related Deformation 9

S5 Benchmarking **12**

S6 Tectonic Model - Relative Plate Motion **17**

S7 Stress and Stress Changes **19**
S7.1 Stress in the Dike Plane 19
S7.2 Stress change $\Delta\sigma_3$ caused by the dike 22

S8 Comparison of LOS-Residual to Mapped Fault Traces **23**

S9 Difference between Tectonic Stress- and Pressure-driven Models 24

S10 Loading Conditions on the Dike 25
S10.1 Fraction of Released Tectonic Stress 25
S10.2 Distributed Opening Model by Sigmundsson et al. (2022) 26
S10.3 Entire Tectonic Stress Released 28
S10.4 40% of Tectonic Stress Released 29
S10.5 Influence of dike geometry 30

S11 Additional Limitations 31

S1 Model Coordinate System

Although the model results in this study are presented in the WSG84 format, the Finite Element model was in a metrical reference frame. We defined a local cartesian, east-west/north-south oriented coordinate system, which has an origin corresponding to 63.882240°N and 22.433715°W. This point corresponds to the location of GNSS station SENG near the Svartsengi geothermal power plant, which is located west of Fagradalsfjall and North of the town of Grindavík. We then used the Matlab-functions "local2latlon()" and "latlon2local()" to convert between the coordinate systems.

S2 Model Setup, Parameters and Mesh

S2.1 Model Setup and Parameters

The model domain had a width, height and length corresponding each to 200 km. Two blocks are added to allow for mesh-refinement later on. One corresponds approximately to the size of the Reykjanes Peninsula (orange in Figure S1) and measures 60 km in East-West direction and 40 km in North-Sotuh direction and reaches from the surface down to 15 km. The smaller block (blue in Figure S1) measures 10 km x 10 km x 13 km and encases the entire dike. All three blocks are laterally centered around the center of the dike and vertically positioned that their top surfaces are at z=0 m.

The outline of the plate boundary axis (based on Michalczewska et al., 2014) was vertically extended to cut through the entire model domain. The $10^{21}\,Pa\,s$-isoviscous surface as well as the two dike segments were implemented as para-

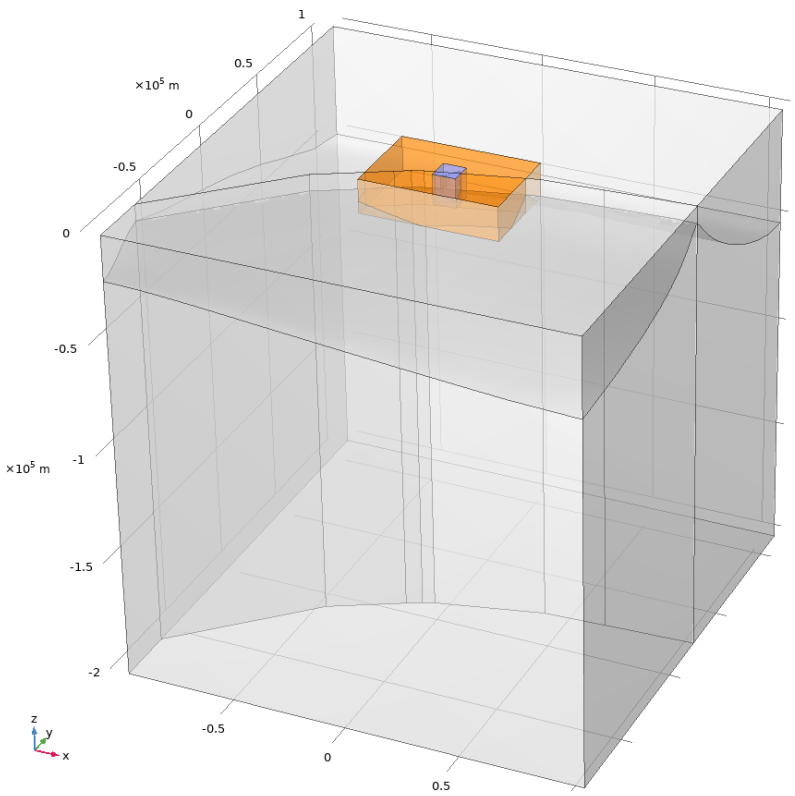

Figure S1 : Model geometry and domain. Colours mark blocks outlining approximately the size of the Reykjanes Peninsula (orange) and the location of the dike (blue). Furthermore visible are the outlines of the plate boundary axis (horizontally curved, vertical surface) and the approximately bellshaped base of the elastic crust defined by the $10^{21}\,Pa\,s$-isoviscous surface.

metric surfaces.

Table Table S1 lists all parameters related to the geometry and rheology of the Finite-Element models presented in the main text. The model domain length, height and width were chosen large enough to avoid edge effects.

Both model steps were time-dependent studies. The tectonic model simulated plate spreading over the course of 800 years. The dike model ran for 1 year and results shown in the main text correspond to t=0.1 yr. The dike model was set up as time-dependent to allow for consistent boundary conditions for both model steps. However, on the time-scales of the dike model, the contribution of viscoelastic relaxation is negligible, so that this step of the model behaves effectively elastic.

S2.2 Mesh

The mesh for the presented study consisted of 71 348 vertices which spanned 394 344 tetrahedral elements. The mesh resolution was finest at and above the dike, where the maximum mesh size was set to be no larger than 200 m. This was applied to the dike plane and to the 10 km x 10 km square corresponding to the top surface of the innermost block shown in blue in Figure S1 . The growth rate for these elements was set to equal 1.1, i.e. the size of neighbouring elements was not allowed to differ by more than 10%. THis was done to prevent rapid changes in mesh resolution. Elements along the intersection of the plate-boundary axis and the 10^{21} $Pa\,s$-isoviscous surface were not allowed to be larger than 500 m with a maximum growth rate of 1.3. The top surface of the orange block in Figure S1 and the parts of the plate boundary axis located above the 10^{21} $Pa\,s$-isoviscous surface were not allowed to exceed a length of more than 1000 m.

Table S1: List pf parameters and properties used in the numerical models. References for values listed below.

Parameter	Variable name	Value
Model length	L	200 km
Model width	W	200 km
Model height	h_b	200 km
Thermal conductivity	k	2.6 W/(m K)[a]
Heat capacity	c	1050 J/(kg K)[a]
Plate spreading direction		N100°E[b]
Full spreading rate	u_{full}	$20\frac{mm}{yr}$[b]
Density	rho	depth-dependent[c]
Poisson's ratio	ν	0.27[d]
Young's modulus	E	depth-dependent[c,d]
Scaling factor	s	7 km [b]
Universal gas constant	R	8.3145 J/(K mol)
Dimension of undeformed crystals	h	3 mm[e]
Activation energy	E_a	300 kJ/mol[f]
Activation volume	V_a	6 cm^3/mol[f]
Frequency factor	D_0	0.0001 m^2/s[a]
Strike of southern dike segment	δ_s	23.5°[g]
Strike of northern dike segment	δ_n	45°[g]
Length of indiviual dike segments	L_d	4.5 km[g]
Maximum depth of southern dike segment	$d_{s,max}$	6 km[g]
Maximum depth of northern dike segment	$d_{n,max}$	7 km[h]
Top of both dike segments	d_{min}	1 km[h]
Released fraction of tectonic stress	f	60%

[a] Turcotte and Schubert (2014)
[b] Keiding et al. (2008)
[c] Sigmundsson et al. (2020b)
[d] Weir et al. (2001)
[e] Turner et al. (2017)
[f] Karato and Wu (1993)
[g] Directly from Sigmundsson et al. (2022)
[h] Modified from Sigmundsson et al. (2022); changed from the original to increase distance to constrained base of the brittle crust/surface

S3 Heat-Transfer Model

The 3D viscosity-model used in the deformation models (Figure 1f in the main text) is based on a simple, stationary heat transfer model. We assume that the temperature profile at the plate boundary axis is constant on the modeled time scales and that heat is transported away from the plate boundary axis by advection due to plate motion and conduction. The temperature profile applied to the plate boundary axis is based on the one used by Islam et al. (2016) for the

nearby Western Volcanic Zone (Figure 1a in the main text), but we placed the depth corresponding to 700°C at 5 km depth based on estimates of the brittle-ductile transition in the western part of the peninsula (Keiding et al., 2009). The model surface is kept at 5°C and the base at 1200°C. The sides allow for outflow only. The Eurasian and North American plates each move away from the plate boundary axis at a rate of 1 cm/yr in the direction of N100°E and N280°E, respectively (Keiding et al., 2008).

Due to the curved plate boundary, the resulting temperature structure is asymmetric with higher temperatures on the Eurasian (southeastern) side of the plate boundary compared to the those at the same distance and depth on the North-American (northwestern) side (Figure S2). This likely relates to the conductive component of the heat flux (Figure S2 c), where thermal energy collects in the concave-shaped southern side of the plate boundary axis. The total heat flux appears largely dominated by advective heat transport, but shows rotation close to the plate boundary axis, which indicates the effects of conductive transport(Figure S2 d).

The asymmetry in the temperature model directly translates into the viscosity

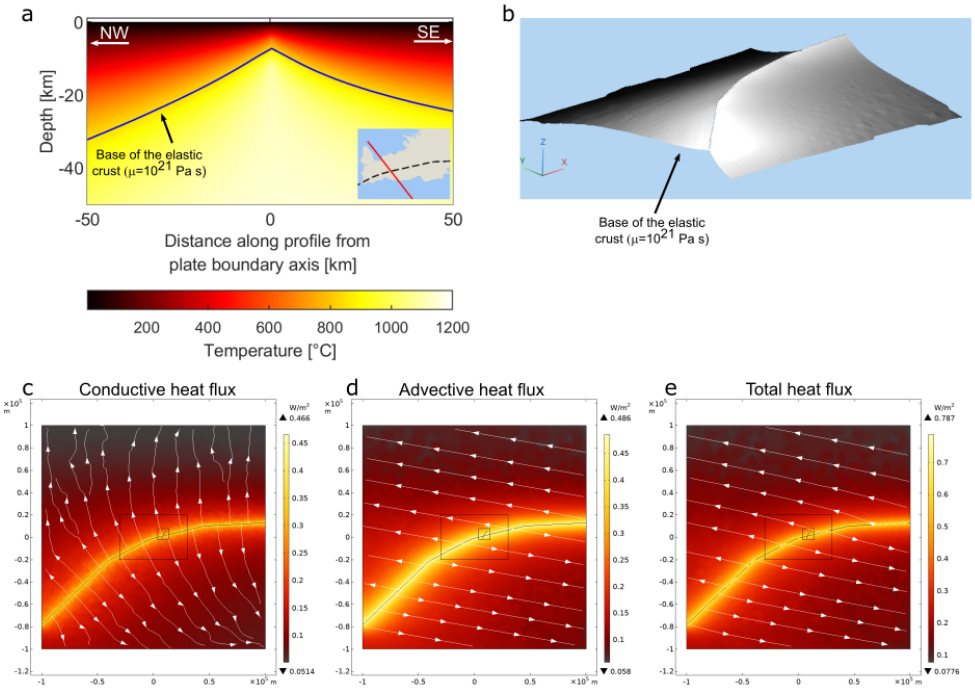

Figure S2 : a) Temperature in a cross-section along the direction of the least compressive stress from the tectonic model. Base of the elastic crust indicated in blue. b) Isosurface corresponding to the viscosity of $10^{21} Pa\,s$, taken here as the base of the elastic crust. The curved shape of the surface comes from the curved plate boundary. c) Conductive, d) advective and e) total heat flux at 4 km depth below the model surface.

model. Additionally, the estimated viscosities are high in the upper crust (up to the order of 10^{62}Pa s). However, this implies that relaxation times are very long and it can be assumed that above viscosities of 10^{21} Pa s, the model behaves effectively elastic on the timescales of our model.

It should be noted that applying the same temperature profile along the entire plate boundary axis is a simplification. There are indications that the depth of the brittle-ductile transition and magma storage depths vary along the peninsula and are shifted to larger depth further east (Weir et al., 2001; Caracciolo et al., 2023). Furthermore, we ignore here local anomalies associated with high-temperature geothermal areas, that are found in most volcanic systems other than Fagradalsfjall (Figure 1a in the main text). Lastly, there are likely temperature variations due to cooling intrusions, so a steady-state model is a strong simplification. While future studies could benefit from more detailed temperature models, the present study should be sufficient to capture first-order structures.

S4 Preparation of Surface Deformation Data

The modelling results in this study are compared to surface deformation data, which was published by Keiding et al. (2008) and Sigmundsson et al. (2022).

S4.1 GNSS-velocities for the Tectonic Model

The total amount of spreading that accumulated since the end of the last eruptive period on the Reykjanes Peninsula is somewhat poorly constrained. We therefore compare the results of the tectonic model to geodetically observed velocities. Keiding et al. (2008) presented and analyzed surface deformation from campaign GNSS measurements spanning the period of 2000-2006. All velocities were calculated relative to the continuous GNSS station REYK, which is considered to be outside of the main deformation field of the plate boundary zone.

We evaluated the surface velocity at locations corresponding to the GNSS-stations from Keiding et al. (2008). A number of these points were affected by coseismic displacement related to an earthquake in Krýsuvík in August 2003, in which case we used the corrected velocities, which where also presented by Keiding et al. (2008).

S4.2 Dike-related Deformation

The surface deformation during formation of the 2021 Fagradalsfjall dike was geodetically well documented by both GNSS and InSAR. We compare our modelling results to 18 GNSS stations and an ascending InSAR track (Sentinel 1 satellite on Track 16) published by Sigmundsson et al. (2022). The dike intrusion was accompanied by intense seismic activity and the model presented by Sigmundsson et al. (2022) comprised distributed opening/shearing on two dike segments as well as coseismic deformation of the two largest earthquakes, slip along the plate boundary axis and a subsidence signal attributed to a shallow, contracting Mogi-source. These two earthquakes occurred on the 24th of Feburary and on the 14th of March and had magnitudes of $M_W = 5.64$ and $M_W = 5.33$, respectively. The earlier earthquake was located east of Fagradalsfjall, the later one west of it (see Figure 1b in the main text).

To compare our model to observations, we removed the coseismic displacement of the two earthquakes from the data provided by Sigmundsson et al. (2022) using their best-fitting source parameters for the two faults(Figure S3 & S4). Coseismic displacement was calculated using the Okada-solution from the dMODELS package (Battaglia et al., 2013). We decided to not remove other signals, since it is less clear how they relate to the dike-induced deformation.

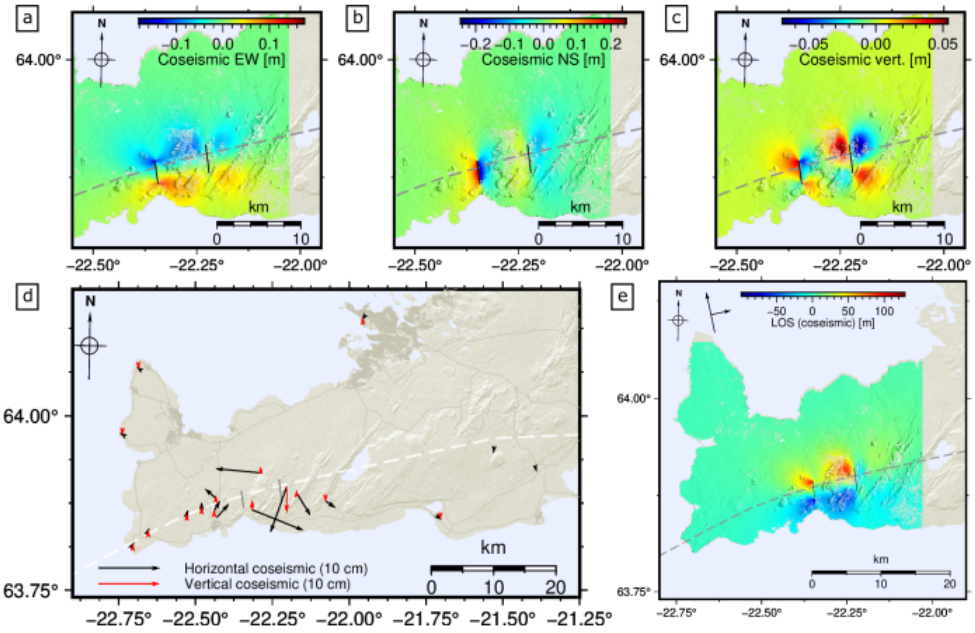

Figure S3 : Modelled coseismic deformation of the two largest earthquakes that occurred during the dike intrusion. Fault parameters are from Sigmundsson et al. (2022). a) East-west, b) north-south and c) vertical component of motion. d) shows the horizontal and vertical motion at recording GNSS stations. e) Line of Sight (LOS) displacement of an ascending Sentinel-1 satellite on Track 16. Faults are marked by black lines (darkgrey in d).

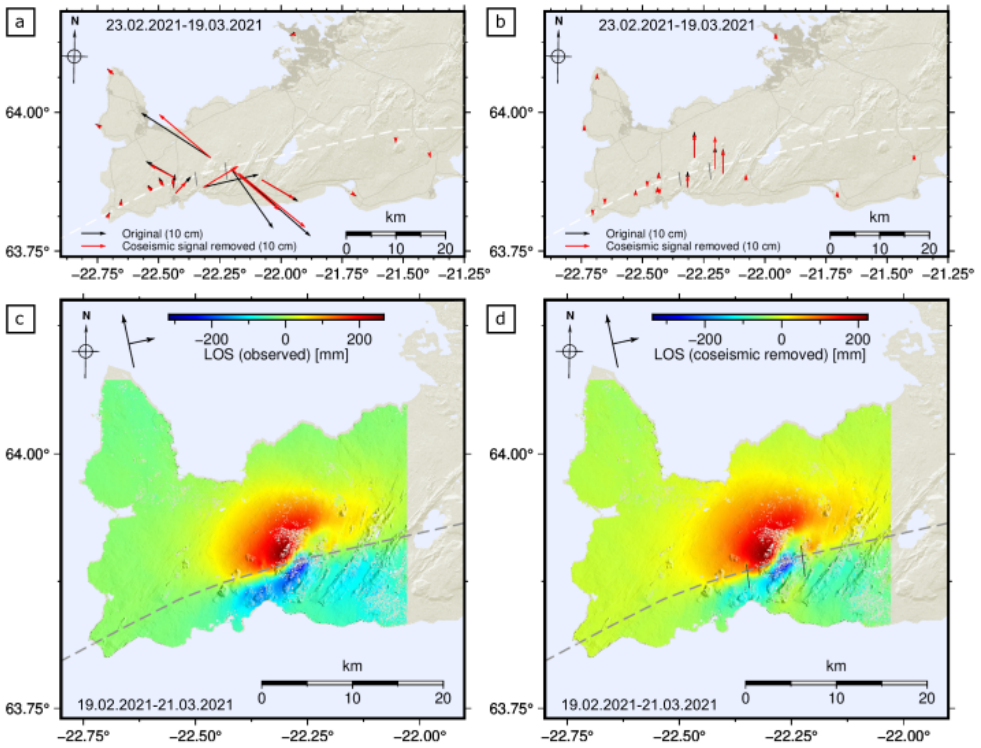

Figure S4 : Observed deformation by Sigmundsson et al. (2022) before and after removal of the coseismic signal. a) Horizontal and b) vertical displacement of GNSS stations. c) Original LOS-displacement of the ascending Sentinel-1 satellite on Track 16. d) LOS displacement after the coseismic signal (Figure S3 e) has been removed.

S5 Benchmarking

There is no direct equivalent which we could benchmark tectonic and the dike model against. We constrained the tectonic model with observed surface velocities by Keiding et al. (2008). For the dike model, we simplify the crustal structure and boundary conditions to evaluate 1) if there are mesh-effects in the model and 2) to what degree the final solution is affected by constraining the base of the elastic crust.

For the dike-model, we decided to benchmark a simplified version of the model against the Okada-dislocation model using the implementation from the dMODELs package (Okada, 1985; Battaglia et al., 2013). It is important to note that while in the Okada-model the dislocation experiences uniform dislocation, a uniformly pressurized crack results in even loading, but variable opening (e.g., Currenti et al., 2011). Therefore, the misfit between the FEM- and the analytical model contains some differences due to variable opening. We compared the Root-Mean-Square (RMS) between the analytical and numerical models

$$RMS = \sqrt{\sum_{i}^{N} \frac{\left(u_{num,i} - u_{ana,i}\right)^2}{N}} \tag{S1}$$

and evaluated the analytical model at points corresponding to surface mesh-nodes of the numerical model.

To simplify the numerical model, we only considered linearly elastic host-rock with a constant Young's modulus and Poisson-ratio ($E = 50\,GPa$, $\nu = 0.27$). To avoid effects of superposition, we only considered the southern dike segment during benchmarking rather than both segments. However, although no loading is applied to the northern segment, the same mesh resolution was applied to both segments. An overpressure of $P = 13\,MPa$ was applied to the southern segment.

We compare the analytical model to two simplified versions of the numerical model. One where the only applied conditions are the following: Uniform overpressure at the crack, roller conditions at the sides of the model domain and fixed base of the model domain. A roller-condition implies that boundary-parallel motion is free, but no deformation normal to the boundary can occur. The second model has the surface, which in the main text corresponds to the base of the elastic crust, constrained by applying horizontal spreading and preventing vertical motion. We test this to estimate how strongly constraining the base of the elastic crust affects surface deformation.

The amount of opening applied to the analytical model was varied and we chose the value, that had the lowest RMS to the unconstrained numerical model. We find that this value corresponds to 1.01 m of uniform opening, which is very close to the mean opening of 0.93 m of the unconstrained numerical model. The volume of the dike is very similar for both of these models with $22.725\,mio.\,m^3$ for the analytical model and $22.718\,mio.\,m^3$ for the unconstrained numerical model.

Despite differing opening patterns, surface deformation patterns are very similar between the unconstrained numerical and the Okada model with a maximum RMS of less than 0.5 cm for individual components (Table S2 and Figure S5).

Table S2: Root-mean square of the difference for each deformation component between the Okada model and the two tested numerical models as well as a comparison between the numerical models.

Compared models	RMS_{EW}	RMS_{NS}	RMS_{vert}
Okada & Unconstrained	4.5 mm	2.5 mm	4.2 mm
Okada & Constrained	4.4 mm	2.6 mm	4.0 mm
Unconstrained & Constrained	6.4 mm	1.8 mm	8.7 mm

Residual patterns are overall strongly concentrated to the proximity of the dike and are smooth, i.e. they do not show traces of individual mesh elements. This indicates that the resolution of mesh-elements close to the dike is not a significant issue. Furthermore, strong concentration of the residual above the dike suggests that this could mainly relate to the variable opening of the two models in the shallowest parts of the dike. In the numerical model, the maximum mesh resolution above the dike and in the dike plane is limited to 200 m.

The comparison between the Okada model and the numerical model, where the base of the crust in constrained shows overall also similar deformation (Figure S6). However, especially in the EW-component, a low-amplitude signal that stretches farther away from the dike along the plate boundary axis (Figure S6 g) indicates that constraining the base of the crust indeed has minor effects on surface deformation, even if the RMS of the residual slightly decreased.

The effect of restricting motion at the base of the elastic crust on surface deformation also becomes evident when comparing both numerical models. When subtracting the deformation of the constrained model from that of the unconstrained model, it becomes evident that there are up to 1.5 cm difference between both models(Figure S7 j-l). Of all three components, the vertical direction is affected the strongest and the NS-component the least (Table S2).

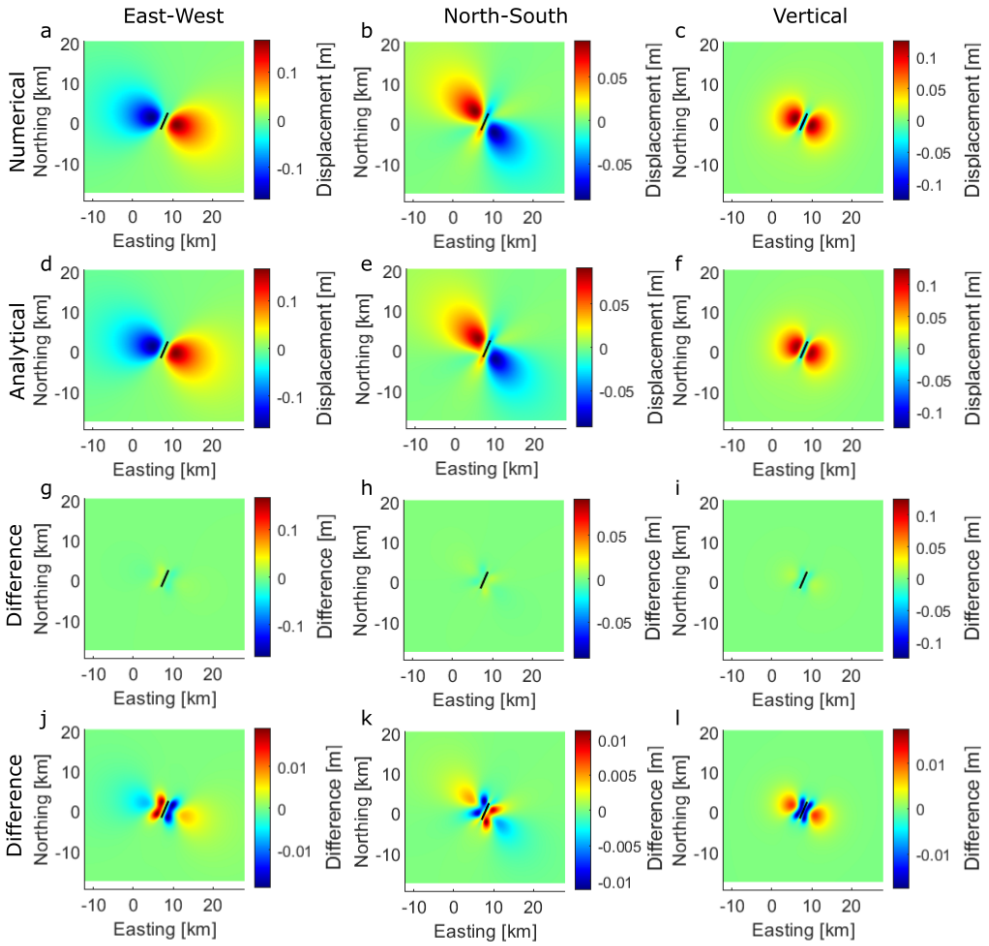

Figure S5 : Linear-elastic version of the dike model with the base of the crust being unconstrained. a)-c) East-West, North-South and vertical displacements predicted by the numerical model. d)-f) East-West, North-South and vertical displacements predicted by the analytical Okada model (Okada, 1985; Battaglia et al., 2013). g)-i) Difference between the models if the analytical model is subtracted from the numerical one. j)-l) Same as g)-i), but with the adjusted to match the range of the difference for each component.

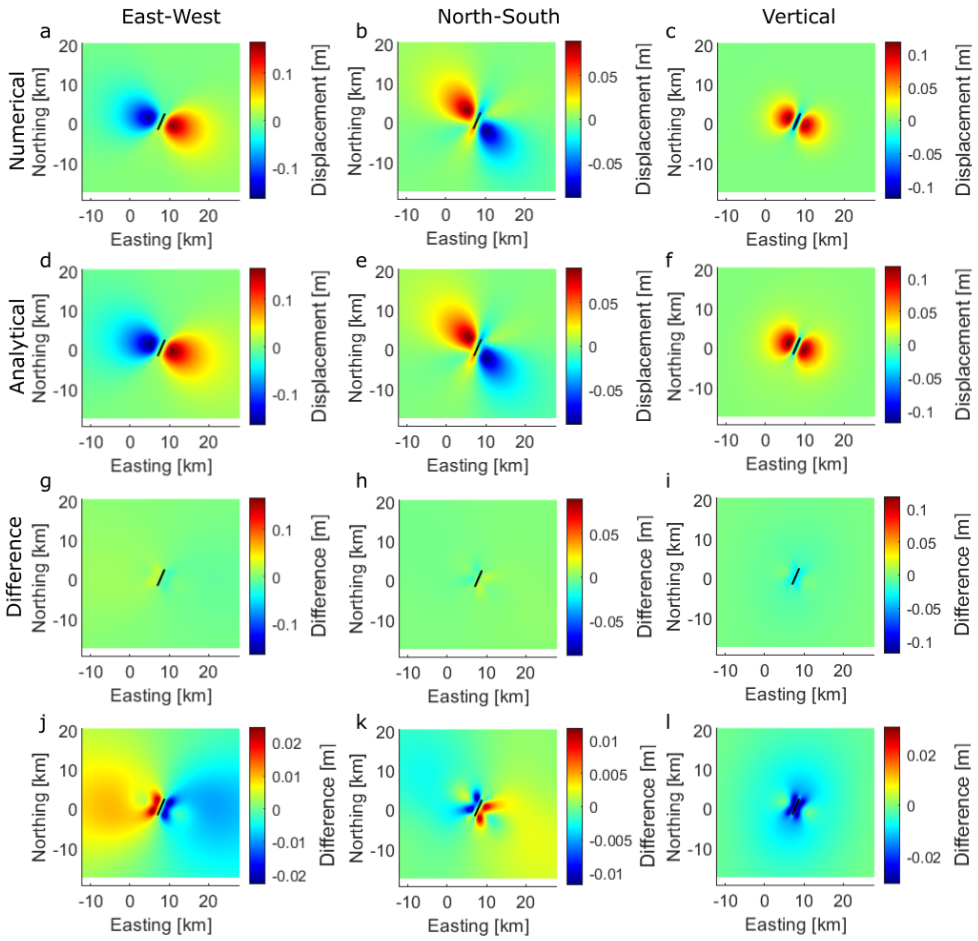

Figure S6 : Linear-elastic version of the dike model with the base of the crust being constrained. a)-c) East-West, North-South and vertical displacements predicted by the numerical model. d)-f) East-West, North-South and vertical displacements predicted by the analytical Okada model (Okada, 1985; Battaglia et al., 2013). g)-i) Difference between the models if the analytical model is subtracted from the numerical one. j)-l) Same as g)-i), but with the adjusted to match the range of the difference for each component.

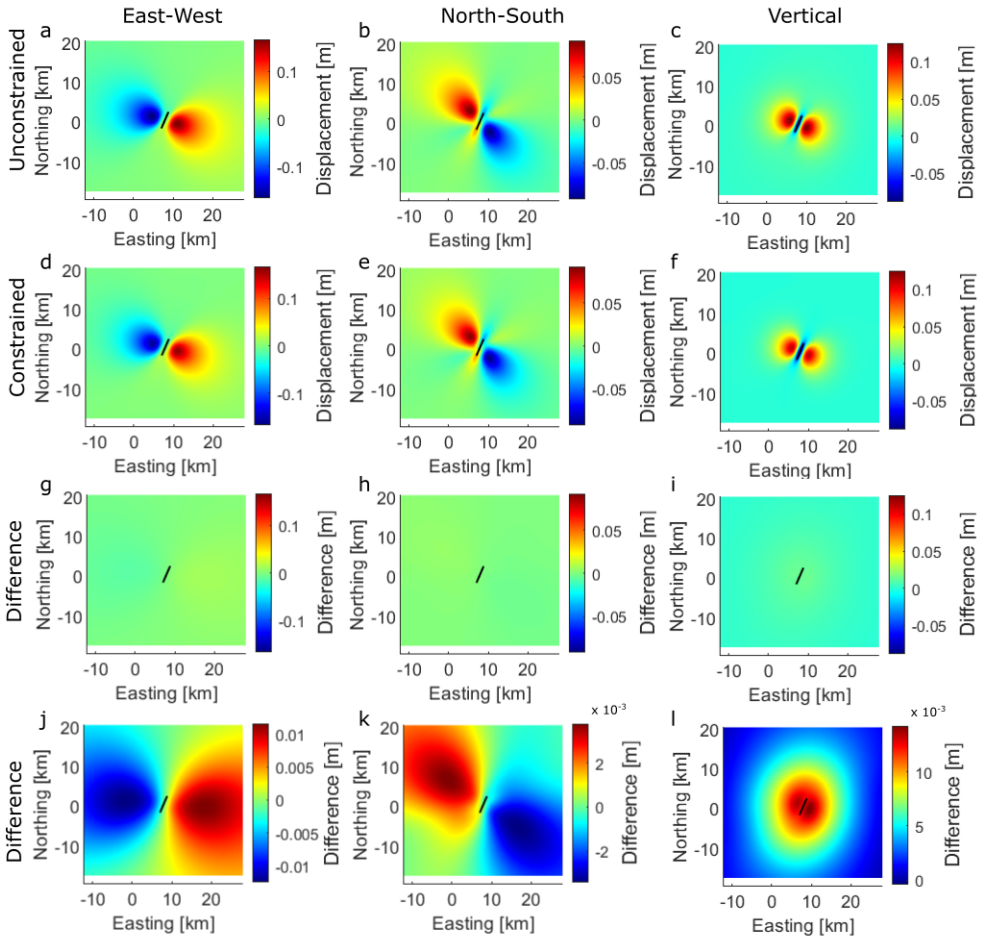

Figure S7 : Comparison between the models with an unconstrained and constrained base of the crust. a)-c) East-west, north-south and vertical displacements predicted by the unconstrained model. d)-f) East-west, north-south and vertical displacements predicted by the constrained model. g)-i) Difference between the models if the constrained model is subtracted from the unconstrained one. j)-l) as g)-i) but with the color scale adjusted to match the range of the difference for each component.

S6 Tectonic Model - Relative Plate Motion

Plate spreading at the Reykjanes Peninsula and elsewhere in Iceland has been modeled primarily with elastic srew-dislocation models (Árnadóttir et al., 2006; Keiding et al., 2008; Árnadóttir et al., 2009) or as elastic slabs (Heimisson and Segall, 2020; Spaans and Hooper, 2018). Both of these types of models solve for a locking depth, above which the plates are locked and being stretched, and below which the plates are unlocked and move freely. In the model presented here spreading is applied at depths, which change as a function of distance from the plate boundary (Equation 2 and Figure 1g in the main text) based on Savage and Burford (1973). In this equation, the locking depth corresponds to the depth, above which the plates are locked, while they can freely move away from or past each other. Eq. (2) describes well the velocity field across plate boundaries (Heimisson et al., 2015; Islam et al., 2016). However, the obliqueness of the plate motion on Reykjanes brings up the question if the distance from the plate boundary axis in the arctan-function should be the actual (perpendicular) distance from the axis or along the direction of plate motion and we found that the first option fits well (Figure S8).

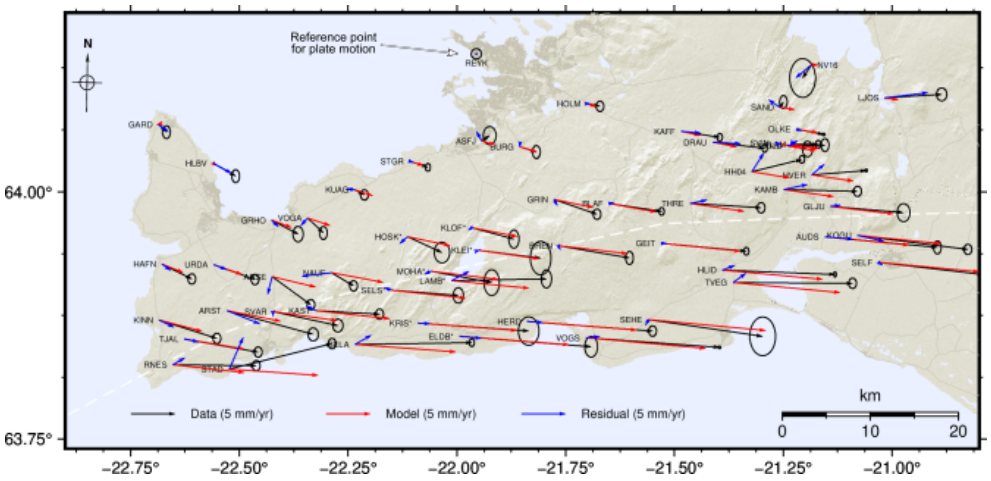

Figure S8 : Modelled and geodetically observed horizontal surface velocities at the end of the tectonic model (after 800 years of spreading). Observed velocities from Keiding et al. (2008). All velocities are given relative to station REYK, which is located in Reykjavik.

Comparison of modelled and observed surface velocities relative to the GNSS-station REYK shows that the spreading directions are to a large extent similar (Figure S8). Deviations are found close to the geothermal powerplants at Svartsengi and Hengill, where residuals show inward motion, since we did not consider deformation or changes in material properties related to geothermal processes in our models. The model underpredicts deformation at the stations positioned along the northern and southern coast of the Reykjanes Peninsula. It is possible that the velocities applied to the base of the crust do not increase fast enough (i.e.,

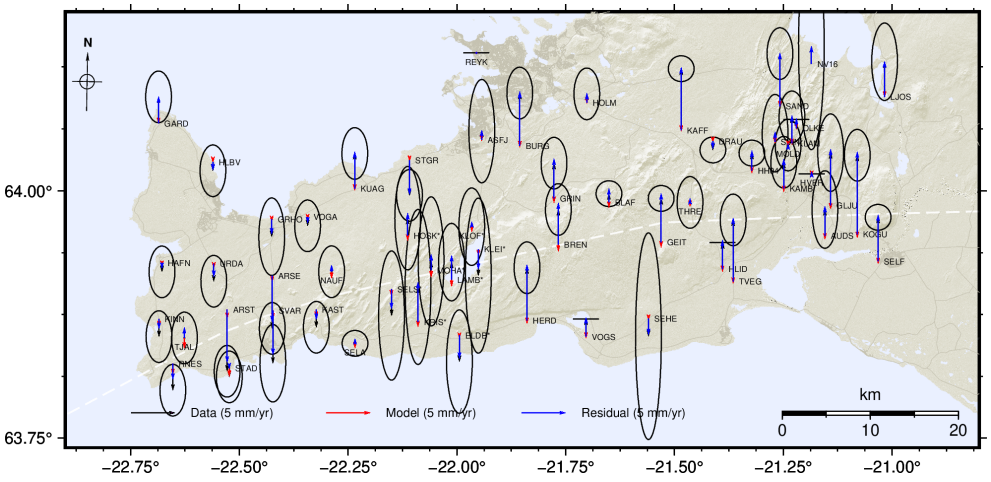

Figure S9 : Modelled and geodetically observed vertical surface velocities at the end of the tectonic model (after 800 years of spreading). Observed velocities from Keiding et al. (2008). All velocities are given relative to station REYK, which is located in Reykjavik.

the applied arctan-function is not steep enough) or it could relate to the crustal structure, i.e. that the spreading is applied to deeply, which would imply that the temperature in the model decreases too fast away from the plate boundary. Other possibilities are changes in the crustal properties, which are not considered in the model or that an overall different mechanism is needed to focus the plate boundary deformation. The vertical spreading rates show a much poorer fit to observations than the horizontal (Figure S9), although it should be noted that the vertical component of observed velocities is also less well constrained. The poor fit could relate to constraints introduced by preventing vertical motion at the base of the elastic crust. This however was required to focus the horizontal deformation. Alternatively, the observed subsidence could relate to geological processes, which are not considered in our model To some extent this could relate to geothermal exploration (Keiding et al., 2010; Parks et al., 2020), aspects of the crustal structure, which are not represented here (Lanzi et al., 2024) or glacio-isostatic adjustment (e.g., Drouin and Sigmundsson, 2019).

The aim of this study is however to reproduce the first-order features of the tectonic stress field and we decided that based on the horizontal component, the predicted plate spreading is similar enough to observed plate motion to justify its use in the dike model. It should be pointed out that because the strain is largely constrained by the forced motion at depth, the deformation field itself does not much depend on the chosen elastic properties of the crust. There is for example little variation between a model with a constant Young's modulus or a variable one. The choice of Young's modulus mainly affects the associated stresses, which in turn affect the opening of the dike in the second model step.

S7 Stress and Stress Changes

S7.1 Stress in the Dike Plane

The opening angles based on deformation predicted by the dike model were calculated as

$$\mu_{def} = atan\left(\frac{s}{o}\right) \tag{S2}$$

with s as the shear and o as the opening across the crack plane. Positive opening angles are associated with right-lateral shear, negative with left-lateral shear and $\mu = 0°$ corresponds to purely tensile opening. Delaney et al. (1986) and Jolly and Sanderson (1997) derived the expected opening angle from loading conditions as

$$\mu_{load} = atan\left(\frac{\tau}{P_f - \sigma_n}\right) \tag{S3}$$

where τ, P_f and σ_n are the shear stress, the fluid pressure and the normal stress acting on the dike plane, respectively. For the Fagradalsfjall dike, we set $P_f = 0\,MPa$ and multiplied the total normal stress by 0.6 to account for the partial release of tectonic stress. When handeling stresses in Comsol, it should be noted that tensional stress is positive, not negative as is conventional in Earth Sciences. Therefore, the fluid pressure and normal stress in Eq. S3 need to be added rather than subtracted when calculating the opening angles Figure S11 .

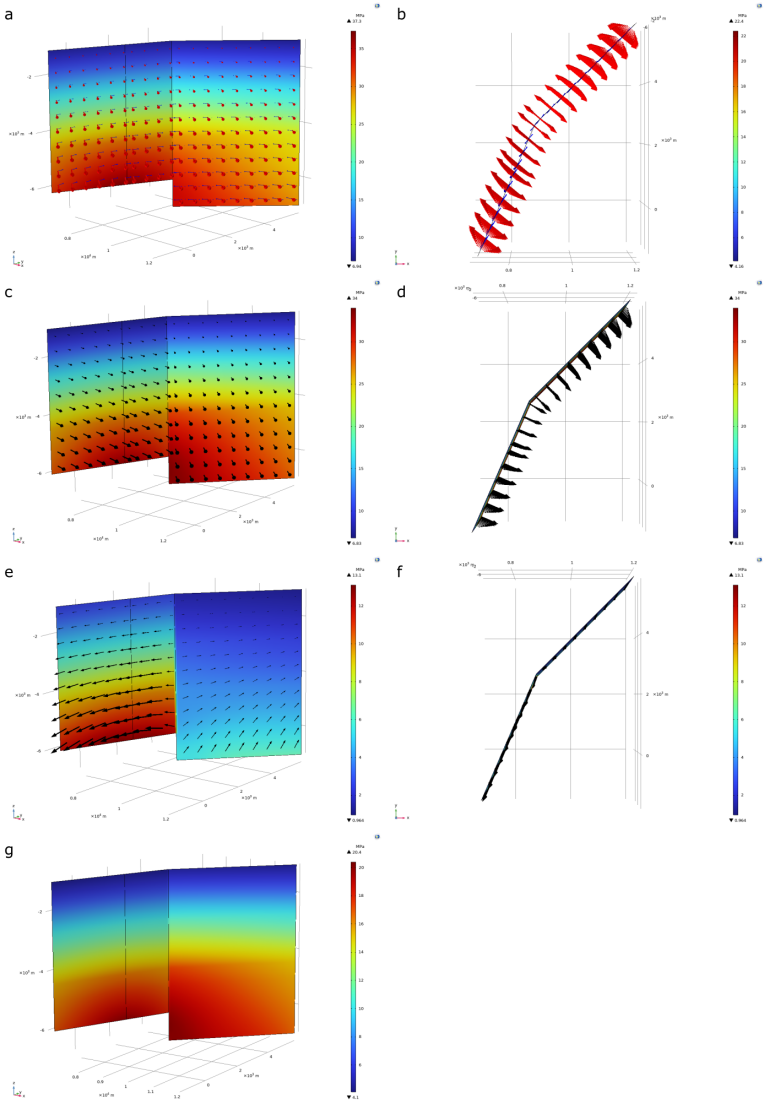

Figure S10 : Loading conditions in the dike plane due to tectonic motion (after 800 years of plate spreading). a) Sideview and b) Top view of the least compressive stress. Arrows indicate directions of principal stresses (red: least compressive, blue: most compressive stress). The top view shows that the principal stresses are almost parallel to the northern segment, but oblique to the southern dike segment. c) Side view and d) top view of the stress acting normal to the dike plane. Black arrows indicate directions. e) Side view and f) Top view of the tangential (shearing) component of the stress field. Black arrows indicate directions. g) Side view of 60% of the normal loading. The stresses acting on the dike plane during the dike model correspond to a superposition of e) and g).

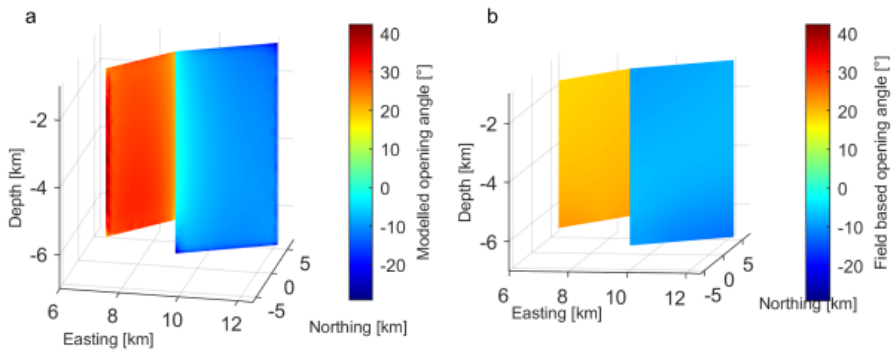

Figure S11 : Opening angle based on a) opening and shear predicted by the dike model and b) normal and tangential loading due to tectonic stress.

S7.2 Stress change $\Delta\sigma_3$ caused by the dike

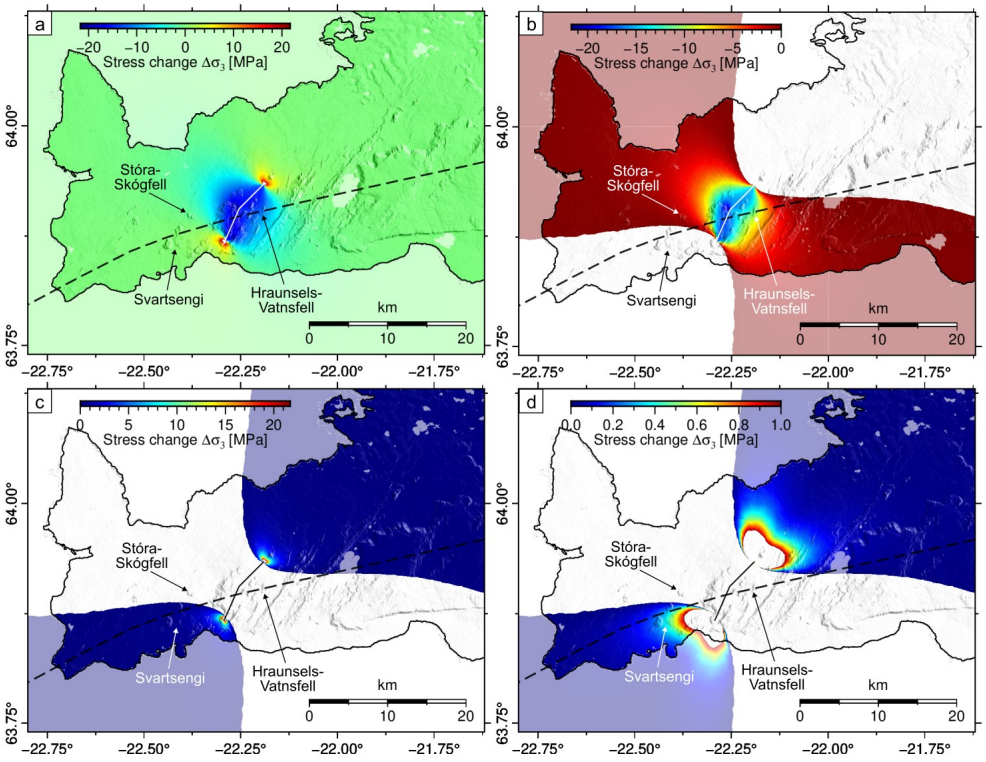

Figure S12 : a) Stress change of the least compressive stress σ_3 in response to the dike at 4 km depth. Dike and plate boundary are marked by solid and dashed lines. Negative change corresponds to stress decrease, poisitve change to stress increase. b)-d) use different color scale limits to highlight b) area of reduced stress, c) area of increased stress and d) area of low-amplitude stress increase, specifically the area around Svartsengi, where magmatic and volcanic activity moved in fall 2023.

S8 Comparison of LOS-Residual to Mapped Fault Traces

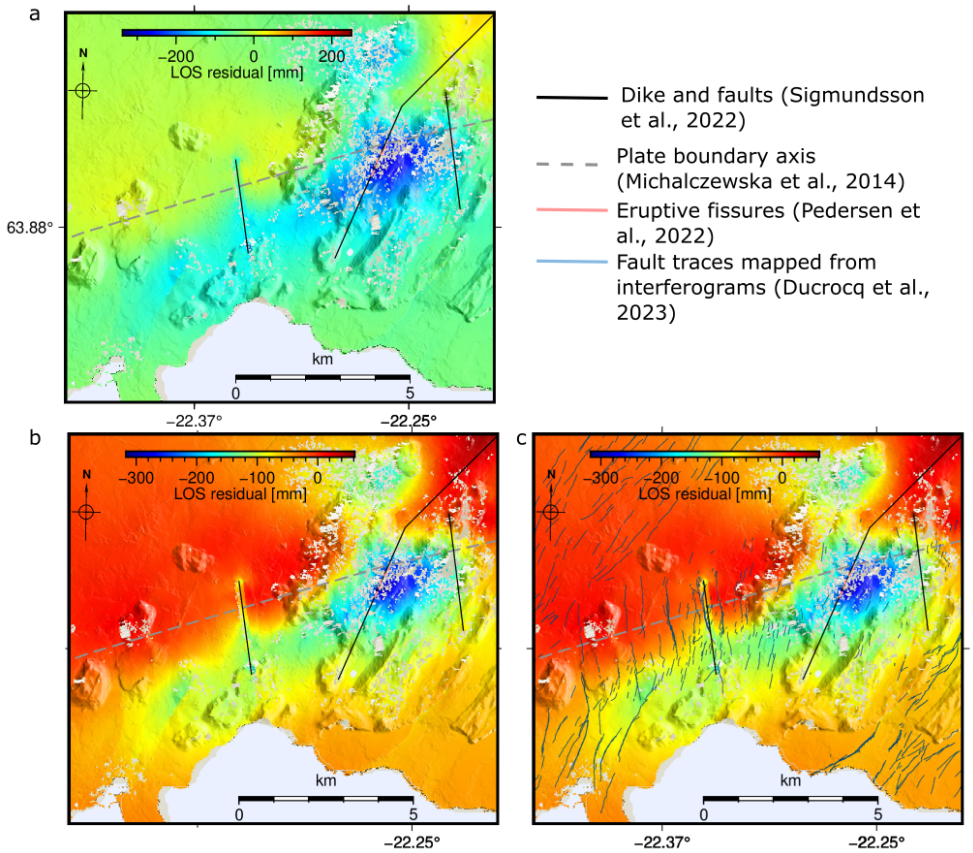

Figure S13 : Residual between observed and modelled surface deformation related to dike opening around the southwest corner of the dike. a) Part of Figure 2d of the main text. b) Same as a), but with adjusted colormap. c) Same as b), but with fault traces mapped by Ducrocq et al. (2024). Data from Ducrocq et al. (2023).

Large parts of the residual signal southwest of the dike can be directly connected to fault traces, which were mapped by Ducrocq et al. (2024). While most fractures in this area strike approximately NS, one fault located just south of the plate boundary strikes closer to NE and shows prominent offset of several centimeters. Additionally, the left of the two faults, whose coseismic deformation was removed from the image in Section S4.2 appears to continue further south than initially estimated, since a sharp step in the residual appears to continue beyond the mapped signal until almost all the way to the coast (Figure S13 b).

S9 Difference between Tectonic Stress- and Pressure-driven Models

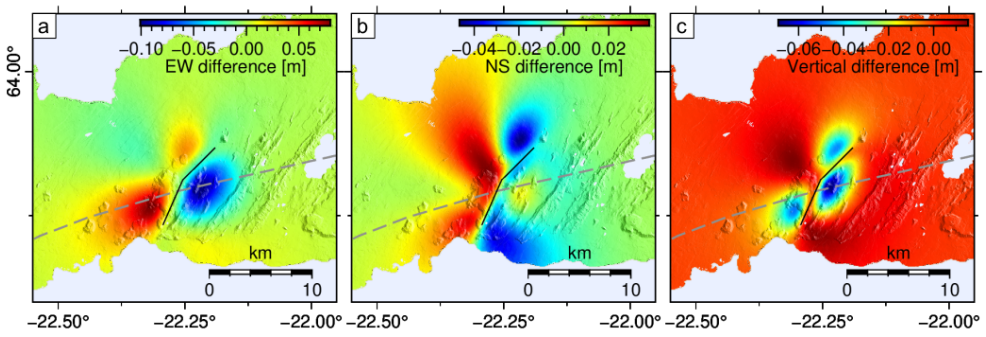

Figure S14 : Difference between the models driven by tectonic stress and uniform overpressure, respectively. The panels correspond to Figure 4 g-i in the main text, but have the colorscales adjusted to the largest differences of each component. a) East-west deformation component, b) north-south component and c) vertical component.

S10 Loading Conditions on the Dike

S10.1 Fraction of Released Tectonic Stress

When evaluating the fit between the observed and modelled surface deformation associated with the dike, we compared the RMS of the LOS-displacement as well as of each of the GNSS components for fractions of released tectonic stress that were varied in 10%-increments (Figure S15). While the horizontal components of the GNSS-displacement are best reproduced if 60% of the normal component of the tectonic stress field are released, the LOS- and vertical GNSS-deformation are best reproduced if 40% of the tectonic stress are released.

However, the vertical component of GNSS displacements typically has larger uncertainties than the horizontal components and variations in the LOS-displacement were relatively minor, which is likely related to relatively more far-field data compared to GNSS. We therefore decided that the model which released 60% of the tectonic stress was preferable.

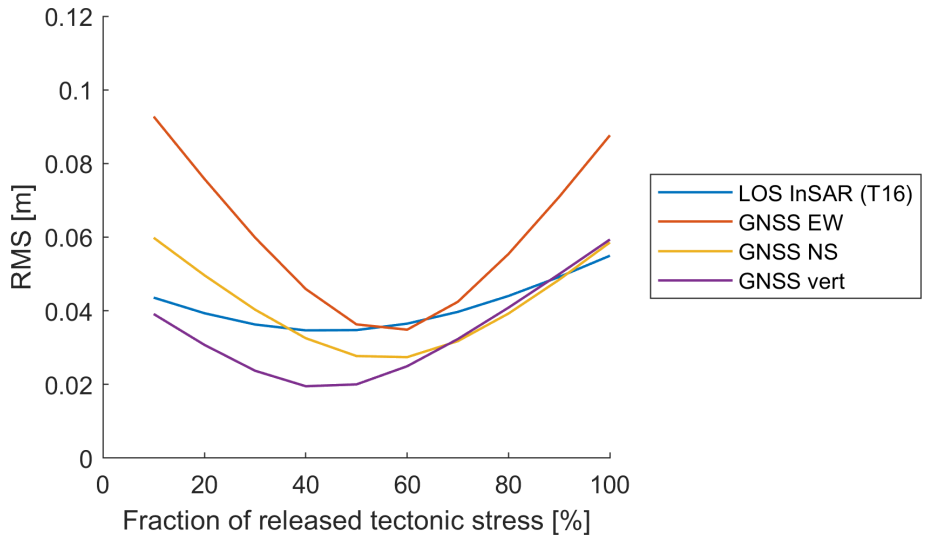

Figure S15 : RMS of dike models for which varying fractions of the accumulated tectonic stress are released. Observed data from Sigmundsson et al. (2022).

S10.2 Distributed Opening Model by Sigmundsson et al. (2022)

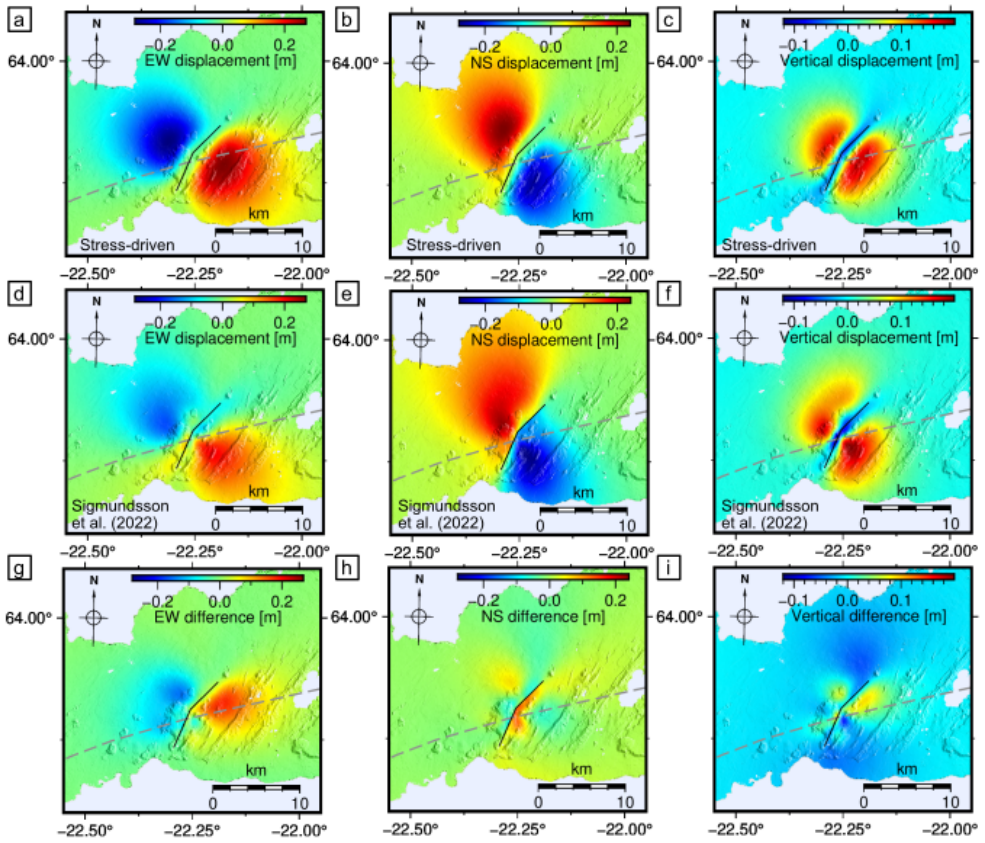

Figure S16 : Comparison between the surface deformation of the dike-model form the main text (a-c) and the distributed opening model by Sigmundsson et al. (2022) (d-f) as well as the associated differences (g-i). For the difference, the deformation predicted from the model by Sigmundsson et al. (2022) was subtracted from the model from this study.

The difference between the dike model from this study and the distributed opening model by Sigmundsson et al. (2022) reaches a significant fraction of the predicted signals (Figure S16). Especially in the horizontal components, the distributed opening model by Sigmundsson et al. (2022) predicts more deformation directly above the dike. This relates to that in their model, the dike reached to the surface and there is both opening and shearing close to or at the surface especially close to the center of the dike (Figure S16 d,e).

The RMS between models and observations for the model from this study and the multi-source model by Sigmundsson et al. (2022) are surprisingly similar, even though our study only considers the dike itself and the two major earthquakes, while the model by Sigmundsson et al. (2022) also considers shear along a plate boundary segment and a contracting point source (Table S3). The worse fit in

Table S3: Comparison of RMS-values for the interferogram and GNSS-signals between the stress driven model from this study and the model by Sigmundsson et al. (2022). Their model considers distributed opening/shear on the dike, shear on the plate boundary segment, the two M>5 earthquakes, which were removed from the geodetic signals in this study, as well as a contracting Mogi-source.

Model	LOS [m]	GNSS, EW [m]	GNSS, NS [m])	GNSS, vertical [m]
Stress-model	0.037	0.035	0.027	0.025
Sigmundsson et al. (2022)	0.034	0.011	0.020	0.024

the horizontal components of the GNSS-data for the model form this study likely relates to that near-surface coseismic deformation around Svartsengi/Grindavík is not considered specifically in our study, but covered by the plate-boundary shear by Sigmundsson et al. (2022). The small difference between our model and their model in the RMS for the LOS may be related to that there are many data points in the far field with overall little deformation. This may to some degree reduce the sensitivity to changes in the near field.

S10.3 Entire Tectonic Stress Released

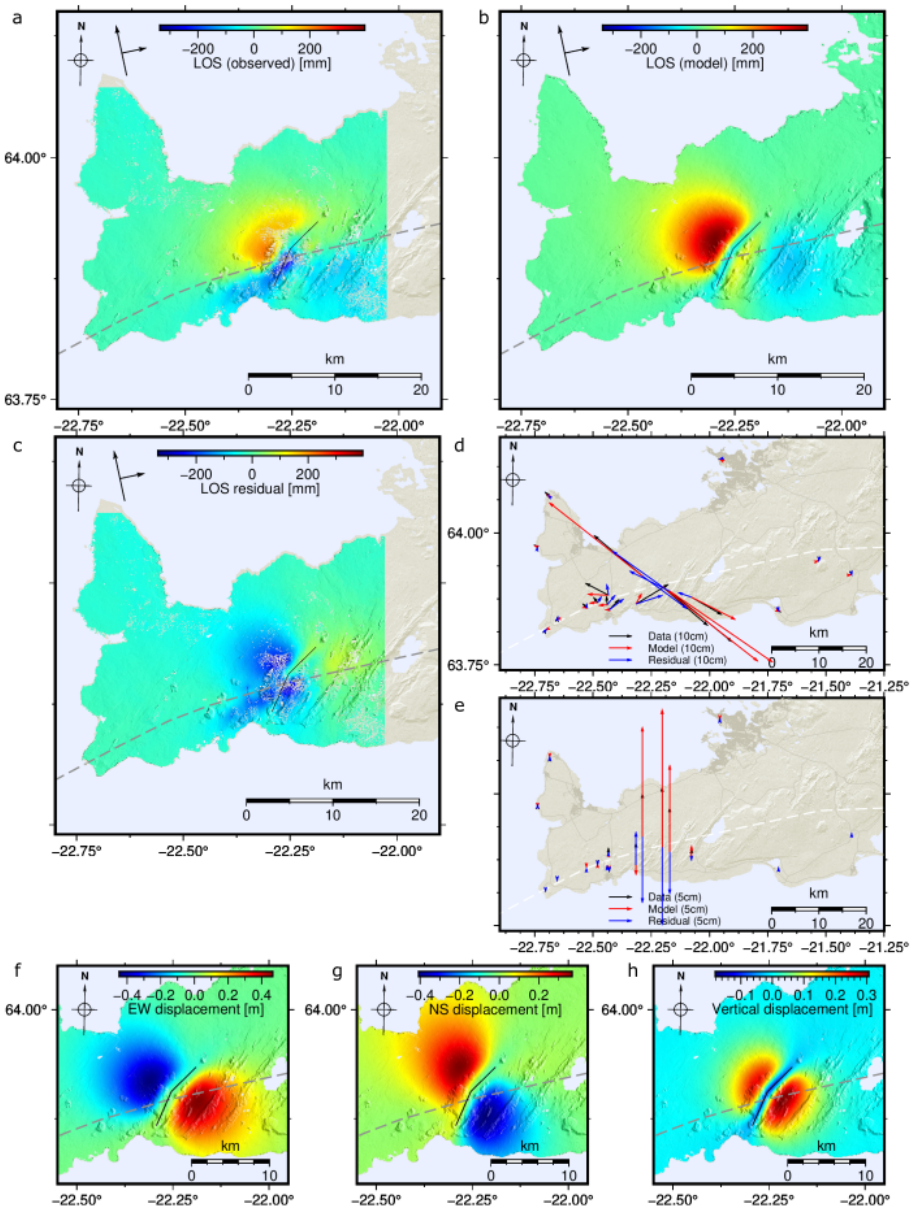

Figure S17 : Surface deformation predicted by the dike model if the entire tectonic stress were released. a) Observed LOS-displacement (Sigmundsson et al., 2022) with two major earthquakes removed. b) Projection of predicted deformation onto the LOS vector. c) Residual between a and b. d) Horizontal and e) vertical deformation at GNSS-benchmarks. f) East-west, g) north-south and h) vertical component of the predicted surface displacement.

S10.4 40% of Tectonic Stress Released

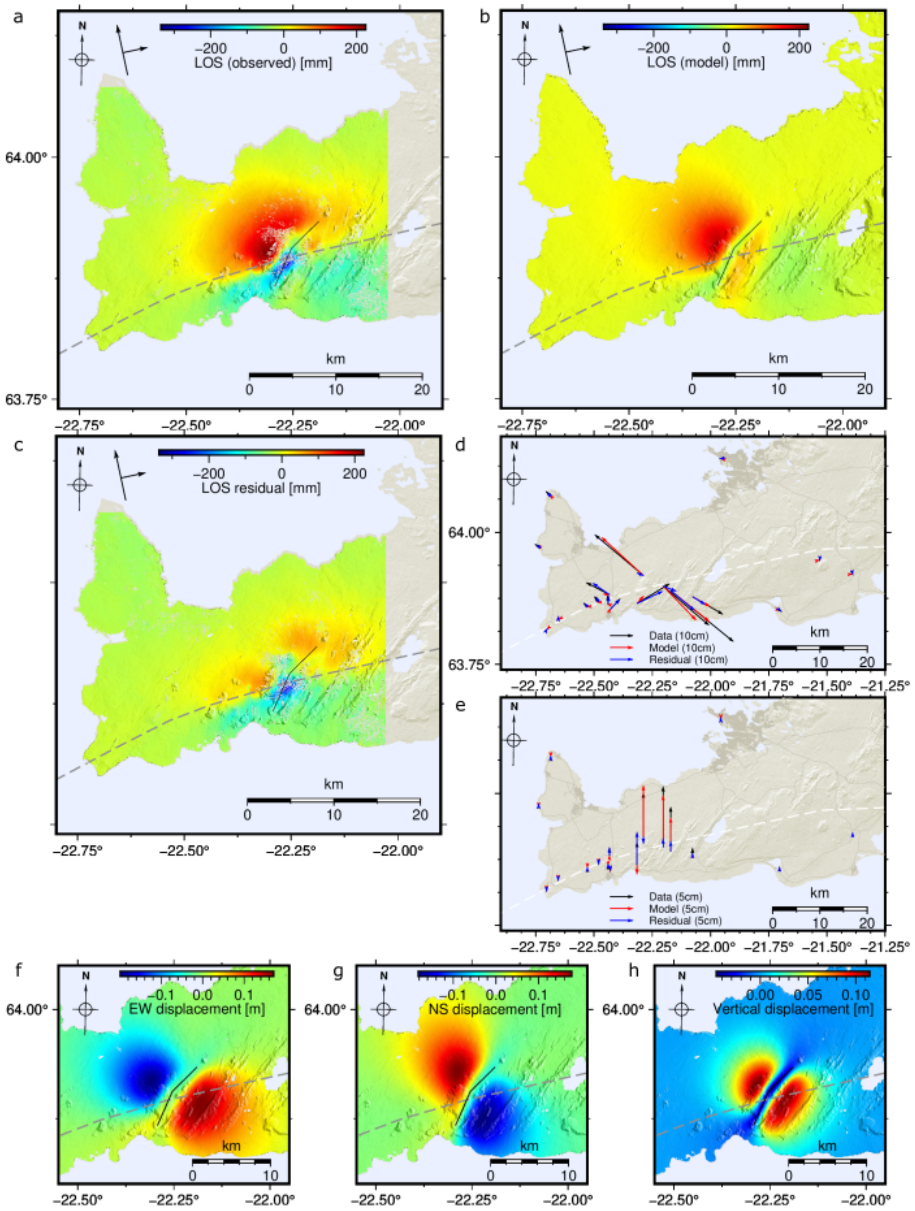

Figure S18 : Surface deformation predicted by the dike model if the 40% of the normal component of the tectonic stress were released. a) Observed LOS-displacement (Sigmundsson et al., 2022) with two major earthquakes removed. b) Projection of predicted deformation onto the LOS vector. c) Residual between a and b. d) Horizontal and e) vertical deformation at GNSS-benchmarks. f) East-west, g) north-south and h) vertical component of the predicted surface displacement.

S10.5 Influence of dike geometry

The fraction of tectonic stress that best reproduces the surface deformation is to some degree dependent on the dimensions of the dike. A detailed study of how the geometry and dimensions of the dike affect surface deformation and the best-fitting fraction of released tectonic stress was beyond the scope of this study. However, we performed some preliminary tests of how this released fraction changes if the top edge of the dike was moved to shallower or larger depths, respectively. The top of the dike was moved to 500 m and 1.5 km below the surface compared to the 1 km depth for the model in the main text (Figure S19). The lower depth and the segment length remain unchanged compared to the model in the main text.

The RMS between between observed and modeled surface deformation for the three GNSS-displacement components as well as for thr LOS-vector of the InSAR image are shows a shift of the minima towards higher released fractions with increasing top-depth of the dike (Figure S19 a-c). The RMS of all four displacement components is on a similar order of magnitude both between the components and across the different top depths. However, the GNSS-displacement shows a higher sensitivity to changes of the top depth of the dike compared to the LOS-displacement. This may in part relate to the large number of pixels of the InSAR image and that far-field points do not experience significant changes of the top depth is varied. Determining the best-fitting fraction of released stress may be somewhat subjective since it depends on the weight put on individual displacement components. The horizontal GNSS components show good agreement across all three tested top depths, while the vertical GNSS component agrees better with the LOS-displacement. Both favour slightly lower fractions of released stress compared to the horizontal GNSS-displacement, i.e. the vertical displacement overestimates observed deformation if the horizontal deformation amplitudes match well. Moving the top of the dike to shallower depth has very limited effects, but the best-fitting fraction of tectonic stress may be closer to 50% than the 60% indicated for the model presented in the main text. Opening of the shallow crust would be expected to create higher and more concentrated surface deformation. Similarly, if opening is restricted to deeper parts of the crust, a higher fraction of stress needs to be released to create deformation of the same amplitude. Because of the larger depth, these effects are distributed over a larger area, which results in overall stronger effects on the RMS-curves, which differ more between Figure S19 b) and c) compared to a) and b), i.e. the change to the shallower depth.

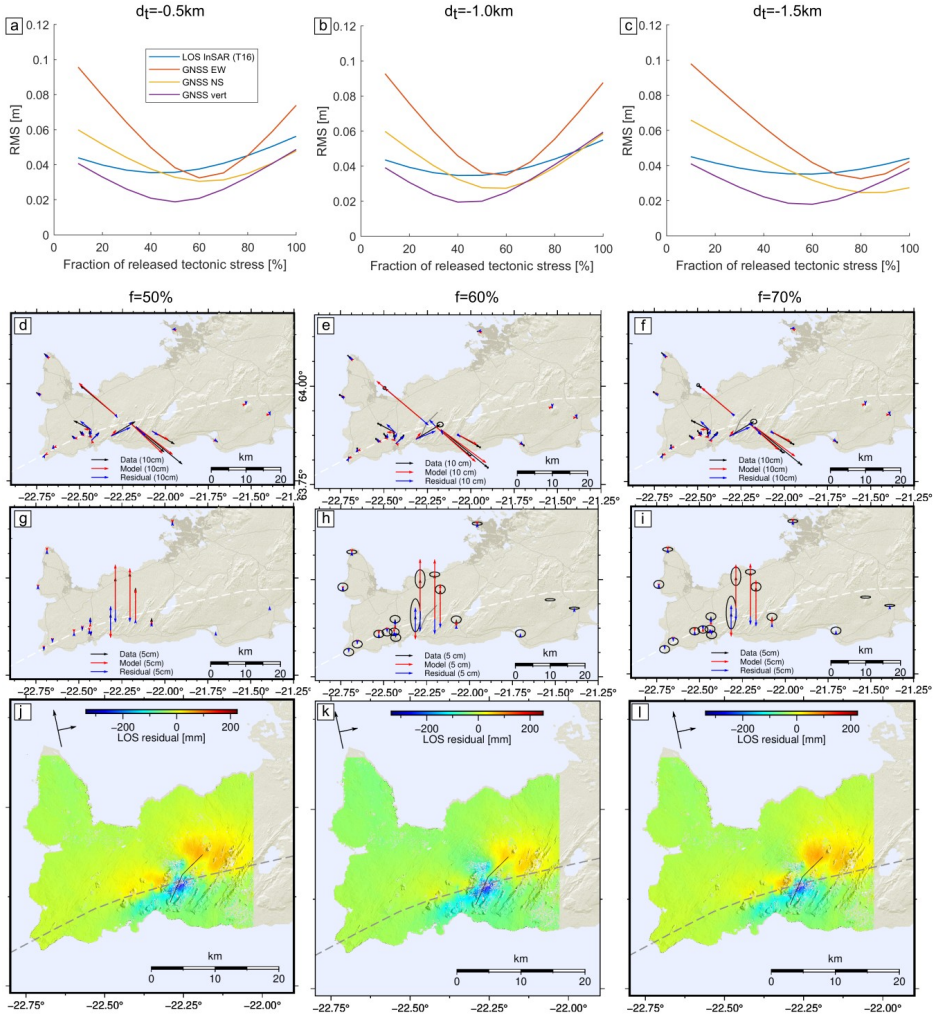

Figure S19 : Surface deformation predicted by models with varying depth of the upper edge of the dike d_t. a)-c) Root-mean-square of different deformation components (legend in panel a). d)-f) Horizontal displacement of GNSS-stations. Fraction of released tectonic stress f listed above the panels. g)-i) Vertical GNSS-displacement. j)-l) Residual between observed and modeled ground deformation along the Line-of-Sight vector of the InSAR-satellite used in the main text. The middle column ($d_t = -1\,km$) corresponds to the model shown in the main text.

S11 Additional Limitations

There are a number of limitations and things to consider that are common for numerical models and/or dislocation models.

Small parts of the model domain close to sharp corners show stress-singularities. This is a common issue when modelling dislocations or cracks and in the present model this occurs e.g., at the intersection between the base of the crust and the

plate boundary axis and at the edges of the dike. This affects only individual elements and we adjusted the colormaps in stress-plots to exclude the affected elements. In nature, brittle or plastic deformation would prevent the buildup of such high stresses, but this was considered beyond the scope of this study.

The model in this study is based on simplified models of the temperature and elastic properties of the Reykjanes Peninsula. While future models may be able to provide more realistic models based on more sophisticated crustal properties, the first-order effects of tectonic stress for dike-emplacement can still be investigated with the simplified structures used in the present study. 3D-seismic velocity models form seismic tomography may be valuable for future, more detailed models.

Lastly, the current model does not directly consider brittle-plastic deformation and assumes that the crust behaves as a continuous medium apart from the crack-boundary condition representing the dike. While widespread fault motion during the dike emplacement has been shown by Ducrocq et al. (2024), this is challenging to implement in deformation models at this time. Nonetheless, efforts to represent distributed fault motion would be of great value for areas such as the Reykjanes Peninsula.

References

Battaglia, M., P. F. Cervelli, and J. R. Murray. "dMODELS: A MATLAB software package for modeling crustal deformation near active faults and volcanic centers". In: *Journal of Volcanology and Geothermal Research* 254 (2013), pp. 1–4. ISSN: 0377-0273. DOI: https://doi.org/10.1016/j.jvolgeores.2012.12.018. URL: https://www.sciencedirect.com/science/article/pii/S0377027312003836.

Caracciolo, A., E. Bali, S.A. Halldórsson, G.H. Gudfinnsson, M. Kahl, I. Thórdardóttir, G.L. Pálmadóttir, and V. Silvestri. "Magma plumbing architectures and timescales of magmatic processes during historical magmatism on the Reykjanes Peninsula, Iceland". In: *Earth and Planetary Science Letters* 621 (2023), p. 118378. ISSN: 0012-821X. DOI: https://doi.org/10.1016/j.epsl.2023.118378. URL: https://www.sciencedirect.com/science/article/pii/S0012821X23003916.

Currenti, G., R. Napoli, A. Di Stefano, F. Greco, and C. Del Negro. "3D integrated geophysical modeling for the 2008 magma intrusion at Etna: Constraints on rheology and dike overpressure". In: *Physics of the Earth and Planetary Interiors* 185.1 (2011), pp. 44–52. ISSN: 0031-9201. DOI: https://doi.org/10.1016/j.pepi.2011.01.002. URL: https://www.sciencedirect.com/science/article/pii/S0031920111000124.

Delaney, P. T., D. D. Pollard, J. I. Ziony, and E. H. McKee. "Field relations between dikes and joints: Emplacement processes and paleostress analysis". In: *Journal of Geophysical Research: Solid Earth* 91.B5 (1986), pp. 4920–4938. DOI: https://doi.org/10.1029/JB091iB05p04920. URL: https://agupubs.onlinelibrary.wiley.com/doi/abs/10.1029/JB091iB05p04920.

414 Drouin, V. and F. Sigmundsson. "Countrywide Observations of Plate Spreading
415 and Glacial Isostatic Adjustment in Iceland Inferred by Sentinel-1 Radar
416 Interferometry, 2015–2018". In: *Geophysical Research Letters* 46.14 (2019),
417 pp. 8046–8055. DOI: https://doi.org/10.1029/2019GL082629. eprint:
418 https://agupubs.onlinelibrary.wiley.com/doi/pdf/10.1029/2019GL
419 082629. URL: https://agupubs.onlinelibrary.wiley.com/doi/abs/10.
420 1029/2019GL082629.
421 Ducrocq, C., Th. Árnadóttir, P. Einarsson, S. Jónsson, V. Drouin, H. Geirsson,
422 and Á. R. Hjartardóttir. "Widespread fracture movements during a volcano-
423 tectonic unrest: the Reykjanes Peninsula, Iceland, from 2019–2021 TerraSAR-
424 X interferometry". In: *Bulletin of Volcanology* 86.2 (2024), p. 14. DOI: https:
425 //doi.org/10.1007/s00445-023-01699-0.
426 Ducrocq, C., Th. Árnadóttir, P. Einarsson, S. Jónsson, V. Drouin, H. Geirsson,
427 and Á. Rut. Hjartardóttir. *Additional material for the article "Widespread
428 fracture movements during a volcano-tectonic unrest: the Reykjanes Penin-
429 sula, Iceland, from 2019–2021 TerraSAR-X interferometry"*. Dec. 2023. DOI:
430 10.5281/zenodo.10433761. URL: https://doi.org/10.5281/zenodo.
431 10433761.
432 Heimisson, E. R., A. Hooper, and F. Sigmundsson. "Forecasting the path of a
433 laterally propagating dike". In: *Journal of Geophysical Research: Solid Earth*
434 120.12 (2015), pp. 8774–8792. DOI: https://doi.org/10.1002/2015JB
435 012402. eprint: https://agupubs.onlinelibrary.wiley.com/doi/pdf/10.
436 1002/2015JB012402. URL: https://agupubs.onlinelibrary.wiley.com/
437 doi/abs/10.1002/2015JB012402.
438 Heimisson, E. R. and P. Segall. "Physically Consistent Modeling of Dike-Induced
439 Deformation and Seismicity: Application to the 2014 Bárdarbunga Dike, Ice-
440 land". In: *Journal of Geophysical Research: Solid Earth* 125.2 (2020). e2019JB018141
441 10.1029/2019JB018141, e2019JB018141. DOI: https://doi.org/10.1029/
442 2019JB018141. eprint: https://agupubs.onlinelibrary.wiley.com/doi/
443 pdf/10.1029/2019JB018141. URL: https://agupubs.onlinelibrary.
444 wiley.com/doi/abs/10.1029/2019JB018141.
445 Islam, Md. Tariqul, Erik Sturkell, Peter LaFemina, Halldór Geirsson, Freysteinn
446 Sigmundsson, and Halldór Ólafsson. "Continuous subsidence in the Thingvel-
447 lir rift graben, Iceland: Geodetic observations since 1967 compared to rhe-
448 ological models of plate spreading". In: *Journal of Geophysical Research:
449 Solid Earth* 121.1 (2016), pp. 321–338. DOI: https://doi.org/10.1002/
450 2015JB012306. eprint: https://agupubs.onlinelibrary.wiley.com/doi/
451 pdf/10.1002/2015JB012306. URL: https://agupubs.onlinelibrary.
452 wiley.com/doi/abs/10.1002/2015JB012306.
453 Jolly, R.J.H. and D.J. Sanderson. "A Mohr circle construction for the opening of a
454 pre-existing fracture". In: *Journal of Structural Geology* 19.6 (1997), pp. 887–
455 892. ISSN: 0191-8141. DOI: https://doi.org/10.1016/S0191-8141(97)
456 00014-X. URL: https://www.sciencedirect.com/science/article/pii/
457 S019181419700014X.
458 Karato, S.i. and P. Wu. "Rheology of the Upper Mantle: A Synthesis". In: *Science*
459 260.5109 (1993), pp. 771–778. DOI: 10.1126/science.260.5109.771. eprint:

https://www.science.org/doi/pdf/10.1126/science.260.5109.771. URL: https://www.science.org/doi/abs/10.1126/science.260.5109.771.

Keiding, M., B. Lund, and T. Árnadóttir. "Earthquakes, stress, and strain along an obliquely divergent plate boundary: Reykjanes Peninsula, southwest Iceland". In: *Journal of Geophysical Research: Solid Earth* 114.B9 (2009). DOI: https://doi.org/10.1029/2008JB006253. eprint: https://agupubs.onlinelibrary.wiley.com/doi/pdf/10.1029/2008JB006253. URL: https://agupubs.onlinelibrary.wiley.com/doi/abs/10.1029/2008JB006253.

Keiding, M., T. Árnadóttir, S. Jónsson, J. Decriem, and A. Hooper. "Plate boundary deformation and man-made subsidence around geothermal fields on the Reykjanes Peninsula, Iceland". In: *Journal of Volcanology and Geothermal Research* 194.4 (2010), pp. 139–149. ISSN: 0377-0273. DOI: https://doi.org/10.1016/j.jvolgeores.2010.04.011. URL: https://www.sciencedirect.com/science/article/pii/S0377027310001290.

Keiding, M., T. Árnadóttir, E. Sturkell, H. Geirsson, and B. Lund. "Strain accumulation along an oblique plate boundary: The Reykjanes Peninsula, southwest Iceland". In: *Geophysical Journal International* 172.2 (Feb. 2008), pp. 861–872. ISSN: 0956-540X. DOI: 10.1111/j.1365-246X.2007.03655.x. eprint: https://academic.oup.com/gji/article-pdf/172/2/861/5985592/172-2-861.pdf. URL: https://doi.org/10.1111/j.1365-246X.2007.03655.x.

Lanzi, C., F. Sigmundsson, M. M. Parks, H. Geirsson, and V. Drouin. "Strain Localization at Volcanoes Undergoing Extension: Investigation of Long-Term Deformation at Krafla and Askja Volcanic Systems in North Iceland". In: *Geophysical Research Letters* 51.21 (2024). e2024GL110299 2024GL110299, e2024GL110299. DOI: https://doi.org/10.1029/2024GL110299. eprint: https://agupubs.onlinelibrary.wiley.com/doi/pdf/10.1029/2024GL110299. URL: https://agupubs.onlinelibrary.wiley.com/doi/abs/10.1029/2024GL110299.

Michalczewska, K., S. Hreinsdóttir, S. Dumont, and F. Sigmundsson. *Crustal deformation on the Western Reykjanes Peninsula 2009 to 2014 mapped by InSAR and GPS measurements*. Tech. rep. Sturlugata 7, 101 Reykjavík, Iceland: Institute of Earth Sciences, 2014.

Okada, Y. "Surface deformation due to shear and tensile faults in a half-space". In: *Bulletin of the Seismological Society of America* 75.4 (Aug. 1985), pp. 1135–1154. ISSN: 0037-1106. DOI: 10.1785/BSSA0750041135. eprint: https://pubs.geoscienceworld.org/ssa/bssa/article-pdf/75/4/1135/5332841/bssa0750041135.pdf. URL: https://doi.org/10.1785/BSSA0750041135.

Parks, M., F. Sigmundsson, Ó. Sigurdsson, A. Hooper, S. Hreinsdóttir, B. Ófeigsson, and K. Michalczewska. "Deformation due to geothermal exploitation at Reykjanes, Iceland". In: *Journal of Volcanology and Geothermal Research* 391 (2020), p. 106438. ISSN: 0377-0273. DOI: https://doi.org/10.1016/j.jvolgeores.2018.08.016. URL: https://www.sciencedirect.com/science/article/pii/S0377027317305887.

Savage, J. C. and R. O. Burford. "Geodetic determination of relative plate motion in central California". In: *Journal of Geophysical Research (1896-1977)* 78.5 (1973), pp. 832–845. DOI: https://doi.org/10.1029/JB078i005p00832. eprint: https://agupubs.onlinelibrary.wiley.com/doi/pdf/10.1029/JB078i005p00832. URL: https://agupubs.onlinelibrary.wiley.com/doi/abs/10.1029/JB078i005p00832.

Sigmundsson, F., M. Parks, A. Hooper, H. Geirsson, K. S. Vogfjörd, V. Drouin, B. G. Ófeigsson, S. Hreinsdóttir, S. Hjaltadóttir, K. Jónsdóttir, P. Einarsson, S. Barsotti, J. Horálek, and Th. Ágústsdóttir. "Deformation and seismicity decline before the 2021 Fagradalsfjall eruption". In: *Nature* 609.7927 (2022), pp. 523–528. DOI: https://doi.org/10.1038/s41586-022-05083-4. URL: https://doi.org/10.1038/s41586-022-05083-4.

Sigmundsson, F., V. Pinel, R. Grapenthin, A. Hooper, S. A Halldórsson, P. Einarsson, B. G. Ófeigsson, E. R. Heimisson, K. Jónsdóttir, M. T. Gudmundsson, K. Vogfjörd, S. Li, V. Drouin, H. Geirsson, S. Dumont, H. M. Fridriksdottir, G. B. Gudmundsson, T. J. Wright, and T. Yamasaki. "Unexpected large eruptions from buoyant magma bodies within viscoelastic crust". In: *Nature Communications* 11.1 (2020b), p. 2403. DOI: https://doi.org/10.1038/s41467-020-16054-6.

Spaans, Karsten and Andrew Hooper. "Insights Into the Stress Field Around Bárdarbunga Volcano From the 2014/2015 Holuhraun Rifting Event". In: *Journal of Geophysical Research: Solid Earth* 123.4 (2018), pp. 3238–3249. DOI: https://doi.org/10.1002/2017JB015274. eprint: https://agupubs.onlinelibrary.wiley.com/doi/pdf/10.1002/2017JB015274. URL: https://agupubs.onlinelibrary.wiley.com/doi/abs/10.1002/2017JB015274.

Turcotte, D. L. and G. Schubert. *Geodynamics*. 3rd. Cambridge university press, 2014, p. 350.

Turner, A. J., R. F. Katz, M. D. Behn, and T. Keller. "Magmatic Focusing to Mid-Ocean Ridges: The Role of Grain-Size Variability and Non-Newtonian Viscosity". In: *Geochemistry, Geophysics, Geosystems* 18.12 (2017), 4342–4355. DOI: https://doi.org/10.1002/2017GC007048. eprint: https://agupubs.onlinelibrary.wiley.com/doi/pdf/10.1002/2017GC007048. URL: https://agupubs.onlinelibrary.wiley.com/doi/abs/10.1002/2017GC007048.

Weir, N. R. W., R. S. White, B. Brandsdóttir, P. Einarsson, H. Shimamura, and H. Shiobara. "Crustal structure of the northern Reykjanes Ridge and Reykjanes Peninsula, southwest Iceland". In: *Journal of Geophysical Research: Solid Earth* 106.B4 (2001), pp. 6347–6368. DOI: https://doi.org/10.1029/2000JB900358. eprint: https://agupubs.onlinelibrary.wiley.com/doi/pdf/10.1029/2000JB900358. URL: https://agupubs.onlinelibrary.wiley.com/doi/abs/10.1029/2000JB900358.

Árnadóttir, T., W. Jiang, K. L. Feigl, H. Geirsson, and E. Sturkell. "Kinematic models of plate boundary deformation in southwest Iceland derived from GPS observations". In: *Journal of Geophysical Research: Solid Earth* 111.B7 (2006). DOI: https://doi.org/10.1029/2005JB003907. eprint: https://agupubs.onlinelibrary.wiley.com/doi/pdf/10.1029/2005JB003907. URL: https://agupubs.onlinelibrary.wiley.com/doi/abs/10.1029/2005JB003907.

551 Árnadóttir, T., B. Lund, W. Jiang, H. Geirsson, H. Björnsson, P. Einarsson,
552 and T. Sigurdsson. "Glacial rebound and plate spreading: Results from the
553 first countrywide GPS observations in Iceland". In: *Geophysical Journal In-*
554 *ternational* 177.2 (May 2009), pp. 691–716. ISSN: 0956-540X. DOI: 10.1111/
555 j.1365-246X.2008.04059.x. eprint: https://academic.oup.com/gji/
556 article-pdf/177/2/691/5930359/177-2-691.pdf. URL: https://doi.
557 org/10.1111/j.1365-246X.2008.04059.x.

